Chapter 1

Surprising Challenges

V. Adrian Parsegian
Department of Physics, University of Massachusetts, Amherst 01003, USA
parsegian@physics.umass.edu

I have been asked to write a scientific reminiscence of my experiences for the book *Electrostatics of Soft and Disordered Matter* The fashionable emphasis on "soft" is relatively new. We want to think "new" although many of the important unsolved or avoided questions are old. If anything, during the years since I random-walked into this business in the early 1960s, there has been a continuing tension between enduring theory that rests on dubious assumptions and experiment that gives unpalatable information.

That tension probably goes back to the old joke that Debye–Huckel theory works only for poorly distilled water. The worries about theory are still part of proper training, but they have been pushed aside in the rush to compute and to publish. I will not dwell on this part, but it is a dominant feature of how people work. Where the theory has been surprisingly correct—up to a point—is in colloid and macromolecular systems where, surprisingly at first, the theory is more reliable despite the greater number of variables that come into simple salt solutions. When there is a massive amount of fixed charge on a large surface, there is necessarily a comparably massive amount of net countercharge nearby. The repulsion keeps

Electrostatics of Soft and Disordered Matter
Edited by David Dean, Jure Dobnikar, Ali Naji, and Rudolf Podgornik

ISBN 978-981-4411-85-1 (Hardcover), 978-981-4411-86-8 (eBook)
www.panstanford.com

the fluctuations down so mean-field thinking is okay—or at least we hope that it is.

The big change has been, of course, the ability to solve equations by computer. The shift has been from worrying whether the theory works to learning how to solve its equations numerically or, better, to simulate solutions with various simplifying assumptions suggested by theory. It's exciting and, if one ignores reasonable worries and ignores conflicting data, it has become quite a respectable enterprise in colloid science and biophysics Many of the old worries have simply been forgotten.

I wish I could tell you that I had a serious purpose in working in this subject, but the truth is that I was lucky to meet good people who continually brought my attention to unexpected ideas, projects, and collaborations.

Like most people I first heard of double layer theory in a chemistry course, physical chemistry at Harvard in my particular case. There was the derivation of the Debye–Huckel theory, and that was it. A couple of years earlier, in college, I had heard a talk by Aharon Katchalsky visiting from the Weizmann Institute. That's when I had my first glimpse of a polyelectrolyte. The talk struck me for his ability to emphasize words in a way that made one think about a concept. When he said of a polyelectrolyte that its ionic movements could confer the property of an "electric quadrupole," the idea of ionic fluctuation stuck with me forever.

A few years later, when I was in graduate school at Harvard, Katchalsky came to give a course on the thermodynamics of irreversible processes. This time, like so many people, I was entranced by the man and, given his powers of persuasion, by the subject as well. I was not very happy at Harvard, but this subject appealed to me. Wanting to do something more in thermodynamics, I asked to do my PhD research with Irwin Oppenheim at MIT down the street. There was no one at Harvard at that time doing much on biophysics and thermodynamics. The PhD program chairman, Arthur Solomon summarily denied my request with, "We are not a prep school for MIT." But then he surprised me by offering me the chance to do my PhD work at the Weizmann Institute. Apparently a visiting professor at Harvard was "Harvard and not-MIT" enough.

I took the chance to leave for the Weizmann Institute, was treated as a more advanced student than I really was, and found I could talk with all kinds of people.

Going to Weizmann was the best thing that I ever did at Harvard. But I digress.

I was "assigned" to work with the remarkable Shneior Lifson. He had been on a kibbutz until his late twenties when he met Katchalsky who offered him some work on polyelectrolytes at the Institute. Shneior went on to be a stunning scientist and Scientific Manager of the Institute. He told me that when Katchalsky made him the offer, he had only two questions. "Will there be a job also for Hanna [his kibbutz math-teacher wife]?" and "What is a polyelectrolyte?" Between Aharon and Shneior and the large group with them in the Institute's Polymer Department, the romance with double layers and electrostatics began.

My thesis using double layer theory was on the stability of fatty acid soaps in the salt-free limit where, we tell ourselves, the theory is more reliable. To get me going, I was told to read Verwey and Overbeek's "Theory of the stability of lyophobic colloids." I started to play with double layer theory, embarrassed myself once or twice thinking I had discovered something that turned out to have been known for decades, then managed to do some work that Katchalsky announced in a lecture was a major step in double layer theory. That was another unexpected connection. A physician at the Tel Hashomer Hospital Moshe Wolman had asked a question about charged surfaces. Aharon sent me to talk with him. I solved it as favor for Moshe, showed the solution to Aharon and Shneior but I didn't even think to publish it until many years later when I was working with Barry Ninham and we needed it for something or other. Barry did some of his neat math to put it in more elegant form, and that became our paper on "charge regulation" in double layers.

I finished my thesis, spent obligatory residence time at Harvard in order to get my PhD in May 1965. Then, after a few months at Stanford, I went to MIT in September to work with Irwin Oppenheim as I had wanted to do before. It turned out that Irwin was soon going on sabbatical in Amsterdam. Theo Overbeek was then a visiting professor at MIT. I went to see him, told him of reading his work and my possibly going to Holland. He immediately encouraged a visit to

his Utrecht University lab, and said he would introduce me to people at Utrecht as well as write to Verwey who was head of the Philips lab, at the Gloeilampenfabriken (glow-lamp factory) in Eindhoven, the Netherlands. Overbeek assured me that Verwey would invite me. He also expressed the commonly held opinion that we did not know enough of the absorption spectra to make good calculations of fluctuation forces. Nevertheless, he encouraged me every way he could, and sent letters to Verwey to receive me.

Life got crazy good. I was even invited to present my thesis work at a meeting in Paris where I actually first met Verwey and several of his colloidal confreres before the actual Eindhoven visit.

During this time in Amsterdam, Irwin told me that his friend in Utrecht, Nico van Kampen had just done a simplified version of the Lifshitz theory of van der Waals forces. I went to see Nico who sat me down and showed me everything he had done. The new way was so easy that it would be possible to generalize the original Lifshitz result, a product of arduous argumentation. Van Kampen and his two coauthors, Nijboer and Schram, not only walked me through the derivation but also suggested how to generalize the result. That conversation informed the next few years of the work with Barry Ninham, who came to our NIH lab in 1968, as we worked to compute forces as well as to create more appropriate formulae that used the strengths for the Lifshitz approach to electrodynamic charge-fluctuation forces. The paradox for me was that the Dutch people studying colloidal systems were still using the earlier theory in their own research. No matter. The big thing was their remarkable generosity that for me became a lifetime benchmark of good scientific behavior.

Barry describes our happy time together as our “high moment” a best-of-times period. I described it as “mental leap frog” with each of us jumping over the part he did better, thus adding our strengths, compensating our weaknesses, and jumping over the hurdles in math, physics, material properties, etc. in a liberating walk. I had spent a year reading Landau and Lifshitz for an hour each morning. Barry had been teaching math and he particularly loved transforms. It added up because each of us understood enough of the other’s expertise to learn and to build together.

When one stops to think about "electrostatic", it is used in many ways. Charges in vacuum or in ideal dielectric materials set up fields that mediate interactions. When those fields are so strong that they reorganize the medium beyond the weak-field limit, the restructuring of the medium becomes important. We think of charges being hydrated in ways that reflect the structure of the medium and of the source charges. Does "electrostatic" suffice then, or should we be thinking of solvent structure in more specific ways than continuum dielectric? Probably the biggest mistake I ever made, published in a 1967 *Science* paper was to treat the repulsion between surfaces covered with zwitterions as an electrostatic double layer interaction. There was plenty of electrostatic interaction going on, but the charges were not able to move as in a double layer of fixed charge plus counterions, and the electric fields were far too strong to let us think of the medium as a simple dielectric. A few years later, Peter Rand and I measured the forces between zwitterionic phosphatidylcholine bilayers in distilled distille, and we realized that the interactions could not be simple double layer forces, and that they were in fact connected with surface hydration, which can mean many things and were a general feature of interactions at distances less than the order of a nanometer. We can call these "electrostatic" in the sense that charge is the initial cause, but the perturbation of the solvent seems more the issue. Similar forces are measured between surfaces of zwitterions as are seen if these zwitterions are cut to create surface charge plus counterions. Solvation forces are partly electrostatic, but the structure of the solvent shows up as a theme in the exponential decay of forces between many kinds of surfaces, charge-plus-counterion or net-neutral with bound counterion. Huge differences in magnitude are seen with different surface chemistry, but the decay of repulsive solvation forces with distance is stubbornly exponential with decay rates that do not resemble what is predicted by double layer theory.

Even the measurements with Peter Rand were a bit of an accident. David Gingell and I had been thinking how a solution, which would have different dielectric properties than a pure solvent, would in fact be a different medium that would modify charge fluctuation forces from those in water. We asked Peter if he could measure separations between lipid bilayers, held in a multilayer

stack by attractive van der Waals forces, when the water solution included sugars. The spacings with added glucose or sucrose more or less confirmed the expectation of measured forces, a progressive weakening and then strengthening of attraction as sugar was added. But Peter was on sabbatical in France. His graduate student Denis Leneveu thought to add another sugar, Dextran, to see what happened. The bilayers only moved together. This stumped us Why would the multilayers not swell then shrink as they did with small sugars? An NIH colleague, Bill Hagins, said disgustedly, "All you are doing is putting osmotic pressure from excluded large molecules." It was a downer for me for about five minutes until I realized that if we knew the osmotic pressure of Dextran we knew the force pushing the bilayers together. We could then add spacings from X-ray scattering and measure force–distance curves. I ran the rest the way from Bill's building to mine and called Peter, back from France, "Do you have an osmometer?" The first papers on exponential hydration forces came out not long after [1, 2].

Contrary to our formally good understanding of van der Waals and electrostatic forces, we are still far short of good explanations (or even correct language) for these "hydration forces" despite the number of places they have been measured, even to the extent that they are now understood to be the principal form of interaction between closely approaching soft and at least partly disorderly surfaces. The general $\sim$3Å exponential forms hold out to separations of a couple of nanometers, but the measured coefficients of strength of interaction vary widely. Geometry seems to be a secondary factor. With simple correction for curvature, forces between double-helical DNA molecules scale remarkably well with those between phospholipids of similar ionic composition. Disorder must be playing a role. Hard surfaces are different. Oscillatory forces are seen there but not between soft surfaces. Melted chain phospholipids show much stronger repulsion than those with frozen chains. The apparent hydration plays on many features of the structure.

Not only are these forces hard to describe beyond the simplest language of order-parameter theory [3], we do not bring in enough of the personalities of the solvent-perturbing bodies. Ions are not just charges: they have polarizabilities that likely act in the steep gradients of molecules distributed near surfaces [Ninham ions].

Ions are not just spherical bits of metallic charges as they were imagined in the earliest theory of self-energies. A positive ion is the result of emptying an electronic orbital. At close range the negative lone electron pair of a water molecule has an affinity for that empty orbital. It's a real place and puts a real condition on how the water can sit around the ion. There is all the more need to look at structure closeup. What I mention here is very well known. What is remarkable to me is that it is so conveniently ignored much of the time, much as measured hydration forces are ignored when discussing the interaction of charged surfaces.

Reading the early literature, I am struck by how much more flexible the thinking was in the 1930s and 1940s when bold and brilliant people were feeling their way, when the big ideas were being doubted and developed. Part of this is normal science—staying with old ideas as long as possible, a practice facilitated by focus on computation. Part of this is that good reliable measurements at short distance are relatively recent.

Many years ago I heard a story about Hamaker, that his kid came in and asked if he were related to the 1937 Hamaker mentioned in a lecture on colloids, to which the reportedly incredulous father replied, "Are they still using that?"

Of course, the more heroic story and lesson is the good example of taking time to think: Verwey and Overbeek working secretly on their part of the Derjaguin–Landau–Verwey–Overbeek (DLVO) theory during WWII. It was probably not as romantic as it sounds decades later, they worked on what they wanted to understand and pretended to do something else as the Nazi guards used to come around to see what was going on. They were waiting for the war to end, as they had no opportunity to write papers to share their research. Fortunately, they were writing it out as a coherent book [4]. (Verwey told me about it in 1967. It deserves a movie.)

Today, there seems to be the beginning of new optimism about the ability to distinguish models. When do we include structure? When do we ignore entire classes of interaction? Still, I am in search of measurement strategies that will distinguish different models as well as of models would bring in real experimental detail.

There are so many models, and still not enough measurements to distinguish them. What I conclude from the good thinking presented

in this book is that we are in a position to think more critically than before. I hope we live up to the boldness of the people who started this subject, taking the time to think about the models we reflexively apply, and to look boldly at data that are frequently ignored.

The other big lesson for me is also personal, not scientific. I have made many friends during these random walks and bumps against unexpected reality. The good feelings that are evident through this book here promise more good learning. I hope there will be more happy stories a few years from now. I hope that we will understand "electrostatics", "hydration", "steric", "dispersion", and so on much better than we do now.

References

1. LeNeveu, D. M., Rand, R. P., Parsegian, V. A. (1976). Measurement of forces between lecithin bilayers, *Nature* **259**, 601–603.
2. LeNeveu, D. M., Rand, R. P., Parsegian, V. A., Gingell, D. (1977). Measurement and modification of forces between lecithin bilayers, *Biophys. J.* **18**, 209–230.
3. Marçelja, S., Radiç, N. (1976). Repulsion of interfaces due to boundary water, *Chem. Phys. Lett.* **42**, 129–130.
4. Verwey, E. J. W. and Overbeek, J. Th. G. (1948). *Theory of the Stability of Lyophobic Colloids*, Elsevier, Amsterdam.

Part I

COULOMB FLUIDS: FROM WEAK TO STRONG COUPLING

Chapter 2

A Field Theory Approach for Modeling Electrostatic Interactions in Soft Matter

Paul Duncan,[a] Marius M. Hatlo,[b] and Leo Lue[a]

[a] *Department of Chemical and Process Engineering, University of Strathclyde, James Weir Building, 75 Montrose Street, Glasgow G1 1XJ, UK*
[b] *Institute for Theoretical Physics, Utrecht University, Leuvenlaan 4, 3584 CE Utrecht, The Netherlands*
leo.lue@strath.ac.uk

2.1 Introduction

Field theoretic approaches have been particularly useful in studying colloidal and biological systems, in which long-range electrostatic interactions are important. For weakly coupled systems, the field theoretic methods reduce to the commonly known Poisson-Boltzmann (PB) theory [Chapman (1913); Gouy (1910)], which has been shown to be very accurate for these systems and has been used with great success to understand and solve numerous problems in soft matter. However, in recent decades, focus has turned toward strongly coupled systems, where highly charged surfaces or multivalent counterions introduce strong correlations, that cannot be treated by a mean field theory or approaches in which

Electrostatics of Soft and Disordered Matter
Edited by David Dean, Jure Dobnikar, Ali Naji, and Rudolf Podgornik

ISBN 978-981-4411-85-1 (Hardcover), 978-981-4411-86-8 (eBook)
www.panstanford.com

the fluctuations are assumed to be weak (e.g., loop expansions). These correlations are important in many systems [Levin (2002); Naji *et al.* (2005); Messina (2009)] and can lead to many effects that cannot be explained by the PB theory, such as attraction between like-charged surfaces.

This work reviews a general field theoretic method to describe the behavior of systems interacting with electrostatics. This approach allows approximations that yield fairly accurate predictions, from the weak coupling regime, in which mean field theories work well, to the strong coupling regime, as well as in between. In addition, these approximations can, in principle, be systematically improved. The method provides a single, unified theoretical approach that is applicable to systems of arbitrary geometries and particles with general shapes and charge distributions. The method is, in general, in good agreement with Monte Carlo simulations, may be systematically improved, and is mathematically similar to the Poisson-Boltzmann theory.

In the next section, we present this general theoretical framework, introducing physical motivation and mathematical details. Then, in the Section 2.3, we discuss the application of the theory to various systems. Finally, the main aspects of the theory are summarized in Section 2.4.

2.2 Basic Formalism

In this work, we consider a system of mobile particles with an extended charge distribution that are immersed in a spatially varying continuum dielectric $\epsilon(\mathbf{r})$. The charge density of a particle of type α that is located at the origin and is in an orientation Ω is $Q_\alpha(\mathbf{r}, \Omega)$. In addition, there may also be a fixed background charge $\Sigma(\mathbf{r})$.

The total electrostatic energy of the system is

$$E_{\text{elec}} = \frac{1}{2}\int d\mathbf{r}d\mathbf{r}'\mathcal{Q}(\mathbf{r})G_0(\mathbf{r}, \mathbf{r}')\mathcal{Q}(\mathbf{r}') \tag{2.1}$$

where G_0 is the Green's function of the Poisson equation

$$-\frac{1}{4\pi}\nabla\cdot[\epsilon(\mathbf{r})\nabla G_0(\mathbf{r}, \mathbf{r}')] = \delta^d(\mathbf{r}-\mathbf{r}'), \tag{2.2}$$

and $\mathcal{Q}(\mathbf{r})$ is the total charge density of the system

$$\mathcal{Q}(\mathbf{r}) = \sum_{\alpha,k} Q_\alpha(\mathbf{R}_{\alpha,k}, \Omega_{\alpha,k}) + \Sigma(\mathbf{r}), \tag{2.3}$$

where $\mathbf{R}_{\alpha,k}$ and $\Omega_{\alpha,k}$ are the position and orientation, respectively, of the kth particle of type α. Physically, $G_0(\mathbf{r}, \mathbf{r}')$ is the electrostatic potential at a position $\mathbf{r}$ due to a unit point charge located at $\mathbf{r}'$; it dictates how the electrostatic potential emanates from a charge.

Formally, the grand partition function of this system can be written exactly as an integral over all the positions and orientations of the particles in the system [Hansen and McDonald (2006)]; however, the direct evaluation of the resulting integral is intractable for most systems. Liquid state approaches to evaluating the partition function (e.g., hypernetted chain theory) focus on the particles in the system and how to develop approximations for correlations between them. These approaches work well in capturing the short-range correlations and fluctuations that occur in the system.

Another perspective is to use a field theoretic approach. In this case, the focus is no longer on the particles in the system but rather on collective modes, such as the density or an effective one-body interaction potential generated by the particles. Mathematically, this is done by representing the grand partition function as a functional integral over an interaction field through the use of the Hubbard–Stratonovich transformation [Stratonovich (1957); Hubbard (1959)]. In the case of our system of charged particles, the grand partition function Z_G becomes

$$Z_G[\gamma, \Sigma] = \left\langle Z_G^{\text{ref}}[\gamma - qi\psi] \exp\left[-\int d\mathbf{r}\Sigma(\mathbf{r})i\psi(\mathbf{r})\right]\right\rangle_0 \tag{2.4}$$

where $\psi(\mathbf{r})$ is a Gaussian random field with mean zero and a spatial correlation of $\beta G_0(\mathbf{r}, \mathbf{r}')$ (where $\beta = 1/(k_B T)$, k_B is the Boltzmann constant, and T is the absolute temperature), the angle brackets denote the average with respect to ψ, and Z_G^{ref} is the grand partition function of the system without electrostatic interactions. The partition function of a system with electrostatic interactions is the same as the partition function of the same system without electrostatic interactions, but with the particles coupled to a randomly fluctuating Gaussian field with a covariance given by the Green's function of the Poisson equation.

This transformation is formally exact, but the resulting functional integral is just as intractable as the original, particle-based partition function. Several different approximation schemes have been developed to evaluate this functional integral, including the mean-field approximation, loop expansions, and variational methods. These approximation schemes are better able to handle the long wavelength correlations that occur in the system.

Neither the particle-based theories nor the functional integral formulations lead to a theory that works well when the system contains highly charged particles (e.g., colloidal particles). For these systems, fluctuations at both short and long wavelengths become important. At short length scales, oppositely charged particles interact strongly with each other, forming bound objects, whereas at large length scales, these composite objects screen and interact through effective electrostatic forces. To describe these systems, very successful *ad hoc* approaches have been developed, such as the strong coupling expansion [Shklovskii (1999); Moreira and Netz (2000)] and dressed colloid theories [Colla and Levin (2010); Lu and Denton (2010)], in which the charge of the colloids is renormalized due to counterion binding. However, we are interested in developing an approach in which this binding arises naturally from the theory, without explicitly putting it into the theory. This is important when the electrostatic interaction leads to binding and aggregation over multiple length scales (e.g., binding of counterions onto charged rods that can themselves bundle to form larger objects that organize).

2.2.1 *Splitting*

Particle-based approaches work well for describing short wavelength correlations, whereas field theory based approaches work well for long wavelength correlations. The idea behind our approximation scheme is to divide the fluctuations of the system into short and long wavelength contributions and to treat each of these contributions in an appropriate approximation [Hatlo and Lue (2009, 2010)].

To achieve this, the Green's function is divided as $G_0 = G_\mathrm{s} + G_\mathrm{l}$, where $G_\mathrm{l} = \mathcal{P}G_0$, $G_\mathrm{s} = (1 - \mathcal{P})G_0$, and $\mathcal{P}$ is an operator that projects

out the long wavelength components of a function. The precise form of $\mathcal{P}$ is fairly arbitrary, but in most of our work, we use $\mathcal{P} = [1 - \sigma^2\nabla^2 + \sigma^4\nabla^4]^{-1}$, where σ is the splitting parameter and is a length that separates short and long wavelength phenomena.

The Hubbard–Stratonovich transformation is performed separately for both G_s and G_l, which leads to functional integrals over the associated random fields ψ_s (correlated at short wavelengths) and ψ_l (correlated at long wavelengths). The averages over these fields are performed using different approximations, which are described in the next sections.

2.2.2 *Short Wavelength Field*

The short wavelength field ψ_s is strongly fluctuating, and we approximate averages over it using a truncated cumulant expansion. The resulting expression becomes equivalent to a virial series in which the particles interact with an effective one-body potential

$$\begin{aligned} u_\alpha(\mathbf{R}, \Omega) = \sum_\alpha \int d\mathbf{r}\, Q_\alpha(\mathbf{r} - \mathbf{R}, \Omega)\Sigma(\mathbf{r}) \\ + \sum_\alpha \frac{\beta}{2} \int d\mathbf{r}d\mathbf{r}'\, Q_\alpha(\mathbf{r} - \mathbf{R}, \Omega)\Delta G_0(\mathbf{r}, \mathbf{r}')Q_\alpha(\mathbf{r}' - \mathbf{R}, \Omega) \\ - \sum_\alpha \frac{\beta}{2} \int d\mathbf{r}d\mathbf{r}'\, Q_\alpha(\mathbf{r} - \mathbf{R}, \Omega)G_l(\mathbf{r}, \mathbf{r}')Q_\alpha(\mathbf{r}' - \mathbf{R}, \Omega) \end{aligned} \tag{2.5}$$

and a two-body potential, given by the short wavelength contribution of the electrostatics

$$v_{\alpha\alpha'}(\mathbf{R}, \Omega, \mathbf{R}', \Omega') = \int d\mathbf{r}d\mathbf{r}'\, Q_\alpha(\mathbf{r} - \mathbf{R}, \Omega)G_s(\mathbf{r}, \mathbf{r}')Q_{\alpha'}(\mathbf{r}' - \mathbf{R}', \Omega'),$$

as well as other nonelectrostatic interactions present in the system.

2.2.3 *Long-wavelength Field*

A single configuration of the long-wavelength field, which is slowly varying in space, is expected to dominate the contributions to the partition function. Configurations that deviate substantially from this main configuration are not expected to make a significant contribution. The contribution of fluctuations is weak.

To approximate this, we use a variational perturbation approximation [Kleinert (1995); Curtis and Lue (2005)], where fluctuations in $\psi_{\rm l}$ are evaluated with respect to a Gaussian distribution with mean $\bar{\psi}_{\rm l}$ and a covariance $\beta G_{\mathcal{K}}(\mathbf{r}, \mathbf{r}')$, a renormalized Green's function, defined through $G_{\mathcal{K}}^{-1}(\mathbf{r}, \mathbf{r}') = G_0^{-1}(\mathbf{r}, \mathbf{r}') + \mathcal{K}(\mathbf{r}, \mathbf{r}')$. Physically, $\mathcal{K}$ is a screening function that describes the influence of mobile charges, and $G_{\mathcal{K}}$ describes the propagation of the electric potential under the influence of these charges. A cumulant expansion is used to account for deviations from this Gaussian distribution. The case $\mathcal{K} = 0$ corresponds to the mean field approximation.

2.2.4 *Free Energy*

With a first-order variational perturbation approximation used to evaluate the averages over $\psi_{\rm l}$ and a second-order cumulant expansion for the averages over $\psi_{\rm s}$, the free energy is given by

$$\begin{aligned} F[\rho, \Sigma] = & \sum_{\alpha} \int d\mathbf{R} d\Omega \, \rho_{\alpha}(\mathbf{R}, \Omega)[\ln \rho_{\alpha}(\mathbf{R}, \Omega)\Lambda_{\alpha}^{d} - 1] \\ & + \sum_{\alpha} \int d\mathbf{R} d\Omega \, \rho_{\alpha}(\mathbf{R}, \Omega)\beta u_{\alpha}(\mathbf{R}, \Omega) \\ & + \frac{1}{2} \sum_{\alpha, \alpha'} \int d\mathbf{R} d\Omega \, d\mathbf{R}' d\Omega' \, [e^{-\beta v_{\alpha\alpha'}(\mathbf{R}, \Omega, \mathbf{R}', \Omega')} - 1] \\ & - \frac{1}{2\beta} \int d\mathbf{r} d\mathbf{r}' i\bar{\psi}_{\rm l}(\mathbf{r}) G_{\rm l}^{-1}(\mathbf{r}, \mathbf{r}') i\bar{\psi}_{\rm l}(\mathbf{r}') + \int d\mathbf{r} \Sigma(\mathbf{r}) i\bar{\psi}_{\rm l}(\mathbf{r}) \\ & + \int d\mathbf{r} \sum_{\alpha} \int d\mathbf{R} d\Omega \, \rho_{\alpha}(\mathbf{R}, \Omega) Q_{\alpha}(\mathbf{r} - \mathbf{R}, \Omega) i\bar{\psi}_{\rm l}(\mathbf{r}) \\ & + \frac{1}{2} \int_0^1 d\zeta \, \mathrm{Tr} \mathcal{K}(G_{\zeta\mathcal{K}} - G_{\rm l}). \end{aligned} \tag{2.6}$$

The first two terms in the expression for the free energy functional is the ideal gas contribution. The second term is the interaction of the particles with a renormalized external potential $u_{\alpha}(\mathbf{R}, \Omega)$. The third term is second virial contribution of the short wavelength electrostatic interaction between particles. The next three terms are the long-wavelength electrostatic energy of the system. The final term represents the contribution of long-wavelength fluctuations of the electrostatic potential to the free energy.

To complete the theory, we need to specify the forms of $\bar{\psi}_1$, $\mathcal{K}$, and σ. If we were able to exactly evaluate the averages over the fluctuations of the fields ψ_s and ψ_1, then the free energy would be independent of the choice of $\bar{\psi}_1$, $\mathcal{K}$, and σ. However, because of the approximations used, the free energy will depend on these quantities; in order to minimize this dependence, we select these quantities such that the free energy is stationary with respect to small variations in their values.

Making the free energy stationary with respect to variations in $\bar{\psi}_1(\mathbf{r})$ leads to the Poisson equation:

$$-\frac{1}{4\pi}\nabla\cdot\epsilon(\mathbf{r})\nabla\phi(\mathbf{r}) = \sum_\alpha \int d\mathbf{R}d\Omega Q_\alpha(\mathbf{r}-\mathbf{R},\Omega)\rho_\alpha(\mathbf{R},\Omega) + \Sigma(\mathbf{r}) \tag{2.7}$$

where $\phi(\mathbf{r}) = \beta^{-1}\mathcal{P}\psi_1(\mathbf{r})$ is the mean electric potential in the system.

The value of the screening function is determined by making the free energy stationary with respect to variations in $\mathcal{K}(\mathbf{r},\mathbf{r}')$. For systems in which electrostatics is the only mode of interaction and neglecting the third term in Eq. (2.6), the screening function becomes:

$$\mathcal{K}(\mathbf{r},\mathbf{r}') = \beta\sum_\alpha \int d\mathbf{R}d\Omega\, Q_\alpha(\mathbf{r}-\mathbf{R},\Omega)\rho_\alpha(\mathbf{R},\Omega)Q_\alpha(\mathbf{r}'-\mathbf{R},\Omega) \tag{2.8}$$

This is a simple generalization of the Debye-Hückel theory for systems with extended charge distributions.

The value of the splitting parameter is determined from $\partial F/\partial\sigma = 0$. Simply setting $\sigma = 0$ corresponds to using the variational approximation for all the fluctuations in the system. In the limit where $\sigma\to\infty$, the theory reduces to a virial expansion or other liquid state theory approximations. In this case, the theory resembles the strong coupling expansions [Shklovskii (1999); Moreira and Netz (2000)], which are able to accurately describe systems in which electrostatic interactions dominate.

2.3 Applications

The theoretical approach developed in the previous section is quite versatile and applicable to a wide variety of problems. In this section,

we present its application to the one-component plasma (OCP), counterions confined between two charged plates, and counterions around a single charged dielectric sphere within the cell model.

2.3.1 *One-component Plasma*

In the OCP model, ions of charge q are contained within a rigid, uniform charge density $\Sigma = -q\rho$, where ρ is the ion number density, so that the system is electrically neutral. Typically, these ions are point charges, but here we generalize the model slightly, so that they are linear charge distributions of length L, such as a uniform line charge or a linear sequence of rigidly bonded point charges. The key parameters that govern the properties of this OCP model are the coupling parameter $\Gamma = \rho^{1/3} l_B$ (the ratio of the mean spacing between the counterions and the range of the interaction), and the ratio L/l_B.

In Fig. 2.1(a), we show the interaction energy of the OCP for 8-mer rods of various lengths. The lines are the predictions of the splitting theory, and the symbols are from molecular dynamics simulations [Hatlo *et al.* (2009)]. The dashed line is the prediction of the Debye-Hückel theory for point charges, which corresponds to the splitting theory with $\sigma = 0$.

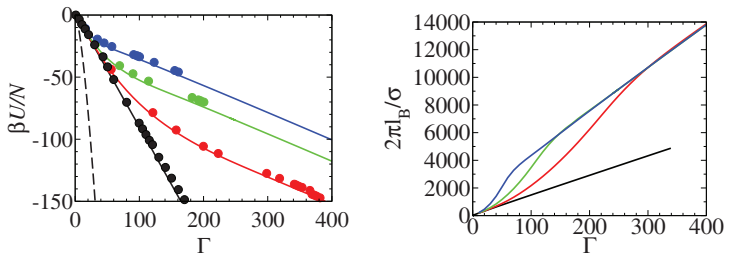

(a) (b)

Figure 2.1 (a) Electrostatic interaction energy for 8-mer rods with: (i) $L/l_B = 0$ (black), (ii) $L/l_B = 0.025$ (red), and (iii) $L/l_B = 0.05$ (green), (iv) $L/l_B = 0.1$ (blue). The solid lines are the predictions of the splitting theory, and the dashed line is the prediction of the Debye-Hückel theory ($\sigma = 0$). The symbols are from molecular dynamics simulations. (b) Splitting parameter.

The corresponding values of the splitting parameter σ are shown in Fig. 2.1(b). The splitting parameter shrinks as the mean spacing between particles decreases. We find that it corresponds to the size of the "correlation hole," [Nordholm (1984); Forsman and Nordholm (2012)] which develops around each ion due to their strong repulsion at short distances.

Interestingly, the rod-like counterion systems show an ordering transition from an isotropic phase when the length of the counterions are much smaller than the Bjerrum length to a nematic phase at sufficiently high values of L/l_B, similar to that observed for long thin rods with only excluded volume interactions [Onsager (1949)].

2.3.2 *Planar Geometry*

Now, we examine the case wherein ions of charge q are confined between two plates with a uniform charge density Σ and separated by a distance D. The two length scales that characterize this system are [Moreira and Netz (2001)] the Bjerrum length $l_B = \beta q^2$ and the Gouy-Chapman length $\mu = (2\pi\beta\Sigma q)^{-1}$.

In Fig. 2.2, we plot the equilibrium curve of the two-plate system. The symbols are from Monte Carlo simulations [Moreira and Netz (2001)]. The solid line is the splitting theory with the mean field approximation for the long wavelength fluctuations and the cumulant expansion truncated at zeroth order. The dashed line is the prediction of the same splitting theory but with the cumulant expansion truncated at first order. As a comparison, we also present the predictions of a theory developed by Šamaj and Trizac (2011), based on a low temperature expansion around a two-dimensional Wigner crystal condensed on both plates (dotted line in Fig. 2.2).

As in the case of the OCP discussed previously, the splitting theory can be extended for two-plate system to the situation in which the counterions consist of extended charge distributions. In the case in which the counterions are a linear collection of point charges, there are two mechanisms for an attraction between the plates: correlations between counterions (similarly to the point charge) and correlations within a counterion, which leads to "bridging" of the counterion across the two plates. These two mechanisms can lead to two separate regions of attraction between

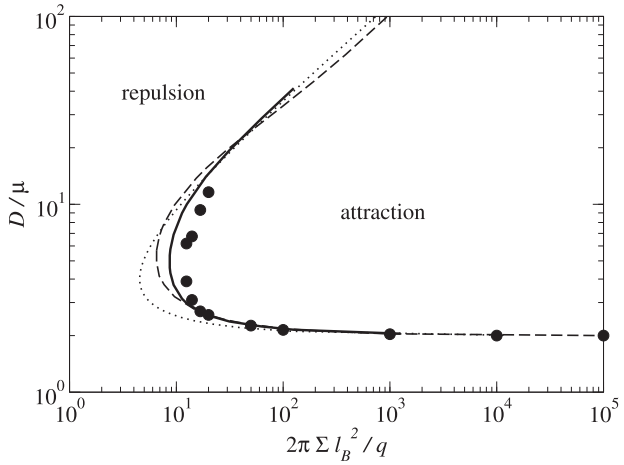

Figure 2.2 Equilibrium distance between two charged plates. The solid line is the prediction of the splitting theory with the second virial correction, and the dashed line is without the correction. The dotted line is the prediction of the Šamaj and Trizac [Šamaj and Trizac (2011)]. The symbols are Monte Carlo simulation data [Moreira and Netz (2001)].

the plates if the length of the counterions is sufficiently large [Hatlo *et al.* (2010); Bohinc and Lue (2011); Bohinc *et al.* (2012)].

2.3.3 *Spherical Cell Model*

Finally, we examine systems of spherical macroions of radius R_{M} and total charge Q, which occupy a volume fraction 0.01, along with a neutralizing number of point counterions of charge q. The interior of the sphere has a dielectric constant ε', whereas outside the sphere, the dielectric constant is ε.

This system is studied [Lue and Linse (2011)] within the cell model, wherein the environment around a single macroion is examined. We focus on four systems, which span a range of conditions: (I) $Q/q = -10$ and $R_{\mathrm{M}}/l_{\mathrm{B}} = 2.81$; (II) $Q/q = -80$ and $R_{\mathrm{M}}/l_{\mathrm{B}} = 2.81$; (III) $Q/q = -40$ and $R_{\mathrm{M}}/l_{\mathrm{B}} = 0.703$; and (IV) $Q/q = -80$ and $R_{\mathrm{M}}/l_{\mathrm{B}} = 22.5$.

The counterion density profiles for each of the systems are shown in Fig. 2.3(a). The predictions of PB theory (dotted lines)

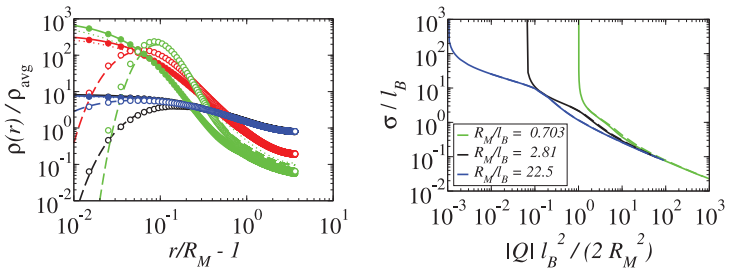

(a) (b)

Figure 2.3 (a) Normalized counterion number density as a function of the distance from the center of the sphere for System I (black), II (red), III (green), and IV (blue). The solid lines are predictions of the splitting theory for $\varepsilon'/\varepsilon = 1$, the dashed lines are the predictions of the splitting theory for $\varepsilon'/\varepsilon = 1/78.4$, and the dotted lines are predictions of PB theory. The symbols are Monte Carlo simulation data for $\varepsilon'/\varepsilon = 1$ (filled) and $\varepsilon'/\varepsilon = 1/78.4$ (open). (b) Reduced splitting parameter.

are only in good agreement with the simulation data (symbols) for the weakly coupled systems. The predictions of the splitting theory (given by the solid and dashed lines) are in fairly good agreement with the simulation data, even for the strongly coupled system.

In Fig. 2.3(b), we show the variation of the splitting parameter with the macroion charge. One interesting feature is that σ diverges when the macroion charge becomes less than that of one counterion. In this case, the splitting theory reduces exactly to that of a single ion. The PB theory is unable to reproduce this limit, even in the region of very low surface charge densities, because it does not account for the discreteness of the counterions.

2.4 Conclusions

We have presented a general theoretical framework for treating electrostatic interactions in soft matter, which can be particularly useful in studying charged colloidal suspensions and electrolyte solutions wherein long-range interactions are important. The key physical motivation behind the theory is to treat the short and long wavelength fluctuations in the system within different approxima-

tion schemes. At short range, the systems are strongly coupled, and at long range, the systems are weakly coupled. To describe both these regimes within a single theory, we split the interaction into a short and long-range contribution. The long-range behavior is often well approximated by a mean field theory, or including first-order fluctuation corrections, whereas the short-range behavior can be captured by a virial expansion, or other liquid state methods suitable to describe particles with short range pair interactions. For weakly coupled systems, this theory approaches the Poisson-Boltzmann theory, whereas for strongly coupled systems, the theory resembles the strong coupling expansion. The theory also performs well for intermediate couplings. In addition, the accuracy of the theory can, in principle, be systematically improved. The theory can be applied to a wide variety of problems, such as systems with different geometries and conditions (e.g., dielectric interfaces) and particles with different shapes and charge distributions. As examples of how the theory may be used, we presented results for systems involving charged objects with neutralizing counterions. These fairly simple systems show a range of interesting phenomena, such as electrostatically driven isotropic-nematic transition and like-charge attraction, which cannot be captured with mean field approximations.

References

Bohinc, K., Grime, J. M. A. and Lue, L. (2012). The interactions between charged colloids with rod-like counterions, *Soft Matter* **8**, pp. 5679–5686.

Bohinc, K. and Lue, L. (2011). Interaction of similarly charged surfaces mediated by nanoparticles, *Chin. J. Polymer Sci.* **29**, 4, pp. 414–420.

Chapman, D. L. (1913). A contribution to the theory of electroencapillarity, *Philos* **25**, pp. 475–481.

Colla, T. E. and Levin, Y. (2010). The renormalized jellium model of colloidal suspensions with multivalent counterions, *J. Chem. Phys.* **133**, p. 234105.

Curtis, R. A. and Lue, L. (2005). Electrolytes at spherical dielectric interfaces, *J. Chem. Phys.* **123**, p. 174702.

Forsman, J. and Nordholm, S. (2012). Polyelectrolyte mediated interactions in colloidal dispersions: Hierarchical screening, simulations, and a new classical density functional theory, *Langmuir* **28**, 9, pp. 4069–4079.

Gouy, G. (1910). Sur la constitution de la charge electique a la surface d'un electrolyte, *J. Phys. Radium* **9**, pp. 468–475.

Hansen, J.-P. and McDonald, I. R. (2006). *Theory of Simple Liquids*, 2nd edn. (Academic Press, London).

Hatlo, M. M., Bohinc, K. and Lue, L. (2010). The properties of dimers confined between two charged plates, *J. Chem. Phys.* **132**, 11, 114102.

Hatlo, M. M., Karatrantos, A. and Lue, L. (2009). One-component plasma of point charges and of charged rods, *Phys. Rev. E* **80**, 6, 061107.

Hatlo, M. M. and Lue, L. (2009). A field theory for ions near charged surfaces valid from weak to strong couplings, *Soft Matter* **5**, pp. 125–133.

Hatlo, M. M. and Lue, L. (2010). Electrostatic interactions of charged bodies from the weak- to the strong-coupling regime, *EPL (Europhysics Letters)* **89**, 2, p. 25002.

Hubbard, J. (1959). Calculation of partition functions, *Phys. Rev. Lett.* **3**, pp. 77–78.

Šamaj, L. and Trizac, E. (2011). Counterions at highly charged interfaces: From one plate to like-charge attraction, *Phys. Rev. Lett.* **106**, p. 078301.

Kleinert, H. (1995). *Path Integrals in Quatum Mechanics, Statistics, and Polymer Physics*, 2nd edn. (World Scientific, Singapore).

Levin, Y. (2002). Electrostatic correlations: from plasma to biology, *Reports on Progress in Physics* **65**, pp. 1577–1632.

Lu, B. and Denton, A. R. (2010). Charge renormalization, thermodynamics, and structure of deionized colloidal suspensions, *Commun. Comput. Phys.* **7**, 2, pp. 235–249.

Lue, L. and Linse, P. (2011). Macroion solutions in the cell model studied by field theory and Monte Carlo simulations, *J. Chem. Phys.* **135**, 22, 224508.

Messina, R. (2009). Electrostatics in soft matter, *J. Phys.: Condens. Matter* **21**, 11, p. 113102.

Moreira, A. G. and Netz, R. R. (2000). Strong-coupling theory for counter-ion distributions, *Europhys. Lett.* **52**, 6, pp. 705–711.

Moreira, A. G. and Netz, R. R. (2001). Binding of similarly charged plates with counterions only, *Phys. Rev. Lett.* **87**, 7, p. 078301.

Naji, A., Jungblut, S., Moreira, A. G. and Netz, R. R. (2005). Electrostatic interactions in strongly coupled soft matter, *Physica A: Statistical Mechanics and its Applications* **352**, 1, pp. 131 – 170.

Nordholm, S. (1984). Simple analysis of the thermodynamic properties of the one-component plasma, *Chem. Phys. Lett.* **105**, 3, pp. 302–7.

Onsager, L. (1949). The effects of shape on the interaction of colloidal particles, *NY Acad. Sci.* **51**, pp. 627–659.

Shklovskii, B. I. (1999). Screening of a macroion by multivalent ions: Correlation-induced inversion of charge, *Phys. Rev. E* **60**, 5, pp. 5802–5811.

Stratonovich, R. L. (1957). A method for the computation of quantum distribution functions, *Dokl. Akad. Nauk SSSR* **115**, 6, pp. 1097–1100.

Chapter 3

Extended Poisson–Boltzmann Descriptions of the Electrostatic Double Layer: Implications for Charged Particles at Interfaces

Derek Frydel[a] and Martin Oettel[b]

[a] *Universidade Federal do Rio Grande do Sul, Porto Alegre, Brazil and Theoretical Chemical Physics Laboratory, ESPCI CNRS Gulliver, Paris, France*
[b] *Institut für Theoretische Physik II, Heinrich Heine Universität Düsseldorf, Germany and Institut für Angewandte Physik, Eberhard Karls Universität Tübingen, Germany*
martin.oettel@uni-tuebingen.de, dfrydel@gmail.com

3.1 Introduction

Whenever a charged surface is immersed in a thermal solvent with mobile co– and counterions (usually an aqueous electrolyte), a screening layer of counterions will form in the vicinity of the charged surface, giving rise to the so-called "double layer." Systematic investigations of the double-layer physics and chemistry have been conducted for more than 100 years and have been motivated by various practical questions such as the behavior of battery electrodes or the stability of charged colloid solutions.

Electrostatics of Soft and Disordered Matter
Edited by David Dean, Jure Dobnikar, Ali Naji, and Rudolf Podgornik

ISBN 978-981-4411-85-1 (Hardcover), 978-981-4411-86-8 (eBook)
www.panstanford.com

Very often, surfaces can be highly charged (e.g., colloid surfaces attain charge densities of about one elementary charge e per nm^2) such that the electrostatic potential ψ near the surface exceeds the equivalent of the thermal energy $k_{\mathrm{B}}T = 1/\beta$ by far (for room temperature $k_{\mathrm{B}}T/e$ corresponds to a potential of 25 mV). Thus, the arrangements of water molecules and counterions near and at the surface should display fairly strong correlations, resulting in, for example, nontrivial potential and dielectric profiles.

Such correlations are neglected in the "work horse" model of charges in solutions, the Poisson–Boltzmann theory. Here, Poisson's equation $\nabla(\epsilon\nabla\psi(\mathrm{r})) = -e(c_+(\mathrm{r}) - c_-(\mathrm{r}))$ is coupled with a strongly simplifying assumption on the density distribution of positive and negative ions, $c_\pm = c_{\mathrm{s}} \exp(\mp e\beta\psi(\mathrm{r}))$, that is, a Boltzmann distribution of charged point particles (having no correlations) subject to the electrostatic potential (the ions are monovalent for simplicity and ϵ is the dielectric constant of the solvent, c_{s} is the bulk number density of positive/negative ions in the solvent). The resulting Poisson–Boltzmann equation for the electrostatic potential

$$\nabla \cdot (\epsilon\nabla\psi) = 2c_{\mathrm{s}}e \sinh(\beta e\psi)\,. \tag{3.1}$$

still poses a formidable nonlinear problem, analytically solvable only in special circumstances such as the geometry of a charged wall. For $\epsilon = \text{const.}$, it is convenient to introduce the Debye–Hückel screening length via $\kappa^{-1} = (\epsilon/(2c_{\mathrm{s}}\beta e^2))^{1/2}$ and the dimensionless potential $\phi = \beta e\psi$. Using these quantities, the Poisson–Boltzmann equation becomes $\nabla \cdot \nabla\phi = \kappa^2 \sinh\phi$, and the significance of the screening length becomes immediately obvious in its linearized form, $(\nabla \cdot \nabla - \kappa^2)\phi = 0$, which entails an exponentially decaying potential with characteristic length κ^{-1} around a localized charge distribution.

Very often, charged particles in electrolytes are characterized using properties of the linearized Poisson–Boltzmann equation. The *effective* or *renormalized charge* or *charge density* is the one appropriate for the charged particle immersed in a hypothetical "linear Poisson–Boltzmann" medium, which exhibits the same asypmptotic potential decay as the "real" charged particle in the "real" (and complicated) electrolyte. If two particles immersed in the electrolyte are sufficiently far apart, then their interaction

energy is proportional to the product of their effective charges—this illustrates that the charge renormalization concept is very useful in characterizing charged colloid suspensions. However, the effective charge density of particles in bulk electrolytes contains very little information about the precise structure and potential profile in the double layer. This is best illustrated by the well-known solution for a charged wall immersed in an electrolyte in Poisson–Boltzmann theory. Using dimensionless charge densities given by $\tilde{\sigma} = \beta e/(\kappa\epsilon)\,\sigma$ the effective charge density $\tilde{\sigma}^{\mathrm{eff}}$ of the wall is given in terms of the bare charge density $\tilde{\sigma}_{\mathrm{c}}$ by

$$\tilde{\sigma}^{\mathrm{eff}} = 4\left(\sqrt{1+\frac{4}{\tilde{\sigma}_{\mathrm{c}}^2}}-\frac{2}{\tilde{\sigma}_{\mathrm{c}}^2}\right)\,. \tag{3.2}$$

For colloidal matter, $\sigma_{\mathrm{c}} \lesssim 1\ e/\mathrm{nm}^2$ and except for situations where $\kappa^{-1} \lesssim 0.3$ nm (or $c_{\mathrm{s}} \gtrsim 1$ M), we are in the saturated regime where $\tilde{\sigma}^{\mathrm{eff}} = 4$. We can draw an important conclusion from this result: Although we might expect the Poisson–Boltzmann description to fail near the charged particles for typical colloid charge densities, we must expect that the dimensionless effective charge density is *roughly constant for modest variations of* σ_{c} *and* κ^{-1} and its determination will not allow to discriminate between different models of the double layer. Thus, by measuring pair interactions between charged particles, we mostly learn which area A of the particle's surface is covered with charge (as $q^{\mathrm{eff}} = A\sigma^{\mathrm{eff}}$) and we do not have access to, say, the potential at the particle surface.

3.2 Charged Particles at Electrolyte Interfaces

The situation is different for charged particles at the interface between an electrolyte and a nonpolar medium (air, oil), see Fig. 3.1. If the dielectric constant of the nonpolar medium is low ($\epsilon/\epsilon_0 \lesssim 2, \epsilon_0$ is the dielectric constant of vacuum) then surface charges can only reside on the colloid surface exposed to the electrolyte. The double layer screens the colloid charge only to the extent that no monopole field is present along the interface. However, higher multipole fields are present, and the leading multipole is a dipole with moment p_{z} oriented perpendicular to the interface (regardless of the charge

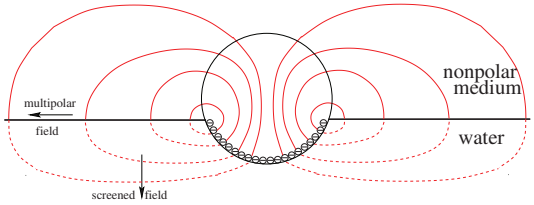

Figure 3.1 Sketch of electric field lines around a charged colloid located at the interface between water and a nonpolar medium. The asymptotics of the electrostatic potential and the associated electric field at the interface is mainly determined by field lines originating from the colloid charges and passing through the colloid and the nonpolar medium. Field lines through the water (containing ions) are screened (indicated by the dashing of the lines).

distribution on the colloid [Dominguez *et al.* (2008)]). Consequently, the electrostatic interaction energy between two charged colloids at the interface with mutual distance d is long-ranged and $\propto p_z^2/d^3$. If the local curvature at the colloid surface is smaller than κ, then the double layer can be approximated by the double layer of a charged wall in the vicinity of each point at the colloid–electrolyte interface. The dipole moment $p_z = A^{\text{eff}} p'_{\text{wall}}$ can be calculated from the aerial dipole moment density p'_{wall} and an effective area A^{eff} that depends on the precise colloid geometry. The crucial observation is that $p'_{\text{wall}} = \epsilon_0 \psi_{\text{wall}}$ is proportional to the contact potential at the wall.[a] Thus, the interaction energy at large distances between two colloids is proportional to the square of the wall contact potential, and such a dependence is very much different from the dependence on the effective (saturated) charges for the interaction between colloids in bulk electrolyte [Frydel *et al.* (2007)]. The Poisson–Boltzmann equation gives $\beta e p'_{\text{wall}} \approx 2\epsilon_0 \ln \tilde{\sigma}_c$ for $\tilde{\sigma}_c \gg 1$, so already here is seen that the dipole moment will not saturate with increasing charge density on the colloid and depends logarithmically on both screening length and charge density, $p_z \propto \ln(\kappa^{-1}\sigma_c) + \text{const.}$ (see the definition of $\tilde{\sigma}$).

[a] Let the wall be located at $z = 0$ and the double layer be located in the half-space $z > 0$. Then, $p'_{\text{wall}} = \int_{0^+}^{\infty} (z\rho(z) + P(z))dz$ where $\rho(z)$ is the charge density in the double layer and $P(z) = -(\epsilon(z) - \epsilon_0)\partial_z \psi(z)$ is the polarization density of the solvent. As $\partial_z(\epsilon \partial_z \psi) = \rho$, we have $p'_{\text{wall}} = \int_{0^+}^{\infty} \epsilon_0 \partial_z \psi = \epsilon_0 \psi_{\text{wall}}$.

Experiments. The dipole moment can be calculated from the interaction potential between charged colloids and this can be inferred through laser tweezers on isolated pairs of colloids, from inversion of measured pair correlations or from elasticity measurements on 2d crystals at the interface. Whereas the logarithmic dependence on κ^{-1} has received much support from laser tweezer data [Park *et al.* (2008)], the absolute magnitude of p_z from the Poisson–Boltzmann equation is too small by about a factor of 5 compared with results of careful measurements using all three routes [Masschaele *et al.* (2010)]. This points to a severe underestimation of the contact potential at a charged wall in the Poisson–Boltzmann equation.

3.3 Modification Strategies for Improving the Poisson–Boltzmann Description

The deficiencies of and possible amendments to the Poisson–Boltzmann equation (3.1) have been discussed for a long time, starting with the work of Bikerman [Bikerman (1942)]. Recently, starting with Ref. [Borukhov *et al.* (1997)], the modified Poisson–Boltzmann approach received renewed interest. We are interested in modifications that preserve the type of equation as a differential equation for the potential ψ. The electrostatic interactions thus remain on the mean-field level, and the modifications introduce contributions that do not stem from correlations. This approach is suitable to investigate certain aspects of "ion specificity" in the weak-coupling limit.

(1) *Finite size effects.* A finite size of the co– and counterions (e.g., through a hard–sphere volume v) will inevitably lead to layering effects in the density profile of the ions near the charged surface. In aqueous solution, the effective ion size is increased as a result of hydration. Thus, in a strict sense, the finite ion size contributions require nonlocal treatment, however, one can capture these effects using local corrections, for example, by taking into account a local change in the ion chemical potential $\mu_\pm$ (or ion osmotic pressure p) through local density changes. In the Poisson–Boltzmann equation, ions are treated

as ideal, thus $\beta\mu_{\pm} = \ln vc_{\pm}$ (or $\beta p = \rho$). A popular modification (MPB, modified Poisson–Boltzmann equation) [Borukhov *et al.* (1997)] has been derived by lattice gas considerations, leading to $\beta\mu_{\pm} = \ln vc_{\pm} - \ln(1 - vc_{+} - vc_{-})$ (or $\beta p = -v^{-1}\ln(1 - vc_{+} - vc_{-})$), where the excess chemical potential, $v^{-1}\ln(1 - vc_{+} - vc_{-})$, accounts for the repulsive (excluded volume) ionic interactions. Such a local correction places an upper bound on the local density, leading to density "saturation" in the region of high ionic concentration. Far from the concentrated region, the density is merely shifted by some length d, $c^{\mathrm{MPB}}(x) = c^{\mathrm{PB}}(x - d)$, in relation to the Poisson–Boltzmann result. Thus, the screening behavior far from the concentrated region is not exactly altered, but rather the effective position of a charged surface is shifted into the solution. Roughly, the changes associated with the finite size effects can be quantified with an additional length scale $v\sigma_c$, which is the size of a layer of counterions that would form if all counterions were forced into a close-packed configuration. The extent of the finite size effects is estimated as the ratio of this length with other relevant lengths, such as the screening or Gouy–Chapman length. Although the lattice gas modification corresponds to a not very precise equation of state for hard spheres, application of MPB to inhomogeneous ionic solutions yields predictions that compare rather well with exact results. This points to some internal cancellation of errors.

(2) *Dielectric inhomogeneity of the solvent.* The solvent medium, made up of water molecules with permanent dipoles, acts as a dielectric that is polarized in an external electrostatic field and thus screens the electrostatic potential within the medium. Thermal fluctuations favor isotropic orientation of dipoles, and the electrostatic interactions favor alignment with the field lines. As long as the thermal energy exceeds the electrostatic counterpart, the polarization is proportional to an external field and the dielectric constant is field independent. But if the two energy scales become comparable, polarization saturation takes place: the dipoles reach perfect alignment with the field lines and no longer dissipate electrostatic energy above a certain threshold. This behavior is described through the Langevin function $\mathcal{L}(x) = \coth x - 1/x$, and the

polarization with nonlinear dependence on the field strength is $P = p_0 c_d \mathcal{L}(\beta p_0 |\nabla\psi|)$, where p_0 is the dipole moment of a solvent molecule and c_d is the dipole density. This amounts to a change in dielectric constant according to

$$\epsilon_{\text{eff}} \to \epsilon_0 + p_0 c_d \frac{\mathcal{L}(\beta p_0 |\nabla\psi|)}{|\nabla\psi|}. \tag{3.3}$$

Here, it is assumed that the solvent is incompressible and the modification leads to the Langevin Poisson–Boltzmann equation (LPB) [Frydel and Oettel (2011)]. For small electrostatic field, $\epsilon \simeq \epsilon_0 + \beta p_0^2 c_d/3$ and in the limit of large field $\epsilon \to \epsilon_0$. Uniform external fields affect only the dipole orientation. Nonuniform fields exert, in addition, a translational (dielectrophoretic) force, so that a dipole migrates toward regions with stronger fields. If one treats the solvent as consisting of point dipoles, as in Ref. [Abrashkin *et al.* (2007)] (DPB, dipolar Poisson–Boltzmann equation), this force leads to the strong dependence of the solvent density on the field, $c_d(\beta p_0 |\nabla\psi|)$, with the functional form $c_d(x) = \sinh x/x$. However, due to hydrogen bonds that lead to a high density of water at ambient conditions, the assumption of incompressibility is more realistic and the resulting ϵ qualitatively reproduces the drop with increasing field strength as seen in the simulations [Yeh and Berkowitz (1999)].

(3) *Ionic polarizabilities.* Ions can further be characterized by including their polarizability α, so that they acquire an induced dipole moment in an external field. Part of the electrostatic energy is dissipated when it polarizes ions. This leads to a dielectric constant with a term linear in the ion concentration,

$$\epsilon_{\text{eff}} \to \epsilon + \alpha(c_+ + c_-). \tag{3.4}$$

The presence of induced dipoles, in turn, contributes to a dielectrophoretic interaction of an ion with a field. Accordingly, the density distribution of ions becomes [Frydel (2011)],

$$c_\pm = c_s \exp(\mp e\beta\psi + \beta\alpha|\nabla\psi|^2/2). \tag{3.5}$$

The above theoretical framework can be used to describe a somewhat different but related situation. A dissolved charged particle (for simplicity taken to be a point) is tightly bound to

solvent dipoles forming its hydration shell so that the dipoles become unresponsive to presumably a weaker external field. This produces a dielectric cavity that reduces the dielectric constant of a solvent, on the one hand, and leads to a migration of a hydrated ion away from a strong field, on the other hand. These trends are captured with a polarizable model in which the "effective" polarizability is a negative valued quantity [Hatlo *et al.* (2012)]. Interestingly enough, both negative and positive α lead to a spreading out of a diffuse double layer.

(4) *Stern layer.* A layer of solvent in direct contact with an interface has different properties from the bulk solvent. First of all, ions cannot penetrate into it due to their finite size. Second of all, the solvent within this layer tends to be more structured so that its dielectric response is expected to be suppressed in relation to that in the bulk. A frequent solution to incorporating this contribution is to introduce the Stern layer adjacent to a sharp interface with the width corresponding to a radius of a bare or hydrated ion and the dielectric constant being the same as or lower than the bulk value. The introduction of this layer does not change anything far from an interface, but it increases the contact potential, $\psi_c \rightarrow \psi_c + \sigma_c R/\epsilon_{stern}$, where R is the radius of an ion and ϵ_{stern} is the dielectric constant with the Stern layer [Frydel and Oettel (2011)]. Incorporation of the Stern layer at an air–water interface was found to give an accurate predictions for the excess surface tension of strong electrolytes [Levin and Flores-Mena (2001)].

As an example, in Fig. 3.2, we present a comparison between PB and MPB, LPB [routes (1) and (2) from above] for the contact potential dependence at a charged wall on the charge density. Finite ion size and dielectric saturation lead to a noticeable increase in the contact potential, which is in line with the experimental results (discussed above) for the dipole moment of charged colloids at interfaces.

Figure 3.3 compares counterion density profiles for various models. The "saturation" effect is clearly seen for the MPB model. The mechanism behind the spreading-out of the diffuse layer for the PPB model is connected with the dielectrophoretic repulsive force

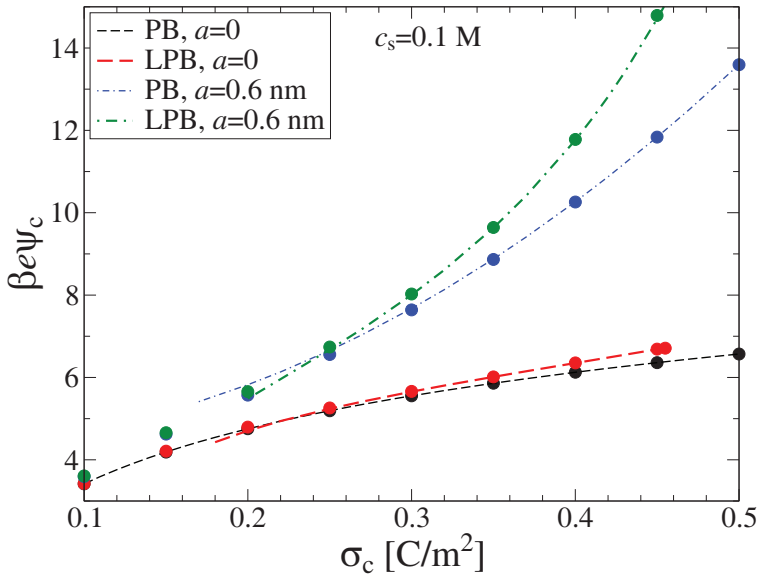

Figure 3.2 Contact potential (proportional to a colloid dipole moment at an interface) for PB and LPB, with and without steric corrections due to finite ion size ($v = a^3$). The symbols correspond to numerical data points and dashed lines correspond to analytical expressions derived in reference Frydel and Oettel (2011). Clearly, the contact potential in PB is noticeably smaller than in the modified theories for higher charge densities; thus, dipole moments will be underestimated by PB alone.

of ions with negative polarizability. Only the LPB model causes a stronger attraction toward the wall. This is caused by the lowering of the dielectric constant close to a wall. The combination of effects would require an appropriately combined model, an example is the combination of LPB and MPB as seen in the thick green dot-dashed curve in Fig. 3.2.

3.4 Outlook to Nonlocal Descriptions

In the models outlined above, the electrostatic interactions are described on the mean-field level, and the repulsive–core interactions among hydrated ions and solvent molecules are incorporated

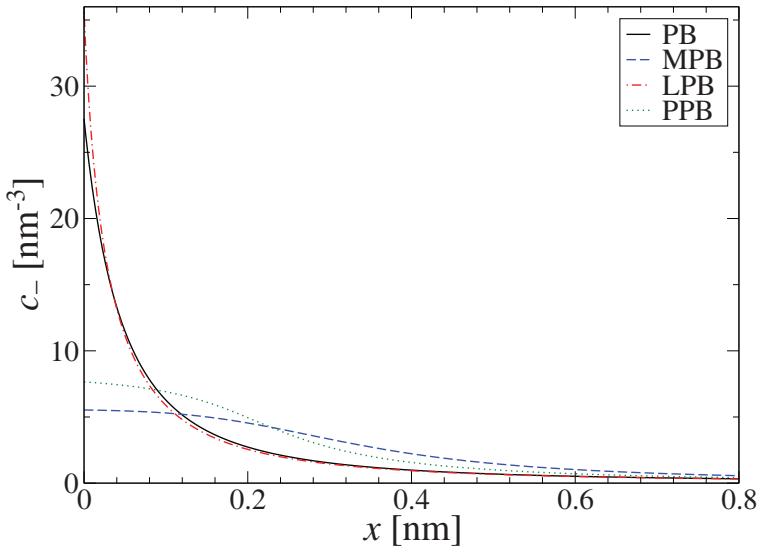

Figure 3.3 Counterion density near a charged wall for the models discussed in Sec. 3.3. The common parameters are $\sigma_c = 0.4$ C/m^2, $c_s = 0.1$ M, and $\lambda_B = 0.7$ nm. Specific parameters for each model are for MPB, the ion radius is 0.35 nm, for LPB (point ions) the dipole concentration is $c_d = 55$ M (as in water) and the permanent dipole moment is $p_0 = 4.85$ D, for PPB, the polarizability is $\alpha/(4\pi\epsilon_0) = -8$ M^{-1}. Only LPB leads to an increased concentration near a wall, whereas the other contributions tend to spread out a diffuse layer.

as local contributions. These models, even if quantitatively not precise, are able to capture correct trends. The drawback of the local approximation for the excluded volume interactions is that the "saturated" density profile is an unphysical artifact of the method itself. This leads to a violation of the contact value theorem (the relation between the density at the wall, solvent pressure and wall potential). Despite this, the electrostatic properties at a charged wall and far from the wall are captured with reasonable accuracy, despite the unphysical details in-between. A possibly more accurate treatment of the repulsive–core interactions can be achieved via density functional theory. In the example of reference Frydel and Levin (2012), ions are treated as charged hard spheres using the accurate fundamental measure theory, but for simplicity in

the background of a structureless solvent. This corresponds to a nonlocal extension of the MPB modification discussed above. Finally, the mean-field treatment of electrostatics neglects correlated fluctuations, which not only correct, but, in the so-called strong-coupling limit, also give rise to altogether new phenomena, such as the attraction between the same-charged macroparticles [Naji *et al.* (2005); Samaj and Trizac (2011)]. Although the applicability of the mean-field treatment breaks down in the strong-coupling limit, the correct theoretical treatment of correlations continues to be a challenge. This challenge is increased if both the correlations due to the short-range solvent and the long-range electrostatic interactions are important. Currently, the solutions are looked for using either the density functional theory approach or the field-theoretical methods.

Acknowledgments

M.O. thanks the DFG (German Research Foundation) for support through the Collaborative Research Center TR6 (Colloids in External Fields) and D.F. acknowledges support of CNPq (Brazil).

References

Abrashkin, A., D., A. and Orland, H. (2007). Dipolar poisson-boltzmann equation: Ions and dipoles close to charge interfaces, *Phys. Rev. Lett.* **99**, p. 077801.

Bikerman, J. J. (1942). Structure and capacitance of electrical double layer, *Phil. Mag. Series 7* **33**, p. 384.

Borukhov, I., Andelman, D. and Orland, H. (1997). Steric effects in electrolytes: A modified poisson-boltzmann equation, *Phys. Rev. Lett.* **79**, p. 435.

Dominguez, A., Frydel, D. and Oettel, M. (2008). Multipole expansion of the electrostatic interaction between charged colloids at interfaces, *Phys. Rev. E* **77**, p. 020401(R).

Frydel, D. (2011). Polarizable poisson–boltzmann equation: The study of polarizability effects on the structure of a double layer, *J. Chem. Phys.* **134**, p. 234704.

Frydel, D., Dietrich, S. and Oettel, M. (2007). Charge renormalization for effective interactions of colloids at water interfaces, *Phys. Rev. Lett.* **99**, p. 118302.

Frydel, D. and Levin, Y. (2012). A close look into the excluded volume effects within a double layer, *J. Chem. Phys.* **137**, p. 163703.

Frydel, D. and Oettel, M. (2011). Charged particles at fluid interfaces as a probe into structural details of a double layer, *Phys. Chem. Chem. Phys.* **13**, p. 4109.

Hatlo, M. M., van Roij, R. and Lue, L. (2012). The electric double layer at high surface potentials: The influence of excess ion polarizability, *EPL* **97**, p. 28010.

Levin, L. and Flores-Mena, J. E. (2001). Surface tension of strong electrolytes, *EPL* **56**, p. 187.

Masschaele, K., Park, B. J., Furst, E. M., Fransaer, J. and Vermant, J. (2010). Finite ion-size effects dominate the interaction between charged colloidal particles at an oil-water interface, *Phys. Rev. Lett.* **105**, p. 048303.

Naji, A., Jungblut, S., Moreira, A. G. and Netz, R. R. (2005). Electrostatic interactions in strongly coupled soft matter, *Physica A* **352**, p. 131.

Park, B. J., Pantina, J. P., Furst, E. M., Oettel, M., Reynaert, S. and Vermant, J. (2008). Direct measurements of the effects of salt and surfactant on interaction forces between colloidal particles at water-oil interfaces, *Langmuir* **24**, p. 1686.

Samaj, L. and Trizac, E. (2011). Counterions at highly charged interfaces: From one plate to like-charge attraction, *Phys. Rev. Lett.* **106**, p. 078301.

Yeh, I. C. and Berkowitz, M. L. (1999). Dielectric constant of water at high electric fields: Molecular dynamics study, *J. Chem. Phys.* **110**, p. 7935.

Chapter 4

Aspects of One-Dimensional Coulomb Gases

Ronald R. Horgan,[a] David S. Dean,[b] Vincent Démery,[c] Thomas C. Hammant,[a] Ali Naji,[d] and Rudolf Podgornik[e]

[a] *Department of Applied Mathematics and Theoretical Physics, University of Cambridge, Centre for Mathematical Sciences, Cambridge CB3 0WA, UK*
[b] *Université de Bordeaux and CNRS, Laboratoire Ondes et Matière d'Aquitaine (LOMA), UMR 5798, F-33400 Talence, France*
[c] *Institut Jean Le Rond d'Alembert, CNRS and UPMC Univ Paris 6, UMR 7190, F-75005 Paris, France*
[d] *School of Physics, Institute for Research in Fundamental Sciences (IPM), Tehran 19395-5531, Iran*
[e] *Department of Physics, J. Stefan Institute and Faculty of Mathematics and Physics, University of Ljubljana, SI-1000 Ljubljana, Slovenia*

4.1 Introduction

Field-theoretic functional integral methods can be used to study exact solutions of models on the basis of a one-dimensional (1D) Coulomb gas with charged boundaries. In 1D, exactly solvable Coulomb gas models can be then used as a testbed for assessing the accuracy of various approximations: the weak coupling expansion, Poisson–Boltzmann (PB)/mean-field (MF) equations, and the strong

Electrostatics of Soft and Disordered Matter
Edited by David Dean, Jure Dobnikar, Ali Naji, and Rudolf Podgornik

ISBN 978-981-4411-85-1 (Hardcover), 978-981-4411-86-8 (eBook)
www.panstanford.com

coupling expansion [1]. We review these approximations in the context of three 1D Coulomb gas systems and remark on whether or not they fail to predict important effects present in the exact solution.

Some physical properties of the 1D system can be applicable at least qualitatively for dimensions $d > 1$ and can help us to understand whether pertaining approximation methods are reliable or not. In particular, our analysis gives insight into systems such as an array of charged smectic layers or lipid multilayers, and ionic liquids near charged interfaces, treated as effectively 1D systems. An important aspect of these endeavors is that we can test and develop the analysis and especially numerical methods that can then be tentatively applied also for $d > 1$.

4.2 Theoretical Methods

The method of functional integrals applied to Coulomb gas systems has been developed over many years [4, 7, 9, 10]. In any dimension, this approach allows for both strong and weak coupling to be studied explicitly, but specifically in 1D, the functional integral representation can be applied using a variety of methods to obtain exact solutions to a number of models. These are generally characterized by a Coulomb gas of ions of possibly non-zero size confined between boundaries with properties that allow their potential or charge to be determined either dynamically or as an external field condition. Three varieties of a 1D Coulomb gas model discussed below are presented in Fig. 4.1.

The functional integral representation of the Coulomb gas partition function allows us to formulate two effective solution techniques. The *Schrödinger kernel technique* is applicable in all dimensions and has been used to analyze a number of models [3]. In 1D, it corresponds to solving the Schrödinger equation [7], which is in principle exact. In $d > 1$ the Schrödinger kernel field-theoretic representation of the partition function is derived, often using a Hubbard–Stratonovich transformation, and is analyzed by perturbative and graphical methods. For $d > 1$, this approach does require that a preferred coordinate can be designated as the Euclidean time

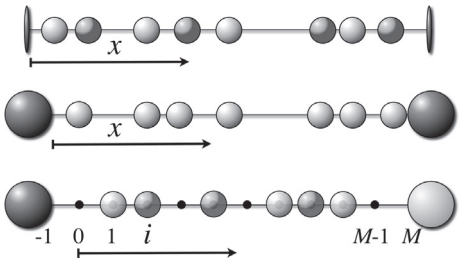

Figure 4.1 Top: The 1D Coulomb fluid configuration in the case of the soap film model (positively and negatively charged particles and adsorbing surfaces), middle: counterions between charged surfaces (positively charged particles and oppositely charged bounding surfaces), and bottom: an ionic liquid lattice capacitor (positively and negatively charged particles on a lattice with one positive and one negative bounding surface). Positively (negatively) charged particles are shown schematically as light (dark) gray spheres.

and so the approach is limited to symmetrically layered systems [3]. The *transfer matrix and Fourier methods technique* is an alternative to the Schrödinger kernel approach. Although it is more general, it is only practical in 1D. Its implementation exploits periodicity in the (imaginary) electrostatic potential ϕ, which also restricts its general applicability. Examples of this technique in 1D are the counterion gas and lattice ionic liquids.

The actual formulation of the functional integral method relies on the action for the full QED of a general system that is then reduced to the electrostatic action proper. The relevant *electrostatic Lagrangian* is then

$$\mathcal{L}(\psi) = \frac{1}{2}\varepsilon \int d\mathrm{x}(\nabla\psi(\mathrm{x}))^2 - e\sum_i q_i\psi(\mathrm{x}_i) - \int d\mathrm{x}\rho_e(\mathrm{x})\psi(\mathrm{x}).$$

Here, q_i is the charge of the i-th ion at position x_i and $\rho_e(\mathrm{x})$ is the external charge distribution. The partition function is obtained by tracing the Boltzmann weight of the above Lagrangian over the electrostatic field $[\psi]$. Tracing furthermore over ion positions, changing the axis of functional integration $\psi = i\phi$, and introducing fugacity $\mu_- = \mu_+ \equiv \mu$ by the Gibbs technique, the partition function for monovalent ions (with $q_i = \pm 1$) assumes the form

$$\mathcal{Z} = \int d[\phi]\exp(S(\phi))\,, \tag{4.1}$$

with the "field action"

$$S(\phi) = -\frac{\beta}{2}\varepsilon \int d\mathrm{x}(\nabla\phi(\mathrm{x}))^2 + 2\mu \int d\mathrm{x}\ \cos(e\beta\phi(\mathrm{x}))\,, \quad (4.2)$$

where $\beta = 1/(k_{\mathrm{B}}T)$. The charge density operator is then given by

$$\rho = \mu\frac{d}{d\mu}\log\mathcal{Z}(\mu) \ \Rightarrow\ \rho = 2\mu\langle\cos(e\beta\phi)\rangle, \quad (4.3)$$

where $\langle\cdots\rangle$ stands for the ϕ average.

4.3 Bilayer Soap Film in Ionic Solution

Because hydrophobic heads of the surfactant molecules preferentially migrate to the surfaces charging them up dynamically, the configuration of the bilayer soap film consists of two planar (surfactant) surfaces separated by a distance L confining a solution of a symmetric electrolyte.

We calculate the surface charge, the density profile of electrolyte near the interfaces, and the disjoining pressure P as a function of the thickness L of the soap film, defined as

$$P = P_{\mathrm{film}} - P_{\mathrm{bulk}} = -\frac{1}{\beta}\left(\frac{\partial J_{\mathrm{film}}}{\partial L} - \frac{\partial J_{\mathrm{bulk}}}{\partial L}\right).$$

i.e., the difference between the film and bulk pressures. Here, J is the grand-canonical partition function/unit area. An important phenomenon to predict is the first-order collapse transition of the film to a Newton black film expected, as the electrostatic coupling in the film is increased.

We model this system by a Coulomb gas confined to $z \in [0, L]$, schematically presented in Fig. 4.1 (top), with potentials on the boundaries that account for the hydrophillic nature of the head group of the surfactant molecule. The Debye length is given by $l_{\mathrm{D}} = \sqrt{\varepsilon k_{\mathrm{B}}T/2\rho e^2}$, and the Bjerrum length in 1D by $l_{\mathrm{B}} = 2k_{\mathrm{B}}T\varepsilon/e^2$. Perturbation theory is an expansion in the coupling parameter $g = l_{\mathrm{D}}/l_{\mathrm{B}}$.

We use the partition function described earlier but now include surface free energy $f(\phi)$ to model the surface potentials, which are attractive for the negatively charged hydrophillic surfactant head groups whose surface density is denoted by $\rho_-(\phi)$:

$$f(\phi) = e^{\lambda\rho_-(\phi)},$$

where λ controls the potential strength. To simplify the notation, we scale the variables: $\phi \to e\beta\phi$, $\mathrm{x} \to \mathrm{x}\, l_{\mathrm{B}}$. The charge density operators for $\pm$ charges are then given by the Boltzmann weights $\rho_{\pm}(\phi) = e^{\pm i\phi}$. The 1D partition function then becomes

$$\mathcal{Z} = \frac{1}{2\pi}\int_0^{2\pi} d\phi_0 d\phi_L\, f(\phi_0) K(\phi_0, \phi_L; L) f(\phi_L)\ ,$$

where

$$K(\phi_0, \phi_x; x) \ = \ \int \mathcal{D}\phi(x)\ \exp \int_0^x dx'\, \mathcal{L}(\phi(x'))$$

is the Schrödinger kernel for evolution in the "Euclidean time" x:

$$\Psi(\phi, x) = \int d\phi'\, K(\phi, \phi'; x) f(\phi').$$

It satisfies the Schrödinger (Feynman-Kac) equation

$$H\Psi = \frac{2\varepsilon}{\beta e^2}\frac{\partial}{\partial x}\Psi\ , \qquad H = \frac{\partial^2}{\partial\phi^2} \ + \ \frac{Z(g)}{2g^2}\cos(\phi),$$

with $Z(g) \ = \ 1/\langle\cos(\phi)\rangle$. The above equation is also known as the *Mathieu equation*, and the harmonic term gives the Debye length in units of l_{B}. $Z(g) \ = \ 2\mu/\rho$ is the renormalization that relates the fugacity to the observable charge density and is given by Eq. (4.3). We now consider the solution in various limiting regimes.

4.3.1 *Large L: Bulk Pressure*

Strong coupling (SC) $g \to \infty$: The Mathieu ground state dominates in this regime, and so, we can use the Schrödinger perturbation theory for the ground-state energy of H. The result, derived originally in [7], is

$$P_{\mathrm{bulk}} = \frac{1}{2}\rho k_{\mathrm{B}} T\left[1 + \frac{7}{32}\frac{1}{g^2} - \frac{23}{4608}\frac{1}{g^4} - \frac{4897}{7826432}\frac{1}{g^6} + \ldots\right].$$

The leading term is the free gas term but for density $\rho/2$, which therefore signals the onset of the dimerization process, *i.e.*, the Bjerrum pair formation of positive and negative mobile charges.

Weak coupling (WC) $g \to 0$: Feynman perturbation theory is applicable in this case, and so we use the Feynman diagram expansion to find

$$P_{\mathrm{bulk}} = \rho k_{\mathrm{B}} T\left(1 - \frac{1}{2}g + \frac{1}{128}g^3 + \ldots\right).$$

The leading term is the free gas term and the second-order term is the familiar Debye-Hückel result in its 1D variant. Note that there is no $O(g^2)$ term; this is cancelled by the counter term in $Z(g)$.

The strong and weak coupling dependencies of the bulk pressure $P_{\rm bulk}$ on g compare well with the exact solution of the problem. Both approximations are accurate across a wide range of g in their regime of validity. More details can be found in [4].

4.3.2 *Finite L: Exact Methods*

For finite L, we expand the kernel $K(\phi_0, \phi_L; L)$ over periodic eigenfunctions of the Mathieu equation. We can then use a numerical approach for eigenfunctions/eigenenergies, which will give an exact solution for all L. This method is described fully in [4] and we do not delve into details here. It gives the same answers as the Fourier approach that we describe below.

The Fourier method for obtaining an exact solution to problems in 1D is more general than the Schrödinger approach, as it works also when the Hamiltonian is not hermitian, which is the case for the counterion gas considered in the next section. It also forms the basis for the transfer matrix method. The theory is periodic under $\phi \to \phi + 2\pi$ and we can define

$$\Psi(\phi, x) = \int K(\phi, \phi'; x) f(\phi')\, d\phi' = e^{x/2g^2} \sum_{n=-\infty}^{n=\infty} b_n(x) e^{in\phi},$$

where the coefficients $b_n(x)$ obey the evolution equation

$$\frac{db_n}{dx} = -n^2 b_n + \frac{1}{4g^2}(b_{n+1} + b_{n-1} - 2b_n).$$

This is the Fourier version of the Schrödinger equation but can be derived generally from the convolution property of the Schrödinger kernel. The partition function can then be obtained from

$$\mathcal{Z}(T, L) = \int_0^{2\pi} f(\phi)\Psi(\phi, L)\, d\phi = e^{L/2g^2} \sum_{n=0}^{n=\infty} \frac{\lambda^n}{n!} b_n(L),$$

The exact solution for the disjoining pressure as a function of the separation L for different values of the surface potential strength parameter λ clearly predicts a collapse transition to a Newton black film that cannot be accounted for by the MF theory, which we address next.

4.3.3 *Classical or Mean-field Theory*

Standard variational methods applied to the expression for the partition function give the classical MF equation: the PB equation for $\phi_{\rm cl}(x)$ as the saddle point equation of the corresponding field theory. In this case, the disjoining pressure P is given by the value of ion density at the midpoint $x = L/2$ between the bounding surfaces. The MF theory predicts that universally $P > 0$, contrary to our exact result and also to experiment; it does not predict any collapse transition, which is thus obviously a consequence of the non-MF correlation effects and is intrinsically a fluctuation phenomenon.

4.4 Counterions Between Charged Surfaces

The 1D model here is a Coulomb gas of counterions confined between two oppositely charged surfaces; the system is overall neutral. We compare exact results with strong and weak coupling calculations, which are the same as in a 3D system. More details can be found in [5].

The system is shown in Fig. 4.1 (middle) and consists of N counterions, each of valency q, with surface charges σ_1 and σ_2, respectively. We define $\zeta = \sigma_2/\sigma_1$, with $-1 < \zeta < 1$, and define $\alpha = 1/(1+\zeta)$. The 1D Bjerrum length is $l_{\rm B} = 2k_{\rm B}T\varepsilon/e^2$, and the Gouy–Chapman length is $\mu \equiv \mu_1 = l_{\rm B}e/q|\sigma_1|$, where we have chosen σ_1 to be non-zero and have $\mu_2 = \mu/|\zeta|$. The electrostatic coupling constant, g, is then given by

$$g \equiv \frac{q^2\mu}{l_{\rm B}} = \frac{1+\zeta}{N} \ ,$$

where $N \to \infty$ corresponds to the MF/PB theory and $N \to 1$ to the SC theory. The partition function is derived as

$$\mathcal{Z}_N = \frac{1}{2\pi}\int_0^{2\pi} d\phi(0) \int_{-\infty}^{\infty} d\phi(L)\, e^{i\frac{\sigma_1}{qe}\phi(0)} \left(\int_{\phi(0)}^{\phi(L)} d\phi\ e^{-S(\phi)}\right)\ e^{i\frac{\sigma_2}{qe}\phi(L)},$$

with

$$S(\phi) = \int_0^L dx\ \left[\frac{1}{2q^2e^2\beta}\left(\frac{d\phi(x)}{dx}\right)^2 - e^{i\phi(x)}\right] \ .$$

The integral over $d\phi(0)$ ensures charge neutrality: $Nqe + \sigma_1 + \sigma_2 = 0$. The corresponding Hamiltonian (Feynman-Kac) and the partition function are then

$$H = -\frac{q^2e^2\beta^2}{2}\frac{d^2}{d\phi^2} - e^{i\phi}, \quad \mathcal{Z}_N = \int_0^{2\pi} d\phi \; e^{i\frac{\sigma_1}{qe}\phi} \left[e^{-LH}\right] e^{i\frac{\sigma_2}{qe}\phi}.$$

4.4.1 *Exact Results*

In this system, H is not hermitian because the counterions are, by definition, of one charge only. We therefore analyze the model using the Fourier method. We exploit periodicity in H of $\phi \to \phi + 2\pi$ in order to write

$$f(\phi; x) = e^{-xH} f(\phi; 0) \quad \text{with} \quad f(\phi; x) = \sum b(n, x) e^{in\phi} .$$

By introducing $\sigma_1 = -M_1 qe$, $\sigma_2 = -M_2 qe$, $M_1 = \text{Int}(\alpha N)$, $M_2 = N - M_1 - 1$, $\eta_1 = \alpha N - M_1$, and $\eta_2 = 1 - \eta_1$ and $\alpha = 1/(1+\zeta)$, we can derive the Fourier evolution equation from surface 2 to surface 1 in the form

$$\frac{db(n, M_2, L)}{dL} = -\frac{(n-\eta_2)^2}{2}\beta q^2 e^2 b(n, M_2, L) + b(n-1, M_2, L), \tag{4.4}$$

with $b(n, M_2, 0) = \delta_{n,-M_2}$. This Fourier evolution equation can be integrated numerically and the corresponding partition function

$$Z(\sigma_1, \zeta, N, L) = b(M_1 + 1, M_2, L),$$

and disjoining pressure

$$P(L) = -\frac{(M_1 + 1 - \eta_2)^2}{2} q^2 e^2 \; + \; \frac{b(M_1, M_2, L)}{Z(\sigma_1, \zeta, N, L)}$$

can be evaluated exactly. As the second term in the above equation can be seen to be just the counterion density at the boundary of the system, the above form of the pressure is thus a clear example of the contact value theorem; it connects the pressure with the value of the particle density at the confining wall of the system.

4.4.2 *Weak Coupling*

We consider the WC expansion $g \to 0$, which is equivalent in the lowest order to the MF/PB theory. In the $d > 1$ case, the MF theory

treats the potential field $\phi(\mathrm{x})$ as constant in the directions transverse to the normal to the bounding interfaces, and so the results are independent of the dimensionality.

The leading contribution arises from the saddle-point configuration $\phi_0(x) = i\psi_0(x)$ with ψ_0 real. The PB equation and the boundary conditions have the form

$$\frac{d^2\psi_0(x)}{dx^2} = -q^2e^2\beta\, e^{-\psi_0(x)} ,$$

with

$$\left.\frac{d\psi_0}{dx}\right|_0 = -\sigma_1\beta qe, \qquad \left.\frac{d\psi_0}{dx}\right|_L = \sigma_2\beta qe.$$

The leading PB contribution to the disjoining pressure, P, is then expressed as

$$\beta P = -\frac{1}{2q^2e^2\beta}\left(\frac{d\psi_0}{dx}\right)^2 + \rho_0(x),$$

where $\rho_0(x)$ is the density of counterions between the boundaries, given by the standard Boltzmann form $\rho_0(x) = Ce^{-\psi_0(x)}$, where C is a normalization constant. This furthermore implies that the MF/PB disjoining pressure P is obtained as follows: When the pressure is repulsive ($P > 0$), we have $P = \mu^2\sigma_1^2\Gamma^2/2$, where Γ satisfies

$$\tan(\Gamma L) = \frac{\Gamma(1+\zeta)\mu}{\Gamma^2\mu^2 - \zeta},$$

and when the pressure is attractive ($P < 0$), which may be the case within the MF/PB theory only for $\zeta < 0$, we have $P = -\mu^2\sigma_1^2\Gamma^2/2$, where Γ is now given as a solution of

$$\coth(\Gamma L) = -\frac{\zeta + \mu^2\Gamma^2}{\mu\Gamma(1+\zeta)}.$$

4.4.3 *Strong Coupling*

The strong coupling limit is formally identical to the one-particle limit [1]. In the present case, it is easily evaluated from the partition function in the case of a single counterion in the system. The partition function in an explicit one-particle form leads to the

disjoining pressure

$$P(L) = \frac{\sigma_1^2}{2}\left(-\frac{1}{2}(1+\zeta^2) + \frac{1}{2}(1-\zeta^2)\coth\left[(1-\zeta)\frac{L}{2\mu}\right]\right).$$

The range of validity of this limiting expression is of course defined by the number of counterions in the system. As this number decreases toward one, $N \to 1$, the above expression for the disjoining pressure becomes exact.

4.4.4 *Comparison*

Both the weak and strong coupling approximations are independent of dimension d and the comparison with the exact results can test their validity. For symmetric surface charges ($\zeta = 1$), the PB/MF pressure is positive (repulsive) for all intersurface separations, whereas the SC expansion and the exact result for $N = 1$ predict attraction at large separations; this distinction holds for $0 < \zeta \leq 1$. For the asymmetric configuration with $\zeta < 0$, there is little difference between the different approaches; on trivial grounds, there is attraction for large separations, but there is repulsion for sufficiently small separations, see Fig. 4.2, wherein a comparison is made with Monte-Carlo (MC) simulations at different numbers of counterions N [5].

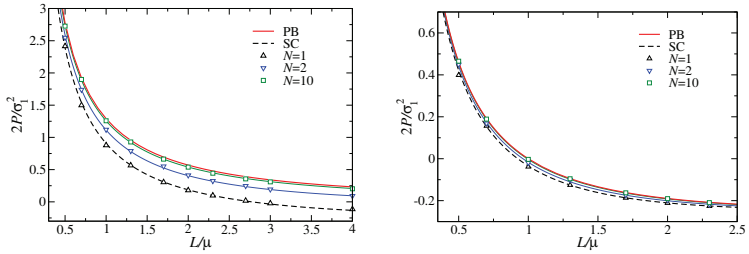

Figure 4.2 Rescaled disjoining pressure, $2P/\sigma_1^2$, for a 1D counterion gas between charged surfaces as function of the rescaled intersurface separation L/μ. Thick (red) solid lines represent the PB result (Section 4.4.2), dashed lines are the SC results (Section 4.4.3) and thin solid lines are the exact results (Section 4.4.1) compared with MC simulations data (symbols) at different numbers of counterions N and for $\zeta = 0.5$ (left pane) and $\zeta = -0.5$ (right pane).

4.5 Ionic Liquid Lattice Capacitor

In the models above, the ions have been chosen to be point-like. Here, we address the question of changes wrought by their finite size. In this case, the system consists of a 1D lattice of M sites with spacing a, with the i-th site, $0 \leq i < M$, occupied by ion with charge qS_i with $S_i \in [-q, 0, q]$, see Fig. 4.1 (bottom). Within this model, the finite ion size is $\sim a$, which is crucial to the phenomena observed in experiments on confined ionic liquids.

The configuration described is one of the 1D *ionic liquid capacitor*. The external fields are imposed either by fixing the charges of the boundaries at $i = -1$ and $i = M$ to be $\pm qQ$, respectively, or by imposing a fixed voltage/potential difference, Δv, across the capacitor. More details can be found in [6].

The electrostatic Hamiltonian in this case is expressed through a spin-like variable $S_i = 0, \pm 1$

$$\beta\mathcal{H} = -\frac{\gamma}{4}\sum_{i.j=0}^{M-1} |i-j| S_i S_j \qquad \gamma = \frac{\beta q^2 a}{\varepsilon}.$$

After a Hubbard-Stratonovich transformation this yields the action

$$S(\phi) = \sum_{j=0}^{M-2} \frac{(\phi_{j+1} - \phi_j)^2}{2\gamma} - \sum_{j=0}^{M-1} \ln[1 + 2\mu\, \cos(\phi)] + iQ(\phi_{-1} - \phi_M).$$

The system includes boundary charges $\pm qQ$ at sites -1, M. The electrostatic potential is defined as $V = -i\phi/\beta q$. In limit $a \to 0$, q/a fixed, the MF equations obtained from the saddle-point of the above field action reduce to those of Kornyshev [8] and Borukhov et al. [2].

For non-zero a, the action is not positive definite for $\mu \geq 0.5$ and so we seem to have a sign problem and certainly cannot use the Schrödinger approach *a priori*. Nevertheless, in the case of 1D, the partition function can be computed exactly by using the transfer matrix approach, with the Fourier method described earlier. This can be seen as follows:

Write $y_i = \phi_i$ and define

$$p^{1/2}(y, y') = \frac{1}{\sqrt{\pi\gamma}} e^{-(y-y')^2/\gamma},$$

with

$$K(y, y') = \int dz\; p^{1/2}(y, z)[1 + \mu\, \cos(z)]\, p^{1/2}(z, y') \qquad (4.5)$$

with $Kf(y) = \int_{-\infty}^{\infty} dy'\ K(y, y') f(y')$. The free energy for the fixed Q ensemble, Ω_Q, then follows as

$$e^{-\beta\Omega_Q} = \int_{-\pi}^{\pi} dx\ e^{iQx} \left[p^{1/2} K^M p^{1/2}\right] e^{-iQx} \equiv \langle\psi_Q|K^M|\psi_Q\rangle$$

with

$$\langle\psi_Q|y\rangle = e^{iQy}, \quad \langle y|K|y'\rangle = K(y, y')$$

The conjugate free energy for the fixed Δv ensemble, $\Omega_{\Delta v}$, then follows from a Legendre transform,

$$e^{-\beta\Omega_{\Delta v}} = \int dQ\ e^{-\Delta v Q - \beta\Omega_Q},$$

while the capacitance $C_{\Delta v}$ is obtained from the first derivative of $\partial\langle Q\rangle_{\Delta v}$ w.r.t. Δv. and can thus be calculated directly from the partition function.

4.5.1 *Results*

The transfer matrix and Fourier approach can be formulated in order to evaluate the free energy explicitly. Details of this procedure can be found in Ref. [6]. Enthalpy $\mathcal{G}_M = \Omega_M + MP_{\text{bulk}}$, the disjoining pressure $P = \mathcal{G}_M - \mathcal{G}_{M+1}$, and the capacitance $C_{\Delta v}$ can all be calculated as a function of μ, Q, Δv.

We show explicitly only the capacitance results, $C_{\Delta v}$, as a function of Δv in Fig. 4.3, both for large μ and small μ. For large μ, the curve shows the typical "bell" shape in contrast to the curve for smaller

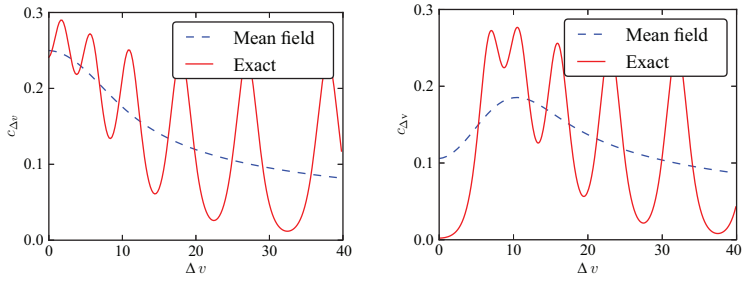

Figure 4.3 (Left) Bell-shaped $C_{\Delta v}$ as a function of Δv for large $\mu = 0.5$. (Right) Camel-shaped $C_{\Delta v}$ as a function of Δv for small $\mu = 0.03$. In both cases, we have $\gamma = 1$. The dashed line is the MF result.

μ, which shows the nonmonotonic "camel" shape, and so, $C_{\Delta v}$ has a minimum at the point of zero charge confirming the Fermi MF results of Kornyshev [8].

For smaller γ (increasing T), the periodic nonmonotonicity both for large μ and small μ disappears and the solution approaches the Fermi MF result of Kornyshev [8]. It is interesting that the exact solution dances around the Kornyshev solution with an ever-increasing amplitude, but the system nevertheless always remains thermodynamically stable, as can be straightforwardly ascertained.

4.6 Conclusion

We have demonstrated that in 1D, one can use the Schrödinger approach for continuum models of Coulomb fluids, but that for discrete models, a more general approach is needed that exploits the transfer matrix and the periodicity of the field to use Fourier methods. We tested the PB/MF and the strong coupling limiting expressions and demonstrated that they need correcting, although the exact analytic result clearly supports the two limiting analyses. We also confirmed that the MF theory does not capture the important effects that are due to correlations, either the attractive intersurface forces in the case of a counterion-only system or nonmonotonic periodic variation of the capacitance in the confined ionic liquid case.

References

1. Boroudjerdi, H., Kim, Y.-W., Naji, A., Netz, R. R., Schlagberger, X. and Serr, A. (2005). Statics and dynamics of strongly charged soft matter, *Phys. Rep.* **416**, p. 129.
2. Borukhov, I., Andelman, D. and Orland, H. (2000). Adsorption of large ions from an electrolyte solution: a modified Poisson-Boltzmann equation, *Electrochem. Acta* **46**, p. 221.
3. Dean, D. S. and Horgan, R. R. (2005). The field theory of symmetrical layered electrolytic systems and the thermal casimir effect, *J. Phys. C* **17**, p. 3473.

4. Dean, D. S., Horgan, R. R. and Sentenac, D. (1998). Boundary Effects in the One Dimensional Coulomb Gas, *J. Stat. Phys.* **90**, p. 899.
5. Dean, D. S., Horgan, R. R., Naji, A. and Podgornik, R. (2009). One-dimensional counterion gas between charged surfaces: Exact results compared with weak- and strong-coupling analysis, *J. Chem. Phys.* **130**, p. 094504.
6. Demery, V., Dean, D. S., Hammant, T. C., Horgan, R. R. and Podgornik, R. (2012). The one-dimensional coulomb lattice fluid capacitor, *J. Chem. Phys.* **137**, p. 064901.
7. Edwards, S. F. and Lenard, J. (1962). Exact Statistical Mechanics of a 1 Dimensional System with Coulomb Forces. 2. Method of Functional Integrals, *J. Math. Phys.* **3**, p. 778.
8. Kornyshev, A. A. (2007). Double-Layer in Ionic Liquids: Paradigm Change? *J. Phys. Chem. B* **111**, p. 5545.
9. Netz, R. R. and Orland, H. (1999). Field Theory for Charged Fluids and Colloids, *Europhys. Lett.* **45**, p. 726.
10. Podgornik, R. and Žekš, B. (1988). Inhomogeneous Coulomb Fluid – A Functional Integral Approach, *J. Chem. Soc. – Farad. Trans.* **84**, p. 611.

Chapter 5

Electrostatics in Electrolytes Expressed in an Exact Formalism Reminiscent of the Poisson–Boltzmann Picture

Roland Kjellander
Department of Chemistry and Molecular Biology, University of Gothenburg, SE-412 96 Gothenburg, Sweden
rkj@chem.gu.se

5.1 Poisson–Boltzmann Approximation in Perspective

Consider a particle in a bulk electrolyte solution. It can be one of the ions, a solvent molecule or some other particle that may be charged or not. The distribution of other particles in the neighborhood of the particle is affected by the interactions with the latter; one may say that the particles are correlated with each other. The concentration there is increased or decreased depending on whether the interaction is attractive or repulsive. For non-spherical molecules the distribution of orientations is also affected by the interactions.

It is common to say that the particle has an "ion cloud" around it, that is, a region in the neighborhood where the ion concentrations

Electrostatics of Soft and Disordered Matter
Edited by David Dean, Jure Dobnikar, Ali Naji, and Rudolf Podgornik

ISBN 978-981-4411-85-1 (Hardcover), 978-981-4411-86-8 (eBook)
www.panstanford.com

deviate from the average bulk values. Since, for example, anions and cations have opposite electrostatic interactions with a charged particle, the enhanced concentration of one ionic species and the reduced concentration of the other implies that there is a nonzero charge density in the cloud. Sufficiently far away from the particle, where the concentrations are equal to the average bulk values, the charge density is zero. Since the density and the orientation distribution of solvent molecules also deviate due the interactions with the particle, one may say that the particle in fact has an "ion and solvent cloud" around it where the values deviate from the bulk. The charge density distribution in the cloud has contributions from both the ion and solvent distributions. This charge distribution is the *polarization response* of the surrounding solution to the interactions with the particle. The presence of the cloud affects the electrostatic field due to the particle; the total field is equal to the sum of the field from the particle itself and that from the charge density of the surrounding cloud. The interaction felt by some charge near the particle is with the total field, not only the field from the particle itself.

When the electrostatic interaction between two particles in an electrolyte solution is calculated, one must consider that the distributions of ions and solvent molecules are affected by *both* particles. The field at one of the particles due to the other is the total field including the contributions from the "shared" cloud around them. In the Poisson–Boltzmann (PB) approximation this is, however, not considered. It is based on a so-called *mean field approximation* where the interaction force on an ion due to a charged particle ("particle A") is calculated without considering that the former has a cloud "of its own". Only the cloud of the charged particle A is considered, which will be explained shortly. Furthermore, in the PB approximation the solvent is modeled as a dielectric continuum so the only effect of the solvent is that the electrostatic interactions between the particles are reduced compared to vacuum with a factor $1/\epsilon_r$, where ϵ_r is the dielectric constant of the pure solvent.

Generally, this treatment of the solvent is also used in the *primitive model* of electrolytes, where the ions are charged hard spheres and the solvent is a dielectric continuum. The PB theory is hence obtained when the mean field approximation is applied to this model.

To calculate the ion distributions around a charged particle A, that is, the ion concentrations as functions of distance from the particle, one needs to know the total potential energy $w_{\mathrm{A}j}(\mathbf{r})$ of an ion of species j at various positions $\mathbf{r} = (x, y, z)$ near A (we here assume for simplicity that the origin of the coordinate system is placed at a fixed point inside particle A and the coordinate axes are fixed relative to this particle). The mean force $\mathbf{f}_{\mathrm{A}j}$ that acts on the ion when its center is located at the point $\mathbf{r}$ is the negative gradient of this potential, $\mathbf{f}_{\mathrm{A}j}(\mathbf{r}) = -\nabla w_{\mathrm{A}j}(\mathbf{r})$. The potential energy $w_{\mathrm{A}j}(\mathbf{r})$ is a free energy quantity that is called the *potential of mean force*. Like for any other potential energy, the variation of $w_{\mathrm{A}j}(\mathbf{r})$ is related to work. The (reversible) work one has to do to move the ion from $\mathbf{r}_1$ to $\mathbf{r}_2$ near A equals $w_{\mathrm{A}j}(\mathbf{r}_2) - w_{\mathrm{A}j}(\mathbf{r}_1)$.

The ion concentration of species j at a point $\mathbf{r}_2$ in the neighborhood of particle A is most conveniently expressed as the number density $n_{\mathrm{A}j}(\mathbf{r}_2)$, where index Aj indicates that we are considering the density of species j around particle A. The interpretation of $n_{\mathrm{A}j}(\mathbf{r}_2)$ is that inside an infinitesimal volume element $d\mathbf{r}_2 = dx_2 dy_2 dz_2$ that surrounds the point $\mathbf{r}_2$ there are on average $n_{\mathrm{A}j}(\mathbf{r}_2)d\mathbf{r}_2$ ion centers (a time average). The density $n_{\mathrm{A}j}(\mathbf{r}_2)$ can be expressed in terms of the potential of mean force $w_{\mathrm{A}j}(\mathbf{r}_2)$ as a simple Boltzmann distribution. We have

$$n_{\mathrm{A}j}(\mathbf{r}_2) = n_j^{\mathrm{bulk}} e^{-\beta w_{\mathrm{A}j}(\mathbf{r}_2)}, \tag{5.1}$$

where n_j^{bulk} is the number density in bulk for species j, $\beta = 1/(k_{\mathrm{B}}T)$, k_{B} is Boltzmann's constant, T is the absolute temperature and $w_{\mathrm{A}j}$ is set equal to zero in the bulk far away from particle A. The relationship (5.1) is exact and holds in general.

The PB mean field approximation is now done in the following way. As mentioned above the electrostatic field felt by an ion at position $\mathbf{r}_2$ is the *total* field, that is, the field from particle A and the cloud that surrounds particle A and the ion. The charge distribution of this cloud is in reality affected by the interaction both with particle A *and* the ion at $\mathbf{r}_2$, see Fig. 5.1a. The ion density distribution is not equal to $n_{\mathrm{A}j}(\mathbf{r})$ since this is the density when *all* ions around A are free to move and no ion is placed at $\mathbf{r}_2$. However, when one calculates the force on an ion placed at $\mathbf{r}_2$ in the PB approximation, one assumes that the charge distribution is *only* affected by particle

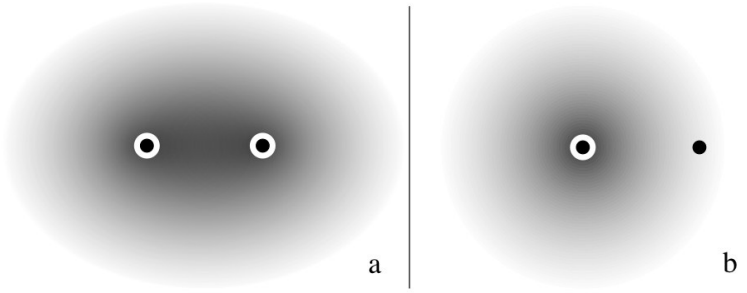

Figure 5.1 (a) Sketch of the charge density around two particles, particle A to the left and another particle to the right. In this case the particles are ions of the same species. (b) The charge density used in the PB approximation when calculating the potential felt by the right ion, which is located at $\mathbf{r}_2$. Then the density is assumed to be affected by particle A only.

A, that is, the density *is* equal to $n_{\mathrm{A}j}(\mathbf{r})$, see Fig 5.1b. It is as if the ion at $\mathbf{r}_2$ is a "ghost" that the other ions do not "see". This ion interacts electrostatically with all other ions, but they do not interact with it. One does this approximation for all ions around particle A, so when $w_{\mathrm{A}j}(\mathbf{r}_2)$ is calculated for any ion of species j we include its interaction with particle A and with the ion cloud around A.

At any point $\mathbf{r}_3$ the cloud around A has the charge density $\rho_{\mathrm{A}}^{\mathrm{cloud}}(\mathbf{r}_3)$, which can be obtained from the ion densities $n_{\mathrm{A}j}$ for all species j as

$$\rho_{\mathrm{A}}^{\mathrm{cloud}}(\mathbf{r}_3) = \sum_j q_j n_{\mathrm{A}j}(\mathbf{r}_3), \tag{5.2}$$

where q_j is the charge of an ion of species j and the sum is over all j.

Let $\rho_{\mathrm{A}}(\mathbf{r}_3)$ denote the interior charge density of particle A itself (ρ_{A} is zero outside the particle). The total charge density of particle A and its surrounding cloud is $\rho_{\mathrm{A}}^{\mathrm{tot}}(\mathbf{r}_3) = \rho_{\mathrm{A}}(\mathbf{r}_3) + \rho_{\mathrm{A}}^{\mathrm{cloud}}(\mathbf{r}_3)$. The electrostatic potential $\psi_{\mathrm{A}}(\mathbf{r}_2)$ from this charge density is given by Coulomb's law

$$\psi_{\mathrm{A}}(\mathbf{r}_2) = \int d\mathbf{r}_3 \rho_{\mathrm{A}}^{\mathrm{tot}}(\mathbf{r}_3)\phi_{\mathrm{Coul}}(r_{32}) = \int d\mathbf{r}_3 \frac{\rho_{\mathrm{A}}^{\mathrm{tot}}(\mathbf{r}_3)}{4\pi\alpha r_{32}}, \tag{5.3}$$

where $\phi_{\mathrm{Coul}}(r) = 1/(4\pi\alpha r)$ is the unit Coulomb potential, $\alpha = \varepsilon_{\mathrm{r}}\varepsilon_0$, ε_0 is the permittivity of vacuum, $r_{32} = |\mathbf{r}_{32}|$, $\mathbf{r}_{32} = \mathbf{r}_2 - \mathbf{r}_3$ and

the integral is taken over the whole space. Equivalently, ψ_A can be obtained as the solution to Poisson's equation

$$-\alpha\nabla^2\psi_A(\mathbf{r}) = \rho_A^{tot}(\mathbf{r}) \tag{5.4}$$

with the boundary condition $\psi_A(\mathbf{r}) \to 0$ infinitely far away from particle A. This solution is given explicitly by Eq. (5.3).

In the PB approximation, an ion at $\mathbf{r}_2$ feels only the electrostatic potential ψ_A and the non-electrostatic short-ranged interactions with particle A, which we denote u_{Aj}^{short}. Thus we have

$$w_{Aj}(\mathbf{r}_2) = u_{Aj}^{short}(\mathbf{r}_2) + \psi_A(\mathbf{r}_2)q_j \quad \text{(PB)} \tag{5.5}$$

(the notation (PB) after an equation means that it is valid only in the PB approximation). Equations (5.1–5.4) together with the PB approximation, Eq. (5.5), constitute a set of equations for the unknown functions $n_{Aj}(\mathbf{r})$, $\rho_A^{cloud}(\mathbf{r})$ and $\psi_A(\mathbf{r})$ that can be solved. By eliminating all unknowns except $\psi_A(\mathbf{r})$ from these equations one obtains the *PB equation*

$$-\alpha\nabla^2\psi_A(\mathbf{r}) = \rho_A(\mathbf{r}) + \sum_j q_j n_j^{bulk} e^{-\beta[u_{Aj}^{short}(\mathbf{r})+\psi_A(\mathbf{r})q_j]}. \text{ (PB)} \tag{5.6}$$

For a particle A with a hard core, the usual case, both $u_{Aj}^{short}(\mathbf{r}) = 0$ and $\rho_A(\mathbf{r}) = 0$ for all $\mathbf{r}$ outside the particle. Then this equation takes on the commonly used form of the PB equation for such $\mathbf{r}$ values: $-\alpha\nabla^2\psi_A(\mathbf{r}) = \sum_j q_j n_j^{bulk} \exp(-\beta\psi_A(\mathbf{r})q_j)$. For $\mathbf{r}$ inside the hard core $u_{Aj}^{short}(\mathbf{r}) = \infty$ so the exponential function in Eq. (5.6) becomes zero and the PB equation becomes $-\alpha\nabla^2\psi_A(\mathbf{r}) = \rho_A(\mathbf{r})$.

The PB approximation implies that the correlations between the ions in the surroundings of the particle A are entirely neglected. Both correlations due to electrostatic and short range interactions, for example ion size effects, are thereby ignored. The surrounding ions are thus modeled as non-correlating point ions in their interaction between themselves. The only correlations that are included are those between particle A and each surrounding ion, whereby effects of the finite size of particle A and electrostatic interactions with it *are* included.

Particle A can be any kind of particle including an ion of the electrolyte solution. Consider, for example, a pure electrolyte

solution of simple ions, which we assume are spherical. Then, if particle A is an ion of species i we have $n_{\mathrm{A}j}(\mathbf{r}) \equiv n_{ij}(r) = n_j^{\mathrm{bulk}} g_{ij}(r)$, where $r = |\mathbf{r}|$ and $g_{ij}(r)$ is, by definition, the radial distribution function of the electrolyte. The latter satisfies $g_{ij}(r) = \exp(-\beta w_{ij}(r))$.

Note that the quantity $\psi_i(\mathbf{r})/q_i$ is in general not the same as $\psi_j(\mathbf{r})/q_j$. This implies that $\psi_i(\mathbf{r})q_j \neq \psi_j(\mathbf{r})q_i$ and hence $w_{ij}(r) \neq w_{ji}(r)$ in the PB approximation and therefore $g_{ij}(r) \neq g_{ji}(r)$, a well-known fact. For a correct theory one *must* have $w_{ij}(r) = w_{ji}(r)$ and $g_{ij}(r) = g_{ji}(r)$. Furthermore, particle A is treated in the PB approximation entirely differently than the surrounding particles of the same kind. In a correct treatment all particles should in principle be handled on an equal basis and those of the same kind must be treated in the same manner.

The main task of this treatise is to show how these shortcomings of the PB approximation can be eliminated without loosing too much of the rather simple structure of this theory. Before we do this we will write the PB approximation in a different manner which is simpler to generalize.

5.2 Relationships with Screened Coulomb Potential

The right hand side (RHS) of the PB equation (5.6), which is equal to $\rho_{\mathrm{A}}(\mathbf{r}) + \rho_{\mathrm{A}}^{\mathrm{cloud}}(\mathbf{r})$, is nonlinear in ψ_{A}. For simplicity, we consider particles with hard cores. The exponential function in $\rho_{\mathrm{A}}^{\mathrm{cloud}}$ can be expanded in a Taylor series. For positions $\mathbf{r}$ outside particle A we have

$$\begin{aligned}\rho_{\mathrm{A}}^{\mathrm{cloud}}(\mathbf{r}) &= \sum_j q_j n_j^{\mathrm{bulk}}[1 - \beta\psi_{\mathrm{A}}(\mathbf{r})q_j + (\beta\psi_{\mathrm{A}}(\mathbf{r})q_j)^2/2 - \ldots] \\ &= -\beta \sum_j q_j^2 n_j^{\mathrm{bulk}} \psi_{\mathrm{A}}(\mathbf{r}) + \text{nonlinear terms}, \qquad \text{(PB)}\end{aligned}$$

where we have used that $\sum_j q_j n_j^{\mathrm{bulk}} = 0$ due to electroneutrality. The term that is linear in ψ_{A} is the *linear polarization response* of the electrolyte to the *total* electrostatic field due to particle A (or rather the linear part of the response), while $\rho_{\mathrm{A}}^{\mathrm{cloud}}$ is the entire polarization response which is nonlinear. This linear term is equal to $-\alpha\kappa_{\mathrm{D}}^2\psi_{\mathrm{A}}$,

where κ_D is the Debye parameter defined by

$$\kappa_D^2 = \frac{\beta}{\alpha} \sum_j q_j^2 n_j^{\text{bulk}} \tag{5.7}$$

and $1/\kappa_D$ is the usual Debye length. By subtracting the linear response term from both sides of Poisson's equation (5.4) we can write this equation for *all* $\mathbf{r}$ values as

$$-\alpha[\nabla^2 \psi_A(\mathbf{r}) - \kappa_D^2 \psi_A(\mathbf{r})] = \rho_A^*(\mathbf{r}) \quad \text{(PB)} \tag{5.8}$$

where $\rho_A^* = \rho_A^{\text{tot}} + \alpha\kappa_D^2\psi_A = \rho_A + \rho_A^{\text{cloud}} + \alpha\kappa_D^2\psi_A$. Note that the function ρ_A^* is equal to the *nonlinear* terms of ρ_A^{cloud} outside particle A, while it is equal to $\rho_A + \alpha\kappa_D^2\psi_A$ inside.

Now, consider the function $\phi_{\text{Coul}}^*(r)$ that is the solution of

$$-\alpha[\nabla^2 \phi_{\text{Coul}}^*(r) - \kappa_D^2 \phi_{\text{Coul}}^*(r)] = \delta^{(3)}(r), \quad \text{(PB)} \tag{5.9}$$

where $\delta^{(3)}(r)$ is the three-dimensional Dirac delta function, and that satisfies the boundary condition $\phi_{\text{Coul}}^*(r) \to 0$ when $r \to \infty$. This function is the *screened Coulomb potential* in the PB approximation,

$$\phi_{\text{Coul}}^*(r) = \frac{e^{-\kappa_D r}}{4\pi\alpha r}. \quad \text{(PB)} \tag{5.10}$$

It is the so-called *Green's function* for Eq. (5.8) and gives the spatial propagation of electrostatic interactions in the electrolyte in the PB approximation. The concept of a Green's function means that the solution ψ_A of Eq. (5.8) for a given ρ_A^* is given by

$$\psi_A(\mathbf{r}_2) = \int d\mathbf{r}_3 \rho_A^*(\mathbf{r}_3) \phi_{\text{Coul}}^*(r_{32}) \tag{5.11}$$

$$\text{i.e., } \psi_A(\mathbf{r}_2) = \int d\mathbf{r}_3 \rho_A^*(\mathbf{r}_3) \frac{e^{-\kappa_D r_{32}}}{4\pi\alpha r_{32}} \quad \text{(PB)} \tag{5.12}$$

for all $\mathbf{r}_2$. One can easily show this by inserting Eq. (5.11) in Eq. (5.8) and using Eq. (5.9).

Note that the potential $\psi_A(\mathbf{r}_2)$ in Eqs. (5.3) and (5.11) is exactly the same. In the latter equation we have written $\psi_A(\mathbf{r}_2)$ in terms of the screened Coulomb potential $\phi_{\text{Coul}}^*(r)$ instead of the ordinary (unscreened) Coulomb potential $\phi_{\text{Coul}}(r)$. The source charge distribution ρ_A^{tot} in Coulomb's law (5.3) has thereby been

replaced by another source charge distribution ρ_A^* in Eq. (5.11). The mathematical form of Coulomb's law is, however, maintained for the screened case. The distribution $\rho_A^*(\mathbf{r}_3)$ has the role of an "effective" charge distribution of A to be used in conjunction with the screened Coulomb potential. It is more short-ranged than $\rho_A^{\text{cloud}}(\mathbf{r}_3)$ of the ion cloud; the latter decays for large r like $\psi_A(\mathbf{r}_3)$ while $\rho_A^*(\mathbf{r}_3)$ decays like $\psi_A^2(\mathbf{r}_3)$. The linear response of the electrolyte due to the electrostatic interactions with particle A is in Eq. (5.11) taken care of by $\phi_{\text{Coul}}^*(r)$ while all nonlinear effects are contained in ρ_A^*. We will say that ρ_A^* is the charge distribution of the *dressed particle* A, where $\rho_A^* - \rho_A$ constitutes the "dress". Note that the dress is different from the cloud since these two entities differ by the linear response term.

A general formula for the decay of $\psi_A(\mathbf{r}_2)$ for large r_2 can easily be obtained from Eq. (5.12). To the leading order we have

$$\frac{e^{-\kappa|\mathbf{r}_2-\mathbf{r}_3|}}{|\mathbf{r}_2-\mathbf{r}_3|} \sim \frac{e^{-\kappa(r_2-\hat{\mathbf{r}}_2\cdot\mathbf{r}_3)}}{r_2} = \frac{e^{-\kappa r_2}}{r_2}\, e^{\kappa\hat{\mathbf{r}}_2\cdot\mathbf{r}_3} \quad \text{when } r_3 \ll r_2 \to \infty,$$

where $\hat{\mathbf{r}}_2 = \mathbf{r}_2/r_2$. Since $\rho_A^*(\mathbf{r}_3)$ decays fast we obtain from Eq. (5.12) to the leading order

$$\psi_A(\mathbf{r}_2) \sim \phi_{\text{Coul}}^*(r_2) \int d\mathbf{r}_3 \rho_A^*(\mathbf{r}_3) e^{\kappa\hat{\mathbf{r}}_2\cdot\mathbf{r}_3} \quad \text{when } r_2 \to \infty, \qquad (5.13)$$

where $\kappa = \kappa_D$ in the present PB case. The distance dependence of the potential is accordingly the same as for the screened Coulomb potential $\phi_{\text{Coul}}^*(r)$, that is, decays as $\exp(-\kappa_D r)/r$. Note, however, that the value of the integral is dependent on the direction of the vector $\mathbf{r}_2$. The electrostatic potential from a non-spherical particle in an electrolyte accordingly has a complicated direction dependence even at large distances (cf. Refs. [1–4]).

For the special case when particle A is spherically symmetric, for example, when it is a simple ion, $\rho_A^*(\mathbf{r}_3)$ depends only on the distance r_3 therefore in Eq. (5.13) one can perform the angular integration in spherical polar coordinates for $\mathbf{r}_3$. One then obtains

$$\psi_A(r_2) \sim \phi_{\text{Coul}}^*(r_2) \int_0^\infty dr_3 4\pi r_3^2 \rho_A^*(r_3) \frac{\sinh(\kappa r_3)}{\kappa r_3} \quad \text{when } r_2 \to \infty,$$

where $\kappa = \kappa_D$ presently. By analogy to the expression for the potential from a charge q in vacuum $\psi(r_2) = \phi_{\text{Coul}}(r_2)q$, we can

write this as (cf. Refs. [5, 6])

$$\psi_{\mathrm{A}}(r_2) \sim \phi^*_{\mathrm{Coul}}(r_2) q^*_{\mathrm{A}} \quad \text{when } r_2 \to \infty \tag{5.14}$$

where

$$q^*_{\mathrm{A}} = \int d\mathbf{r}_3 \rho^*_{\mathrm{A}}(\mathbf{r}_3) \frac{\sinh(\kappa r_3)}{\kappa r_3} \tag{5.15}$$

is the *effective charge* of particle A, which gives the magnitude of the potential when the particle is seen from a large distance. Thus, the effective charge q^*_{A} of particle A in an electrolyte is different from its charge q_{A}, which is given by $q_{\mathrm{A}} = \int d\mathbf{r}_3 \rho_{\mathrm{A}}(\mathbf{r}_3)$. However, in the limit of infinite dilution of the electrolyte we have $q^*_{\mathrm{A}} \to q_{\mathrm{A}}$. (Incidentally, it can be mentioned that q^*_{A} is the Fourier transform $\widetilde{\rho}^*_{\mathrm{A}}(k)$ of $\rho^*_{\mathrm{A}}(r)$ evaluated at $k = \mathrm{i}\kappa$ with i = the imaginary unit.)

For a particle that is not spherical $\phi^*_{\mathrm{Coul}}(r_2) q^*_{\mathrm{A}}$ gives the direction independent part of the potential $\psi_{\mathrm{A}}(\mathbf{r}_2)$ (the average of $\psi_{\mathrm{A}}(\mathbf{r}_2)$ over all directions of $\hat{\mathbf{r}}_2$), but as we have seen there is also a direction dependent part that decays with distance in exactly the same manner. One can, in fact, define effective dipole, quadrupole contributions etc. to $\psi_{\mathrm{A}}(\mathbf{r}_2)$ that all decay with distance as $\exp(-\kappa_{\mathrm{D}} r_2)/r_2$, for details see Refs. [7, 8].

Now, let us look at the potential of mean force in Eq. (5.5). The electrostatic part of it is $w^{\mathrm{el}}_{\mathrm{A}j}(\mathbf{r}_2) = \psi_{\mathrm{A}}(\mathbf{r}_2) q_j$. By inserting Eq. (5.11) we obtain

$$w^{\mathrm{el}}_{\mathrm{A}j}(\mathbf{r}_2) = \int d\mathbf{r}_3 \rho^*_{\mathrm{A}}(\mathbf{r}_3) \phi^*_{\mathrm{Coul}}(r_{32}) q_j. \quad \text{(PB)} \tag{5.16}$$

When particle A is a simple ion of species i we have from Eq. (5.14)

$$w^{\mathrm{el}}_{ij}(r_2) \sim \phi^*_{\mathrm{Coul}}(r_2) q^*_i q_j \quad \text{when } r_2 \to \infty. \quad \text{(PB)} \tag{5.17}$$

If particle A instead would be an ion of species j and we were looking at its interaction with an ion of species i in its ion cloud, we would instead have $w^{\mathrm{el}}_{ji}(r_2) \sim \phi^*_{\mathrm{Coul}}(r_2) q^*_j q_i$. This vividly illustrates the asymmetry $w^{\mathrm{el}}_{ij} \neq w^{\mathrm{el}}_{ji}$ of the PB approximation that is incorrect. A reasonable behavior of a correct theory where all particles are treated on the same basis would rather be $w^{\mathrm{el}}_{ij}(r_2) \sim \phi^*_{\mathrm{Coul}}(r_2) q^*_i q^*_j$, where effective charges appear for both ions. Since Eq. (5.10) follows from the PB approximation, one would furthermore expect that the function $\phi^*_{\mathrm{Coul}}(r)$ is different in such a theory. However, since the PB approximation approaches the correct behavior in the limit of

infinite dilution, the correct $\phi^*_{\text{Coul}}(r)$ is expected to approach Eq. (5.10) in this limit, at least for large r.

Consider the more general case where the i ion is located at $\mathbf{r}_1$ (rather than at the origin) and the j ion is at $\mathbf{r}_2$. In the PB expression $w^{\text{el}}_{ij}(r_{12}) = \psi_i(r_{12})q_j = \int \rho^*_i(r_{13})\phi^*_{\text{Coul}}(r_{32})q_j d\mathbf{r}_3$, the dressed particle charge distribution ρ^*_i appears for one ion and the bare charge q_j for the other. In a symmetrical expression the dressed particle charge distribution ρ^*_j rather than the bare charge q_j would appear and thus interact with the potential ψ_i, that is

$$w^{\text{el}}_{ij}(r_{12}) = \int d\mathbf{r}_3 d\mathbf{r}_4 \rho^*_i(r_{13})\phi^*_{\text{Coul}}(r_{34})\rho^*_j(r_{24}) \tag{5.18}$$
$$= \int d\mathbf{r}_4 \psi_i(r_{14})\rho^*_j(r_{24}) = \int d\mathbf{r}_3 \rho^*_i(r_{13})\psi_j(r_{23}),$$

where we have used Eq. (5.11) for species i and j, respectively, to obtain the last two equalities from the first one. The first integral gives the electrostatic energy between ρ^*_i and ρ^*_j interacting via the screened Coulomb potential. In the second line of the equation the first integral expresses the interaction energy for ρ^*_j with the electrostatic potential from the i ion, while the second integral expresses the interaction energy for ρ^*_i with the potential from the j ion. Eq. (5.18) gives, as we shall see, *the correct expression for the screened Coulomb interaction between two ions in exact theory*. The replacement of the bare charge q_j by the dressed particle charge distribution ρ^*_j is a simple, but important correction to the PB approximation. As we shall also see, in exact theory there are other contributions to w_{ij} in addition to w^{el}_{ij} and u^{short}_{ij}. They constitute the remaining corrections.

5.3 The General Exact Case

All equations above that are not marked (PB) are, in fact, valid in general, so we need only to complement them with equations that replace the PB relationships. First, we will define the screened Coulomb potential ϕ^*_{Coul} and the charge distributions ρ^*_l, $l = i, j$, that appear in Eq. (5.18). In the PB approximation we considered the linear (part of the) polarization response to the total electrostatic field due to particle A. We obtained Eq. (5.8) by subtracting

this response from Poisson's equation (5.4). In the PB case the polarization charge density at a point is proportional to the potential at *the same* point; the response is entirely local. In the general case the response is, however, *nonlocal*: the potential at one point affects the polarization charge density in a whole region around that point. This is due to the intermolecular correlations in the liquid.

Let us first consider the linear polarization response of a bulk liquid to a *weak* electrostatic field from some charge external to the system. The polarization charge density is then given by

$$\rho^{\text{pol}}(\mathbf{r}_2) = \int d\mathbf{r}_3 \Psi^{\text{ext}}(\mathbf{r}_3)\chi(r_{32}) = \int d\mathbf{r}_3 \Psi(\mathbf{r}_3)\chi^*(r_{32}) \qquad (5.19)$$

where Ψ^{ext} is the electrostatic potential from the external charge itself and Ψ is the total electrostatic potential due to the charge including the contributions from ρ^{pol}. The function $\chi(r)$ is the polarization response function for the external potential and $\chi^*(r)$ is that for the total potential (these two functions can be expressed in terms of the pair distribution functions of the solution, see Refs. [9, 10]). In our case $\chi^*(r)$ is of most interest since we will deal with the total potential.

Let us now consider the polarization response $\rho_{\text{A}}^{\text{cloud}}$ due to particle A in an electrolyte. The total electrostatic potential ψ_{A} due to A is, as before, given by Eq. (5.3). It is not weak in general. The *linear part* of the polarization response to ψ_{A} is $\int d\mathbf{r}_3 \psi_{\text{A}}(\mathbf{r}_3)\chi^*(r_{32}) \equiv \rho_{\text{A}}^{\text{lin}}(\mathbf{r}_2)$. If we subtract $\rho_{\text{A}}^{\text{lin}}$ from both sides of Poisson's equation (5.4) we obtain

$$-\alpha\nabla_2^2\psi_{\text{A}}(\mathbf{r}_2) - \int d\mathbf{r}_3 \psi_{\text{A}}(\mathbf{r}_3)\chi^*(r_{32}) = \rho_{\text{A}}^*(\mathbf{r}_2) \qquad (5.20)$$

where ∇_2^2 is the Laplacian with respect to $\mathbf{r}_2$ and $\rho_{\text{A}}^* = \rho_{\text{A}}^{\text{tot}} - \rho_{\text{A}}^{\text{lin}} = \rho_{\text{A}} + \rho_{\text{A}}^{\text{cloud}} - \rho_{\text{A}}^{\text{lin}}$. As before ρ_{A}^* contains the *nonlinear* contributions to $\rho_{\text{A}}^{\text{cloud}}$ outside particle A, while it is equal to $\rho_{\text{A}} - \rho_{\text{A}}^{\text{lin}}$ inside. The part of $\rho_{\text{A}}^{\text{lin}}$ inside the particle is not a real charge density; it is the charge density that linear response "would like to put there" if it could.

Now, the screened Coulomb potential ϕ_{Coul}^* can be defined from

$$-\alpha\nabla_2^2\phi_{\text{Coul}}^*(r_2) - \int d\mathbf{r}_3 \phi_{\text{Coul}}^*(r_3)\chi^*(r_{32}) = \delta^{(3)}(r_2). \qquad (5.21)$$

It is the Green's function for Eq. (5.20) and gives the spatial propagation of electrostatic interactions in the electrolyte. Thus, for

a given ρ_{A}^* the potential ψ_{A} is the solution of Eq. (5.20) and is, as before, given by Eq. (5.11), which is the generalized Coulomb's law for the screened potential.

A physical way to interpret Eq. (5.21) is to consider the potential $\psi_{[q]}$ from a point charge q placed at the origin. In the limit when $q \to 0$ the nonlinear terms vanish and $\rho_{[q]}^*(\mathbf{r}) \to q\delta^{(3)}(r)$. Then, Eq. (5.20) goes over to Eq. (5.21) multiplied by q, so it follows that $\psi_{[q]}(r) \to q\phi_{\mathrm{Coul}}^*(r)$ and accordingly

$$\phi_{\mathrm{Coul}}^*(r) = \lim_{q\to 0} \frac{\psi_{[q]}(r)}{q}. \tag{5.22}$$

This is an alternative definition of the screened Coulomb potential.

An important point is now that if we take the polarization response function equal to that for an electrolyte with explicit molecular solvent, the response contains the appropriate effects of the polarization of the solvent. Then $\rho_{\mathrm{A}}^{\mathrm{cloud}}$ is the charge density of the "ion and solvent cloud" that we mentioned in the beginning. Thereby Eqs. (5.20–5.21) yield the screened Coulomb potential and the generalized Coulomb's law (5.11), which then *includes solvent effects in a correct manner*. In this case $\alpha = \epsilon_0$ in the formulas above since the background for all particles is vacuum. If we instead model the solvent as a dielectric continuum, as done in the primitive model, $\alpha = \epsilon_{\mathrm{r}}\epsilon_0$ as before.

For a simple ion of species i, the charge density $\rho_i^{\mathrm{tot}}(r) = q_i\delta^{(3)}(r) + \rho_i^{\mathrm{cloud}}(r)$ associated with it can be written in terms of the pair distribution functions g_{ij} as $\rho_i^{\mathrm{tot}}(r) = q_i\delta^{(3)}(r) + \sum_j q_j n_j^{\mathrm{bulk}} g_{ij}(r)$ + similar contributions from the solvent. Likewise, one can write $\rho_i^*(r) = q_i\delta^{(3)}(r) + \sum_j q_j n_j^{\mathrm{bulk}} g_{ij}^*(r)$ + similar solvent contributions, where g_{ij}^* contains the nonlinear contributions to g_{ij} (this is analogous to the fact that ρ_i^* contains the nonlinear contributions in ρ_i^{tot}). One can show that [6, 10]

$$g_{ij}(r_{12}) = g_{ij}^*(r_{12}) - \beta \int d\mathbf{r}_3 \psi_i(r_{13}) \rho_j^*(r_{23}), \tag{5.23}$$

where the last term is the contribution that is linear in ψ_i and that corresponds to the term ρ_i^{lin} in ρ_i^{cloud}. This is a key result in the exact theory.

Next we turn to the potential of mean force w_{ij} and start with spherical particles. As will be shown below we have

$$w_{ij}(r) = u_{ij}^{\mathrm{short}}(r) + w_{ij}^{\mathrm{el}}(r) + w_{ij}^*(r) \tag{5.24}$$

where $w_{ij}^{\rm el}$, as defined in Eq. (5.18), constitutes the screened electrostatic interaction between the particles (with $\phi_{\rm Coul}^*$ and $\rho_l^*, l = i, j$, from the definitions above) and where w_{ij}^* contains complicated effects of the short range interactions and indirect effects of the electrostatic ones. In many cases electrostatic interactions dominate the long range behavior of the potential of mean force and then

$$w_{ij}(r) \sim w_{ij}^{\rm el}(r) \quad \text{when } r \to \infty. \tag{5.25}$$

Exceptions occur, for example, at high electrolyte concentration when the strong screening makes the electrostatic interactions more short ranged than effects of other kinds of interactions.

For two non-spherical particles A and B with centers located at $\mathbf{r}_1$ and $\mathbf{r}_2$ respectively and with fixed orientations relative to the coordinate frame we have instead

$$w_{AB}^{\rm el}(\mathbf{r}_{12}) = \int d\mathbf{r}_3 d\mathbf{r}_4 \rho_{\rm A}^*(\mathbf{r}_{13}) \phi_{\rm Coul}^*(r_{34}) \rho_{\rm B}^*(\mathbf{r}_{24}), \tag{5.26}$$

which is the obvious generalization of Eq. (5.18). The screened Coulomb interaction of the two particles accordingly takes place between their dressed particle charge distributions $\rho_{\rm A}^*$ and $\rho_{\rm B}^*$.

[We will for completeness show how Eq. (5.24) can be obtained, but the current paragraph may be skipped in a first reading. A well-known exact formula from liquid state theory [9] is that $w_{ij} = u_{ij} - \beta^{-1}(h_{ij} - c_{ij} + b_{ij})$, where $u_{ij} = u_{ij}^{\rm el} + u_{ij}^{\rm short}$ is the pair interaction potential, $u_{ij}^{\rm el}$ is the electrostatic interaction (i.e., $q_i q_j \phi_{\rm Coul}$ for simple ions), $h_{ij} \equiv g_{ij} - 1$, and c_{ij} and b_{ij} are the, so called, direct correlation and bridge functions, respectively. The latter is a short range function that contains complicated effects of correlations between the particles in a fluid. (The hyper-netted chain (HNC) approximation is obtained if b_{ij} is set equal to zero.) The functions h_{ij} and c_{ij} are related to each other via the Ornstein–Zernike (OZ) equation [9], a subject we do not need to enter in this treatise. The direct correlation function is a long-ranged function that decays for large distances like $c_{ij} \sim -\beta u_{ij}^{\rm el}$, while the "non-electrostatic part" of it $c_{ij}^* \equiv c_{ij} + \beta u_{ij}^{\rm el}$ is short-ranged. Now, by introducing $h_{ij}^* \equiv g_{ij}^* - 1$ and using Eq. (5.18) we can write Eq. (5.23) as $h_{ij} = h_{ij}^* - \beta w_{ij}^{\rm el}$ and we obtain $w_{ij} = u_{ij}^{\rm short} + w_{ij}^{\rm el} - \beta^{-1}(h_{ij}^* - c_{ij}^* + b_{ij})$, which is Eq. (5.24) with $w_{ij}^* = -\beta^{-1}(h_{ij}^* - c_{ij}^* + b_{ij})$. In this manner we have separated out the "simple" screened electrostatic interaction $w_{ij}^{\rm el}(r)$

from the rest for all separations r between the i and j particles. The function $w_{ij}^*(r)$ contains the entangled, nonlinear correlation effects in the surroundings of the two particles at close range, including contributions from overlaps of the particle dresses. (Incidentally, it can be mentioned that h_{ij}^* and c_{ij}^* are related to each other via the OZ equation, exactly like h_{ij} and c_{ij}, see Refs. [6, 10])]

Finally, we shall show how $\phi_{\text{Coul}}^*(r)$ and $w_{ij}^{\text{el}}(r)$ decay for large r in many cases of interest, namely electrolyte solutions at low to medium salt concentrations for systems where the ions and solvent molecules have u_{ij}^{short} of sufficiently short range, for example, hard cores. (Note, however, that the formalism in the current section is general up to this point in the text and is not limited to these cases.)

One can show that ϕ_{Coul}^* defined in Eq. (5.21) or, equivalently, (5.22) decays like (see Refs. [6, 10])

$$\phi_{\text{Coul}}^*(r) \sim \frac{e^{-\kappa r}}{4\pi\alpha^* r} \quad \text{when } r \to \infty, \tag{5.27}$$

where $\kappa \neq \kappa_{\text{D}}$ and $\alpha^* \neq \alpha$. The differences from the PB case, Eq. (5.10), are that the $\exp(\kappa r)/r$ decay occurs for large r only and that the amplitude and decay length $1/\kappa$ are not the same. The parameter α^* can be denoted as an effective permittivity of the electrolyte solution. Both κ and α^* are entirely determined by the response function χ^* of the solution. For small r the function $\phi_{\text{Coul}}^*(r)$ is more complicated than Eq. (5.27) and depends on the discrete nature of the ions and the solvent molecules.

Now, since Eq. (5.11) holds in general, the analysis leading up to Eq. (5.13) shows that the latter equation is valid in the current case too. For spherical particles we accordingly have Eq. (5.14) with an effective charge defined by Eq. (5.15), but now with the correct ρ_{A}^* of course. Thus the potential from a particle behaves at large distances like in the PB approximation, but with a different amplitude and decay length. However, in contrast to the PB case, the potential of mean force is now completely symmetrical and we have from Eqs. (5.18) and (5.25)

$$w_{ij}(r_{12}) \sim \phi_{\text{Coul}}^*(r_{12}) q_i^* q_j^* \quad \text{when } r_{12} \to \infty \tag{5.28}$$

for spherical particles as anticipated above. For two non-spherical particles A and B with fixed orientations we have from Eq. (5.26)

$$w_{AB}(\mathbf{r}_{12}) \sim \int d\mathbf{r}_3 d\mathbf{r}_4 \rho_{\text{A}}^*(\mathbf{r}_{13}) \frac{e^{-\kappa r_{34}}}{4\pi\alpha^* r_{34}} \rho_{\text{B}}^*(\mathbf{r}_{24}) \tag{5.29}$$

for large r_{12}. For the interaction between particle A at $\mathbf{r}_1$ and a simple ion at $\mathbf{r}_2$ we have

$$w_{Aj}(\mathbf{r}_{12}) \sim \psi_A(\mathbf{r}_{12}) q_j^* \quad \text{when } r_{12} \to \infty \tag{5.30}$$

in contrast to the PB approximation $\psi_A q_j$ in Eq. (5.5).

Let us consider a primitive model electrolyte of simple ions. The charge distribution of the ion cloud around an ion of species i is given by Eq. (5.2) with A = i. From Eqs. (5.1) and (5.30) it follows that $\rho_i^{\text{cloud}}(r) \sim \sum_j q_j n_j^{\text{bulk}} \exp(-\beta \psi_i(r) q_j^*)$ for large r. Since ψ_A goes to zero for large r we can linearize the RHS and obtain $\rho_i^{\text{cloud}}(r) \sim -\beta \sum_j q_j q_j^* n_j^{\text{bulk}} \psi_i(r)$.

We shall now investigate Poisson's equation (5.4), which in spherical geometry is $-\alpha r^{-1} d^2[r\psi_A(r)]/dr^2 = \rho_A^{\text{tot}}(r)$. Now, since $\psi_i(r)$ is proportional to $\exp(-\kappa r)/r$ for large r it follows that the left hand side (LHS) of Poisson's equation decays like $-\alpha\kappa^2 \psi_i(r)$. The RHS decays like ρ_i^{cloud} which goes like $-\beta \sum_j q_j q_j^* n_j^{\text{bulk}} \psi_i(r)$. By equating the prefactors in the LHS and RHS we see that

$$\kappa^2 = \frac{\beta}{\alpha} \sum_j q_j q_j^* n_j^{\text{bulk}}, \tag{5.31}$$

which is the exact version of Eq. (5.7) for κ in the primitive model. Since the effective charge q_j^* of an ion is different from its bare charge q_j, it follows that $\kappa \neq \kappa_D$ as anticipated above.

For an electrolyte with discrete solvent molecules each particle is surrounded by an ion and solvent cloud and ρ_i^{cloud} has a contribution from the polarization of the solvent that is linear in ψ_i for large r. Then, there is also a term $\left\langle \tilde{\rho}_s \underline{\tilde{\rho}_s^*} \right\rangle \Big|_{i\kappa} n_s^{\text{bulk}}$ for solvent species s in the sum of Eq. (5.31), where $\langle \cdot \rangle$ is an average over orientations, underline indicates complex conjugation and the term is evaluated at $k = i\kappa$ in Fourier space, see Refs. [7, 10]. (Any nonspherical particle species present in the solution would contribute with such a term.)

5.4 Summary and Concluding Remarks

In the PB approximation for electrolyte systems one assumes that the solvent behaves like a dielectric continuum and that the charge

of each ion interacts with the average electrostatic potential from other ions in the system, neglecting the correlations. In reality an ion does not "feel" the mean potential since the ions and the solvent molecules in its neighborhood correlate with it—each ion has a local "ion and solvent cloud" of its own where the ion distribution deviate from the average one and where the locations and orientations of solvent molecules are affected. This cloud affects the interactions felt by the ion. In this treatise it is shown how it is possible to include such effects in an exact manner for the screened electrostatic interactions. Thereby, the exact theory of electrolyte solutions with discrete solvent molecules is reformulated in a manner that has a similar structure as the PB approximation theory. The screened electrostatic interaction between any two particles in the system is then written in terms of the average electrostatic potential due to one of them interacting with an effective charge distribution of the other (rather than with the bare charges as assumed in the PB approximation). This effective charge distribution also has the role as the source of the average electrostatic potential when the latter is expressed in terms of the screened rather than the ordinary (unscreened) Coulomb potential. The resulting exact formalism maintains a large part of the physical transparency of the PB theory. The primary advantage is conceptual since the formalism separates out the screened electrostatics among complex consequences of the various interactions. Since the theory is exact, the task to obtain numerical results is the same as earlier. To do any numerical work one needs to do computer simulations or use some other approximate analytical or numerical method. One can take such results as input to analyze the behavior of electrolytes using the present formalism. The theory can also be used as a guide to invent new approximations.

References

1. Rowan, D. G., Hansen, J.-P., and Trizac, E. (2000). *Molec. Phys.* **98**, 1369–1378.
2. Trizac, E., Bocquet, L., Agra, R., Weis, J.-J., and Aubouy, M. (2002). *J. Phys.: Condens. Matter* **14**, 9339–9352.

3. Agra, R., Trizac, E., and Bocquet, L. (2004). *Eur. Phys. J. E* **15**, 345–357.
4. Hoffmann, N., Likos, C. N., and Hansen, J.-P. (2004). *Molec. Phys.* **102**, 857–867.
5. Kjellander, R. and Mitchell, D. J. (1992). *Chem. Phys. Lett.* **200**, 76–82.
6. Kjellander, R. and Mitchell, D. J. (1994). *J. Chem. Phys.* **101**, 603–626.
7. Kjellander, R. and Ramirez, R. (2008). *J. Phys.: Condens. Matter* **20**, 494209–1–16.
8. Ramirez, R. and Kjellander, R. (2006). *J. Chem. Phys.* **125**, 144110–1–13.
9. Hansen, J.-P. and McDonald, I. R. (2006). *Theory of Simple Liquids* 3rd edition (Academic Press).
10. Ramirez, R. and Kjellander, R. (2003). *J. Chem. Phys.* **119**, 11380–11395.

Chapter 6

Legendre Transforms for Electrostatic Energies

Justine S. Pujos and A. C. Maggs
CNRS Gulliver, ESPCI, 10 rue Vauquelin, Cedex 05, 75231 Paris.
anthony.maggs@espci.fr

We review the use of Legendre transforms in the formulation of electrostatic energies in condensed matter. We show how to render standard functionals expressed in terms of the electrostatic potential, ϕ, convex—at the cost of expressing them in terms of the vector field $\mathbf{D}$. This leads to great simplification in the formulation of numerical minimization of electrostatic energies coupled to other physical degrees of freedom. We also demonstrate the equivalence of recent functionals for dielectrics derived using field theory methods to classical formulations in terms of the electric polarization.

6.1 Introduction

The Legendre transform is a powerful tool with multiple applications in physics [Zia *et al.* (2009)]. In classical mechanics it allows one to interchange the Lagrangian and Hamiltonian viewpoints; in thermodynamics one regularly transforms ensembles to simplify

Electrostatics of Soft and Disordered Matter
Edited by David Dean, Jure Dobnikar, Ali Naji, and Rudolf Podgornik

ISBN 978-981-4411-85-1 (Hardcover), 978-981-4411-86-8 (eBook)
www.panstanford.com

calculations, choosing the ensemble which most closely idealizes a given experimental setup. In this article we will demonstrate the utility of Legendre transforms in reformulating energies and free energies in electrostatics, with a particular eye for numerical applications and mean field theory.

Our principle motivation for a deeper study of this transformation applied to electrostatic problems is quite practical. Many formulations of (free) energy functions in condensed matter physics involve the electrostatic potential, an important example is the Poisson–Boltzmann energy functional in the theory of ionic solutions. However when we examine closely these functionals we see that they are concave functions of the potential. While the stationary value of the functional is indeed the correct value of the energy that we wish to study, the concavity leads to complications in many situations. In particular we cannot perform a simultaneous minimization of both electrostatic and configurational energies in a simulation. One is generally obliged to fully solve by iterative methods the electrostatic problem at each time step of the iteration over the configurational degrees of freedom—such as densities or polymer configuration. This leads to codes which are complicated to write, and sometimes slow to run.

We remind the reader that for a convex function $f(x)$, its Legendre transform is defined [Zia *et al.* (2009)] from the expression

$$\mathcal{L}[f](s) = g(s) = sx - f(x) \tag{6.1}$$

where on the right hand side (RHS) of Eq. (6.1) we express x as a function of s from the equation $s = \frac{df}{dx}$. This transformation is an involution: $\mathcal{L}[g](x) = f(x)$. The simplest example is an Hookian spring for which $f(x) = kx^2/2$; then the transformation of Eq. (6.1) gives $g(s) = s^2/(2k)$. We will also use the notation $\mathcal{L}(f) = \tilde{f}$. In this article we show that by introducing new variational parameters in a free energy with the help of Lagrange multipliers and then performing a Legendre transform of the resulting free energy we can find functionals that are convex in all degrees of freedom; we will illustrate this with a mean field formulation of phase separation coupled to electrostatic interactions.

We will now illustrate the approach with the simplest possible electrostatic problem, interaction between free charges, ρ_{f}, in a

heterogeneous dielectric medium: Consider the energy functional expressed in terms of the electric potential ϕ.

$$U = \int \left\{ -\frac{\epsilon(\mathbf{r})(\nabla\phi)^2}{2} + \rho_f\phi \right\} d^3\mathbf{r} \tag{6.2}$$

The variational equation for the field is then the Poisson equation:

$$\text{div}\, \epsilon(\mathbf{r})\text{grad}\, \phi = -\rho_f(\mathbf{r}) \tag{6.3}$$

Substituting the solution of the Poisson equation in the electrostatic energy we find

$$U = \frac{1}{2} \int \phi(\mathbf{r})\rho_f(\mathbf{r})\, d^3\mathbf{r} \tag{6.4}$$

We convert the variational problem for the potential by introducing the new variable $\mathbf{E} = -\nabla\phi$. To do this we introduce the (vector) Lagrange multiplier $\mathbf{D}$. The stationary point of Eq. (6.2) is identical to that of the following expression [Courant and Hilbert (1989)]:

$$U = \int \left\{ -\frac{\epsilon(\mathbf{r})\mathbf{E}^2}{2} + \rho_f\phi + \mathbf{D}\cdot(\mathbf{E} + \nabla\phi) \right\} d^3\mathbf{r} \tag{6.5}$$

It is at this point that we recognize that the variational equations for $\mathbf{E}$ correspond to a Legendre transform with dual variable $\mathbf{D}$. We also integrate by parts the product $\mathbf{D}\cdot\nabla\phi$ to find $-\phi$ div $\mathbf{D}$, dropping boundary terms assumed to be zero. Thus the stationary point of Eq. (6.2) is identical to the stationary point of

$$U = \int \left\{ \frac{\mathbf{D}^2}{2\epsilon(\mathbf{r})} + \phi(\rho - \text{div}\, \mathbf{D}) \right\} d^3\mathbf{r} \tag{6.6}$$

Variations in ϕ now impose Gauss' law, div $\mathbf{D} - \rho_f = 0$, while the energy has been rendered convex by the transformations introduced, [Maggs (2002, 2004)].

We now illustrate applications of this transformation to two problems: (i) in phase separation of immiscible fluids in the presence of electrostatic interactions due to ions and (ii) in translation between two very different visions of the theory of dielectrics. Recent formulations of implicit dielectrics pass by elaborate field-theory mappings and find a generalized Poisson–Boltzmann equation with a Langevin correction. We will show how to map this description onto a free energy expressed in terms of a polarization field with long-ranged dipolar interactions. We

believe that these equivalent descriptions can lead to a deeper understanding of the underlying physics.

In the following section we will work with free energy densities, rather than the integrated energies and we (silently) integrate by parts when needed.

6.2 Phase Separation Coupled to Electrostatics

A mixture of two solvents (A and B) near their miscibility limit and in the presence of salt displays interesting properties which have been explored in recent experiments [Bonn *et al.* (2009)]. Density fluctuations couple to the dielectric properties of the medium, and in turn influence the partition of ions in the fluctuating solvent field. The experimental system has turned out to be very rich, and allows one to adjust the effective interaction between colloidal particles using temperature as a control parameter.

A simplified theoretical description of such systems is given in [Tsori and Leibler (2007); Onuki (2006)] who propose the following free energy density expressed in terms of the densities and potentials:

$$f(\phi, \Psi, c_+, c_-) = f_m(\Psi) - \frac{1}{2}\epsilon(\Psi)(\nabla\phi)^2 + (c_+ - c_-)e\phi - \left(\Delta u^+ c_+ + \Delta u^- c_-\right)\Psi + k_B T \sum_j (c_j \ln(c_j/c_{j0}) - c_j) \quad (6.7)$$

Ψ describes the composition fluctuations of the fluid mixture. c_+ and c_- are the concentration of positive and negative monovalent ions, with Δu^+ and Δu^- their relative preferences between liquid-A environment and liquid-B environment. As above ϕ is the electrostatic potential. We see that fluctuation in fluid concentration Ψ couple through the electrostatic field ϕ via $\epsilon(\Psi)$ with the concentration fluctuations of the ions.

$f_m(\Psi)$ includes all the terms that are only dependent on Ψ: $f_m(\Psi) = f_0(\Psi) + \frac{c}{2}(\nabla\Psi)^2 - \mu\Psi$; with $f_0(\Psi)$ the free energy due to mixing of the two solvents. It can, for example, be written as a binary mixture free energy density: $f_0(\Psi) \propto \Psi\log(\Psi) + (1-\Psi)\log(1-\Psi) + \chi\Psi(1-\Psi)$, with χ the Flory parameter [Marcus *et al.* (2008); Samin *et al.* (2013)], or as a Landau expansion $f_0(\Psi) \propto$

$\alpha\,(\Psi-\Psi_c)^2+\gamma\,(\Psi-\Psi_c)^4$, with α being temperature dependent, γ positive, and Φ_c the critical composition [Tsori and Leibler (2007)].

Optimising Eq. (6.7) over c_+ and c_-, the density becomes

$$f(\Psi,\phi)=f_m(\Psi)-\frac{1}{2}\epsilon(\Psi)(\nabla\phi)^2-k_{\mathrm{B}}T\,c_{0+}\exp(\beta\Delta u^{+}\Psi-\beta e\phi)\\ -k_{\mathrm{B}}T\,c_{0-}\exp(\beta\Delta u^{-}\Psi+\beta e\phi) \tag{6.8}$$

With a symmetric electrolyte: $c_{0+}=c_{0-}$, and if we assume the ions are similar in their interaction with the solvents: $\Delta u^{+}=\Delta u^{-}$, $f(\Psi,\phi)$ simplifies into

$$f(\Psi,\phi)=f_m(\Psi)-\frac{1}{2}\epsilon(\Psi)(\nabla\phi)^2-2k_{\mathrm{B}}T\,c_0\exp(\beta\Delta u\Psi)\cosh(\beta e\phi) \tag{6.9}$$

We recognize here a generalization of the well known Poisson–Boltzmann functional for a symmetric electrolyte. The description is adapted to analytical solutions but in the monophase region of the phase diagram $f(\Psi,\phi)$ is convex in Ψ but concave in ϕ. In complicated geometries if one wishes to minimize this free energy numerically one has to solve saddle point equations, simple minimization will not give the correct answer. We now implement the transformation introduced above from the potential ϕ to the electric displacement $\mathbf{D}$ and use the fact that the Legendre transform of cosh is

$$\mathcal{L}[A\cosh(B\phi)](\xi)=A\left[\xi/(AB)\,\mathrm{asinh}\,(\xi/AB)-\sqrt{(\xi/AB)^2+1}\right]\\ =Ag\,(\xi/AB) \tag{6.10}$$

After some calculation we find

$$f(\Psi,\mathbf{D})=f_m(\Psi)+\frac{\mathbf{D}^2}{2\epsilon(\Psi)}+2k_{\mathrm{B}}T\,c_0e^{\beta\Delta u\Psi}g\left(\frac{\mathrm{div}\,(\mathbf{D})e^{-\beta\Delta u\Psi}}{2c_0e}\right) \tag{6.11}$$

We have thus reached our objective: we have built an equivalent description of the system with the stationary conditions conserved and a local and convex function. The disadvantage is that there are more degrees of freedom in the vector field $\mathbf{D}$ than in the scalar field ϕ, but the advantage is that a global minimizing principle can be used and the functional can be directly programmed for the solution of the coupled electrostatic-phase separation problem.

We note that mean field description of the packing of DNA in a virus [Šiber and Podgornik (2008)] contains many similar theoretical features and is also amenable to similar transformations. In this problem the field Ψ corresponds to the square root of the monomer density.

6.3 From Poisson–Langevin to Polarization

We now consider theories of explicit Langevin dipoles and how these can be incorporated into the formulation of the free energy in terms of convex free energy functions. Recent work on improving the description of solvation of proteins [Azuara *et al.* (2008)] has considered an explicit model for the solvent in terms of Langevin dipoles. If we neglect the volume of ions and dipoles we find the free energy density for a mixture of symmetric ions and neutral dipoles as

$$f = \rho_{\mathrm{f}}\phi - \frac{\epsilon_0(\nabla\phi)^2}{2} - 2\lambda_{\mathrm{ion}}\cosh(\beta q\phi) - \lambda_{\mathrm{dip}}\frac{\sinh(\beta p_0|\nabla\phi|)}{\beta p_0|\nabla\phi|} \quad (6.12)$$

where to simplify the presentation we have neglected effects of finite ion size. The parameters λ are related to the chemical activities of the ions and the dipoles.

As in previous work [Maggs (2012)] we start by using a Lagrangian multiplier, $\mathbf{D}$ to replace $(\nabla\phi)$ by its electrostatic equivalent $-\mathbf{E}$. We find

$$f = \rho_{\mathrm{f}}\phi - \frac{\epsilon_0\mathbf{E}^2}{2} - g(\phi) - h(\mathbf{E}) + \mathbf{D}\cdot(\nabla\phi + \mathbf{E}) \quad (6.13)$$

where $h(\mathbf{E})$ is the free energy density due to the dipoles and $g(\phi)$ the free energy due to free ions. We now diverge from our previous treatment and introduce a new variable $\mathbf{P}$ which we will show is the physical polarization variable. We do this by performing a Legendre transform on $h(\mathbf{E})$ to find $\tilde{h}(\mathbf{P})$; we then find

$$f = \phi(\rho_{\mathrm{f}} - \mathrm{div}\,\mathbf{D}) - \frac{\epsilon_0\mathbf{E}^2}{2} - g(\phi) + \tilde{h}(\mathbf{P}) + \mathbf{E}\cdot(\mathbf{D} - \mathbf{P}) \quad (6.14)$$

Clearly by definition of the Legendre transform performing variations with respect to $\mathbf{P}$ on Eq. (6.14) gives Eq. (6.13).

We now perform two more transforms, first to eliminate the potential and second to eliminate the electric field **E**. We find

$$f = \frac{(\mathbf{D}-\mathbf{P})^2}{2\epsilon_0} + \tilde{h}(\mathbf{P}) + \tilde{g}(\rho_{\mathrm{f}} - \mathrm{div}\ \mathbf{D}) \tag{6.15}$$

In the absence of free ions the function $\tilde{g}$ reduces to the constraint of Gauss' law. This is exactly the form postulated in [Maggs and Everaers (2006)]. It is particularly transparent for understanding the physical limits on response functions [Dolgov *et al.* (1981); Kornyshev and Sutmann (1997)] and the origin of the negative dielectric constant observed in structured fluids.

We will now work on Eq. (6.15) to demonstrate its equivalence to other formulations of electrostatic interactions expressed in terms of the polarization **P**. To do this we will eliminate the variable **D**, which will bring us back to other more familiar forms for the electrostatic energy at the cost of re-introducing long-ranged dipole–dipole interactions between the polarization variables.

Eliminating the Displacement field

Let us work in the limit where linear response is valid. Expanding $\tilde{h}$ to quadratic order, we get

$$\tilde{h}(\mathbf{P}) = \frac{P^2}{2\epsilon_0\chi} \tag{6.16}$$

where χ is a material parameter. Taking variations of Eq. (6.14) with respect to **P** and then **E** we find that

$$\mathbf{P} = \epsilon_0\chi\mathbf{E}, \quad \epsilon_0\mathbf{E} = \mathbf{D} - \mathbf{P} \tag{6.17}$$

Thus the parameter χ is the electric susceptibility of the medium. The polarization variable is indeed playing the role we expect from standard treatments of Maxwell's equations. The free energy of the fluctuating dipoles (in the absence of free ions) can then be found from the functional

$$f = \frac{(\mathbf{D}-\mathbf{P})^2}{2\epsilon_0} + \frac{\mathbf{P}^2}{2\epsilon_0\chi(\mathbf{r})} - \phi(\mathrm{div}\ \mathbf{D} - \rho_{\mathrm{f}}) \tag{6.18}$$

where the last term is a Lagrange multiplier for the constraint of Gauss' law. On taking variations of Eq. (6.18) with respect to **D** we find that

$$\mathbf{D} - \mathbf{P} = -\epsilon_0\nabla\phi \tag{6.19}$$

Thus the free energy density can be written as

$$f = \epsilon_0 \frac{(\nabla\phi)^2}{2} + \frac{\mathbf{P}^2}{2\epsilon_0\chi} \tag{6.20}$$

where

$$\epsilon_0\nabla^2\phi = -\rho_{\rm f} + \text{div } \mathbf{P}$$
$$\phi(\mathbf{r}) = \int \frac{1}{4\pi\epsilon_0|\mathbf{r}-\mathbf{r}'|}\left(\rho(\mathbf{r}') - \text{div } \mathbf{P}(\mathbf{r}')\right)\, d^3\mathbf{r}' \tag{6.21}$$

We now substitute Eq. (6.21) in Eq. (6.20) and introduce the bare electric field $\mathbf{E}_0$ as follows: $\mathbf{E}_0 = -\nabla\phi_0$ with $\epsilon_0\nabla^2\phi_0 = -\rho_{\rm f}$. The free energy density can then be expressed in terms of the polarization as

$$U = \frac{1}{2}\int \frac{\text{div } \mathbf{P}(\mathbf{r})\text{div } \mathbf{P}(\mathbf{r}')}{4\pi\epsilon_0|\mathbf{r}-\mathbf{r}'|}\, d^3\mathbf{r}\, d^3\mathbf{r}' + \int\left\{\frac{\epsilon_0\mathbf{E}_0^2}{2} - \mathbf{E}_0\cdot\mathbf{P} + \frac{\mathbf{P}^2}{2\epsilon_0\chi(\mathbf{r})}\right\} d^3\mathbf{r} \tag{6.22}$$

This formulation of the free energy is widely used in theoretical chemistry and is that used by [Marcus (1956)].

The energy Eq. (6.22) can be expressed in an even more physically transparent manner by integrating by parts the first double integral to transfer the derivatives from the polarization to the function $1/|\mathbf{r}-\mathbf{r}'|$. If we do this we find that the double integral is transformed to

$$\frac{1}{2}\int \mathbf{P}(\mathbf{r})T(\mathbf{r}-\mathbf{r}')\mathbf{P}(\mathbf{r}')\, d^3\mathbf{r}\, d^3\mathbf{r}' \tag{6.23}$$

where the dipole operator is

$$T(\mathbf{r}) = \left[\frac{1-3|\mathbf{r}\rangle\langle\mathbf{r}|}{4\pi r^3\epsilon_0} + \frac{\delta(\mathbf{r})}{3\epsilon_0}\right] \tag{6.24}$$

We now proceed in a more abstract manner, considering that the polarization variables are assembled into a vector and the dipolar interactions form a matrix, $\bar{T}$. Eq. (6.22) is simply a quadratic form in $\mathbf{P}$, so that

$$U = \frac{\mathbf{P}(\bar{K}+\bar{T})\mathbf{P}}{2} - \mathbf{E}_0\cdot\mathbf{P} + \epsilon_0\frac{\mathbf{E}_0^2}{2} \tag{6.25}$$

with the diagonal matrix $\epsilon_0 K_{\mathbf{r},\mathbf{r}} = \chi_{\mathbf{r}}^{-1}$. If we now calculate the response of the polarization field to an external perturbation $\mathbf{E}_0$ we find

$$P = \frac{1}{\bar{K}+\bar{T}}\mathbf{E}_0 \tag{6.26}$$

The total electric field is then given by two contributions, the original imposed field $\mathbf{E}_0$ and that due to the dipole density $\mathbf{P}$

$$\mathbf{E} = \mathbf{E}_0 - \bar{T}\mathbf{P} \tag{6.27}$$

$$= \frac{\bar{K}}{\bar{K} + \bar{T}}\mathbf{E}_0 \tag{6.28}$$

We also use

$$\mathbf{D} - \mathbf{P} = \epsilon_0 \mathbf{E} \tag{6.29}$$

to find

$$\mathbf{D} = \frac{I + \epsilon_0 \bar{K}}{\bar{K} + \bar{T}}\mathbf{E}_0 \tag{6.30}$$

Again all these equations are non-local—since they involve the long-ranged operator $\bar{T}$—but we find that

$$\mathbf{D} = (1 + \chi_{\mathbf{r}})\epsilon_0 \mathbf{E} = \epsilon \mathbf{E} \tag{6.31}$$

a purely local constitutive equation between the electric field and the electric displacement.

We conclude that by careful study of the mean field equations arising from the formulation of the dielectric properties of a medium in Eq. (6.12) we have been able to derive the equivalence to the standard continuum formulation of electrostatic arising from Maxwell's equations.

6.4 Conclusions

We have shown that the Legendre transform can be used to translate between multiple forms of the energy in mean field theories. All the formulations are numerically equivalent but different forms put the emphasis on different degrees of freedom in electromagnetism. For numerical work it is advantageous to work with a formulation which is both convex and local. This is achieved in Poisson–Boltzmann theory by choosing the electric displacement $\mathbf{D}$ as the fundamental thermodynamic field. In this way all physical degrees of freedom can be treated in an equivalent manner in numerical solvers. It is no longer necessary to completely solve the electrostatic problem for each iteration of other external degrees of freedom. Very similar

conclusions have also been found in quantum chemistry [Stengel *et al.* (2009)].

We have also demonstrated that energy functionals for dielectrics can be translated into equivalent forms by introducing the physical polarization. We then mapped a linearized form of the theory to the Marcus energy function, widely used in the theoretical chemistry literature.

References

Azuara, C., Orland, H., Bon, M., Koehl, P. and Delarue, M. (2008). Incorporating dipolar solvents with variable density in Poisson-Boltzmann electrostatics, *Biophysical journal* **95**, 12, pp. 5587–5605.

Bonn, D., Otwinowski, J., Sacanna, S., Guo, H., Wegdam, G. and Schall, P. (2009). Direct observation of colloidal aggregation by critical casimir forces, *Phys. Rev. Lett.* **103**, p. 156101.

Courant, R. and Hilbert, D. (1989). *Methods of Mathematical Physics: Volume I, Chapter 4.9* (John Wiley and Sons).

Dolgov, O. V., Kirzhnits, D. A. and Maksimov, E. G. (1981). On an admissible sign of the static dielectric function of matter, *Rev. Mod. Phys.* **53**, 1, pp. 81–94.

Šiber, A. and Podgornik, R. (2008). Nonspecific interactions in spontaneous assembly of empty versus functional single-stranded rna viruses, *Phys. Rev. E* **78**, p. 051915.

Kornyshev, A. A. and Sutmann, G. (1997). Nonlocal dielectric saturation in liquid water, *Phys. Rev. Lett.* **79**, pp. 3435–3438.

Maggs, A. C. (2002). Dynamics of a local algorithm for simulating Coulomb interactions, *The Journal of Chemical Physics* **117**, 5, pp. 1975–1981.

Maggs, A. C. (2004). Auxiliary field monte carlo for charged particles, *The Journal of Chemical Physics* **120**, 7, pp. 3108–3118.

Maggs, A. C. (2012). A minimizing principle for the Poisson-Boltzmann equation, *EPL (Europhysics Letters)* **98**, 1, p. 16012.

Maggs, A. C. and Everaers, R. (2006). Simulating nanoscale dielectric response, *Phys. Rev. Lett.* **96**, 23, p. 230603.

Marcus, G., Samin, S. and Tsori, Y. (2008). Phase-separation transition in liquid mixtures near curved charged objects, *The Journal of Chemical Physics* **129**, 6, 061101.

Marcus, R. A. (1956). On the theory of oxidation-reduction reactions involving electron transfer. i, *J. Chem. Phys.* **24**, 5, pp. 966–978.

Onuki, A. (2006). Ginzburg-landau theory of solvation in polar fluids: Ion distribution around an interface, *Phys. Rev. E* **73**, p. 021506.

Samin, S., Galanis, J. and Yoav, T. (2013). *this volume: Electrostatics of liquid mixtures - phase transitions and colloidal stabilization* (Pan Standford).

Stengel, M., Spaldin, N. A. and Vanderbilt, D. (2009). Electric displacement as the fundamental variable in electronic-structure calculations, *Nature Physics* **5**, 4, pp. 304–308.

Tsori, Y. and Leibler, L. (2007). Phase-separation in ion-containing mixtures in electric fields, *Proceedings of the National Academy of Sciences* **104**, 18, pp. 7348–7350.

Zia, R. K. P., Redish, E. F. and McKay, S. R. (2009). Making sense of the Legendre transform, *American Journal of Physics* **77**, 7, pp. 614–622.

Chapter 7

Ionic Liquids and Ionic Liquid+Solvent Mixtures, Studied by Classical Density Functional Theory

Ryan Szparaga,[a] Clifford E. Woodward,[b] and Jan Forsman[a]
[a] *Theoretical Chemistry, Chemical Centre, S-221 00 Lund, Sweden*
[b] *School of Physical, Environmental and Mathematical Sciences, ADFA, University of New South Wales, Canberra, Australia*
ryan.szparaga@teokem.lu.se

7.1 Introduction

Ionic liquids (ILs) have been known to scientists for close to a century [Walden (1914)]. However, the area has recently attracted a flurry of activity. Their applications include: specific solvents for heterogeneous as well as homogeneous catalysis, selective solvents for removal of heavy metal contaminants, electrolytes in various electrochemical processes, and as dispersive agents for the stabilization of nanoparticles. In all of these applications, the behavior of ILs and IL solutions at interfaces is crucial to their performance [Maier *et al.* (2010)].

The strongly coupled conditions that are found in typical ILs would normally cause a simple salt to crystallize. The size and

Electrostatics of Soft and Disordered Matter
Edited by David Dean, Jure Dobnikar, Ali Naji, and Rudolf Podgornik

ISBN 978-981-4411-85-1 (Hardcover), 978-981-4411-86-8 (eBook)
www.panstanford.com

complex molecular architecture of ionic liquids, however, can lower the freezing point considerably below room temperature. In other words, in ILs steric interactions are generally of crucial importance, contrary to the case in most aqueous salt solutions. Thus, the convenient Poisson–Boltzmann approximation (PBA), which is commonly used to describe the latter systems, will normally fail for IL systems. Given these problems, many theoretical studies have instead resorted to detailed all-atom simulations. Unfortunately, these simulations require large computational resources and are not practical for rapid, exploratory calculations. Furthermore, the number of poorly known force field parameters is a major concern, and tends to thwart straightforward interpretations in terms of simple physical mechanisms. Here, we shall describe an alternative theoretical approach that aims to play a similar role for ILs as the PBA does for aqueous electrolytes. We will use rather coarse-grained models of ILs and IL+solvent mixtures. The inevitable loss of information, associated with an approximate theory, and a coarse-grained model, is outweighed by computational speed as well as a "complete" knowledge of the model system, including phase diagrams etc. The latter are very hard, if not practically impossible, to obtain by simulation methods.

7.2 Model and Theory

The polymer density functional theory (DFT) is designed to treat flexible [Woodward (1991)] as well as semi-flexible (Forsman and Woodward, 2003) chains, and has the added advantage that solvent molecules can be included explicitly. These can in turn be modeled as simple particles, but polymeric or star-like structures can also be accounted for. We shall here limit ourselves to neat ILs or IL+solvent mixtures wherein the latter are implicit, that is, the solvent enters via an incompressibility constraint. Specifically, the total local volume fraction, which is the sum of the IL and solvent components, is constant. This assumption removes the explicit dependence on the solvent density, and the free energy is effectively only a functional of the densities of the ionic liquid components. In other words, we use McMillan–Mayer arguments [McMillan and Mayer (1945)] to

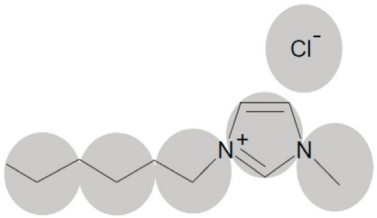

Figure 7.1 A schematic picture, illustrating our coarse-grained IL model, and its crude relation to a "real" IL.

integrate out the solvent degrees of freedom, wherein the osmotic pressure is directly related to the solvent chemical potential. We emphasize that our main findings in this study, with emphasis on a fluctuation-enhanced differential capacitance, are robust in the sense that they rely on well-established thermodynamic relations, which are independent of model details. Specifically, analogous behaviors can be established in a model comprising an explicit solvent representation.

With an oligomeric/simple particle model for the IL constituents, as illustrated in Fig. 7.1, the semi-grand free energy[a], $\mathcal{G}$, can be written as

$$\begin{aligned}\beta\mathcal{G} = {} & \beta\mathcal{F}_{cat}^{id}[N(\mathbf{R})] + \int n_a(\mathbf{r})(\ln[n_a(\mathbf{r})] - 1)d\mathbf{r} \\ & + \beta\mathcal{F}_{hs}[\bar{n}_m(\mathbf{r}), \bar{n}_a(\mathbf{r})] + \beta\int w_{LJ}(\mathbf{r})(n_m(\mathbf{r}) + n_a(\mathbf{r}))d\mathbf{r} \\ & + \frac{\beta}{2}\int\int{}' \sum_g \sum_d n_g(\mathbf{r})n_d(\mathbf{r}')\phi_{LJ}(|\mathbf{r}-\mathbf{r}'|)d\mathbf{r}d\mathbf{r}' \\ & + \frac{\beta}{2}\int\int \sum_\gamma \sum_\delta n_\gamma(\mathbf{r})n_\delta(\mathbf{r}')\Phi_{el}^{\gamma\delta}(|\mathbf{r}-\mathbf{r}'|)d\mathbf{r}d\mathbf{r}' \\ & + \int \sum_\gamma (\beta V_{el}(\mathbf{r}) + f_{DHH}[\bar{n}_\gamma(\mathbf{r})] - \beta\mu_\gamma)n_\gamma(\mathbf{r})d\mathbf{r} \qquad (7.1)\end{aligned}$$

The sums extend over all particle types, except where Greek subscripts are used, whereby the sums only include the charged monomers.

[a]We use the notation "semi-grand" as the density is allowed to fluctuate, though subject to the constraint of overall electroneutrality.

The first two terms on the RHS of Eq. 7.1 represent the *exact* ideal contributions to the free energy, $\beta\mathcal{G}^{id}$, due to cations and anion. We define the (approximate) excess free energy, $\mathcal{G}^{ex}$, as: $\beta\mathcal{G}^{ex} = \beta\mathcal{G} - \beta\mathcal{F}^{id}_{cat}[N(\mathbf{R})] + \int n_a(\mathbf{r})(\ln[n_a(\mathbf{r})] - 1)d\mathbf{r}$. As the cations are made up of chain like molecules, their ideal free energy, $\mathcal{F}^{id}_{cat}[N(\mathbf{R}]$, must reflect this. It can be exactly expressed as a functional of the density distribution $N(\mathbf{R})$, where $\mathbf{R} = (\mathbf{r}_1, \ldots, \mathbf{r}_5)$, with $\mathbf{r}_i$ the coordinate of the ith cationic monomer, [Woodward (1991)].

$$\beta\mathcal{F}^{id}_{cat}[N(\mathbf{R})] = \int N(\mathbf{R})\,(\ln[N(\mathbf{R})] - 1)\,d\mathbf{R} + \beta \int N(\mathbf{R})V_B(\mathbf{R})d\mathbf{R}, \tag{7.2}$$

where $V_{\mathrm{B}}(\mathbf{R})$ is the "bonding potential" that maintains the oligomeric structure. This is assumed to be a freely jointed chain in our model. The third term in Eq. (7.1) is the steric contribution, $\mathcal{F}_{hs}[\bar{n}_m(\mathbf{r}), \bar{n}_a(\mathbf{r})]$, which describes the hard core interactions between the fluid species. As in other treatments [Forsman *et al.* (2011b)] it is assumed to be a functional only of the total monomer densities of the cationic oligomer, $n_m(\mathbf{r})$ and the anion density, $n_a(\mathbf{r})$. Note that these appear as weighted densities in the functional (denoted by the *bar* over densities). We choose the simple weighting scheme originally used by Nordholm, [Nordholm *et al.* (1980)] which gives a simple and reasonably accurate representation of excluded volume effects. For example, the weighted monomer density, $\bar{n}_m(\mathbf{r})$, is given by,

$$\bar{n}_m(\mathbf{r}) = \frac{3}{4\pi\sigma^3} \int_{|\mathbf{r}-\mathbf{r}'|<\sigma} n_m(\mathbf{r}')\mathbf{d}\mathbf{r}' \tag{7.3}$$

The explicit form for $\mathcal{F}_{hs}$ is obtained by integrating a suitably modified generalized Flory-dimer equation of state [Wichert *et al.* (1996); Forsman and Woodward (2004)]. In this work, we have set $\sigma = 5$ Å.

The fourth and fifth terms represent the non-electrostatic, solvent-mediated Hamaker contributions to the free energy. The prime above the L–J pair interaction integral, indicates that regions where $|\mathbf{r} - \mathbf{r}'| \leq \sigma$ should be excluded. Specifically, we have used an effective L–J interaction, $\phi_{LJ}(r) = 4\epsilon_{LJ}((\sigma/r)^{12} - (\sigma/r)^6)$, with $\epsilon_{LJ} = 120k_BK$. The effective L–J wall potential, w_{LJ} (acting on

monomers and counterions), is modeled by the same LJ parameters, assuming cubic close packing within the electrode.

The sixth term gives the Coulombic interaction between fluid particles, while the quantity $V_{\rm el}$ represents the electrostatic interaction between particles and the electrodes. These two terms describe a mean field treatment for the electrostatics, and would be the only contributions in a conventional Poisson–Boltzmann treatment of charged fluids. In dense ionic liquids, and other highly-coupled charged fluids, the neglect of electrostatic correlations constitutes a significant error. While we are considering solutions of ILs, the electrostatic coupling is large, due to the relatively low dielectric constant, $\epsilon_{\rm r} = 18$, that we have used for the IL+solvent mixture. We shall estimate electrostatic correlations using concepts derived from the "hole corrected Debye–Hückel" theory [Nordholm (1984); Penfold and Nordholm (1991)] for the one-component plasma. f_{DHH} is the electrostatic correlation free energy per charged particle and is given by

$$4\beta f_{DHH}[\bar{n}_\alpha(\mathbf{r})] = 1 + \frac{2\pi}{3\sqrt{3}} - \ln[3] + \ln[\omega^2 + \omega + 1] - \omega^2 - \frac{2}{\sqrt{3}}\tan^{-1}[\frac{2\omega+1}{\sqrt{3}}] \tag{7.4}$$

where $\omega = [1 + c\bar{n}_\alpha^{1/2}]^{1/3}$ and $c = |\frac{q_\alpha}{e}|^3(3l_B)^{3/2}\sqrt{\frac{4\pi}{3}}$. The Bjerrum length is, $l_{\rm B} = e^2\beta/(4\pi\epsilon_0\epsilon_r)$.

Finally, μ_α is the electrochemical potential of the charged species α and the terms containing these quantities maintain chemical equilibrium with the bulk solution and electroneutrality via the Donnan equilibrium.

We will in this work focus on an IL+solvent mixture in narrow electrode capillaries. An electrode pore is modeled by two charged flat surfaces, separated a distance h. The direction normal to the surfaces is defined as z, while the x, y directions are integrated out, using standard mean field arguments. Since the cation has an oligomeric structure, we have utilized polymer density functional methods to work out monomer density profiles [Woodward (1991)]. For each monomer, i, along the chain, an auxiliary "end monomer field", $c(i, z)$ is constructed from a series of integrations of Boltzmann-weighted distributions, across spherical surfaces, each

with a diameter σ (one bond length). Such an integral represents a sum of Boltzmann-weighted probabilities, for the $(i-1)$-mer that is connected to end i. The final probability for monomer i to be located at z is obtained as a product of the two end probability fields, $c(i, z)$ and $c(6-i, z)$. This means that the total monomer density profile is given by the following sum (ρ_p^b is the bulk polymer density):

$$n_m(z) = \rho_p^b \sum_{i=1}^{5} c(i, z)c(6-i, z) \tag{7.5}$$

$c(i, z)$ fulfills a recursive relation, $c(1, z) = 1$ and for $i \in [2, 5]$:

$$c(i, z) = e^{\lambda_{i,b}} \int c(i-1, z')T_{i,i-1}(z', z)dz' \tag{7.6}$$

where the connectivity matrix $T_{i,i-1}(z', z)$ is defined in terms of the excess monomer free energies $\lambda_i(z)$ ($\lambda_{i,b}$ is the bulk value):

$$T(z', z) = \frac{1}{2\sigma} e^{-\lambda_i(z)/2} \Theta(|z-z'|-\sigma) e^{-\lambda_{i-1}(z')/2} \tag{7.7}$$

$$\lambda_i(z) = \frac{\delta \mathcal{G}^{ex}[n(z)]}{\delta n_i(z)} \tag{7.8}$$

We note that the second monomer requires special consideration (different local field, λ), as it is charged.

The semi-grand free energy describes an electrode with a fixed surface charge density. The electrode potential is then determined by the response of the fluid, which minimizes the free energy. The total density of the fluid ions can fluctuate, while their total excess charge is constrained to be equal in magnitude, but opposite in sign to that of the electrode. However, many experiments are performed under constant surface potential. In this case the surface charge density is allowed to fluctuate, while the surface potential remains constant. This corresponds to a Grand Ensemble, with the appropriate thermodynamic potential given by the following Legendre transform of the semi-grand free energy,

$$\Omega = \mathcal{G} - \sigma_s \psi_s. \tag{7.9}$$

where the surface potential, ψ_s, is fixed. Ω denotes the Grand potential per unit electrode area.

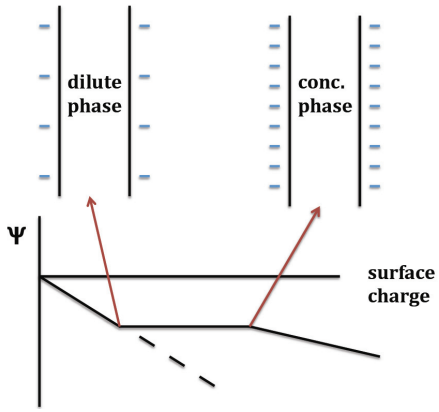

Figure 7.2 An illustration of how the surface charge density might vary between concentrated and dilute phases in an electrode pore. The lower graph highlights the fact that the applied (surface) potential is identical, for both phases.

The differential capacitance, C_{D}, is a thermodynamic response function, defined as,

$$\begin{aligned} C_{\mathrm{D}} &= \partial\sigma_{\mathrm{s}}/\partial\Psi_{\mathrm{s}} \\ &= \partial^2\mathcal{G}/\partial\Psi_{\mathrm{s}}^2 \\ &= \left\{\partial^2\Omega/\partial\sigma_{\mathrm{s}}^2\right\}^{-1} \end{aligned} \tag{7.10}$$

Experimentally, this quantity is often measured as a function of the surface potential, Ψ_{s}. If the electrolyte undergoes a phase change, finite fluctuations in the surface charge density occur for a very small potential change (ideally zero), with a corresponding spike in the differential capacitance. This is because the surface charge density, at a given surface potential, generally is different for the two different phases. This is illustrated in Fig. 7.2, for the case of a capillary-induced phase separation (CIPS) where a dilute phase in a narrow pore of an electrode, may undergo a transition to a concentrated phase (or vice versa).

Here, we see that while the surface potential is identical for the dilute and concentrated phases, the surface charge density, σ_{s}, is not.

In Fig. 7.3, we exemplify how the grand potential, Ω, might vary with "density". This is just a cartoon, illustrating qualitatively

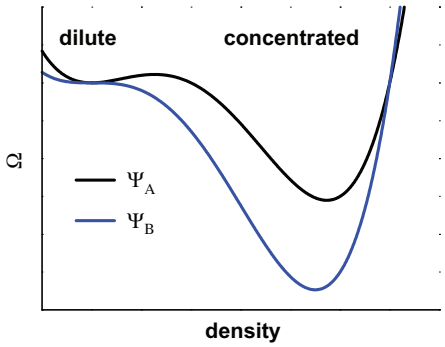

Figure 7.3 A cartoon of how the grand potential, Ω, might vary with density (average IL density in pore, and/or surface charge density). In these cases, the high density phase is more stable, and the dilute phase spinodal is reached for a potential Ψ_B.

relevant features, so "density" could in this case either mean "average IL pore density", or "surface charge density".

7.3 Results

Numerous direct comparisons with simulation results have demonstrated that the DFT is able to predict differential capacitance as well as detailed structural properties, with a remarkably high accuracy [Forsman *et al.* (2011b,a)]. Here, we will instead focus on some interesting predictions obtained via our DFT of IL+solvent mixtures. First, in Fig. 7.4, we give an example of monomer density distributions of a dilute and a concentrated phase, in the vicinity of a CIPS. The surface charge density is actually the same for both systems, but it should be noted that the surface potential ("applied potential") is not.

A specific example of fluctuation-enhanced differential capacitance, is given in Fig. 7.5.

Upon increasing the surface potential from zero to positive values, the dilute phase becomes metastable, and as the spinodal is approached, C_D will display a dramatic increase, as the system undergoes CIPS. At higher potentials, there is only the concentrated phase. If we instead make the surface potential increasingly

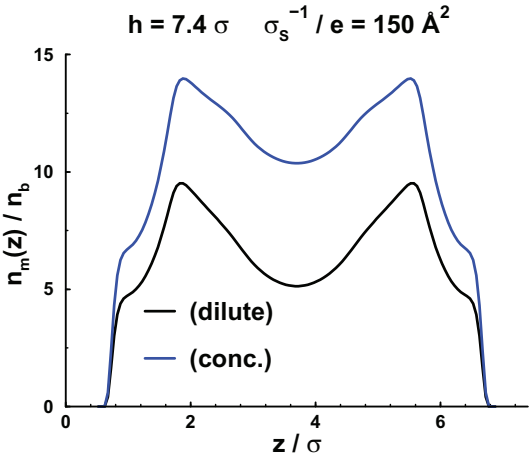

Figure 7.4 Monomer density distributions for the dilute and the concentrated phase, at a relatively high positive surface charge density, $\sigma_s = 152e/\text{Å}^2$. Note that the surface potential is different for these two phases. n_b is the bulk monomer density.

more negative, starting from a zero level, the corresponding C_D-peak is finite and reversible. This is because the system actually never undergoes a first-order transition, although CIPS-proximity is implied by the height of the peak. The peak established at a

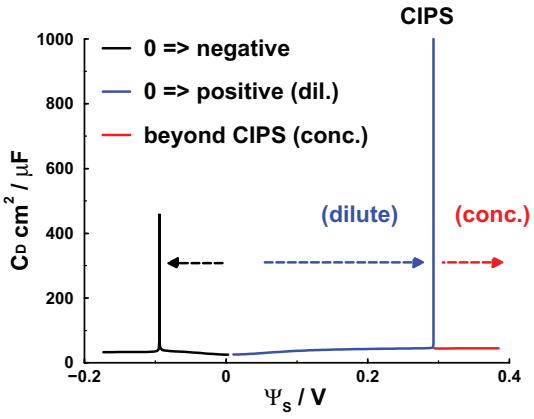

Figure 7.5 Fluctuation-enhanced differential capacitance.

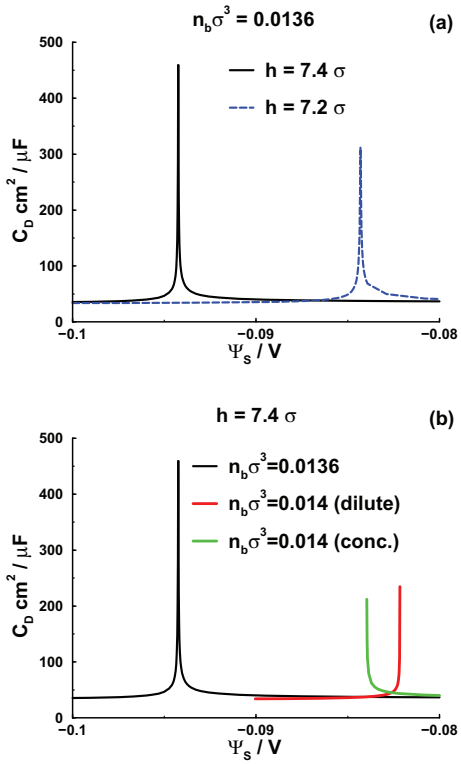

Figure 7.6 (a) Second-order (reversible) transitions, with concomitant finite C_D peaks, for two different pore sizes, at constant bulk conditions. (b) Here we see, for a given pore width, how a first-order CIPS may disappear at a lower bulk IL concentration. Nevertheless, it does show some reflection of the nearby critical point, that is, although the capacitance no longer diverges, it does display a rather distinct peak. Note the considerable hysteresis effect of the differential capacitance, that is typically obtained for first-order transitions.

positive potential, however, does correspond to a first-order CIPS, and is thus diverging. In this case, there are inevitable hysteresis effects. Specifically, the spinodal for the dilute → concentrated transition is reached at a different (larger) surface potential than the corresponding concentrated → dilute spinodal. This mechanism is illustrated in

Figure 7.6, where we also exemplify how a first-order irreversible CIPS may vanish for narrow pores and/or lower bulk densities. Such a response is not unexpected, but it does serve to illustrate the complexities one might encounter in an experimental setup, where pores generally are polydisperse. Nevertheless, such complexities also suggest interesting possibilities, and for a system with a range of pore sizes, one might observe a broad peak, which in turn could be of significant practical interest. Note that one of the major drawbacks of supercapacitors, as compared with batteries, is that the former displays a strongly varying potential upon discharging, which is a major problem for many applications.

References

Forsman, J., Szparaga, R., Nordholm, S., Woodward, C. E. and Penfold, R. (2011a). *Ionic Liquids - Classes and Properties* (InTech, Rijeka), pp. 127–150.

Forsman, J. and Woodward, C. E. (2003). An improved density functional description of hard sphere polymer fluids at low density, *J. Chem. Phys.* **119**, p. 1889.

Forsman, J. and Woodward, C. E. (2004). Evaluating the accuracy of a density functional theory of polymer density functional theory of polymer solutions with additive hard sphere diameters, *J. Chem. Phys.* **120**, p. 506.

Forsman, J., Woodward, C. E. and Trulsson, M. (2011b). A classical density functional theory of ionic liquids, *J. Phys. Chem. B* **115**, p. 4606.

Maier, F., Cremer, T., Kolbeck, C., Lovelock, K. R. J., Paape, N., Schulz, P. S., Wasserscheid, P. and Steinruck, H.-P. (2010). Insights into the surface composition and enrichment effects of ionic liquids and ionic liquid mixtures. *Phys. Chem. Chem. Phys.* **12**, p. 1905.

McMillan, W. G. and Mayer, J. E. (1945). The statistical thermodynamics of multicomponent systems, *J. Chem. Phys.* **13**, p. 276.

Nordholm, S. (1984). Simple analysis of the thermodynamic properties of the one-component plasma, *Chem. Phys. Lett.* **105**, p. 302.

Nordholm, S., Johnson, M. and Freasier, B. C. (1980). Generalized van der waals theory. iii. the prediction of hard sphere structure, *Aust. J. Chem.* **33**, p. 2139.

Penfold, R. and Nordholm, S. (1991). A simple analysis of the classical hard sphere one component plasma. i. hole corrected debye-hückel theory, *J. Chem. Phys.* **95**, p. 2048.

Walden, P. (1914). Über die molekulargrösse und elektrische leitfähigkeit einiger geschmolzenensalze. *Bull. Acad. Imper. Sci. St. Petersburg* **8**, p. 405.

Wichert, J. M., Gulati, H. S. and Hall, C. K. (1996). Binary hard chain mixtures. i. generalized flory equations of state, *J. Chem. Phys.* **105**, p. 7669.

Woodward, C. E. (1991). A density functional theory for polymers: Application to hard chain-hard sphere mixtures in slit-like pores, *J. Chem. Phys.* **94**, p. 3183.

Chapter 8

The Wigner Strong-Coupling Approach

Ladislav Šamaj[a,b] and Emmanuel Trizac[b]
[a] *Institute of Physics, Slovak Academy of Sciences, Bratislava, Slovakia*
[b] *LPTMS, Université Paris-Sud, UMR CNRS 8626, Orsay, France*
Ladislav.Samaj@savba.sk

8.1 Model

Two equivalent charges in vacuum repel each other. Let the two charges, say macro-ions, be immersed in an electrolyte of mobile micro-ions which is in thermal equilibrium at some inverse temperature $\beta = 1/(k_{\mathrm{B}}T)$. Since the micro-ions are repelled/attracted by the macro-ions, the Coulomb interaction between macro-ions is modified by tracing out microscopic degrees of freedom. An important question is whether the ensuing effective interaction can become attractive in some distance range between macro-ions. This question is essential in various fields of colloid science from physics (1) to biochemistry (2). It was first answered from numerical investigations (3) showing that the effective interaction, which is always repulsive in the high-temperature (weak-coupling) region described adequately by the Poisson–Boltzmann mean field theory (4), can become attractive at low temperatures (strong-coupling regime).

Electrostatics of Soft and Disordered Matter
Edited by David Dean, Jure Dobnikar, Ali Naji, and Rudolf Podgornik

ISBN 978-981-4411-85-1 (Hardcover), 978-981-4411-86-8 (eBook)
www.panstanford.com

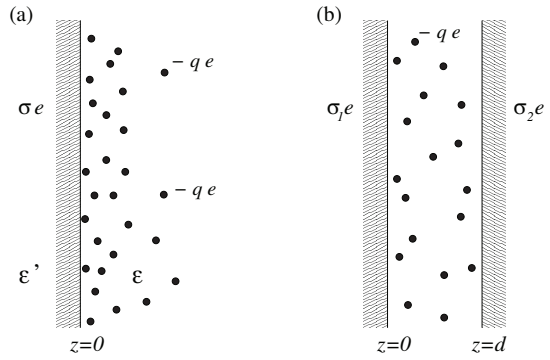

Figure 8.1 The two geometries considered: (a) one plate and (b) two parallel plates at distance d.

A simplified model system may be proposed, for the sake of analytical understanding. Firstly, spherical macro-ions are usually big colloids of several thousand elementary charges e, and we represent their boundaries as plates with the fixed surface charge density $\sigma e \simeq$ electron/(nm)^2. Secondly, we shall consider the no-salt regime, with only one type of mobile micro-ions (counterions) having charge $-qe$ (valence $q = 1, 2, \ldots$), under the requirement of global electroneutrality.

The considered 3D geometries are shown in Fig. 8.1.

- In the one-plate geometry (a), the charged (x, y)-surface is located at $z = 0$. The mobile counterions, confined to the half-space $z > 0$, are immersed in a solvent of dielectric permittivity ϵ. In realistic biological systems, the permittivity of the polarizable colloid $z < 0$ ($\epsilon' \leq 10$) is much smaller than that of the solvent ($\epsilon \simeq 80$ for water).
- In the geometry of two parallel plates (b), the counterions are confined to the region $0 < z < d$. Global electroneutrality requires that the surface charge densities of the plates are constrained by $\sigma_1 + \sigma_2 > 0$. Only the homogeneous dielectric case $\epsilon = \epsilon'$ will be worked out for this geometry.

Here, we shall concentrate on the strong-coupling (SC) regime, defined as the limit where the appropriately defined coupling

parameter Ξ [see Eq. (8.3)] is large. Based on a field-theoretical representation, Netz and his collaborators (5) proposed a virial strong-coupling (VSC) approach. A comparison with Monte–Carlo (MC) simulations confirms the adequacy of the leading SC behavior which is a single-particle theory in the potential of the charged wall(s). However, the VSC method fails to describe the subleading SC corrections. The *leading* order of the VSC theory was generalized to asymmetrically charged plates, image charge effects, presence of salt and curved (spherical and cylindrical) geometries (6).

Recently, we put forward a different SC approach (7; 8) based on a large coupling expansion in particle deviations around the ground state formed by the 2D Wigner crystal of counterions at the plate(s). It was hence coined Wigner–SC (WSC). It will be shown that in doing so, one can address situations where the VSC approach is invalid, such as the one plate problem with dielectric mismatch. In cases where the VSC provides the correct dominant SC behavior, the WSC yields the exact subsequent correction, a task where VSC is unsuccessful. The reason is, in both cases and even if the dominant SC behavior stems from a single-particle picture, that the problem should be envisioned as an N-body one, and does not comply by the virial idea that two-body interactions are a perturbative correction to one-body results. In this respect, the failure of the virial route is here reminiscent of its breakdown for critical property studies of electrolytes (9).

8.2 One-Plate Geometry

8.2.1 *Homogeneous Dielectric Case*

First we consider the one-plate geometry in Fig. 8.1 (a) with no image charges, $\epsilon' = \epsilon$. There are two relevant length scales describing counterion interactions. The potential energy of an isolated counterion at distance z from the wall is given, in Gauss units, by the dimensionless relation

$$\beta E_1(z) = \frac{2\pi q \beta e^2 \sigma}{\epsilon} z \equiv \frac{z}{\mu} \equiv \widetilde{z}, \tag{8.1}$$

where μ is the Gouy–Chapman length. The interaction energy of two counterions at distance r is given by

$$\beta E_2(r) = \beta \frac{(qe)^2}{\epsilon} \frac{1}{r} \equiv \frac{q^2 \ell_B}{r}, \tag{8.2}$$

where $\ell_B = \beta e^2/\epsilon$ is the Bjerrum length. This defines another length scale $q^2\ell_B$. The dimensionless coupling parameter Ξ, quantifying the strength of electrostatic correlations, is defined as the ratio

$$\Xi = \frac{q^2 \ell_B}{\mu} = 2\pi q^3 \ell_B^2 \sigma. \tag{8.3}$$

The SC regime $\Xi \gg 1$ can be realized in a number of ways, for example, low temperatures or large valence q/surface charge density σe.

We are interested in the counterion density profile defined by $\rho(\mathbf{r}) \equiv \rho(z) = \langle \sum_{j=1}^{N} \delta(\mathbf{r} - \mathbf{r}_j) \rangle$, where j runs over N counterions at spatial positions $\{\mathbf{r}_j\}$ and $\langle \cdots \rangle$ means thermal equilibrium average. The profile will be considered in the rescaled form $\widetilde{\rho}(\widetilde{z}) \equiv \rho(\mu\widetilde{z})/(2\pi\ell_B\sigma^2)$. The electroneutrality condition $q\int_0^\infty \mathrm{d}z\, \rho(z) = \sigma$ can be rewritten as follows: $\int_0^\infty d\widetilde{z}\, \widetilde{\rho}(\widetilde{z}) = 1$. The contact theorem (10) reads as $\beta P = \rho(0) - 2\pi\ell_B\sigma^2$ and since the fluid pressure P vanishes for a single isolated double layer, we have $\widetilde{\rho}(0) = 1$.

According to the VSC method (5), the density profile of counterions can be formally expanded in the SC regime as a power series in $1/\Xi$:

$$\widetilde{\rho}(\widetilde{z}, \Xi) = \widetilde{\rho}_0(\widetilde{z}) + \frac{1}{\Xi}\widetilde{\rho}_1(\widetilde{z}) + O\left(\frac{1}{\Xi^2}\right), \tag{8.4}$$

where

$$\widetilde{\rho}_0(\widetilde{z}) = \mathrm{e}^{-\widetilde{z}}, \quad \widetilde{\rho}_1(\widetilde{z}) = \mathrm{e}^{-\widetilde{z}} \left(\frac{\widetilde{z}^2}{2} - \widetilde{z}\right). \tag{8.5}$$

The leading single-particle term $\widetilde{\rho}_0(\widetilde{z})$ is in agreement with MC simulations, the subleading $\widetilde{\rho}_1(\widetilde{z})$ has the expected functional form, butthe prefactor $1/\Xi$ is incorrect. In particular, the MC data (5) were treated by using $\widetilde{\rho}(\widetilde{z}, \Xi) - \widetilde{\rho}_0(\widetilde{z}) = \widetilde{\rho}_1(\widetilde{z})/\theta$ with θ as a fitting parameter. As seen in the log–log plot of Fig. 8.2, the MC numerical values of θ (filled circles) are much smaller than the VSC prediction $\theta = \Xi$ (dashed line). Note that the difference even grows with increasing Ξ.

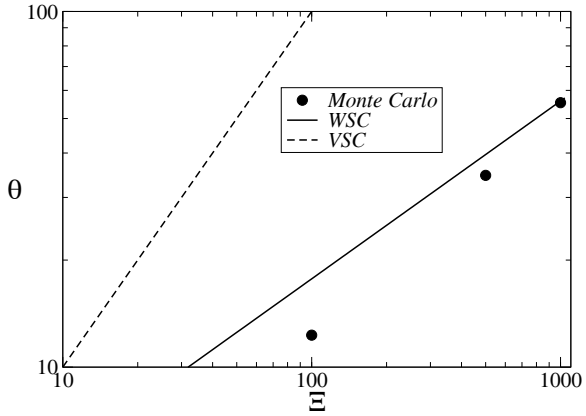

Figure 8.2 The fitting parameter θ versus the coupling constant Ξ.

The WSC approach (7) is based on the fact that in the asymptotic ground-state limit $\Xi \to \infty$ all counterions collapse on the oppositely charged surface $z = 0$, forming a 2D hexagonal (equilateral triangular) Wigner lattice (11). The lattice points are indexed by $j = (j_1, j_2)$, j_1 and j_2 being any two integers: $\mathbf{R}_j \equiv (R_j^x, R_j^y) = j_1\boldsymbol{a}_1 + j_2\boldsymbol{a}_2$, where $\boldsymbol{a}_1 = a(1, 0)$ and $\boldsymbol{a}_2 = (a/2)(1, \sqrt{3})$ are the primitive translation vectors of the Bravais lattice. The lattice spacing a is fixed by the condition of global electroneutrality, $q = \sqrt{3}a^2\sigma/2$. Note that in the large-Ξ limit, the lateral distance between nearest-neighbor counterions in the Wigner crystal a is much larger than the characteristic length μ in the perpendicular z-direction, $a/\mu \propto \sqrt{\Xi} \gg 1$.

We denote the ground-state energy of counterions on the Wigner lattice plus the fixed surface charge by E_0. For Ξ large but not infinite, the vibrations of counterions around their lattice positions play a role. Let us first shift one of the particles, say $j = 1$, from its Wigner lattice position ($\mathbf{R}_1$, $z_1 = 0$) by a small vector $\delta\mathbf{r} = (x, y, z > 0)$ ($|\delta\mathbf{r}| \ll a$) and look for the corresponding change in the total energy $\delta E = E - E_0 \geq 0$. The first contribution to δE comes from the one-body interaction of the shifted counterion with the fixed surface charge density,

$$\delta E_1(z) = \frac{2\pi q e^2 \sigma}{\epsilon} z. \tag{8.6}$$

The second contribution comes from the two-body interactions of the shifted counterion 1 with all other particles $j \neq 1$ on the 2D hexagonal lattice:

$$\delta E_2(x, y, z) = \frac{(qe)^2}{\epsilon} \sum_{j\neq 1} \left[\frac{1}{\sqrt{(R_{1j}^x + x)^2 + (R_{1j}^y + y)^2 + z^2}} - \frac{1}{R_{1j}} \right]$$
$$\sim \frac{(qe)^2}{2\epsilon a^3} C_3 \left[\frac{1}{2}(x^2 + y^2) - z^2 \right], \tag{8.7}$$

where $\mathbf{R}_{1j} \equiv \mathbf{R}_1 - \mathbf{R}_j$ and the dimensionless lattice sum $C_3 = \sum_{j\neq 1}(R_{1j}/a)^{-3} = 11.034\ldots$. It can be shown (7) that harmonic deviations in the (x, y) plane and higher-order deviation terms do not contribute to the first SC correction and we can write

$$-\beta\delta E = -\widetilde{z} + \frac{3^{3/4} C_3}{2(4\pi)^{3/2}} \frac{1}{\sqrt{\Xi}} \widetilde{z}^2 + \cdots . \tag{8.8}$$

The generalization to shifts of all $j = 1, 2, \ldots$ counterions from their lattice positions $(\mathbf{R}_j, z_j = 0)$ by a small vector $\delta\mathbf{r}_j = (x_j, y_j, z_j > 0)$ $(|\delta\mathbf{r}_j| \ll a)$ is straightforward and leads to

$$-\beta\delta E \sim -\sum_j \widetilde{z}_j + \frac{3^{3/4}}{2(4\pi)^{3/2}} \frac{1}{\sqrt{\Xi}} \sum_{j<k} \frac{(\widetilde{z}_j - \widetilde{z}_k)^2}{(|\mathbf{R}_j - \mathbf{R}_k|/a)^3} + \cdots . \tag{8.9}$$

Two-body interactions are only a perturbation with respect to the one-body terms, which explains why a single-particle picture provides the leading SC behavior. Introducing a generating field (7), the cumulant perturbation expansion yields the density profile

$$\widetilde{\rho}(\widetilde{z}) = \underbrace{\mathrm{e}^{-\widetilde{z}}}_{\widetilde{\rho}_0(\widetilde{z})} + \underbrace{\frac{3^{3/4}}{(4\pi)^{3/2}} \frac{C_3}{\sqrt{\Xi}}}_{1/\theta} \underbrace{\mathrm{e}^{-\widetilde{z}} \left(\frac{\widetilde{z}^2}{2} - \widetilde{z} \right)}_{\widetilde{\rho}_1(\widetilde{z})} + \cdots . \tag{8.10}$$

Comparing with the VSC result (8.4) we see that the first corrections have the same functional dependence on $\widetilde{z}$, but different prefactors. In terms of the fitting parameter θ, the VSC estimate $\theta = \Xi$ is compared with the present value

$$\theta = \frac{(4\pi)^{3/2}}{3^{3/4}} \frac{1}{C_3} \sqrt{\Xi} = 1.771\ldots \sqrt{\Xi}. \tag{8.11}$$

As seen from Fig. 8.2, this formula (solid curve) is in full agreement with MC data (filled circles).

8.2.2 *Dielectric Inhomogeneity*

In the inhomogeneous dielectric case, we define the dielectric jump between the solvent and the wall as $\Delta = (\epsilon - \epsilon')/(\epsilon + \epsilon')$. The image of a charge e at position $\mathbf{r} = (x, y, z > 0)$ has the charge of strength $e^* = e\Delta$ and is localized at $\mathbf{r}^* = (x, y, -z < 0)$. Counterions interact via the Coulomb interaction potential $u(\mathbf{r}, \mathbf{r}') = u_0(\mathbf{r}, \mathbf{r}') + u_{\rm im}(\mathbf{r}, \mathbf{r}')$, where

$$u_0(\mathbf{r}, \mathbf{r}') = \frac{1}{\varepsilon|\mathbf{r} - \mathbf{r}'|}, \quad u_{\rm im}(\mathbf{r}, \mathbf{r}') = \frac{\Delta}{\varepsilon|\mathbf{r}^* - \mathbf{r}'|} \tag{8.12}$$

are the direct and image Coulomb potentials, respectively. The total interaction energy of the counterions at positions $\{\mathbf{r}_j\}_{j=1}^N$ in the half-space $z > 0$ reads

$$E = \sum_{j=1}^{N} \left[\frac{2\pi q e^2 \sigma}{\varepsilon}(1 + \Delta) z_j + \frac{(qe)^2}{4\varepsilon} \frac{\Delta}{z_j} \right] + \frac{(qe)^2}{2} \sum_{\substack{j,k=1 \\ (j \neq k)}}^{N} u(\mathbf{r}_j, \mathbf{r}_k). \tag{8.13}$$

Here, the two one-body terms in the square brackets originate in the interaction of the particle with the surface charge plus its image (therefore the factor $1 + \Delta$) and with its own charge image.

We shall restrict ourselves to the case of repulsive $\Delta > 0$ image charges which is of special interest. The counterions on the one hand are attracted to the wall by the fixed surface charge σe and on the other hand repelled from the wall by their images. It is natural to assume that the ground state of the system is formed by the standard 2D hexagonal Wigner crystal of counterions with lattice spacing a, localized at some nonzero distance l from the wall. This distance is determined by balancing the attractive and repulsive forces. The energy per particle for the Wigner crystal at distance z from the wall is given by

$$\frac{\beta E_0(z)}{N} = (1 + \Delta)\frac{z}{\mu} + \frac{q^2 \ell_{\rm B}}{2} \sum_{j \neq 1} \frac{1}{R_{1j}} + \frac{q^2 \ell_{\rm B}}{2} \Delta \left[\frac{1}{2z} + \sum_{j \neq 1} \frac{1}{\sqrt{R_{1j}^2 + (2z)^2}} \right]. \tag{8.14}$$

On the RHS, the first term describes the interaction of the particle with the surface charge, the second (z-independent) one the direct

interaction with all other particles, and the last two terms the interaction of the particle with its own self-image and with images of all other particles. The distance of the Wigner crystal from the wall l is determined by the stationarity condition $\partial_z[\beta E_0(z)/N]|_{z=l} = 0$. Introducing the variable $t = 2l/a$, this requirement can be written as

$$\sum_{j,k=-\infty}^{\infty} \frac{1}{[t^2 + (j^2 + jk + k^2)]^{3/2}} = \frac{4\pi}{\sqrt{3}} \frac{1+\Delta}{\Delta} \frac{1}{t}, \tag{8.15}$$

where the hexagonal structure was used. The lattice sum appearing here can be represented as an integral over Jacobi theta functions (8), which can be evaluated with a high precision. The numerical solution of Eq. (8.15) for the extreme case $\Delta = 1$ is $t \simeq 0.295$. In the limit of small Δ, we have $t \sim 3^{1/4}\sqrt{\Delta/(4\pi)}$. To examine the ground-state stability of the Wigner crystal along the z direction, we shift one particle (say $j = 1$) from its lattice position by a small deviation $z-l$. The corresponding change in the energy $\beta\delta E = (z-l)^2/\xi^2$ turns out to be positive. The Wigner lattice is therefore thermodynamically stable, for all $\Delta \in [0, 1]$ (8).

The distance of the Wigner crystal from the wall l is of the order of the Wigner lattice spacing a. Shifting a particle from its lattice position along the z-axis, its pair interactions with all counterions is of the same relevance as its one-body interaction with the charged wall. We thus anticipate the failure of the VSC route. In the leading WSC order, we consider the particle potential induced by the charged wall plus the frozen hexagonal Wigner crystal (excluding the particle under consideration) at distance l from the wall:

$$\beta u(z) = (1+\Delta)\frac{z}{\mu} + q^2\ell_{\rm B}\sum_{j\neq 1}\frac{1}{\sqrt{R_{1j}^2 + (z-l)^2}} + q^2\ell_{\rm B}\Delta\left[\frac{1}{4z} + \sum_{j\neq 1}\frac{1}{\sqrt{R_{1j}^2 + (z+l)^2}}\right]. \tag{8.16}$$

We have at our disposal MC results of the density profile only for the dielectric jump $\Delta = 0.95$ and the relatively small coupling $\Xi = 10$ (12), see filled circles in Fig. 8.3. The VSC density profile is represented by the dashed curve, in disagreement with MC. On the other hand, the WSC density profile (solid curve) is calculated by

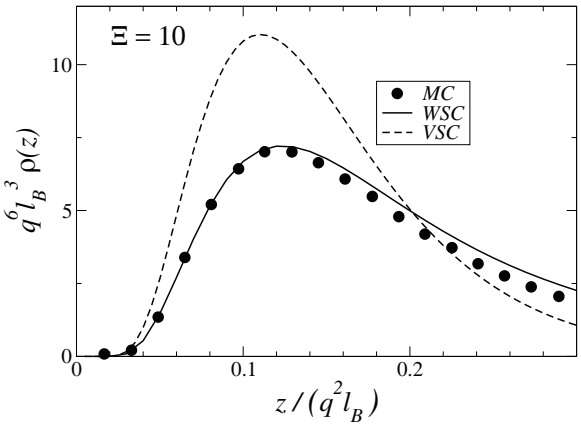

Figure 8.3 The density profile in various approaches, for the dielectric jump $\Delta = 0.95$ and the coupling constant $\Xi = 10$. The value $q = 1$ was used in (12) for the MC simulations.

using the potential (8.16) and shows good agreement with MC data up to $z \sim 0.2q^2\ell_{\rm B} = 2\mu$, even for such a small value of Ξ.

8.3 Two-Plate Geometry

We next consider symmetric like-charged plates $\sigma_1 = \sigma_2 \equiv \sigma$. The electric field between the plates vanishes for this case. At $T = 0$, the classical system is defined furthermore by the dimensionless separation

$$\eta = d\sqrt{\frac{\sigma}{q}} = \frac{1}{\sqrt{2\pi}}\frac{\widetilde{d}}{\sqrt{\Xi}}. \tag{8.17}$$

A minor complication comes from the fact that counterions form, on the opposite plate surfaces, a bilayer Wigner crystal whose structure depends on η (13). Here, we aim at performing expansions of thermodynamic quantities in powers of $\eta \propto \widetilde{d}/\sqrt{\Xi} \ll 1$ since we fix the scale $\widetilde{d}$ while Ξ becomes large. At the smallest separation $\eta = 0$, a single hexagonal Wigner crystal is formed. Its lattice spacing b is determined by global neutrality as $q = \sqrt{3}b^2\sigma$. Since $\eta \ll 1$ is equivalent to $d/b \ll 1$, we shift particles along the z-axis around this

structure. The corresponding energy change is

$$\delta E = \text{cst.} - \frac{(qe)^2}{4\epsilon} \sum_{\substack{j,k=1 \\ j\neq k}}^{N} \frac{(z_j - z_k)^2}{|\mathbf{R}_j - \mathbf{R}_k|^3}. \tag{8.18}$$

The cumulant technique (7) then implies the density profile

$$\widetilde{\rho}(\widetilde{z}) = \frac{2}{\widetilde{d}} + \frac{1}{\theta}\frac{2}{\widetilde{d}}\left[\left(\widetilde{z} - \frac{\widetilde{d}}{2}\right)^2 - \frac{\widetilde{d}^2}{12}\right] + O\left(\frac{\widetilde{d}^2}{\theta^{3/2}}\right), \tag{8.19}$$

where the θ-parameter is now obtained in the form

$$\theta = \frac{(4\pi)^{3/2}}{3^{3/4}} \frac{1}{C_3} \frac{1}{\sqrt{2}} \sqrt{\Xi} = 1.252\ldots\sqrt{\Xi}. \tag{8.20}$$

The previous VSC result was $\theta = \Xi$ (5). Defining the rescaled (temperature-independent) pressure $\widetilde{P} \equiv \beta P/(2\pi\ell_B\sigma^2)$, the contact-value theorem $\widetilde{P} = \widetilde{\rho}(0) - 1 = \widetilde{\rho}(\widetilde{d}) - 1$ implies

$$\widetilde{P} = -1 + \frac{2}{\widetilde{d}} + \frac{\widetilde{d}}{3\theta} + O\left(\frac{\widetilde{d}^2}{\theta^{3/2}}\right). \tag{8.21}$$

The phase diagram in the $(\Xi, \widetilde{d})$ plane, following from this WSC equation, is shown in Fig. 8.4. The shape of the isobaric phase boundary $P = 0$ (solid curve), which divides the plane into its attractive ($P < 0$) and repulsive ($P > 0$) parts, shows striking

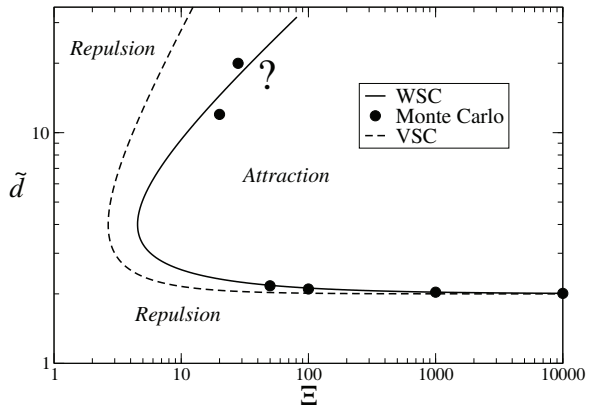

Figure 8.4 Phase diagram in the $(\Xi, \widetilde{d})$ plane for symmetric like-charged plates.

similarity with its counterpart obtained numerically (5) (filled circles). The question mark is a reminder that the upper branch where $\widetilde{d} \propto \sqrt{\Xi}$ exceeds the validity domain of Eq. (8.21), which is $\widetilde{d} \propto \Xi^{1/4}$. The dashed line is the inaccurate VSC prediction.

The WSC formalism can be readily generalized to plates with the asymmetry parameter $\zeta = \sigma_2/\sigma_1 \in [-1, 1]$. The final result for the rescaled pressure reads $\widetilde{P} = \widetilde{P}_0 + \widetilde{P}_1/\sqrt{\Xi} + O(1/\Xi)$, where

$$\widetilde{P}_0 = -\frac{1}{2}(1+\zeta^2) + \frac{1}{2}(1-\zeta^2)\coth\left(\frac{1-\zeta}{2}\widetilde{d}\right) \tag{8.22}$$

is the leading SC contribution, already obtained within the VSC method (6), and the coefficient of the first $1/\sqrt{\Xi}$ correction

$$\widetilde{P}_1 = \frac{3^{3/4}(1+\zeta)^{5/2}C_3}{4(4\pi)^{3/2}} \frac{\widetilde{d}}{\sinh^2\left(\frac{1-\zeta}{2}\widetilde{d}\right)} \times \left[\left(\frac{1-\zeta}{2}\widetilde{d}\right)\coth\left(\frac{1-\zeta}{2}\widetilde{d}\right) - 1\right]. \tag{8.23}$$

For the coupling constant $\Xi = 10^3$, the phase diagram in the whole range of the asymmetry parameter ζ is shown in Fig. 8.5. The dashed line corresponds to the leading-order (common to VSC and WSC) result of the phase boundary $\widetilde{P}_0 = 0$, which is equivalent to $\widetilde{d}^* = -2\ln|\zeta|/(1-\zeta)$. The solid line corresponds to the full WSC phase boundary $\widetilde{P} = \widetilde{P}_0 + \widetilde{P}_1/\sqrt{\Xi} = 0$. For oppositely charged plates $-1 < \zeta \leq 0$, the difference between the solid and dashed curves is

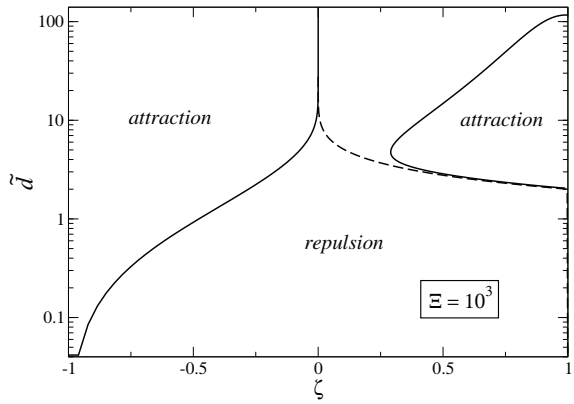

Figure 8.5 Phase diagram of asymmetrically charged plates.

invisible. On the other hand, the first correction affects significantly the positive ζ part of the phase diagram: no like-charge attraction is found in the range $0 < \zeta < 0.29$, whereas the leading-order result (dashed line) predicts an attraction region for all ζ.

8.4 Conclusion

Although the Wigner crystal becomes thermodynamically unstable for relatively large coupling constants $\Xi \sim 10^5 - 10^6$, it can serve as the starting point for WSC expansions valid for much smaller values of $\Xi \sim 10 - 100$. This is remarkable but not exceptional in statistical mechanics, for example, a low-temperature expansion of an Ising model around its ground state can be interpolated into the critical region.

Here are the main advantages of our WSC approach comparing to the original VSC method.

- The WSC approach is technically simple, the treatment of harmonic and higher vibrations requires an elementary technique of cumulants. On the other hand, there were no attempts to go beyond the leading term in nontrivial applications of the technically complicated VSC method such as for asymmetric plates.
- In contrast to the VSC method, the WSC theory also implies accurately the first correction to the leading SC behavior, see Fig. 8.2. As was shown for two asymmetrically charged plates in Fig. 8.5, this correction can significantly modify the phase diagram.
- More importantly, the WSC method applies also to the physical situations when the leading SC description is not of single-particle type. We documented this on the one-plate geometry with repulsive image charges, where the Wigner structure formed at a finite distance from the plate contributes to the leading order (Fig. 8.3). There, the VSC approach fails severely. Other problems of this kind include curved surfaces, and will be the focus of future work.

References

1. Ben-Tal, N. (1995) *J. Phys. Chem.* **99**, 9642; Wu, J. Z., Bratko, D., Blanch, H. W., and Prausnitz, J. M. (2000) *Phys. Rev. E* **62**, 5273; Dahirel, V. and Hansen, J.-P. (2009) *J. Chem. Phys.* **131**, 084902.
2. Jönsson, B. and Stahlberg, J. (1999) *Colloid Surf. B* **14**, 67.
3. Gulbrand, L., Jönsson, B., Wennerström, H., and Linse, P. (1984) *J. Chem. Phys.* **80**, 2221; Kjellander, R. and Marčelja, S. (1984) *Chem. Phys. Lett.* **112**, 49; Kékicheff, P., Marčelja, S., Senden, T. J., and Shubin, V. E. (1993) *J. Chem. Phys.* **99**, 6098.
4. Andelman, D. (2006) in *Soft Condensed Matter Physics in Molecular and Cell Biology*, edited by Poon, W. C. K. and Andelman, D. (Taylor & Francis, New York, 2006).
5. Moreira, A. G. and Netz, R. R. (2000) *Europhys. Lett.* **52**, 705; (2001) *Phys. Rev. Lett.* **87**, 078301; (2002) *Eur. Phys. J. E* **8**, 33; Netz, R. R. (2001) *Eur. Phys. J. E* **5**, 557.
6. Kanduč, M., Trulsson, M., Naji, A., Burak, Y., Forsman, J., and Podgornik, R. (2008) *Phys. Rev. E* **78**, 061105; Kanduč M. and Podgornik, R. (2007) *Eur. Phys. J. E* **23**, 265; Kanduč, Naji, A., Forsman, J., and Podgornik, R. (2010) *J. Chem. Phys.* **132**, 124701; Naji, A., Jungblut, S., Moreira A. G., and Netz, R. R., (2005) *Physica A* **352**, 131.
7. Šamaj, L. and Trizac, E. (2011) *Phys. Rev. Lett.* **106**, 078301; *Phys. Rev. E* **84**, 041401;
8. Šamaj, L. and Trizac, E. (2012) *Contrib. Plasma Phys.* **52**, 53.
9. Fisher, M. E. and Levin, Y. (1993) *Phys. Rev. Lett.* **71**, 3826.
10. Henderson, D. and Blum, L. (1978) *J. Chem. Phys.* **69**, 5441; Carnie, S. L. and Chan, D. Y. C. (1981) *J. Chem. Phys.* **74**, 1293.
11. Bonsall, L. and Maradudin, A. A. (1977) *Phys. Rev. B* **15**, 1959; Shklovskii, B. I. (1999) *Phys. Rev. Lett.* **82**, 3268; Levin, Y. (2002) *Rep. Prog. Phys.* **65**, 1577.
12. Moreira, A. G. and Netz, R. R. (2002) *Europhys. Lett.* **57**, 911.
13. Goldoni, G. and Peeters, F. M. (1996) *Phys. Rev. B* **53**, 4591; Messina, R. and Löven, H. (2003) *Phys. Rev. Lett.* **91**, 146101; Šamaj, L. and Trizac, E. (2012) *Europhys. Lett.* **98**, 36004.

Chapter 9

Moderately Coupled Charged Fluids Near Dielectric Interfaces and in Confinement

J. W. Zwanikken[a]

[a] *Department of Materials Science and Engineering, Northwestern University, 2220 Campus Drive, 60208 Evanston, Illinois, USA*
J-Zwanikken@Northwestern.edu

9.1 Summary

An overview of classic theories is presented that describes the structural and thermodynamic properties of fluids of charged particles, such as (poly-)electrolyte solutions, ionic liquids, plasmas, and charged colloids, and their relevance is discussed for current challenges, both in materials design and in fundamental research on soft and biological matter. The chapter is illustrated with examples of novel applications, and complemented with recent improvements on theoretical and numerical methods. Initially, the structural properties of homogeneous fluids of charged hard spheres are studied by means of Debye–Hückel (DH) and Ornstein–Zernike (OZ) theory. A recently derived closure for the OZ equation is highlighted that approximates the accuracy of the hyper-netted chain (HNC), but with a superior numerical efficiency and stability. The results

Electrostatics of Soft and Disordered Matter
Edited by David Dean, Jure Dobnikar, Ali Naji, and Rudolf Podgornik

ISBN 978-981-4411-85-1 (Hardcover), 978-981-4411-86-8 (eBook)
www.panstanford.com

shed light on charge ordering and clustering behavior in charged fluids. Classical density functional theory (DFT) is then addressed as a powerful framework to study fluids that are inhomogeneous, whether due to a wall, a membrane, or an ensemble of nanoparticles, using the information obtained for bulk fluids to estimate the position-dependent excess chemical potential, which accounts for the correlations between the particles. In the special case of planar symmetry, the rigorous method proposed by Kjellander and Marčelja can be applied, known as the anisotropic hyper-netted chain (AHNC), in which the excess chemical potential is actually calculated instead of heuristically estimated, using a mathematical mapping of the inhomogeneous system to a more polydisperse, yet homogeneous system of lower dimension. The AHNC reveals how walls and dielectric interfaces deform the screening cloud around charged particles, and how the average force between the particles is modified. The chapter is concluded by a perspective on different origins for like-charge attractions.

9.2 Introduction

Systems of inorganic ions and charged macromolecules near dielectric interfaces are omnipresent on Earth. In fact, they host the vital processes of life, govern the atmospheric chemistry, and form the main subject for the petrochemical, food, and pharmaceutical industry. Interfaces can enable and accelerate chemical processes by attracting reactive components, by allowing components in two different phases to meet, and by confining components to a lower dimension, which drastically increases the likelihood of collisions. These catalytic properties determine the reaction rates between sea salt and air on water droplets and snow, by which the entire atmospheric composition is regulated (Jungwirth and Tobias, 2002). Interfaces are also heavily exploited by organisms. Each life form is highly compartmentalized by specialized subunits such as organs and vessels, and by the elementary units, cells, bounded by walls or membranes that coordinate the processes with the environment. It is even conjectured that life itself originated on an interface, for example, inside a porous rock or a lipid vesicle

(Kuhn, 2008; Sowerby *et al.*, 2001; Luisi *et al.*, 1999), rather than a bulky ocean. Also for industrial applications, understanding of the microscopic behavior near interfaces is of prime importance, for example, for catalysis in chemical processing, cleaning waste, metal extraction, emulsion (de-)stabilization, colloids, encapsulation and drug delivery. From a more fundamental scientific point of view, these systems pose several open challenges in physics, which will be the focus of this chapter. The solutions may lead to a better understanding of interfacial processes in general, and an increased potential and control in industrial applications.

9.3 New Physics in Between

From the perspective of a physicist, the energy scales in biology are somewhere in between two well-explored regimes. Organic systems display more structure than an ideal gas, but are not necessarily as rigid as a metal, and do evolve by thermal motion over timescales that span the complete gap between the atomic and galactic ones. In more physical terms, the kinetic and potential energy are on an equal footing, which appears to be a characteristic, or even a necessity for the vastly complex, adaptive structures that represent life. The consequence is that high-temperature expansions and mean field theories that proved so useful for weakly-coupled fluids, and zero-temperature approaches that provided insight in the physical aspects of frozen systems, all fall short by underestimating either the energetic or the entropic aspects. Although some models seek (and find) answers in linear combinations of the results of high and low-temperature approaches, their predictions do not cover the complete experimental complexity, demonstrating that a more rigorous approach is required for charged fluids at intermediate temperatures, in order to get more insight in such aspects as the local structure near interfaces, and to understand the different mechanisms behind the observed attractions between like-charged objects. Although we may aim for transparency and simplicity, the biological conditions force us to go beyond the theories that were developed for simpler, inorganic fluids and solids. As discussed here, even relatively simple systems of charged hard spheres near

dielectric boundaries may show a complex behavior that is missed by mean field theories, zero-temperature analyses or combinations thereof, although the usefulness of these methods has been proven for a plethora of soft condensed matter systems. Many biological processes are not even ergodic, are chemically driven, and far from equilibrium. We turn our eyes away from those facts, into the direction of the (sub-)systems where statistical thermodynamics is applicable. We run through a history of research, and take a theoretical path that gradually leads deeper into the moderately coupled domain.

9.4 Primitive Model

From this point, ions are modeled as charged, hard spheres with diameter $\sigma_{\pm}$ and charge $\pm qe$, and the solvent is modeled as a homogeneous structureless background medium with permittivity ϵ; known as the primitive model (PM). Effects due to solvent structure and solvent-ion interactions are not explicitly considered, nor the softness, polarizability or anisotropy that may characterize real ions (Levin, 2009), or effects due to the zoo of impurities that are so common in real solutions (Ninham, 1999). One hopes to correct for these mostly short-ranged effects by choosing an appropriate hard core diameter, for example, one that includes the hydration shells of an ion in water. On the other hand, further refinement of the model may only lead to better results if the Coulomb interactions are properly treated in the first place. So we focus on the PM, and use the words 'ions' and 'solvent' here and there, being aware that we simplify their aspects, which could nuance our results (Ninham, 1999).

9.5 Debye–Hückel

In 1923, Debye and Hückel developed a theory, which still stands as the principal method to grasp the thermodynamic properties of electrolyte solutions (Debye and Hückel, 1923). Simple expressions for the typical correlation length and the equations of state appeared

useful to estimate both structural and thermodynamic aspects such as the double layer (Kornyshev, 2007) and the critical behavior (Fisher and Levin, 1993; Levin and Fisher, 1996), and opened the door for an initial understanding of charged fluids. Kirkwood demonstrated in statistical terminology (Kirkwood, 1934) that the sole approximation of DH theory consists of a replacement of the potential of mean force by the mean electrostatic potential, nowadays referred to as a mean field approximation, or, using a modern field-theoretical formalism (Podgornik and Žekš, 1988; Attard, 1996; Netz and Orland, 2000), a saddle point approximation. The mean electric potential is obtained by solving the Poisson–Boltzmann equation, either analytically after linearization, or just numerically (with a hard sphere cut-off), which is no effort for modern computers (Zwanikken and de La Cruz, 2010; Zwanikken *et al.*, 2011c). The consequences of the linearization are obvious in Fig. 9.1. Figure 9.1 shows the radial distribution function $g(r)$ for

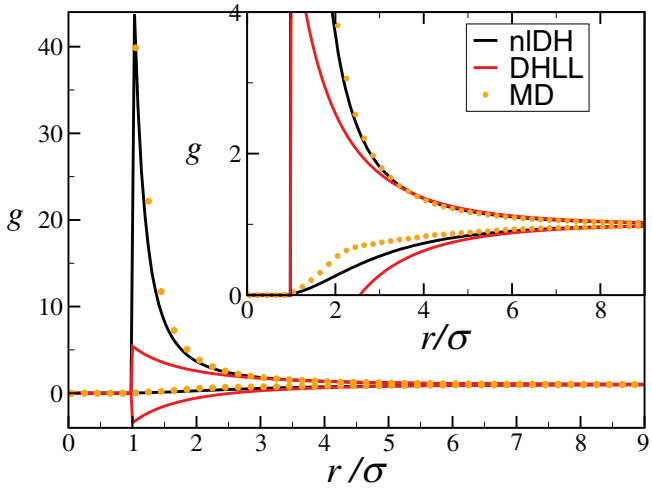

Figure 9.1 Radial distribution functions between oppositely charged spheres (upper curves) and like-charged spheres (lower curves) with an electrostatic potential at contact of 6 $k_{\mathrm{B}}T$ at a concentration of 5 mM, according to non-linearized DH theory (nlDH, black lines), linearized DH theory (DHLL, red lines), and MD simulations (orange dots). The results of nlDH and MD show close agreement. The results of DHLL lie far off.

a homogeneous system of hard, charged spheres. The electrostatic pair potential at contact is 6 $k_{\mathrm{B}}T$ ($\sim$ divalent ions in water), and the density is 5 mM. It is clear from the picture that the results of DH theory are very close to those of a molecular dynamics (MD) simulation, whereas the results of the linearized DH theory (DHLL) are far off. DH theory agrees closely with MD as long as the density is sufficiently but not unreasonably low, especially regarding the macroscopic properties of the fluid such as the pressure or compressibility, which are calculated from (integrals of) the radial distribution function. Also for charged molecular fluids, DH theory has predicted accurate phase diagrams, for example, polyelectrolytes (González-Mozuelos and De la Cruz, 1995; González-Mozuelos and de la Cruz, 2003; Ermoshkin and Olvera de La Cruz, 2003; Kudlay *et al.*, 2004).

The commonly used statement that 'mean field theory ignores correlations' can be nuanced. In Gouy-Chapman theory (Gouy, 1910), the global concentration of ions is calculated near a fixed planar wall, which 'ignores all correlations' by presuming $g(\mathrm{r}, \mathrm{r}') = 1$. In DH theory, the local concentration of ions is calculated around a mobile ion, calculating $g(|\mathrm{r} - \mathrm{r}'|)$ at a mean field level, and ignoring higher order correlations. Although DH theory seems less crude, it is applicable only for bulk fluids. These results speak for Poisson-Boltzmann cell models (Zwanikken *et al.*, 2011a,b; Von Grünberg *et al.*, 2007; Deserno and von Grünberg, 2002), and were an inspiration to formulate a new closure for the OZ equation (Zwanikken *et al.*, 2011c).

9.6 Ornstein–Zernike Theory

Almost a century ago, Ornstein and Zernike (Ornstein and Zernike, 1914) formulated the equation

$$h(\mathrm{r}, \mathrm{r}') = c(\mathrm{r}, \mathrm{r}') + \int \mathrm{r}'' c(\mathrm{r}, \mathrm{r}'')\rho(\mathrm{r}'')h(\mathrm{r}'', \mathrm{r}') \qquad (9.1)$$

with the total correlation function $h(\mathrm{r}, \mathrm{r}') = g(\mathrm{r}, \mathrm{r}') - 1$ and density of particles ρ, which for a long time was considered as the definition of the direct correlation function c. Alternatively, one can define the correlation functions as functional derivatives of the (grand)

partition function and derive the OZ equation (9.1) (Hansen and McDonald, 2006), which has the bonus that one can derive a second relation between h and c (Van Leeuwen *et al.*, 1959), and the pair potential u:

$$c(\mathrm{r}, \mathrm{r}') = -\beta u(\mathrm{r}, \mathrm{r}') + h(\mathrm{r}, \mathrm{r}') - \ln(h(\mathrm{r}, \mathrm{r}') + 1) + d(\mathrm{r}, \mathrm{r}'). \quad (9.2)$$

by comparing the diagrammatic expansions of c and h in terms of Mayer cluster diagrams (Mayer, 1950). The function d, known as the bridge function (thanks to the topology of the diagrams of its expansion), is practically as hard to calculate as the initial partition function, but in practice often negligible compared to the other terms. Equation (9.2) without d is an approximate closure known as the HNC, which is particularly accurate for fluids with soft, long-range potentials such as plasmas, electrolyte solutions, and all fluids where the Coulomb force is dominantly present. For homogeneous systems, equations (9.1) and (9.2) can be solved iteratively, by making use of a Fourier transformation of (9.1) to get rid of the convolution. When ρ has an explicit r-dependence, the equations become intractable, unless one can make clever use of symmetries, discussed in the last section (Kjellander and Marčelja, 1984). Some improvements on the HNC have been made by estimating the contribution of d, borrowing it from a reference system of hard spheres (RHNC). In a personal attempt to improve the numerical stability of the HNC (Zwanikken *et al.*, 2011c), the right hand side of (9.2) was estimated ab initio by DH theory and the Percus-Yevick closure for hard spheres (Verlet and Weis, 1972), which simplifies the iteration procedure, and has better convergence properties than the HNC. This closure was called the Debye–Hückel extended mean spherical approximation (DHEMSA). Although from a rigorous point of view, one would expect the DHEMSA to be strictly worse than the HNC, the distribution functions are generally almost indistinguishable, and at least very close, as shown in Fig. 9.2.

9.7 Oscillations in the Potential of Mean Force

In Fig. 9.2, the radial distributions are plotted for a moderately coupled system. The electrostatic pair-potential at contact is 16.7

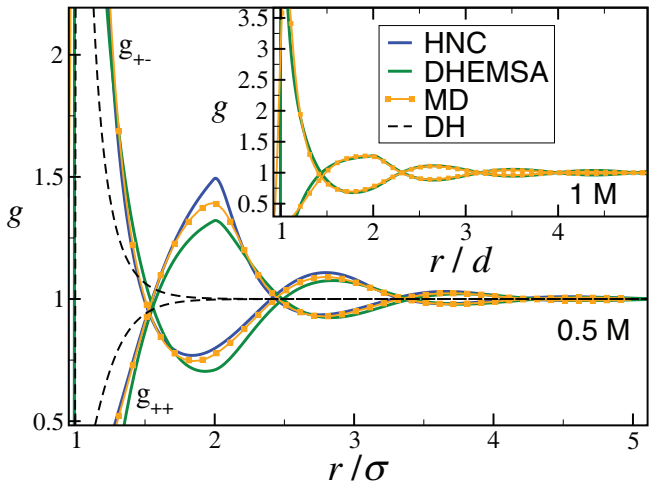

Figure 9.2 Radial distribution functions between oppositely charged spheres (upper curves) and like-charged spheres (lower curves), using DH theory, two closures for the OZ equations, and MD. The electrostatic pair-potential at contact is 16.7 $k_{\mathrm{B}}T$. A pronounced layering of charge is visible.

$k_{\mathrm{B}}T$ ($\sim$ ions with a valency of 4 in water), and the density is 0.5 M and 1 M (inset). Both the HNC and the DHEMSA are close to the MD results, and for 1 M the DHEMSA performs excellently, whereas we could not let the HNC converge. DH theory is not useful under these conditions. The oscillatory behavior of the distribution functions tells us that the mean force between two positive ions can be attractive, depending on their separation. On average the ions are enveloped by layers of positive and negative charge, a qualitative feature already predicted by Kirkwood and Poirier (Kirkwood and Poirier, 1954) by means of a charging procedure. Kirkwood and Stillinger (Stillinger Jr and Kirkwood, 1960) predicted a similar stratification near a rigid wall.

Any number $n = 1, 2, 3\ldots$ of layers can be found by variation of the parameters, and the additional possibilities in three- or multicomponent fluids are hard to oversee. Features such as charge reversal (when the first layer of counterions overcompensates the charge of the central object) or like-charge attractions may appear in many different ways, and for different reasons, even within the

PM. At intermediate densities (0.1–10 mM), all the above methods break down and simulations cope with long relaxation times, except for specialized routines (Caillol *et al.*, 2002; Orkoulas and Panagiotopoulos, 1999; Yan and De Pablo, 1999; Luijten *et al.*, 2002) such as the Monte-Carlo algorithm developed by Valeriani (Valeriani *et al.*, 2010a,b) that revealed a dilute phase of small clusters. In the next sections we shall describe fluids that are inhomogeneous due to an external field or by confinement, and sketch how external fields can induce like-charge attractions.

9.8 Density Functional Theory

DFT offers convenient calculation rules and notations to describe inhomogeneous fluids, avoiding partition functions with many degrees of freedom, and in quantum mechanics, cumbersome $N-$body wave functions. Once the intrinsic properties of the system have been formulated, one can calculate the density distributions for any external potential as exerted by a rigid wall, a molecule, a lattice of fixed charges, a laser beam, or other source, making DFT a highly effective theory to calculate the electronic structure in metals and molecules, and ion and particle distributions in soft matter. The greater challenge rests in the formulation of the intrinsic properties; to find a form for the excess chemical potential μ_{exc} as a functional of ρ, or a form for a free energy functional from which μ_{exc} can be derived. For more information about DFT we refer to a rich literature (Parr and Weitao, 1994; Evans, 1979; Hansen and McDonald, 2006), and jump to the Boltzmann distribution

$$\rho(\mathrm{r}) = \exp(\mu - V_{\text{ext}}(\mathrm{r}) - \beta\mu_{\text{exc}}[\rho; r]). \tag{9.3}$$

with the equilibrium density ρ depending on the position r (can also be another degree of freedom, such as angle, spin,…), μ the chemical potential and V_{ext} the external potential. One can assume that $\mu_{\text{exc}}[\rho; \mathrm{r}]$ is locally equal to the chemical potential of a homogeneous system with density $\rho(\mathrm{r})$,

$$\mu_{\text{exc}}[\rho; r] = \mu_{\text{exc}}(\rho)|_{\rho=\rho(\mathrm{r})}, \tag{9.4}$$

which corresponds to a local density approximation (LDA). The LDA is particularly suitable for systems where the density varies weakly

over a typical correlation length (and if the correlation functions vary weakly with the density). A more advanced approach makes a similar assumption as (9.4), but then with $\mu_{\rm exc}(\bar{\rho})$ evaluated for a $\bar{\rho}$ averaged around r, which is known as a Weighted Density Approach. The approach introduces a weight function, to define the weighted density, in a semi-empiric (Tarazona, 1985) or in a self-consistent (Curtin and Ashcroft, 1985; Denton and Ashcroft, 1989) way, based on what is known about bulk fluids. A very accurate functional for inhomogeneous hard sphere fluids was formulated by Rosenfeld (Rosenfeld *et al.*, 1997), based on fundamental measures. There is no expression for charged systems with an equivalent success, and the challenge is still open to find accurate functional forms for the chemical potential and free energy functional in terms of ρ. The theory of the next chapter actually calculates the position-dependent $\mu_{\rm exc}(\mathrm{r})$ in inhomogeneous systems with planar symmetry, using OZ theory with the HNC, and also yields the anisotropic correlation functions.

9.9 The Anisotropic HNC

As remarked earlier, the OZ equation cannot be solved for inhomogeneous systems, because of computational limitations. Typically one would need N^9 grid points, with N the number of grid points in one dimension, such that for $N = 1000$ one shoots beyond Avogadro's number. However, by a smart mathematical mapping (involving no additional assumptions) Kjellander and Marčelja (Kjellander and Marcělja, 1984; Kjellander and Marčelja, 1985; Kjellander, 1988) were able to solve the OZ equation for systems with planar symmetry, using the HNC as the only assumption, and called it the AHNC. Carefully and completely explained in their works, the procedure is illustrated here in Fig. 9.3.

An inhomogeneous system with translational symmetry in the x–y plane appears homogeneous, if considered in the z-direction (see Fig. 9.3). One can map the 3D inhomogeneous system to a 2D homogeneous one without loss of information about the z-coordinate, if the particles are 'colored' in parallel layers, and considered as a distinct species. The number of layers correspond to

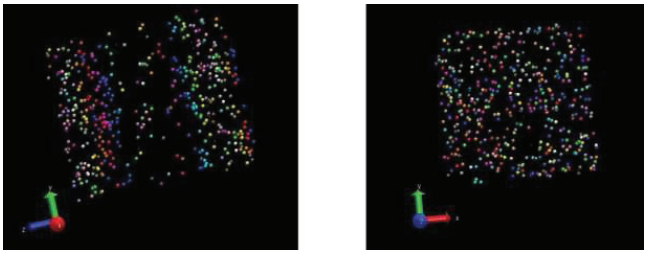

Figure 9.3 Just by a different angle of inspection, the inhomogeneous system (left) appears homogeneous (right). Ergo, one can map the 3D inhomogeneous system to a 2D homogeneous one. Particles in parallel layers have to be 'colored' first, and considered a distinct species in order to retain information about the coordinate that is lost by projection. One trades inhomogeneity for polydispersity.

a discretization of the z-axis. One trades inhomogeneity for polydispersity, and the latter is easily accounted for in OZ theory. Instead of a single equation (9.1), one needs M^2 equations, with M the number of layers (i.e., z-coordinates). The correlation functions are labeled to denote the species, so $c_{ij}(r)$ denotes the direct correlation between particles of species i and j separated by the in-plane distance r, and ρ_i is the density of particles in layer i. The OZ equation can be written as a matrix equation, and solved with the HNC closure, which is the only approximation in the theory. The set of equations is closed by the Boltzmann distributions for the densities ρ_i, Eq. (9.3), where the excess chemical potential has an explicit expression in terms of the correlation functions within the HNC (Hansen *et al.*, 1977). The final solution for the 2D system can be mapped back onto the original 3D system, yielding density profiles, anisotropic correlation functions, and an accurate thermodynamics of moderately coupled charged fluids near flat interfaces. These interfaces can be neutral, hard, soft, attractive, (discretely) charged, ionizable (Ninham and Parsegian, 1971), or polarizable (Kjellander, 1988; Jadhao *et al.*, 2012), and the same procedure is also applicable to dense neutral fluids, with other closures than the HNC (Kjellander and Sarman, 1990; Lang *et al.*, 2010; Boţan *et al.*, 2009). Some results for the PM, and interpretations, are given in the next section. Only a small part of the phenomenology is presented here.

9.10 Double Layer Deformation and Like-Charge Attraction

A few test systems are considered using the AHNC, to highlight a few characteristic effects in charged fluids under external fields. Figure 9.4 (left) shows the distribution of divalent ions between two neutral walls, with an external potential that follows a step function with a jump of 1 $k_{\mathrm{B}}T$ at $z = 0$. We leave the origin of the external field unspecified, but it could model the solubility of the ions, in two different phases that meet at $z = 0$ (two immiscible liquids (Luo *et al.*, 2006), a gel and a solvent (Jha *et al.*, 2011), a polymer brush…). There is no external influence that induces charge separation and the ions are of equal size, so one can expect in advance that $\rho_+ = \rho_- = \rho$. A mean field theory would predict the density to be a step function, like the external potential. Electrostatic correlations, though, cause a depletion near the walls and near the right side of the phase boundary, and an accumulation near the left side of the boundary, due to cohesion of the ion cloud, taken into account by the AHNC. The screening cloud around the ions becomes highly anisotropic as shown in the right figure, where the colors correspond to the total charge density Q given that there is a negative ion at the interface $z = 0$, and the vertical axis corresponds to the coordinate x perpendicular to z. The ions have a spherical double layer structure in bulk, which gets deformed near the phase boundary (alluded to in (Zwanikken and van Roij, 2007; Leunissen *et al.*, 2007) without knowledge of the correlation functions). Another example of an anisotropic double layer is shown in Fig. 9.5, around an ion between two sticky walls, and around an ion adsorbed at one of the sticky walls (right). The attractive potential of the wall is such that positive ions adsorb equally well as negative ions. The density of counterions is much higher in the adsorbed layers than in between the walls. Entropically it is more favorable to polarize the dense layer near the walls, rather than attracting counterions in the dilute phase in between. A simple illustration how two walls that are neutral on average still correlate electrostatically, by modifying the local environment around the confined ions. Not unlike (critical) Casimir forces, that arise by

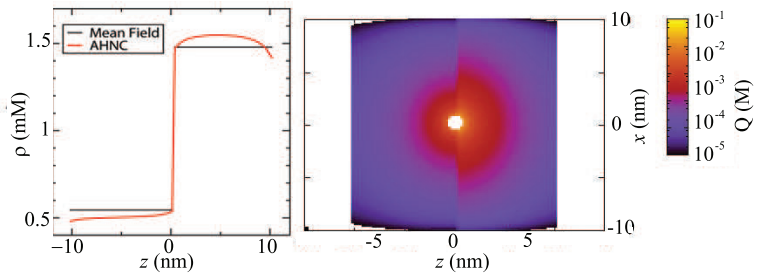

Figure 9.4 Equilibrium distributions of divalent ions between two neutral walls (left) with an the external potential that makes a jump of 1 $k_{\mathrm{B}}T$ at $z = 0$, predicted by the AHNC (red line) revealing typical effects due to the cohesion of the ion cloud that are missed by a mean field theory (black line). The right figure shows the anisotropic distribution of countercharge Q around a negative ion situated at the interface, causing a mean electrostatic force to the right.

constraining the fluctuation spectrum of the electromagnetic field (Casimir, 1948) or in a critical solvent mixture (Hertlein *et al.*, 2008; Bier *et al.*, 2011). The sign and magnitude of the correlation-induced interaction between the walls depend strongly on the coupling strength between the ions, the density in the solvent, the density near the walls, and the area of the walls. A more detailed overview is presented in Zwanikken and Olvera de la Cruz (2013). Also the question how confinement can induce like-charge attractions, or the opposite, how interfaces can locally destroy a stratification of charge around the ions is not addressed here. Several effects have been revealed by Greberg, Kjellander and Åkesson (Greberg *et al.*, 1997).

9.11 Conclusion

Several classical theories for charged structured fluids are discussed, with recent adaptations and applications. The moderately coupled regime has a rich phenomenology that is incompletely explored, even for simplified model systems as the PM. With the modern computational potential, we are able to evaluate classical theories numerically without additional (traditional) approximations, and

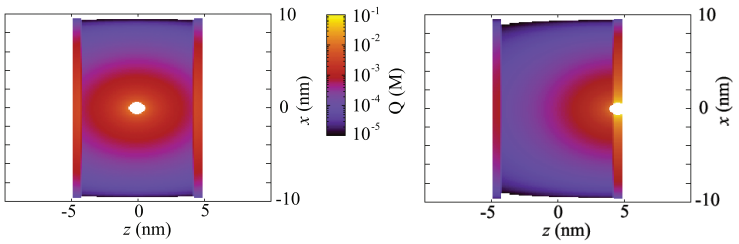

Figure 9.5 The net charge concentration around a negative ion, placed between two sticky walls (left), and in the adsorbed layer of the right wall (right), calculated by the AHNC. The majority of countercharge is located in the adsorbed layers. It is entropically favorable for ions to be screened by a dense rather than a dilute phase, causing effective interactions between the plates.

can develop and learn from new quantitative predictive algorithms. From the rigorous AHNC it may be possible to learn more about the anisotropic correlations in charged fluids near (dielectric) boundaries, and formulate an effective DFT for more general geometries. A few examples showed the screening cloud around a charged sphere being deformed in the presence of an interface, affecting the interactions between spheres near the interface, and the excess pressure between two nearby walls. After a long history of research, we seem closer to a clear categorization of the structure in moderately coupled Coulomb fluids, and manifestations of like-charge attractions, with expectable consequences for industrial applications involving catalysis, emulsion stabilization, charged colloids, and biomaterials.

9.12 Acknowledgment

Monica Olvera de la Cruz is gratefully acknowledged for advice and the realization of this chapter. The author acknowledges the support by the NSEC program on integrated nanopatterning (EEC-0647560) at Northwestern University. MD simulations presented in the manuscript were performed by Prateek K. Jha.

References

Attard, P. (1996). *Adv. Chem. Phys. XCII* **1**.

Bier, M., Gambassi, A., Oettel, M. and Dietrich, S. (2011). Electrostatic interactions in critical solvents, *EPL (Europhysics Letters)* **95**, 6, p. 60001.

Boţan, V., Pesth, F., Schilling, T. and Oettel, M. (2009). Hard-sphere fluids in annular wedges: Density distributions and depletion potentials, *Physical Review E* **79**, 6, p. 061402.

Caillol, J., Levesque, D. and Weis, J. (2002). Critical behavior of the restricted primitive model revisited, *arXiv preprint cond-mat/0201301* .

Casimir, H. (1948). On the attraction between two perfectly conducting plates, in *Proc. K. Ned. Akad. Wet*, Vol. 51, p. 793.

Curtin, W. and Ashcroft, N. (1985). Weighted-density-functional theory of inhomogeneous liquids and the freezing transition, *Physical Review A* **32**, 5, p. 2909.

Debye, P. and Hückel, E. H. (1923). *Phys. Zeits.* **24**, 185, p. 305.

Denton, A. and Ashcroft, N. (1989). Modified weighted-density-functional theory of nonuniform classical liquids, *Physical Review A* **39**, 9, p. 4701.

Deserno, M. and von Grünberg, H. (2002). Osmotic pressure of charged colloidal suspensions: A unified approach to linearized poisson-boltzmann theory, *Physical Review E* **66**, 1, p. 011401.

Ermoshkin, A. and Olvera de La Cruz, M. (2003). Polyelectrolytes in the presence of multivalent ions: gelation versus segregation, *Physical review letters* **90**, 12, p. 125504.

Evans, R. (1979). See for example adv, *Phys* **28**, p. 143.

Fisher, M. and Levin, Y. (1993). Criticality in ionic fluids: Debye-hückel theory, bjerrum, and beyond, *Physical review letters* **71**, 23, pp. 3826–3829.

González-Mozuelos, P. and De la Cruz, M. (1995). Ion condensation in salt-free dilute polyelectrolyte solutions, *The Journal of chemical physics* **103**, p. 3145.

González-Mozuelos, P. and de la Cruz, M. (2003). Association in electrolyte solutions: Rodlike polyelectrolytes in multivalent salts, *The Journal of chemical physics* **118**, p. 4684.

Gouy, M. (1910). Sur la constitution de la charge electrique a la surface d'un electrolyte, *J. Phys. Theor. Appl.* **9**, 1, pp. 457–468.

Greberg, H., Kjellander, R. and Akesson, T. (1997). Ion-ion correlations in electric double layers from monte carlo simulations and integral equation calculations part 2. case of added salt, *Molecular physics* **92**, 1, pp. 35–48.

Hansen, J. and McDonald, I. (2006). *Theory of simple liquids* (Academic press).

Hansen, J., Torrie, G. and Vieillefosse, P. (1977). Statistical mechanics of dense ionized matter. vii. equation of state and phase separation of ionic mixtures in a uniform background, *Physical Review A* **16**, 5, p. 2153.

Hertlein, C., Helden, L., Gambassi, A., Dietrich, S. and Bechinger, C. (2008). Direct measurement of critical casimir forces, *Nature* **451**, 7175, pp. 172–175.

Jadhao, V., Solis, F. and de la Cruz, M. (2012). Fast simulations of charges moving in response to varying dielectric media, *arXiv preprint arXiv:1208.4113* .

Jha, P., Zwanikken, J., de Pablo, J. and Olvera de La Cruz, M. (2011). Electrostatic control of nanoscale phase behavior of polyelectrolyte networks, *Current Opinion in Solid State and Materials Science* **15**, 6, pp. 271–276.

Jungwirth, P. and Tobias, D. (2002). Ions at the air/water interface, *The Journal of Physical Chemistry B* **106**, 25, pp. 6361–6373.

Kirkwood, J. (1934). On the theory of strong electrolyte solutions, *The Journal of Chemical Physics* **2**, p. 767.

Kirkwood, J. and Poirier, J. (1954). The statistical mechanical basis of the debye–hüekel theory of strong electrolytes, *The Journal of Physical Chemistry* **58**, 8, pp. 591–596.

Kjellander, R. (1988). Inhomogeneous coulomb fluids with image interactions between planar surfaces. ii. on the anisotropic hypernetted chain approximation, *The Journal of chemical physics* **88**, p. 7129.

Kjellander, R. and Marcělja, S. (1984). Correlation and image charge effects in electric double layers, *Chemical physics letters* **112**, 1, pp. 49–53.

Kjellander, R. and Marčelja, S. (1985). Inhomogeneous coulomb fluids with image interactions between planar surfaces. i, *The Journal of chemical physics* **82**, 4, pp. 2122–2135.

Kjellander, R. and Sarman, S. (1990). A study of anisotropic pair distribution theories for lennard-jones fluids in narrow slits, *Molecular Physics* **70**, 2, pp. 215–237.

Kornyshev, A. (2007). Double-layer in ionic liquids: paradigm change? *The Journal of Physical Chemistry B* **111**, 20, pp. 5545–5557.

Kudlay, A., Ermoshkin, A. and de la Cruz, M. (2004). Complexation of oppositely charged polyelectrolytes: effect of ion pair formation, *Macromolecules* **37**, 24, pp. 9231–9241.

Kuhn, H. (2008). Origin of lifesymmetry breaking in the universe: Emergence of homochirality, *Current Opinion in Colloid & Interface Science* **13**, 1, pp. 3–11.

Lang, S., Boţan, V., Oettel, M., Hajnal, D., Franosch, T. and Schilling, R. (2010). Glass transition in confined geometry, *Physical review letters* **105**, 12, p. 125701.

Leunissen, M., Zwanikken, J., van Roij, R., Chaikin, P. and van Blaaderen, A. (2007). Ion partitioning at the oil–water interface as a source of tunable electrostatic effects in emulsions with colloids, *Phys. Chem. Chem. Phys.* **9**, 48, pp. 6405–6414.

Levin, Y. (2009). Polarizable ions at interfaces, *Physical review letters* **102**, 14, p. 147803.

Levin, Y. and Fisher, M. (1996). Criticality in the hard-sphere ionic fluid, *Physica A: Statistical Mechanics and its Applications* **225**, 2, pp. 164–220.

Luijten, E., Fisher, M. and Panagiotopoulos, A. (2002). Universality class of criticality in the restricted primitive model electrolyte, *Physical review letters* **88**, 18, p. 185701.

Luisi, P., Walde, P. and Oberholzer, T. (1999). Lipid vesicles as possible intermediates in the origin of life, *Current opinion in colloid & interface science* **4**, 1, pp. 33–39.

Luo, G., Malkova, S., Yoon, J., Schultz, D., Lin, B., Meron, M., Benjamin, I., Vanỳsek, P. and Schlossman, M. (2006). Ion distributions at the nitrobenzene–water interface electrified by a common ion, *Journal of Electroanalytical Chemistry* **593**, 1, pp. 142–158.

Mayer, J. (1950). The theory of ionic solutions, *The Journal of Chemical Physics* **18**, 11, pp. 1426–1436.

Netz, R. and Orland, H. (2000). Beyond poisson-boltzmann: Fluctuation effects and correlation functions, *The European Physical Journal E: Soft Matter and Biological Physics* **1**, 2, pp. 203–214.

Ninham, B. (1999). On progress in forces since the dlvo theory, *Advances in colloid and interface science* **83**, 1, pp. 1–17.

Ninham, B. and Parsegian, V. (1971). Electrostatic potential between surfaces bearing ionizable groups in ionic equilibrium with physiologic saline solution, *Journal of theoretical biology* **31**, 3, pp. 405–428.

Orkoulas, G. and Panagiotopoulos, A. (1999). Phase behavior of the restricted primitive model and square-well fluids from monte carlo

simulations in the grand canonical ensemble, *The Journal of chemical physics* **110**, 3, pp. 1581–1590.

Ornstein, L. and Zernike, F. (1914). Accidental deviations of density and opalescence at the critical point of a single substance, in *Proc. Akad. Sci.(Amsterdam)*, Vol. 17, p. 793.

Parr, R. and Weitao, Y. (1994). *Density-functional theory of atoms and molecules*, Vol. 16 (Oxford University Press, USA).

Podgornik, R. and Žekš, B. (1988). Inhomogeneous coulomb fluid. a functional integral approach, *J. Chem. Soc., Faraday Trans. 2* **84**, 6, pp. 611–631.

Rosenfeld, Y., Schmidt, M., Löwen, H. and Tarazona, P. (1997). Fundamental-measure free-energy density functional for hard spheres: Dimensional crossover and freezing, *Physical Review E* **55**, 4, p. 4245.

Sowerby, S., Cohn, C., Heckl, W. and Holm, N. (2001). Differential adsorption of nucleic acid bases: Relevance to the origin of life, *Proceedings of the National Academy of Sciences* **98**, 3, pp. 820–822.

Stillinger Jr, F. and Kirkwood, J. (1960). Theory of the diffuse double layer, *The Journal of Chemical Physics* **33**, p. 1282.

Tarazona, P. (1985). Free-energy density functional for hard spheres, *Physical Review A* **31**, 4, p. 2672.

Valeriani, C., Camp, P., Zwanikken, J., Van Roij, R. and Dijkstra, M. (2010a). Computer simulations of the restricted primitive model at very low temperature and density, *Journal of Physics: Condensed Matter* **22**, 10, p. 104122.

Valeriani, C., Camp, P., Zwanikken, J., van Roij, R. and Dijkstra, M. (2010b). Ion association in low-polarity solvents: comparisons between theory, simulation, and experiment, *Soft Matter* **6**, 12, pp. 2793–2800.

Van Leeuwen, J., Groeneveld, J. and De Boer, J. (1959). New method for the calculation of the pair correlation function. i, *Physica* **25**, 7, pp. 792–808.

Verlet, L. and Weis, J. (1972). Equilibrium theory of simple liquids, *Physical Review A* **5**, 2, p. 939.

Von Grünberg, H., Van Roij, R. and Klein, G. (2007). Gas-liquid phase coexistence in colloidal suspensions? *EPL (Europhysics Letters)* **55**, 4, p. 580.

Yan, Q. and De Pablo, J. (1999). Hyper-parallel tempering monte carlo: Application to the lennard-jones fluid and the restricted primitive model, *The Journal of chemical physics* **111**, p. 9509.

Zwanikken, J. and de La Cruz, M. (2010). Correlated electrolyte solutions and ion-induced attractions between nanoparticles, *Physical Review E* **82**, 5, p. 050401.

Zwanikken, J., Guo, P., Mirkin, C. and Olvera de la Cruz, M. (2011a). Local ionic environment around polyvalent nucleic acid-functionalized nanoparticles, *The Journal of Physical Chemistry C* **115**, 33, pp. 16368–16373.

Zwanikken, J., Ioannidou, K., Kraft, D. and van Roij, R. (2011b). Reversible emulsification controlled by ionic surfactants and responsive nanoparticles, *Soft Matter* **7**, 23, pp. 11093–11097.

Zwanikken, J., Jha, P. and de la Cruz, M. (2011c). A practical integral equation for the structure and thermodynamics of hard sphere coulomb fluids, *The Journal of chemical physics* **135**, p. 064106.

Zwanikken, J. and van Roij, R. (2007). Charged colloidal particles and small mobile ions near the oil-water interface: Destruction of colloidal double layer and ionic charge separation, *Physical review letters* **99**, 17, p. 178301.

Zwanikken, J. W. and Olvera de la Cruz, M. (2013). Tunable soft structure in charged fluids confined by dielectric interfaces, *Proceedings of the National Academy of Sciences* **110**, 14, pp. 5301–5308.

Part II

Ions at Interfaces and in Nanoconfinement

Chapter 10

Dielectric Profiles and Ion-Specific Effects at Aqueous Interfaces

Douwe Jan Bonthuis[a] and Roland R. Netz[b]

[a] *Rudolf Peierls Centre for Theoretical Physics, University of Oxford, Oxford OX1 3NP, UK*
[b] *Fachbereich Physik, Freie Universität Berlin, 14195 Berlin, Germany*
douwe.bonthuis@physics.ox.ac.uk

10.1 Introduction

Unlike bulk water, water at aqueous interfaces exhibits a pronounced anisotropic molecular ordering. The water density shows a depletion in the interfacial region, to an extent depending on ambient pressure and temperature [Mamatkulov *et al.* (2004)] and on the hydrophobicity of the surface [Sendner *et al.* (2009)]. Moreover, at soft surfaces, such as air–water interfaces, the density increases monotonically, whereas at most solid surfaces, the water molecules arrange in distinct layers, leading to an oscillating density profile [Sedlmeier *et al.* (2008)]. Finally, vibrational spectroscopy experiments show that the water molecules in the interfacial region are preferentially oriented with their dipole moments pointing roughly along the surface plane at both air–water interfaces [Du

Electrostatics of Soft and Disordered Matter
Edited by David Dean, Jure Dobnikar, Ali Naji, and Rudolf Podgornik

ISBN 978-981-4411-85-1 (Hardcover), 978-981-4411-86-8 (eBook)
www.panstanford.com

et al. (1993)] and quartz–water interfaces [Du *et al.* (1994a,b)]. For macroscopic solutes, this molecular structure strongly affects both their static properties, such as double-layer capacitance, and their dynamic behavior, such as electro-osmotic mobility and surface conductance.

In this chapter, we present a modeling approach by which we calculate the molecular properties, in particular the dielectric profile, from molecular dynamics (MD) simulations and incorporate the results into a modified Poisson–Boltzmann equation. Our MD simulations show that the aqueous interface can be characterized by two largely independent characteristic length scales: the dielectric-dividing surface, based on the dielectric profile, and the Gibbs-dividing surface, based on the water density profile. Using these two interface characteristics, we estimate two of the main contributions to the interaction between a surface and a single ion.

10.2 Calculation of the Dielectric Profile

If the electric field is independent of the spatial coordinates $\boldsymbol{r}$, $\boldsymbol{E}(\boldsymbol{r}) = \boldsymbol{E}$, a change in the global electric field $\Delta\boldsymbol{E}$ is related to a change in the local displacement field $\Delta\boldsymbol{D}(\boldsymbol{r})$ by the tensorial local response function $\varepsilon(\boldsymbol{r})$,

$$\Delta\boldsymbol{D}(\boldsymbol{r}) = \varepsilon_0\varepsilon(\boldsymbol{r}) \cdot \Delta\boldsymbol{E}, \tag{10.1}$$

with ε_0 being the permittivity of vacuum and $\varepsilon(\boldsymbol{r})$ being the integral over one argument of the nonlocal dielectric response function [Bonthuis *et al.* (2012)]. Similarly, a change in the homogeneous displacement field, $\Delta\boldsymbol{D}$, is related to a change in the local electric field $\Delta\boldsymbol{E}(\boldsymbol{r})$ by the inverse dielectric response function $\varepsilon^{-1}(\boldsymbol{r})$,

$$\Delta\boldsymbol{E}(\boldsymbol{r}) = \varepsilon_0^{-1}\varepsilon^{-1}(\boldsymbol{r}) \cdot \Delta\boldsymbol{D}. \tag{10.2}$$

To calculate the dielectric function from the polarization of the medium, the electric field $\boldsymbol{E}(\boldsymbol{r})$ is separated into the displacement field $\boldsymbol{D}(\boldsymbol{r})$, associated with the monopole density $P_0(\boldsymbol{r})$, and the polarization $\boldsymbol{m}(\boldsymbol{r})$, generated by all higher order multipole moments, $\varepsilon_0\boldsymbol{E}(\boldsymbol{r}) = \boldsymbol{D}(\boldsymbol{r}) - \boldsymbol{m}(\boldsymbol{r})$. We consider water at a planar surface, having translational invariance in the x and y directions

and a dielectric discontinuity in the z direction. In this planar geometry, the dielectric tensor is diagonal with only two unique components, one parallel and one perpendicular to the surface, and the electric field and the polarization density depend on the z direction only. Maxwell's equation $\nabla \times \boldsymbol{E}(z) = 0$ implies that $E_\parallel$, corresponding to E_x or E_y, is independent of z everywhere. With the symmetry condition $\Delta E_\parallel = E_\parallel$, the parallel component of Eq. 10.1 becomes

$$\varepsilon_\parallel(z) = 1 + \frac{\Delta m_\parallel(z)}{\varepsilon_0 E_\parallel}. \tag{10.3}$$

When the monopole density $P_0(z) = 0$, Maxwell's equation for the displacement field, $\nabla \cdot \boldsymbol{D}(z) = P_0(z)$, shows that the displacement field is constant in space. Using the boundary condition $\Delta D_\perp(z) = D_\perp$, the perpendicular component of the inverse dielectric function given in Eq. 10.2 becomes

$$\varepsilon_\perp^{-1}(z) = 1 - \frac{\Delta m_\perp(z)}{D_\perp}. \tag{10.4}$$

Applying an external electric field, the dielectric tensor can be calculated directly from Eqs. 10.3 and 10.4. To estimate the dielectric response from the fluctuations of the polarization in absence of an external field, we use a statistical mechanical expression for the excess polarization $\Delta\boldsymbol{m}(\boldsymbol{r})$ upon application of an external field. For small applied field $\boldsymbol{F}$, the linearized ensemble average of the excess polarization vector is given by [Kirkwood (1939); Fröhlich (1949); Ballenegger and Hansen (2005)]

$$\Delta\boldsymbol{m}(\boldsymbol{r}) \approx \beta\left[\langle \boldsymbol{m}(\boldsymbol{r})\,\boldsymbol{M}\rangle_0 - \langle \boldsymbol{m}(\boldsymbol{r})\rangle_0\langle \boldsymbol{M}\rangle_0\right]\cdot\boldsymbol{F}, \tag{10.5}$$

where $\langle \ldots \rangle_0$ denotes the ensemble average without applied electric field. In order to determine the dielectric tensor, we need to know the relation between the applied field $\boldsymbol{F}$ in Eq. 10.5 and $\Delta\boldsymbol{E}$ or $\Delta\boldsymbol{D}$ in Eqs. 10.1 and 10.2. In the direction parallel to the surface, the homogeneous applied field $F_\parallel$ in Eq. 10.5 must correspond to the homogeneous field $E_\parallel$. Therefore, combining Eqs. 10.3 and 10.5 leads to

$$\varepsilon_\parallel(z) \approx 1 + \varepsilon_0^{-1}\beta\left[\langle m_\parallel(z)\,M_\parallel\rangle_0 - \langle m_\parallel(z)\rangle_0\langle M_\parallel\rangle_0\right]. \tag{10.6}$$

In the direction perpendicular to the surface, the spatially constant field $F_\perp$ must be associated with the homogeneous displacement

field $D_\perp/\varepsilon_0$. Consequently, combining Eqs. 10.4, 10.5, and 10.8, we arrive at the fluctuation equation for the inverse perpendicular permittivity,

$$\varepsilon_\perp^{-1}(z) \approx 1 - \varepsilon_0^{-1}\beta\left[\langle m_\perp(z)\, M_\perp\rangle_0 - \langle m_\perp(z)\rangle_0\langle M_\perp\rangle_0\right]. \qquad (10.7)$$

The polarization $\boldsymbol{m}(\boldsymbol{r})$ can be calculated in two different ways. The first method is to express $\boldsymbol{m}(\boldsymbol{r})$ in terms of the multipole densities [Jackson (1998); Bonthuis *et al.* (2012)]

$$\boldsymbol{m}(\boldsymbol{r}) = \boldsymbol{P}_1(\boldsymbol{r}) - \nabla\cdot \mathrm{P}_2(\boldsymbol{r}) + \nabla\nabla : \mathrm{P}_3(\boldsymbol{r}) - \ldots. \qquad (10.8)$$

The terms written explicitly are the dipole density $\boldsymbol{P}_1$, the quadrupole density P_2, and the octupole density P_3. When each molecule i is composed of atoms j with point charges q_j^i at positions $\boldsymbol{r}_j^i$, the terms of Eq. 10.8 are set by the spatial distribution of partial charges,

$$\mathrm{P}_l(\boldsymbol{r}) = \sum_i \mathrm{p}_{li}\,\delta(\boldsymbol{r}-\boldsymbol{r}_i) \quad \text{with} \quad \mathrm{p}_{li} = \frac{1}{l!}\sum_{j(i)} q_j^i\left(\boldsymbol{r}_j^i - \boldsymbol{r}_i\right)^l, \quad (10.9)$$

where p_{li} denotes the molecular multipole moment of order $l \in \{0, 1, 2, \ldots\}$, and $\boldsymbol{r}_i$ is some reference point in the molecule. Alternatively, the perpendicular polarization density in absence of free charges, $P_0(z) = 0$, is calculated from an integral over the total charge density $\rho(z) = \sum_{i,j} q_j^i \delta\left(\boldsymbol{r} - \boldsymbol{r}_j^i\right)$,

$$m_\perp(z) = -\int_0^z \rho\left(z'\right)\, dz'. \qquad (10.10)$$

To calculate the polarization $m_\parallel$ in the direction parallel to the surface, we introduce a virtual cut perpendicular to the x-axis, where the x direction can be any direction parallel to the surface. We only cut the water molecules at the position of the virtual cut, closing the volume without cutting any other molecules. By cutting the volume, some water molecules are split, forming a nonzero monopole density $P_0(x, z)$ on either side of the virtual cut, where the x dependence of $P_0(x, z)$ has the form of a Dirac delta function at the position of the cut. For more details, see [Bonthuis *et al.* (2012)]. The parallel polarization density is calculated from

$$m_\parallel(z) = \pm\int P_0(x, z)\, dx, \qquad (10.11)$$

where the different signs apply to closing the volume and integrating $P_0(x, z)$ on the different sides of the cut. To calculate $m_\parallel(z)$, Eq. 10.11 is averaged over many different cut positions along the x-axis.

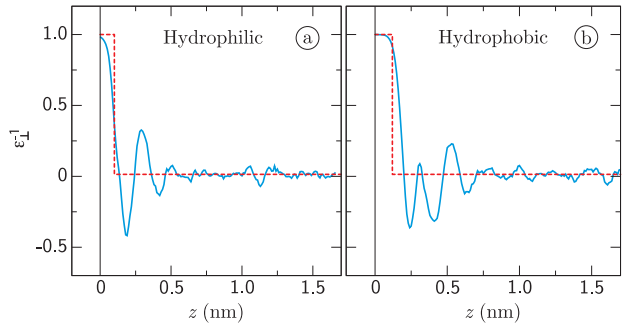

Figure 10.1 The inverse perpendicular dielectric profile (blue solid lines), calculated using Eqs. 10.7 and 10.10, for SPC/E water at (a) a hydrophilic (hydroxide-terminated) and (b) a hydrophobic (hydrogen-terminated) diamond surface. See [Bonthuis *et al.* (2012)] for details of the MD simulations. Also shown is the step-function approximation of Eq. 10.12 (red dashed lines).

The dielectric profiles calculated from either the fluctuations or the response to an applied field, and using either of the methods described above to calculate $\boldsymbol{m}(\boldsymbol{r})$, all coincide [Bonthuis *et al.* (2012)]. Interestingly, $\varepsilon_\perp^{-1}(z)$ shows strong oscillations—even passing through zero several times—within the first few water layers, reflecting the molecular structure at the interface (Fig. 10.1).

10.2.1 *Construction of the Dielectric Dividing Surface*

For further investigation of the effect of the dielectric profile on macroscopic interfacial properties, such as the double-layer capacitance, the electrophoretic mobility, and the surface conductivity, it is convenient to simplify the dielectric profile. We approximate the profile shown in Fig. 10.1 with a step function,

$$\varepsilon_\perp(z) = \begin{cases} 1 & \text{if } z < z_\perp^{\text{DDS}} \\ \varepsilon_{\text{bulk}} & \text{otherwise.} \end{cases} \tag{10.12}$$

The dielectric-dividing surface position in Eq. 10.12 is defined as

$$z_\perp^{\text{DDS}} = z_v + \int_{z_v}^{z_l} \frac{\varepsilon_\perp^{-1}(z_l) - \varepsilon_\perp^{-1}(z)}{\varepsilon_\perp^{-1}(z_l) - \varepsilon_\perp^{-1}(z_v)}\, dz, \tag{10.13}$$

with z_v and z_l being positions in the solid and liquid phase, respectively. The profile in Eq. 10.12 is designed to reproduce the

electrostatic potential calculated in molecular dynamics simulations at positions $z \gtrsim 1$ nm from the interface [Bonthuis *et al.* (2011)]. The definition of the dielectric-dividing surface in Eq. 10.13 is analogous to the definition of the Gibbs-dividing surface, which follows from Eq. 10.13 by replacing the dielectric profile $\varepsilon_\perp^{-1}(z)$ by the water density profile. On a simple level, the effects of the dielectric profile and the density profile can be quantified using these two length scales. For $z_\perp^{\mathrm{DDS}}$, we use two different values: $z_\perp^{\mathrm{DDS}} = 0.10$ nm, corresponding to a hydrophilic surface, and $z_\perp^{\mathrm{DDS}} = 0.12$ nm, corresponding to a very hydrophobic surface [Bonthuis *et al.* (2012)]. The insensitivity of $z_\perp^{\mathrm{DDS}}$ to the surface type stands in strong contrast to the Gibbs-dividing surface z^{GDS}, which lies much closer to the surface at hydrophilic surfaces ($z^{\mathrm{GDS}} = 0.07$ nm) than at hydrophobic surfaces ($z^{\mathrm{GDS}} = 0.22$ nm). The inverse dielectric profiles $\varepsilon_\perp^{-1}(z)$ in the step-function approximation of Eq. 10.12 are shown as red dashed lines in Fig. 10.1.

10.3 Modified Poisson–Boltzmann Equation

At charged surfaces, the monopole density $P_0(z)$ is nonzero, and consequently, the displacement field $D_\perp(z)$ is not homogeneous. Therefore, we use the local assumption that the electric field $E_\perp(z)$ is linearly related to $D_\perp(z)$ by $\varepsilon_\perp^{-1}(z)$,

$$\varepsilon_0 E_\perp(z) = \varepsilon_\perp^{-1}(z)\, D_\perp(z)\,. \tag{10.14}$$

Eq. 10.14 is a good approximation in case of a slowly varying $D_\perp(z)$ [Bonthuis *et al.* (2011); Kornyshev *et al.* (1982)]. Taking the derivative of Eq. 10.14 and using $\nabla\psi(z) = -E_\perp(z)$, with $\psi(z)$ the electrostatic potential, and $\nabla D_\perp(z) = P_0(z)$, with $P_0(z)$ the ionic charge density, the Poisson equation is transformed into an integro-differential equation,

$$\varepsilon_0 \nabla^2 \psi(z) = -\varepsilon_\perp^{-1}(z)\, P_0(z) - D_\perp(z)\, \nabla \varepsilon_\perp^{-1}(z)\,, \tag{10.15}$$

with the displacement field $D_\perp(z)$ being given by

$$D_\perp(z) = \int_0^z P_0\left(z'\right) \mathrm{d}z'. \tag{10.16}$$

Considering a solution of monovalent ions, the free charge density is calculated from the ionic densities $c_+(z)$ and $c_-(z)$,

$$P_0(z) = e\left(c_+(z) - c_-(z)\right), \tag{10.17}$$

with e the absolute charge of an electron. To ensure that the ionic density does not exceed its physical limit set by the ionic volume, we include a fermionic steric interaction to calculate the ionic densities from the unrestricted ionic densities $\tilde{c}_+(z)$ and $\tilde{c}_-(z)$ [Bikerman (1942); Eigen and Wicke (1954); Kralj-Iglič and Iglič (1994); Borukhov *et al.* (1997, 2000)],

$$c_\pm(z) = \frac{\sqrt{2}\,\tilde{c}_\pm(z)}{\sqrt{2} + a_+^3\left(\tilde{c}_+(z) - c_0\right) + a_-^3\left(\tilde{c}_-(z) - c_0\right)}, \tag{10.18}$$

with c_0 the bulk salt concentration and a_+ and a_- the diameters of positive and negative ions, respectively. The denominator in Eq. 10.18 restricts the maximum density $c_\pm(z)$ to $\sqrt{2}\,a_\pm^{-3}$, which is the maximum density of close-packed (face-centered cubic or hexagonal close-packed) spheres of diameter $a_\pm$. The unrestricted ionic densities $\tilde{c}_+(z)$ and $\tilde{c}_-(z)$ follow the Boltzmann distribution

$$\tilde{c}_\pm(z) = c_0 \exp\left[-\mu_\pm(z) \mp \beta e\psi(z)\right], \tag{10.19}$$

with β being the inverse thermal energy and $\mu_+(z)$ and $\mu_-(z)$ being the nonelectrostatic contributions to the potentials of the positive and negative ions, respectively. Combining Eqs. 10.15–10.19 yields the modified Poisson–Boltzmann equation. It should be noted that the steric interaction of Eq. 10.18 becomes important only in case of high surface charge density, high salt concentration, or large ion size [Bazant *et al.* (2009)]; its effect on the calculations presented here is minor.

For the nonelectrostatic potential $\mu_\pm(z)$, we use a heuristic function of the form

$$\mu_\pm(z) = \alpha \exp\left[1 - 2z/a_\pm\right]. \tag{10.20}$$

Beyond 1 nm away from the interface, the potential of mean force—which includes dielectric as well as nonelectrostatic effects—typically shows a decreasing shape that can be well approximated with the exponential form of Eq. 10.20 [Horinek *et al.* (2008); Schwierz *et al.* (2010)].

10.3.1 *Double-Layer Capacitance*

To demonstrate the experimentally relevant consequences of the dielectric profile determined in Section 10.3, we calculate the double-layer capacitance and compare the result with experimental data. We solve Eqs. 10.15–10.19 at a surface with surface charge density σ_0, using the boundary conditions $\lim_{z\to\infty} \psi(z) = 0$ and overall charge neutrality. The capacitance C is calculated in the limit $\sigma_0 \to 0$ from $C = d\sigma_0/d\psi_0$, with ψ_0 the potential at $z = 0$. Assuming $\varepsilon_\perp(z) = \varepsilon_{\text{bulk}}$ (dashed lines in Fig. 10.2), the result of the Poisson–Boltzmann equation overestimates the experimental data by one order of magnitude. Better agreement with the experimental data is obtained when the dielectric profile is taken into account via Eq. 10.12 (solid lines in Fig. 10.2), which effectively introduces an interfacial layer with a low dielectric constant, much alike the Stern layer [Stern (1924)]. The experimental results can be fitted quantitatively using the nonelectrostatic potential $\mu_\pm(z)$ of Eq. 10.20 in addition to the dielectric profile (dotted lines in Fig. 10.2), where the interaction strength α is used as a fitting parameter to account for the data spread due to the different surface materials and ion types used in the experiments. The interaction strength

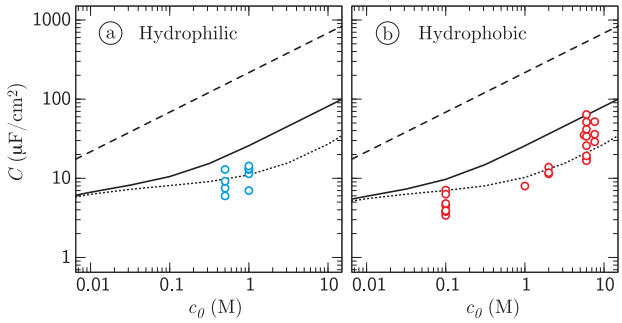

Figure 10.2 Double-layer capacitance C as a function of the bulk salt concentration c_0. Symbols represent experimental results on different kinds of (a) hydrophilic and (b) hydrophobic carbon-based surfaces [Bonthuis *et al.* (2011)]. Curves represent theoretical results using $\varepsilon_\perp(z) = \varepsilon_{\text{bulk}}$ with $\mu_\pm(z) = 0$ (dashed lines), $\varepsilon_\perp(z)$ from Eq. 10.12 with $\mu_\pm(z) = 0$ (solid lines), and $\varepsilon_\perp(z)$ from Eq. 10.12 with $\mu_\pm(z)$ from Eq. 10.20 using $\alpha = 1$ (dotted lines).

needed to fit the data is of order unity; for the dotted curves in Fig. 10.2, we have used $\alpha = 1$. Interestingly, the experimental data demonstrate that the hydrophobicity of the surface has no significant influence on the double-layer capacitance, which can be viewed as a confirmation of our result that the values of $z_\perp^{\text{DDS}}$ hardly differ between the two surface types.

Using the modeling approach presented in Sections 10.2 and 10.3 in conjunction with a modified Navier Stokes equation, we have also been able to theoretically model electrokinetic measurements, in particular the electrophoretic mobility and the so-called anomalous surface conductivity [Bonthuis and Netz (2012)].

10.4 Ion-Specific Effects

In the calculations expounded in Section 10.3, the potential energy of an ion consists of the electrostatic energy of a point charge in the mean electrostatic potential, and a nonelectrostatic term for which the simplified form of Eq. 10.20 is used. Experimentally, however, the energy of interaction between an ion and a surface is found to depend on the ion's chemical properties, such as size, charge, and polarizability, and is strongly ion-specific [Kunz (2010)]. Models of the specific ion-surface interaction have been developed on the basis of polarizability and hydration effects [Levin (2009); Dos Santos *et al.* (2010)]. Equally important for the ion-specific interaction are the molecular structure of the interfacial water and the chemical properties of the surface [Schwierz *et al.* (2010)]. The combined potential due to the aforementioned effects is termed the potential of mean force (PMF), which can be incorporated into the Poisson–Boltzmann equation as a nonelectrostatic contribution to the potential. Previous attempts, however, to split the PMF into contributions from the Lennard–Jones potential, the polarizability, the image charge potential, and the electrostatics of the ordered water molecules, have failed to capture the results from atomistic MD simulations [Horinek *et al.* (2008)].

On the basis of the two length scales discussed above, the Gibbs-dividing surface z^{GDS} and dielectric-dividing surface $z_\perp^{\text{DDS}}$, we design a model for ion–surface interactions that combines the image charge

potential, which does not appear in a proper mean-field formulation, and the nonelectrostatic hydration energy. The model is aimed at capturing the main features of the ionic PMF. The image potential depends on the distance z' to the dielectric-dividing surface position, $z' = z - z_{\perp}^{\mathrm{DDS}}$, and on the size of the ion. For the latter, we introduce the dielectric diameter $d_{\pm}$ as a second ionic diameter next to the ionic hard-sphere diameter $a_{\pm}$. The dielectric diameter can be estimated by equating the experimental solvation free energy to the sum of the electrostatic energy and the cavity hydration energy. Because the cavity contribution to the solvation free energy can be neglected for small ions, the dielectric diameter can be approximated by equating the ionic solvation free energy to the electrostatic energy $U_{\mathrm{b}}\,(1 - \varepsilon_{\mathrm{bulk}})$, with U_{b} being the Born free energy, given by

$$U_{\mathrm{b}} = \frac{e^2}{4\pi\, d_{\pm}\varepsilon_0\varepsilon_{\mathrm{bulk}}}. \tag{10.21}$$

For small ions, we expect that $d_{\pm} > a_{\pm}$, reflecting the observation that diameters inferred from the solvation free energy are larger than cavity diameters measured with diffraction methods [Marcus (1988)]. Given the hydrophilic nature of small ions, it also conforms with our result that $z_{\perp}^{\mathrm{DDS}} > z^{\mathrm{GDS}}$ at hydrophilic surfaces. However, the relation between $a_{\pm}$ and $d_{\pm}$ may be different for larger ions. In the following calculations, we choose $a_{\pm} = d_{\pm}$ for simplicity. The image potential $U_{\mathrm{i}}\,(z)$ with respect to the Born energy U_{b} is calculated numerically for a nonpolarizable finite-sized ion with $d_{\pm} = 0.3$ nm ($U_{\mathrm{TC}}\,(z)$ in Fig. 10.3a) [Tamashiro and Constantino (2010)]. Also shown in Fig. 10.3a are an approximate expression for a perfectly polarizable ion, denoted $U_{\mathrm{L}}\,(z)$ [Levin (2009)], and the flawed expression $U_{\mathrm{KU}}\,(z)$ [Kharkats and Ulstrup (1991); Markin and Volkov (2002)] used in previous studies [Bonthuis *et al.* (2012)], the latter of which lies in between the results for a perfectly polarizable and a nonpolarizable ion. In order to compare to MD simulations with nonpolarizable force fields, we use $U_{\mathrm{i}}\,(z) = U_{\mathrm{TC}}\,(z)$ to calculate the total interaction energy.

In addition to the repulsive image potential, the ions are subject to an attractive hydration potential, scaling with the hydrated volume of the ion [Horinek *et al.* (2009); Huang *et al.* (2001); Hummer *et al.* (1998)]. Calculating the ionic volume from the hard-

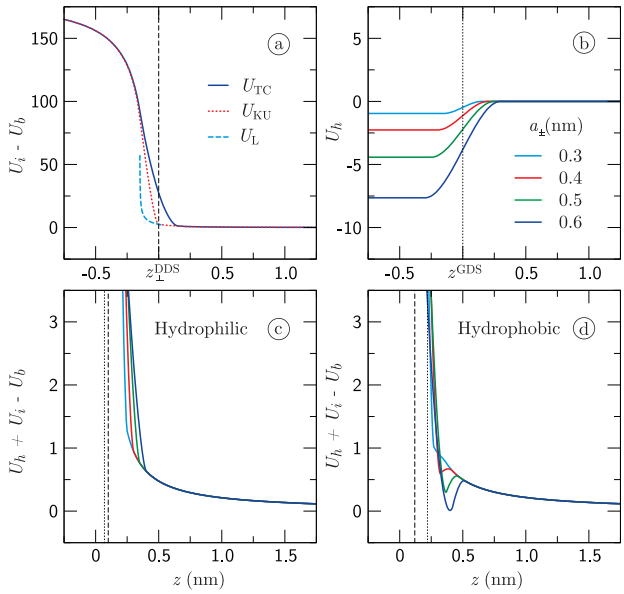

Figure 10.3 (a) Image charge potential $U_{\rm i}(z) - U_{\rm b}$ of a non-polarizable ($U_{\rm TC}(z)$ [Tamashiro and Constantino (2010)]) and a perfectly polarizable ($U_{\rm L}(z)$ [Levin (2009)]) ion of diameter $d_\pm = 0.3$ nm in the dielectric profile of Eq. 10.12. Also shown is the flawed Kharkats & Ulstrup potential $U_{\rm KU}(z)$ [Kharkats and Ulstrup (1991); Markin and Volkov (2002)]. (b) Hydration potential $U_{\rm h}(z)$ (Eq. 10.22) and the sum $U_{\rm h}(z)+U_{\rm i}(z)-U_{\rm b}$ at (c) hydrophilic and (d) hydrophobic surfaces, using $U_{\rm i}(z) = U_{\rm TC}(z)$, for ions of different diameter $a_\pm = d_\pm$ (legend as in b). Positions of the dielectric-dividing surface (dashed vertical lines) and Gibbs-dividing surface (dotted vertical lines) are also shown.

sphere cavity diameter $a_\pm$, the hydration energy is given by

$$U_{\rm h}(z) = \begin{cases} -\dfrac{\pi}{6} a_\pm^3 \beta C & \text{if } 2z'' < -a_\pm \\ 0 & \text{if } 2z'' > a_\pm \\ -\dfrac{\pi}{12}\left(a_\pm - 2z''\right)^2 \left(z'' + a_\pm\right) \beta C & \text{otherwise,} \end{cases} \tag{10.22}$$

with $z'' = z - z^{\rm GDS}$, β being the inverse thermal energy and $C = 2.8 \times 10^{-19}$ J/nm^3 being the hydration energy of an uncharged cavity in bulk water [Huang *et al.* (2008)]. Importantly, $U_{\rm i}(z)$ and $U_{\rm h}(z)$ act with respect to different surface positions: although the image potential acts with respect to $z^{\rm DDS}_\perp$ (Fig. 10.3a),

the hydration potential of Eq. 10.22 acts with respect to z^{GDS} (Fig. 10.3b). A major difference between hydrophilic and hydrophobic surfaces is that whereas $z^{\mathrm{GDS}} < z_{\perp}^{\mathrm{DDS}}$ at hydrophilic surfaces, their order is reversed at hydrophobic surfaces. Because $z^{\mathrm{GDS}} > z_{\perp}^{\mathrm{DDS}}$ at hydrophobic surfaces, the influence of the attractive hydration potential is much more pronounced than it is at hydrophilic surfaces. The total interaction potential $U_{\mathrm{h}}(z) + U_{\mathrm{i}}(z) - U_{\mathrm{b}}$ clearly reflects this difference between hydrophilic (Fig. 10.3c) and hydrophobic (Fig. 10.3d) surfaces: whereas big ions ($d_{\pm} = 0.6$ nm, corresponding to iodide) are repelled from hydrophilic surfaces, they are adsorbed on to hydrophobic surfaces, similar to the results of recent MD simulations [Schwierz *et al.* (2010)]. Small ions ($d_{\pm} = 0.3$ nm, corresponding to fluoride and sodium) are repelled from both surface types.

10.5 Summary and Conclusion

We have presented the theoretical framework to extract the dielectric profile of interfacial water from MD simulations. Incorporating the dielectric profile into a modified mean-field description of the interfacial electrostatics, we have shown that taking the dielectric properties of pure interfacial water into account is necessary to capture the experimental values of the double-layer capacitance. Characterizing the dielectric profile and the density profile of water with two independent length scales, namely the dielectric-dividing surface and the Gibbs-dividing surface, a simple calculation of the ion-surface interaction potential exhibits a conspicuous difference between hydrophilic and hydrophobic surfaces: large ions that are readily adsorbed on to hydrophobic surfaces are still repelled from hydrophilic ones.

References

Ballenegger, V. and Hansen, J. (2005). Dielectric permittivity profiles of confined polar fluids, *J. Chem. Phys.* **122**, p. 114711.

Bazant, M. Z., Kilic, M. S., Storey, B. D. and Ajdari, A. (2009). Towards an understanding of induced-charge electrokinetics at large applied voltages in concentrated solutions, *Adv. Colloid Interface Sci.* **152**, p. 48.

Bikerman, J. J. (1942). Structure and capacity of electrical double layer, *Philos. Mag.* **33**, p. 384.

Bonthuis, D. J., Gekle, S. and Netz, R. R. (2011). Dielectric profile of interfacial water and its effect on double-layer capacitance, *Phys. Rev. Lett.* **107**, p. 166102.

Bonthuis, D. J., Gekle, S. and Netz, R. R. (2012). Profile of the static permittivity tensor of water at interfaces: Consequences for capacitance, hydration interaction and ion adsorption, *Langmuir* **28**, p. 7679.

Bonthuis, D. J. and Netz, R. R. (2012). Unraveling the combined effects of dielectric and viscosity profiles on surface capacitance, electro-osmotic mobility, and electric surface conductivity, *Langmuir* **28**, p. 16049.

Borukhov, I., Andelman, D. and Orland, H. (1997). Steric effects in electrolytes: A modified Poisson-Boltzmann equation, *Phys. Rev. Lett.* **79**, p. 00319007.

Borukhov, I., Andelman, D. and Orland, H. (2000). Adsorption of large ions from an electrolyte solution: A modified Poisson-Boltzmann equation, *Electrochim. Acta* **46**, p. 221.

Dos Santos, A. P., Diehl, A. and Levin, Y. (2010). Surface tensions, surface potentials, and the hofmeister series of electrolyte solutions, *Langmuir* **26**, p. 10778.

Du, Q., Freysz, E. and Shen, Y. R. (1994a). Surface vibrational spectroscopic studies of hydrogen bonding and hydrophobicity, *Science* **264**, p. 826.

Du, Q., Freysz, E. and Shen, Y. R. (1994b). Vibrational spectra of water molecules at quartz/water interfaces, *Phys. Rev. Lett.* **72**, p. 238.

Du, Q., Superfine, R., Freysz, E. and Shen, Y. R. (1993). Vibrational spectroscopy of water at the vapor water interface, *Phys. Rev. Lett.* **70**, p. 2313.

Eigen, M. and Wicke, E. (1954). The thermodynamics of electrolytes at higher concentration, *J. Phys. Chem.* **58**, p. 702.

Fröhlich, H. (1949). *Theory of Dielectrics* (Clarendon Press, Oxford).

Horinek, D. *et al.* (2008). Molecular hydrophobic attraction and ion-specific effects studied by molecular dynamics, *Langmuir* **24**, p. 1271.

Horinek, D. *et al.* (2009). Specific ion adsorption at the air/water interface: The role of hydrophobic solvation, *Chem. Phys. Lett.* **479**, p. 173.

Huang, D. M., Cottin-Bizonne, C., Ybert, C. and Bocquet, L. (2008). Aqueous electrolytes near hydrophobic surfaces: Dynamic effects of ion specificity and hydrodynamic slip, *Langmuir* **24**, p. 1442.

Huang, D. M., Geissler, P. L. and Chandler, D. (2001). Scaling of hydrophobic solvation free energies, *J. Phys. Chem. B* **105**, p. 6704.

Hummer, G., Garde, S., García, A. E., Paulaiti, M. E. and Pratt, L. R. (1998). Hydrophobic effects on a molecular scale, *J. Phys. Chem. B* **102**, p. 10469.

Jackson, J. D. (1998). *Classical Electrodynamics*, 3rd edn. (John Wiley & Sons, USA).

Kharkats, Y. I. and Ulstrup, J. (1991). The electrostatic Gibbs energy of finite-size ions near a planar boundary between 2 dielectric media, *J. Electroanal. Chem.* **308**, p. 17.

Kirkwood, J. G. (1939). The dielectric polarization of polar liquids, *J. Chem. Phys.* **7**, p. 911.

Kornyshev, A. A., Schmickler, W. and Vorotyntsev, M. A. (1982). Nonlocal electrostatic approach to the problem of a double layer at a metal-electrolyte interface, *Phys. Rev. B* **25**, p. 5244.

Kralj-Iglič, V. and Iglič, A. (1994). Influence of finite size of ions on elecrostatic properties of electric double layer, *Electrotechnical Review (Ljubljana, Slovenija)* **61**, p. 127.

Kunz, W. (2010). Specific ion effects in colloidal and biological systems, *Curr. Opin. Colloid Interface Sci.* **15**, p. 34.

Levin, Y. (2009). Polarizable ions at interfaces, *Phys. Rev. Lett.* **102**, p. 147803.

Mamatkulov, S. I., Khabibullaev, P. K. and Netz, R. R. (2004). Water at hydrophobic substrates: Curvature, pressure, and temperature effects, *Langmuir* **20**, p. 4756.

Marcus, Y. (1988). Ionic radii in aqueous solutions, *Chem. Rev.* **88**, p. 1475.

Markin, V. S. and Volkov, A. G. (2002). Quantitative theory of surface tension and surface potential of aqueous solutions of electrolytes, *J. Phys. Chem. B* **106**, p. 11810.

Schwierz, N., Horinek, D. and Netz, R. R. (2010). Reversed anionic Hofmeister series: The interplay of surface charge and surface polarity, *Langmuir* **26**, p. 7370.

Sedlmeier, F. *et al.* (2008). Water at polar and nonpolar solid walls, *Biointerphases* **3**, p. FC23.

Sendner, C., Horinek, D., Bocquet, L. and Netz, R. R. (2009). Interfacial water at hydrophobic and hydrophilic surfaces: Slip, viscosity, and diffusion, *Langmuir* **25**, p. 10768.

Stern, O. (1924). Zur Theorie der elektrolytischen Doppelschicht, *Z. Elektrochem.* **30**, p. 508.

Tamashiro, M. N. and Constantino, M. A. (2010). Ions at the water-vapor interface, *J. Phys. Chem. B* **114**, p. 3583.

Chapter 11

Hydration Repulsion between Polar Surfaces: An Atomistic Simulation Approach

Matej Kanduč,[a,b] Emanuel Schneck,[c] and Roland R. Netz[a]

[a] *Department of Physics, Free University Berlin, D-14195 Berlin, Germany*
[b] *Department of Theoretical Physics, J. Stefan Institute, SI-1000 Ljubljana, Slovenia*
[c] *Institut Laue-Langevin, 6 Rue Jules Horowitz, F-38000 Grenoble, France*

11.1 Introduction

11.1.1 *Hydration Repulsion*

Soft and biological matter is governed by three fundamental interactions. Two of them are long-ranged, namely the van der Waals and electrostatic forces. For large separations, these two contributions can be treated in a continuum formulation in terms of Derjaguin-Landau-Verwey-Overbeek (DLVO) theory [1]. In this approximation, the interacting particles or molecules and the intervening water are treated as continuum media with homogeneous properties (such as dielectric constant and surface charge density. The third important and very strong repulsive

Electrostatics of Soft and Disordered Matter
Edited by David Dean, Jure Dobnikar, Ali Naji, and Rudolf Podgornik

ISBN 978-981-4411-85-1 (Hardcover), 978-981-4411-86-8 (eBook)
www.panstanford.com

fundamental force is the hydration interaction. It results from the removal of water molecules from hydrophilic groups and is not well captured by continuum approximations. The hydration repulsion was experimentally quantified in 1970s in diffraction experiments of membrane multilayers [2, 3] and by surface force apparatus measurements of pairs of membranes [4].

Experiments revealed that the hydration repulsion is a very short-ranged force, acting typically on the nanometer range. It approximately obeys an exponential decay law with a decay constant λ between 0.1 nm and 0.6 nm [5]. More recently, also a multiexponential law with several decay lengths has been suggested [6]. The hydration forces can easily reach repulsive pressures of several kilobars at small separations, overcoming the other attractive DLVO force contributions. It is responsible for the stabilization of membrane surfaces and stops vesicles from close contact with cell membranes, making spontaneous fusion difficult [7].

The mechanism of the hydration repulsion is still not fully understood. An attempt to rationalize the repulsion between membranes has been proposed by Marcelja et al. [8]. They predicted an exponential decay of the repulsion on the basis of a general order-parameter description. Despite some progress of continuum models, it has become a consensus view during the last decades that in order to explain the hydration interaction on a quantitative level, the structure of the solvent has to be taken into account explicitly [5]. In recent years, this insight has drawn the attention toward the application of atomistic simulations, wherein water molecules are treated explicitly including all relevant degrees of freedom. In this article, we review an approach to study the interactions between surfaces in aqueous environments using atomistic simulations with a focus on the hydration interaction.

11.2 Modeling Lipid Bilayers

11.2.1 *Atomistic Molecular Dynamics Simulations*

Computer simulations are able to provide exact results for models of many-body problems, which could in general not be solved

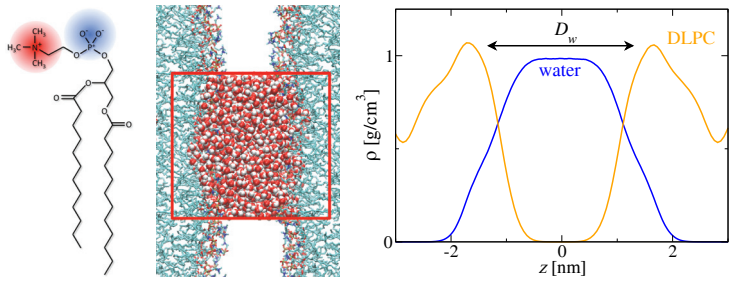

Figure 11.1 (a) Amphiphilic DLPC molecule with polar head group and alkyl tails. (b) Snapshot of the simulated system of membrane layers with $N = 2016$ water molecules in between. The simulation box with dimensions $L_x = 4.2\,\text{nm}$, $L_y = 5.1\,\text{nm}$, and $L_z = 5.7\,\text{nm}$ is shown as a red rectangle and is repeated infinitely many times in all three directions via periodic boundary conditions. Water is shown only in the red rectangle for clarity. (c) Measured density profiles of water and DLPC bilayer for the system shown in (b).

exactly in terms of analytical approaches. Molecular dynamics (MD) constitutes one branch of molecular modeling, as it refers to the use of classical Newtonian mechanics to describe the physical basis behind atomistic models [9, 10].

We focus on a typical system of biological membranes, composed of dilinoleoyl-phosphatidyl-choline (DLPC) lipids. Each DLPC molecule is composed of two 12-carbon atom long aliphatic chains, $CH_3(CH_2)_{10}COOH$, which are attached to a polar head group, Fig. 11.1a. Tails are hydrophobic and build the interior of the membranes. On the contrary, the polar head groups, which are exposed to water, are hydrophilic. Water in our system is modeled in terms of the simple point charge/extended (SPC/E) model. Here, each water molecule is represented by three Coulomb point charges (comprising the oxygen and two hydrogen atoms) as well as an additional Lennard-Jones dispersion interaction on the oxygen atom [11].

We have used the OPLS/Berger forcefield, which determines effective interactions between lipids and water molecules. The parameters were determined by a combination of ab initio calculations and empirical optimization in such a way as to reproduce correct lipid densities [12].

11.2.2 *Keeping the Water Chemical Potential Constant: Thermodynamic Extrapolation*

The next important challenge in our modeling is keeping the water chemical potential constant. The experimentally relevant ensemble is the one where water is allowed to freely exchange with an external bulk reservoir. In other words, the water is at constant chemical potential. At given temperature T, the interacting pressure p between the surfaces is related to the derivative of the free energy G with respect to the inter-surface distance D_{w} at constant water chemical potential, viz.

$$p = -\frac{1}{A}\left(\frac{\partial G}{\partial D_{\mathrm{w}}}\right)_{\mu,T}, \tag{11.1}$$

where A is the surface area. However, simulating an explicit bulk water reservoir in computer simulations is very time-consuming and the systems suffer from edge-effects. Alternatively, the constant chemical potential can be assured through frequent deletions and insertions of individual water molecules. This approach was established by Grunze, Pertsin, and coworkers by using a grand canonical Monte Carlo (GCMC) approach [13]. However, the bottleneck of this method is the pressure resolution as determined by the precision with which the chemical potential of water can be controlled. In the GCMC approach, the pressure resolution has reached about 200 bars, such that interactions can only be studied under conditions of high pressures, which correspond to small surface separations [14].

In order to achieve fast numerical convergence, we use the recently introduced thermodynamic extrapolation (TE) method [15]. We perform simulations in the canonical NpT ensemble, that is, with constant number of water molecules N and constant isotropic pressure p. During simulations, a constant pressure is maintained in all three directions by independent adjustments of the box dimensions. The actual pressure is continuously measured during simulations via the pressure tensor $\mathbf{P}$, which is calculated from the difference between kinetic energy $\mathbf{E}_{\mathrm{kin}}$ and the virial Ξ [16],

$$\mathbf{P} = \frac{2}{V}(\mathbf{E}_{\mathrm{kin}} - \Xi), \tag{11.2}$$

where V is the volume of the simulation box. The virial Ξ tensor is defined as:

$$\Xi = -\frac{1}{2}\sum_{i<j} \mathbf{r}_{ij} \otimes \mathbf{F}_{ij}. \tag{11.3}$$

The simulated system at prescribed pressure does not necessarily correspond to the wanted chemical potential μ_0. Instead, the chemical potential μ_1 in our simulation differs from the wanted chemical potential μ_0. The standard ways of measuring chemical potential in computer simulations are the Widom particle insertion method (TPI) or the thermodynamic integration method (TI) [9].

The crucial part of TE, on a simplified level, follows from the Gibbs–Duhem equation, $Nd\mu = -SdT + Vdp$. Under constant temperature, a chemical potential deviation $\Delta\mu$ is linearly proportional to a pressure change Δp. By measuring the actual pressure in our simulations $p(\mu_1)$ at a certain chemical potential μ_1, we can predict the pressure $p(\mu_0)$ that would correspond to the chemical potential μ_0 in terms of the linear relationship,

$$p(\mu_0) = p(\mu_1) + \frac{\mu_0 - \mu_1}{v_\mathrm{w}}, \tag{11.4}$$

which corresponds to the extrapolated pressure. Here, $v_\mathrm{w} = V/N \approx 0.030\,\mathrm{nm}^3$ is the volume occupied by a single water molecule. This linear relationship turns out to work fairly well on a range of several hundred bars, as water is quite incompressible, and therefore, v_w remains almost constant [15]. For a formal derivation and an estimate of correction terms, see Ref. [15].

11.3 Results and Discussion

In order to carry out MD simulations of the system, we use the GROMACS simulation package [16]. We perform two sets of MD simulations, both in the canonical NpT ensemble at $T = 300\,\mathrm{K}$. The first set, which we will refer to as MD1, was done under actual pressure of 1 bar. The measured chemical potential μ_1 in this case depends on the surface separation. The interacting pressure between the membranes that corresponds to the bulk water chemical potential μ_0 is then calculated via the TE, Eq. (11.4). In the second set of simulations, MD2, we have used the extrapolated

pressure results from MD1 as the actual pressure in the simulations. By this iteration, the chemical potential in MD2 is very close to the bulk water chemical potential μ_0 for all surface separations. Consequently, the extrapolated pressure is also very close to the actual pressure in MD2. A comparison of the extrapolated pressure results from both simulations enables us to estimate how good the results in the first step MD1 really are.

In fact, the two simulation sets correspond to two different experimental set-ups. Namely, the MD2 simulations, which are done at approximately bulk chemical potential, correspond to the experiment in which a membrane stack is under hydrostatic pressure and in contact with a water reservoir. This hydrostatic method is usually used for smaller pressures and larger separations, typically $D_{\mathrm{w}} = 0.5 - 1.7$ nm [2]. In contrast, in the MD1 set, the chemical potential depends on the membrane separation. This method mimics the experimental technique in which the lipids are equilibrated at constant atmospheric pressure and with known partial pressures generated by a polymer or a saturated salt solution [2, 17]. With this measurement method, the pressures at prescribed chemical potential are estimated by using the same TE relationship, Eq. (11.4). The latter method is suitable for smaller separation ranges $D_{\mathrm{w}} = 0.3 - 0.5$ nm and can therefore complement the hydrostatic method.

Either set of MD simulations, be it MD1 or MD2, can be performed for the entire separation range from 0.3 nm up to 3.0 nm. Their comparison therefore allows for checking the consistency of both experimental methods.

Figure 11.1b shows a simulation snapshot of 72 DLPC lipids hydrated by $N = 2016$ water molecules under isotropic actual pressure 1 bar. As can be seen from Fig. 11.1c, the water density profile does not show abrupt changes but a continuous decay at the membrane surfaces, meaning that water penetrates around 1 nm deep into the membranes. We define surface–surface separation as the width of the corresponding water slab of bulk density, that is,

$$D_{\mathrm{w}} = \frac{v_{\mathrm{w}} N}{L_x L_y}, \tag{11.5}$$

where v_{w} is a volume of one water molecule in the bulk, and N is the number of water molecules in the simulation box.

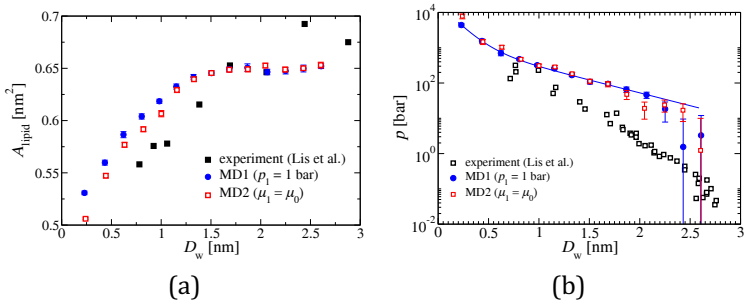

Figure 11.2 (a) Area per lipid as a function of water-slab thickness. (b) Pressure as obtained from the TE expression is compared with experimental data. The solid line is a double exponential fit to the MD1 data.

The lateral surface area that each lipid occupies depends on the level of hydration, hence D_w. As seen from Fig. 11.2a, the area per lipid at full hydration is $A = 0.64\,\mathrm{nm}^2$ in both simulation sets, which is only slightly lower than the experimental value from Ref. [3]. At lower hydration, that is, at smaller surface–surface separations, the lipids tend to squeeze together and the area shrinks. As expected, the area decreases more in MD2, as the actual pressure in simulations gets larger at smaller separations. However, the difference between both ensembles is small.

Figure 11.2b shows the simulated pressure–distance curves at constant chemical potential in a semi-logarithmic plot. The MD1 (blue circles) and MD2 (red empty squares) are compared with experimental values (black filled squares). The hydration force exhibits large pressures of several kilobars at very small separations and decays rapidly on a nanometer scale.

The two MD sets of simulations mimicking vapor and hydrostatic method do not show any significant difference. Namely, the small changes in area per lipid do not alter the hydration interaction much. Therefore, we can conclude that also vapor and hydrostatic experimental methods are consistent and do not show significant systematic differences.

The comparison with experiment is nearly quantitative in terms of the pressure scale at small separations, and qualitative in terms of the exponential decay at larger distances. At short distances below

0.5 nm, the opposing head groups tend to overlap, which results in an enhanced steric repulsion with a decay length of around $\lambda = 0.24$ nm. At separations above 0.5 nm, the decay length is larger by around a factor of 2, namely $\lambda = 0.5$ nm. The experimental results exhibit an almost perfect exponential decay with a decay length of $\lambda = 0.26$ nm, which agrees with simulations only at shorter separations. We obtain a similar value of $\lambda = 0.44$ nm in a related study of DPPC membranes, which have slightly longer hydrophobic tails than DLPC [15].

In fact, various MD simulations of phospholipids give a quite large span of measured decay lengths. The simulations by Pertsin et al. [14] of DLPE membranes and TIP4P water model give a value of $\lambda = 0.17$ nm. Furthermore, Eun and Berkowitz [18] showed that their models of attached PC-head groups to graphene plates with the SPC/E water model exhibit a separation-dependent decay length. At very short distances below 1 nm, the pressure can be fitted with decay length $\lambda = 0.08$ nm, at intermediate distances with $\lambda = 0.295$ nm, and with $\lambda = 0.782$ nm at distances above 1.6 nm.

Moreover, the hydration decay length has also been much discussed in experimental measurements, which reveal several repulsion regimes depending on the surface separation [19]. Measured decay lengths of various lipid experiments range from 0.08 nm to 0.64 nm [5, 20]. There is still no consensus on what determines the strength and decay length of the hydration repulsion.

We now discuss the contribution of dispersion interactions to the pressure. As the used force field of molecular interactions in our simulations is *ad hoc* designed on the basis of particular physical properties of lipids in order to correctly reproduce the area per lipid, it does not necessarily reproduce the van der Waals interaction correctly. In addition to that, also the Helfrich undulation repulsion is not fully included in the simulations. Both contributions have roughly the same functional pressure behavior, $\sim 1/D_{\mathrm{w}}^3$, the van der Waals being attractive, whereas Helfrich undulations are repulsive.

In order to assess the importance of both contributions, we first subtract the intrinsic van der Waals interaction from the obtained pressure, which is included in the force field in terms of Lennard-Jones interactions [21], and on top of that, we add the van der Waals contribution with an effective Hamaker constant H, viz.,

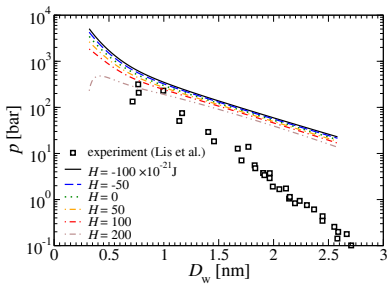

Figure 11.3 Pressure–distance curves with modified van der Waals like interaction are compared with experimental data.

$$p_{\mathrm{vdW}} = -\frac{H}{6\pi D_{\mathrm{w}}^3}. \tag{11.6}$$

The tunable parameter H can account for the sum of attractive van der Waals and repulsive Helfrich interactions. Fig. 11.3 shows fitted curves of MD1 simulations with the added van der Waals term Eq. (11.6) for various values of the parameter H. The measured Hamaker constant for lipids across water ranges from $H = 5 - 10 \times 10^{-21}$ J [2, 3, 22]. The Helfrich contribution is usually even smaller than that. However, by tuning the parameter H almost an order of magnitude out of experimental range in both directions, the overall contribution remains small compared with the hydration force obtained from simulations, Fig. 11.3. The mismatch between experiments and MD simulations can therefore not be attributed to poorly defined van der Waals or Helfrich interactions in our simulations. The reason lies presumably in the hydration interaction itself, that is, in the way water interacts with head groups and mediates the interaction between the surfaces. This shows that the hydration force is still not fully understood and that we are still lacking satisfactory comparison of theory and experimental measurements [23].

11.4 Conclusion

Four decades after the first experimental measurements of hydration forces between polar surfaces their mechanisms still elude

a quantitative theoretical description. Hydration forces become important at surface separations below several nanometers. They cannot be described by standard continuum DLVO approaches but require a detailed atomistic treatment. However, in recent years, computer simulations have enabled precise modeling of biological systems on atomic level and contributed significantly to their understanding.

We examined the interactions between DLPC lipid membranes where we have employed a recently proposed TE technique for measuring interacting pressures at prescribed chemical potential. The method allows for much more precise pressure measurements than other conventional approaches. We have performed two sets of MD simulations, the first at constant actual pressure, which mimics the hydrostatic experimental method, and the second at constant chemical potential, which mimics the experimental vapor pressure method. Comparing both MD sets, we find differences in surface area per lipid, which are smaller in constant chemical-potential simulations, as actual pressures build up to several kilobars. On the contrary, the final extrapolated interacting pressures do not depend significantly on the ensemble. Therefore, we conclude that also both aforementioned experimental techniques, which are usually used complementary, exhibit no significant systematic differences in measuring the pressure. The simulation pressure results agree quantitatively with experiment at smaller separations in magnitude and decay length. Some mismatch appears at larger separations, wherein MD simulations show too large repulsive pressures. The reason for this discrepancy is not resolved, but on the basis of other atomistic simulations, it is suggested to be related to the subtle interactions between water and surface molecules. We have shown that van der Waals and Helfrich contributions are too small to attribute for this discrepancy.

With the progress made in accounting for the constant chemical potential of water and other molecules in MD simulations, the predictions of interaction pressures from atomistic simulations are becoming more precise. The range of interactions that can be studied in MD simulations will thus become larger, and we will gain a more comprehensive picture of hydration interactions in the near future.

Acknowledgments

M. K. is supported by the Alexander von Humboldt Foundation. E. S. acknowledges support from a Marie Curie Intra-European Fellowship within the European Commission 7th Framework Program.

References

1. Israelachvili, J. N. (ed.) (1991). *Intermolecular and Surface Forces* (2nd ed. London: Academic Press Inc.).
2. Parsegian, V. A.; Fuller, N.; Rand, R. P. (1979). *Proc. Natl. Acad. Sci. USA* **76**, pp. 2750.
3. Lis, L. J.; McAlister., M.; Fuller, N.; Rand, R. P.; Parsegian, V. A. (1982). *Biophys. J.* **37**, pp. 657.
4. Israelachvili, N. and Adams, G. E. (1978). *J. Chem. Soc. Faraday. Trans.* **74**, pp. 975.
5. Rand, R. P. and Parsegian, V. A. (1989). *Biochim. Biophys. Acta.* **988**, pp. 351.
6. Stanley, C. and Rau, D. C. (2011). *Curr. Opp. Coll. Sci.* **16**, pp. 551.
7. Pagano, R. E. and Weinstein, J. N. (1978). *Ann. Rev. Biophys. Bioeng.* **7**, pp. 435.
8. Marcelja, S. and Radic, N. (1976). *Chem. Phys. Lett.*, pp. 42.
9. Frenkel, D. and Smit, B. (eds.) (2002). *Understanding molecular simulation: from algorithms to applications* (Academic Press Inc.).
10. Allen, M. P. and Tildesley, D. J. (eds.) (1991). *Computer simulation of liquids* (Oxford University Press, New York).
11. Berendsen, H. J. C.; Grigera, J. R.; Straatsma, T. P. (1987). *J. Phys. Chem.* **91**, pp. 6269.
12. Berger, O.; Edholm, O.; Jähnig, F. (1997). *Biophys. J.* **72**, pp. 2002.
13. Hayashi, T.; Pertsin, A.; Grunze, M. (2002). *J. Chem. Phys.* **117**, pp. 6271.
14. Pertsin, A.; Platonov, D.; Grunze M. (2007). *Langmuir* **23**, pp. 1388.
15. Schneck, E.; Sedlmeier, F.; Netz, R. R. (2012). *Proc. Natl. Acad. Sci. USA* **36**, pp. 14405.
16. van der Spoel, D.; Lindahl, E.; Hess, B.; Groenhof, G.; Mark, A. E.; Berendsen, H. J. (2005). *J. Comp. Chem.* **26**, pp. 1701.

17. Schneider, M. J. T. and Schneider, A. S. (1972). *J. Membr. Biol.* **8**, pp. 127.
18. Eun, C. and Berkowitz, M. (2009). *J. Phys. Chem. B* **113**, pp. 13222.
19. Hammer, M.; Anderson, T.; Chaimovich, A.; Shell, M.; Israelachvili, J. (2010). *Faraday Discuss.* **146**, pp. 299.
20. Marsh, D. (1989). *Biophys. J.* **55**, pp. 1093.
21. Sendner, C.; Horinek, H.; Bocquet, L.; Netz, R. R. (2009). *Langmuir* **25**, pp. 10768.
22. Parsegian, V. A. (ed.) (2006). *Van der Waals forces: a handbook for biologists, chemists, engineers, and physicists* (Cambridge University Press).
23. Parsegian, V. A. and Zemb, T. (2011). *Curr. Op. Coll. Int. Sci.* **16**, pp. 618.

Chapter 12

The Electrode–Ionic Liquid Interface: A Molecular Point of View

Céline Merlet,[a] Mathieu Salanne,[a] Paul A. Madden,[b] and Benjamin Rotenberg[a]

[a] *UPMC University Paris 06, CNRS, ESPCI, UMR 7195, PECSA, F-75005 Paris, France*
[b] *Department of Materials, University of Oxford, Oxford OX1 3PH, UK*
benjamin.rotenberg@upmc.fr

12.1 Introduction

Ionic liquids are room-temperature molten salts, composed mostly of organic ions that may undergo almost unlimited structural variations. They are currently under intense examination as potential electrolytes for future electrochemical systems [Armand *et al.* (2009)], as they present a number of highly appropriate properties such as low vapor pressure, low combustibility, high thermal stability, good ionic conductivity, and wide electrochemical windows. In particular, it is worth underlining the case of electrical double-layer capacitors (EDLCs), which have attracted much attention in recent years [Simon and Gogotsi (2008)]. The discovery of nanoporous electrode materials with enhanced performances when using an ionic liquid with ion sizes matching the pore size opens the way for

Electrostatics of Soft and Disordered Matter
Edited by David Dean, Jure Dobnikar, Ali Naji, and Rudolf Podgornik

ISBN 978-981-4411-85-1 (Hardcover), 978-981-4411-86-8 (eBook)
www.panstanford.com

a widespread use of supercapacitors in many contexts in which high power electrical output is required [Miller and Simon (2008)].

From the theoretical point of view, the description of the interface between an electrode and an ionic liquid is much more challenging than that with an electrolyte dissolved in a solvent. The latter has been the subject of over a century of theoretical work, from the early studies of Gouy and Chapman and the concept of double layer to the most recent molecular simulations. The interface between electrodes and ionic liquids has remained unexplored—with a relatively unnoticed exception of [Heyes and Clarke (1981)]—until the last decade. Then, several studies have focused on the structure of ionic liquids on charged flat surfaces [Lanning and Madden (2004); Pinilla *et al.* (2007)], showing that the ions exhibit a pronounced oscillatory structure close to the interface. In parallel, the development of a mean-field theory based on the Poisson–Boltzmann lattice-gas model showed that it is mandatory to account for the finite volume occupied by the ions, resulting in a dramatic departure from the Gouy–Chapman law for the capacitance-potential curves [Kornyshev (2007)]. Nevertheless, most of the recent theoretical advances in this field have been possible only by resorting to molecular simulations. In the following, we briefly present the state of the art for the realistic simulation of metallic electrodes in contact with ionic liquids. We then illustrate the main features observed at a planar graphite interface, both from electrolyte and electrode points of view. We finally introduce current developments in the study of more complex electrode geometries.

12.2 Methods and Models

Classical molecular dynamics and Monte Carlo simulations rely on an accurate description of the interactions between the constituents of the system. One could thus expect, in principle, that the observed results crucially depend on the choice of a force field. In practice, however, one observes little impact of the latter on the qualitative results for the structure in the context of ionic liquids: Similar conclusions can be reached with force fields differing both in the analytic expression and in the parametrization scheme [Canongia

Lopes *et al.* (2004); Borodin (2009); Dommert *et al.* (2012); Canongia Lopes and Pádua (2012)], or even with coarse-grained models used to decrease the computational cost [Wang *et al.* (2009); Roy and Maroncelli (2010); Roy *et al.* (2010)].

The main difficulty when dealing with interfaces with a metallic electrode is rather the treatment of the electrostatic problem. In some studies, the electrode is represented by a planar surface with a fixed uniform charge density (i.e., with no explicit atomic sites) or with fixed partial charges on fixed atomic positions. This approach has the great advantage of being simple and not requiring specific developments in the simulation codes. However, a metallic electrode is more accurately described by an ideal conductor in which induction charges appear in order to maintain a constant potential, rather than a constant charge. Several strategies have been introduced to that end, such as solving on a grid the Poisson equation with corresponding boundary conditions [Raghunathan and Aluru (2007)], using analytical expressions for the screened interactions between ions in specific geometries [Kondrat *et al.* (2011)] or introducing explicit image charges [Petersen *et al.* (2012)].

Another approach, which is not restricted to any particular geometry and does not require insights from continuous theories, has been introduced by Siepmann and Sprik [Siepmann and Sprik (1995)], and adapted by Reed *et al.* to the case of electrochemical cells [Reed *et al.* (2007)]. In this method, the electrode consists of explicit atoms bearing a Gaussian charge distribution $\rho_j(\mathbf{r}) = q_j A \exp\left(- \mid \mathbf{r} - \mathbf{r}_j \mid^2 \eta^2\right)$, where $A = \eta^3 \pi^{3/2}$ is a normalization constant and where the atomic charge q_j of each atom is determined at each time step of the simulation so as to impose a prescribed value V_0 (one value per electrode) to the potential V_j experienced by the atom. This can be achieved by adding to the Coulomb energy U_c a constraint term $U_\mathrm{constraint} = -\sum_{j=1}^{M} V_0 q_j$, with M the number of electrode atoms. As the potential experienced by any charge is:

$$V_j = \left[\frac{\partial U_\mathrm{c}}{\partial q_j}\right]_{\{q_i\}_{i\neq j}}, \tag{12.1}$$

it is easy to see that minimizing the total potential energy $U_\mathrm{c} + U_\mathrm{constraint}$ with respect to all the variable charges simultaneously

enforces $V_j = V_0$ for all atoms. This procedure induces an additional computational cost, which can be limited to less than an order of magnitude. Although we refer to studies using different methods, all the simulations performed by us discussed in the following section use this approach.

12.3 Ionic Liquids at Graphite Electrodes

Most of the simulation work has been so far devoted to the description of ionic liquids at planar electrodes. These studies differ not only by the simulation method, briefly discussed in the previous section, but also in the considered system, that is, the nature of ionic liquids (molten salts [Heyes and Clarke (1981); Lanning and Madden (2004); Reed *et al.* (2007); Pounds *et al.* (2009); Tazi *et al.* (2010); Vatamanu *et al.* (2010a)], imidazolium-based ionic liquids [Kislenko *et al.* (2009); Vatamanu *et al.* (2010b, 2011); Merlet *et al.* (2011, 2012b)], primitive models [Fedorov and Kornyshev (2008a,b); Fedorov *et al.* (2010); Georgi *et al.* (2010)]) and of the electrode (graphite/graphene [Kislenko *et al.* (2009); Merlet *et al.* (2011, 2012b)], smooth surface [Fedorov and Kornyshev (2008a,b); Fedorov *et al.* (2010); Georgi *et al.* (2010)], generic metal [Vatamanu *et al.* (2010a)] or solid aluminum [Pounds *et al.* (2009); Tazi *et al.* (2010)]). Nevertheless, all the investigated systems share the same main structural features, which we now illustrate in the case of a liquid composed of hexafluorophosphate (PF_6^-) and 1-butyl-3-methylimidazolium (BMI^+) ions between graphite electrodes.

Figure 12.1 illustrates the pronounced layering of the liquid at the interface, even in the absence of a potential difference $\Delta\Psi^0$ between the two electrodes. The liquid inside the first layer, which contains both cations and anions, also displays a rather ordered structure (not shown). Such a behavior differs markedly from the double-layer picture of dilute electrolyte solutions. It originates from ionic correlations due to the finite size of the ions (excluded volume) and to electrostatic effects, which prevent local charge separation.

The layered structure persists upon application of a potential difference and even extends further away from the surface. As can be seen in Figure 12.1, each ion layer is then polarized by a

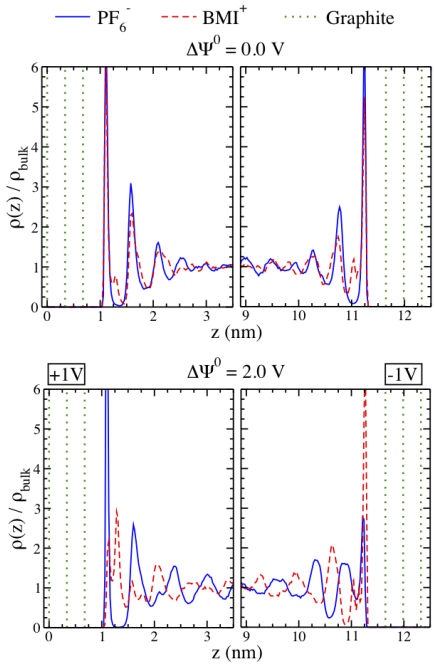

Figure 12.1 Density profiles of hexafluorophosphate (blue) and 1-butyl-3-methylimidazolium (red) ions between graphite electrodes, in the absence (top) and presence (bottom) of a potential difference $\Delta\Psi^0$. The vertical dotted lines indicate the location of the graphite planes. Note that the bulk region has been omitted in this figure to emphasize the interfacial regions and that the densities have been normalized by that in the bulk.

shift in the average position of cations and anions. An important feature observed at these interfaces is the so-called *overscreening* effect [Fedorov and Kornyshev (2008a,b); Feng *et al.* (2011); Bazant *et al.* (2011); Merlet *et al.* (2011)]: The first adsorbed layer carries a charge that is greater than that of the electrode and is therefore counterbalanced in the following layer. This phenomenon is progressively damped in the next layers until the bulk behavior is recovered. As a consequence of these polarized layers, the Poisson potential also displays oscillations. An asymmetry between the positive and negative electrode can also be observed, which arises from the difference in the size and shape of the cations and anions.

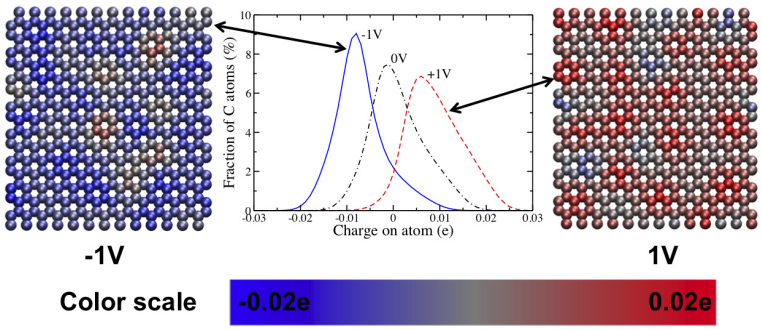

Figure 12.2 Charge on each carbon atom inside the negative (-1 V) and positive ($+1$ V) electrodes, for an instantaneous configuration. The central figure indicates the charge distribution inside both electrodes and in the absence of potential difference (0 V).

Let us now turn to the counterpart of the ionic liquid, namely the electrode. The charge of each electrode atom fluctuates in response to its local environment. Figure 12.2 illustrates the charge distribution in the positive and negative electrodes. At each time step (see the snapshots), the charge distribution is very inhomogeneous. Moreover, one can observe the presence of negatively (respectively positively) charged atoms on the positive (respectively negative) electrode. This counterintuitive fact is a consequence of the presence of cations (respectively anions) in the liquid adsorbed at the surface. Such a feature cannot be captured in constant charge simulations. The average charge distribution, also reported in Fig. 12.2, is not Gaussian and gets more skewed upon application of a potential difference. The asymmetry between the two electrodes arising from the different ionic sizes is also evident in this distribution.

Finally, molecular simulation allows to determine the capacitance of each electrode as illustrated in Fig. 12.3. The total surface charge density of each electrode fluctuates in response to the thermal motion of the ionic liquid. Its average value σ_S is determined as a function of the potential drop $\Delta\Psi^{\pm}$ between the (positive or negative) surface and the bulk. For sufficiently small voltages, σ_S is proportional to $\Delta\Psi^{\pm}$ and the slope is the differential capacitance C_{diff}. Once again, the size difference between cations and anions results in an asymmetry between the two electrodes.

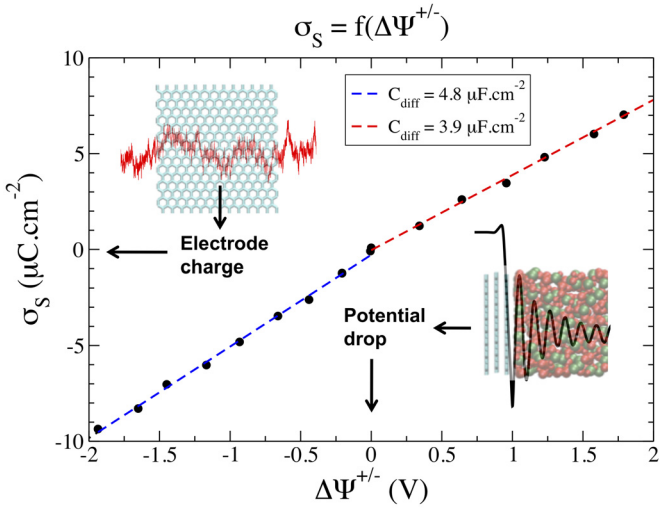

Figure 12.3 The total charge of each electrode fluctuates as the liquid moves in its vicinity. The average surface charge density σ_S, plotted as a function of the potential drop $\Delta\Psi^{\pm}$ between the surface and the bulk electrolyte, varies linearly for sufficiently small voltages. The slope on each side (positive or negative) is the differential capacitance C_{diff}.

The results presented here, obtained with a coarse-grained representation of the ionic liquid, are in good agreement with that obtained using an all-atom model [Merlet *et al.* (2011)]. This coarse-grained level of description is computationally less intensive than the latter and lends itself better to systematic studies. For example, Merlet *et al.* have recently investigated ionic liquids composed of BMI^+ and PF_6^- ions as well as EMI^+ (1-ethyl-3-methylimidazolium) and BF_4^- (tetrafluoroborate) ions [Merlet *et al.* (2012b)].

12.4 Beyond Planar Electrodes

As mentioned in the Introduction, excellent charge storage performances can be obtained in supercapacitors on the basis of nanoporous carbon electrodes, which cannot be explained by the simple increase in specific surface area. The search for the underlying microscopic mechanism has motivated a number of

theoretical studies on porous materials. Simulations involving slit-like pores [Vatamanu *et al.* (2010a)] or carbon nanotubes [Yang *et al.* (2009); Shim and Kim (2010)] provided a first insight of the structure of ionic liquids in a confined environment. Then, the account of polarization effects by the metallic walls and of the resulting screening of interactions between ions revealed the possibility of forming a superionic state [Kondrat and Kornyshev (2011); Kondrat *et al.* (2011)], in which a slit pore contains a single type of ions (e.g., cations) whose charge is compensated by the electrode itself and not by counter-ions. But it is only the use of a realistic carbon structure, determined by Palmer *et al.* [Palmer *et al.* (2010)], in conjunction with the accurate treatment of polarization described above, which allowed the prediction of capacitances in agreement with the large experimental values and the analysis of the microscopic mechanism at play [Merlet *et al.* (2012a)].

Figure 12.4 illustrates the simulation setup used by Merlet *et al.* to investigate CDC-based supercapacitors and the complex structure

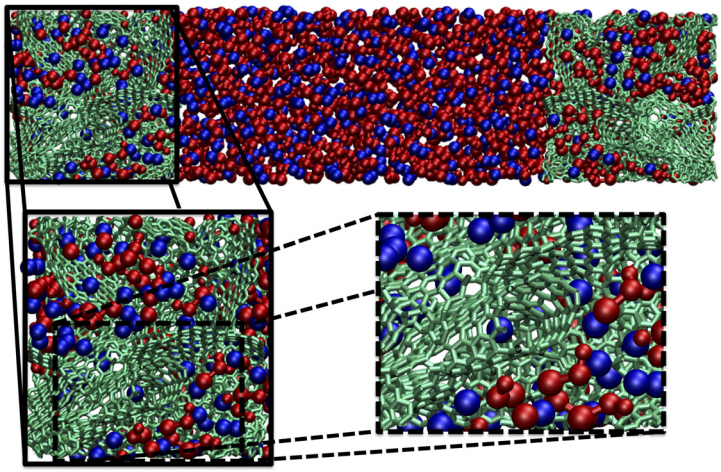

Figure 12.4 Supercapacitor based on carbide-derived carbon (CDC) electrodes. The electrode atoms are in green, while blue and red molecules represent the PF_6^- and BMI^+ ions, respectively. The complex local structure, featuring nanotube-like and graphitic domains, influences the structure of the liquid and the charge storage mechanism differs from that at a planar surface.

of the nanoporous electrode. The simulations revealed in particular that the confinement prevents the formation of liquid layers and the occurrence of overscreening effects. Moreover, the charge distribution inside the electrode, in the presence of an applied voltage, is much broader and more skewed than in graphite. Finally, the charging mechanism involves the exchange of ions between the electrode and the bulk electrolyte, in qualitative agreement with the idea of a superionic state. All these factors contribute to the larger capacitance observed with these materials [Merlet *et al.* (2012a)]. The comparison of two CDC structures with similar average pore sizes but different local features such as graphitic domains confirmed both the validity of the model, as the simulations were able to reproduce the different capacitances observed experimentally, and the importance of the local structure in determining the performances of the material. Such a simulation approach might thus also be useful to investigate other electrode geometries, such as "onion-like" carbons.

12.5 Conclusion and Perspectives

Classical molecular simulation has provided many insights into the structure of the interface between metallic electrode and ionic liquids. Such interfaces appear to be much more complex than the double-layer picture valid for dilute electrolyte solutions. Important advances have been made possible only recently through the correct account of the electrode polarization and the simulation under constant potential conditions. Nevertheless, significant progress can still be expected in the coming years. In particular, studies on the dynamics of the interface and the charging/discharging processes are still scarce. The influence of the simulation method (constant charge or potential) on the dynamics might prove more important than for the structural properties. Moreover, although most published work has been devoted to the simulation of pure ionic liquids, most experimental devices use in fact ions dissolved in a solvent such as acetonitrile or propylene carbonate. It is therefore important to investigate the properties of interfaces involving concentrated solutions of organic ions such as the ones presented

here in order to assess the influence of the solvent on the charging process.

Finally, one can also anticipate further improvements of the models, both in terms of the descriptions of the system (porous electrode structure, presence of defects, functionalization) and of the simulation method (algorithm efficiency for constant potential conditions, for example). Although the importance of using realistic electrode structure to capture the microscopic charging process has been recently demonstrated, resort to simplified theories remains necessary to predict generic trends, for example, of the ratio between molecular and pore sizes or of polydispersity [Kondrat *et al.* (2012)]. One can thus confidently assume that both routes will still provide useful insights.

Acknowledgments

The authors acknowledge the support of the French Agence Nationale de la Recherche (ANR) under grant ANR-2010-BLAN-0933-02 ("Modeling the Ion Adsorption in Carbon Micropores").

References

Armand, M., Endres, F., MacFarlane, D. R., Ohno, H. and Scrosati, B. (2009). Ionic-liquid materials for the electrochemical challenges of the future, *Nature Mater.* **8**, pp. 621–629.

Bazant, M. Z., Storey, B. D. and Kornyshev, A. A. (2011). Double layer in ionic liquids: Overscreening versus crowding, *Phys. Rev. Lett.* **106**, p. 046102.

Borodin, O. (2009). Polarizable force field development and molecular dynamics simulations of ionic liquids, *J. Phys. Chem. B* **113**, 33, pp. 11463–11478.

Canongia Lopes, J. N., Deschamps, J. and Pádua, A. A. H. (2004). *J. Phys. Chem. B* **108**, pp. 2038–2047.

Canongia Lopes, J. N. and Pádua, A. A. H. (2012). Cl&p: A generic and systematic force field for ionic liquids modeling, *Theor. Chem. Acc.* **131**, 3, p. 1129.

Dommert, F., Wendler, K., Berger, R., Delle Site, L. and Holm, C. (2012). Force fields for studying the structure and dynamics of ionic liquids: A critical review of recent developments, *ChemPhysChem* **13**, 7, pp. 1625–1637.

Fedorov, M. V., Georgi, N. and Kornyshev, A. A. (2010). Double layer in ionic liquids: the nature of the camel shape of capacitance, *Electrochem. Commun.* **12**, 2, pp. 296–299.

Fedorov, M. V. and Kornyshev, A. A. (2008a). Ionic liquid near a charged wall: structure and capacitance of electrical double layer, *J. Phys. Chem. B* **112**, 38, pp. 11868–11872.

Fedorov, M. V. and Kornyshev, A. A. (2008b). Towards understanding the structure and capacitance of electrical double layer in ionic liquids, *Electrochim. Acta* **53**, pp. 6835–6840.

Feng, G., Huang, J., Sumpter, B. G., Meunier, V. and Qiao, R. (2011). A "counter-charge layer in generalized solvents" framework for electrical double layers in neat and hybrid ionic liquid electrolytes, *Phys. Chem. Chem. Phys.* **13**, pp. 14723–14734.

Georgi, N., Kornyshev, A. A. and Fedorov, M. V. (2010). The anatomy of the double layer and capacitance in ionic liquids with anisotropic ions: Electrostriction vs lattice saturation, *J. Electroanal. Chem.* **649**, 1–2, pp. 261–267.

Heyes, D. M. and Clarke, J. H. R. (1981). Computer-simulation of molten-salt interphases - effect of a rigid boundary and an applied electric-field, *J. Chem. Soc., Faraday Trans. 2* **77**, pp. 1089–1100.

Kislenko, S., Samoylov, I. and Amirov, R. (2009). Molecular dynamics simulation of the electrochemical interface between a graphite surface and the ionic liquid [BMIM][PF_6], *Phys. Chem. Chem. Phys.* **11**, pp. 5584–5590.

Kondrat, S., Georgi, N., Fedorov, M. V. and Kornyshev, A. A. (2011). A superionic state in nano-porous double-layer capacitors: insights from Monte Carlo simulations, *Phys. Chem. Chem. Phys.* **13**, pp. 11359–11366.

Kondrat, S. and Kornyshev, A. A. (2011). Superionic state in double-layer capacitors with nanoporous electrodes, *J. Phys.: Condens. Matter* **23**, p. 022201.

Kondrat, S., Perez, C. R., Presser, V., Gogotsi, Y. and Kornyshev, A. A. (2012). Effect of pore size and its dispersity on the energy storage in nanoporous supercapacitors, *Energy Environ. Sci.* **5**, 4, pp. 6474–6479.

Kornyshev, A. A. (2007). Double-layer in ionic liquids: paradigm change? *J. Phys. Chem. B* **111**, 20, pp. 5545–5557.

Lanning, O. and Madden, P. A. (2004). Screening at a charged surface by a molten salt, *J. Phys. Chem. B* **108**, 30, pp. 11069–11072.

Merlet, C., Rotenberg, B., Madden, P. A., Taberna, P.-L., Simon, P., Gogotsi, Y. and Salanne, M. (2012a). On the molecular origin of supercapacitance in nanoporous carbon electrodes, *Nature Mater.* **11**, pp. 306–310.

Merlet, C., Salanne, M. and Rotenberg, B. (2012b). New coarse-grained models of imidazolium ionic liquids for bulk and interfacial molecular simulations, *J. Phys. Chem. C* **116**, 14, pp. 7687–7693.

Merlet, C., Salanne, M., Rotenberg, B. and Madden, P. A. (2011). Imidazolium ionic liquid interfaces with vapor and graphite: Interfacial tension and capacitance from coarse-grained molecular simulations, *J. Phys. Chem. C* **115**, pp. 16613–16618.

Miller, J. R. and Simon, P. (2008). Electrochemical capacitors for energy management, *Science* **321**, pp. 651–652.

Palmer, J. C., Llobet, A., Yeon, S.-H., Fisher, J. E., Shi, Y., Gogotsi, Y. and Gubbins, K. E. (2010). Modeling the structural evolution of carbide-derived carbons using quenched molecular dynamics, *Carbon* **48**, pp. 1116–1123.

Petersen, M. K., Kumar, R., White, H. S. and Voth, G. A. (2012). A computationally efficient treatment of polarizable electrochemical cells held at a constant potential, *J. Phys. Chem. C* **116**, pp. 4903–4912.

Pinilla, C., Del Pópolo, M. G., Kohanoff, J. and Lynden-Bell, R. M. (2007). Polarization relaxation in an ionic liquid confined between electrified walls, *J. Phys. Chem. B* **111**, 18, pp. 4877–4884.

Pounds, M., Tazi, S., Salanne, M. and Madden, P. A. (2009). Ion adsorption at a metallic electrode: an *ab initio* based simulation study, *J. Phys.: Condens. Matter* **21**, 42, p. 424109.

Raghunathan, A. V. and Aluru, N. R. (2007). Self-consistent molecular dynamics formulation for electric-field-mediated electrolyte transport through nanochannels, *Phys. Rev. E* **76**, p. 011202.

Reed, S. K., Lanning, O. J. and Madden, P. A. (2007). Electrochemical interface between an ionic liquid and a model metallic electrode, *J. Chem. Phys.* **126**, 8, p. 084704.

Roy, D. and Maroncelli, M. (2010). An improved four-site ionic liquid model, *J. Phys. Chem. B* **114**, 39, pp. 12629–12631.

Roy, D., Patel, N., Conte, S. and Maroncelli, M. (2010). Dynamics in an idealized ionic liquid model, *J. Phys. Chem. B* **114**, pp. 8410–8424.

Shim, Y. and Kim, H. J. (2010). Nanoporous carbon supercapacitors in an ionic liquid: A computer simulation study, *ACS Nano* **4**, 4, pp. 2345–2355.

Siepmann, J. and Sprik, M. (1995). Influence of surface-topology and electrostatic potential on water electrode systems, *J. Chem. Phys.* **102**, 1, pp. 511–524.

Simon, P. and Gogotsi, Y. (2008). Materials for electrochemical capacitors, *Nature Mater.* **7**, pp. 845–854.

Tazi, S., Salanne, M., Simon, C., Turq, P., Pounds, M. and Madden, P. A. (2010). Potential-induced ordering transition of the adsorbed layer at the ionic liquid/electrified metal interface, *J. Phys. Chem. B* **114**, 25, pp. 8453–8459.

Vatamanu, J., Borodin, O. and Smith, G. (2010a). Molecular dynamics simulations of atomically flat and nanoporous electrodes with a molten salt electrolyte, *Phys. Chem. Chem. Phys.* **12**, pp. 170–182.

Vatamanu, J., Borodin, O. and Smith, G. D. (2010b). Molecular insights into the potential and temperature dependences of the differential capacitance of a room-temperature ionic liquid at graphite electrodes, *J. Am. Chem. Soc.* **132**, pp. 14825–14833.

Vatamanu, J., Cao, L., Borodin, O., Bedrov, D. and Smith, G. D. (2011). On the influence of surface topography on the electric double layer structure and differential capacitance of graphite/ionic liquid interfaces, *J. Phys. Chem. Lett.* **2**, pp. 2267–2272.

Wang, Y. T., Feng, S. L. and Voth, G. A. (2009). Transferable coarse-grained models for ionic liquids, *J. Chem. Theory Comput.* **5**, 4, pp. 1091–1098.

Yang, L., Fishbine, B. H., Migliori, A. and Pratt, L. R. (2009). Molecular simulation of electric double-layer capacitors based on carbon nanotube forests, *J. Am. Chem. Soc.* **131**, 34, pp. 12373–12376.

Chapter 13

Modeling Electrokinetics Through Varying Length and Time Scales

I. Pagonabarraga[a] and B. Rotenberg[b]
[a] *Departament de Física Fonamental, Universitat de Barcelona, Carrer Martí i Franqués 1, Barcelona 08028, Spain*
[b] *CNRS, UPMC University, Paris 06, ESPCI, UMR 7195 PECSA, 75005 Paris, France*
ipagonabarraga@ub.edu

13.1 Introduction

Charged materials are ubiquitous in nature due to the high permittivity of water that favors ionic dissociation. The strong electrostatic attraction favors electroneutrality. However, ion entropy due to their dissociation in water allows for local charges. The Bjerrum length, l_B, the distance beyond which the thermal energy dominates the electrostatic interaction between unit charges, is only of $l_B \sim 7$ Å for water at room temperature. The competition between entropy and electrostatics results in a distribution of ions around a given charge over distances of the order of the Debye length, κ^{-1}, a characteristic of the screening of electrostatic interactions by the ionic atmosphere (in the nanometer range for usual conditions) [Hunter (2001)]. Hence, the dynamics of charged fluids poses a number of challenges because one needs to capture the behavior from the molecular scales

Electrostatics of Soft and Disordered Matter
Edited by David Dean, Jure Dobnikar, Ali Naji, and Rudolf Podgornik

ISBN 978-981-4411-85-1 (Hardcover), 978-981-4411-86-8 (eBook)
www.panstanford.com

(ion size and solvation), to the micron scale of colloids without overlooking the collective ion distribution and response, which evolves naturally on the nanometer and nanosecond scales.

In the simple case of electro-osmosis near a charged fixed wall, an electric field accelerates the fluid in the so-called double-layer region in which the fluid is charged; momentum is then slowly transferred to the rest of the fluid by viscous stresses even in the regions wherein it is electrically neutral. Such a coupling between ionic and solvent flows, defining electrokinetic phenomena, is exploited, for example, for pumping in microfluidic devices [Harrison *et al.* (1993)]. The interplay between the different scales gives rise to a rich phenomenology. For example, the ion distribution around a colloid, polymer, or charged solid surface, forming the so-called double layer, can be deformed by the fluid flow that develops when the fluid is forced. This induced polarization acts back on the fluid, modifying its motion and, in turn, the effective interaction between suspended colloids or polymers. The feedback between the stresses that local charges induce in the solvent and the distortion in the ionic distribution due to advection by the solvent is at the origin of the complexity of electrokinetic phenomena.

From a modeling perspective, the large variety of length scale and the corresponding diversity of time regimes make it impossible to carry out first principle simulations to analyze electrokinetic phenomena. Therefore, one needs to understand the phenomena at play and to appropriately coarse grain the description in order to analyze the dynamics of the relevant degrees of freedom. Electrokinetics constitutes a paradigmatic, relevant class of phenomena wherein mutiscaling opens new possibilities to perform a more quantitative and accurate modeling. We discuss here some of the different strategies that have been proposed to study numerically the dynamics of charged fluids by judiciously choosing the relevant degrees of freedom depending on the specific phenomena to be addressed. A more complete discussion can be found in [Pagonabarraga *et al.* (2010)].

13.2 Simulation Strategies

There exist different simulation strategies to address the properties of heterogeneous charged materials. All-atom molecular dynam-

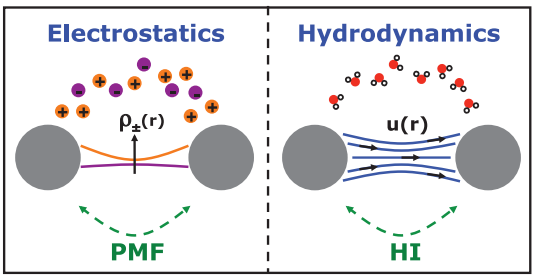

Figure 13.1 Different levels of coarse-graining are necessary to capture the dynamics of charged fluids, which involve different length scales. In a suspension of charged colloids, both the microions and the solvent can be described with different degrees of specificity: (1) explicitly as ions and molecules; (2) explicitly as continuous fields such as ionic densities $\rho_{\pm}(\mathbf{r})$ and fluid velocity $\mathbf{u}(\mathbf{r})$; and (3) implicitly as effective interactions between colloids. The latter can be approximated by analytical expressions such as the Oseen tensor for hydrodynamic interactions (HI) or the screened Coulomb interaction for the potential of mean force (PMF).

ics (MD) simulations provide a rigorous framework to analyze electrokinetic phenomena in generic complex charged materials [Rotenberg and Pagonabarraga (2013)]. The computational cost of such simulations prevents their use to study the properties of materials at large length and time scales. The long-range nature of electrostatic interactions requires a proper treatment of the interactions with all charged image particles. Ewald sums or particle mesh constitutes standard techniques that account for the impact of image charges on the behavior of the system particles and introduce additional computational costs [Hockney and Eastwood (1981)]. Despite the fast growth in computational power, MD cannot reach, for examples, the typical time scales over which charged colloid evolves dynamically.

To overcome this bottleneck, a variety of coarse-grained approaches have been proposed, which differ in how they deal both with the charged species and with the embedding solvent. These different approaches are complementary to each other both conceptually, as illustrated in Figure 13.1, and computationally, as summarized in Table 13.1. As the ion concentration is rather dilute in electrolytes, a standard approach keeps the molecular specificity of the ions treating them individually while the solvent is simplified

Table 13.1 Simulation strategies discussed in the text, depending on how they account for the solvent and the microions (see text for abbreviations)

	Explicit Solvent	Implicit Solvent
Explicit Ions	MD	BD with HI
	LB + MD	
Implicit Ions	DPD, LA, or SRD	BD with PMF and HI
	Hybrid LB	or Green Function

and treated as an effective continuous medium. This constitutes a hybrid approach that selects the individual degrees of freedom of the ions and charged particles (such as colloids of polyelectrolytes).

In equilibrium, the restricted primitive model (RPM) considers the solvent as a passive medium whose polarizability determines the effective electric permittivity and is able to predict the thermodynamic properties of charged systems keeping the molecular specificity of the charged species [Dufrêche *et al.* (2005)]. The dynamics are usually analyzed disregarding the flows generated by the solutes and lumping all hydrodynamics in an effective viscosity that determines the friction coefficient that opposes ion or atom motion. A random force (noise) is also included to ensure that in the absence of external forcing, the system reaches thermal equilibrium. Friction and noise lead to a Langevin dynamics (LD) of charged systems. If the friction is large and ion or atom inertia is negligible, the particle velocities relax instantaneously and the system follows a Brownian dynamics (BD).

Such an approach is useful to study how external forces modify the structure of electrolyte solutions or other charged suspensions. However, momentum exchange between ions and solvent is lost, which does not allow to predict a number of electrokinetic phenomena. The flow induced by the ions does not need to be resolved. It can be accounted for in the drag force that a moving ion induces on the rest of suspended charged particles. To lowest order, this coupling is quantified by the Oseen tensor (OT), for an unbounded system or the Blake hydrodynamic tensor in the presence of a planar solid wall [Kim and Netz (2006)]. The finite size of the ions, characteristic of the RPM, can be accounted by an appropriate generalization of the Oseen tensor, resulting in the Rotne–Prager form. BD

simulations assuming pairwise additivity of the OT have been extensively exploited to analyze long-time diffusivity of charged colloidal suspensions. Due to the long-range nature of hydrodynamic interactions (HI), analogous to the slow decay of electrostatic interactions, a proper treatment of system finite size is required. For an unbounded system, a method analogous to the Ewald summation for electrostatics has been implemented to compute HI; recent studies have also generalized ideas of P3M methods in electrostatics to speed up the slow convergence due to the long-range nature of HI. The pairwise additivity assumption, though computationally useful, does not recover generically the electrokinetic properties of charged suspensions [Nägele (1996)].

Resolving explicitly the dissolved ions provides a means to obtain quantitative detailed information on the molecular impact of ions on the local distribution of ions on solid walls and around colloids and polymers. However, in many cases, the atomic details of the ions only enter in the structure of the double layer that characterizes how ions organize around charged surfaces. For example, for colloidal particles, in equilibrium, the DLVO theory provides the PMF between particles [Verwey and Overbeek (1948)]. Only colloids are then resolved and all the ion information is encoded in the effective parameters determining colloid potentials. An analogous approach can be carried out to describe the electro-hydrodynamics of electrolyte solutions. In the Debye–Hückel limit, the system's Green function only in response to applied electric fields can be derived [Ajdari and Long (2001)]. Once the equivalent of the OT is known, the colloid or polymer dynamics can be carried out without the need to account for the ion dynamics. The derived propagators can be used in a BD scheme without including the dynamics of salt and counterions explicitly [Rex and Löwen (2008)].

In parallel to the need to develop efficient computational tools to address the electrostatic interactions in charged molecular systems, the long-range nature of HI has also led to the development of coarse-grained computational schemes that resolve the combined dynamics of the solute and solvent on the same footing. To this end, the solvent needs to be treated explicitely, but avoiding at the same time any molecular or atomic detail. Dissipative particle dynamics (DPD) models the solvent as point particles that interact through conservative and dissipative and random forces satisfying

detailed balance, isotropy, and Galilean invariance [Español and Warren (1995)]. The appropriate hydrodynamic limit is recovered at long scales and the soft interaction among effective solvent particles allows long time scales to be covered numerically. Groot [Groot (2003)] extended DPD to model electrolytes. Due to the absence of a finite size associated with the particles, to avoid the collapse of particles with opposite charges, he smeared the particle charge at the expense of introducing a new length scale related to the charge distribution around each particle. This method deals with electrostatics in a standard way, and the total force of the smeared charge distribution is then applied to the point particle. As the charge distribution in the system is affected by hydrodynamic flow, this approach provides a natural coupling between electrostatics and fluid motion. However, the hydrodynamic regime requires that this new length scale (which is of the order of the Bjerrum length) is small compared with any other relevant scale in the system. Alternative momentum conserving thermostats, such as the Lowe–Anderson (LA) thermostat [Lowe (1999)] allows combining molecular methods enforcing appropriate momentum conservation. The possibility to use an ideal dissipative solvent becomes a flexible tool to concentrate the computational efforts in the description of the charged solutes and electrolytes. Multiparticle collision dynamics (MPC) constitutes an alternative means to account for the solvent dynamics [Kapral (2008)]; it is composed of point particles, which in equilibrium behave as an ideal gas; yet, the effective interactions among them impart the fluid with a finite viscosity (hence, it is referred as an ideal dissipative gas). The dynamics of this effective solvent (which captures the essentials of the hydrodynamics of the fluid) can be straitghforwardly combined with a molecular description of the solute. The coarse-grained solvent in DPD, MPC, or LA introduces an effective solvent viscosity.

13.3 Kinetic Models: Lattice Boltzmann

The different methods discussed in the previous section are based on identifying the relevant degrees of freedom and building a mechanical approach for the relevant subsystem analogously to MD.

The mechanics of a system can also be understood, complementarily, on the basis of kinetic equations, starting from the Liouville equation or the BBGKY hierarchy. This perspective can also be exploited to identify coarse-grained approaches for a given system.

If the molecular specificity of the electrolyte is not relevant, and only their collective dynamics matters, it is then possible to solve the electrolyte dynamics in terms of their number densities, ρ_k, $k = \pm$. Using the analogy between the Nernst–Planck and Fokker–Planck equations, one can propose lattice methods on the basis of the phase space distribution, $f_k(\mathbf{r}, \mathbf{v}, t)$ [Moroni *et al.* (2006)]. Such an approach is very efficient numerically and can be exploited to achieve large time and length scales. They reproduce the diffusive dynamics of the electrolyte (disregarding the dynamic correlations between ions) but do not recover the well-known coupling between the ion motion and the solvent.

It is possible to account for the combined motions of charges and fluid solvent within this kinetic framework, which typically includes charged species on a pre-existing kinetic approach for hydrodynamics. One flexible and powerful tool is to exploit the potentiality of the lattice-Boltzmann method (LB) [Succi (2001)]. The LB can be thought of as a discretized, linearized version of the Boltzmann equation. It follows the evolution of the one-particle distribution function, $f(\mathbf{r}, \mathbf{v}, t)$. Its time evolution is divided into two steps. In the collision, f relaxes to a prescribed local equilibrium that corresponds to a low-velocity expansion of a Maxwell–Boltzmann distribution. It can be easily extended to account for complex fluids and solid particle inclusions [Stratford *et al.* (2005)]. In order to model electrolytes, charged ions can be included through their local number densities, $\rho_k(\mathbf{r}, t)$, and their dynamics follows Poisson–Nernst–Planck for their relaxation toward local equilibrium (as prescribed by the ion diffusivity and the local electrostatic force) together with a local advection determined by the fluid velocity as derived from the corresponding moment of $f(\mathbf{r}, \mathbf{v}, t)$.

Due to the long-range nature of the electrostatic interactions, the numerical implementation of the ion dynamics has to ensure local charge conservation to numerical accuracy. In the presence of solid boundaries, it is important to avoid any charge leakage from the fluid into the solid; an implementation of the diffusive

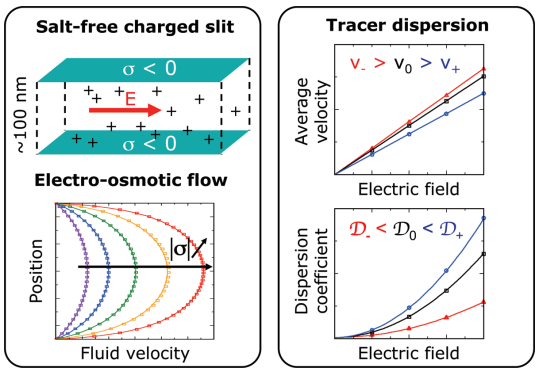

Figure 13.2 Electro-osmotic flow in a slit pore, without added salt. The fluid velocity (profiles bottom left) increases with surface charge density σ. The average velocity of tracers, proportional to the applied electric field, and their dispersion coefficient that varies quadratically depend on their charge. All results from Lattice–Boltzmann simulations (symbols) are in perfect agreement with the analytical expressions (lines).

dynamics of the ions based on link fluxes allows to overcome some of the numerical inaccuracies of older proposals [Capuani *et al.* (2004); Rotenberg *et al.* (2010)]. The electrostatic potential can be obtained from the local charge distribution using standard methods to compute electrostatic fields, such as successive overrelaxation, or P3M [Deserno and Holm (1998)]. The probabilistic nature of kinetic models further allows to determine statistical information over the particle trajectories. The moment propagation method allows, for example, to compute quantities such as the velocity auto-correlation function, from which diffusion of dispersion coefficients can be determined [Rotenberg *et al.* (2008)].

Figure 13.2 illustrates the LB simulation of electro-osmotic flows in a slit pore with a size (100 nm), which renders the use of molecular simulation impossible, in the absence of added salt. The average velocity of tracers results both from the direct action of the electric field and the advection by the electro-osmotic flow. Depending on their charge, which controls their distribution inside the pore, they feel the effect of the flow differently. More details can be found in [Rotenberg *et al.* (2008)]. LB also constitutes a flexible framework to analyze the electrokinetics of colloidal suspensions and other

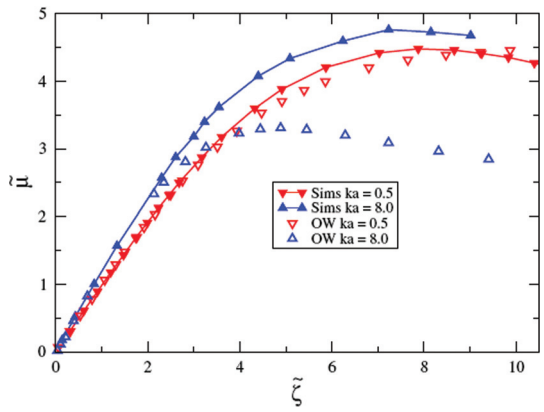

Figure 13.3 Electrophoretic mobility of a charged colloid subject to a uniform applied electric field as a function of the colloid charge, expressed in terms of the dimensionless surface potential, $\tilde{\zeta}$ for different values of the ratio between the colloid radius and the Debye length, κa (from Ref. [Giupponi and Pagonabarraga (2011)]). Empty symbols correspond to the theoretical prediction of [O'Brien and White (1978)].

complex fluids. Adding colloidal dynamics to the solvent described by LB through a hybrid MD scheme is rather straightforward [Stratford and Pagonabarraga (2008)]. For example, Figure 13.3 shows the dimensionless electrophoretic mobility, $\tilde{\mu} \equiv 6\pi\eta l_B v/eE$ of a colloid of radius R moving at velocity v due to an applied electric field of magnitude E in a fluid of viscosity η as a function of the colloid charge expressed in terms of the dimensionless electrostatic potential at the colloid surface, $\tilde{\zeta} \equiv e\zeta/k_B T$. For small charges, $\hat{\zeta} \leq 3$, the colloid velocity increases linearly, and it develops a maximum at larger charges. The agreement with the linearized theoretical prediction [O'Brien and White (1978)] agrees well in this regime. The LB simulations always show a maximum in $\hat{\mu}$, whereas the linearized theory predicts it only for narrow double layers.

If molecular specificity is relevant, it is possible to couple the LB treatment of the solvent with an MD description of individually resolved ions. In this case, one is limited in the length and time scales that can be covered (wherein solute objects can be typically of nanoscopic size), but it is possible to account for details of the interactions between ions and polymers or colloids. The description

again builds on the RPM and focuses on the computational effort in the electrostatic and electrokinetic properties of the system because it neglects the molecular nature of the solvent even if its size is comparable to that of ions. A self-consistent approach that includes the finite size nature of all components of the system (solvent, ions, solutes) requires a generalization of the LB approach to account for the correlations associated with the finite size of the interacting components during the collision, for example, by constructing a lattice generalization of the Enskog theory for fluid mixtures [Melchionna and Marini Bettolo Marconi (2011)].

13.4 Conclusion

We have described the challenges associated with accounting for the disparate length scales, and corresponding time scales that are involved in the dynamics of charged fluids. We have identified the relevant length scales associated with the ionic motion in a solvent and have exploited their magnitudes to gain insight in how to coarse grain the dynamics of charged solutes in a polar solvent. Such an analysis allows to put forward schemes that minimize the computational cost by focusing on the relevant degrees of freedom selected on a systematic basis according to whether or not the molecular specificity of ions or solutes is relevant.

We have discussed the complementarity of particle-based and kinetic methods and their computational advantages. Coping with the complex nature of electrokinetics constitutes a challenging area wherein multiscale approaches will offer new venues to keep molecular details into account while reaching the long length and time scales associated with the motion of large charged aggregates and their structural evolution.

References

Ajdari, A. and Long, D. (2001). A note on the screening of hydrodynamic interactions, in electrophoresis, and in porous media, *Europ. J. Phys. E* **4**, pp. 29–32.

Capuani, F., Pagonabarraga, I. and Frenkel, D. (2004). Discrete solution of the electrokinetic equations, *J. Chem. Phys.* **121**, pp. 973–986.

Deserno, M. and Holm, C. (1998). How to mesh up Ewald sums. i. a theoretical and numerical comparison of various particle mesh routines, *J. Chem. Phys.* **109**, 18, pp. 7678–7693.

Dufrêche, J.-F., Bernard, O., Durand-Vidal, S. and Turq, P. (2005). Analytical theories of transport in concentrated electrolyte solutions from the msa, *J. Phys. Chem. B* **109**, pp. 9873–9884.

Español, P. and Warren, P. B. (1995). Statistical-mechanics of dissipative particle dynamics, *Europhys. Lett.* **30**, pp. 191–196.

Giupponi, G. and Pagonabarraga, I. (2011). Colloid electrophoresis for strong andweak ion diffusivity, *Phys. Rev. Lett.* **106**, p. 248304.

Groot, R. D. (2003). Electrostatic interactions in dissipative particle dynamics-simulation of polyelectrolytes and anionic surfactants, *J. Chem. Phys.* **118**, pp. 11265–11277.

Harrison, D. J., Fluri, K., Seiler, K., Fan, Z., Effenhauser, C. S. and Manz, A. (1993). Micromachining a Miniaturized Capillary Electrophoresis-Based Chemical Analysis System on a Chip, *Science* **261**, 5123, pp. 895–897, doi:10.1126/science.261.5123.895.

Hockney, R. and Eastwood, J. (1981). *Computer Simulation Using Particles* (McGraw-Hill Inc., US).

Hunter, R. (2001). *Foundations of Colloid Science* (Oxford University Press, Oxford).

Kapral, K. (2008). *Adv. Chem. Phys.* **140**, p. 89.

Kim, Y. and Netz, R. (2006). Electro-osmosis at inhomogeneous charged surfaces: Hydrodynamic versus electric friction, *J. Chem. Phys.* **124**, p. 114709.

Lowe, C. (1999). An alternative approach to dissipative particle dynamics, *Europhys. J.* **47**, pp. 145–151.

Melchionna, S. and Marini Bettolo Marconi, U. (2011). Electro-osmotic flows under nanoconfinement: A self-consistent approachs, *EPL* **95**, p. 44002.

Moroni, D., Rotenberg, B., Hansen, J. P., Succi, S. and Melchionna, S. (2006). Solving the fokker-planck kinetic equation on a lattice, *Phys. Rev. E* **73**, p. 066707.

Nägele, G. (1996). On the dynamics and structure of charge-stabilized suspensions, *Phys. Rep.* **272**, pp. 216–372.

O'Brien, R. and White, L. (1978). Electrophoretic mobility of a spherical colloidal particle, *J. Chem. Soc. Faraday Trans.* **74**, p. 1607.

Pagonabarraga, I., Rotenberg, B. and Frenkel, D. (2010). Recent advances in the modelling and simulation of electrokinetic effects: bridging the gap between atomistic and macroscopic descriptions, *Phys. Chem. Chem. Phys.* **12**, p. 9566.

Rex, M. and Löwen, H. (2008). Influence of hydrodynamic interactions on lane formation in oppositely charged driven colloids, *Europ. J. Phys. E* **26**, pp. 143–150.

Rotenberg, B. and Pagonabarraga, I. (2013). Electrokinetics: insights from simulation on the microscopic scale (Topical Review), *Mol. Phys.* **111**, pp. 827–842.

Rotenberg, B., Pagonabarraga, I. and Frenkel, D. (2008). Dispersion of charged tracers in charged porous media, *EPL* **83**, p. 34004.

Rotenberg, B., Pagonabarraga, I. and Frenkel, D. (2010). Coarse-grained simulations of charge, current and flow in heterogeneous media, *Faraday Discussions* **144**, pp. 223–243.

Stratford, K., Adhikari, R., Pagonabarraga, I. and Desplat, J.-C. (2005). Lattice boltzmann for binary fluids with suspended colloids, *J. Stat. Phys.* **121**, p. 163.

Stratford, K. and Pagonabarraga, I. (2008). Parallel simulation of particle suspensions with the lattice Boltzmann method, *Comp. Math. Appl.* **55**, p. 1585.

Succi, S. (2001). *The Lattice Boltzmann Equation for Fluid Dynamics and Beyond* (Oxford University Press).

Verwey, J. and Overbeek, J. (1948). *Theory of the Stability of Lyotropic Colloids* (Elsevier, Amsterdam).

Chapter 14

Polarizable Surfaces: Weak and Strong Coupling Regimes

Alexandre P. dos Santos[a] and Yan Levin[b]

[a] *Departamento de Física, Universidade Federal de Santa Catarina, 88040-900, Florianópolis, Santa Catarina, Brazil*

[b] *Instituto de Física, Universidade Federal do Rio Grande do Sul, Caixa Postal 15051, CEP 91501-970, Porto Alegre, RS, Brazil*

levin@if.ufrgs.br

14.1 Introduction

Study of charged surfaces in electrolyte solutions is of fundamental importance, as these can model lamellar liquid crystals, clays, biological membranes, electrodes, and so on. Interesting phenomena such as like-charge attraction between similarly charged surfaces have been observed in the presence of multivalent counterions [Guldbrand *et al.* (1984); Pellenq *et al.* (1997); Levin (2002)]. There has been a great theoretical [Engstrom and Wennerstrom (1978); Kjellander and Mitchell (1997); Netz (2001); Moreira and Netz (2001); Lau and Pincus (2002); Jho *et al.* (2007); Abrashkin *et al.* (2007); Jho *et al.* (2008); Hatlo and Lue (2009, 2010); Samaj and Trizac (2011a,b)], simulational [Guldbrand *et al.* (1984); Pellenq *et al.* (1997); Moreira and Netz (2002); Wang and Ma (2012)], and experimental [Duval *et al.* (2004)] effort to clarifying the behavior

Electrostatics of Soft and Disordered Matter
Edited by David Dean, Jure Dobnikar, Ali Naji, and Rudolf Podgornik

ISBN 978-981-4411-85-1 (Hardcover), 978-981-4411-86-8 (eBook)
www.panstanford.com

of double layers near charged surfaces. In many approaches, the theories assume that the entire system is composed of the same dielectric material. This, however, is not very realistic, as clays, colloidal particles, and hydrocarbon membranes have dielectric constant significantly smaller than that of the surrounding aqueous medium. The dielectric discontinuity across the interface results in polarization effects [Jho *et al.* (2007, 2008); Hatlo and Lue (2009, 2010); dos Santos *et al.* (2011); Lue and Linse (2011); Wang and Ma (2012); Gan *et al.* (2012)], which can significantly affect the ionic distribution near the surface. In the current chapter, we present a simple theoretical approach that allows us to accurately predict the counterion distribution near a charged wall, which separates two environments with different dielectric constants. We consider separately the weak and the strong coupling regimes. Monte Carlo (MC) simulations are also performed in order to test our theoretical predictions.

14.2 Monte Carlo Simulations

The simulations of long-range interacting systems are much more difficult than that of systems with short-range forces. The difficulty is that one can not arbitrarily cut off the long-range Coulomb potential by using periodic boundary conditions, as is the case of the usual Lennard–Jones fluids. Instead, one needs to consider an infinite number of periodic images of the system and then sum over these using Ewald summation methods [Allen, M. P. and Tildesley, D. J. (1987)]. For systems with a planar geometry, such as an infinite charged wall in contact with an electrolyte, there is an additional complication that comes from the broken translational symmetry. In this section, we describe an approach that allows us to simulate such systems taking into account the dielectric discontinuity at the interface. The MC simulations are performed in the NVT ensemble. The system is located in the right-hand half of a rectangular simulation box of dimensions $L_x \times L_y \times L_z$, centered at the origin of coordinate system. A charged wall of surface charge density $-\sigma$ is located at $z = 0$. $N_c = \text{int}\left[\sigma L_{xy}^2/q\alpha\right]$ neutralizing counterions of charge αq and effective radius r_c are confined to the region $0 < z < L_z/2$, where q is the proton charge and α is the ionic valence.

The dielectric constants on the two sides of the wall are different, given by ϵ_c and ϵ_w, for $z < 0$ and $z > 0$, respectively. Note that the dielectric discontinuity results in the appearance of the image charges in the region $-L_z/2 < z < 0$, which will be discussed later. The Ewald summation [Allen, M. P. and Tildesley, D. J. (1987)] is used in order to calculate the electrostatic potentials between the ions in the periodic replicas of the simulation box. To account for the slab geometry, we use the correction proposed by Yeh and Berkowitz [Yeh and Berkowitz (1999)]. The complete derivation of the electrostatic energy is presented in the appendix.

14.3 Theory: Weak Regime

We first present a theory that accounts for the results of the MC simulations in the weak coupling limit, when the characteristic Coulomb interaction between the counterions is smaller than the thermal energy, $\Gamma \equiv \alpha^2 q^2/\epsilon_w d k_B T \ll 1$, where d is the characteristic distance between the condensed counterions. Using $\alpha q/\pi d^2 = \sigma$, the plasma parameter becomes $\Gamma = \sqrt{\alpha^3 q^3 \pi \sigma}/\epsilon_w k_B T$. The Bjerrum length is defined as $\lambda_B = \beta q^2/\epsilon_w$ and is 7.2 Å, for water at room temperature.

Before studying the ionic distribution near a charged wall, we first need to understand the role of electrostatic correlations and the induced charges when $\sigma = 0$. To this end, we consider a symmetric α:α electrolyte at concentration c_s confined to infinite half-space, Fig. 14.1. The work necessary to bring an ion from the bulk to a distance z_q from the (uncharged) surface that separates the two regions with the different dielectric constants, ϵ_w and ϵ_c, can be calculated in terms of the electrostatic Green's function [Levin and Flores-Mena (2001)].

To account for the interionic correlations and induced surface charge, we use the linearized Poisson–Boltzmann (Debye–Hückel) equation. For symmetry reasons, it is convenient to work in a cylindrical coordinate system. Suppose that an ion of charge q is located at z_q, see Fig. 14.1. The electrostatic potential inside the

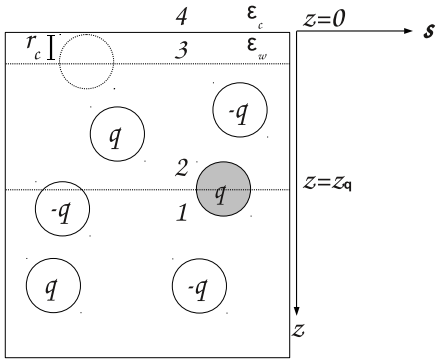

Figure 14.1 Representation of an electrolyte in the region $z > r_c$.

regions 1 and 2 satisfies

$$\nabla^2\phi(\boldsymbol{s}, z) - \kappa^2\phi(\boldsymbol{s}, z) = -\frac{4\pi\alpha q}{\epsilon_w}\delta(\boldsymbol{s})\delta(z - z_q)\,, \tag{14.1}$$

whereas in the regions 3 and 4, it satisfies the Laplace equation,

$$\nabla^2\phi(\boldsymbol{s}, z) = 0\,, \tag{14.2}$$

where $\kappa = \sqrt{8\pi\alpha^2\lambda_B c_s}$ is the inverse Debye length.

Writing the potential as a Fourier transform,

$$\phi(\boldsymbol{s}, z) = (1/4\pi^2)\int_{-\infty}^{+\infty} d\boldsymbol{k}\, e^{i\boldsymbol{k}\cdot\boldsymbol{s}}\,\hat{\phi}(\boldsymbol{k}, z),$$

we obtain the following equation for the regions 1 and 2,

$$\frac{\partial^2\hat{\phi}(\boldsymbol{k}, z)}{\partial z^2} - (k^2 + \kappa^2)\hat{\phi}(\boldsymbol{k}, z) = -\frac{4\pi\alpha q}{\epsilon_w}\delta(z - z_q)\,, \tag{14.3}$$

and for the regions 3 and 4,

$$\frac{\partial^2\hat{\phi}(\boldsymbol{k}, z)}{\partial z^2} = k^2\hat{\phi}(\boldsymbol{k}, z)\,, \tag{14.4}$$

where we have used a Fourier representation of the delta function

$$\delta(\boldsymbol{s}) = \frac{1}{(2\pi)^2}\int_{-\infty}^{+\infty} d\boldsymbol{k}\, e^{i\boldsymbol{k}\cdot\boldsymbol{s}}\,. \tag{14.5}$$

As the electrostatic potential must remain finite in the limits $z \to \infty$ and $z \to -\infty$, we obtain the following solutions for each region:

$$\begin{aligned}
\hat{\phi}_1(\boldsymbol{k}, z) &= B_1 e^{-pz}\,,\\
\hat{\phi}_2(\boldsymbol{k}, z) &= A_2 e^{pz} + B_2 e^{-pz}\,,\\
\hat{\phi}_3(\boldsymbol{k}, z) &= A_3 e^{kz} + B_3 e^{-kz}\,,\\
\hat{\phi}_4(\boldsymbol{k}, z) &= A_4 e^{kz}\,,
\end{aligned} \tag{14.6}$$

where $p = \sqrt{k^2 + \kappa^2}$.

To calculate the integration constants, we use the conditions of continuity of the electrostatic potential, $\hat{\phi}_3(\boldsymbol{k}, z) = \hat{\phi}_4(\boldsymbol{k}, z)$ at $z = 0$, $\hat{\phi}_2(\boldsymbol{k}, z) = \hat{\phi}_3(\boldsymbol{k}, z)$ at $z = r_c$ and $\hat{\phi}_2(\boldsymbol{k}, z) = \hat{\phi}_1(\boldsymbol{k}, z)$ at $z = z_q$, and of the normal components of the displacement field,

$$\begin{aligned}
&\epsilon_c \frac{\partial \hat{\phi}_4(\boldsymbol{k}, z)}{\partial z} - \epsilon_w \frac{\partial \hat{\phi}_3(\boldsymbol{k}, z)}{\partial z} = 0 \text{ , at } z = 0 \text{ ,} \\
&\epsilon_w \frac{\partial \hat{\phi}_3(\boldsymbol{k}, z)}{\partial z} - \epsilon_w \frac{\partial \hat{\phi}_2(\boldsymbol{k}, z)}{\partial z} = 0 \text{ , at } z = r_c \text{ ,} \\
&\epsilon_w \frac{\partial \hat{\phi}_2(\boldsymbol{k}, z)}{\partial z} - \epsilon_w \frac{\partial \hat{\phi}_1(\boldsymbol{k}, z)}{\partial z} = 4\pi\alpha q \text{ , at } z = z_q \text{ .}
\end{aligned} \tag{14.7}$$

The last equation has been obtained by integrating Eq. 14.3 across the singularity at z_q.

The Fourier transform of the electrostatic potential in the region 2 is found to be

$$\hat{\phi}_2(\boldsymbol{k}, z) = \frac{2\pi\alpha q}{\epsilon_w p} \left[e^{-p(z_q - z)} + e^{-p(z + z_q - 2r_c)} \frac{f_1(k)}{f_2(k)} \right] , \tag{14.8}$$

where

$$\begin{aligned}
f_1(k) = {} & p \cosh(kr_c) - k \sinh(kr_c) + \frac{\epsilon_c}{\epsilon_w} p \sinh(kr_c) \\
& - \frac{\epsilon_c}{\epsilon_w} k \cosh(kr_c) \text{ ,}
\end{aligned} \tag{14.9}$$

$$\begin{aligned}
f_2(k) = {} & p \cosh(kr_c) + k \sinh(kr_c) + \frac{\epsilon_c}{\epsilon_w} p \sinh(kr_c) \\
& + \frac{\epsilon_c}{\epsilon_w} k \cosh(kr_c)
\end{aligned} \tag{14.10}$$

and the inverse Fourier transform is

$$\phi_2(\boldsymbol{s}, z) = \frac{1}{2\pi} \int_0^\infty dk\, k J_0(ks) \hat{\phi}_2(\boldsymbol{k}, z) \text{ ,} \tag{14.11}$$

where $J_0(ks)$ is the Bessel function of order 0.

We are interested in calculating the potential felt by an ion, located at distance z_q from the interface. Subtracting the self-potential $q/\epsilon_w(z_q - z)$, after performing the explicit integration of the first term in Eq. 14.8, we find

$$\phi_{\text{pol}}(z_q) = -\frac{\alpha q \kappa}{\epsilon_w} + \frac{\alpha q}{\epsilon_w} \int_0^\infty dk\, e^{-2p(z_q - r_c)} \frac{k}{p} \frac{f_1(k)}{f_2(k)} \text{ .} \tag{14.12}$$

Performing the Güntelberg charging process [Güntelberg (1926)], we obtain the work necessary to bring an ion from the bulk to a distance z_q from the interface [Levin and Flores-Mena (2001)],

$$W_{\rm i}(z_q) = \frac{\alpha^2 q^2}{2\epsilon_{\rm w}} \int_0^\infty dk\, e^{-2p(z_q - r_{\rm c})} \frac{k\, f_1(k)}{p\, f_2(k)} \,. \tag{14.13}$$

A very accurate approximation to the above expression is

$$W_{\rm ap}(z_q) = \frac{W_{\rm i}(r_{\rm c}) r_{\rm c}}{z_q}\, e^{-2\kappa(z_{\rm q} - r_{\rm c})} \,. \tag{14.14}$$

This approximate form is much more convenient for numerical implementation [Levin *et al.* (2009); dos Santos *et al.* (2010a)], as it requires calculating only one integral to determine $W_{\rm i}(r_{\rm c})$ at the beginning of the calculation.

We now return to the problem of interest. The system now is an infinite dielectric wall of charge density $-\sigma$, located at $z = 0$, and the neutralizing counterions of charge αq and radius $r_{\rm c}$, confined to $0 < z < L_z/2$. The dielectric constants are $\epsilon_{\rm c}$ and $\epsilon_{\rm w}$, for $z < 0$ and $z > 0$, respectively. For $\Gamma < 1$ (weak coupling limit), the electrostatic potential and the ionic density profile can be determined from the solutions of the modified PB equation

$$\nabla^2 \phi(z) = -\frac{4\pi}{\epsilon_{\rm w}} \left[-\sigma \delta(z) + \alpha q \rho(z) \right] \,, \tag{14.15}$$

where the counterion density is given by

$$\rho(z) = \frac{\sigma\, e^{-\alpha q \beta \phi(z) - \beta W_{\rm ap}(z)}}{\alpha q \int_{r_{\rm c}}^{L_z/2} dz\, e^{-\alpha q \beta \phi(z) - \beta W_{\rm ap}(z)}} \,. \tag{14.16}$$

The ionic correlations and the surface polarization are taken into account through the potential $W_{\rm ap}(z)$, with $\kappa = \sqrt{8\pi \lambda_{\rm B} \alpha \sigma / q L_z}$. In Fig. 14.2, we compare our results with the MC simulations, for various dielectric constants. As can be seen, the agreement between the theory and the simulations is excellent.

14.4 Strong Coupling Regime

When $\Gamma > 1$, the mean field theory—such as the PB equation—is not able to accurately predict the ionic density distribution because of

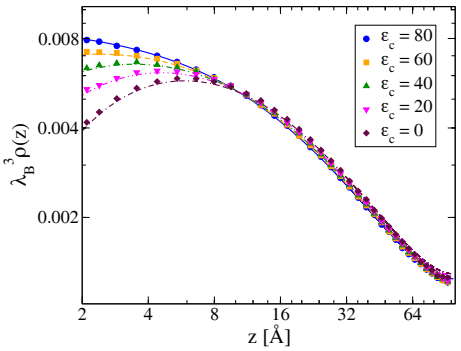

Figure 14.2 The symbols are the simulation data, whereas the lines represent the solutions of the modified PB equation (Eq. 14.15). The surface charge density is $\sigma = 6.25 \times 10^{-4}\ q/\text{Å}^2$ and the monovalent counterion radius is $r_c = 2$ Å. The lengths of the rectangular simulation box are $L_x = L_y \equiv L_{xy} = 231.08$ Å, and $L_z = 200$ Å.

the strong correlations between the counterions. In the limit $\Gamma \gg 1$, the counterions form a quasi-two dimensional strongly correlated liquid near the wall [Shklovskii (1999); Levin (2002)], with an approximately hexagonal geometry [Totsuji (1975)]. Consider one counterion. The electric fields produced by the other counterions of the double layer approximately cancel each other. The counterion then interacts predominantly with the wall and with the ionic image charges, see Fig. 14.3. The potential produced by the charged plate that separates the two environments with different dielectric constants is given by

$$\phi_p(z) = -\frac{4\pi\sigma}{(\epsilon_w + \epsilon_c)} z\,. \tag{14.17}$$

As an approximation, we consider that the ion interacts only with the self-image and with the image charges of the six first neighbors in the hexagonal lattice, see Fig. 14.3.

This approximation was used previously in the study of colloidal double layers [Bakhshandeh *et al.* (2011)]. The electrostatic energy of a counterion at distance z from the plate is then

$$U(z) = \alpha q \phi_p(z) + \frac{\gamma \alpha^2 q^2}{\epsilon_w 4z} + \frac{6\gamma\alpha^2 q^2}{\epsilon_w \sqrt{4z^2 + h^2}}\,, \tag{14.18}$$

where $\gamma = (\epsilon_w - \epsilon_c)/(\epsilon_w + \epsilon_c)$ and h is the distance between the ions of the hexagonal lattice. h can be calculated by considering that

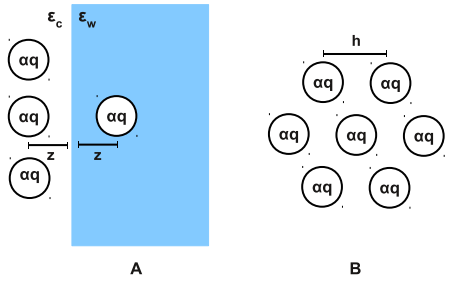

Figure 14.3 Hexagon of images at the surface. (A) The side view. (B) The self-image and the nearest neighbors. In order to illustrate we consider $\epsilon_c = 0$.

$N_c = \sigma A/\alpha q$ ions are distributed on the surface of area A. The unitary cell of a hexagonal lattice is a parallelogram of area $h^2\sqrt{3}/2$, which gives the result

$$h = \sqrt{\frac{2\alpha q}{\sigma\sqrt{3}}}\,. \tag{14.19}$$

The ionic density profile near the surface is obtained from

$$\rho(z) = Ce^{-\beta U(z)} \tag{14.20}$$

where $C = \sigma/\alpha q \int_0^L dz\ e^{-\beta U(z)}$ is the normalization constant. In Fig. 14.4, we compare our theoretical results with the MC simulations. The agreement is very good in the region in which the strong coupling approximation applies.

In the far field, we expect that the counterions will be very dilute so that the electrostatic potential will, once again, satisfy the PB equation. The boundary condition at the colloidal surface, however, must be modified to account for the strong counterion condensation induced by the electrostatic correlations. The new boundary condition can be derived by equating the electrochemical potential of the condensed counterions and of the counterions that remain in the bulk [Shklovskii (1999); dos Santos *et al.* (2009); dos Santos *et al.* (2010b)]. This results in a new boundary condition for the standard PB equation, which requires that the concentration of the counterions near the surface be

$$\rho_{\rm PB}(0) = \rho_{\rm sc}e^{\beta\mu_c}\,, \tag{14.21}$$

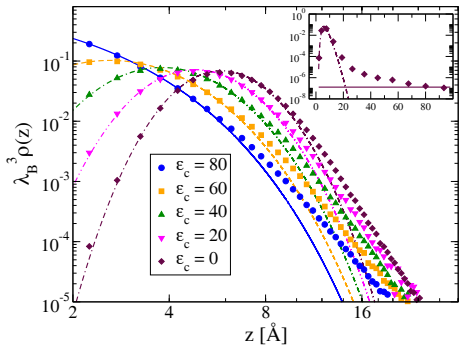

Figure 14.4 The symbols are simulation data, whereas the lines represent the theory. The surface charge density is $\sigma = 3.74 \times 10^{-3}\ q/\text{Å}^2$ and the pentavalent counterions radius is $r_c = 2$ Å, whereas the lengths of the rectangular simulation box are $L_x = L_y \equiv L_{xy} = 231.08$ Å, and $L_z = 200$ Å. The solid line in the inset shows the solution of the regular PB equation with the boundary condition given by Eq. 14.21.

where $\beta\mu_c = -1.65\Gamma + 2.61\Gamma^{1/4} - 0.26 \ln \Gamma - 1.95$ is the chemical potential of the strongly correlated counterions [Totsuji (1975)]. The density ρ_{sc} is obtained using the coarse-graining of the near-field density profile, Eq. 14.20, in the region near the surface [dos Santos *et al.* (2009)],

$$\rho_{sc} = \frac{\int_{r_c}^{r_c+3.6\lambda_{GC}} dz\, \rho(z)}{3.6\lambda_{GC}}\,, \tag{14.22}$$

where $\lambda_{GC} = 1/2\pi\alpha\lambda_B\sigma$ is the Gouy–Chapman length. In the inset of the Fig. 14.4, we present the solution of the usual PB equations with the renormalized boundary condition given by Eq. 14.21. Only the case with $\epsilon_c = 0$ is shown, as in the far field, the ionic density distribution is highly insensitive to the value of ϵ_c.

14.5 Conclusion

We have presented a method for performing MC simulations in a cell geometry that includes a dielectric discontinuity at one of the boundaries. The results of the simulation have been used to study the counterion density profiles and to develop the weak and the strong coupling theories, which account very accurately for the

simulation data. In the weak coupling regime, the image charges repel the counterions from the wall. The contact density predicted by the present theory is substantially smaller than what is found using the usual PB equation, and is in excellent agreement with the MC simulations. In the strong coupling limit, the contact density is found to be even lower, as in this case, the counterions are repelled both by the self-image and by the images of the others counterions. Finally, we show how for $\Gamma \gg 1$ the counterion density distribution can be calculated in the far field using a renormalized boundary condition for the standard PB equation.

In presenting the theory, we have restricted ourselves to the systems containing only counterions and no coions. In the weak coupling limit, the approach developed here can be easily extended to systems, which also contain 1:1 electrolyte. The situation, however, is much more difficult for multivalent electrolytes. For such systems, strong electrostatic interactions between the counterions and coions lead to formation of Bjerrum clusters. Thus, to be able to account for the distribution of multivalent ions near a charged surface, one must first have an accurate description of the bulk of solution. This already presents a formidable challenge, see Ref. [Levin (2002)]. Nevertheless, one can make some progress by considering a chemical picture of electrolyte in which there is an equilibrium between the free ions and the clusters; such calculations, however, very rapidly become quite involved [dos Santos *et al.* (2010b)].

14.6 Acknowledgments

This work was partially supported by the CNPq, FAPERGS, INCT-FCx, and by the US-AFOSR under the grant FA9550-09-1-0283.

A.7 Appendix: Energy Calculation for Monte Carlo Simulations

We consider a charge neutral system of N ions of charges q_i. The electrostatic potential at the position $\boldsymbol{r}$, created by all ions (excluding

ion i), their image charges (including the image of ion i), and the periodic replicas is

$$\phi_i(\boldsymbol{r}) = \sum_{\boldsymbol{n}}^{\infty} \sum_{j=1}^{N}{}' \int \frac{\rho_j(\boldsymbol{s})}{\epsilon_{\rm w}|\boldsymbol{r}-\boldsymbol{s}+\boldsymbol{r}_{\rm ep}|} d^3\boldsymbol{s} + \sum_{\boldsymbol{n}}^{\infty} \sum_{j=1}^{N} \int \frac{\rho'_j(\boldsymbol{s})}{\epsilon_{\rm w}|\boldsymbol{r}-\boldsymbol{s}+\boldsymbol{r}_{\rm ep}|} d^3\boldsymbol{s}\,, \tag{A.1}$$

where $\rho_j(\boldsymbol{s}) = q_j\delta(\boldsymbol{s}-\boldsymbol{r}_j-\boldsymbol{r}_{\rm ep})$ and $\rho'_j(\boldsymbol{s}) = \gamma q_j\delta(\boldsymbol{s}-\boldsymbol{r}'_j-\boldsymbol{r}_{\rm ep})$ are the charge densities of ions and their replicas; and of dielectric images and their replicas. The replication vector is defined as $\boldsymbol{r}_{\rm ep} = L_{xy}n_x\hat{\boldsymbol{x}} + L_{xy}n_y\hat{\boldsymbol{y}} + L_z n_z\hat{\boldsymbol{z}}$ and $\boldsymbol{r}'_j = \boldsymbol{r}_j - 2z_j\hat{\boldsymbol{z}}$. The vectors $\boldsymbol{n} = (n_x, n_y, n_z)$, where n_x, n_y and n_z are integers, represent the infinite replicas of the main cell. The constant γ is defined as $\gamma = (\epsilon_{\rm w} - \epsilon_{\rm c})/(\epsilon_{\rm w} + \epsilon_{\rm c})$ and the prime on the summation means that $j \neq i$, when $\boldsymbol{n} = (0, 0, 0)$. The total electrostatic energy of the system is given by

$$U = \frac{1}{2}\sum_{i=1}^{N} q_i\phi_i(\boldsymbol{r}_i)\,. \tag{A.2}$$

The energy above is very difficult to calculate because of the slow convergence of the series in Eq. A.1. To speed up the convergence, we use the Ewald method in which the ionic charge is partially screened by placing a Gaussian-distributed charge of opposite sign on top of each ion [Allen, M. P. and Tildesley, D. J. (1987)]. We then add and subtract opposite Gaussian charge at the position of each ion and its image, $\rho_j(\boldsymbol{s})$ and $\rho'_j(\boldsymbol{s})$, respectively. The potential, Eq. A.1, then becomes

$$\phi_i(\boldsymbol{r}) = \phi_i^S(\boldsymbol{r}) + \phi^{\rm L}(\boldsymbol{r}) - \phi_i^{\rm self}(\boldsymbol{r})\,, \tag{A.3}$$

where

$$\phi_i^S(\boldsymbol{r}) = \sum_{\boldsymbol{n}}^{\infty} \sum_{j=1}^{N}{}' \int \frac{\rho_j(\boldsymbol{s}) - \rho_j^G(\boldsymbol{s})}{\epsilon_{\rm w}|\boldsymbol{r}-\boldsymbol{s}+\boldsymbol{r}_{\rm ep}|} d^3\boldsymbol{s} + \sum_{\boldsymbol{n}}^{\infty} \sum_{j=1}^{N} \int \frac{\rho'_j(\boldsymbol{s}) - \rho'^G_j(\boldsymbol{s})}{\epsilon_{\rm w}|\boldsymbol{r}-\boldsymbol{s}+\boldsymbol{r}_{\rm ep}|} d^3\boldsymbol{s}\,, \tag{A.4}$$

$$\phi^{\rm L}(\boldsymbol{r}) = \sum_{\boldsymbol{n}}^{\infty} \sum_{j=1}^{N} \int \frac{\rho_j^G(\boldsymbol{s})}{\epsilon_{\rm w}|\boldsymbol{r}-\boldsymbol{s}+\boldsymbol{r}_{\rm ep}|} d^3\boldsymbol{s} + \sum_{\boldsymbol{n}}^{\infty} \sum_{j=1}^{N} \int \frac{\rho'^G_j(\boldsymbol{s})}{\epsilon_{\rm w}|\boldsymbol{r}-\boldsymbol{s}+\boldsymbol{r}_{\rm ep}|} d^3\boldsymbol{s} \tag{A.5}$$

and

$$\phi_i^{\rm self}(\boldsymbol{r}) = \int \frac{\rho_i^G(\boldsymbol{s})}{\epsilon_{\rm w}|\boldsymbol{r}-\boldsymbol{s}|} d^3\boldsymbol{s}\,, \tag{A.6}$$

where $\rho_j^G(\boldsymbol{s}) = q_j(\kappa_{\rm e}^3/\sqrt{\pi^3})\exp(-\kappa_{\rm e}^2|\boldsymbol{s}-\boldsymbol{r}_j-\boldsymbol{r}_{\rm ep}|^2)$, $\rho_j'^G(\boldsymbol{s}) = \gamma q_j(\kappa_{\rm e}^3/\sqrt{\pi^3})\exp(-\kappa_{\rm e}^2|\boldsymbol{s}-\boldsymbol{r}_j'-\boldsymbol{r}_{\rm ep}|^2)$ and $\kappa_{\rm e}$ is a dumping parameter. We subtracted the self potential, Eq. A.6, from the Eq. A.3, in order to remove the prime over the summation in the long-range (L) part of the potential, Eq. A.5. The electrostatic potential produced by the Gaussian charges can be easily calculated using the Poisson equation, yielding

$$\phi^{\rm L}(\boldsymbol{r}) = \sum_{\boldsymbol{n}}^{\infty}\sum_{j=1}^{N} q_j \frac{\mathrm{erf}(\kappa_{\rm e}|\boldsymbol{r}-\boldsymbol{r}_j+\boldsymbol{r}_{\rm ep}|)}{\epsilon_{\rm w}|\boldsymbol{r}-\boldsymbol{r}_j+\boldsymbol{r}_{\rm ep}|} + \sum_{\boldsymbol{n}}^{\infty}\sum_{j=1}^{N} \gamma q_j \frac{\mathrm{erf}(\kappa_{\rm e}|\boldsymbol{r}-\boldsymbol{r}_j'+\boldsymbol{r}_{\rm ep}|)}{\epsilon_{\rm w}|\boldsymbol{r}-\boldsymbol{r}_j'+\boldsymbol{r}_{\rm ep}|}\,, \tag{A.7}$$

where $\mathrm{erf}(x)$ is the error function. The short-range part of the potential (S), Eq. A.4, can then be obtained in terms of the complementary error function, $\mathrm{erfc}(x) = 1-\mathrm{erf}(x)$,

$$\phi_i^S(\boldsymbol{r}) = \sum_{\boldsymbol{n}}^{\infty}{\sum_{j=1}^{N}}' q_j \frac{\mathrm{erfc}(\kappa_{\rm e}|\boldsymbol{r}-\boldsymbol{r}_j+\boldsymbol{r}_{\rm ep}|)}{\epsilon_{\rm w}|\boldsymbol{r}-\boldsymbol{r}_j+\boldsymbol{r}_{\rm ep}|} + \sum_{\boldsymbol{n}}^{\infty}\sum_{j=1}^{N} \gamma q_j \frac{\mathrm{erfc}(\kappa_{\rm e}|\boldsymbol{r}-\boldsymbol{r}_j'+\boldsymbol{r}_{\rm ep}|)}{\epsilon_{\rm w}|\boldsymbol{r}-\boldsymbol{r}_j'+\boldsymbol{r}_{\rm ep}|}\,. \tag{A.8}$$

This potential decays very rapidly and can be truncated by setting the dumping parameter to $\kappa_{\rm e} = 5/V^{1/3}$, where $V = L_{xy}^2 L_z$, corresponding to the minimum image convention. It is then sufficient to consider in the sum only the term $\boldsymbol{n} = (0,0,0)$, with the usual periodic boundary condition,

$$\phi_i^S(\boldsymbol{r}) = {\sum_{j=1}^{N}}' q_j \frac{\mathrm{erfc}(\kappa_{\rm e}|\boldsymbol{r}-\boldsymbol{r}_j|)}{\epsilon_{\rm w}|\boldsymbol{r}-\boldsymbol{r}_j|} + \sum_{j=1}^{N} \gamma q_j \frac{\mathrm{erfc}(\kappa_{\rm e}|\boldsymbol{r}-\boldsymbol{r}_j'|)}{\epsilon_{\rm w}|\boldsymbol{r}-\boldsymbol{r}_j'|}\,. \tag{A.9}$$

The self-potential, Eq. A.6, reduces to

$$\phi_i^{\rm self}(\boldsymbol{r}) = q_i \frac{\mathrm{erf}(\kappa_{\rm e}|\boldsymbol{r}-\boldsymbol{r}_i|)}{\epsilon_{\rm w}|\boldsymbol{r}-\boldsymbol{r}_i|}\,. \tag{A.10}$$

We next calculate the long-range part of the potential, Eq. A.7. This is most easily obtained using the Fourier representation, $\hat{\phi}^L(\boldsymbol{k}) = (1/V)\int_V d^3\boldsymbol{r}\ \exp(-i\boldsymbol{k}\cdot\boldsymbol{r})\phi^{\mathrm{L}}(\boldsymbol{r})$, since in the reciprocal space all the sums, once again, converge very rapidly. The Fourier transform $\hat{\rho}^T(\boldsymbol{k}) = (1/V)\int_V d^3\boldsymbol{r}\ \exp(-i\boldsymbol{k}\cdot\boldsymbol{r})\rho^T(\boldsymbol{r})$, of the Gaussian charge density,

$$\rho^T(\boldsymbol{r}) = \sum_{\boldsymbol{n}}^{\infty}\sum_{j=1}^{N} q_j \frac{\kappa_{\mathrm{e}}^3}{\sqrt{\pi^3}} \exp(-\kappa_{\mathrm{e}}^2|\boldsymbol{r}-\boldsymbol{r}_j-\boldsymbol{r}_{\mathrm{ep}}|^2) + \sum_{\boldsymbol{n}}^{\infty}\sum_{j=1}^{N} \gamma q_j \frac{\kappa_{\mathrm{e}}^3}{\sqrt{\pi^3}} \exp(-\kappa_{\mathrm{e}}^2|\boldsymbol{r}-\boldsymbol{r}'_j-\boldsymbol{r}_{\mathrm{ep}}|^2)\,, \quad \text{(A.11)}$$

is

$$\hat{\rho}^T(\boldsymbol{k}) = \frac{1}{V}\exp(-\frac{|\boldsymbol{k}|^2}{4\kappa_{\mathrm{e}}^2})\left[\sum_{j=1}^{N} q_j \exp(-i\boldsymbol{k}\cdot\boldsymbol{r}_j) + \sum_{j=1}^{N}\gamma q_j \exp(-i\boldsymbol{k}\cdot\boldsymbol{r}'_j)\right]\,, \quad \text{(A.12)}$$

where $\boldsymbol{k} = (2\pi n_x/L_{xy}, 2\pi n_y/L_{xy}, 2\pi n_z/L_z)$. Using the Poisson equation, $|\boldsymbol{k}|^2\hat{\phi}^L(\boldsymbol{k}) = (4\pi/\epsilon_{\mathrm{w}})\hat{\rho}^T(\boldsymbol{k})$, we can evaluate the Fourier transform of the potential,

$$\hat{\phi}^L(\boldsymbol{k}) = \frac{4\pi}{\epsilon_{\mathrm{w}} V|\boldsymbol{k}|^2}\exp(-\frac{|\boldsymbol{k}|^2}{4\kappa_{\mathrm{e}}^2})\left[\sum_{j=1}^{N} q_j \exp(-i\boldsymbol{k}\cdot\boldsymbol{r}_j) + \sum_{j=1}^{N}\gamma q_j \exp(-i\boldsymbol{k}\cdot\boldsymbol{r}'_j)\right]\,. \quad \text{(A.13)}$$

The corresponding real-space electrostatic potential is calculated using the inverse Fourier transform, $\phi^{\mathrm{L}}(\boldsymbol{r}) = \sum_{\boldsymbol{k}}\hat{\phi}^L(\boldsymbol{k})\exp(i\boldsymbol{k}\cdot\boldsymbol{r})$,

$$\phi^{\mathrm{L}}(\boldsymbol{r}) = \sum_{\boldsymbol{k}}\frac{4\pi}{\epsilon_{\mathrm{w}} V|\boldsymbol{k}|^2}\exp(-\frac{|\boldsymbol{k}|^2}{4\kappa_{\mathrm{e}}^2})\exp(i\boldsymbol{k}\cdot\boldsymbol{r})\times \left[\sum_{j=1}^{N} q_j \exp(-i\boldsymbol{k}\cdot\boldsymbol{r}_j) + \sum_{j=1}^{N}\gamma q_j \exp(-i\boldsymbol{k}\cdot\boldsymbol{r}'_j)\right]\,. \quad \text{(A.14)}$$

The long-range contribution to the total electrostatic energy is given by $U_{\mathrm{L}} = (1/2)\sum_{i=1}^{N} q_i\phi^{\mathrm{L}}(\boldsymbol{r}_i)$, where $\phi^{\mathrm{L}}(\boldsymbol{r})$ is obtained

from Eq. A.14. It is convenient to rewrite this in terms of functions: $A(\boldsymbol{k}) = \sum_{i=1}^{N} q_i \cos(\boldsymbol{k}\cdot\boldsymbol{r}_i)$, $B(\boldsymbol{k}) = -\sum_{i=1}^{N} q_i \sin(\boldsymbol{k}\cdot\boldsymbol{r}_i)$, $C(\boldsymbol{k}) = \sum_{i=1}^{N} \gamma q_i \cos(\boldsymbol{k}\cdot\boldsymbol{r}'_i)$ and $D(\boldsymbol{k}) = -\sum_{i=1}^{N} \gamma q_i \sin(\boldsymbol{k}\cdot\boldsymbol{r}'_i)$. The electrostatic energy then becomes,

$$U_{\mathrm{L}} = \sum_{\boldsymbol{k}} \frac{2\pi}{\epsilon_{\mathrm{w}} V |\boldsymbol{k}|^2} \exp(-\frac{|\boldsymbol{k}|^2}{4\kappa_{\mathrm{e}}^2}) \times \left[A(\boldsymbol{k})^2 + B(\boldsymbol{k})^2 + A(\boldsymbol{k})C(\boldsymbol{k}) + B(\boldsymbol{k})D(\boldsymbol{k})\right] . \tag{A.15}$$

These functions are easily updated for each new configuration in a Monte Carlo simulation. The electrostatic energy coming from the short-range part of the potential is $U_S = (1/2)\sum_{i=1}^{N} q_i \phi_i^S(\boldsymbol{r}_i)$, where $\phi_i^S(\boldsymbol{r})$ is given by the Eq. A.9, and the self-energy contribution is $U_{\mathrm{self}} = (1/2)\sum_{i=1}^{N} q_i \phi_i^{\mathrm{self}}(\boldsymbol{r}_i)$. In the limit $x \to 0$, the $\mathrm{erf}(x)$ function vanishes as $(2/\sqrt{\pi})x$ and the self-energy contribution reduces to, $U_{\mathrm{self}} = (\kappa_{\mathrm{e}}/\epsilon_{\mathrm{w}}\sqrt{\pi})\sum_{i=1}^{N} q_i^2$. The total electrostatic interaction energy of the ions is given by the above expressions plus the correction for the slab geometry. Yeh and Berkowitz [Yeh and Berkowitz (1999)] found that the regular 3D Ewald summation method with an energy correction, can reproduce the same results as the 2D Ewald method, with a significant gain in performance. Taking into account the dielectric discontinuity and the induced image charges, we find the correction for the slab geometry to be

$$U_{\mathrm{cor}} = -\frac{\pi}{\epsilon_{\mathrm{w}} V} \sum_{i=1}^{N} q_i \left[\sum_{j=1}^{N} q_j (z_i - z_j)^2 + \sum_{j=1}^{N} \gamma q_j (z_i - z'_j)^2 \right] , \tag{A.16}$$

where $z'_j = -z_j$. Using the electroneutrality, this expression can be written as

$$U_{\mathrm{cor}} = \frac{2\pi}{\epsilon_{\mathrm{w}} V} M_z^2 (1-\gamma) , \tag{A.17}$$

where $M_z = \sum_{i=1}^{N} q_i z_i$ is the magnetization in the $\hat{z}$ direction.

Now suppose that the system consists of N_{c} counterions of charge αq and a wall of uniform surface charge density $-\sigma$, located at $z = 0$. We first derive the functions A, B, C and D appearing in

the long-range part of the potential, Eq. A.15. For the surface charge we find

$$A_{\rm p}(\boldsymbol{k}) = -\int_{-L_{xy}/2}^{L_{xy}/2}\int_{-L_{xy}/2}^{L_{xy}/2} \sigma\, dx\, dy \cos\left(k_x x + k_y y\right) = -\frac{4\sigma}{k_x k_y}\sin\left(k_x L_{xy}/2\right)\sin\left(k_y L_{xy}/2\right),$$

$$B_{\rm p}(\boldsymbol{k}) = \int_{-L_{xy}/2}^{L_{xy}/2}\int_{-L_{xy}/2}^{L_{xy}/2} \sigma\, dx\, dy \sin\left(k_x x + k_y y\right) = 0\,,$$

$$C_{\rm p}(\boldsymbol{k}) = -\int_{-L_{xy}/2}^{L_{xy}/2}\int_{-L_{xy}/2}^{L_{xy}/2} \gamma\sigma\, dx\, dy \cos\left(k_x x + k_y y\right) = -\frac{4\gamma\sigma}{k_x k_y}\sin\left(k_x L_{xy}/2\right)\sin\left(k_y L_{xy}/2\right)$$

and

$$D_{\rm p}(\boldsymbol{k}) = \int_{-L_{xy}/2}^{L_{xy}/2}\int_{-L_{xy}/2}^{L_{xy}/2} \gamma\sigma\, dx\, dy \sin\left(k_x x + k_y y\right) = 0\,.$$

The corresponding functions for $N_{\rm c}$ counterions and the charged wall are then: $A(\boldsymbol{k}) = \alpha q \sum_{i=1}^{N_{\rm c}} \cos\left(\boldsymbol{k}\cdot\boldsymbol{r}_i\right) + A_{\rm p}(\boldsymbol{k})$, $B(\boldsymbol{k}) = -\alpha q \sum_{i=1}^{N_{\rm c}} \sin\left(\boldsymbol{k}\cdot\boldsymbol{r}_i\right)$, $C(\boldsymbol{k}) = \gamma\alpha q \sum_{i=1}^{N_{\rm c}} \cos\left(\boldsymbol{k}\cdot\boldsymbol{r}_i'\right) + C_{\rm p}(\boldsymbol{k})$ and $D(\boldsymbol{k}) = -\gamma\alpha q \sum_{i=1}^{N_{\rm c}} \sin\left(\boldsymbol{k}\cdot\boldsymbol{r}_i'\right)$, and the total long-range part of the energy, $U_{\rm L}$, is given by the Eq. A.15.

The short-range contribution to the electrostatic potential created by the charged surface at distance z_i is

$$\phi_{\rm p}(z_i) = -\frac{2\sigma}{(\epsilon_{\rm c}+\epsilon_{\rm w})} \times \int_{-L_{xy}/2}^{L_{xy}/2} dx \int_{-L_{xy}/2}^{L_{xy}/2} dy\, \frac{\operatorname{erfc}(\kappa_{\rm e}\sqrt{x^2+y^2+z_i^2})}{\sqrt{x^2+y^2+z_i^2}}\,. \quad \text{(A.18)}$$

The limits of integration are defined in order to keep the minimum image convention. We calculate the potential on a grid in the $\hat{z}$ direction with spacing between the points 0.01 Å. The calculation is performed once at the beginning of the simulation, and the potential is tabulated. The total short range electrostatic interaction energy

is then given by $U_S = (\alpha q/2)\sum_{i=1}^{N_c}\phi_i^S(\boldsymbol{r}_i) + \alpha q\sum_{i=1}^{N_c}\phi_p(z_i)$, where $\phi_i^S(\boldsymbol{r})$ is

$$\phi_i^S(\boldsymbol{r}) = \alpha q\sum_{j=1}^{N_c}{}' \frac{\mathrm{erfc}(\kappa_e|\boldsymbol{r}-\boldsymbol{r}_j|)}{\epsilon_w|\boldsymbol{r}-\boldsymbol{r}_j|} + \gamma\alpha q\sum_{j=1}^{N_c}\frac{\mathrm{erfc}(\kappa_e|\boldsymbol{r}-\boldsymbol{r}'_j|)}{\epsilon_w|\boldsymbol{r}-\boldsymbol{r}'_j|}. \quad \text{(A.19)}$$

The self energy can be written as $U_{self} = (\kappa_e/\epsilon_w\sqrt{\pi})(N_c\alpha^2q^2 + \sigma^2L_{xy}^4)$. Since the charged surface is located at $z = 0$, it does not contribute to the correction potential, Eq. A.17, so that the magnetization remains $M_z = \alpha q\sum_{i=1}^{N_c} z_i$. The total energy used in the simulations is

$$U = U_S + U_L - U_{self} + U_{cor}. \quad \text{(A.20)}$$

We use 1×10^6 MC steps to equilibrate the system. The configurations are saved each 100 MC steps. The counterionic density profiles are obtained with 80×10^3 saved uncorrelated states.

References

Abrashkin, A., Andelman, D. and Orland, H. (2007). *Phys. Rev. Lett.* **99**, p. 077801.

Allen, M. P. and Tildesley, D. J. (1987). *Computer Simulations of Liquids* (Oxford: Oxford University Press, New York).

Bakhshandeh, A., dos Santos, A. P. and Levin, Y. (2011). *Phys. Rev. Lett.* **107**, p. 107801.

dos Santos, A. P., Bakhshandeh, A. and Levin, Y. (2011). *J. Chem. Phys.* **135**, p. 044124.

dos Santos, A. P., Diehl, A. and Levin, Y. (2009). *J. Chem. Phys.* **130**, p. 124110.

dos Santos, A. P., Diehl, A. and Levin, Y. (2010a). *Langmuir* **26**, p. 10778.

dos Santos, A. P., Diehl, A. and Levin, Y. (2010b). *J. Chem. Phys.* **132**, p. 104105.

Duval, J. F. L., Leermakers, F. A. M. and van Leeuwen, H. P. (2004). *Langmuir* **20**, p. 5052.

Engstrom, S. and Wennerstrom, H. (1978). *J. Phys. Chem.* **82**, p. 2711.

Gan, Z., Xing, X. and Xu, Z. (2012). *J. Chem. Phys.* **137**, p. 034708.

Guldbrand, L., Jonsson, B., Wennerstrom, H. and Linse, P. (1984). *J. Chem. Phys.* **80**, p. 2221.

Güntelberg, E. Z. (1926). *Z. Phys. Chem.* **123**, p. 199.

Hatlo, M. M. and Lue, L. (2009). *Soft Matter* **5**, p. 125.

Hatlo, M. M. and Lue, L. (2010). *Europhys. Lett.* **89**, p. 25002.

Jho, Y. S., Kanduc, M., Naji, A., Podgornik, R., Kim, M. W. and Pincus, P. A. (2008). *Phys. Rev. Lett.* **101**, p. 188101.

Jho, Y. S., Park, G., Chang, C. S., Pincus, P. A. and Kim, M. (2007). *Phys. Rev. E* **76**, p. 011920.

Kjellander, R. and Mitchell, D. J. (1997). *Mol. Phys.* **91**, p. 173.

Lau, A. W. C. and Pincus, P. (2002). *Phys. Rev. E* **66**, p. 041501.

Levin, Y. (2002). *Rep. Prog. Phys.* **65**, p. 1577.

Levin, Y., dos Santos, A. P. and Diehl, A. (2009). *Phys. Rev. Lett.* **103**, p. 257802.

Levin, Y. and Flores-Mena, J. E. (2001). *Europhys. Lett.* **56**, p. 187.

Lue, L. and Linse, P. (2011). *J. Chem. Phys.* **135**, p. 224508.

Moreira, A. G. and Netz, R. R. (2001). *Phys. Rev. Lett.* **87**, p. 078301.

Moreira, A. G. and Netz, R. R. (2002). *Eur. Phys. J. E* **8**, p. 33.

Netz, R. R. (2001). *Eur. Phys. J. E* **5**, p. 557.

Pellenq, R. J. M., Caillol, J. M. and Delville, A. (1997). *J. Phys. Chem. B* **101**, p. 8584.

Samaj, L. and Trizac, E. (2011a). *Phys. Rev. E* **84**, p. 041401.

Samaj, L. and Trizac, E. (2011b). *Phys. Rev. Lett.* **106**, p. 078301.

Shklovskii, B. I. (1999). *Phys. Rev. E* **60**, p. 5802.

Totsuji, H. (1975). *J. Phys. Soc. Jpn.* **39**, p. 253.

Wang, Z. Y. and Ma, Y. Q. (2012). *J. Chem. Phys.* **136**, p. 234701.

Yeh, I. C. and Berkowitz, M. L. (1999). *J. Chem. Phys.* **111**, p. 3155.

Part III

COMPLEX COLLOIDS

Chapter 15

Coarse-Grained Modeling of Charged Colloidal Suspensions: From Poisson–Boltzmann Theory To Effective Interactions

Alan R. Denton
Department of Physics, North Dakota State University, Fargo, North Dakota, USA
alan.denton@ndsu.edu

15.1 Introduction

Electrostatic forces—the strongest interparticle forces outside of the nucleus—account for the stability of matter over a broad range of length scales, from atoms to macromolecules to the myriad materials that surround us. Colloidal particles (nanometers to microns in size) and polymers can become charged in a polar solvent (e.g., water) through dissociation of counterions [1]. Repulsive Coulomb interactions between ions can then stabilize a suspension or solution against aggregation due to ubiquitous van der Waals attractive interactions [2]. Electrostatic interactions between ions largely govern the equilibrium thermodynamic and dynamical properties of charge-stabilized colloidal suspensions and polyelectrolyte solutions. Controlling mechanical and thermal stability is essential

Electrostatics of Soft and Disordered Matter
Edited by David Dean, Jure Dobnikar, Ali Naji, and Rudolf Podgornik

ISBN 978-981-4411-85-1 (Hardcover), 978-981-4411-86-8 (eBook)
www.panstanford.com

to many applications, from foods and pharmaceuticals to filters and photonic materials.

Predicting the properties of such complex, multicomponent systems with accuracy sufficient to guide and interpret experiments requires realistic modeling of the interparticle interactions and collective behavior of many-particle systems. Although the fundamental interactions are simple, the sheer number of particles and the broad ranges of length and time scales confront the modeler with significant computational challenges. A general strategy for mitigating such challenges is to "coarse grain" or "integrate out" the degrees of freedom of some components, reducing the original multicomponent model to a simpler model of fewer components [3–6]. The trade-off for so reducing complexity is that the simpler model is governed by modified (effective) interparticle interactions.

This chapter is a "how-to" manual of sorts for implementing coarse-graining methods to derive effective interactions. For simplicity, we focus here on charge-stabilized colloidal suspensions. The same basic concepts apply, however, to a wide variety of soft (and hard) materials. To set the stage, we begin by defining the primitive and one-component models and outlining the Poisson–Boltzmann (PB) theory of charged colloids. After reviewing the well-known cell model implementation of PB theory, we turn to an alternative implementation, based on perturbation theory, and derive microion distributions around colloids and effective electrostatic interactions. After some effort, a happy result emerges: the effective interactions remain relatively simple, at least in systems with monovalent microions. This fortunate outcome provides the foundation for further theoretical and simulation modeling to explore and facilitate design of novel materials. Finally, we peer over the horizon at the outlook for possible future research directions in the field.

15.2 Primitive Model

The primitive model of charged colloids and polyelectrolytes [1, 2] idealizes the solvent as a homogeneous dielectric continuum of relative permittivity ϵ. Dispersed throughout the solvent are

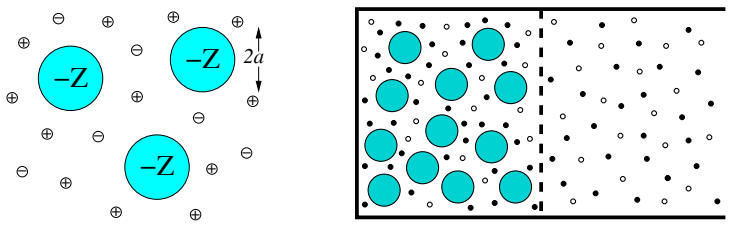

Figure 15.1 Primitive model of charged colloids: spherical macroions (radius a, valence Z) and point microions dispersed in a dielectric continuum (left). Colloidal suspension in Donnan equilibrium across semi-permeable membrane with electrolyte reservoir (right).

macroions and microions, modeled here as charged hard spheres of radius a and valence Z (charge $-Ze$) and point ions of valence z. In a closed suspension, all particles are confined to the same volume V. In Donnan equilibrium, only the macroions are confined, whereas the microions can exchange (e.g., across a semi-permeable membrane) with a salt reservoir, here assumed to be a 1:1 electrolyte of monovalent ions.

If sufficiently dilute, the reservoir can be reasonably modeled as an ideal gas. The reservoir fixes the chemical potential of salt in the suspension, $\mu_s = 2k_BT \ln(n_0\Lambda^3)$, where n_0 is the number density of ion pairs, T is the absolute temperature, and Λ is the thermal wavelength, defining the arbitrary zero of the chemical potential. A bulk suspension of N_m macroions, N_c counterions, and N_s dissociated pairs of oppositely charged salt ions contains $N_+ = N_c + N_s$ positive and $N_- = N_s$ negative microions, for a total of $N_\mu = N_c + 2N_s$ microions. Global electroneutrality constrains the macroion and counterion numbers by the condition $Z N_m = zN_c$.

Accounting for excluded-volume and electrostatic (Coulomb) pairwise interparticle interactions, the Hamiltonian separates naturally into three terms:

$$H = H_m + H_\mu + H_{m\mu} \,. \tag{15.1}$$

The first term on the right side is the macroion Hamiltonian

$$H_m = H_{hs} + \frac{1}{2} \sum_{i \neq j=1}^{N_m} v_{mm}(r_{ij}) \,, \tag{15.2}$$

where $H_{\rm hs}$ is the hard sphere Hamiltonian (including kinetic energy), $v_{\rm mm}(r_{ij}) = Z^2\lambda_{\rm B}/r_{ij}$ is the Coulomb pair potential between a pair of macroions with center–center separation r_{ij}, and $\lambda_{\rm B} = e^2/(\epsilon k_{\rm B}T)$ defines the Bjerrum length, the distance at which the Coulomb interaction energy between a pair of monovalent ions rivals the thermal energy. To simplify notation, in this chapter, Hamiltonians, pairpotentials, and all other quantities having dimensions of energy are expressed in thermal ($k_{\rm B}T$) units. The remaining two terms on the right side of Eq. (15.1) are the microion Hamiltonian

$$H_\mu = K_\mu + \frac{\lambda_{\rm B}}{2}\sum_{i\neq j=1}^{N_\mu}\frac{z_i z_j}{r_{ij}}\,, \tag{15.3}$$

with kinetic energy K_μ and microion valences $z_i = \pm 1$, and the macroion–microion interaction energy

$$H_{{\rm m}\mu} = Z\lambda_{\rm B}\sum_{i=1}^{N_{\rm m}}\sum_{j=1}^{N_\mu}\frac{z_j}{r_{ij}}\,. \tag{15.4}$$

15.3 One-Component Model: Effective Hamiltonian

Significant concentrations of salt pose severe computational challenges for large-scale simulations of bulk suspensions [7–9]. Consider that a suspension of macroions of radius $a = 10$ nm at 1% volume fraction and just 1 mM salt concentration contains, *per macroion*, $\mathcal{O}(10^3)$ particles, all interacting via long-range Coulomb forces. Therefore, salt-dominated suspensions usually are modeled by first mapping the mixture onto a one-component model (OCM).

For a suspension in Donnan equilibrium, this mapping (or coarse graining) operates on the semigrand partition function:

$$\mathcal{Z} = \langle\langle\exp(-H)\rangle_\mu\rangle_{\rm m}\,, \tag{15.5}$$

where $\langle\,\rangle_\mu$ denotes a grand canonical trace over microion coordinates and $\langle\,\rangle_{\rm m}$ denotes a canonical trace over macroion coordinates. The partition function may be formally expressed in the form

$$\mathcal{Z} = \langle\exp(-H_{\rm eff})\rangle_{\rm m}\,, \tag{15.6}$$

where

$$H_{\rm eff} = H_{\rm m} + \Omega_\mu \tag{15.7}$$

is an effective Hamiltonian of a one-component system of pseudo-macroions and

$$\Omega_\mu = -\ln\langle \exp(-H_\mu - H_{\mathrm{m}\mu})\rangle_\mu \tag{15.8}$$

is the grand potential functional of the microions in the presence of fixed macroions. Practical applications of the OCM require approximating Ω_μ. For this purpose, PB theory [1, 2, 10, 11] is a powerful approach. Below, we briefly review PB theory and two common implementations: the cell model and the effective interaction model.

15.4 Poisson–Boltzmann Theory

PB theory is most elegantly formulated within the framework of classical density-functional theory of nonuniform fluids [12–16]. Corresponding to the primitive model Hamiltonian [Eqs. (15.2)–(15.4)], there exists a Helmholtz free energy functional $F[n_{\mathrm{m}}(\mathbf{r}), n_\pm(\mathbf{r})]$, which (for a given external potential) is a unique functional of the macroion and microion number density profiles, $n_{\mathrm{m}}(\mathbf{r})$ and $n_\pm(\mathbf{r})$, varying with position $\mathbf{r}$ [13]. This free energy functional separates, according to $F = F_{\mathrm{id}} + F_{\mathrm{ex}} + F_{\mathrm{ext}}$, into a (purely entropic) ideal gas free energy functional of all ions,

$$F_{\mathrm{id}} = \int \mathrm{d}\mathbf{r} \sum_{i=m,\pm} n_i(\mathbf{r})\{\ln[n_i(\mathbf{r})\Lambda^3] - 1\}\,, \tag{15.9}$$

an excess free energy functional, $F_{\mathrm{ex}} = F_{\mathrm{hs}} + F_{\mathrm{el}}$, due to hard-sphere (hs) and electrostatic (el) interparticle interactions, and a contribution F_{ext} due to an external potential. Neglecting interparticle correlations (mean-field approximation), the electrostatic part of the excess free energy functional may be approximated as

$$F_{\mathrm{el}} = \frac{1}{e}\int \mathrm{d}\mathbf{r}\, \rho(\mathbf{r})\Psi(\mathbf{r})\,, \tag{15.10}$$

where $\rho(\mathbf{r}) = e[n_+(\mathbf{r}) - n_-(\mathbf{r}) - n_{\mathrm{f}}(\mathbf{r})]$ is the total charge density, including the negative charge fixed on the macroion surfaces of number density $n_{\mathrm{f}}(\mathbf{r})$, and

$$\Psi(\mathbf{r}) = \frac{\lambda_{\mathrm{B}}}{e}\int \mathrm{d}\mathbf{r}'\, \frac{\rho(\mathbf{r}')}{|\mathbf{r}-\mathbf{r}'|} \tag{15.11}$$

is the reduced electrostatic potential at position $\mathbf{r}$ due to all ions. The reduced potential and total ion density are related via the Poisson equation, which may be expressed in the form

$$\nabla^2\psi(\mathbf{r}) = -4\pi\lambda_{\mathrm{B}}[n_+(\mathbf{r})-n_-(\mathbf{r})]\,; \quad \nabla\psi|_{\mathrm{surface}} = Z\lambda_{\mathrm{B}}/a^2\,, \quad (15.12)$$

where the macroion charges are absorbed into a boundary condition at the macroion surfaces and the microion densities implicitly vanish inside the macroion cores.

In a given external potential, the equilibrium densities of all ions minimize the total grand potential functional of the system [13]. Alternatively, fixing the macroions and regarding their charges as the source of the external potential, the equilibrium microion densities alone minimize the *microion grand potential functional*

$$\Omega_\mu[n_\pm(\mathbf{r})] = F_\mu[n_\pm(\mathbf{r})]-\mu_+\int \mathrm{d}\mathbf{r}\, n_+(\mathbf{r})-\mu_-\int \mathrm{d}\mathbf{r}\, n_-(\mathbf{r})\,, \quad (15.13)$$

a Legendre transform of the microion free energy functional

$$F_\mu[n_\pm(\mathbf{r})] = F_{\mu,\mathrm{id}}[n_\pm(\mathbf{r})] + \frac{1}{2e}\int \mathrm{d}\mathbf{r}\,\rho(\mathbf{r})\Psi(\mathbf{r})\,, \quad (15.14)$$

where

$$F_{\mu,\mathrm{id}}[n_\pm(\mathbf{r})] = \int \mathrm{d}\mathbf{r}\sum_{i=\pm} n_i(\mathbf{r})\{\ln[n_i(\mathbf{r})\Lambda^3]-1\} \quad (15.15)$$

is the ideal gas free energy functional and the microion (electro)chemical potentials $\mu_\pm$ are identified as the Legendre variables. Note that Ω_μ depends parametrically on the macroion coordinates and that F_μ includes macroion–macroion Coulomb interactions for electroneutrality. Under the assumption that either the electrostatic potential or the electric field vanishes everywhere on the boundary of the volume V, the microion free energy functional may be also expressed in the form

$$F_\mu[n_\pm(\mathbf{r})] = \int \mathrm{d}\mathbf{r}\sum_{i=\pm} n_i(\mathbf{r})\{\ln[n_i(\mathbf{r})\Lambda^3]-1\} + \frac{1}{8\pi\lambda_{\mathrm{B}}}\int \mathrm{d}\mathbf{r}\,|\nabla\psi|^2\,. \quad (15.16)$$

Minimizing $\Omega_\mu[n_\pm(\mathbf{r})]$ with respect to $n_\pm(\mathbf{r})$ now yields the Boltzmann approximation for the equilibrium microion densities

$$n_\pm(\mathbf{r}) = n_\pm^{(0)}\exp[\mp\psi(\mathbf{r})] \quad \text{(fixed macroions)}\,, \quad (15.17)$$

where the reference densities, $n_{\pm}^{(0)} = \Lambda^{-3}\exp(\mu_{\pm})$, are the microion densities at the reference potential $\psi = 0$. The microion grand potential is the value of the grand potential functional [Eq. (15.13)] evaluated at the equilibrium density profiles [Eq. (15.17)]:

$$\Omega_{\mu} = -\int \mathrm{d}\mathbf{r}\,[n_{+}(\mathbf{r})+n_{-}(\mathbf{r})] - \frac{1}{2}\int \mathrm{d}\mathbf{r}\,[n_{+}(\mathbf{r})-n_{-}(\mathbf{r})+n_{f}(\mathbf{r})]\psi(\mathbf{r})\,. \tag{15.18}$$

For a closed suspension (fixed particle numbers), the chemical potentials of the two microion species differ because of asymmetric interactions with the macroions: $\mu_{+} \neq \mu_{-}$. Correspondingly, the reference densities also differ: $n_{+}^{(0)} \neq n_{-}^{(0)}$. In Donnan equilibrium, however, exchange of microions with a salt reservoir shifts the intrinsic microion chemical potentials, $\mu_{\pm}^{\mathrm{in}} = [\delta F_{\mu}/\delta n_{\pm}(\mathbf{r})]_{\mathrm{eq}}$, by the Donnan potential ψ_D:

$$\mu_{\pm} = \mu_{\pm}^{\mathrm{in}} \pm \psi_D = \ln(n_0\Lambda^3)\,. \tag{15.19}$$

The total chemical potentials, and so too the reference densities, of the two microion species are thus equalized. The equilibrium microion density profiles are then given by

$$n_{\pm}(\mathbf{r}) = n_0 \exp[\mp\psi(\mathbf{r})]\,. \tag{15.20}$$

The Donnan potential is interpreted physically as the change in electrostatic potential across the reservoir–suspension interface, and mathematically as a Lagrange multiplier for the constraint of global electroneutrality.

Combining the Poisson equation for the potential [Eq. (15.12)] with the Boltzmann approximation for the microion densities [Eq. (15.17) or (15.20)], the PB equation becomes

$$\nabla^2\psi(\mathbf{r}) = \kappa_0^2 \sinh\psi(\mathbf{r})\,; \quad \nabla\psi|_{\mathrm{surface}} = Z\lambda_{\mathrm{B}}/a^2\,, \tag{15.21}$$

where $\kappa_0 = \sqrt{8\pi\lambda_{\mathrm{B}}n_0}$ is the screening constant in the reservoir. Note that Eq. (15.21) is highly nonlinear. In the case of weak electrostatic potentials ($\psi \ll 1$), the right side of Eq. (15.21) may be expanded in powers of ψ. Truncating at linear order yields the linearized PB equation:

$$\nabla^2\psi(\mathbf{r}) = \kappa_0^2\psi(\mathbf{r})\,; \quad \nabla\psi|_{\mathrm{surface}} = Z\lambda_{\mathrm{B}}/a^2\,. \tag{15.22}$$

Beyond the boundary condition at the macroion surfaces, the boundary value problem is fully specified only by imposing another condition at the outer boundary of the system, which depends on the practical implementation of the theory.

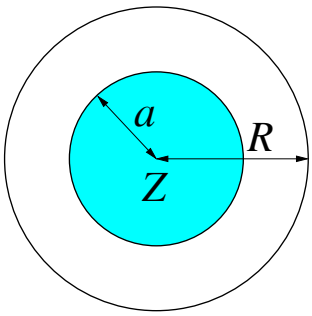

Figure 15.2 Cell model: a single macroion in a spherical cell.

15.5 Cell Model Implementation

The anisotropic boundary conditions on the nonlinear PB equation [Eq. (15.21)] imposed by an arbitrary configuration of macroions render a general solution computationally daunting. In recent years, powerful *ab initio* methods have been developed for combining PB theory of microion density profiles with molecular dynamics [15–18] or Brownian dynamics [19, 20] simulation to evolve macroion coordinates according to derived forces. Despite such advances, most applications of PB theory have been implemented within a cell model to facilitate numerical solution.

In a seemingly bold reduction, the cell model represents a bulk suspension by a single macroion, neutralizing counterions, and salt ions confined to a cell of the same shape as the macroion (see Fig. 15.2). Microion-induced correlations between macroions are simply ignored. For spherical colloids, the natural choice is a spherical cell centered on the macroion. Gauss's law then dictates that the electric field must vanish everywhere on the boundary of the electroneutral cell. With the potential and microion densities depending on only the radial coordinate r, the PB equation reduces to an ordinary differential equation for $\psi(r)$ with boundary conditions $\psi'(a) = Z\lambda_B/a^2$ and $\psi'(R) = 0$, where the cell radius R is commensurate with the average macroion density: $n_m = N_m/V = 3/(4\pi R^3)$. For a closed suspension, the arbitrary location of the reference point of the electrostatic potential (where $\psi = 0$) is usually chosen as the cell boundary: $\psi(R) = 0$. In Donnan

equilibrium, the potential is conventionally chosen to vanish in the reservoir, in which case the boundary value of the electrostatic potential is identified as the Donnan potential: $\psi(R) = \psi_D \neq 0$.

An appealing feature of the cell model is the simple analytic relation between the bulk pressure p (in thermal units) and the microion densities at the cell boundary:

$$p = n_+(R) + n_-(R)\,. \tag{15.23}$$

Although first derived within the mean-field PB framework [21], this pressure theorem proves to be exact within the cell model [22], that is, valid also for correlated microions. In Donnan equilibrium with an ideal gas reservoir, the osmotic pressure Π, defined as, the difference in pressure between suspension and reservoir, is then given by

$$\Pi = n_+(R) + n_-(R) - 2n_0\,. \tag{15.24}$$

Within PB theory, the osmotic pressure is strictly positive [23], which follows directly from Eqs. (15.20) and (15.24) and the inequality, $\cosh x > 1$.

The cell model provides one means of implementing PB theory by approximating the microion grand potential [Eq. (15.7)] in the one-component mapping of the primitive model (Sec. 15.3). Reducing a suspension to a single macroion in a cell with isotropic boundary conditions facilitates solution of the nonlinear PB equation. The cost of incorporating nonlinear microion screening, however, is neglect of correlations between macroions.

15.6 Effective-Interaction Implementation

An alternative implementation of PB theory, based on the one-component mapping, focuses on effective interactions derived from perturbative expansion of the microion grand potential about a reference system, namely, a uniform plasma of microions unperturbed by the macroions. By incorporating macroion interactions, this approach can model both thermodynamic and structural properties of colloidal suspensions. For reviews of effective interactions in colloidal suspensions, see refs. [3–6]. Several statistical mechanical frameworks have been developed. Density functional theories [24–27] expand the ideal gas part of the microion free energy functional

[Eq. (15.15)] in a Taylor series in powers of deviations of the microion density profiles from their mean values $n_\pm$:

$$F_{\mu,\mathrm{id}}[n_\pm(\mathbf{r})] = \sum_{i=\pm}\left(N_i[\ln(n_i\Lambda^3)-1] + \int \mathrm{d}\mathbf{r}\,\frac{[n_i(\mathbf{r})-n_i]^2}{2n_i} + \cdots\right). \tag{15.25}$$

Distributon function theories are based on extensions of the Debye–Hückel theory of electrolytes [28]. Response theories [29–32] are based on a similar perturbative expansion of the microion grand potential functional [Eq. (15.8)]:

$$\Omega_\mu = \Omega_0 + \int_0^1 d\lambda\,\langle H_{\mathrm{m}\mu}\rangle_\lambda\,, \tag{15.26}$$

where $\Omega_0 = -\ln\langle\exp(-H_\mu)\rangle_\mu$ is the grand potential of a reference suspension in the absence of an external colloidal potential and $\langle H_{\mathrm{m}\mu}\rangle_\lambda$ denotes an ensemble average of the macroion–microion interaction energy in a system in which the macroions are "charged" to a fraction λ of their full charge, which can be related to the macroion–microion pair potentials $v_{\mathrm{m}\pm}(r) = \pm Z\lambda_\mathrm{B}/r$ and the densities, $n_\mathrm{m}(\mathbf{r})$ and $n_\pm(\mathbf{r})$, of macroions and microions:

$$\langle H_{\mathrm{m}\pm}\rangle_\lambda = \int d\mathbf{r}\int d\mathbf{r}'\,v_{\mathrm{m}\pm}(|\mathbf{r}-\mathbf{r}'|)n_\mathrm{m}(\mathbf{r})\left\langle n_\pm(\mathbf{r}')\right\rangle_\lambda\,. \tag{15.27}$$

Expanding the microion densities about a reference microion plasma in powers of the macroion "external" potential,

$$\phi_\pm(\mathbf{r}) = \int \mathrm{d}\mathbf{r}'\,v_{\mathrm{m}\pm}(|\mathbf{r}-\mathbf{r}'|)n_\mathrm{m}(\mathbf{r}')\,, \tag{15.28}$$

and truncating the series at linear order yields the linear-response approximation

$$n_\pm(\mathbf{r}) = \sum_{i=\pm}\int \mathrm{d}\mathbf{r}'\,\chi_{\pm i}(|\mathbf{r}-\mathbf{r}'|)\phi_i(\mathbf{r}')\,. \tag{15.29}$$

The linear response functions

$$\chi_{ij}(|\mathbf{r}-\mathbf{r}'|) = \left(\frac{\delta n_i(\mathbf{r})}{\delta\phi_j(\mathbf{r}')}\right)_{Z=0} \tag{15.30}$$

describe the response of the reference plasma to the macroions and are related to the plasma pair correlation functions $h_{ij}(r)$ via [33]

$$\chi_{ij}(r) = -n_i[\delta_{ij}\delta(r) + n_j h_{ij}(r)]\,. \tag{15.31}$$

The neglected higher-order terms in Eq. (15.29) involve nonlinear response functions and many-particle correlations.

Approximating the pair correlation functions of the uniform plasma by their asymptotic (long-range) limits yields the so-called random phase approximation

$$h_{ij}(r) = -z_i z_j \lambda_B \frac{e^{-\kappa r}}{r} , \tag{15.32}$$

where $\kappa = \sqrt{4\pi\lambda_B n_\mu}$ is the screening constant in the system, which differs from that in the reservoir κ_0 [*cf.* Eq. (15.21)]. For consistency, n_μ here represents the total density of microions in the *free* volume, that is, the volume not excluded by the macroion hard cores.

Inserting the linearized microion densities [Eq. (15.29)] into Eq. (15.27) recasts the effective Hamiltonian (microion grand potential) in the form of a sum of effective interactions:

$$H_{\text{eff}} = E_v + H_{\text{hs}} + \frac{1}{2}\sum_{i\neq j=1}^{N_m} v_{\text{eff}}(r_{ij}) , \tag{15.33}$$

where the volume energy E_v is the microion grand potential for a single macroion, $v_{\text{eff}}(r)$ is an *effective* electrostatic pair potential between macroions, and neglected higher-order terms involve sums over effective many-body interactions. The volume energy takes the general form

$$E_v = \Omega_0 + \frac{1}{2}N_m v_{\text{ind}}(0) + \frac{1}{2}(N_+ - N_-)\Psi_D , \tag{15.34}$$

where the first term on the right side accounts for the microion entropy, the second term for the macroion–microion interaction energy, and the last term is the Donnan potential energy resulting from the electroneutrality constraint. The effective macroion–macroion pair potential can be expressed as

$$v_{\text{eff}}(r) = v_{\text{mm}}(r) + v_{\text{ind}}(r) , \tag{15.35}$$

which comprises the bare Coulomb pair potential $v_{\text{mm}}(r)$ and a *microion-induced* pair potential

$$v_{\text{ind}}(r) = \int \mathrm{d}\mathbf{r}' \, [n_+(r') - n_-(r')] v_{\text{m+}}(|\mathbf{r} - \mathbf{r}'|) . \tag{15.36}$$

To evaluate $v_{\rm ind}(r)$, it is helpful first to consider the isotropic microion density profiles around a single macroion, which are obtained from Eqs. (15.29)–(15.32):

$$n_{\pm}(r) = \sum_{i=\pm} \int \mathrm{d}\mathbf{r}'\, \chi_{\pm i}(|\mathbf{r}-\mathbf{r}'|) v_{\rm m+}(r') = \pm n_{\pm} \left(n_{\mu} \lambda_{\rm B} \int d\mathbf{r}' \, \frac{e^{-\kappa r'}}{r'} v_{\rm m+}(|\mathbf{r}-\mathbf{r}'|) - v_{\rm m+}(r) \right). \quad (15.37)$$

To ensure exclusion of microions from the macroion hard cores, the macroion–microion pair potentials can be extended inside the core:

$$v_{\rm m\pm}(r) = \pm Z \lambda_{\rm B} f(r); \qquad f(r) = \begin{cases} 1/r\,, & r > a \\ \alpha/a\,, & r < a\,, \end{cases} \quad (15.38)$$

where α is a constant to be chosen such that $n_{\pm}(r) = 0$ for $r < a$. After evaluating the convolution integral

$$\int_0^{\infty} dr'\, r' e^{-\kappa r'} g(r, r') = \frac{2}{\kappa^2} \begin{cases} \frac{1}{r} - \frac{e^{\kappa a}}{1+\kappa a} \frac{e^{-\kappa r}}{r}\,, & r > a \\ \frac{1}{a + \kappa^{-1}}\,, & r < a\,, \end{cases} \quad (15.39)$$

with

$$g(r, r') = \int_{-1}^{1} d\mu\, f(|\mathbf{r}-\mathbf{r}'|)\,; \quad \mu \equiv \mathbf{r}\cdot\mathbf{r}'/(rr')\,, \quad (15.40)$$

one finds [from Eqs. (15.37) and (15.38)] $\alpha = \kappa a/(1+\kappa a)$ and

$$n_{\pm}(r) = \mp n_{\pm} Z \lambda_{\rm B} \left(\frac{e^{\kappa a}}{1+\kappa a} \right) \frac{e^{-\kappa r}}{r}\,, \qquad r > a\,. \quad (15.41)$$

Substituting Eq. (15.41) into Eqs. (15.35) and (15.36), and evaluating the integral (for $r > 2a$)

$$\int_a^{\infty} dr'\, r' e^{-\kappa r'} g(r, r') = \frac{2}{\kappa^2 r} \left(\frac{1+\kappa a}{e^{\kappa a}} - \frac{e^{\kappa a}}{1+\kappa a} e^{-\kappa r} \right), \quad (15.42)$$

yields a screened Coulomb (Yukawa) effective pair potential:

$$v_{\text{eff}}(r) = Z^2\lambda_{\text{B}}\left(\frac{e^{\kappa a}}{1+\kappa a}\right)^2\frac{e^{-\kappa r}}{r}\,, \qquad r > 2a\,. \tag{15.43}$$

Finally, from Eqs. (15.36) and (15.41), we have

$$v_{\text{ind}}(0) = -\frac{Z^2\lambda_{\text{B}}}{a+\kappa^{-1}}\,, \tag{15.44}$$

which allows the volume energy to be written more explicitly:

$$E_{\text{v}} = \Omega_0 - \frac{1}{2}N_{\text{m}}\frac{Z^2\lambda_{\text{B}}}{a+\kappa^{-1}} - \frac{1}{2}\frac{(N_+ - N_-)^2}{N_\mu}\,. \tag{15.45}$$

In passing, we recall that Eq. (15.43) is the basis of the classic Derjaguin–Landau–Verwey–Overbeek (DLVO) theory [34, 35] of charged colloids, wherein it was first derived within a Debye–Hückel approximation, without the associated volume energy and without excluded-volume corrections.

It is important to remember that the one-body volume energy, although independent of macroion coordinates, does depend on the *average* macroion density, and therefore can influence thermodynamic properties. Similarly, the effective pair potential is density-dependent. Implications of density-dependent effective interactions for thermodynamic stability and consistency have been discussed extensively in recent years [36–41].

Bulk thermodynamic and structural properties can be calculated ultimately by inputting the effective interactions, E_{v} and $v_{\text{eff}}(r)$, into statistical mechanical theories or simulations of the OCM. Figures 15.3 and 15.4 show sample results for the osmotic pressure of highly charged colloidal suspensions, calculated using methodologies described in Refs. [11, 42, 43]. Predictions of the PB cell and effective interaction (one-component) models agree closely with simulations of the primitive model [7] (Fig. 15.3) up to moderate electrostatic coupling strengths ($\Gamma \equiv \lambda_{\text{B}}/a < 1$) and with experimental data [44, 45] (Fig. 15.4) over a considerable range of colloid volume fractions. To achieve such agreement, the linear response theory has been merged with charge renormalization theory to incorporate the important concept of an effective macroion valence [46]. By subsuming within the effective valence those counterions that are strongly associated with the

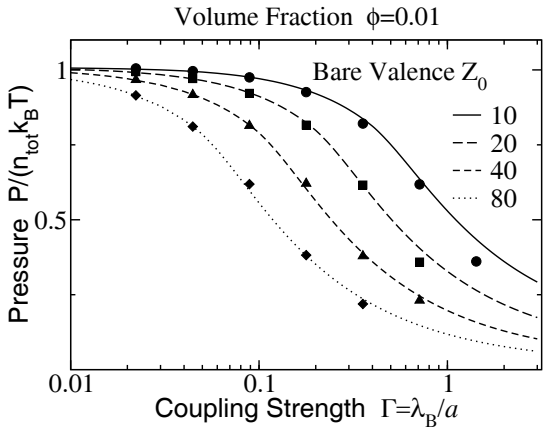

Figure 15.3 Pressure vs. electrostatic coupling constant $\Gamma \equiv \lambda_B/a$ for salt-free suspensions with colloid volume fraction $\phi = 0.01$ and several bare valences Z_0. Predictions of the effective interaction model (curves) are compared with primitive model simulation data (symbols) [7].

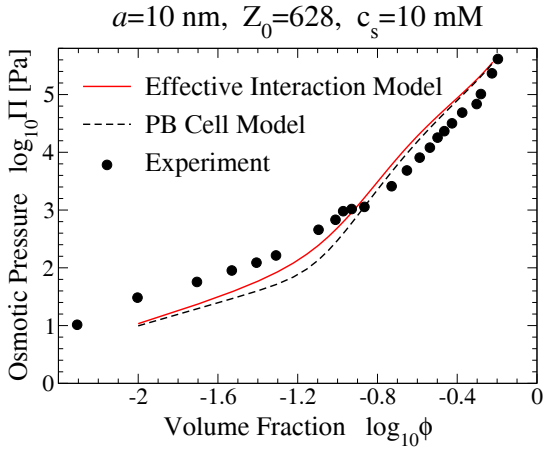

Figure 15.4 Osmotic pressure vs. colloid volume fraction for suspensions with macroion radius $a = 10$ nm, bare valence $Z_0 = 628$, and salt concentration $c_s = 10$ mM. Predictions of the effective interaction model (solid curve) and the PB cell model (dashed curve) are compared with experimental data (symbols) [44, 45].

macroions, the renormalized theory includes most of the nonlinear response inherent in the PB equation. Comparably accurate results are obtained with a renormalized jellium theory [47–49]. The effective interaction model also predicts radial distribution functions in close agreement with simulations of the primitive model [41, 42].

15.7 Outlook

To illustrate the essence of coarse-grained modeling in a friendly context, the discussion in this chapter is limited to the primitive model of charged colloids, focusing on monodisperse suspensions of microspheres. For this system, the effective electrostatic interactions derived using the coarse-graining scheme described in Section 15.6 are relatively simple and lead to predictions for thermodynamic and structural properties that agree closely with the PB cell model, detailed simulations of the primitive model, and experiment. Tremendous opportunities now lie ahead for extending the general methods outlined here and applying them to more complex systems, such as mixtures of colloids differing in size, shape, and charge, to suspensions of particles with anisotropic (patchy) charge distributions (e.g., Janus particles), as well as to different interparticle interactions, such as dipolar interactions. As computing power grows, the demand for coarse-grained models will likely persist, to guide and interpret simulations and to facilitate exploration of increasingly complex materials.

Acknowledgments

It is a pleasure to thank Jun Kyung Chung and Sylvio May for helpful discussions. This work was supported by the National Science Foundation under Grant No. DMR-1106331.

References

1. Evans, D. F. and Wennerström, H. (1999). *The Colloidal Domain*, 2nd ed. (Wiley-VCH, New York).

2. Israelachvili, J. (1992). *Intermolecular and Surface Forces* (Academic, London).
3. Belloni, L. (2000). Colloidal interactions, *J. Phys. Condens. Matter* **12**, pp. R549–R587.
4. Hansen, J. P. and Löwen, H. (2000). Effective interactions between electric double layers, *Annu. Rev. Phys. Chem.* **51**, pp. 209–242.
5. Likos, C. N. (2001). Effective interactions in soft condensed matter physics, *Phys. Rep.* **348**, pp. 267–439.
6. Denton, A. R. (2007). Effective interactions in soft materials. In *Nanostructured Soft Matter: Experiment, Theory, Simulation and Perspectives*, edited by A. V. Zvelindovsky (Springer, Dordrecht).
7. Linse, P. (2000). Structure, phase stability, and thermodynamics in charged colloidal solutions, *J. Chem. Phys.* **113**, pp. 4359–4373.
8. Brukhno, A. V., Åkesson, T., and Jönsson, B. (2009). Phase behavior in suspensions of highly charged colloids, *J. Phys. Chem.* B **113**, pp. 6766–6774.
9. Hynninen, A.-P. and Panagiotopoulos, A. Z. (2007). Disappearance of the gas-liquid phase transition for highly charged colloids, *Phys. Rev. Lett.* **98**, pp. 198301-1-4.
10. Deserno, M. and Holm, C. (2001). In *Electrostatic Effects in Soft Matter and Biophysics*, vol. 46, NATO Advanced Studies Institute, Series II: Mathematics, Physics and Chemistry, edited by C. Holm *et al.* (Kluwer, Dordrecht).
11. Denton, A. R. (2010). Poisson-Boltzmann theory of charged colloids: limits of the cell model for salty suspensions, *J. Phys. Condens. Matter* **22**, pp. 364108-1-12.
12. Evans, R. (1992). In *Inhomogeneous Fluids*, edited by D. Henderson (Dekker).
13. Evans, R. (1979). The nature of the liquid-vapour interface and other topics in the statistical mechanics of nonuniform, classical fluids, *Adv. Phys.* **28**, pp. 143–200.
14. Oxtoby, D. W. (1991). Crystallization of liquids: A density-functional approach, in *Liquids, Freezing and Glass Transition*, Les Houches session 51, edited by Hansen, J.-P., Levesque, D. and Zinn-Justin, J., 145–189 (North-Holland, Amsterdam).
15. Löwen, H., Madden, P. A., and Hansen, J.-P. (1992). Description of counterion screening in colloidal suspensions, *Phys. Rev. Lett.* **68**, pp. 1081–1084.

16. Löwen, H., Madden, P. A., and Hansen, J.-P. (1993). Nonlinear counterion screening in colloidal suspensions, *J. Chem. Phys.* **98**, pp. 3275–3289.
17. Löwen, H. and Kramposthuber, G. (1993). Optimal effective pair potential for charged colloids, *Europhys. Lett.* **23**, pp. 673–678.
18. Tehver, R., Ancilotto, F., Toigo, F., Koplik, J., and Banavar, J. R. (1999). Absence of many-body effects in interactions between charged colloidal particles, *Phys. Rev.* E **59**, pp. R1335–R1338.
19. Dobnikar, J., Chen, Y., Rzehak, R., and von Grünberg, H. H. (2003). Many-body interactions and the melting of colloidal crystals, *J. Chem. Phys.* **119**, pp. 4971–4985.
20. Dobnikar, J., Haložan, D., Brumen, M., von Grünberg, H. H., and Rzehak, R. (2004). Poisson-Boltzmann brownian dynamics of charged colloids in suspension, *Comp. Phys. Comm.* **159**, pp. 73–92.
21. Marcus, R. A. (1955). Calculation of thermodynamic properties of polyelectrolytes, *J. Chem. Phys.* **23**, pp. 1057–1068.
22. Wennerström, H., Jönsson, B., and Linse, P. (1982). The cell model for polyelectrolyte systems. Exact statistical mechanical relations, Monte Carlo simulations, and the Poisson-Boltzmann approximation, *J. Chem. Phys.* **76**, pp. 4665–4670.
23. Deserno, M. and von Grünberg, H. H. (2002). Osmotic pressure of charged colloidal suspensions: A unified approach to linearized Poisson-Boltzmann theory, *Phys. Rev.* E **66**, pp. 011401-1-15.
24. van Roij, R. and Hansen, J.-P. (1997). Van der Waals-like instability in suspensions of mutually repelling charged colloids, *Phys. Rev. Lett.* **79**, pp. 3082–3085.
25. Graf, H. and Löwen, H. (1998). *Density jumps across phase transitions in soft-matter systems*, *Phys. Rev.* E **57**, pp. 5744–5753.
26. van Roij, R., Dijkstra, M., and Hansen, J.-P. (1999). Phase diagram of charge-stabilized colloidal suspensions: van der Waals instability without attractive forces, *Phys. Rev.* E **59**, pp. 2010–2025.
27. Zoetekouw, B. and van Roij, R. (2006). Nonlinear Screening and Gas-Liquid Separation in Suspensions of Charged Colloids, *Phys. Rev. Lett.* **97**, 258302–258305.
28. Warren, P. B. (2000). A theory of void formation in charge-stabilised colloidal suspensions at low ionic strength, *J. Chem. Phys.* **112**, 4683–4698.
29. Grimson, M. J. and Silbert, M. (1991). A self-consistent theory of the effective interactions in charge-stabilized colloidal dispersions, *Mol. Phys.* **74**, 397–404.

30. Denton, A. R. (1999). Effective interactions and volume energies in charge-stabilized colloidal suspensions, *J. Phys. Condens. Matter* **11**, pp. 10061–10071.
31. Denton, A. R. (2000). Effective interactions and volume energies in charged colloids: Linear response theory, *Phys. Rev.* E **62**, pp. 3855–3864.
32. Denton, A. R. (2007). Electroneutrality and phase behavior of colloidal suspensions, *Phys. Rev.* E **76**, 051401-1-11.
33. Hansen, J.-P. and McDonald, I. R. (1986). *Theory of Simple Liquids*, 2nd edition (Academic, London).
34. Derjaguin, B. V. and Landau, L. (1941). Theory of the stability of strongly charged lyophobic sols and the adhesion of strongly charged particles in solutions of electrolytes, *Acta Physicochimica (URSS)* **14**, 633.
35. Verwey, E. J. W. and Overbeek, J. T. G. (1948). *Theory of the Stability of Lyophobic Colloids* (Elsevier, Amsterdam).
36. Louis, A. A. (2002). Beware of density dependent pair potentials, *J. Phys. Condens. Matter* **14** 9187.
37. Dobnikar, J., Castañeda-Priego, R., von Grünberg, H. H., and Trizac, E. (2006). Testing the relevance of effective interaction potentials between highly-charged colloids in suspension, *New J. Phys.* **8**, 277.
38. Castañeda-Priego, R., Rojas-Ochoa, L. F., Lobaskin, V., and Mixteco-Sánchez, J. C. (2006). Macroion correlation effects in electrostatic screening and thermodynamics of highly charged colloids, *Phys. Rev.* E **74**, 051408-1-6.
39. Trizac, E., Belloni, L., Dobnikar, J., von Grünberg, H. H., and Castañeda-Priego, R. (2007). Macroion virial contribution to the osmotic pressure in charge-stabilized colloidal suspensions, *Phys. Rev.* E **75**, 011401-1-8.
40. Rojas-Ochoa, L. F., Castañeda-Priego, R., Lobaskin, V., Stradner, A., Scheffold, F., and Schurtenberger, P. (2008). Density dependent interactions and structure of charged colloidal dispersions in the weak screening regime, *Phys. Rev. Lett.* **100**, 178304-1-4.
41. Castañeda-Priego, R., Lobaskin, V., Mixteco-Sánchez, J. C., Rojas-Ochoa, L. F., and Linse, P. (2012). On the calculation of the structure of charge-stabilized colloidal dispersions using density-dependent potentials, *J. Phys. Condens. Matter* **24**, pp. 065102-1-7.
42. Lu, B. and Denton, A. R. (2010). Charge renormalization, thermodynamics, and structure, of deionized colloidal suspensions, *Commun. Comput. Phys.* **7**, pp. 235–249.

43. Denton, A. R. (2008). Charge renormalization, effective interactions, and thermodynamics of deionized colloidal suspensions, *J. Phys. Condens. Matter* **20**, pp. 494230-1-8.
44. Jönsson, B., Persello, J., Li, J., and Cabane, B. (2011). *Equation of state of colloidal dispersions*, *Langmuir* **27**, 6606–6614.
45. Chang, J., Lesieur, P., Delsanti, M., Belloni, L., Bonnet-Gonnet, C., Cabane, B. (1995). Structural and Thermodynamic Properties of Charged Silica Dispersions, *J. Phys. Chem.* **99**, pp. 15993–16001.
46. Alexander, S., Chaikin, P. M., Grant, P., Morales, G. J., and Pincus, P. (1984). Charge renormalization, osmotic pressure, and bulk modulus of colloidal crystals, *J. Chem. Phys.* **80**, 5776–5781.
47. Pianegonda, S., Trizac, E., and Levin, Y. (2007). The renormalized jellium model for spherical and cylindrical colloids, *J. Chem. Phys.* **126**, pp. 014702-1-10.
48. Colla, T. E., Levin, Y., and Trizac, E. (2009). A self-consistent renormalized jellium approach for calculating structural and thermodynamic properties of charge stabilized colloidal suspensions, *J. Chem. Phys.* **131**, pp. 074115-1-6.
49. Falcón-González, J. M. and Castañeda-Priego, R., (2010). Note: Renormalized jellium model for charged colloids revisited, *J. Chem. Phys.* **133**, pp. 216101-1-3.

Chapter 16

Many-Body Interactions in Colloidal Suspensions

Jure Dobnikar[a,b]

[a] *Department of Chemistry, University of Cambridge, Lensfield Road, CB2 1EW, Cambridge, UK*
[b] *Department for Theoretical Physics, Jožef Stefan Institute, Jamova 39, 1000 Ljubljana, Slovenia*
jure.dobnikar@ijs.si; jd489@cam.ac.uk

16.1 Introduction

Most soft matter systems are complex mixtures in which several species with widely different characteristic time and space scales coexist. Typically, they consist of particles suspended in an aqueous solvent wherein they acquire electric charge. This is due to high dielectric permittivity of water favoring dissociation of surface charge groups. Consequently, electrostatic interactions often play a crucial role in many processes on the scales from nanometers to micrometers. Here, we will not discuss the role of the solvent granularity [Bocquet and Charlaix (2010)] but will focus on approaches wherein the solvent is treated as a continuous dielectric medium with a macroscopic permittivity ϵ. Mesoscopic colloidal

Electrostatics of Soft and Disordered Matter
Edited by David Dean, Jure Dobnikar, Ali Naji, and Rudolf Podgornik

ISBN 978-981-4411-85-1 (Hardcover), 978-981-4411-86-8 (eBook)
www.panstanford.com

particles ($\approx$ μm) are immersed into the solvent surrounded by the electrolyte consisting of counterions and dissociated salt ions ($\approx$ 0.1 nm). The interactions among colloidal particles are mediated by the microions and their correct description is challenging due to the large asymmetry in the length and time scales.

16.2 Modeling Colloidal Suspensions

The most direct approach to modeling charged colloidal suspensions (assuming a homogeneous solvent) is the so-called primitive model. Here, the degrees of freedom of all the particles (colloids and the electrolyte ions) are taken into account. Numerical simulations of the primitive model are demanding due to the large number of degrees of freedom, especially in systems with finite salt concentration. Consequently, most work has been done on salt-free suspensions, wherein all electrolyte ions come from the dissociation of the surface charge groups on the colloids. Linse [Linse (1991)] studied asymmetric two-component electrolytes (charge asymmetry 1:20) within the primitive model and explored pair and triplet correlations among colloidal particles in concentrated suspensions. He compared his data with the results of a simulation of an effective one-component system, consisting only of colloids interacting via effective pair potentials, chosen such that the pair correlations in the original two-component system and in the reference one-component system are identical. Although in general rather similar triplet correlation functions were obtained, considerable differences became visible at small distances, pointing to the relevance of many-body forces.

When studying the properties of colloidal suspensions, the discrete nature of the microions often does not play a crucial role. Therefore, it is tempting to describe the microions in terms of density fields, generally termed density-functional theory [Lowen *et al.* (1993); Hansen and McDonald (1986)]. In the mean-field Poisson-Boltzmann (PB) approach (one version of the density-functional theory), the microions are treated as an ideal gas, neglecting any microion–microion correlations. In the grand canonical ensemble, the microions are coupled to the reservoir with a fixed chemical

potential (fixed concentration c_S of the salt ions); this leads to a nonlinear differential equation for the electrostatic potential $\phi(\boldsymbol{r})$:

$$\nabla\left[\epsilon\nabla\left(\frac{e\phi}{k_B T}\right)\right] = \frac{2e_0^2 c_S}{\epsilon_0 k_B T}\sinh\left[\frac{e_0\phi}{k_B T}\right] . \qquad (16.1)$$

Here, e_0 is the basic charge, k_B is the Boltzxmann constant, ϵ_0 is the dielectric constant, and ϵ is the relative dielectric permitivity (could be position–dependent). The PB equation has to be coupled with appropriate boundary conditions at the colloidal surfaces. Usually, fixed surface charge density or fixed surface potential is assumed. The relation between microscopic physiochemical processes governing the charging of colloidal surfaces (i.e., preferential adsorption or dissociation of surface molecules) and the boundary conditions in the coarse-grained description is not trivial [Strubbe *et al.* (2007)]. In general, the realistic description should take into account dynamic charge regulation [Gisler *et al.* (1994); Pujar and Zydney (1997); El Masri *et al.* (2011)] that results in electrostatic potentials in-between those obtained by the fixed charge density and fixed surface potential assumptions. Often, however, the surface charge groups are strongly dissociated and immobile and the constant charge density boundary condition is sufficient. The PB theory predicts repulsive interactions between like-charged colloids. On the pair level, the interactions have a Yukawa-like functional form $V(r) \propto e^{-\kappa r}/r$ as predicted by the DLVO theory; however, all many-body interaction terms are taken into account in systems with $N > 2$. The PB description is a valid approach for systems with monovalent microions, where microion–microion interactions are not strong enough to induce significant correlations among them. The relative significance of the microion correlations can be assessed by the coupling constant $\Xi = q^2\lambda_B/\mu \propto q^3$, where $\lambda_B \equiv e_0^2/4\pi\epsilon\epsilon_0 k_B T$ is the Bjerrum length, $\mu \equiv (2\pi q\lambda_B\sigma)^{-1}$ is the Gouy–Chapman length (σ is the surface charge density of a planar colloid), and q is the valency of the microions. For monovalent ions ($q = 1$), the value of Ξ is always much less than 1: no known material would have $\Xi \approx 1$. Raising the microions valency quickly diminishes the validity of the PB theory: divalent and trivalent microions mediate effective attractions between like-charged objets, which leads to aggregation of colloidal clusters. Such microion correlation driven

phenomena cannot be correctly captured by the PB theory. Some attempts have been made to modify the PB equation (16.1) in order to introduce the correlations a posteriori [Borukhov *et al.* (1997)]. In the limit of high $\Xi \gg 1$, the correlations completely govern the behavior and the microion distribution can be evaluated by the strong coupling theory [Moreira and Netz (2000); Grosberg *et al.* (2002); Naji *et al.* (2005); Messina *et al.* (2001); Šamaj and Trizac (2011)] (for a recent discussion regarding the strong coupling electrostatic theory, see also the chapter by Samai and Trizac in this book).

16.3 Effective Interactions

A precise knowledge of the interactions among the constituent particles is the basis for understanding the structural, thermodynamic, and dynamic properties of matter. In complex systems such as soft matter, the interactions among the colloids mediated by the smaller components (microions) are inherently many-body interactions: a change in the arrangement of the colloids nonlinearly affects the distribution of the microions. Strictly speaking, a correct description of any liquid or solid must explicitly take into account many-body interactions.

It is common practice in theoretical physics to resort to a coarse-grained description by integrating out of the partition function all degrees of freedom that do not belong to the larger (i.e., in our case colloidal) constituents. This leads to a state-dependent effective Hamiltonian for the colloids, thereby allowing a one-component model (OCM) description. The motivation for such a procedure is not only to facilitate contact with experiments, wherein most of the time the small constituents cannot be probed directly (most experimental techniques such as small angle X-ray or neutron scattering, or video-microscopy, probe the colloidal degrees of freedom only), but also to simplify the theoretical treatment: in frame of the OCM, one can use the well developed statistical mechanics tools from the theory of simple liquids. In the case of electrostatic interactions in colloidal suspensions, such a reduction results in the classic Derjaguin–Landau–Verwey–Overbeek (DLVO) theory [Verwey and Overbeek

(1948)] of colloidal interactions: an isolated pair of charged colloidal spheres in an aqueous salt solution interacts via a repulsive Yukawa potential at large separations. The DLVO theory correctly describes the pair interactions, as has been confirmed by direct experimental measurements [Crocker and Grier (1994)].

Not surprisingly, the theory is commonly extended in order to design effective descriptions of dense colloidal suspensions. As the physical equations governing the systems' behavior are typically nonlinear, the colloidal interactions in dense suspensions are inherent *many-body* in nature. The interaction between two particles is modified by other colloids in their surrounding and the total interaction energy is not given by the sum of the pair potentials corresponding to the isolated pairs

$$U_{\text{int}}(\boldsymbol{r}_1, \ldots, \boldsymbol{r}_N) = \sum_{\text{pairs}} u_{ij}^{(2)}(\boldsymbol{r}_i, \boldsymbol{r}_j) + \sum_{\text{triplets}} u_{ijk}^{(3)}(\boldsymbol{r}_i, \boldsymbol{r}_j, \boldsymbol{r}_k) + \ldots . \quad (16.2)$$

The way around the problem is to construct an *effective pair potential* [Belloni (2000)] that correctly predicts the total interaction energy:

$$U_{\text{int}}(\boldsymbol{r}_1, \ldots, \boldsymbol{r}_N) \equiv \sum_{\text{pairs}} V_{ij}^{\text{eff}}(\boldsymbol{r}_i, \boldsymbol{r}_j) . \quad (16.3)$$

Clearly, construction of such effective potentials V^{eff} is state-dependent, but hopefully in a broad enough range of parameters, the dependence is not too severe and a single set of effective parameters can be used to design the pairwise additive model of the system [Belloni (2000); Levin (2002); Trizac (2000)]. Instead of the total interaction energy, it is practical to construct effective pair potentials so as to reproduce the structural properties determined in the experiments, that is, the radial distribution function $g(r)$ or the structure factor $s(q)$ (both based on the pair correlations). In principle, the Henderson theorem [Henderson (1974)] guarantees that every (perfect) pair correlation function $g(r)$) can be uniquely associated with an effective pair potential. Given the structural information, the effective pair potential can therefore be constructed by inverted Monte Carlo simulations [M. Brunner *et al.* (2002)]. This procedure, however, is computationally demanding and it is not free of technical difficulties (defining the appropriate cut-off value for the potentials), which introduce a degree of arbitrariness. Alternative

approach to reverse-engineering the interactions are the integral equation theories [Hansen and McDonald (1986)]. Combined with a proper closure relation, they provide an analytical expression (in an integral form) relating the interactions and the structure. Integral equations can provide a useful framework to study the thermodynamical properties of colloidal suspensions, providing that one can justify the specific choice of the closure relation.

Despite the fact that it is being frequently attempted, the transposition from complex to simple fluids is therefore not straightforward and is often paved with fundamental difficulties, see, for example, [Louis (2002)]. It is important to realize that effective potentials—in contrast to the true pair potentials—cannot be regarded as fundamental quantities because their parameters depend on the state of the system. An an effective potential that reproduces the structure of the system at a given density will not correctly reproduce it at another value of it [M. Brunner *et al.* (2002)]). But even at a fixed density, the effective potentials still depend on the exact colloidal positions [Dobnikar *et al.* (2003); Dahirel and Hansen (2009)]: the effective pair interactions derived from the full PB solutions are different in FCC and BCC crystals of equal densities [Dobnikar *et al.* (2003)]. In addition to being state-dependent, no unique way to derive the effective potentials exists: even if we were able to construct the effective potentials to correctly reproduce the structural properties of the many-body system at all parameters, they will in principle not do well in describing the thermodynamics [Colla *et al.* (2012)] or dynamic properties of the same system.

The relevance of the effective pair interactions has been further explored in [Dobnikar *et al.* (2006)] where PB cell and Jellium [Colla *et al.* (2009); Pianegonda *et al.* (2007); Trizac and Levin (2004)] models have been used to derive the effective potentials, which were later used in a one-component simulation to extract the compressibility of the system as a function of the density. Using the Kirkwood–Buff relation [Kirkwood and Buff (1951)], such thermodynamic behavior is related to the structural information and this provided a means to test the consistency of the applied approximations. Roughly speaking, the conclusions are that at large salt concentration, when the charges on colloids are heavily

screened, the pairwise additive effective picture works well for both the structural and thermodynamic properties. At very low salinity, the double layers overlap and the pair picture completely fails. Here, however, the microion-dominated descriptions such as cell or Jellium model work well for thermodynamics. In the overlapping region, none of the approaches is perfect.

16.4 Three-Body Interactions

Already in 1943, it has been supposed by Axilrod and Teller [Axilrod and Teller (1943)] and later also by Barker and Henderson [Barker and Henderson (1976, 1972)] that three-body interactions may significantly contribute to the total interaction energy in noble gas systems. This seems to be surprising because noble gas atoms possess a closed-shell electronic structure and are therefore often (and erroneously) regarded as examples of a simple liquid. The conjecture of Axilrod and Teller, however, was confirmed only very recently, when large-scale molecular dynamics simulations for liquid xenon and krypton were compared with the structure factor measurements at small q-vectors performed with small-angle neutron scattering. In these studies, it has clearly been demonstrated that only a combination of pair-potentials and three-body interactions, the latter in the form of the AT triple-dipole term, leads to a satisfactory agreement with the experimental data [Barker *et al.* (1969)]. In the meantime, it was realized that many-body interactions also have to be considered for nuclear interactions, interatomic potentials, electron screening in metals, photoionization, molecular island distribution on surfaces [Österlund *et al.* (1999)], and even for the simplest chemical processes in solids [Ovchinnikov and Apkarian (1999)] such as the making and breaking of a bond. In view of the general importance of many-body effects, it seems surprising that until recently, no direct measurements of these interactions had been performed.

This is largely due to the fact that in atomic or molecular systems, positional information is typically provided by structure factors or pair-correlation functions, that is, in an integrated form. Direct measurements of many-body interactions, however, require direct

positional information beyond the level of pair-correlations, which is not accessible at molecular length scales. In contrast, owing to the more convenient time and length scales, direct microscopic information is accessible in colloidal suspensions. In addition, the interactions in colloidal suspensions can be varied over large ranges, for example, from short-ranged steric to long-ranged electrostatic or dipolar interactions. The colloidal electrostatic interactions can be tuned by simply changing the salt concentration (in contrast to atoms in which interactions are unchangeably dictated by their electronic structure). At sufficiently small salt concentrations, the screening of the colloidal charges provided by the microions is weak; the range of the interactions amounts to several colloidal diameters. If more than two colloids are within their interaction range, the pairwise description naturally breaks down and many-body interactions become substantial. Triplet interactions in colloidal suspensions have been numerically studied in [Löwen and Allahyarov (1998)]. Recently, the three-body [Brunner *et al.* (2004)] and four-body [Dobnikar *et al.* (2004a)] electrostatic interactions have been directly measured in an experiment in which three colloidal particles were trapped by laser tweezers [Brunner *et al.* (2004); Dobnikar *et al.* (2004b)], providing the first direct observation of many-body interaction terms in a microscopic system. Surprisingly, the three-body interaction terms prove to be comparable both in the magnitude and in the range to the pair interactions, therefore not at all a small perturbation to the later. A similar conclusion was drawn in [Frischknecht and Yethiraj (2011)] wherein three-body interactions among nanoparticles in polymer melts have been investigated. An interesting collapse of data has been observed in numerical work [Russ *et al.* (2002)]: for a range of parameters studied, the three-body electrostatic interaction term seems to depend on a single positional degree of freedom (rather than on six), which is the perimeter of the triangle formed by the three particles. The generality of the conclusions in [Russ *et al.* (2002)] has yet to be investigated; however, the reported results suggest a promising route towards a coarse-grained description of the three-body interactions.

A recent study [Sinkovits *et al.* (2013)] has focused on the three-body interactions in a system of charged cylinders with the coupling constant $\Xi \gtrsim 1$, in the intermediate regime between the weak

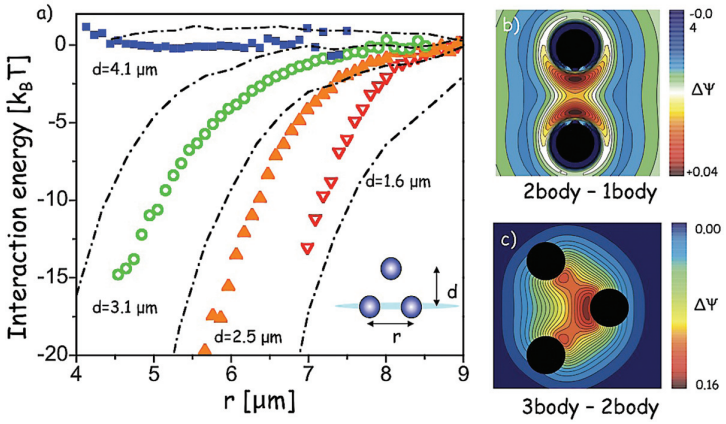

Figure 16.1 The three-body interaction term measured in the experiment and calculated by solving the PB equation [Brunner *et al.* (2004)]. (a) The three-body term $u^{(3)}$ as a function of distance r between two colloids in the line trap with a fixed position of the third colloid along the symmetry line d (see schematic inset). Experimental measurements (symbols) are compared with the PB calculations (lines). (b) The difference between the two-body solution and the superposition of two one-body solutions of the PB equation (16.1). (c) The difference between the three-body solution and the superposition of three three-body solutions. Reproduced with permission from [Brunner *et al.* (2004)].

coupling (PB) and strong coupling electrostatics. Such a regime is relevant for many biological systems with multivalent counterions, such as DNA bundle formation. The observation there was that the three-body term seems to oppose the two-body one. In the PB case, the two-body interactions are repulsive and the three-body term is attractive, reducing the repulsion between pairs (also true for helically charged cylinders [Kanduc *et al.* (2009)]). In the transition regime with $\Xi \gtrsim 1$, the pair forces are attractive, whereas the three-body term is repulsive, again effectively reducing the strength of the pair interactions.

16.5 Many-Body Interactions in Dense Suspensions

Experiments with four colloidal particles reported in [Dobnikar *et al.* (2004a)] demonstrate that the four-body terms are again

comparable with the three-body terms suggesting that the many-body series (16.2) is poorly converging. In dense suspensions, therefore, it is insufficient to take into account two-body and three-body terms. Instead, all many-body terms need to be considered. However, as the series is alternating [the consecutive N–body terms are repulsive ($N = 2$), attractive ($N = 3$), repulsive ($N = 4$), ...], the question arises whether the net effect on macroscopic behavior is significant at all. In [Dobnikar *et al.* (2003)], the melting of charge-stabilized colloidal crystals has been studied with Brownian dynamics simulations coupled to solving the full nonlinear PB equation (thus taking into account all many-body terms). The many-body interactions result in a macroscopic phase behavior (shift of the melting line), not reproducible by pairwise-additive effective interactions: the region of stability of the fluid phase is expanded in comparison to the pairwise-additive system. In [Baumgartl *et al.* (2008)], many-body interactions had to be invoked in order to explain the phonon dispersion in 2D colloidal crystals. In [Reinke *et al.* (2007)], elastic constants in 3D (FCC) crystals of charged colloids have been determined. In crystals with cubic symmetry, there are in principle three independent elastic constants. The Cauchy theorem states that—if the forces between constituents are pairwise additive and central—two of them must be the same. Any deviation from the Cauchy relation signals the presence of many-body interaction terms. As the values of the elastic constants, as well as the phonon band gap structure in [Reinke *et al.* (2007)] could not be described in terms of pairwise additive interactions, we can conclude that the many-body interactions affect the elastic response of colloidal crystals. Similar behavior was later confirmed by numerical calculations in 2D [Dyshlovenko (2005)] and in 3D [Dyshlovenko and Dobnikar (2013)].

Even more pronounced macroscopic effects of many-body colloidal interactions can be found in other colloidal systems. In [Osterman *et al.* (2009)], a system of superparamagnetic colloids in precessing external magnetic field has been studied experimentally and theoretically. In magnetic colloidal systems in aqueous solutions, the medium is not magnetized; therefore, the interactions are inherently less complex than in the electrostatic case. However, the induced dipoles on the colloids mutually depolarize, which still

leads to state-dependent many-body interactions. When the external driving field precesses at the so-called magic angle, the induced magnetic interactions are—on the pair level—formally equivalent to molecular van der Waals interactions. However, the strong many-body effects (the three-body compared with the two-body term is much larger than the corresponding AT three-body term in the van der Waals systems [Axilrod and Teller (1943)]) govern a surprising aggregation scenario leading to the formation of thin colloidal membranes in the bulk. Another example of inherently many-body colloidal systems is a mixture of polymers and colloidal particles. Here, colloidal interactions are of entropic origin, mediated by the polymers. In numerical simulations of crystallization of DNA functionalized colloids [Mladek *et al.* (2012)], the assumption of pairwise additivity leads to substantial errors in the estimate of the free energy of the crystal phase. Ordering of polymer-grafted nanoparticles in homopolymer matrix [Akcora *et al.* (2009)] and hard sphere nanoparticles in grafted polymer layers [Curk *et al.* (2013)] is also governed by strong many-body effects.

16.6 Conclusion

The present review discusses the importance of many-body effects in charged colloidal suspensions, as well as limitations of the effective pairwise additive pictures commonly applied to study such systems. Numerous studies have demonstrated that many-body interactions are often crucial in order to correctly describe structural and thermodynamic properties. The observability and tunability of colloidal suspensions make them an ideal model system for systematic investigations of many-body interactions, which is one of the pertinent problems in statistical physics.

One of the exciting questions that needs to be further explored in the future concerns downscaling to the nanoscale [Walker *et al.* (2011)], where the physics is governed by the predominance of the surfaces and the granularity of the solvent becomes important. Fluid water is a highly complex medium due to the presence of the hydrogen bonds between the water molecules. Close to the surfaces or interfaces, and in nano-confinement, the classical

description of the fluid therefore breaks down. Ion-specific effects at interfaces [dos Santos and Levin (2011)], the interfacial viscosity and dielectric profile of water [Sendner *et al.* (2009)], as well as its flow through nanochannels [Falk *et al.* (2010)] have recently been addressed.

Acknowledgments

I would like to acknowledge my long-term collaborations with H. H. von Grünberg, C. Bechinger, and E. Trizac on many-body interactions in charged colloidal suspensions. I acknowledge the financial support of the 7th Framework Program of European Union through grants ARG-ERC-COLSTRUCTION 227758 and ITN-COMPLOIDS 234810, and by the Slovenian research agency through Grant P1-0055.

References

Akcora, P., Liu, H., Kumar, S. K., Moll, J., Li, Y., Benicewicz, B. C., Schadler, L. S., Acehan, D., Panagiotopoulos, A. Z., Pryamitsyn, V., Ganesan, V., Ilavsky, J., Thiyagarajan, P., Colby, R. H. and Douglas, J. F. (2009). Anisotropic self-assembly of spherical polymer-grafted nanoparticles, *Nature Materials* **8**, 4, pp. 354–U121, doi:{10.1038/NMAT2404}.

Axilrod, B. M. and Teller, E. (1943). Interaction of the van der waals type between three atoms, *The Journal of Chemical Physics* **11**, 6, pp. 299–300, doi:10.1063/1.1723844, http://link.aip.org/link/?JCP/11/299/1.

Barker, J. and Henderson, D. (1972). Theories of liquids, *Annual Review of Physical Chemistry* **23**, pp. 439–&, doi:{10.1146/annurev.pc.23.100172.002255}.

Barker, J. and Henderson, D. (1976). What is liquid—understanding states of matter, *Reviews of Modern Physics* **48**, 4, pp. 587–671, doi:{10.1103/RevModPhys.48.587}.

Barker, J., Henderson, D. and Smith, W. (1969). Pair and triplet interactions in argon, *Molecular Physics* **17**, 6, pp. 579–&, doi:{10.1080/00268976900101451}.

Baumgartl, J., Dietrich, J., Dobnikar, J., Bechinger, C. and von Grunberg, H. H. (2008). Phonon dispersion curves of two-dimensional colloidal crystals: the wavelength-dependence of friction, *Soft Matter* **4**,

pp. 2199–2206, doi:10.1039/B807881E, http://dx.doi.org/10.1039/B807881E.

Belloni, L. (2000). Colloidal interactions, *Journal of Physics: Condensed Matter* **12**, 46, p. R549, http://stacks.iop.org/0953-8984/12/i=46/a=201.

Bocquet, L. and Charlaix, E. (2010). Nanofluidics, from bulk to interfaces, *Chem. Soc. Rev.* **39**, pp. 1073–1095, doi:10.1039/B909366B, http://dx.doi.org/10.1039/B909366B.

Borukhov, I., Andelman, D. and Orland, H. (1997). Steric effects in electrolytes: A modified Poisson-Boltzmann equation, *Phys. Rev. Lett.* **79**, pp. 435–438, doi:10.1103/PhysRevLett.79.435, http://link.aps.org/doi/10.1103/PhysRevLett.79.435.

Brunner, M., Dobnikar, J., von Grünberg, H.-H. and Bechinger, C. (2004). Direct measurement of three-body interactions amongst charged colloids, *Phys. Rev. Lett.* **92**, p. 078301, doi:10.1103/PhysRevLett.92.078301, http://link.aps.org/doi/10.1103/PhysRevLett.92.078301.

Colla, T. E., dos Santos, A. P. and Levin, Y. (2012). Equation of state of charged colloidal suspensions and its dependence on the thermodynamic route, *The Journal of Chemical Physics* **136**, 19, 194103, doi:10.1063/1.4718367, http://link.aip.org/link/?JCP/136/194103/1.

Colla, T. E., Levin, Y. and Trizac, E. (2009). A self-consistent renormalized jellium approach for calculating structural and thermodynamic properties of charge stabilized colloidal suspensions, *The Journal of Chemical Physics* **131**, 7, 074115, doi:10.1063/1.3211305, http://link.aip.org/link/?JCP/131/074115/1.

Crocker, J. C. and Grier, D. G. (1994). Microscopic measurement of the pair interaction potential of charge-stabilized colloid, *Phys. Rev. Lett.* **73**, pp. 352–355, doi:10.1103/PhysRevLett.73.352, http://link.aps.org/doi/10.1103/PhysRevLett.73.352.

Curk, T., Martinez-Veracoechea, F. J., Frenkel, D. and Dobnikar, J. (2013). Collective ordering of colloids in grafted polymer layers, *Soft Matter* **9**(23), pp. 5565–5571, DOI: 10.1039/C3SM50486G.

Dahirel, V. and Hansen, J. P. (2009). Ion-mediated interactions in suspensions of oppositely charged nanoparticles, *The Journal of Chemical Physics* **131**, 8, 084902, doi:10.1063/1.3193556, http://link.aip.org/link/?JCP/131/084902/1.

Dobnikar, J., Brunner, M., Baumgartl, J., Bechinger, C. and von Grünberg, H.-H. (2004a). Three- and four-body interactions in colloidal systems, *Proc. SPIE 5514, Optical Trapping and Optical Microma-*

nipulation **5514**, pp. 340–351, doi:10.1117/12.554610, http://dx.doi.org/10.1117/12.554610.

Dobnikar, J., Brunner, M., von Grünberg, H.-H. and Bechinger, C. (2004b). Three-body interactions in colloidal systems, *Phys. Rev. E* **69**, p. 031402, doi:10.1103/PhysRevE.69.031402, http://link.aps.org/doi/10.1103/PhysRevE.69.031402.

Dobnikar, J., Castaneda-Priego, R., von Grünberg, H. H. and Trizac, E. (2006). Testing the relevance of effective interaction potentials between highly-charged colloids in suspension, *New Journal of Physics* **8**, 11, p. 277, http://stacks.iop.org/1367-2630/8/i=11/a=277.

Dobnikar, J., Chen, Y., Rzehak, R. and von Grünberg, H. H. (2003). Many-body interactions and the melting of colloidal crystals, *The Journal of Chemical Physics* **119**, 9, pp. 4971–4985, doi:10.1063/1.1595642, http://link.aip.org/link/?JCP/119/4971/1.

dos Santos, A. P. and Levin, Y. (2011). Ion specificity and the theory of stability of colloidal suspensions, *Phys. Rev. Lett.* **106**, p. 167801, doi:10.1103/PhysRevLett.106.167801, http://link.aps.org/doi/10.1103/PhysRevLett.106.167801.

Dyshlovenko, P. (2005). Evidence of many-particle interactions in two-dimensional charge-stabilized colloidal crystals, *Physical Review Letters* **95**, 3, doi:{10.1103/PhysRevLett.95.038302}.

Dyshlovenko, P. and Dobnikar, J. (2013). Many–body effects on elastic constants of colloidal crystals, *preprint*.

El Masri, D., van Oostrum, P., Smallenburg, F., Vissers, T., Imhof, A., Dijkstra, M. and van Blaaderen, A. (2011). Measuring colloidal forces from particle position deviations inside an optical trap, *Soft Matter* **7**, 7, pp. 3462–3466, doi:{10.1039/c0sm01295e}.

Falk, K., Sedlmeier, F., Joly, L., Netz, R. R. and Bocquet, L. (2010). Molecular origin of fast water transport in carbon nanotube membranes: Superlubricity versus curvature dependent friction, *Nano Letters* **10**, 10, pp. 4067–4073, doi:10.1021/nl1021046, http://pubs.acs.org/doi/abs/10.1021/nl1021046.

Frischknecht, A. L. and Yethiraj, A. (2011). Two- and three-body interactions among nanoparticles in a polymer melt, *The Journal of Chemical Physics* **134**, 17, 174901, doi:10.1063/1.3585979, http://link.aip.org/link/?JCP/134/174901/1.

Gisler, T., Schulz, S. F., Borkovec, M., Sticher, H., Schurtenberger, P., D'Aguanno, B. and Klein, R. (1994). Understanding colloidal charge renormalization

from surface chemistry: Experiment and theory, *The Journal of Chemical Physics* **101**, 11, pp. 9924–9936, doi:10.1063/1.467894.

Grosberg, A. Y., Nguyen, T. T. and Shklovskii, B. I. (2002). *Colloquium*: The physics of charge inversion in chemical and biological systems, *Rev. Mod. Phys.* **74**, pp. 329–345, doi:10.1103/RevModPhys.74.329, http://link.aps.org/doi/10.1103/RevModPhys.74.329.

Hansen, J. and McDonald, I. (1986). *Theory of simple liquids*, 2nd ed. (Academic Press, London, UK), ISBN 0 12 323851 X.

Henderson, R. (1974). A uniqueness theorem for fluid pair correlation functions, *Physics Letters A* **49**, 3, pp. 197–198, doi:10.1016/0375-9601(74)90847-0, http://www.sciencedirect.com/science/article/pii/0375960174908470.

Šamaj, L. and Trizac, E. (2011). Wigner-crystal formulation of strong-coupling theory for counterions near planar charged interfaces, *Phys. Rev. E* **84**, p. 041401, doi:10.1103/PhysRevE.84.041401, http://link.aps.org/doi/10.1103/PhysRevE.84.041401.

Kanduc, M., Dobnikar, J. and Podgornik, R. (2009). Counterion-mediated electrostatic interactions between helical molecules, *Soft Matter* **5**, pp. 868–877, doi:10.1039/B811795K, http://dx.doi.org/10.1039/B811795K.

Kirkwood, J. G. and Buff, F. P. (1951). The statistical mechanical theory of solutions. *The Journal of Chemical Physics* **19**, 6, pp. 774–777, doi:10.1063/1.1748352, http://link.aip.org/link/?JCP/19/774/1.

Levin, Y. (2002). Electrostatic correlations: From plasma to biology, *Reports on Progress in Physics* **65**, 11, p. 1577, http://stacks.iop.org/0034-4885/65/i=11/a=201.

Linse, P. (1991). Highly asymmetric electrolyte: Triplet correlation functions from simulation in one- and two-component model systems, *The Journal of Chemical Physics* **94**, 12, pp. 8227–8233, doi:10.1063/1.460720, http://link.aip.org/link/?JCP/94/8227/1.

Louis, A. A. (2002). Beware of density dependent pair potentials, *Journal of Physics: Condensed Matter* **14**, 40, p. 9187, http://stacks.iop.org/0953-8984/14/i=40/a=311.

Löwen, H. and Allahyarov, E. (1998). The role of effective triplet interactions in charged colloidal suspensions, *Journal of Physics: Condensed Matter* **10**, 19, p. 4147, http://stacks.iop.org/0953-8984/10/i=19/a=003.

Lowen, H., Hansen, J.-P. and Madden, P. A. (1993). Nonlinear counterion screening in colloidal suspensions, *The Journal of Chemical Physics*

98, 4, pp. 3275–3289, doi:10.1063/1.464099, http://link.aip.org/link/?JCP/98/3275/1.

M. Brunner, C. Bechinger, W. Strepp, V. Lobaskin and H. H. von Grünberg (2002). Density-dependent pair interactions in 2d, *Europhys. Lett.* **58**, 6, pp. 926–965, doi:10.1209/epl/i2002-00105-4, http://dx.doi.org/10.1209/epl/i2002-00105-4.

Messina, R., Holm, C. and Kremer, K. (2001). Strong electrostatic interactions in spherical colloidal systems, *Phys. Rev. E* **64**, p. 021405, doi:10.1103/PhysRevE.64.021405, http://link.aps.org/doi/10.1103/PhysRevE.64.021405.

Mladek, B. M., Fornleitner, J., Martinez-Veracoechea, F. J., Dawid, A. and Frenkel, D. (2012). Quantitative prediction of the phase diagram of DNA-functionalized nanosized colloids, *Physical Review Letters* **108**, 26, doi:{10.1103/PhysRevLett.108.268301}.

Moreira, A. G. and Netz, R. R. (2000). Strong-coupling theory for counter-ion distributions, *EPL (Europhysics Letters)* **52**, 6, p. 705, http://stacks.iop.org/0295-5075/52/i=6/a=705.

Naji, A., Jungblut, S., Moreira, A. G. and Netz, R. R. (2005). Electrostatic interactions in strongly coupled soft matter, *Physica A: Statistical Mechanics and its Applications* **352**, 1, pp. 131–170, doi:10.1016/j.physa.2004.12.029, http://www.sciencedirect.com/science/article/pii/S037843710401619X.

Österlund, L., Pedersen, M. O., Stensgaard, I., Lægsgaard, E. and Besenbacher, F. (1999). Quantitative determination of adsorbate-adsorbate interactions, *Phys. Rev. Lett.* **83**, pp. 4812–4815, doi:10.1103/PhysRevLett.83.4812, http://link.aps.org/doi/10.1103/PhysRevLett.83.4812.

Osterman, N., Poberaj, I., Dobnikar, J., Frenkel, D., Ziherl, P. and Babić, D. (2009). Field-induced self-assembly of suspended colloidal membranes, *Phys. Rev. Lett.* **103**, p. 228301, doi:10.1103/PhysRevLett.103.228301, http://link.aps.org/doi/10.1103/PhysRevLett.103.228301.

Ovchinnikov, M. and Apkarian, V. A. (1999). Practical formulation of accurate many-body potentials through the perturbative extension of diatomics-in-ionic-systems: Applied to hf clusters, *The Journal of Chemical Physics* **110**, 20, pp. 9842–9852, doi:10.1063/1.478038, http://link.aip.org/link/?JCP/110/9842/1.

Pianegonda, S., Trizac, E. and Levin, Y. (2007). The renormalized jellium model for spherical and cylindrical colloids, *The Journal of Chemical Physics* **126**, 1, 014702, doi:10.1063/1.2387168, http://link.aip.org/link/?JCP/126/014702/1.

Pujar, N. S. and Zydney, A. L. (1997). Charge regulation and electrostatic interactions for a spherical particle in a cylindrical pore, *Journal of Colloid and Interface Science* **192**, 2, pp. 338–349, doi:10.1006/jcis.1997.5017, http://www.sciencedirect.com/science/article/pii/S0021979797950177.

Reinke, D., Stark, H., von Grünberg, H.-H., Schofield, A. B., Maret, G. and Gasser, U. (2007). Noncentral forces in crystals of charged colloids, *Phys. Rev. Lett.* **98**, p. 038301, doi:10.1103/PhysRevLett.98.038301, http://link.aps.org/doi/10.1103/PhysRevLett.98.038301.

Russ, C., von Grünberg, H. H., Dijkstra, M. and van Roij, R. (2002). Three-body forces between charged colloidal particles, *Phys. Rev. E* **66**, p. 011402, doi:10.1103/PhysRevE.66.011402, http://link.aps.org/doi/10.1103/PhysRevE.66.011402.

Sendner, C., Horinek, D., Bocquet, L. and Netz, R. R. (2009). Interfacial water at hydrophobic and hydrophilic surfaces: Slip, viscosity, and diffusion, *Langmuir* **25**, 18, pp. 10768–10781, doi:10.1021/la901314b, http://pubs.acs.org/doi/abs/10.1021/la901314b, pMID: 19591481.

Sinkovits, D. W., Barros, K., Kanduč, M., A., N., Podgornik, R., Dobnikar, J. and Luijten, E. (2013). Many-body electrostatic interactions between charged polarizable rods, *preprint*.

Strubbe, F., Beunis, F., Marescaux, M. and Neyts, K. (2007). Charging mechanism in colloidal particles leading to a linear relation between charge and size, *Phys. Rev. E* **75**, p. 031405, doi:10.1103/PhysRevE.75.031405, http://link.aps.org/doi/10.1103/PhysRevE.75.031405.

Trizac, E. (2000). Effective interactions between like-charged macromolecules, *Phys. Rev. E* **62**, pp. R1465–R1468, doi:10.1103/PhysRevE.62.R1465, http://link.aps.org/doi/10.1103/PhysRevE.62.R1465.

Trizac, E. and Levin, Y. (2004). Renormalized jellium model for charge-stabilized colloidal suspensions, *Phys. Rev. E* **69**, p. 031403, doi:10.1103/PhysRevE.69.031403, http://link.aps.org/doi/10.1103/PhysRevE.69.031403.

Verwey, E. J. W. and Overbeek, J. T. G. (1948). *Theory of Stability of Lyophobic Colloids* (Elsevier, Amsterdam, NL).

Walker, D. A., Kowalczyk, B., de la Cruz, M. O. and Grzybowski, B. A. (2011). Electrostatics at the nanoscale, *Nanoscale* **3**, pp. 1316–1344, doi:10.1039/C0NR00698J, http://dx.doi.org/10.1039/C0NR00698J.

Chapter 17

Controlling the Fluid–Fluid Mixing–Demixing Phase Transition with Electric Fields

Jennifer Galanis, Sela Samin, and Yoav Tsori
Department of Chemical Engineering, Ben Gurion University of the Negev, Beer-Sheva 84105, Israel
tsori@bgu.ac.il

Various properties of a material (viscosity, refractive index, and so on) can dramatically change after a phase transition. Investigating exactly when and how this change occurs potentially elucidates the dominant molecular forces working within the material, thus fueling significant scientific interest. Similarly, the analysis of idealized molecular models provides a framework for predicting the behavior of real, and often more complicated, materials. Understanding phase behavior is not just limited to fundamental research, as the ability to switch on or off various desirable properties with a simple "turn of the knob" can lead to interesting technological applications.

Traditionally, intrinsic thermodynamic variables, such as temperature or pressure, act as the "knobs" that control phases. However, the application of *external* fields, such as gravitational, magnetic, and electric fields, can play an equally vital role, as they often offer a reversible, easily tunable, and localized method of

Electrostatics of Soft and Disordered Matter
Edited by David Dean, Jure Dobnikar, Ali Naji, and Rudolf Podgornik

ISBN 978-981-4411-85-1 (Hardcover), 978-981-4411-86-8 (eBook)
www.panstanford.com

control. The necessary key for practical use resides in a strong coupling between the field and a material property, for example, the applied electric field with the material's dielectric response function. If such a strong coupling can be obtained, large changes to the phase diagram can occur even with a weak field.

In this chapter, we will specifically focus on theoretical advancements for how electric fields induce a mixing–demixing phase transition between two dielectric fluids (oils), presenting results from both equilibrium and dynamics. Moreover, we will highlight how strong coupling between the field and dielectric function naturally occurs with *nonuniform* electric fields originating from small curved charged objects.

17.1 Equilibrium Phase Behavior

Using a mean-field approach, we consider a binary mixture of two fluids, A and B, in an electric field $\mathbf{E}$, and write the total free energy $\mathcal{F}$ for a volume V as

$$\mathcal{F} = \int_V (f_{\mathrm{m}} + f_{\mathrm{e}} + f_{\mathrm{i}})\,\mathrm{d}V \tag{17.1}$$

where f_{m}, f_{e}, and f_{i} are the free energy densities for mixing, electrostatics, and fluid–fluid interfaces, respectively.

The fluids, in the absence of an electric field, can mix or demix due to a competition between entropy and enthalpy, where temperature T adjusts the relative balance. For concreteness, we consider the Bragg–Williams form

$$f_{\mathrm{m}} = \frac{kT}{v_0}\Big[\phi\ln\phi + (1-\phi)\ln(1-\phi) + \chi\phi(1-\phi)\Big] \tag{17.2}$$

where k is Boltzmann's constant, v_0 is the molecular volume of both components, ϕ such that $0 < \phi < 1$ is the volume fraction of component A, and $\chi \sim 1/T$ is the Flory interaction parameter [Safran (1994)]. The first two terms account for entropy, while the third term accounts for the energy of mixing.

Equation 17.2 gives rise to an upper critical solution temperature-type phase diagram. The shape of $f_{\mathrm{m}}(\phi)$ transitions from a single minimum at $\phi = 1/2$ to a double minimum curve as T

shifts from above to below the critical temperature T_c. By using the well-known double tangent construction, we obtain the two binodal compositions ϕ_b for each temperature $T < T_c$. These compositions mark the mixing–demixing boundary in the $\phi - T$ plane. Specifically, fluids demix when ϕ is located between the two values of ϕ_b, or more simply stated "under the binodal curve." Finally, the phase diagram terminates at the mixture's critical point $(\phi_c, \chi_c) = (1/2, 2)$.

In the following, we will employ a simplified form of Eq. 17.2, namely the Landau expansion of the mixing energy around $\phi = \phi_c$:

$$f_m \approx \frac{kT}{v_0}\left[(2-\chi)\left(\phi - \frac{1}{2}\right)^2 + \frac{4}{3}\left(\phi - \frac{1}{2}\right)^4 + \text{const.}\right] \quad (17.3)$$

Note that the quadratic term in the expansion changes sign at the critical value $\chi_c = 2$.

For electrostatics, the free energy density f_e is given by

$$f_e = \pm\frac{1}{2}\varepsilon_0\varepsilon(\phi)|\nabla\psi|^2 \quad (17.4)$$

where ε_0 is the vacuum permittivity, $\varepsilon(\phi)$ is the relative dielectric constant of the mixture, and ψ is the electrostatic potential ($\mathbf{E} = -\nabla\psi$). The positive (negative) sign corresponds to constant charge (potential) boundary conditions. The relation $\varepsilon(\phi)$ can, in fact, be a complicated function. Using the simplest approximation, we assume a linear relation, $\varepsilon(\phi) = (\varepsilon_A - \varepsilon_B)\phi + \varepsilon_B$, where ε_A and ε_B are the dielectric constants for pure fluids A and B, respectively.

When considering the structure of the interface between phases, f_i is required. This term accounts for the energetic cost of composition gradients and is given by [Safran (1994)]:

$$f_i = \frac{kT}{2v_0}\chi\lambda^2|\nabla\phi|^2 \quad (17.5)$$

where λ is a constant characterizing the interface width. Notice that f_i vanishes when the composition is uniform.

To determine the equilibrium state in the presence of a field, we minimize $\mathcal{F}$ with respect to ϕ and ψ using calculus of variations and

obtain the following Euler–Lagrange equations

$$\frac{\delta \mathcal{F}}{\delta \psi} = \nabla \cdot [\varepsilon_0 \varepsilon(\phi) \nabla \psi] = 0 \tag{17.6}$$

$$\frac{\delta \mathcal{F}}{\delta \phi} = \frac{kT}{v_0}\left[(4-2\chi)\left(\phi - \frac{1}{2}\right) + \frac{16}{3}\left(\phi - \frac{1}{2}\right)^3 - \chi \lambda^2 \nabla^2 \phi\right] - \frac{\varepsilon_0}{2}\frac{\mathrm{d}\varepsilon(\phi)}{\mathrm{d}\phi}|\nabla \psi|^2 = \mu \tag{17.7}$$

The first equation is naturally Laplace's equation (Gauss's law) for the potential ψ, whereas the second equation gives the composition distribution ϕ. Finally, $\varepsilon(\phi)$ and □ couple these two equations, in our case, $\mathrm{d}\varepsilon(\phi)/\mathrm{d}\phi$ is constant.

The Lagrange multiplier μ in Eq. 17.7 differentiates between open and closed systems. For a closed system (canonical ensemble), μ is adjusted to satisfy the mass conservation constraint: $\langle \phi \rangle = \phi_0$, where ϕ_0 is the average composition. A closed system, whose volume increases to infinity, can be related to an open system in contact with a material reservoir (grand canonical ensemble). At this infinite size limit, the mass conservation constraint can be approximated as $\mu = \mu_0(\phi_0)$, basically the chemical potential that corresponds to the reservoir composition ϕ_0. The distinction between open and closed systems confers differences in phase behavior, as will be discussed below.

Before continuing to nonuniform fields, we will briefly review changes in the phase diagram with uniform fields. The effect of a uniform electric field, $\mathbf{E}_0$, on the mixture phase behavior was first studied by Landau and Lifshitz [Landau and Lifshitz (1957)] and later by Onuki [Onuki (1995)]. In the Landau theory, expansion of the electrostatic free energy leaves only a term proportional to $(\phi - \phi_c)^2$, which combines with the quadratic term in Eq. 17.3 to renormalize the critical temperature and the entire binodal curve. The theory predicts a critical temperature shift: $\Delta T_c = v_0 \varepsilon_0 \varepsilon'' \mathbf{E}_0^2/(4k)$ that is controlled by two free parameters $\mathbf{E}_0$ and $\varepsilon'' = \mathrm{d}^2\varepsilon(\phi)/\mathrm{d}\phi^2$. If ε'' is greater (less) than zero, T_c increases (decreases) and the electric field effect is that of demixing (mixing).

As v_0 is small in simple fluids, large electric fields are required to see an effect. For the typical maximal fields used in experiments ($\cong 10^7$ V/m), the predicted ΔT_c is extraordinarily small, on the

order of milliKelvins. Experiments in low molecular weight binary mixtures agree with the theory on the magnitude of ΔT_c, but yield conflicting results on the sign or direction of the shift [Debye and Kleboth (1965); Orzechowski (1999)]. A more rigorous discussion about the effects of uniform electric fields is given in Ref. [Tsori (2009)].

Nonuniform electric fields, however, generate different results and can alter the mixing–demixing phase diagram considerably, compared with uniform fields of the same magnitude [Tsori *et al.* (2004); Marcus *et al.* (2008); Samin and Tsori (2009)]. Large-field gradients occur naturally in systems such as microfluidic and nanoscale devices due to their small size and complex geometry. Detailed investigations of the phase transition have been conducted with three simple yet fundamental shapes: wedge, sphere, and cylinder. Analogous results occur between these shapes; therefore, due to space constraints, we focus on a closed system consisting of two concentric cylinders with radii R_1 and R_2, where $R_2 \to \infty$ produces an open system. We impose cylindrical symmetry such that $\phi = \phi(r)$ and $\psi = \psi(r)$, where r is the distance from the inner cylinder's center. Furthermore, the prescribed charge density σ per unit area on the inner cylinder allows integration of Gauss's law to obtain an explicit expression for the electric field: $\mathbf{E}(r) = \sigma R_1/(\varepsilon_0 \varepsilon(\phi) r)\hat{\mathbf{r}}$. Combining this result with $\mathbf{E} = -\nabla\psi$ in Eq. 17.7, we obtain a single equation determining the composition profile $\phi(r)$:

$$\mu = \frac{kT}{v_0}\left[\frac{\partial f_m}{\partial \phi} - \chi\lambda^2\nabla^2\phi - \chi M\frac{\mathrm{d}\varepsilon(\phi)/\mathrm{d}\phi}{\varepsilon(\phi)^2}\tilde{r}^{-2}\right] \tag{17.8}$$

where $M = \sigma^2 v_0/(4kT_c\varepsilon_0)$ is the dimensionless field, and $\tilde{r} \equiv r/R_1$ is the scaled distance.

Inspection of Eq. 17.8 shows two important differences from the case of uniform fields. First, the equation does not require a nonzero ε'' to shift the phase diagram. This holds irrespective of the three fundamental geometries. Recall that we, in fact, assumed a linear dependence for $\varepsilon(\phi)$. Such a simple constitutive relation is insufficient for changing the phase diagram in a uniform electric field, resulting in $\Delta T_c = 0$.

Second, the nonuniform electric field imposes a nonuniform "pull" on the fluid mixture, manifesting as an r-dependent total free

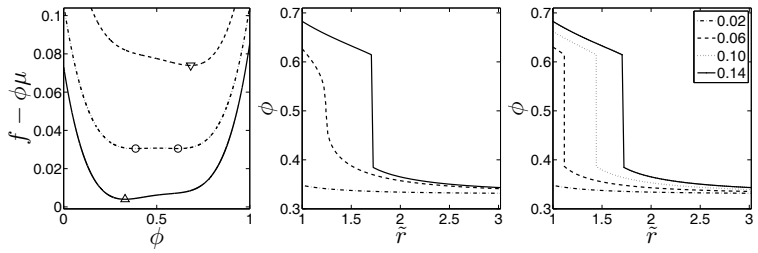

(a) (b) (c)

Figure 17.1 The free energy density $f(\phi, r)$ for a charged cylinder open system. (a) $f(\phi, r) - \phi\mu$ versus ϕ at distance $r = r_1$ (dashed line), r_i (dash-dotted line), and ∞ (solid line) for $\phi_0 = 0.33$, $T/T_c = 0.98$, and $M = 0.14$. Symbols mark minima for each curve. (b) $\phi(r)$ versus dimensionless distance $\tilde{r}$. Solid line is data from (a). Dash-dotted line has same ϕ_0 and T as (a) but with $M = 0.02$. Dashed line has same ϕ_0 and M as (a), but with $T/T_c = 0.995$. (c) $\phi(r)$ versus r for various values of M with ϕ and T as in (a).

energy density $f(\phi, r) = f_m + f_e + f_i$. We will consider, for illustrative clarity, a fluid–fluid interface that is infinitely thin by specifically defining a vanishing interfacial term $\lambda = 0$, which sets $f_i = 0$. With this simplification, the behavior of f in an open system can be conceptualized as a competition between f_m and f_e. As $r \to \infty$, the electric field is weak, $f_e \to 0$, and $f \approx f_m$ governs fluid behavior. The solid line in Fig. 17.1(a) shows a typical example of $f(\phi, r)$ at a large value of r using $\phi_0 = 0.33$, $T/T_c = 0.98$, and $M = 0.14$. The minimum of $f(\phi, r)$, marked by a symbol, gives the value of $\phi(r)$ as $r \to \infty$, which in this case is 0.33. At the other distance extreme, $r = R_1$, the electric field is the strongest, and the dashed line in Fig. 17.1(a) shows the resulting $f(\phi, r)$. Note the dramatic difference in the value of $\phi(r)$ when the value of r is small (R_1) versus large.

By finding the minima of f for all r, it is possible to construct the full concentration profile $\phi(r)$, where the solid line in Fig. 17.1(b) corresponds to the data from Fig. 17.1(a). Whether or not a phase transition occurs resides in how the minimum of $f(\phi)$ changes, as r varies between the two distance extremes. Specifically, if there exists an $r = r_i$ where f contains *two* minima (see dash-dotted line in

Fig. 17.1(a)), then r_i marks the interface between the two fluids. Figure 17.1(b) illustrates how the two minima in $f(r_i)$ translates into a discontinuity at $\phi(r_i)$, thereby creating a distinct boundary between the two phases.

Not all applied fields, however, induce phase separation. Figure 17.1(b) illustrates two such examples, in which the dash-dotted line shows the same ϕ_0 and T with a smaller M and the dashed line shows the same ϕ_0 and M with a higher T. In both cases, f contains a single minimum for all r, resulting in a smooth $\phi(r)$ profile. Despite the absence of a phase transition in these examples, the field still produces an effect, as the more polar (higher ε) fluid accumulates near the high electric field. This phenomenon can be thought of as the molecular version of the "dielectric rise" effect due to a dielectrophoretic force.

Delving more deeply into the requirements for a phase transition, we vary M for a constant ϕ_0 and T. Figure 17.1(c) shows that certain values of M induce a transition, whereas others do not. In fact, there exists a critical M_c that marks the lowest M necessary for fluid–fluid separation. If an electric field can cause phase separation in a region of $\phi_0 - T$ space *above* the binodal curve, a natural question arises: what is the new stability diagram for a particular M? This can be constructed by holding M constant and probing $\phi_0 - T$ space for fluid–fluid demixing. As the electric field breaks the symmetry of the free energy with respect to composition ($\phi_0 \to 1 - \phi_0$), the stability diagram is asymmetric with respect to $\phi_0 - \phi_c$. Figure 17.2(a) compares a typical stability curve for an open system, solid line, with the binodal curve, dashed line. Clearly, nonuniform fields can produce large changes to the phase diagram.

Figure 17.2(a) also includes the stability diagram for a typical closed system, dotted line, highlighting significant differences from open systems. Notably, the same M induces a weaker effect and produces a smaller stability diagram when $\phi_0 < \phi_c$, and the transition can occur when $\phi_0 > \phi_c$. These differences develop as a consequence of material conservation. As there is no infinite bath from which to draw material, accumulation of ϕ in high-field regions leads to depletion of ϕ in low-field regions. Moreover, the penalty in f_m grows faster than the energy gain in f_e with changing ϕ_0 or T. Roughly speaking, however, the area under the stability curves for

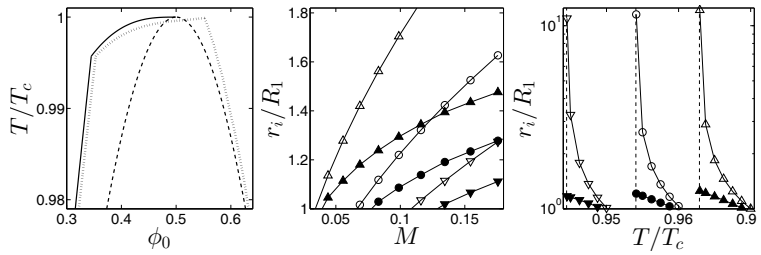

Figure 17.2 Behavior of the fluid–fluid interface r_i. (a) The stability curves in $\phi_0 - T$ space for a constant $M \approx 0.069$ in an open (solid line) and closed (dotted line) cylindrical system. The binodal curve shown with dashes. (b,c) The location of r_i with respect to M with constant $T/T_c = 0.975$ (b) and T with constant $M = 0.02$ (c) for open (open symbols) and closed (filled symbols) systems, wherein $\phi_0 = 0.29(\triangledown)$, $0.31(\bigcirc)$, and $0.33(\triangle)$. In (c), the dashed lines are the binodal temperatures for each value of ϕ_0, and the y-axis is on a log scale. For all figures, $R_2/R_1 = 5$ in the closed system.

both open and closed systems increases (decreases) as M increases (decreases).

Once an interface exists, several parameters control the location of r_i, for example, ϕ_0, T, M and R_2. In general, r_i increases with increasing M (Fig. 17.1(c) and 17.2(b)), decreasing T (Fig. 17.2(c)), increasing R_2 (not shown), and increasing ϕ_0 (Fig. 17.2(b)). The interested reader can find more specific details in Refs. [Tsori *et al.* (2004); Marcus *et al.* (2008); Samin and Tsori (2009); Galanis and Tsori (2013)].

17.2 Phase Separation Dynamics

Let us begin with a fluid–fluid mixture without an electric field and in equilibrium. When the electric field switches "on," the fluid mixture rearranges with time until it reaches a new equilibrium state. To describe the phase ordering dynamics, we follow the model H theoretical framework of the Hohenberg and Halperin classification [Hohenberg and Halperin (1977)]. We assume that the electrostatic potential responds instantaneously to any changes

in the composition and supplement the model with Gauss's law to obtain

$$\frac{\partial \phi}{\partial t} + \mathbf{v} \cdot \nabla \phi = D \nabla^2 \frac{\delta \mathcal{F}}{\delta \phi} \tag{17.9}$$

$$\nabla \cdot (\rho \mathbf{v}) = 0 \tag{17.10}$$

$$\rho \left[\frac{\partial \mathbf{v}}{\partial t} + (\mathbf{v} \cdot \nabla)\mathbf{v} \right] = \eta \nabla^2 \mathbf{v} - \nabla P - \phi \nabla \frac{\delta \mathcal{F}}{\delta \phi} \tag{17.11}$$

$$\nabla \cdot [\varepsilon_0 \varepsilon(\phi) \nabla \psi] = 0 \tag{17.12}$$

where $\mathbf{v}$ is the fluid hydrodynamic velocity field, P is the pressure, ρ is the fluid density, and η is fluid viscosity. The Cahn–Hilliard equation, Eq. 17.9, is the continuity equation for the mixture composition. The composition changes via two mechanisms: (1) a diffusive current that depends on gradients in the chemical potential $\mu = \delta \mathcal{F}/\delta \phi$, where D is the diffusivity constant, and (2) a convective current due to fluid velocity $\mathbf{v}$. Equation 17.10 is the continuity equation for the fluid, while Eq. 17.11 is the Navier–Stokes equation that includes a chemical potential related body force $-\phi \nabla \delta \mathcal{F}/\delta \phi$ [Onuki (2004)]. Lastly, Eq. 17.12 is Gauss's law, which is again coupled through $\varepsilon(\phi)$ to the other equations.

We will solve a simplified version of the model H dynamics, specifically in the over damped limit with no net fluid flow: $\mathbf{v} = 0$. This is known as model B dynamics. The problem is now reduced to solving Eq. 17.9, with only a diffusive current, and Eq. 17.12. When T decreases from above to below the critical point in the absence of an electric field, diffusion governs the exchange of material, and the fluids phase separate locally into small domains that grow in time. Most notably, this process (at late times) can be described by a characteristic length such that the domain structure at all times is self-similar when rescaled by this length [Cahn and Hilliard (1958)]. Adding an electric field, as we shall see, alters this behavior.

Returning to concentric cylinders in a closed system, we use the right-hand side of Eq. 17.8 for the chemical potential in Eq. 17.9 and solve the radially symmetric problem with a dimensionless time $\tilde{t} = (DkT/R_1^2 v_0)t$. When an electric field is turned on, material first accumulates near $r \approx R_1$. If $M > M_c$, a fluid–fluid interface emerges at $r_i(t_i) = R_1$, travels outward to larger r, and asymptotically reaches the long-time steady-state location $r_i(t \to \infty) = r_{i\infty}$. Figure 17.3(a)

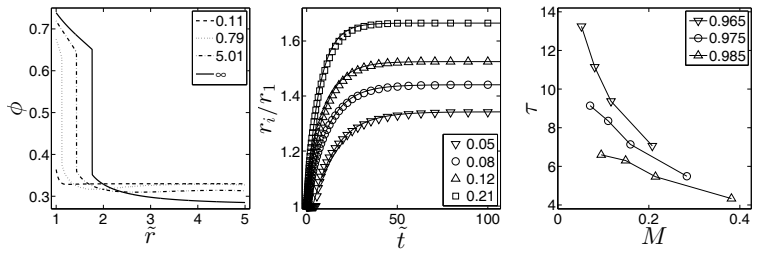

(a) (b) (c)

Figure 17.3 Movement of r_i in time t. (a) $\phi(r)$ versus dimensionless distance $\tilde{r}$ at various dimensionless times $\tilde{t}$, where $\phi_0 = 0.33$, $T/T_c = 0.965$, $M \approx 0.31$. (b) Symbols show interface location r_i versus $\tilde{t}$ for various M, where $\phi_0 = 0.33$, $T/T_c = 0.965$. Lines are fits to Eq. 17.13. (c) The time constant τ as a function of σ for various T/T_c. For all data, $R_2/R_1 = 5$.

shows snapshots of $\phi(r)$ in time, while the symbols in Fig. 17.3(b) mark r_i with time.

The behavior of r_i can be approximated as an exponential relaxation

$$r_i(t) = r_{i\infty} + (r_1 - r_{i\infty}) \exp[-(\tilde{t} - t_i)/\tau] \tag{17.13}$$

which contains two free parameters, the time constant for relaxation τ and the lag time for the interface to emerge t_i. The lines in Fig. 17.3(b) show fits to the data. In general, τ decreases with increasing M (Fig. 17.3(c)), increasing T (Fig. 17.3(c)), and decreasing ϕ_o (not shown).

In conclusion, we briefly reviewed important features of how nonuniform electric fields induce a fluid–fluid mixing–demixing phase transition. The advantage of nonuniform fields, over uniform fields, is that a phase transition can occur with only a simple dielectric difference between the fluids. Moreover, nonuniform fields can dramatically alter the transition temperature, compared with uniform fields.

Because phase changes often lead to different material properties, the ability to easily control a phase transition often translates into the ability to easily tune material behavior. For example, turning "on" an electric field can cause a homogeneous fluid–fluid mixture to phase separate, which creates a refractive index

mismatch and produces an optical interface. Turning the field "off" reverses this process. As nonuniform fields readily occur when electrical components are small, field-induced separation may have an important technological impact.

References

Cahn, J. W. and Hilliard, J. E. (1958). Free energy of a nonuniform system. i. interfacial free energy, *J. Chem. Phys.* **28**, 2, pp. 258–267.

Debye, P. and Kleboth, K. (1965). Electrical field effect on the critical opalescence, *J. Chem. Phys.* **42**, pp. 3155–3162.

Galanis, J. and Tsori, Y. (2013). Mixing-demixing phase diagram for simple liquids in nonuniform electric fields, *Phys. Rev. E* **88**, p. 012304.

Hohenberg, P. C. and Halperin, B. I. (1977). Theory of dynamic critical phenomena, *Rev. Mod. Phys.* **49**, 3, pp. 435–479.

Landau, L. D. and Lifshitz, E. M. (1957). *Elektrodinamika Sploshnykh Sred Chap. II, Sec. 18, Problem 1* (Nauka, Moscow).

Marcus, G., Samin, S. and Tsori, Y. (2008). Phase-separation transition in liquid mixtures near curved charged objects, *J. Chem. Phys.* **129**, 6, 061101.

Onuki, A. (1995). Electric-field effects in fluids near the critical point, *Europhys. Lett* **29**, pp. 611–616.

Onuki, A. (2004). *Phase Transition Dynamics* (Cambridge University Press).

Orzechowski, K. (1999). Electric field effect on the upper critical solution temperature, *Chem. Phys.* **240**, pp. 275–281.

Safran, S. (1994). *Statistical Thermodynamics of Surfaces, Interfaces, and Membranes* (Westview Press, New York).

Samin, S. and Tsori, Y. (2009). Stability of binary mixtures in electric field gradients, *J. Chem. Phys.* **131**, 19, 194102.

Tsori, Y. (2009). *Colloquium* : Phase transitions in polymers and liquids in electric fields, *Rev. Mod. Phys.* **81**, pp. 1471–1494.

Tsori, Y., Tournilhac, F. and Leibler, L. (2004). Demixing in simple fluids induced by electric field gradients, *Nature* **430**, pp. 544–547.

Chapter 18

Dynamic Electric Response of Charged Fibrous Virus (fd) Suspensions: Interactions of charged colloidal rods in AC Electric Fields

Kyongok Kang and Jan K. G. Dhont
Forschungszentrum Juelich, ICS-3 (Soft Condensed Matter), Juelich D- 52425, Germany
k.kang@fz-juelich.de

The electric response of charged fibrous viruses (fd), as charged colloidal rods, to an AC external electric field is explored. Various field-induced phases and dynamical states are characterized in the field-amplitude versus frequency plane. The observed phase/state transitions are due to intercolloidal field-induced interactions as a result of polarization of double layers and/or the layer of condensed ions, and possibly electro-osmotic flow. The concentration of fd-virus is chosen within the isotropic-nematic coexistent phase at a low ionic strength. For low frequencies, chiral-nematic phases and dynamical states are induced on increasing the field amplitude. At high frequencies, (above $\sim$1 kHz), a uniform homeotropic phase is induced, wherein the fd-rods align along the electric field. Also, electrode polarization is described in order to correct applied field amplitudes to obtain the field amplitudes within the bulk

Electrostatics of Soft and Disordered Matter
Edited by David Dean, Jure Dobnikar, Ali Naji, and Rudolf Podgornik

ISBN 978-981-4411-85-1 (Hardcover), 978-981-4411-86-8 (eBook)
www.panstanford.com

of the suspensions, away from the electrodes. Field-induced non-equilibrium criticality is experimentally measured.

18.1 Introduction

The response of many soft matter systems to an external electric field results from permanent or dielectrically induced dipoles. When the colloidal cores are dielectrically polarized, the interacting electrical dipoles can lead to anisotropic structures such as strings and sheets of colloidal particles [1–3]. The frequencies that are used for such dielectric experiments are in the MHz range. At these high frequencies, the electric double layers and the layer of condensed ions of the colloidal particles are not polarized. In the present work, we investigate the response to low frequencies (below a few kHz), wherein the electric double-layer polarization, and/or polarization of the layer of condensed ions, as well as electro-osmotic flow, leads to field-induced interactions between the colloids.

In this study, we use fd-virus particles, which have been used in the past as model systems for very long and thin, highly charged, and stiff colloidal rods. The concentrations are chosen such that, without an external electric field, there is isotropic-nematic coexistence. In the presence of an external electric field, various phase/state transitions are induced, depending on the field amplitude and frequency [4, 5], as a result of field-induced polarization of the double layer, the layer of condensed ions, and possibly electric-osmotic flow.

We use suspensions of fd-viruses at a quite low ionic strength, corresponding to an electric double thickness of 27 nm. Fd-virus suspensions are purified following standard biological protocols, from the XL1 blue strain of *Escherichia coli* as the host bacteria [6]. Fd-virus particles consist of ds-DNA, coated with proteins, with a length of 880 nm and a diameter of 6.7 nm. The coat proteins render the particles quite stiff: the persistence length is about 2500 nm. The surface charge of fd-virus particles, as obtained from titration curves, is -8700e at pH $= 6.9$ [7]. The concentrated fd-suspensions are prepared by dialyzing (for 2 days) against a TRIS/HCl-buffer with a buffer concentration of 1.6×10^{-4} M. The appropriate

fd-concentrations are then obtained by dilution with the same buffer. For such a low buffer concentration, the amount of carbon dioxide that dissolves from the air contributes to the ionic strength and pH [8]. The pH changes from 8.2 to 6.9 due to dissolved carbon dioxide at this low buffer concentration.

A home-made optically transparent in situ electrical cell is used for imaging of the sample morphology through a microscope, for birefringence measurements, and for dynamic light scattering [9]. Commercially available indium-tin-oxide (ITO) coated float glass (from Prazisions Glas und Optik GmbH, CEC500S) is used, with dimensions of 40×70 mm^2, and with a glass thickness of 0.7 mm. Images are taken with an inverted microscope in polarization mode, combined with differential interference contrast (Carl Zeiss, Axiovert 40CFL model). Images are recorded with a CCD camera (AxioCam Color A12-312).

Before describing the experimental observations, a theory is described in the subsequent section, for the correction of the applied electric field amplitude for electrode polarization [5]. At the low frequencies under consideration in the present study, electric double layers build up at the electrodes, which screen the electric field. The electric field amplitude within the bulk of the suspension is thus less than the applied field amplitude. A simple relation between the applied field amplitude and its value in the bulk of the suspension is derived. This relation is used to correct the measured location of phase/state transition lines in the field-amplitude versus frequency plane.

18.2 Electrode Polarization

A simple theory based on the standard electrokinetic equations is used for the correction of electrode polarization [5]. Due to the formation of double layers near the electrodes, the applied electric field amplitude may be different from the field amplitude in the bulk of the suspension. The attenuation of the electric field is frequency dependent due to the finite diffusivity of the salt ions. For a DC field, the double layers can fully develop and completely screen the electric field, in which case the field amplitude in the bulk of the

suspension vanishes. For finite frequencies, the double layers at the electrodes only partially develop, and therefore partially screen the electric field.

The positively charges ions experience a force $\vec{F}_{\pm}$ that sets them into motion with a velocity equal to $\vec{v}_{\pm} = \vec{F}_{\pm}/\zeta$, where ζ is the solvent friction coefficient of the ions. This force has two contributions: First of all, there is an electric force on the (univalent) ions $\mp e\,(\partial\Phi(z,\,t)/\partial z)$ (– for the positive ions, + for the positive ions), where $e > 0$ is the elementary charge and $\Phi(z,\,t)$ is the local electric potential, while z is the distance from the mid-plane between the two electrodes, which varies from $-L/2$ to $+L/2$, with L the distance between the two electrodes. Second, there is a Brownian force $\vec{F}_{\pm}(z,\,t) = -k_{\mathrm{B}}T\,(\partial \ln \rho_{\pm}(z,\,t)/\partial z)$, where $\rho_{\pm}(z,\,t)$ is the local number density of positive ions, k_{B} is the Boltzmann constant, and T is the temperature. The Brownian force describes the diffusive motion induced by concentration gradients. The total force is thus equal to,

$$\vec{F}_{\pm}(z,\,t) = -k_{\mathrm{B}}T\,\frac{\partial}{\partial z}\ln\,\rho_{\pm}(z,\,t)\,\mp\,e\frac{\partial}{\partial z}\Phi(z,\,t) \tag{18.1}$$

Substitution into the conservation equation for the concentration, $\partial\rho_{\pm}(z,\,t)/\partial t = -\,\partial(\rho_{\pm}\,v_{\pm}(z,\,t))/\partial z$, thus leads to the well-known equations of motion (we do not denote position and time dependence explicitly for brevity),

$$\frac{\partial\rho_{\pm}(z,\,t)}{\partial t} = D\,\frac{\partial^2}{\partial z^2}\rho_{\pm} \pm D\,\beta e\,\left[\rho_{\pm}\frac{\partial}{\partial z}\Phi\right] \tag{18.2}$$

where $\beta = 1/k_{\mathrm{B}}T$, and $D = k_{\mathrm{B}}T/\zeta$ is the Einstein diffusion coefficient of the ions. Note that there is no convective contribution for the two-plate geometry under consideration. Assuming that the variation $\Delta\Phi$ of the potential within the double layers near the electrodes is small (in the sense that $\beta e\,\Delta\Phi$ is small), the excess density $\Delta\rho_{\pm} \equiv \rho_{\pm} - \bar{\rho}$, with $\bar{\rho}$ the overall density of ions, is proportional to the potential. A corresponding linearization of Eq. (18.2) with respect to $\Delta\rho_{\pm}$ and Φ leads to,

$$\frac{\partial\,\Delta\rho_{\pm}}{\partial t} = D\,\frac{\partial^2}{\partial z^2}\Delta\rho_{\pm} \pm D\,\frac{1}{2}\kappa^2\,\left[\Delta\rho_{+} - \Delta\rho_{-}\right] \tag{18.3}$$

where $\kappa = \sqrt{2\beta e^2 \bar{\rho}/\varepsilon}$ is the inverse Debye screening length, and ε is the dielectric constant. This equation of motion is the one-dimensional form of a well-known electrokinetic equation in the absence of electro-osmotic flow (see references [10–13]). The value of the applied electric field amplitude sets the first boundary condition for the potential between the electrodes,

$$\Phi(z = \frac{1}{2}L, t) - \Phi(z = -\frac{1}{2}L, t) = E_0 L \cos(\omega t) \tag{18.4}$$

The second boundary condition assures that ion fluxes $\rho_\pm \vec{v}_\pm$ must vanish at the electrodes. As ion velocities are proportional to the force in Eq. (18.1), this implies that,

$$\frac{\partial}{\partial z}\left[-\Delta\rho_\pm(z, t) \mp \varepsilon\kappa^2\Phi(z, t)\right] = 0, \quad \text{for } z = \pm\frac{L}{2} \quad \text{and } t > 0 \tag{18.5}$$

where the same linearization discussed above has been performed. For 1-1 electrolytes, the above equations can be used to derive equations of motion and boundary conditions for the free charge density $\rho = e[\Delta\rho_+ - \Delta\rho_-]$, resulting from differences in the concentrations of positive and negative ions. Subtraction of the equation of motion [in Eq. (18.3)] for $\Delta\rho_+$ and $\Delta\rho_-$ leads to a single equation of motion for the free charge density,

$$\frac{\partial\rho}{\partial t} = D\left[\frac{\partial^2}{\partial z^2} - \kappa^2\right]\rho \tag{18.6}$$

As far as we know, this equation of motion has been derived for the first time by Ferry [14], who used it to describe the capacitance of a single double layer at a flat interface. The potential is connected to the free charge density through the Poisson equation,

$$\frac{\partial^2}{\partial z^2}\Phi = -\frac{\rho}{\varepsilon} \tag{18.7}$$

Subtraction of the boundary condition for ρ_+ from that of ρ_- leads to

$$\frac{\partial}{\partial z}\left[\rho + \varepsilon\kappa^2\Phi(z, t)\right] = 0, \quad \text{for } z = \pm\frac{L}{2} \quad \text{and } t > 0 \tag{18.8}$$

The above set of equations (18.6) and (18.7), together with the boundary conditions (18.4) and (18.8), describe electrode polarization within the Debye–Hueckel approximation for 1-1

electrolytes. The solution of the above equations for the potential and the free charge density is constructed in appendix B in Ref. [5]. As shown there, the in-phase and out-phase response functions for the electric field strength can be written as additive contributions that describe the electric field within the double layers near the electrodes, and contributions that describe the field within the bulk, away from the electrodes. The contributions within the double layers decay exponentially with the distance from the electrodes over a distance that is at most equal to the Debye length, and can therefore be discarded for the calculation of the attenuation factor, which is the ratio of the field amplitude in the bulk of the suspension and the applied amplitude. The attenuation factor is thus found to be equal to,

$$\gamma(L) = \Omega(L)/\sqrt{4 + \Omega^2(L)} \leq 1 \tag{18.9}$$

where the dimensionless frequency is defined as $\Omega \equiv \omega L/D\kappa$. Note that the attenuation factor is a function of the distance L between the electrodes. The attenuation factor tends to unity (no electrode polarization) for large distances between the electrodes. The above expression for the attenuation factor is used later to correct our measured electric phase/state diagram. The electrode polarization is important only for frequencies below about 60–100 Hz, in case of $L = 1.4$ mm thickness.

18.3 Bulk Electric Response: Reversible Electric Phase/State Diagram

The electric phase/state diagram is shown in Fig. 18.1 for a fd-virus concentration of 2.0 mg/ml, in the electric field amplitude versus frequency plane. A detailed characterization of the individual phases and states is given in our Ref. [5]. Below about 60–100 Hz, there are two sets of phase/state transition lines to be seen in Fig. 18.1: the thin lines at relatively high field amplitudes are applied amplitudes, whereas the lower thick lines are the amplitudes corrected for electrode polarization. The phases and states that exist are independent of how the field amplitude and frequency are achieved. In this sense, the phase/state diagram is “reversible”.

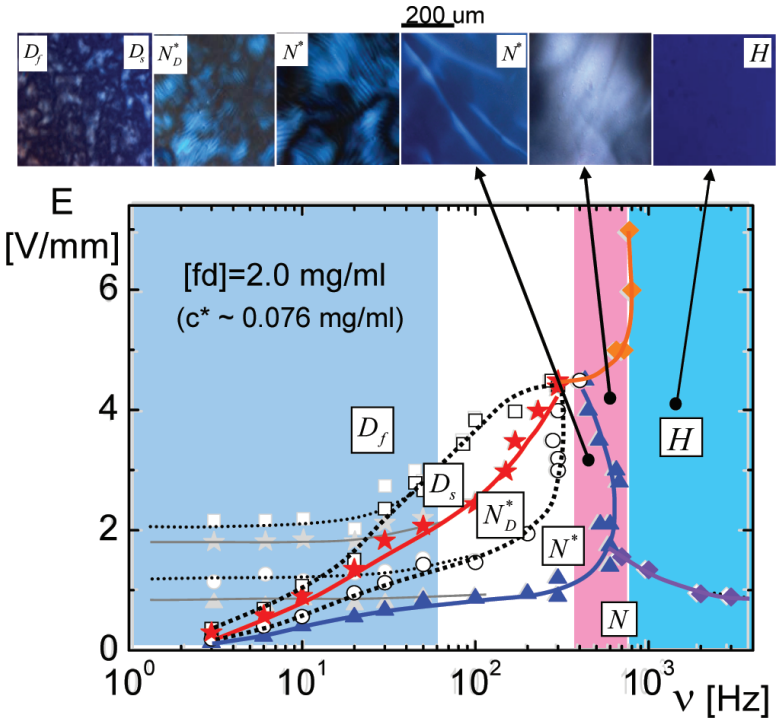

Figure 18.1 The electric phase/state diagram in the amplitude versus frequency plane, with the corresponding depolarized morphology. The solid/dashed lines refer to sharp and gradual phase/state transitions, respectively.

18.3.1 *Low Frequency Induced Chiral-nematic (N^* and N_D^*) Phases and Dynamical (D_S and D_f) States*

At low frequencies, the nematic N-phase (where there is coexistence between nematic domains and isotropic regions) turns into the chiral-nematic N^*-phase on increasing the field amplitude. It is well known that at relatively high ionic strength, the equilibrium nematic of fd is chiral, due to the chiral structure of the ds-DNA core of fd-virus. For the low ionic strength, we use in the present experiments, a non-chiral nematic is found without the electric field, due to the long-ranged electrostatic repulsive interactions. On applying an electric field, the range of electrostatic repulsions is

apparently diminished, and the chiral structure of the core affects inter-rod interactions (such as at high ionic strengths), resulting in a chiral structure of part of the nematic domains. The striped texture, corresponding to chiral-nematic domains, extends over regions that exceed the size of the N-domains, while the chiral-nematic does not nucleate within the N-domains. There is a strong variation in the measured pitch at low field amplitudes, which becomes smaller with increasing amplitudes. The variation of true pitch as a function of field amplitude is decreased and levels off to 10 μm at high field amplitudes within the N_D^*-phase.

There is the second sharp transition line at a low frequencies, where the N_D^*-phase transits to dynamical states (D_S, D_f). In these dynamical states, small nematic domains (∼30 μm) are melting and forming. We measured dynamic image-time intensity autocorrelation functions to explore the kinetics of melting and forming [5, 9, 15]. The of characteristic time for melting and forming of the small nematic domains (∼30 μm size) of D_f state is 10 times faster than that of D_S state.

18.3.2 *High Frequency Induced Orientational Order in the H-phase*

At frequencies larger than about a kHz, a homeotropic phase is formed: the H-phase in Fig. 18.1. Contrary to all other phases/states, this is a uniform phase. The rods are now aligned along the field direction, perpendicular to the electrode surfaces. The orientational order parameter, as well diffusion coefficients as measured by dynamic light scattering, are found to be independent of the frequency and field amplitude throughout the H-phase [16, 17]. This suggests that hydrodynamic interactions are responsible for the stabilization of this phase, rather than interactions through polarization charges. At these relatively high frequencies, polarization of the double layer and the layer of condensed ions is essentially absent. The electro-osmotic flow and/or the flow induced by the electrophoretic motion of the rods might be the driving mechanism for the formation of the H-phase. The diffusive dynamics is observed, within the H-phase and near to the $H \rightarrow N^*$ phase transition line [16].

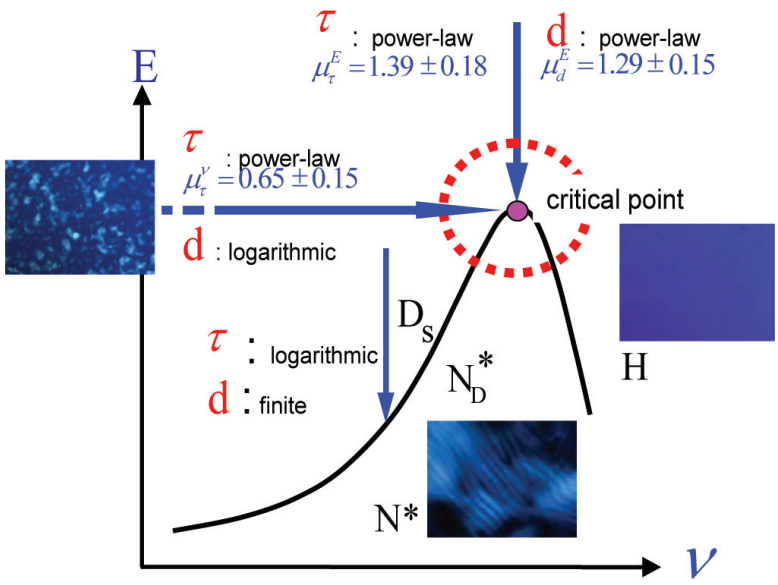

Figure 18.2 Non-equilibrium criticality of the characteristic time τ for melting and forming of small nematic domains and the domain size d.

18.3.3 *Field-induced Non-equilibrium Criticality*

The point in the phase/state diagram where several transition lines meet (also see Fig. 18.2) can be identified as a "non-equilibrium critical point", where a time scale and a length scale diverge. The time scale is the time on which melting and forming of nematic domains occurs, which can be measured by image correlation spectroscopy, based on time traces of CCD images. The nature of the critical divergence is probed for the approach of the critical point on increasing the frequency at constant field amplitude, and on lowering the field amplitude at constant frequency. We found both power-law and logarithmic divergences, as summarized in Fig. 18.2 [18].

18.4 Conclusion

The characteristics of electric field induced phases and dynamical states of charged rods are provided in the reversible bulk field

amplitude versus applied frequency. A simple procedure is proposed to correct for electrode polarization, which is important at lower frequencies. The origin of observed phases and dynamical states is due to the interactions between rods that result from external field induced polarization charges and hydrodynamic interactions. At low frequencies, both electrostatic interactions and hydrodynamic interactions play a role. However, at relatively high frequencies, where a uniform homeotropic phase (the H-phase) is found, charge-polarization is essentially absent, so that this phase is most likely stabilized through hydrodynamic interactions induced by electro-osmotic flow and possibly by the flow induced due to electrophoretic motion of the rods. The mechanism that leads to the dynamical states, as well as the critical phenomena that we observed, are as yet not understood. An understanding of the underlying mechanisms for the observed phenomena requires the evaluation of pair interactions due to polarization charges and hydrodynamics, and the analysis of appropriate equations of motion where these pair-forces are used as an input to make the step to collective phenomena.

References

1. Dassanayake, U., Fraden, S. and van Blaaderen, A. (2000) Structure of rheological fluids, *J. Chem. Phys.*, **112**, pp. 3851–1858.
2. Yethiraj, A., and van Blaaderen, A. (2003) A colloidal model system with an interaction tunable from hard sphere to soft and dipolar, *Nature*, **421**, pp. 513–517.
3. Hynnine, A.-P., and Dijkstra, M. (2005) Phase diagram of dipolar hard and soft spheres: Manipulation of colloidal crystal structures by an external field, *Phys. Rev. Lett.*, **94**, pp. 138303.
4. Kang, K., and Dhont, J. K. G. (2008) Double-layer polarization induced transitions in suspensions of colloidal rods, *Eur. Phys. Lett.*, **84**, pp. 14005
5. Kang, K., and Dhont, J. K. G. (2010) Electric-field induced transitions in suspensions of charged colloidal rods, *Soft Matter*, **6**, pp. 273–286.
6. Sambrook, J., Fritsch, E. F., and Maniatis, T. (1989) *Molecular Cloning: A Laboratory Manual* (Cold Spring Harbor Laboratory, New York).

7. Zimmermann, K., Hagedorn, H., Heuck, C. C., Hinrichsen, M., and Ludwig, H. (1986) The ionic properties of the filamentous bacteriophages Pf1 and fd., *J. Biol. Chem*. **261**, pp. 1653–1655.
8. Kang, K., Wilk, A., Patkowski, A., and Dhont J. K. G. (2007), Diffusion of spheres in isotropic and nematic networks of rods: Electrostatic interactions and hydrodynamic screening, *J. Chem. Phys*. **126**, pp. 214501.
9. Kang, K. (2011) Image time-correlation, dynamic light scattering and birefringence for the study of the response of anisometric colloids to external fields, *Rev. Sci. Instrum.* **82,** pp. 053903.
10. Overbeek, J. Th. G. (1943) Sonderabdruck aus den Kolloid-Beiheften, Band 54, Heft 7-9, pp. 287-364 (in German).
11. Booth, F. (1950) The electroviscous effect for suspensions of solid spherical particles, *Proc. Roy. Soc. Lond. Ser A***, 203**, pp. 533–551.
12. DeLacey, E. H. B., and White, L. R. (1981) Dielectric response and conductivity of dilute suspensions of colloidal particles, *J. Chem. Soc., Faraday Trans*. 2, **77**, pp. 2007–2039.
13. O'Brien, R. W. (1982) The response of a colloidal suspension to an alternating electric field, *Adv. Coll. Int. Sci.* **16**, pp. 281–320.
14. Ferry, J. D. (1948) Frequency dependence of the capacity of a diffuse double layer*, J. Chem. Phys*., **16**, pp. 737–738.
15. Kang, K. (2010) Mesoscopic relaxation time of dynamic image correlation spectroscopy, *J. Biomed. Sci. and Eng*., **3**, pp. 625–632.
16. Kang, K. (2010) Charged fibrous viruses (fd) in external electric fields: Dynamics and orientational order, *New. J. Phys*., **12**, pp. 063017.
17. Kang, K. (2010) Diffusivity in an electric-field-induced homeotropic phase of charged colloidal rods, *Euro. Phys. Lett.* **92**, pp. 18002.
18. Kang, K., and Dhont, J. K. G. (2009) Criticality in a non-equilibrium, driven system: Charged colloidal rods (fd-viruses) in electric fields, *Euro. Phys. J. E*. **30**, pp. 333–340.

Chapter 19

Statistical Thermodynamics of Supercapacitors and Blue Engines

René van Roij
Institute for Theoretical Physics, Utrecht University, Leuvenlaan 4, 3584 CE Utrecht, The Netherlands
r.vanroij@uu.nl

19.1 Introduction

The scarcity of fresh water, the depletion of fossil fuels, and the ever-increasing demand for electric power are important issues that receive increasing attention in a variety of branches of science and technology. In all three cases, nanoporous carbon electrodes, immersed in a liquid medium with charge carriers, are being considered as device elements. For instance, in carbide-derived carbon electrodes with nanometer-sized pores filled with an ionic liquid, electric energy can be stored/released through the adsorption/desorption of ionic charges on/from the surface of the charging/discharging electrodes [Chmiola *et al.* (2006); Miller and Simon (2008); Merlet *et al.* (2012)]. Carbon electrodes are also being explored in capacitive devices to harvest sustainable

Electrostatics of Soft and Disordered Matter
Edited by David Dean, Jure Dobnikar, Ali Naji, and Rudolf Podgornik

ISBN 978-981-4411-85-1 (Hardcover), 978-981-4411-86-8 (eBook)
www.panstanford.com

energy from mixing fresh river water with salty sea water [Brogioli (2009); Brogioli *et al.* (2011); Rica *et al.* (2012); Sales *et al.* (2010)]. This salinity-gradient energy, or "blue" energy, is obtained from charging up a pair of electrodes immersed in sea water (whereby ions adsorb onto the electrodes at a low potential) and discharging them again immersed in fresh water (whereby ions desorb from the electrodes at a higher potential). This capacitive mixing process, with brackish water as a waste product, intercepts the spontaneous diffusion of ions from high to low salinity in much the same way as heat engines intercept the heat flow from hot to cold heat baths; for typical salt concentrations in river and sea water, these "blue engines" can produce of the order of 2 kJ of energy per liter of river water, in principle even completely reversibly [Boon and van Roij (2011)]. The reverse process, which can be seen as a "blue fridge," is a desalination process in which two volumes of initially brackish water are converted into a volume of fresh water and a volume of brine by charging up the electrodes in one of the volumes (which then desalinates due to ion adsorption onto the electrodes, at a high potential) and discharging them in the other volume (which then becomes more salty due to the release of the ions from the electrodes, at a low potential) [Biesheuvel (2009)]. Of course, the "blue fridge" requires a net energy input, and ongoing research questions involve the efficiency and speed of such processes.

In this contribution, we will perform a thermodynamic and statistical-mechanical analysis of supercapacitors and blue engines. We will identify direct similarities between the electric work performed by/onto these devices with mechanical work performed by heat engines or consumed by fridges. Moreover, we will identify a number of Maxwell relations. A distinction emerges between the differential capacity at constant ion number and at constant ion chemical potential, directly equivalent to the heat capacity at constant volume and constant temperature. Finally, we will discuss the charge distribution on a (porous) electrode at a given potential. Throughout we make connection with recently published results, although we start off with a quick reminder of ordinary thermodynamics to clarify the analogies.

19.2 Thermodynamics of Heat Engines: A Reminder

We consider a system of internal energy U, volume V, and entropy S. If the number of particles in the system and all other (geometric, dielectric, magnetic, and so on) characteristics are considered fixed, we can write $U = U(S, V)$ such that

$$dU = T\,dS - p\,dV, \tag{19.1}$$

with temperature T and pressure p of the system defined by

$$T = \left(\frac{\partial U}{\partial S}\right)_{\mathrm{V}} \text{ and } p = -\left(\frac{\partial U}{\partial V}\right)_{\mathrm{S}}. \tag{19.2}$$

Equation (19.1) is a combined formulation of the First and Second Law of Thermodynamics, where $T\,dS$ is the amount of heat that the system takes up reversibly from a heat bath (also at temperature T) and $p\,dV$ is the reversible mechanical work done *by* the system (on the environment also at pressure p).

Consider the system to reversibly go through a cycle in the $p - V$ plane, such that the final state is identical to the initial state. From the fact that U is a state function, we conclude that $\oint dU = 0$, such that the total mechanical work performed by the system during the cycle can be written as $W_{\mathrm{m}} \equiv \oint p\,dV = \oint T\,dS$. Geometrically, this means that the work equals not only the enclosed area in the $p - V$ plane but also the enclosed area of the cycle in the $T - S$ plane. In other words, reversible work of a cyclic heat engine *must* be accompanied by heat exchange. For the system to perform a positive amount of work, that is, for the system to act as a heat engine, it should typically expand at high pressures (and hence at high temperatures), thereby taking up heat from baths during (a part of) the expansion, and compress at lower pressures (and hence at lower temperatures), thereby releasing heat into the colder baths during (a part of) the compression.

Two famous examples of heat engines are the Stirling engine and the Carnot engine, for which the working substance is a classical ideal gas (for which $U \propto T \propto pV$) that cycles in a four-fold fashion. In the (idealized) Stirling engine, the high-temperature expansion and the low-temperature compression are performed isothermally (such that $dU = 0$ and hence $T\,dS = p\,dV$), while the cooling and heating

parts take place isochorically ($dV = 0$ such that $dU = T\,dS$). In the Carnot cycle, the expansion and the compression consist both of an isothermal part ($dU = 0$) and an adiabatic part ($dS = 0$ such that $dU = -pdV$ thereby cooling and heating the gas upon expanding and compressing the gas, respectively.). It is well known that the Carnot engine yields the most efficient conversion of heat into work for given hot and cold heat reservoirs at high and low temperatures T_{h} and T_{l}, respectively, with the mechanical work of the Carnot cycle given by $W_{\mathrm{m}} = \Delta T\,\Delta S$ where $\Delta T = T_{\mathrm{h}} - T_{\mathrm{l}}$ and ΔS is the entropy extracted from the hot bath during the isothermal expansion and delivered to the cold bath during the isothermal compression. In the $T - S$ plane, this Carnot cycle is represented by a rectangular shape at two fixed temperatures and two fixed entropies.

19.3 Thermodynamics of Electrode–Electrolyte Systems

The system of our actual interest here is a macroscopic electrode with total charge Q in contact with a 1:1 electrolyte that contains $N + Q/e$ counterions and N monovalent coions, such that the combined electrode–electrolyte system is charge neutral. Here, e is the proton charge. The temperature T is fixed, and the geometric properties of the electrode (e.g., its surface area, its porosity, the volume, and the curvature of its pores, and so on) are assumed to be fixed as well. Moreover, in the case of an aqueous electrolyte, the water is treated as a structureless dielectric continuum. The Helmholtz free energy of this system can then be written as $F(N,\ Q)$, where we drop the dependence on the fixed temperature T and the fixed geometric variables for notational convenience. Regardless of the functional form of F, which depends on the microscopic details of the ion–electrode and ion–ion interactions, we can write the differential of the state function F generally as

$$dF = \mu dN + \Psi dQ, \tag{19.3}$$

where we define the ionic chemical potential μ and the electrostatic potential of the electrode Ψ as

$$\mu = \left(\frac{\partial F}{\partial N}\right)_{\mathrm{Q}} \text{ and } \Psi = \left(\frac{\partial F}{\partial Q}\right)_{\mathrm{N}}. \tag{19.4}$$

We note that μ and Ψ, which are the intensive conjugate variables of the extensive variables N and Q, respectively, can be seen as equations of state, that is, $\mu = \mu(N, Q)$ and $\Psi = \Psi(N, Q)$, which we leave unspecified for now as we focus on general and universal thermodynamic properties of the electrode–electrolyte system of interest.

We first note that ΨdQ in Eq. (19.3) represents the (isothermal and reversible) electrostatic work done *on* the electrode–electrolyte system by its environment (which is also at electric potential Ψ) when it provides the system with an additional charge dQ. Likewise, μdN is the (reversible and isothermal) chemical work done *on* the system when its environment (at chemical potential μ) provides dN pairs of salt ions. Consider now a reversible and isothermal *cyclic* process due to charging and discharging processes, possibly at various N, under the constraint that the initial and the final states of the electrode–electrolyte system are the same. The total electric work performed *by* the system during the cycle equals $W = -\oint \Psi dQ$, that is, the work performed is the (negative of the) enclosed area in the $\Psi - Q$ plane. Typically, work is done ($W > 0$) by this cyclic "blue engine" if the electrode is charged at low voltage (which usually implies a high concentration of ions to screen the electrode charge) and discharged at high voltage (low salt concentrations). By virtue of F being a state function, such that $\oint dF = 0$ and hence $W = \oint \mu dN$, we indeed find that reversible cyclic blue engines *must* be accompanied by ion exchange processes, whereby $W > 0$ implies by thermodynamic necessity that ions are to be taken up ($dN > 0$) by the system at a high chemical potential [during (a part of) the charging process] and released again ($dN < 0$) at a low chemical potential [during (a part of) the discharging].

If one compares Eqs. (19.1) and (19.3), a striking resemblance appears, not only regarding the (free) energy contribution due to the exchange of heat and ions, TdS and μdN, but also regarding the mechanical and electric work contributions, $-pdV$ and ΨdQ, respectively. In fact, we can make the following mapping: $U \leftrightarrow F$, $T \leftrightarrow \mu$, $S \leftrightarrow N$, $-p \leftrightarrow \Psi$, and $V \leftrightarrow Q$. This identification of variables respects the symmetry of extensivity and intensivity, connects (de)compressions of a gas with (dis)charging of the electrolyte-immersed electrode, and implies that isothermal (constant-T) and

adiabatic (constant-S) volume changes in heat engines are analogous to grand-canonical (constant-μ) and canonical (constant-N) charging processes of electrolyte-immersed electrodes, respectively.

With this mapping of variables between heat engines and blue engines in mind, it is interesting to note that the blue engine recently developed by Brogioli [Brogioli (2009)] to harvest salinity gradient energy is actually equivalent to the (idealised) Stirling engine: Brogioli's electrode charging/discharging processes take place at constant μ, just like Stirling's volume changes take place at constant T, and Brogioli's flushing processes to exchange river and sea water (to change the ion chemical potential) at constant electrode charge are equivalent to Stirling's heat exchanges between hot and cold baths (to change the temperature) at constant volume. In addition, this mapping of variables was exploited in Ref. [Boon and van Roij (2011)] to construct a conceptual Carnot-like blue engine. The key difference with the Brogioli cycle is the replacement of the two flushing steps by a constant-N charging and discharging process, whereby the initially salty water desalinates upon electrode charging due to ion adsorption, and the initially fresh water salinates upon discharging due to ion desorption. This Carnot-like cycle, composed of two iso-μ and two iso-N (dis)charging steps, yields an electric work output $W = \Delta N \Delta\mu$ per cycle, where ΔN is the number of ion pairs that flows during the iso-μ parts of the cycle from the salty to the fresh water through an adsorption-desorption process onto the electrodes, and where $\Delta\mu$ is the chemical potential difference between the salty and the fresh water. The rectangular shape of the enclosed area of the cycle in the μ–N representation is the hallmark for the most efficient process, as it makes explicit that each of the ΔN ion pairs contributes its full chemical potential difference $\Delta\mu$ to the total work; more work (per cycle per transferred ion pair) is thermodynamically impossible.

There is, however, one key difference between the nature of the mapped variables T and μ, as T does have a well-defined absolute zero whereas μ is only defined up to an arbitrary reference potential. For that reason, there is no well-defined analogue of the Carnot heat engine efficiency $\Delta T / T_{\mathrm{h}}$; the analogous expression $\Delta\mu/\mu_{\mathrm{h}}$ with μ_{h} the high chemical potential of the sea water is meaningless.

19.4 Maxwell Relations and Response Functions

Starting from Eq. (19.3) a number of thermodynamic relations for (super)capacitors immersed in an ionic fluid can be constructed in full analogy to the standard relations that follow from Eq. (19.1) for heat exchange and volume work. In the latter case, it proves convenient, for instance, to consider Legendre transformations of $U(S, V)$ to obtain thermodynamic potentials such as the Helmholtz free energy, the Gibbs free energy, or the grand potential, from which a set of Maxwell relations follows by considering second derivatives with respect to two different variables [Callen (1985)]. What emerges from this is a set of five measurable and therefore interesting response functions associated with heat transfer and pressure-volume work: the constant volume and constant pressure heat capacities $c_\mathrm{V} = T(\partial S/\partial T)_\mathrm{V}$ and $c_\mathrm{p} = T(\partial S/\partial T)_\mathrm{p}$, the isothermal and the adiabatic compressibilities $\kappa_\mathrm{T} = -V^{-1}(\partial V/\partial p)_\mathrm{T}$ and $\kappa_\mathrm{S} = -V^{-1}(\partial V/\partial p)_\mathrm{S}$, and the isobaric thermal expansivity $\beta_\mathrm{p} = V^{-1}(\partial V/\partial T)_\mathrm{p}$. However, standard textbook thermodynamics dictates (on the basis of reciprocity relations and Maxwell relations) that these five quantities are not all independent, as they satisfy

$$\frac{c_\mathrm{p}}{c_\mathrm{V}} = \frac{\kappa_\mathrm{T}}{\kappa_\mathrm{S}} \qquad \text{and} \qquad c_\mathrm{p} - c_\mathrm{V} = T\frac{\beta_\mathrm{p}^2}{\kappa_\mathrm{T}}, \tag{19.5}$$

such that there are in fact only *three* independent response functions. As a consequence of the second relation together with $\kappa_\mathrm{T} > 0$, it is guaranteed that $c_\mathrm{p} > c_\mathrm{V}$ and hence from the first one that $\kappa_\mathrm{T} > \kappa_\mathrm{S}$. In the following section, we follow exactly the same thermodynamic arguments for the electrode–electrolyte system of interest here, building on the mapping of the variables as discussed in the previous section.

We consider three Legendre transformations of $F(N, Q)$, which we denote by the Gibbs-like free energy $G(N, \Psi) = F - \Psi Q$, the grand potential $\Omega(\mu, Q) = F - \mu N$, and the thermodynamic potential $Y(\mu, \Psi) = F - \mu N - \Psi Q$. Note that all these potentials depend implicitly also on T and on the geometric properties of the electrode (e.g., the volume), which renders even Y well defined, as any bonafide thermodynamic potential must depend on at least one

extensive variable. The differentials of these potentials are given by

$$\begin{aligned} dG &= \mu dN - Qd\Psi, \\ d\Omega &= -Nd\mu + \Psi dQ, \\ dY &= -Nd\mu - Qd\Psi. \end{aligned} \tag{19.6}$$

By taking "off-diagonal" second derivatives of each of the four potentials, the following four Maxwell equations can straightforwardly be derived:

$$\frac{\partial^2 F}{\partial N \partial Q} = \left(\frac{\partial \Psi}{\partial N}\right)_Q = \left(\frac{\partial \mu}{\partial Q}\right)_N ;$$

$$\frac{\partial^2 G}{\partial N \partial \Psi} = -\left(\frac{\partial Q}{\partial N}\right)_\Psi = \left(\frac{\partial \mu}{\partial \Psi}\right)_N ;$$

$$\frac{\partial^2 \Omega}{\partial \mu \partial Q} = \left(\frac{\partial \Psi}{\partial \mu}\right)_Q = -\left(\frac{\partial N}{\partial Q}\right)_\mu ; \tag{19.7}$$

$$-\frac{\partial^2 Y}{\partial \mu \partial \Psi} = \left(\frac{\partial N}{\partial \Psi}\right)_\mu = \left(\frac{\partial Q}{\partial \mu}\right)_\Psi \equiv \alpha_\Psi. \tag{19.8}$$

We note that an alternative derivation of Eq. (19.7) was recently reported, and in fact, both sides of the equation as obtained from measurements were successfully compared [Rica *et al.* (2012)], where the explicit ideal-solution relation between chemical potential and salt concentration was used. We also note that α_Ψ, as defined in Eq. (19.8), plays the same role here as the isobaric expansivity β_p in "standard" thermodynamics.

By considering "diagonal" second derivatives of the two potentials that depend on Q, we define the iso-μ and the iso-N capacitances C_N and C_μ,

$$\left(\frac{\partial^2 F}{\partial Q^2}\right)^{-1} = \left(\frac{\partial Q}{\partial \psi}\right)_\mathrm{N} \equiv C_\mathrm{N}, \tag{19.9}$$

$$\left(\frac{\partial^2 \Omega}{\partial Q^2}\right)^{-1} = \left(\frac{\partial Q}{\partial \psi}\right)_\mu \equiv C_\mu, \tag{19.10}$$

which we recognize on the basis of our mapping of variables as the analogues of the two compressibilities. Taking "diagonal" second

derivatives of the two potentials that depend on N, we find

$$\left(\frac{\partial^2 F}{\partial N^2}\right)^{-1} = \left(\frac{\partial N}{\partial \mu}\right)_Q \equiv \chi_Q$$
$$\left(\frac{\partial^2 G}{\partial N^2}\right)^{-1} = \left(\frac{\partial N}{\partial \mu}\right)_\Psi \equiv \chi_\Psi, \tag{19.11}$$

where the χ's play the role of the heat capacities.

The five quantities C_μ, C_N, χ_Ψ, χ_Q, and α_Ψ are not all independent and satisfy relations akin to the two standard relations between c_p, c_V, κ_S, κ_T, and β_p of Eq. (19.5). Standard thermodynamic manipulations involving the reciprocal and the reciprocity relations yield

$$\frac{C_\mu}{C_\mathrm{N}} = \frac{\chi_\Psi}{\chi_Q} \qquad \text{and} \qquad \chi_\Psi - \chi_Q = \frac{\alpha_\Psi^2}{C_\mu}. \tag{19.12}$$

With $C_\mu > 0$, which is a stability requirement as we will see below, we thus find that $\chi_\Psi > \chi_Q$ and $C_\mu > C_\mathrm{N}$. Note that thermodynamics does *not* provide numerical values for these quantities, as this would require a microscopic or molecular theory for the electrode–electrolyte system. The strength of these thermodynamic relations lies, however, in their generality: it is thermodynamically *guaranteed* for *any* electrode–electrolyte system that $C_\mu > C_\mathrm{N}$. It is therefore guaranteed that $\Psi(Q)$ rises faster with Q at fixed N than at fixed μ, the difference being larger if α_Ψ is larger, that is, if the electrode exhibits a larger adsorption-to-potential or charge-to-concentration response. Given that a large difference $C_\mu - C_\mathrm{N}$ gives rise to a large area in the enclosed $\Psi - Q$ plane, and hence a large amount of work during a (Carnot-like) cycle, it could be beneficial for these devices to be based on electrode–electrolyte combinations with a large α_Ψ.

19.5 Ensembles and Charge Distribution

We have been concerned with an electrode–electrolyte system of which the thermodynamics can be described by the Helmholtz free energy $F(N, Q)$. This system has an underlying microscopic Hamiltonian, denoted by $\mathcal{H}$ here, which depends on all the degrees of freedom of all the ions and all the surface charges. At temperature

T, the statistical probability of a microscopic configuration is then given by the Boltzmann weight $\exp(-\beta\mathcal{H})/Z(N, Q)$, where the normalization factor $Z(N, Q)$ is the canonical partition function and where $\beta^{-1} = k_B T$. The Helmholtz free energy, with the differential given in Eq. (19.3), follows as $F(N, Q) = -k_B T \ln Z(N, Q)$ as usual.

If we now consider the electrode–electrolyte system at fixed N and Ψ, the total electrode charge Q is a fluctuating quantity that takes values according to the thermal probability distribution

$$P(Q) = \frac{\exp(-\beta F(N, Q) + \beta\Psi Q)}{\mathcal{Z}(N, \Psi)}, \tag{19.13}$$

where the normalization factor is the Gibbs-like partition function $\mathcal{Z}(N, \Psi) = \sum_Q \exp(-\beta F(N, Q) + \beta\Psi Q) \equiv \exp(-\beta G(N, \Psi))$, with $G(N, \Psi)$ the Gibbs-like potential with a differential given by Eq. (19.6). It readily follows that the average electrode charge is given by $\langle Q\rangle_N = \sum_Q P(Q)Q = k_B T \mathcal{Z}^{-1}(\partial\mathcal{Z}/\partial\Psi)_N = -(\partial G/\partial\Psi)_N$, in agreement with the differential of Eq. (19.6). Likewise, one can write $\langle Q^2\rangle_N = (k_B T)^2 \mathcal{Z}^{-1}(\partial^2\mathcal{Z}/\partial\Psi^2)_N$, which after some elementary algebra gives rise to the following identity for the variance

$$\langle Q^2\rangle_N - \langle Q\rangle_N^2 = k_B T C_N, \tag{19.14}$$

with C_N the constant-N differential capacity defined in Eq. (19.9). One can also show that the variance of Q at fixed μ and Ψ is given by $k_B T C_\mu$, which is larger than in the iso-N case as $C_\mu > C_N$ as we have seen above. Expression (19.14) shows that the differential capacitance can be measured from the fluctuations of the electrode charge, completely equivalently to measurements of the heat capacity from energy fluctuations and the compressibility from volume fluctuations in "ordinary" (NVU) and (NVT) ensembles, respectively.

Of course, the differential capacity C (either C_N or C_μ) as well as the average electrode charge $\langle Q\rangle$ (either $\langle Q\rangle_N$ or $\langle Q\rangle_\mu$) are extensive quantities that scale linearly with the system size (in this case the electrode area). Therefore the standard deviation of the charge, $(k_B T C)^{1/2} \equiv \delta Q$, becomes much smaller than the average charge $\langle Q\rangle$ for thermodynamically large electrodes. However, our analysis can also be applied to a small (sub-)system *provided* it is large enough to be statistically independent (in fact $F(N, Q) = F(NM, QM)/M$ for $M > 1$ must hold). An example includes typical

computer simulations of 10^2–10^4 ions near electrode areas of the order of tens of nm^2. For such small electrode areas, the charge fluctuations at fixed Ψ can be significant, and in fact even be of the order of $\langle Q\rangle$. Consider, for instance, a typical carbon-based supercapacitor with an arial capacity of the order of several μF/cm^2 at a potential $\Psi = 1$ V, such that the average charge density is of the order $10^{-2}e$/nm^2. A patch of electrode of the order of 100 nm^2 contains, therefore, a charge $\langle Q\rangle \pm \delta Q$ of the order of $e \pm e$, indicating that a significant fraction of nm-sized patches carries a charge that is opposite to the average charge.

In fact, it is possible to calculate the complete charge distribution $P(Q)$ as defined in Eq. (19.13) from the formalism that we used here by expanding $F(N, Q)$ about the most probable charge Q^*, defined by $P'(Q^*) = 0$, that is, by $F'(N, Q^*) = \Psi$, where a prime denotes a derivative with respect to Q. Skipping the N-depence for notational convenience, we then find

$$\begin{aligned} P(Q) &\propto \exp(-(Q-Q^*)^2 F''(Q^*)/2 + (Q-Q^*)^3 F'''(Q^*)/6 + \dots) \\ &= \exp\left(-\frac{(Q-Q^*)^2}{2k_\mathrm{B}TC^*} + \frac{(Q-Q^*)^3 C'(Q^*)}{6k_\mathrm{B}T(C^*)^2} + \dots\right), \end{aligned} \tag{19.15}$$

where $C^* = C_\mathrm{N}(Q^*)$. On the basis of extensivity arguments, the cubic and higher order terms in the exponent can be ignored in the thermodynamic limit, such that $P(Q)$ is a Gaussian with $Q^* = \langle Q\rangle$ and a variance in accordance with Eq. (19.14). However, for smaller systems, the higher order terms may be relevant, at least in the case when $C'(Q) = (\partial C/\partial Q)_N \neq 0$, that is, when the differential capacity depends significantly on the average charge (and hence on the applied voltage) [Hatlo *et al.* (2012)]. Equation (19.15) appears to be in agreement with the findings in Ref. [Merlet *et al.* (2012)] on graphite electrodes, which give an almost Gaussian charge distribution and an essentially vanishing C'. However, the significantly skewed charge distributions as found Ref. [Merlet *et al.* (2012)] for nanoporous carbide derived carbon electrodes require some further attention, as the capacity is reported to be essentially constant, which should yield a Gaussian distribution according to the present derivation. We speculate that the individual carbon atoms of the electrode may be too small to be viewed as a statistically independent subsystem, although more research is needed to clarify this point.

19.6 Conclusion

We compare the differential of the Helmholtz free energy $F(N, Q)$ of an electrode–electrolyte system with that of the energy $U(S, V)$ of an "ordinary" thermal system, and identified the transferred heat TdS with the ion flow contribution μdN, and the mechanical work $-pdV$ with the electric work ΨdQ. By a mapping of the variables (N, μ, Q, Ψ) of present interest onto $(S, T, V, -p)$, we can define Legendre transformations of $F(N, Q)$, identify Maxwell relations, and formulate Eq. (19.12) analogous to (19.5). With this mapping, we identify the Brogioli blue engine as a Stirling heat engine, and we discuss a Carnot-like blue engine that should have the optimal conversion of mixing entropy to work. Finally, we discuss the charge distribution at fixed electrode potential and show the variance of the charge scales with the differential capacitance.

Acknowledgment

It is a pleasure to thank Niels Boon, Benjamin Rotenberg, Doriano Brogioli, Raul Rica, Francesco Mantegazza, and Maarten Biesheuvel for inspiration and useful discussions.

References

Biesheuvel, P. M., J. *Colloid Interface Sci.* **332**, 258 (2009).

Boon, N., and R. van Roij, *Mol. Phys.* **109**, 1229 (2011).

Brogioli, D., *Phys. Rev. Lett.* **103**, 058501 (2009).

Brogioli, D., R. Zhao, P. M. Biesheuvel, *Energy Environm. Sci.* **4**, 772 (2011).

Callen, H. B., *Thermodynamics and an introduction to thermostatistics*, Wiley, New York (1985).

Chmiola, J., G. Yushun, Y. Gogotsi, C. Portet, P. Simon, and P. L. Taberna, *Science* **313**, 1760 (2006).

Hatlo, M. M., R. van Roij, and L. Lue, *Europhys. Lett.* **97**, 28010 (2012).

Merlet, C., B. Rotenberg, P. A., Madden, P.-L. Taberna, P. Simon, Y. Gogotsi, and M. Salanne, *Nature Mater.* **11**, 306 (2012).

Millar, J. R. and P. Simon, *Science* **321**, 651 (2008).

Porada, S. et al., *Appl. Mater. Interfaces* **4**, 1194 (2012).

Rica, R. A., R. Ziano, D. Salerno, F. Mantegazza, and D. Brogioli, *Phys. Rev. Lett.* **109**, 156103 (2012).

Sales, B. B., M. Saakes, J. Post, C. J. N. Buisman, P. M. Biesheuvel, and H. V. M. Hamelers, *Env. Sci. Techn.* **44**, 5661 (2010).

Part IV

BIOLOGICAL SYSTEMS AND MACROMOLECULAR INTERACTIONS

Chapter 20

Cluster Phases in Colloids and Proteins

Suliman Barhoum,[a] Amit K. Agarwal,[b] and Anand Yethiraj[a]

[a] *Department of Physics and Physical Oceanography, Memorial University St. John's, Newfoundland, Canada*

[b] *Instruments Research and Development Establishment, Dehradun, Uttarakhand, India*

ayethiraj@mun.ca

20.1 Introduction

Since the simulation of the fluid-solid transition in hard spheres (HS) [Alder and Wainwright (1962)], there has been a long-standing question, with answers of progressively increasing complexity: what interactions, in addition to excluded volume, does it take to obtain more complex phases and phase transitions in atomic and molecular systems? Colloidal suspensions have proved to be the ideal experimental testing grounds for addressing this question, because one can control interparticle interactions by both chemical and physical means [Gast and Russel (1998); Yethiraj (2007)].

Different colloidal solid phases have been discovered, even in monodisperse colloids, with carefully controlled interparticle interactions. This includes close-packed fcc or random hexagonal close packed (rhcp) [Kose and Hachisu (1974); Pusey and van Megen

Electrostatics of Soft and Disordered Matter
Edited by David Dean, Jure Dobnikar, Ali Naji, and Rudolf Podgornik

ISBN 978-981-4411-85-1 (Hardcover), 978-981-4411-86-8 (eBook)
www.panstanford.com

(1986)], body-centered cubic [Sirota *et al.* (1989)], body-centered tetragonal [Tao and Sun (1991); Dassanayake *et al.* (2000)], and body-centered orthorhombic [Yethiraj and van Blaaderen (2003)]. For suspensions with more than one species of colloids, the phase behavior is even richer [Bartlett and Pusey (1993); Leunissen *et al.* (2005); Bartlett and Campbell (2005); Shevchenko *et al.* (2006); Talapin *et al.* (2009)]. Colloidal suspensions have been also used to study glassy behavior in the presence of competing (short-range) attractive and (long-range) repulsive interactions [Pham *et al.* (2002); Puertas *et al.* (2002)].

The liquid phase results from a sensitive balance between excluded volume or other forms of repulsive interactions on one hand, and attractive interactions on the other hand. A feature of the gas-liquid phase transition is bulk phase separation of the low-density (gas) and the high-density (liquid) states.

In the presence of competing interactions on different length-scales, for example, a short-ranged attraction and a long-ranged repulsion, a stable non-crystalline phase of finite-sized clusters is possible [Groenewold and Kegel (2001)]. The existence of clusters in equilibrium has been showcased in a recent collection of review articles on cluster phases [Dinsmore *et al.* (2011)]. A class of cluster phases that can form with only short-range interactions are micellar phases. Micelles form due to geometric constraints that arise from amphiphilicity. These micelles can either be spherical and of fixed size, or cylindrical and of fixed diameter but variable length. Due to this geometric constraint, bulk phase separation is replaced by "micro phase separation."

The cluster phases of interest in this overview occur due to a sensitive balance of attractive and repulsive interactions. Because of the absence of the geometric constraint, cluster sizes can be even smaller than for micelles. They have been reported in colloidal systems with electrostatic repulsions and depletion-induced attractions, as well as in globular proteins. It is shown here that colloids interacting *via* the electric field induced dipolar interaction also form stable cluster phases, with percolating crystalline clusters at high densities, non-percolating crystalline cluster islands at intermediate densities, and a re-entrant percolation at low densities of clusters whose internal lateral structure is disordered. The external field

controllability of dipolar interactions enables the study of clustering in the presence of an externally switchable control parameter.

The existence of colloid-like cluster phases in proteins, arising again from competition between short-range attractions and long-range repulsions, has been studied *via* scattering experiments, and is the source of much discussion in the literature. Experiments that use diffusion and relaxation NMR, which confirm the existence of a cluster phase in protein solutions, are discussed in context with previous experiments.

20.2 Clustering in Colloids

20.2.1 *Electrostatics and Depletion Attractions*

Binary colloids and colloid polymer mixtures are ideal systems to study and understand gelation in molecular liquids [Aarts *et al.* (2004); Aarts and Lekkerkerker (2004)]. Similar to molecular liquids, these systems also exhibit spinodal decomposition; this has been studied both theoretically and experimentally [Lekkerkerker *et al.* (1992); Ilett *et al.* (1995); de Hoog *et al.* (2001)].

The presence of smaller particles (or nonadsorbing polymer chains) in between larger particles induces a depletion attraction between the larger colloids [Oosawa and Asakura (1954)]. This interaction between the larger colloids is purely entropic in nature and has been tested *via* comparison of experimental and predicted phase diagrams [Kaplan *et al.* (1994); Ramakrishnan *et al.* (2002)] as well as directly measured using optical tweezers [Crocker *et al.* (1999)] and by total internal reflection microscopy [Rudhardt *et al.* (1998)]. Depletion forces are believed to play a significant role in many biological organization processes, ranging from protein folding to DNA compaction [Marenduzzo *et al.* (2006); Kojima *et al.* (2006)].

The phase diagram of colloid–polymer mixtures has been reported for nanoparticle colloids in which the polymer-colloid size ratio $\xi = R_g/R_c$ is about 0.5. In this case, there is a coexistence region between a colloid-rich liquid phase and a colloid poor gas phase (Fig. 20.1(a)). When ξ is near unity, gas, liquid, and crystal

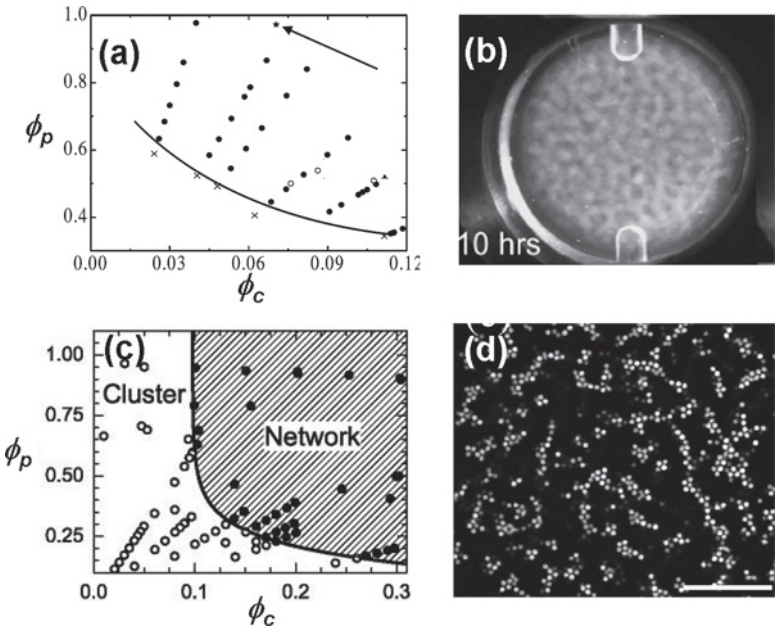

Figure 20.1 (a) Experimental phase diagram for polymer–colloid mixtures as a function of volume fraction of colloids (ϕ_p) and polymer (ϕ_c) for polymer-colloid size ratio (ξ) close to 0.5 [Aarts and Lekkerkerker (2004)]. Liquid–gas phase separation occurs above the solid line, while below it is the one-phase region. The arrow indicates a state point where the system gelled at high ϕ_p. Reprinted with permission from D. G. A. L. Aarts and H. N. W. Lekkerkerker in *J. Phys.: Cond. Mat.* **16** S4231 (2004). (b) Colloid–polymer mixture ($\xi = 0.63$) undergoing spinodal decomposition in micro gravity [Bailey *et al.* (2007)]. A sample cell of 2 cm diameter is shown after 10 h of homogenization. Reprinted with permission from A. E. Bailey *et al.*, *Phys. Rev. Lett.* **99**, 205701 (2007). Copyright (2007) by the American Physical Society. http://prl.aps.org/abstract/PRL/v99/i20/e205701. (c) Phase diagram for colloid-polymer mixture ($\xi \approx 0.11$). A well-defined boundary between the cluster fluid and network phase can be seen [Campbell *et al.* (2005)]. (d) Confocal microscope image of network phase in colloid–polymer mixture [Campbell *et al.* (2005)]. The scale bar is 20 μm. (c) and (d) reprinted with permission from A. I. Campbell *et al.*, *Phys. Rev. Lett.* **94**, 208301 (2005). Copyright (2005) by the American Physical Society. http://prl.aps.org/abstract/PRL/v94/i20/e208301.

phases are expected; however, at highest polymer concentrations, a gel is formed instead, perhaps due to polydispersity in the colloidal particle size [Aarts and Lekkerkerker (2004)].

At higher particle densities (>1 wt%), the yield stress of a gel can compete with gravitational stress. Gravitational stress can induce the collapse of a colloidal gel [Bartlett *et al.* (2012)]. The phase separation of a colloid–polymer mixture was studied in the absence of gravity in an experiment done at the International Space Station [Bailey *et al.* (2007)]. An interconnected domain structure was formed that coarsened with time: Fig. 20.1(b) shows the entire sample of 2 cm extent. In time-averaged zero-gravity conditions obtained on earth by slowly rotating the colloid polymer mixtures [Masri *et al.* (2012)], the average cluster size R was found to grow with the overall volume fraction of the colloids ϕ: $R \propto \phi^{1/3}$. Sedimentation increases the local colloid volume fraction, leading to gel formation, while slowly rotating a suspension of opposite-charged colloids led to stable clusters, avoiding gel formation.

When the size ratio ξ is much less than 1, effective attractions induced between the colloidal particles give rise to two different dynamically arrested states. At higher densities, a glass transition was predicted, and at moderate densities, gelation was predicted to take place [Puertas *et al.* (2002)] consistent with mode coupling theory (MCT). The existence of two qualitatively distinct kind of glasses, dominated by repulsion and attraction, respectively, was indeed observed in experiment with $\xi = 0.08$ [Pham *et al.* (2002)].

The presence of long-range repulsion along with the depletion interaction leads to a stable cluster phase at low volume fraction [Stradner *et al.* (2004a); Campbell *et al.* (2005)]. At higher volume fractions, a percolated network is formed followed by arrested gelation [Campbell *et al.* (2005)] as shown in Fig. 20.1(c) and (d). Density fluctuations triggered by spinodal decomposition in colloid polymer mixtures also give rise to dynamically arrested spanning clusters leading to gelation [Lu *et al.* (2008)]. Simulations [Sciortino *et al.* (2005)] suggest that the formation of low-density arrested states can be modeled as a glass transition, where clusters (as opposed to particles) are trapped in cages generated by the long-range repulsions. Tuning the long-range repulsions by control of

the Debye length, phase separation was found to lead to percolated network structures and gel formation [Tanaka *et al.* (2005)].

20.2.2 *Dipolar Interactions*

Attractions (of any sort) are expected to give rise to a regime in phase space in which gas and liquid phases can coexist, along with a critical point that separates a region where there are distinct gas and liquid states from a region where there is only a fluid state.

In the presence of a uniform electric field of amplitude E_0, two dielectric spheres of radius a and dielectric constant $\epsilon_{\rm p}$ that are suspended in a fluid (dielectric constant $\epsilon_{\rm f}$) have an anisotropic interparticle interaction potential of the form

$$\frac{U_{\rm dipolar}(r)}{k_{\rm B}T} = -\frac{\Lambda}{(r/2a)^3}\frac{3\cos^2\theta - 1}{2} \tag{20.1}$$

where $\Lambda = \pi\epsilon_0\epsilon_{\rm f}\beta^2 a^6 E_0^2/2k_{\rm B}T$ is the dipolar energy in units of $k_{\rm B}T$, $\beta = (\epsilon_{\rm p}-\epsilon_{\rm f})/(\epsilon_{\rm p}+2\epsilon_{\rm f})$, and (r, θ) are the radial and angular positions of one sphere with respect to the other.

In dipolar colloids, the existence of a gas-liquid transition has been a matter of debate. It was found [van Leeuwen and Smit (1993)] that chain-like dipolar spheres showed no propensity toward bulk phase separation into liquid and vapor phases. On the contrary, it was shown [Stevens and Grest (1995)] that phase coexistence between dense and dilute regions did exist. It is not clear, given the system size, whether this is truly bulk phase coexistence or a form of cluster phase.

The stability of finite size clusters in dipolar colloids is seen both in experiment and simulation. At high field strengths, all structures are composed of strings, and string–string positioning along the field direction is either stacked or staggered. The corresponding interaction potential between two strings is purely repulsive for stacked strings (shown in Figure 20.2(a)), but for staggered strings, it is attractive at short distances and weakly repulsive at intermediate distances (shown in Figure 20.2(b)). For large Λ, string undulations are unimportant, and the problem may be treated as quasi-two-dimensional. Shown in Figure 20.2 (c)–(e) are two-dimensional snapshots from experiments (similar to those reported

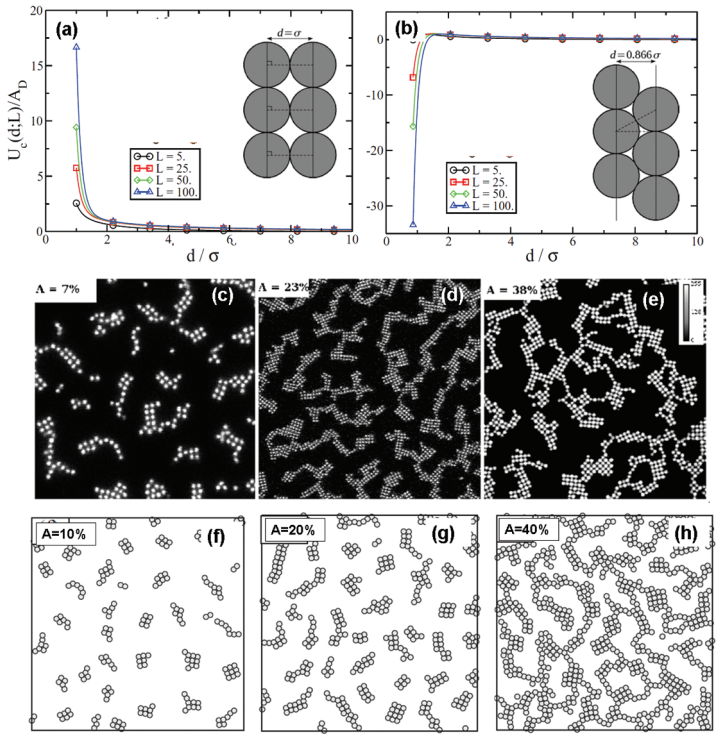

Figure 20.2 (a, b) Chain–chain interaction energy as a function of distance (d) for different chain lengths (L). (a) For stacked configuration and (b) for staggered configuration. Insets show the stacked and staggered configurations of chains, respectively. (c,e) Experimental 2-D snapshots of colloidal systems at different effective area fraction. Particle diameter 2 μm. (f)–(h) 2-D simulation results at comparable area fractions. (a,b,f-h). Reprinted with permission from A. M. Almudallal and I. Saika-Voivod, *Phys. Rev. E* **84**, 011402 (2011). Copyright (2011) by the American Physical Society. http://pre.aps.org/abstract/PRE/v84/i1/e011402.

in [Yethiraj and van Blaaderen (2003)]) at different effective area fractions. Each configuration was taken after equilibrating at a given field for a long time; typical field strengths are of order $E_0 = 1\,\mathrm{V/\mu m}$. Figure 20.2(f)–(h) show the two-dimensional Monte–Carlo simulations based on string–string interaction potentials of the form shown in Figure 20.2(a)–(b). It can be seen that the equilibrium cluster size decreases with decreasing concentration in

both cases [Almudallal and Saika-Voivod (2011)]. Although one does not expect quantitative agreement with a two-dimensional model, the qualitative trends in experiment and simulation are very similar.

At low effective temperatures (high Λ) and low packing, a cluster phase is stable in both colloids interacting with dipolar interactions [Almudallal and Saika-Voivod (2011)] and with competing electrostatic repulsive and depletion attractive interactions [Toledano *et al.* (2009)]. It is reasonable to presume that the gas–liquid critical point at lower temperatures is replaced by a region in which a cluster phase is stable. In the case of depletion, there is a critical point at finite temperatures when there are no electrostatic repulsions. However, upon increasing the strength of long-range repulsions, the tendency toward macroscopic phase separation is suppressed [Toledano *et al.* (2009)].

There is an experimental surprise lurking at low densities. As packing fraction is lowered below 2%, experiments report a new phase [Agarwal and Yethiraj (2009)] wherein the particle-rich regions become disordered (Figure 20.3(a)). These disordered

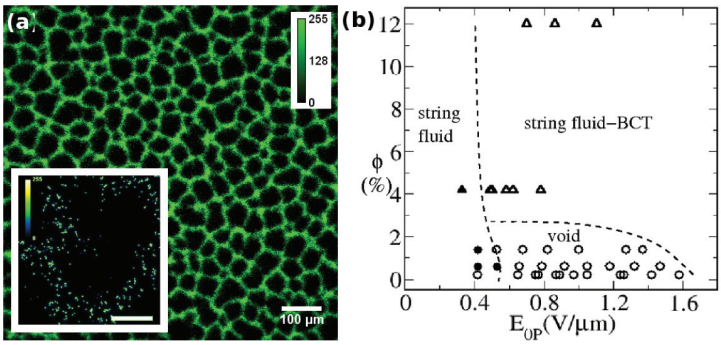

Figure 20.3 (a) Percolating particulate network structure surrounding particle-free voids at ultralow volume fraction ($\phi = 0.6\%$). Inset: The local particle organization on the single void scale (scale bar in inset is 25 μm) is disordered [Agarwal and Yethiraj (2009)]. (b) Phase diagram shows a stable void phase for a range of field strengths and for volume fractions less than $\phi = 2\%$: empty circles, void phase; empty triangles, string fluid-BCT coexistence; filled symbols, string fluid. (a) and (b) reprinted with permission from A. K. Agarwal and A. Yethiraj, *Phys. Rev. Lett.* **102**, 198301 (2009). Copyright (2009) by the American Physical Society. http://prl.aps.org/abstract/PRL/v102/i19/e198301

clusters are more diffuse than the crystalline ones. Associated with this order-disorder transition is a re-entrant percolation of the particle-rich regions to form elongated clusters that form an ultra-low density network. These structures are stable over a range of field strengths and a range of packing fractions below 2% (Figure 20.3(b)). Thus far, simulations carried out [Almudallal and Saika-Voivod (2011); Richardi and Weis (2011); Park and Saintillan (2011)] have failed to observe this void phase. It is feasible that the experiments signal a departure from the dipolar approximation at low densities.

20.3 Cluster Phases in Proteins

Proteins are an essential component of the crowded environment of biological cells and organisms [Campbell *et al.* (2009); Bryant (2006); Ellis (2001)], and play a crucial role in different metabolic, structural, and mechanical functions as long as they are in their native folded state [Voet *et al.* (2008)]. When proteins misfold, they can form insoluble fibrous ("amyloid") aggregates [Schnabel (2010)] that play a significant role in so-called "conformational" diseases [Kopito and Ron (2000); Aguzzi and O'Connor (2010)]. Consequently, the question of how one can achieve, in crowded solutions, the conformational stability that is required to maintain biological activity is a major challenge of contemporary interest [Johnston *et al.* (2012); Ball (2012)]. To this end, it is important to have a deep understanding of the phase behavior of proteins in concentrated aqueous media.

A balance between short-range attraction and long-range repulsion can lead to finite-sized clusters [Groenewold and Kegel (2004)], whose size can be controlled by pH and is of fundamental importance in understanding the nucleation and growth of amyloid aggregates [Sahoo *et al.* (2009)]. Protein solutions have been shown to exhibit metastable liquid-liquid phase separation [Muschol and Rosenberger (1997)], sometimes followed by crystallization or irreversible precipitation [Price *et al.* (2001)]. Protein clusters in equilibrium were reported in small angle neutron scattering (SANS) and small angle X-ray scattering (SAXS) experiments on aqueous

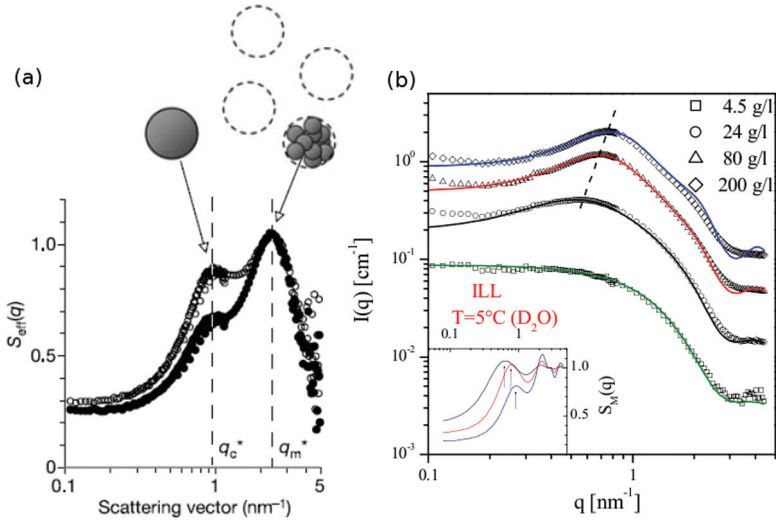

Figure 20.4 (a) The effective structure factor $S_{\text{eff}}(\text{q})$ for aqueous lysozyme solutions with concentrations $C = 254$ mg/ml (filled symbols) and $C = 169$ mg/ml (open symbols) at $T = 25^{\circ}\text{C}$ as recorded from SANS [Stradner *et al.* (2004b)]. (b) The computed structure factor $S_{\text{M}}(\text{q})$ from the scattering intensity as obtained from three SANS/SAXS instruments. The arrows indicate the position of the low-q peak at 5°C [Shukla *et al.* (2008)]. Symbols are experimental data, while continuous lines are a fit model. A. Shukla *et al.*, *PNAS*, **105**, 5075 (2008). Copyright 2008, National Academy of Sciences, U.S.A.

solutions of the globular protein lysozyme using D_2O as solvent and buffered with 20 mM HEPES [Stradner *et al.* (2004b)]. Stradner et al. observed two peaks in the effective structure factor $S_{\text{eff}}(\text{q})$, with the low-q peak (q_{c}^*) identified as the cluster-cluster correlation peak and the high-q peak (q_{m}^*) identified as the monomer-monomer correlation peak in a single cluster (Figure 20.4a). The cluster peak interpretation is that, over a range of protein concentrations, the cluster-cluster separation remains unchanged, although the number of proteins within a cluster increases. Similar experiments carried out independently [Shukla *et al.* (2008)] reported results that were not in agreement. In this work, the low-q peak showed a dependence on the lysozyme volume fraction (Figure 20.4b) and was thus interpreted as distinct from a cluster peak. Although Shukla

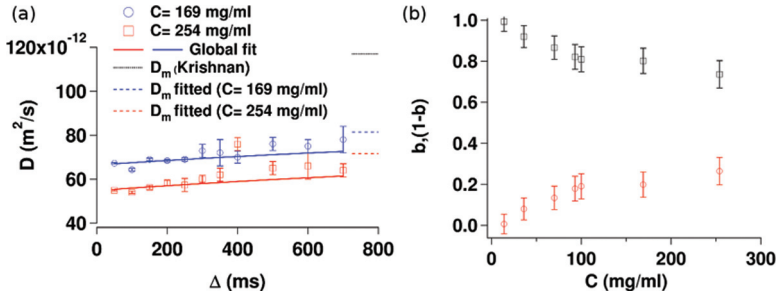

Figure 20.5 (a) Self-diffusion coefficient D versus diffusion time Δ for lysozyme in aqueous solution with concentration $C = 169$ mg/ml ($\Phi = 0.14$) and $C =$ v254 mg/ml ($\Phi = 0.22$) at $T = 25\ ^{\circ}\mathrm{C}$. Dotted lines to the right show fitted values of D_{m}. (b) The fraction b and $(1 - \mathrm{b})$ of lysozyme in monomeric (black empty squares) and aggregate form (red empty circles) respectively, versus C [Barhoum and Yethiraj (2010)]. Reprinted with permission from S. Barhoum and A. Yethiraj. *J. Phys. Chem. B*, **114**, 17062 (2010). Copyright 2010, American Chemical Society.

et al. modeled their results using a two-Yukawa potential model, independent simulations using the same interaction potential indicated coexistence of individual proteins and clusters [Kowalczyk *et al.* (2011)].

NMR diffusometry and relaxometry measurements on concentrated lysozyme solutions in D_2O and 20 mM HEPES buffer [Barhoum and Yethiraj (2010)] provide an independent test. These results presented quantitative evidence for the existence of an equilibrium cluster phase. The diffusion coefficient in NMR is obtained from an exponential fit to the attenuation, due to molecular diffusion, of a pulsed-field gradient stimulated echo signal [Price (1997)]. The signal attenuation associated with lysozyme peaks was monoexponential. Figure 20.5(a) shows the variation of lysozyme self-diffusion coefficient D for 169 and 254 mg/ml lysozyme samples as function of the diffusion time Δ. If the observed diffusion coefficient arose from a single species (e.g., monomers), then D would be independent of Δ. On the contrary, in the limit of short-time self-diffusion, one would expect to see a decrease not an increase in D. Indeed, in the NMR experiments, ($\Delta > 10$ ms) one is accessing long-time self diffusion and D should be independent of Δ. Instead, the lysozyme self-diffusion coefficient D showed an *increase*

as a function of the diffusion time. These observations are consistent with the presence of two species (monomers and aggregates) with different relaxation rates $R_{1,\mathrm{m}}$ and $R_{1,\mathrm{a}}$, such that the observed self-diffusion coefficient is a relaxation-weighted average of monomer and aggregate diffusion coefficient, D_{m} and D_{a} respectively [Price *et al.* (1999, 2001)],

$$D = \frac{bD_m \exp\left(-R_{1,\mathrm{m}}\Delta\right) + (1-b)D_{\mathrm{a}} \exp\left(-R_{1,\mathrm{a}}\Delta\right)}{b \exp\left(-R_{1,\mathrm{m}}\Delta\right) + (1-b) \exp\left(-R_{1,\mathrm{a}}\Delta\right)} \tag{20.2}$$

The observed relaxation rates are phenomenologically fit to contributions from monomer and aggregate, $R_1 = bR_{1,\mathrm{m}} + (1-b)R_{1,\mathrm{a}}$. The results in Figure 20.5(a) are globally fit to equation 20.2, and the monomer diffusion coefficient D_{m} is obtained with relatively small uncertainty. Using the observed longitudinal relaxation rates R_1, as well as the fitted rates $R_{1,\mathrm{m}}$ and $R_{1,\mathrm{a}}$, the fraction b and $(1-b)$ of lysozyme in free monomer form and in aggregate state, respectively, (figure 20.5(b)) are obtained for a range of lysozyme concentrations. NMR measurements validate the existence of the cluster phase; the fraction of monomers in the cluster state can be as high as 25%.

Figure 20.6(a) shows the lysozyme monomer diffusion coefficient D_{m}/D_0, normalized with respect to the theoretically reported monomer self-diffusion coefficient $D_0 = D_{\mathrm{m}}$(Krishnan), which is $11.7 \times 10^{-11}\ \mathrm{m}^2/\mathrm{s}$ [Price *et al.* (1999)]. The functional dependence of D_{m}/D_0 on Φ shows reasonable agreement with a model [Han and Herzfeld (1993)] that considers crowding effects on the self-diffusion of a biological molecule. We compare these results with neutron spin echo (NSE) experiments [Porcar *et al.* (2010); Liu *et al.* (2011); Falus *et al.* (2012)] as well as other NMR diffusion experiments [Liu *et al.* (2011)] (Figure 20.6(b)). NMR diffusometry is used to measure the long-time self-diffusion coefficient, whereas NSE is used to measure the collective diffusion D_{C} over a range of scattering vectors, where the asymptotic value of D_{C} at high value of scattering vectors is the short-time self-diffusion coefficient. For $\phi < 0.15$, the scaled diffusion coefficient results of Barhoum et al. (Figure 20.6(a)) agree with both the other diffusion NMR results and the NSE results (Figure 20.6(b)). For $\phi > 0.15$, however, there are quantitative discrepancies. Most important, the monomer diffusion coefficients of Barhoum et al. are at odds with those of Liu et al. and consistently higher in value. One possible source of the discrepancy

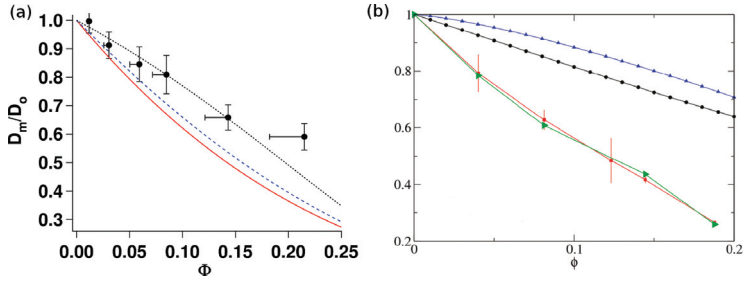

Figure 20.6 (a) Scaled long-time self-diffusion coefficient of lysozyme monomer [Barhoum and Yethiraj (2010)] D_m/D_0 versus volume fraction Φ, plotted alongside different theoretical curves: red [Medina-Noyola (1988); van Blaaderen *et al.* (1992)], blue dashed [Tokuyama and Oppenheim (1994)], and black dotted [Han and Herzfeld (1993)]) lines. Reprinted with permission from S. Barhoum and A. Yethiraj. *J. Phys. Chem. B* **114**, 17062 (2010). Copyright 2010, American Chemical Society. (b) Normalized long-time self-diffusion coefficient (green triangles) equals the short-time self-diffusion coefficient (red squares) [Liu *et al.* (2011)]: Surprising and at odds with the NMR measurements in (a). Reprinted with permission from Liu *et al.*, *J. Phys. Chem. B* **115**. 7338 (2011). Copyright 2011, American Chemical Society.

is a difference in sample preparation. Although Barhoum et al. followed the protocol for sample preparation in the first scattering experiments [Stradner *et al.* (2004b); Shukla *et al.* (2008)], Liu et al. prepared their samples by directly dissolving lysozyme powder into buffer solution. Although there is not yet conclusive resolution of these discrepancies, results are expected to depend sensitively on the electrostatic environment.

20.4 Conclusion

Cluster phases are a generalization of the liquid state, and occur in a diverse range of systems in which there is a sensitive balance between short-range (attractive) and longer range (repulsive) interactions. These phase are of import not only in the classic case of depletion and electrostatics but also for colloids interacting *via* dipolar interactions (where clusters replace bulk phase separation), as well as concentrated globular protein solutions.

References

Aarts, D. G. A. L. and Lekkerkerker, H. N. W. (2004). Confocal scanning laser microscopy on fluid-fluid demixing colloid-polymer mixtures, *Journal of Physics: Condensed Matter* **16**, pp. S4231–S4242.

Aarts, D. G. A. L., Schmidt, M., and Lekkerkerker, H. N. W. (2004). Direct visual observation of thermal capillary waves, *Science* **304**, pp. 847–850.

Agarwal, A. K. and Yethiraj, A. (2009). Low-density ordered phase in brownian dipolar colloidal suspensions, *Physical Review Letters* **102**, p. 198301.

Aguzzi, A. and O'Connor, T. (2010). Protein aggregation diseases: pathogenicity and therapeutic perspectives, *Nature Reviews Drug Discovery* **9**, pp. 237–248.

Alder, B. J. and Wainwright, T. E. (1962). Phase transition in elastic disks, *Physical Review* **127**, pp. 359–361.

Almudallal, A. M. and Saika-Voivod, I. (2011). Simulations of a two-dimensional model for colloids in a uniaxial electric field, *Physical Review E* **84**, p. 11402.

Bailey, A. E., Poon, W. C. K., Christianson, R. J., Schofield, A. B., Gasser, U., Prasad, V., *et al.* (2007). Spinodal decomposition in a model colloid-polymer mixture in microgravity, *Physical Review Letters* **99**, p. 205701.

Ball, P. (2012). Material witness: Cluster control, *Nature Materials* **11**, pp. 185–185.

Barhoum, S. and Yethiraj, A. (2010). NMR detection of an equilibrium phase consisting of monomers and clusters in concentrated lysozyme solutions, *The Journal of Physical Chemistry B* **114**, pp. 17062–17067.

Bartlett, P. and Campbell, A. I. (2005). Three-dimensional binary superlattices of oppositely charged colloids, *Physical Review Letters* **95**, 12.

Bartlett, P. and Pusey, P. N. (1993). Freezing of binary mixtures of hard-sphere colloids, *Physica A* **194**, pp. 415–423.

Bartlett, P., Teece, L. J., and Faers, M. A. (2012). Sudden collapse of a colloidal gel, *Physical Review E* **85**, p. 021404.

Bryant, J. E. (2006). In-cell protein dynamics, *Molecular BioSystems* **407**, pp. 406–410.

Campbell, A. I., Anderson, V. J., van Duijneveldt, J. S., and Bartlett, P. (2005). Dynamical arrest in attractive colloids: The effect of long-range repulsion, *Physical Review Letters* **94**, p. 208301.

Campbell, N. A., Reece, J. B., Urry, L. A., Cain, M. L., Wasserman, S. A., Minorsky, P. V., *et al.* (2009). *Biology*, 8th edn. (Pearson Education Inc, San Francisco).

Crocker, J. C., Matteo, J. A., Dinsmore, A. D., and Yodh, A. G. (1999). Entropic attraction and repulsion in binary colloids probed with a line optical tweezer, *Physical Review Letters* **82**, pp. 4352–4355.

Dassanayake, U., Fraden, S., and van Blaaderen, A. (2000). Structure of electrorheological fluids, *The Journal of Chemical Physics* **112**, pp. 3851–3858.

de Hoog, E. H. A., Kegel, W. K., van Blaaderen, A., and Lekkerkerker, H. N. W. (2001). Direct observation of crystallization and aggregation in a phase-separatingcolloid-polymer suspension, *Physical Review E* **64**, p. 021407.

Dinsmore, A. D., Dubin, P. L., and Grason, G. M. (2011). Clustering in complex fluids, *The Journal of Physical Chemistry B* **115**, pp. 7173–7174.

Ellis, R. J. (2001). Macromolecular crowding: Obvious but underappreciated, *Trends in Biochemical Sciences* **26**, pp. 597–604.

Falus, P., Porcar, L., Fratini, E., Chen, W.-R., Faraone, A., Hong, K., *et al.* (2012). Distinguishing the monomer to cluster phase transition in concentrated lysozyme solutions by studying the temperaturedependence of the short-time dynamics, *Journal of physics: Condensed matter* **24**, p. 064114.

Gast, A. and Russel, W. (1998). Simple ordering in complex fluids - Colloidal particles suspended in solution provide intriguing models for studying phase transitions, *Physics Today* **51**, pp. 24–30.

Groenewold, J. and Kegel, W. (2004). Colloidal cluster phases, gelation and nuclear matter, *Journal of Physics: Condensed Matter* **16**, pp. S4877–S4886.

Groenewold, J. and Kegel, W. K. (2001). Anomalously large equilibrium clusters of colloids, *The Journal of Physical Chemistry B* **105**, pp. 11702–11709.

Han, J. and Herzfeld, J. (1993). Macromolecular diffusion in crowded solutions, *Biophysical Journal* **65**, pp. 1155–1161.

Ilett, S. M., Orrock, A., Poon, W. C. K., and Pusey, P. N. (1995). Phase behavior of a model colloid-polymer mixture, *Physical Review E* **51**, pp. 1344–1352.

Johnston, K. P., Maynard, J. A., Truskett, T. M., Borwankar, A. U., Miller, M. A., Wilson, B. K., *et al.* (2012). Concentrated dispersions of equilibrium

protein nanoclusters that reversibly dissociate into active monomers, *ACS Nano* **6**, pp. 1357–1369.

Kaplan, P. D., Rouke, J. L., and Yodh, A. G. (1994). Entropically driven surface phase separation in binary colloidal mixtures, *Physical Review Letters* **72**, pp. 582–585.

Kojima, M., Kubo, K., and Yoshikawa, K. (2006). Elongation / compaction of giant dna caused by depletion interaction with a flexible polymer, *The Journal of Chemical Physics* **124**, pp. 24902–24904.

Kopito, R. R. and Ron, D. (2000). Conformational disease, *Nature Cell Biology* **2**, pp. E207–E209.

Kose, A. and Hachisu, S. (1974). Kirkwood-Alder Transition In Monodisperse Latexes. 1. Non-Aqueous Systems, *Journal of Colloid and Interface Science* **46**, 3, pp. 460–469.

Kowalczyk, P., Ciach, A., Gauden, P., and Terzyk, A. (2011). Equilibrium clusters in concentrated lysozyme protein solutions, *Journal of Colloid and Interface Science* **363**, pp. 579–584.

Lekkerkerker, H. N. W., Poon, W. C. K., Pusey, P. N., Stroobants, A., and Warren, P. B. (1992). Phase-behavior of colloid plus polymer mixtures, *Europhysics Letters* **20**, pp. 559–564.

Leunissen, M., Christova, C., Hynninen, A., Royall, C., Campbell, A., Imhof, A., *et al.* (2005). Ionic colloidal crystals of oppositely charged particles, *Nature* **437**, 7056, pp. 235–240.

Liu, Y., Porcar, L., Chen, J., Chen, W.-R., Falus, P., Faraone, A., *et al.* (2011). Lysozyme protein solution with an intermediate range order structure, *The Journal of Physical Chemistry B* **115**, pp. 7238–7247.

Lu, P. J., Zaccarelli, E., Ciulla, F., Schofield, A. B., Sciortino, F., and Weitz, D. A. (2008). Gelation of particles with short-range attraction, *Nature* **453**, pp. 499–U4.

Marenduzzo, D., Finan, K., and Cook, P. R. (2006). The depletion attraction: An underappreciated force driving cellular organization, *The Journal of Cell Biology* **175**, pp. 681–686.

Masri, D. E., Vissers, T., Badaire, S., Stiefelhagen, J. C. P., Vutukuri, H. R., Helfferich, P., *et al.* (2012). A qualitative confocal microscopy study on a range of colloidal processes by simulating microgravity conditions through slow rotations, *Soft Matter* **8**, pp. 6979–6990.

Medina-Noyola, M. (1988). Long-time self-diffusion in concentrated colloidal dispersions, *Physical Review Letters* **60**, pp. 2705–2708.

Muschol, M. and Rosenberger, F. (1997). Liquid-liquid phase separation in supersaturated lysozyme solutions and associated precipitate formation/crystallization, *The Journal of Chemical Physics* **107**, pp. 1953–1962.

Oosawa, F. and Asakura, S. (1954). Surface tension of high-polymer solutions, *The Journal of Chemical Physics* **22**, p. 1255.

Park, J. S. and Saintillan, D. (2011). Electric-field-induced ordering and pattern formation in colloidal suspensions, *Physical Review E* **83**, p. 041409.

Pham, K. N., Puertas, A. M., Bergenholtz, J., S. U. Egelhaaf, A. M., Pusey, P. N., Schofield, A. B., *et al.* (2002). Multiple glassy states in a simple model system, *Science* , pp. 104–106.

Porcar, L., Falus, P., Chen, W.-R., Faraone, A., Fratini, E., Hong, K., *et al.* (2010). Formation of the dynamic clusters in concentrated lysozyme protein solutions, *The Journal of Physical Chemistry Letters* **1**, pp. 126–129.

Price, W. S. (1997). Pulsed-field gradient nuclear magnetic resonance as a tool for studying translational diffusion: Part I. basic theory, *Concepts in Magnetic Resonance* **9**, pp. 299–336.

Price, W. S., Tsuchiya, F., and Arata, Y. (1999). Lysozyme aggregation and solution properties studied using PGSENMR diffusion measurements, *Journal of the American Chemical Society* **121**, pp. 11503–11512.

Price, W. S., Tsuchiya, F., and Arata, Y. (2001). Time dependence of aggregation in crystallizing lysozyme solutions probed using NMR self-diffusion measurements. *Biophysical Journal* **80**, pp. 1585–1590.

Puertas, A. M., Fuchs, M., and Cates, M. E. (2002). Comparative simulation study of colloidal gels and glasses, *Physical Review Letters* **88**, p. 098301.

Pusey, P. N. and van Megen, W. (1986). Phase-Behavior of concentrated suspensions of nearly hard colloidal spheres, *Nature* **320**, pp. 340–342.

Ramakrishnan, S., Fuchs, M., Schweizer, K. S., and Zukoski, C. F. (2002). Entropy driven phase transitions in colloid-polymer suspensions:tests of depletion theories, *The Journal of Chemical Physics* **116**, pp. 2201–2212.

Richardi, J. and Weis, J. J. (2011). Low density mesostructures of confined dipolar particles in an external field, *The Journal of Chemical Physics* **135**, p. 124502.

Rudhardt, D., Bechinger, C. and Leiderer, P. (1998). Direct measurement of depletion potentials in mixtures of colloids and nonionic polymers, *Physical Review Letters* **81**, pp. 1330–1333.

Sahoo, B., Nag, S., Sengupta, P., and Maiti, S. (2009). On the Stability of the soluble amyloid aggregates, *Biophysical Journal* **97**, pp. 1454–1460.

Schnabel, J. (2010). Protein folding: The dark side of proteins, *Nature* **464**, pp. 828–829.

Sciortino, F., Tartaglia, P., and Zaccarelli, E. (2005). One-dimensional cluster growth and branching gels in colloidal systems withshort-range depletion attraction and screened electrostatic repulsion, *The Journal of Physical Chemistry B* **109**, pp. 21942–21953.

Shevchenko, E., Talapin, D., Kotov, N., O'Brien, S., and Murray, C. (2006). Structural diversity in binary nanoparticle superlattices, *Nature* **439**, 7072, pp. 55–59.

Shukla, A., Mylonas, E., Cola, E. D., Finet, S., Timmins, P., Narayanan, T., *et al.* (2008). Absence of equilibrium cluster phase in concentrated lysozyme solutions, *Proceedings of the National Academy of Sciences* **105**, pp. 5075–5080.

Sirota, E. B., Ou-Yang, H. D., Sinha, S. K., Chaikin, P. M., Axe, J. D., and Fujii, Y. (1989). Complete phase diagram of a charged colloidal system: A synchrotron X-ray scattering study, *Physical Review Letters* **62**, pp. 1524–1527.

Stevens, M. J. and Grest, G. S. (1995). Structure of soft-sphere dipolar fluids, *Physical Review E* **51**, pp. 5962–5975.

Stradner, A., Sedgwick, H., Cardinaux, F., Poon, W. C. K., Egelhaaf, S. U., and Schurtenberger, P. (2004a). Equilibrium cluster formation in concentrated protein solution and colloids, *Nature* **432**, pp. 492–495.

Stradner, A., Sedgwick, H., Cardinaux, F., Poon, W. C. K., Egelhaaf, S. U., and Schurtenberger, P. (2004b). Equilibrium cluster formation in concentrated protein solutions and colloids, *Nature* **432**, pp. 492–495.

Talapin, D. V., Shevchenko, E. V., Bodnarchuk, M. I., Ye, X., Chen, J., and Murray, C. B. (2009). Quasicrystalline order in self-assembled binary nanoparticle superlattices, *Nature* **461**, 7266, pp. 964–967.

Tanaka, H., Nishikawa, Y., and Koyama, T. (2005). Network-forming phase separation of colloidal suspensions, *Journal of Physics: Condensed Matter* **17**, pp. L143–L153.

Tao, R. and Sun, J. M. (1991). Ground state of electrorheological fluids from monte carlo simulations, *Physical Review Letters* **44**, pp. R6181–R6184.

Tokuyama, M. and Oppenheim, I. (1994). Dynamics of hard-sphere suspensions, *Physical Review E* **50**, pp. R16–R19.

Toledano, J. C. F., Sciortino, F., and Zaccarelli, E. (2009). Colloidal systems with competing interactions: From an arrested repulsive cluster phase to a gel, *Soft Matter* **5**, pp. 2390–2398.

van Blaaderen, A., Peetermans, J., Maret, G., and Dhont, J. K. G. (1992). Long-time self-diffusion of spherical colloidal particles measured with fluorescence recovery after photobleaching, *The Journal of Chemical Physics* **96**, pp. 4591–4603.

van Leeuwen, M. E. and Smit, B. (1993). What makes a polar liquid a liquid? *Physical Review Letters* **71**, pp. 3991–3994.

Voet, D., Voet, J. G. and Pratt, C. W. (2008). *Fundamentals of Biochemistry: Life at the Molecular Level*, 3rd edn. (Wiley, New Jersey).

Yethiraj, A. (2007). Tunable colloids: Control of colloidal phase transitions with tunable interactions, *Soft Matter* **3**, 9, pp. 1099–1115.

Yethiraj, A. and van Blaaderen, A. (2003). A colloidal model system with an interaction tunable from hard sphere to soft and dipolar, *Nature* **421**, pp. 513–517.

Chapter 21

Estimation of Solvation Electrostatic Free Energy of Biomolecular Systems by Numerical Solution of the Poisson–Boltzmann Equation

José Colmenares, Sergio Decherchi, and Walter Rocchia
Drug Discovery and Development Department, Italian Institute of Technology, Via Morego, 30, I-16163 Genova, Italy
walter.rocchia@iit.it

21.1 Introduction

It is widely accepted that electrostatics plays a pivotal role in biological processes. This is because of its long-range influence, its effects on the aqueous solvent, and the highly specific patterns it can engender during biomolecular recognition. Electrostatics also affects the structure and the dynamical behavior of biomolecules and often dominates intermolecular and intramolecular interactions despite the screening exerted by the solvent and the electrolytes [Sheinerman *et al.* (2000); Radic *et al.* (1997)]. Together with the direct Coulombic interaction, the so-called reaction field, that is,

Electrostatics of Soft and Disordered Matter
Edited by David Dean, Jure Dobnikar, Ali Naji, and Rudolf Podgornik

ISBN 978-981-4411-85-1 (Hardcover), 978-981-4411-86-8 (eBook)
www.panstanford.com

the response of the system to the electric field generated by the charge present on the solute molecule, is probably the conceptually simplest and most used model of electrostatic effects adopted in biomolecular simulations. The long-range nature of electrostatics makes these calculations very time-consuming, as in principle, they scale as the square of the charged interacting centers. The computational burden is particularly heavy in atomistic simulations, such as in molecular dynamics, when all the degrees of freedom (DOFs) are treated explicitly. In this kind of simulations, the time evolution of every DOF is calculated for systems at the thermodynamic equilibrium so as to derive an estimate of interesting physical quantities. The computation may have to progress for a long time in order to achieve a good level of accuracy and the electrostatic contribution often represents the major computational bottleneck. To face this issue, several algorithmic solutions have been devised, the Particle Mesh Ewald being probably the most widely adopted [Darden *et al.* (1993)]. On the other side, alternative models try to make an *a priori* average of some DOFs, so as to reduce the overall computational cost. This is the case of so-called *implicit solvent* models, where the DOFs of the solvent, possibly including those of a dissolved salt, are averaged out under some simplifying assumptions. The reason behind this approach is that one is usually not interested in studying the evolution of the individual solvent DOFs but rather to consider the effects of the solvent on the behavior of the solute. In this framework, the Poisson–Boltzmann equation (PBE) proved to be extremely useful in providing a tool that estimates reaction field and electrostatic interaction energy. Here, a basic derivation of the PBE is described as well as the grid-based numerical approach adopted by one widely used PBE solver, the DelPhi software [Honig and Nicholls (1995); Rocchia *et al.* (2001)].

21.2 Electrostatic Continuum Models and the Poisson–Boltzmann Equation

In the continuum description of the electric properties of a molecular system in aqueous solution, the linear response of both the solute and the solvent to the electric field generated by the

charge located on the solute is accounted for by a macroscopic parameter, the dielectric constant. Practically, a medium with a high dielectric constant generates a strong reaction field that locally opposes the applied one [Jackson (1999)]. In the context of systems described at the atomistic or molecular scale, the dielectric constant has not the rigorous meaning intended in macroscopic physics, but rather that of effectively accounting for all the types of reactions, due chiefly to electronic and molecular polarization, which are not considered explicitly [Schutz and Warshel (2001)]. Usually, the solute, that is, the biomolecule, is described as a low dielectric medium containing fixed partial charges, whereas the solvent is described as a high dielectric medium that can contain a simple dissociated salt behaving according to the Debye–Huckel theory [Bockris and Reddy (2002)]. In some more complex models, however, the solute is treated as an inhomogeneous medium, and different dielectric constant values are assigned to different solute subregions [Rocchia *et al.* (2001); Wang *et al.* (2013)]. In others, a continuously varying dielectric constant is also used [Grant *et al.* (2001)]. Under these assumptions, the PBE comes as an application of the laws of the electrostatics of macroscopic media to a microscopic description of the system and adds a term considering the ionic cloud originated by the dissociation of a salt in thermal equilibrium with the bulk. This latter is the Boltzmann term and provides a link between local ionic concentration and electrostatic potential. Similar to the polarization, the unbalance between positive and negative ionic distributions can be interpreted as a reaction to the applied field and originates the so-called Debye screening. The PBE can take the following form, derived from the Gauss' law for the electric displacement:

$$\nabla \cdot [\epsilon(\mathbf{x})\nabla\phi(\mathbf{x})] = -\frac{e}{\epsilon_0 k_B T}[\rho^{\text{fixed}}(\mathbf{x}) + \rho^{\text{solv}}(\mathbf{x})], \tag{21.1}$$

where $\epsilon(\mathbf{x})$ is the local relative dielectric constant, $\phi(\mathbf{x})$ is the dimensionless electrostatic potential obtained multiplying the potential $\phi(\mathbf{x})$ by $\frac{e}{k_B T}$, e is the unit charge, k_B, T, and ϵ_0 are Boltzmann constant, absolute temperature, and vacuum permittivity (SI units), respectively. Fixed and solvent charge densities correspond to the partial charges located on the molecule body and the ionic charge

located in solution. They can be expressed as follows:

$$\rho^{\text{fixed}}(\mathbf{x}) = \sum_{i=1}^{N_\text{f}} q_i \delta(\mathbf{x} - \mathbf{x}_i), \tag{21.2}$$

where $\delta(\cdot)$ is the Dirac's delta, i spans over the N_f fixed charges, and

$$\rho^{\text{solv}}(\mathbf{x}) = e \sum_{j=1}^{N_\text{s}} C_j^b z_\text{j} \exp(-z_\text{j}\phi(\mathbf{x})), \mathbf{x} \in \mathcal{S} \tag{21.3}$$

where j spans over the N_s ionic species, and C_j^b and z_j are the bulk concentration and the valence of the *j-th* ionic species, respectively. $\mathcal{S}$ is the space region containing the ionic solution. In the case of monovalent salt, which is the one in which the PBE is mostly validated, the equation takes the following form:

$$\nabla \cdot [\epsilon(\mathbf{x})\nabla\phi(\mathbf{x})] = -\frac{e}{\epsilon_0 k_\text{B} T}\rho^{\text{fixed}}(\mathbf{x}) + \epsilon_{\text{solv}}\kappa(\mathbf{x})^2 \sinh(\Phi(\mathbf{x})) \tag{21.4}$$

where ϵ_{solv} is the relative dielectric constant of the solvent and

$$\kappa(\mathbf{x}) = \begin{cases} \frac{1}{\lambda_\text{D}} = \sqrt{\frac{2e^2 C_{\text{salt}}}{\epsilon_0 \epsilon_{\text{solv}} k_\text{B} T}} & \text{if } \mathbf{x} \in \mathcal{S} \\ 0 & \text{otherwise} \end{cases} \tag{21.5}$$

C_{salt} is the salt concentration and λ_D is the so-called Debye length, a figure indicating the extension of the electric screening effect exerted by the dissociated salt.

If the solute is low charged, also the potential is expected to be low, and therefore, the hyperbolic sine can be approximated with its argument giving rise to the easier to treat *linearized* PBE. In regions in which the potential turns out to be high, the Boltzmann term can lead to unphysically high ionic concentrations. This can occur in the vicinity of the surface that divides the solute from the solvent, as the latter gets close to the fixed charges originating the potential. This phenomenon occurs more markedly in the nonlinear PBE, due to the exponential behavior of the hyperbolic sine. To alleviate this problem, the *Stern layer* model [Bockris and Reddy (2002)] can be adopted. According to it, ions that are not making any specific interaction with the solute, such as those described by the Boltzmann term, cannot get closer to the surface than a given threshold. In the PBE, this means forcing the $\kappa(\mathbf{x})$ function to be zero also in the solvent within a given distance from the surface of the solute.

21.3 Input to the Model

A typical input to the PBE model in the field of computational biology is the structure of a protein or a nucleic acid. This can be obtained by experimental means via X-ray crystallography or NMR. The Protein Data Bank (http://www.rcsb.org) is a worldwide repository containing many of these experimentally derived structures in a standard format, the *pdb*. Among other information, a pdb file contains the atom types of the resolved structure along with the atomic coordinates, expressed in Åmstrongs ($1\ \text{Å} = 10^{-10}$ m). Other fundamental inputs are radii and partial charges needed to identify the space region occupied by the solute and the sources of the field. However, these values are not unique and several different sets of charges and radii have been devised, based upon theoretical/computational approaches or upon fitting experimental data [Sitkoff *et al.* (1994); Marten *et al.* (1996); Marenich *et al.* (2012)]. Then, solute (ϵ_{in}) and solvent (ϵ_{solv}) relative dielectric constant values are needed. Although the bulk value for water is normally used ($\epsilon_{\text{solv}} = 78.5$ or, frequently, $\epsilon_{\text{solv}} = 80.0$), there is less agreement in the literature on the best dielectric value for the solute. $\epsilon_{\text{in}} = 2$ should account for pure electronic polarization but, in fixed point calculations, it has been seen that higher values, such as $\epsilon_{\text{in}} = 4$ or even larger, provide better agreement with experimental data [Antosiewicz *et al.* (1994)]. To correctly set up the Boltzmann term, the following information is needed (see Eqs. 21.3 and 21.5): concentration of the salt, charge of the dissociated species and width of the Stern layer. A fundamental part in preparing the model is the construction of the so-called *molecular surface*, that is, the surface that separates the solute from the solvent. In order to do this, another parameter is needed, the probe radius of the solvent, which is usually taken as 1.4 Å for water.

21.3.1 *Molecular Surface Construction*

The exact shape of the molecular surface can have a great influence on the reaction field estimation, as it affects the location of the polarization charge, which practically quantifies the entity of the reaction itself, as shown in Figure 21.1. Probably, the most widely

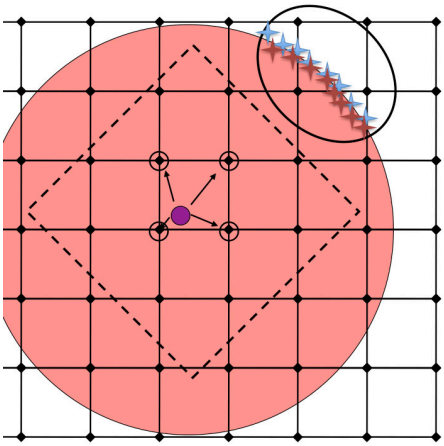

Figure 21.1 2D sketch of the grid mapping of the system. The fixed charge (violet) at atom center is mapped on the nearest grid points. The potential at the grid points in the dashed square is most affected by the grid artifact. In the oval, the dielectric boundary is highlighted, and the polarization charge arising from the solute and the solvent is indicated (dark orange and light blue stars, respectively).

used surfaces in implicit solvent calculations are the van der Waals surface (VDWS), the solvent accessible surface (SAS), and the solvent-excluded surface (SES); other more recent definitions exist, but they will not be discussed here [Decherchi *et al.* (2013)]. All of the cited molecular models represent the system as a set of hard spheres, whose radius is the van der Waals radius immersed in a homogenous solvent. The geometric union of these hard spheres is the so-called van der Waals volume and the resulting enclosing surface is the VDWS. One problem arising when the VDWS is used to separate high from low dielectric regions is that it presents small interstices that are assigned to the continuum solvent, despite that in reality, they are not accessible to the molecular solvent; this results in an overestimation of the reaction field. To alleviate this problem, other surface definition has been devised. The SES is probably the most used molecular surface definition; it identifies the space region accessible to a finite size solvent probe. This definition, based on a hard sphere model of both the solute and the solvent, was suggested by Lee and Richards (1971) (Figure 21.2) and an

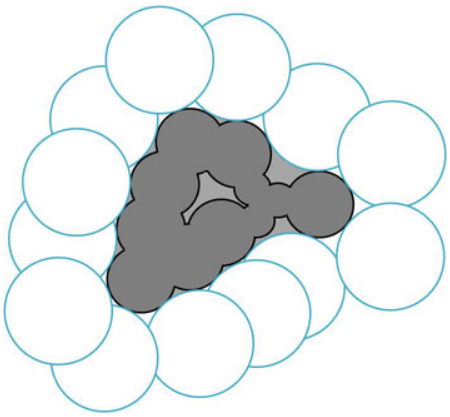

Figure 21.2 Construction of the solvent-excluded surface according to the Lee and Richards definition. The probe (light blue circle) rolls over the VDWS of the solute (dark gray). The small voids that are not accessible to the probe are filled (light gray) by assigning the same dielectric constant to them as that of the solute.

algorithm for its computation was provided by Connolly (1983). His approach became so widespread that the above-described surface is often called Connolly surface, although Connolly algorithm is not the only one developed to this purpose [Sanner *et al.* (1996); Rocchia *et al.* (2002); Totrov and Abagyan (1996)]. One of the interesting features of the SES is that the only geometric primitive used is the sphere: this property is particularly appealing because it allows to define efficient distance-based algorithms for its construction. An iterative algorithm for the construction of the SES on a grid can be found in [Rocchia *et al.* (2002)]: this algorithm is currently used by the DelPhi engine. It iteratively classifies the midpoints of the grid points and iteratively grows the VDWS until it becomes the SES. Although the SES is both an efficient and plausible model for a molecular surface, it is not devoid of deficiencies, such as the nonexistence of the surface normal in some points, and the discontinuity of surface area with respect to atomic positions. To cope with these problems, recent works try to propose other surface definitions that have a different trade-off between physical and geometric soundness [Decherchi *et al.* (2013); Bates *et al.* (2008)].

21.4 Input to the Numerical Solver

There are parameters that influence the simulation but do not depend on the model, the grid spacing is one of them, as well as the percentage filling, which indicates how much of the grid is occupied by the solute. Moreover, if iterative methods are used to solve the equation, a stopping criterion is also necessary. For this purpose, a threshold on the variation of the result between two successive iterations may be provided as an input. Another essential ingredient is the boundary conditions for the PBE. In principle, the equation is defined on an unbounded domain with the condition that the potential tends to zero as the distance from the source of field, that is, the solute, tends to infinity. In reality, the system must be mapped on a finite size grid, and therefore, an updating criterion for the points at the grid boundary is needed. Usually, the potential at the boundary is kept fixed at a potential profile that is derived by asymptotic solutions of particular approximations to the PBE for which analytical solutions exist. The available boundary conditions in the DelPhi software follow: (i) the *zero* option assigns a potential of 0.0 to all boundary points. Computationally, it is the most light weighted, but it provides a good approximation only if the distance between the solute and the boundary of the grid is large. (ii) The *full Coulombic* option calculates the potential at each boundary point due to every charge in the system using the Debye–Hückel approximation, in which the medium of the solute is removed and only charges in solution are left. In this case, the linear PBE has an analytical solution. These conditions are pretty accurate but can be costly, as they require the calculation of the distance between each charge and all the cubes at the grid boundary. (iii) The *approximated dipolar* uses the same asymptotic solution, but it approximates the system with two charges, the overall positive and negative ones located at the respective barycenters. This can be a good trade-off between accuracy and computational cost. (iv) The *focusing* option presents several advantages, but it requires multiple runs. In one calculation, a low resolution, that is, a large grid spacing, is used so as to allow for a low percentage filling and a good validity of the asymptotic boundary conditions. The second calculation uses

a larger percentage filling on the same grid that thus encloses a smaller portion of the molecule. It derives the boundary conditions from the potential values obtained at the previous step.

DelPhi is also capable of using *periodic* boundary conditions, so that the potential values at one side of the grid coincide with those at the opposite side along the given direction. This is useful if the molecule has a repeated portion, such as with biological membranes, so that the whole system does not need to be included in the grid. Using the same approach, an external field can be applied and kept fixed during the simulation, mimicking, for instance, the membrane potential.

21.5 Numerical Solution via Finite-Difference Scheme

The PBE is a nonlinear 3D partial differential equation with discontinuous coefficients, delta functions, (in principle) unbounded domain, and rapid, exponential, nonlinearity. For this equation, analytical solution is impossible in realistic cases and also fast and accurate numerical solution is usually difficult to accomplish. The most used numerical approaches are finite-differences and finite-elements [Honig and Nicholls (1995); Holst and Saied (1993); Baker *et al.* (2000)]. The time and memory requirements for a calculation may heavily depend on the specific method and implementation; a detailed description of these aspects is however out of the scope of this work. Numerical solution of the PBE implies some kind of discretization of both the physical space and the differential operators. Space can be discretized into cubes (finite-differences), or tetrahedra (finite-elements). In the linearized case, the problem can also be mapped on the surface separating low from high dielectric constant (boundary elements) [Boschitsch *et al.* (2002)]. Each of these methods leads to a system of algebraic equations, which can be solved, for instance, by an iterative approach. Here, we will focus on the finite-difference scheme and describe the approach used by the DelPhi solver. In this approach, the solute is positioned at the center of a cubic grid. Then, the PBE is locally integrated over a generic grid cube, converting the Dirac's deltas of ρ^{fixed} to finite values assigned

to the centers of the cubes neighboring the charges (see Fig. 21.1). Then, the left-hand side of Eq. (21.1) is converted into a surface integral by applying the divergence theorem. The function $\kappa(\mathbf{x})$ is evaluated at each grid cube center. After these steps, the equation takes the following form:

$$\iint_{SC_i} [\epsilon(\mathbf{x})\nabla\Phi(\mathbf{x})]dS = -\frac{e}{\epsilon_0 k_B T}[q_i + \epsilon_{\text{solv}}\kappa(\mathbf{x_i})^2 h^3 \sinh(\Phi(\mathbf{x_i}))], \tag{21.6}$$

where SC_i is the surface of the i-th grid cube, and q_i the overall charge in it. As a further processing, the simple geometry of the cubic surface is exploited together with the finite-difference expression of the gradient, so that the left-hand side of Eq. (21.6) becomes:

$$\sum_j^6 \epsilon_{i,j}(\Phi_{i,j} - \Phi_i)h \tag{21.7}$$

where the subscript j enumerates the faces of the cube, that is, the coordinate directions together with their orientation. In this expression, $\epsilon_{i,j}$ is the dielectric constant at the center of the *j-th* face of the *i-th* cube while $\Phi_{i,j}$ is the potential in the center of the adjacent grid cube in the *j-th* direction and h is the side of the cube, that is, the grid spacing. This discretization process leads, for each grid cube, to an algebraic expression where the potential at the grid center is in explicit relationship with the potential values at the six neighboring grid cubes as shown in Eq. (21.8):

$$\phi_i = \frac{\sum_j^6 \epsilon_{i,j}\phi_{i,j} + \frac{eq_i}{\epsilon_0 k_B T h}}{\sum_j^6 \epsilon_{i,j} + \epsilon_{\text{solv}}\kappa_i^2 h^2} - \frac{\epsilon_{\text{solv}}\kappa_i^2 h^2(\sinh(\Phi_i) - \Phi_i)}{\sum_j^6 \epsilon_{i,j} + \epsilon_{\text{solv}}\kappa_i^2 h^2} \tag{21.8}$$

The form of Eq. (21.8) separates the equation used in the linearized PBE, that is, the first term, from the nonlinear correction, which is often approximated via a Taylor expansion. It is worth noting that several terms in this general expression cancel in many regions, leading to much more simplified formulas that are used by the solver to avoid unnecessary calculations. For instance, in solute regions in which charge is null and dielectric constant is uniform, the effect of (21.8) is simply that of a Laplacian smoothing, that is, a local averaging. Eq. (21.8) inspires a possible updating rule to be used in an iterative scheme, which, in the linear case, takes the form:

$$\phi^{(n+1)} = \mathbf{T}\phi^{(n)} + Q \tag{21.9}$$

where n is the iteration counter indicated by the bracketed notation. The updating rule (21.9) can be made explicit with respect to the current iteration of the potential:

$$\phi^{(n)} = \left(\sum_{i=0}^{n-1} \mathbf{T}^i \right) Q + \mathbf{T}^n \phi^{(0)}, \tag{21.10}$$

leading to a series whose limit can be formally written as:

$$\lim_{n \to \infty} \phi^{(n)} = \frac{\mathbf{I}}{\mathbf{I} - \mathbf{T}} Q \tag{21.11}$$

where $\mathbf{I}$ is the identity matrix of the same dimension of $\mathbf{T}$ and the division of matrices can be calculated by power series expansion [Golub and Van Loan (1996)]. This series converges if the eigenvalues of $\mathbf{T}$ are in the $[-1, 1]$ range. A detailed analysis of the spectrum of $\mathbf{T}$ is outside the scope of this work, but it can be shown that this condition is satisfied in this case. The iterative approach adopted by the DelPhi solver is the successive overrelaxation method (SOR), a variant of the well-known Gauss–Seidel scheme [Stoer and Bulirsch (2002)]. One interesting implementation detail is the exploitation of the so-called checkerboard structure of the discretized operator. This structure consists in coloring the grid in "black and white" points, so that each black grid point is surrounded only by white ones and *vice versa*. Eq. (21.8) shows that the update of a point of a given color can be done using only points of the opposite one. Splitting the overall update in these two alternating steps provides a factor 2 of speed up with practically no effort except for a smart indexing of the points. More details about this implementation can be found in [Nicholls and Honig (1991)]. As briefly sketched, the nonlinear case can be treated as a perturbation of the linear one [Rocchia *et al.* (2001)], although convergence in this case is not guaranteed and other approaches can be better suited to this purpose [Boschitsch and Fenley (2003); Simonov *et al.* (2007)].

21.6 Analysis of the Results: Energy Calculation and Partitioning

Once the solution of the equation is obtained, the electric potential is available at each grid point. The classical expression for the energy

of the system is the following:

$$\mathcal{E} = \frac{1}{2}\sum_{i}^{N_f} q_i \phi_i \tag{21.12}$$

where $\{q_i\}$ are the already described fixed charges and ϕ_i is the potential generated by all the field sources at the site where q_i is located except for that generated by q_i itself [Jackson (1999)]. As described more in detail in [Rocchia *et al.* (2001)], the potential can be partitioned according to field sources, which are basically three in number: (i) the fixed charges, (ii) the polarization charges arising at the interface between regions of different dielectric, and (iii) the ions in solution. These are briefly termed as Coulombic reaction and ion direct contributions:

$$\phi(\mathbf{x_j}) = \underbrace{\sum_{i \neq j} \frac{q_i}{4\pi\epsilon_0 \epsilon(\mathbf{x_i}) x_{j,i}}}_{\phi_{\text{coul}}} + \underbrace{\sum_{p} \frac{\delta_p}{4\pi\epsilon_0 x_{j,p}}}_{\phi_{\text{react}}} + \underbrace{\sum_{k} \frac{h^3 d\rho_k^{\text{solv}}}{4\pi\epsilon_0 \epsilon_{\text{solv}} x_{j,k}}}_{\phi_{\text{ion}}} \tag{21.13}$$

Here, $x_{j,a}$ stands for $\|\mathbf{x_j} - \mathbf{x_a}\|$, δ_p is the fractional polarization charge located at the *p-th* grid cube, which is crossed by the dielectric boundary (see Fig. 21.1), and $h^3 d\rho_k^{\text{solv}}$ is the charge contained in the *k-th* grid cube, which in turn is located in the solvent. The distinction between the different field sources can be useful both for interpreting the results and also for numerical reasons. In fact, the finite-difference numerical solution of the PBE leads to some inaccuracies, the so-called *grid artifacts*, which make the potential near charged grid points sensitive to the specific parameters of the simulation, such as the grid spacing and the position/orientation of the solute relative to the grid. If we consider expression (21.13), we observe that ϕ_{coul} can be calculated analytically; δ_p, needed to derive ϕ_{react}, can be calculated by applying Gauss' law to each grid cube crossed by the dielectric boundary. This calculation is quite robust, as it relies on potential values located around the dielectric boundary that usually are not charged (see Fig. 21.1). The explicit calculation of ϕ_{ion} is not devoid of problems, as it requires to sum over all the grid cubes in the solvent. Summing over solvent volume can be extremely time-consuming and can suffer of the finiteness of the grid size. Some approaches have been developed to account for this issue but are not frequently used

[Rocchia (2005)]. An alternative approach, which however suffers from the grid artifact problem, consists in making two or more runs at different ϵ_{solv} or different ionic strengths, but at the same grid spacing and position of the system, and then computing the energy difference according to Eq. (21.12). It is worth stressing the importance of a good estimation of the reaction field energy, as it is one of the major determinants of the solvation energy. The just described energy calculation must be revised in the full nonlinear case, where two more energy terms have to be considered, namely those originated by the osmotic pressure and by the electrostatic stress [Sharp and Honig (1990); Rocchia *et al.* (2001)].

21.7 Conclusion

The PBE is a widely used tool to model biomolecules in physiological solution and to estimate the electrostatic contribution to desolvation and salt effects. It relies on several assumptions, such as the linear response of the media to the electric field generated by the solute, and the Boltzmann approximation to the thermodynamic equilibrium distribution of the counterions in solution, which neglects ion–ion correlation and ion finite size. It also relies on the atom center point charge distribution model, which only partially accounts for the complex behavior of electronic density in molecules. Nonetheless, it provides good agreement with experimental data in many biological cases, which fall into the so-called *weak coupling* regime, where the charge of typical solutes is not extremely high and monovalent salts in solution are considered. Despite its foundations date back to the beginning of the nineteenth century [Debye and Hückel (1923)], the PBE is still subject of research, aimed both at improving the model [Forsman (2004); Shi and Koehl (2008)] and at increasing the performance of its implementations [Wang and Luo (2010)].

Acknowledgments

The authors gratefully acknowledge the support of NIGMS, NIH, grant number 1R01GM093937-01 and of the IIT platform *Computation*.

References

Antosiewicz, J., McCammon, J. and Gilson, M. (1994). Prediction of ph-dependent properties of proteins, *Journal of Molecular Biology* **238**, pp. 415–436.

Baker, N., Holst, M. and Wang, M. (2000). Adaptive multilevel finite element solution of the Poisson-Boltzmann equation i: Refinement at solvent accessible surfaces in biomolecular systems. *Journal of Computational Chemistry* **21**, pp. 1343– 1352.

Bates, P., Wei, G. and Zhao, S. (2008). Minimal molecular surfaces and their applications, *Journal of Computational Chemistry* **29**, 3, pp. 380–391.

Bockris, J. O. and Reddy, A. K. (2002). *Modern Electrochemistry*, 2nd edn. (Plenum Rosetta).

Boschitsch, A. H. and Fenley, M. O. (2003). Hybrid boundary element and finite difference method for solving the nonlinear Poisson-Boltzmann equation, *Journal of Computational Chemistry* **25**, pp. 935–955.

Boschitsch, A. H., Fenley, M. O. and Zhou, H.-X. (2002). Fast boundary element method for the linear Poisson-Boltzmann equation, *Journal of Physical Chemistry B* **106**, pp. 2741–2754.

Connolly, M. (1983). Analytical molecular surface calculation, *Journal of Applied Crystallography* **16**, pp. 548–558.

Darden, T., York, D. and Pedersen, L. (1993). Particle mesh Ewald: An nlog(n) method for Ewald sums in large systems, *Journal of Chemical Physics* **98**, pp. 10089–10092.

Debye, P. and Hückel, E. (1923). On the theory of electrolytes. I. Freezing point depression and related phenomena, *Physikalische Zeitschrift* **24**, pp. 185–206.

Decherchi, S., Colmenares, J., Catalano, C., Spagnuolo, M., Alexov, E. and Rocchia, W. (2013). Between algorithm and model: Different molecular surface definitions for the Poisson-Boltzmann based electrostatic characterization of biomolecules in solution, *Communications in Computational Physics* **13**, pp. 61–89.

Forsman, J. (2004). A simple correlation-corrected Poisson-Boltzmann theory, *Journal of Physical Chemistry B* **108**, pp. 9236–9245.

Golub, G. H. and Van Loan, C. F. (1996). *Matrix computations*, 3rd edn. (Johns Hopkins University, Baltimore), ISBN 0801854148.

Grant, J. A., Pickup, B. T. and Nicholls, A. (2001). A smooth permittivity function for Poisson-Boltzmann solvation methods, *Journal of Computational Chemistry* **22**, 6, pp. 608–640.

Holst, M. and Saied, F. (1993). Multigrid solution of the Poisson-Boltzmann equation, *Journal of Computational Chemistry* **14**, pp. 105–113.

Honig, B. and Nicholls, A. (1995). Classical electrostatics in biology and chemistry, *Science* **268**, pp. 1144–1149.

Jackson, J. D. (1999). *Classical electrodynamics*, 3rd edn. (Wiley, New York), ISBN 9780471309321.

Lee, B. and Richards, F. (1971). The interpretation of protein structures: Estimation of static accessibility, *Journal of Molecular Biology* **55**, pp. 379–400.

Marenich, A. V., Jerome, S. V., Cramer, C. J. and Truhlar, D. G. (2012). Charge model 5: An extension of hirshfeld population analysis for the accurate description of molecular interactions in gaseous and condensed phases, *Journal of Chemical Theory and Computation* **8**, 2, pp. 527–541, doi:10.1021/ct200866d, http://pubs.acs.org/doi/abs/10.1021/ct200866d.

Marten, B., Kim, K., Cortis, C., Friesner, R. A., Murphy, R. B., Ringnalda, M. N., *et al.* (1996). New model for calculation of solvation free energies: Correction of self-consistent reaction field continuum dielectric theory for short-range hydrogen-bonding effects, *Journal of Physical Chemistry* **100**, pp. 11775–11788.

Nicholls, A. and Honig, B. (1991). A rapid finite difference algorithm, utilizing successive over-relaxation to solve the Poisson-Boltzmann equation, *Journal of Computational Chemistry* **12**, pp. 435–445.

Radic, Z., Kirchhoff, P., Quinn, D. M., McCammon, J. and Taylor, P. (1997). Electrostatic influence on the kinetics of ligand binding to acetylcholinesterase distinctions between active center ligands and fasciculin, *The Journal of Biological Chemistry* **272**, pp. 23265–23277.

Rocchia, W. (2005). Poisson-Boltzmann equation boundary conditions for biological applications, *Mathematical and Computer Modelling* **41**, pp. 1109–1118.

Rocchia, W., Alexov, E. and Honig, B. (2001). Extending the applicability of the nonlinear Poisson-Boltzmann equation: Multiple dielectric constants and multivalent ions, *Journal of Physical Chemistry B* **105**, 28, pp. 6507–6514.

Rocchia, W., Sridharan, S., Nicholls, A., Alexov, E., Chiabrera, A. and Honig, B. (2002). Rapid grid-based construction of the molecular surface for both molecules and geometric objects: Applications to the finite difference Poisson−Boltzmann method, *Journal of Computational Chemistry* **23**, pp. 128–137.

Sanner, M. F., Olson, A. J. and Spehner, J. (1996). Reduced surface: An efficient way to compute molecular surfaces, *Biopolymers* **38**, pp. 305–320.

Schutz, C. N. and Warshel, A. (2001). What are the dielectric constants of proteins and how to validate electrostatic models? *PROTEINS: Structure, Function, and Genetics* **44**, pp. 400–417.

Sharp, K. and Honig, B. (1990). Calculating total electrostatic energies with the nonlinear Poisson-Boltzmann equatlon, *Journal of Computational Chemistry* **94**, pp. 7684–1044.

Sheinerman, F. B., Norel, R. and Honig, B. (2000). Electrostatic aspects of protein protein interactions, *Current Opinion in Structural Biology* **10**.

Shi, X. and Koehl, P. (2008). The geometry behind numerical solvers of the Poisson-Boltzmann equation, *Communications in Computational Physics* **3**, 5, pp. 1032–1050.

Simonov, N. A., Mascagni, M. and Fenley, M. O. (2007). Monte Carlo–based linear Poisson-Boltzmann approach makes accurate salt-dependent solvation free energy predictions possible, *Journal of Chemical Physics* **127**, 18, p. 185105.

Sitkoff, D., Sharp, K. A. and Honig, B. (1994). Accurate calculation of hydration free energies using macroscopic solvent models, *Journal of Physical Chemistry* **98**, pp. 1978–1988.

Stoer, J. and Bulirsch, R. (2002). *Introduction to numerical analysis* (Springer, New York).

Totrov, M. and Abagyan, R. (1996). The contour-buildup algorithm to calculate the analytical molecular surface, *Journal of Structural Biology* **116**, pp. 138–143.

Wang, J. and Luo, R. (2010). Assessment of linear finite-difference Poisson–Boltzmann solvers, *Journal of Computational Chemistry* **31**, pp. 1689–1698.

Wang, L., Zhang, Z., Rocchia, W. and Alexov, E. (2013). Using delphi capabilities to mimic protein's conformational reorganization with amino acid specific dielectric constants, *Communications in Computational Physics* **13**, pp. 13–30.

Chapter 22

Modeling DNA in Nanopores

Stefan Kesselheim and Christian Hom
Institute for Computational Physics, University of Stuttgart, Allmandring 3, 70569 Stuttgart, Germany
holm@icp.uni-stuttgart.de

22.1 Introduction

In the past 20 years, nanopores have evolved into powerful and versatile probes for the world of single biomolecules, allowing scientists to detect them and discriminate between them with remarkable precision with relatively lightweight instruments. The basic concept follows the same idea as the Coulter counter [Coulter (1953)], but scaled down to single molecules: The analyte of interest, dissolved in an electrolyte solution, appears as a modulation of the ion current when it crosses a small pore. The attention attracted by these experiments would likely have been far smaller, if—only 4 years after seminal experiments had been published [Branton *et al.* (1996)]—it had not been found that solely based on the current signal it is possible to distinguish single-stranded DNA (ssDNA) molecules by their bases [Meller *et al.* (2000)]: The current blockade e.g., of poly(dC) was less pronounced than that of poly(dA). The

Electrostatics of Soft and Disordered Matter
Edited by David Dean, Jure Dobnikar, Ali Naji, and Rudolf Podgornik

ISBN 978-981-4411-85-1 (Hardcover), 978-981-4411-86-8 (eBook)
www.panstanford.com

idea to build a nanopore-based read-out device, which sequentially reads single DNA molecules, was born. This great leap for science and medicine is not yet made, although many theoretical and experimental hurdles that accompany this enterprise have been cleared. Although DNA sequencing is the most prominent focal point of ongoing research, also other applications in analytic chemistry or clinical diagnosis are of significant interest.

In this chapter, we want to provide an introduction to the topic, with special focus on electrostatic effects, and provide a selection of literature especially suited for newcomers in the field of nanopores. We do not try to compete with the excellent text book of Muthukumar [Muthukumar (2009)], which gives a very broad view and a very educative description of the rich physics involved. We finish this chapter with a discussion of our recent results regarding electrostatic translocation barriers and compare them with a simple Poisson-Boltzmann (PB) model.

22.2 A Brief Overview of Nanopore Translocation Experiments

The first successful experiments were performed with single biological pore proteins embedded in a lipid bilayer membrane [Branton *et al.* (1996)]. When applying a voltage between the two compartments that are separated by this membrane, a small but clearly measurable ion current runs through the pore. When ssDNA molecules that are added to the chamber with negative voltage enter the pore, intermittent events appear, where the current is largely blocked. This allows for the detection of single DNA molecules in the translocation process. The ion blockade events, which can last for milliseconds, contain information on the base sequence of the DNA molecule [Meller *et al.* (2000)]. This has not only stimulated many experiments (see e.g., the reviews [Venkatesan and Bashir (2011)], [Howorka and Siwy (2009)] and [Dekker (2007)]), but also the company Oxford Nanopore Technologies to develop nanopore-based devices for sensing and sequencing, which will reportedly be commercially available by the end of 2012 [Eisenstein (2012)].

Only a few years after the first experiments with biological pores, conceptually identical experiments could be performed with

synthetic pores [Li *et al.* (2001)]. Many different groups developed nanofabrication techniques to create single pores in mostly silicon-based substrates (e.g. [Storm *et al.* (2003); Henrickson *et al.* (2000)]), called *solid-state* nanopores. Their favorable mechanical properties and the possibility to create them in large arrays make them very interesting for sensing applications, although biological pores seem currently to be ahead in sequencing. Since the fabrication of the first solid-state nanopores, a broad range of new ideas has been put forward, each of which might be the key toward a new technological application. We can only mention a few here: Different groups [Fischbein and Drndic (2008); He *et al.* (2011)] combined solid state nanopores with graphene sheets, which can have (at least) two advantages: On the one hand, graphene is very thin, and this allows nanopores with a very short constriction so that only a single base is read at a time. On the other hand, the electronic properties of graphene can be used to obtain more information on the translocation event. In the lab of U. Keyser, glass micropipettes are used as nanopores. In a careful pulling procedure, pores with only $\sim$10 nm diameter can be formed from cheap pipettes, a procedure that could in principle be performed in clinical practice. The same group used the DNA origami technique [Rothemund (2006)] as synthetic replacement of pore proteins [Bell *et al.* (2012)], but inserted into solid state pores. This technique might allow them to combine the advantage of atom-precise equality of pore proteins and the flexibility of solid-state pores.

Although the detection of the ion current might already be sufficient for technological applications, other observables have proved helpful for scientific insight. The lab of C. Dekker managed to attach a double-stranded DNA (dsDNA) molecule to a colloid held in optical tweezers, allowing them to directly measure the force acting on the DNA molecule [Keyser *et al.* (2006)]. Other groups were able to include gold electrodes over the pores to enable the detection of molecules by the tunnel current [Tsutsui *et al.* (2010); Ivanov *et al.* (2011)]. A direct imaging technique allow for visual observation of the translocation of flourescently labeled dsDNA molecules as it occurs [Thacker *et al.* (2012)].

The creativity of the experimental nanopore community continues to produce marvelous new techniques and ideas how to produce

tools that might revolutionize medicine or at least are valuable lab tools.

22.3 Theory of Nanopore Translocation

Nanopores and translocation experiments have also attracted a considerable interest by theoreticians. We will focus here on two aspects that have been of special interest: Theoretical models of the dynamics of a chain molecule translocating through a pore and the different aspects of the motion of small ions and fluid in translocation setups, and how this couples to the translocating molecule.

Translocation and chain dynamics

A quite simple question has attracted much interest since the advent of DNA translocation experiments and yet remains not fully solved: How does the mean translocation time τ of a chain molecule depend on its number of monomers N? In polymer science [Rubinstein and Colby (2003); Doi and Edwards (1986); Grosberg and Khokhlov (1994)] typically, scaling laws are constructed, wherein answers are of the following form: For long enough polymers, a property P of a polymeric molecule equals $P = Af(N)$, where A is a prefactor that is not of interest, but rather the function f. This is expressed as $P \sim f(N)$, which reads as P scales as the function f of N. The fractal nature of long polymers is responsible for f being a power law in many cases. In the Rouse model, in which hydrodynamic interactions are neglected, the time of a polymer to relax to its equilibrium state scales as $N^{1+2\nu}$. Here, ν is the Flory exponent that was found to be important for a large number of properties of polymeric molecules. For so-called self-avoiding chains in three spatial dimensions, wherein monomer overlap is forbidden because of repulsive interaction between monomers, its numerical value is 0.588.

Inserting a polymer into a pore is associated with a decrease in chain entropy, as a large number of conformations is disallowed by steric hindrance. The free energy difference to a free chain can

be expressed in terms of the free energy penalty of tethering two polymer chains of size s and $N-s$ to a wall, if the pore length is much shorter than the contour of the chain. The integer number s denotes the number of monomers that have already crossed the membrane. According to [Muthukumar (1999)] and [Sung and Park (1996)], this is associated with entropic free energy barrier:

$$\mathcal{A}(s)/k_{\mathrm{B}}T = \gamma\left(\log s + \log\left(N-s\right)\right),$$

where γ is a prefactor of order 1 that depends on the chain model ($\gamma = 0.69$ for self-avoiding chains in 3D). The definition of the free energy requires thermodynamic equilibrium, which means that all other degrees of freedom have sufficient time to relax to thermodynamic equilibrium, while changes of the reaction coordinate s happen on a longer timescale. In other words, all degrees of freedom of the system change much more rapidly than the reaction coordinate s—the chain is in *quasi-equilibrium* for every value of s. Under these conditions, the translocation process can be described as a diffusional process of s in an external potential. This would imply a scaling of $\tau \sim N^2$, just as for free diffusional processes, the square distance traveled is linear in time. A simple but very interesting observation brought forward in [Chuang *et al.* (2001)] is that the relaxation time of the chain ends scales as $N^{1+2\nu}$ in the Rouse model and for long enough chains will be larger than the N^2 scaling of the translocation time. Thus, for long enough chains, the relaxation time will be longer than the translocation time, and thus, the quasi-equilibrium assumption is invalid. According to the authors, this implies that the relaxation time of the chains is a lower bound to the translocation time.

A particularly clear account of this intrinsic non-equilbrium effect was given by Gauthier et al. [Gauthier and Slater (2009)], who showed with molecular dynamics (MD) simulations that the escape of a chain from a nanopore changes dramatically if interrupted half-way and given time to relax to its equilibrium. De Haan et al. were able to show that a whole range of exponents can be obtained in computer experiments by systematically varying the solvent viscosity and the friction in the pore [de Haan and Slater (2012)], explaining why so many different apparently contradicting values had been found before. Only very recently, the discussion

appears to converge, at least for the case of unforced translocation, after Sakaue introduced the concept of chain tension propagation [Sakaue (2010)], which was extended by Rowghanian and Grosberg (2011). The simple question, however, has proved to have a quite complicated answer and a full understanding is not yet achieved.

Motion of small ions and electrophoresis

A very simple model of the motion of small ions and the electric field was suggested by Grosberg et al. [Wanunu *et al.* (2009)] following [Hille (1968, 1970); Hall (1975)]: The electrolyte is assumed to possess a position-independent conductivity σ and the pore is assumed to be strictly cylindrical of length L and diameter D. The total electric resistance is then given by the sum of the access resistance (from the electrode to the pore entrance) $1/\sigma D$ and the pore resistance of order $1/\sigma \frac{L}{D^2}$ along the pore. This can be found easily under the assumption that the total electric flux must be identical through hemispheres around the pore openings and planes perpendicular to the cylinder axis. This implies that only for long pores ($L \gg D$), the access resistance is negligible. The general shape of the field lines is as follows: In front of the pore, they point toward (or away from) the pore openings, and in the pore, they are parallel to the pore axis. These electric field lines create a funneling effect that facilitates the rate with which DNA molecules are captured by the pore [Grosberg and Rabin (2010)]. We now present a brief discussion of the motion of charges in electric fields.

Charged objects in solution that are subject to an external electric field undergo a process known as electrophoresis. For many researchers, this effect requires a certain recalibration of the intuition, which we hope to achieve with the next paragraphs.

The fundamental misconception is most clearly seen with the following consideration: We imagine an object with charge q immersed in an electrolyte under an applied field E and held still by a mechanical force. This stall force F_s is not given by $-qE$ but a typically smaller value. Following [Zhang and Shklovskii (2007)], we use the term *stall charge*, the symbol q_s as the proportionality constant between stall force and electric field, although we will

show later that this concept is by far not as general as desired. The difference between bare (usual) and stall charge is related to the fact that the surrounding counterion cloud is accelerated by the same field but in the opposite direction. By viscous drag, a fraction of this force is transferred to the object. In fact, certain conditions can even lead to an inversion of the force (e.g., shown explicitly in atomistic simulations in [Luan and Aksimentiev (2010)]). Although these facts are well known, not all researchers appear to be familiar with them. At the time of writing this article, the German Wikipedia article indeed reports the stall force incorrectly, while the English article is more precise[a]. We will elucidate a few more aspects of the physics of electrophoresis, following the concepts of electric fields, mechanical forces, and drag forces as presented in [Long *et al.* (1996)], which were brought to attention in the nanopore field by [Zhang and Shklovskii (2007)] and [Grosberg and Rabin (2010)]. An interesting review on different consequences of this picture was recently published [Shendruk *et al.* (2012)].

The deep insight that hydrodynamic friction and the stall force in electric fields are the key to understand the motion of charged particles in electric fields dates back to the seminal work of O'Brien and White [O'Brien and White (1978)] who investigated the electrophoresis of a spherical charged particle. They noted that in the limit of low applied forces and velocities, the linearity of the response can be used to superimpose electrical fields, mechanical forces, and the velocity of the particle. This leads to the following consideration: The state of stationary electrophoretic velocity can be considered as a superposition of two situations: (i) The particle is held fixed in an external electric field with the stall force mentioned above; (ii) The particle is held at a constant velocity without any electric field applied. If (i) and (ii) are superimposed so that the applied forces exactly cancel, the stationary electrophoretic state is recovered. This can be expressed in the following way: The electrophoretic mobility μ that relates the electric field and the electrophoretic velocity can be expressed as

$$\mu = q_s/\xi,$$

[a]Wikipedia, the free encyclopedia, http://de.wikipedia.org/wiki/Elektrophorese and http://en.wikipedia.org/wiki/Electrophoresis, accessed September 26, 2012.

where ξ is the drag coefficient, i.e., the ratio of velocity and drag force and the case without applied electric field.

The limitations of the concept of a stall charge q_s become clear, when applying this result to a charged polymer, such as DNA in free solution. It is well known [Nkodo *et al.* (2001); Grass and Holm (2009)] that the electrophoretic mobility for long chains is independent of the chain length and the drag coefficient scales as N^ν. This means that the stall charge has to scale as N^ν as well, which is of course not the linear scaling behavior one would expect from a quantity called *charge*. In addition, q_s depends on the salt concentration, the geometry, and chain conformations, and the definition above is only valid in a homogeneous electric field—it is a quantity that might still fool the physical intuition.

22.4 Electrostatic and Dielectric Translocation Barriers

Beyond the entropic barrier mentioned above, it is interesting whether a purely electrostatic barrier exists that prevents DNA molecules from entering a pore. In recent articles [Suezen (2009); Kesselheim *et al.* (2011, 2012)], estimates of the electrostatic free energy barrier for dsDNA molecules in cylindrical pores of 4–10 nm diameter were calculated. In this section, we recapitulate our applied model and our results and provide an explanation of the obtained forces by means of PB theory.

Our strategy is based on coarse-graining: systematically replacing complex features of the system by simpler ones. So, the number of degrees of freedom is reduced tremendously, but it has to be done with care. Arguments can, however, be formulated much more in the spirit of physics, thus addressing the question of which aspect of matter or a process is responsible for which behavior, especially as physical effects can often be switched on or off. The aspect we concentrated on was the difference in polarizability of water and the membrane material. Indeed, the question of charged objects in pores of low dielectric permittivity goes back to the work of [Parsegian (1969)]. The method we chose was MD.

Our dsDNA model is motivated by the fact that the persistence length of the "usual" B-DNA is between 40 nm and 60 nm

[Kam *et al.* (2004)]. In other words, it is rather stiff on the length scale of the size of small synthetic pores. This allows us to approximate a 10 nm (=30 bp) piece of DNA as a stiff rod. We assume it to be charged with $2e$/bp and approximate it as a rigid object composed of 60 overlapping spheres of diameter 2 nm with a mutual distance of 0.167 nm each carrying one elementary charge. Ions are approximated as spheres with 0.425 nm diameter, thus including a first solvation shell that is generally considered to be tightly bound. Water is treated as a homogeneous dielectric medium with a dielectric constant of $\varepsilon = 80$. DNA and ions repel each other with a truncated and shifted variant of the Lennard–Jones potential, which is known as the Weeks–Chandler–Anderson (WCA) potential:

$$\frac{U(r)}{k_\mathrm{B}T} = \begin{cases} 4\epsilon \left[\left(\frac{\sigma}{r}\right)^{12} - \left(\frac{\sigma}{r}\right)^{6} \right] + 1 & \text{if } r < 2^{1/6}\sigma \\ 0 & \text{otherwise,} \end{cases} \tag{22.1}$$

where the size parameter σ is the arithmetic mean of the diameter of both particles involved. The absolute temperature is denoted by T and the Boltzmann constant by k_B. The prefactor ϵ is set to 1 $k_\mathrm{B}T$. The potential rises steeply from zero to 1 $k_\mathrm{B}T$ between 1.12σ and 1σ so that the particles almost never come closer than σ. It can be considered as an MD-friendly variant of the hard sphere interaction. The pore is treated as a geometric object shaped according to Fig. 22.1 from which we calculate the distance in every MD step for all ions and apply a WCA potential with $\sigma = 1$ nm.

For simplicity, we assumed that the charged rod is confined to the pore axis and characterizes its position by the axial coordinate z of its center. The positional constraint leads to an underestimation of the barrier by a few $k_\mathrm{B}T$, which corresponds to the translational and rotational entropy loss in the constraining geometry of the pore. The advantage, however, is that we can calculate the free energy profile $\mathcal{A}(z)$ as the potential of the mean force necessary to fix the DNA. This stall force corresponds to the negative sum of the force on all DNA particles F. This reads as:

$$\mathcal{A}(z) = -\int \mathrm{d}z' \langle F\left(z'\right)\rangle. \tag{22.2}$$

A sketch illustrating the applied simulation model and a snapshot from an actual simulation are shown in Fig. 22.1.

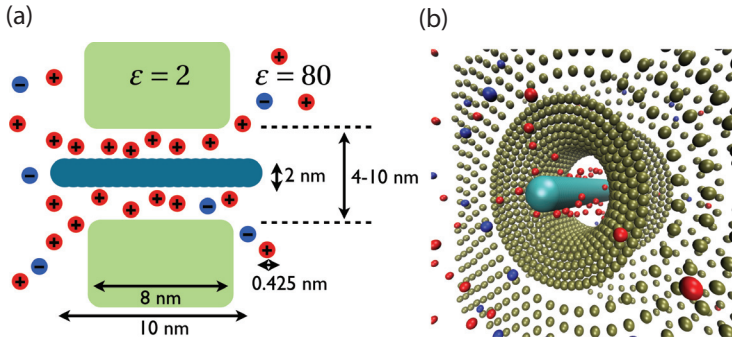

Figure 22.1 (a) Sketch of the simulation setup and (b) Snapshot of the simulation setup. Cyan spheres compose the rigid DNA molecule that is fixed on the pore axis. Blue and red sphere represent counterions and coions and the surface discretization points are represented as green spheres ((b) only). The pore shape is depicted by the rounded rectangles in (a).

The model, as presented up to here, does not take into account dielectric properties of the membrane material. We implicitly assumed its dielectric constant to equal that of the surrounding water. This is, however, not justified, as typical membrane materials such as SiO_2 and Si_3N_4 are much less polarizable than water. The qualitative influence of dielectric boundary forces is depicted in Fig. 22.2a using the picture of image charges that is presented in many textbooks dealing with electrostatics, e.g., [Jackson (1999)]. In contrast to the situation most often considered in textbooks—metallic surfaces—the image charges occurring in our system are of equal sign: The image charge of a charge q equals

$$q' = \frac{\varepsilon_{\text{water}} - \varepsilon_{\text{membrane}}}{\varepsilon_{\text{water}} + \varepsilon_{\text{membrane}}} q, \tag{22.3}$$

thus almost equal to q for $\varepsilon_{\text{membrane}}$ close to unity. The image charge picture allows us to immediately write down the potential energy of a charge q at a distance d from a wall:

$$V(d)/k_{\text{B}}T = qq' \frac{l_{\text{B}}}{2d}, \tag{22.4}$$

where l_{B} is the Bjerrum length, which equals 0.71 nm in water at ambient conditions.

Even though the pore is not a plane, the work necessary to bring a dsDNA molecule of charge 60 into a pore of radius 2.5 nm would

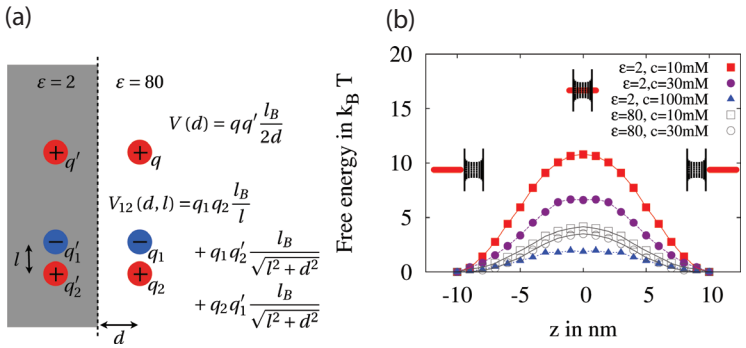

Figure 22.2 (a) Illustration of the effect of a planar dielectric boundary on the potential energy of a point charge and on the pair potential of two point charges. (b) Free energy profile comparing different salt concentrations with and without taking into account dielectric contrast ($\varepsilon = 2/\varepsilon = 80$).

be of similar order. With $q = 60$, d = 2.5 nm, and $\varepsilon_{\text{membrane}} = 2$, we obtain a potential energy of 1000 $k_{\text{B}}T$ from eq. 22.4. As screening by counterions reduces the effective charge and the dielectric contrast enhances the mutual attraction of opposite charges, the barrier will be much smaller. Both effects are discussed in detail below.

In our simulations, the dielectric interface between water and the membrane material is taken into account with the ICC* (induced charge computation) algorithm that was presented in [Tyagi *et al.* (2010)]. In summary, the *induced charge* on the dielectric boundary is determined in an iterative, self-consistent way, which can be combined with any algorithm suited to calculate the long-range electrostatic interaction. We apply the P^3M method developed by Hockney and Eastwood [Hockney and Eastwood (1988)] with parameters tuned for a force accuracy of 10^{-3} $k_{\text{B}}T/\text{nm}$ according to [Deserno and Holm (1998)].

In Fig. 22.2b, we report the free energy profile for a pore of 5 nm diameter comparing cases with different salt concentrations and with and without taking into account the dielectric contrast between water and the membrane material. We observe a barrier of up to 20 $k_{\text{B}}T$ under low-salt conditions that decreases quickly with the addition of salt. The dielectric contrast is responsible for a sharp increase of the barrier, although it stays far below the estimate given

above. We will now try to understand these results by means of PB theory.

The easiest way to derive the PB equation is the following: We assume that the concentration c of univalent ions of two different types $+$ and $-$ distribute according to the Boltzmann distribution in the electrostatic potential. This reads as:

$$c_{\pm}(r) = c_0 \exp \mp\phi.$$

Here, c_0 is the concentration of the electrolyte reservoir and Φ is the electrostatic potential in units of $k_B T/e$. Mutual interaction of ions that is not electrostatic in nature is neglected in PB theory. This is one reason why the validity of the PB equation is restricted to low-ion densities.

The following mean field assumption is the central theme of PB theory: It is assumed that the average electrostatic potential may be inserted in this equation. This is the second reason why the PB equation is limited to low-ion densities: At moderate ion concentrations, correlations between ion positions are important. Then, the electric field felt by an ion is no longer the mean electric field at the same position, but due to correlations with the other ions, it is different. For strongly correlated systems, a different limit can be taken: The *strong coupling limit* that is an alternative continuum theory [see, e.g., Moreira and Netz (2000)].

The mean electrostatic potential can be calculated from the Poisson equation given in this unit system as:

$$\Delta\phi = -4\pi l_B (c_+ - c_-).$$

Here l_B denotes the Bjerrum length. Combining both equations leads to the PB equation:

$$\Delta\phi = \kappa^2 \sinh\phi,$$

where $1/\kappa = l_D$ is the Debye length. It is given by:

$$l_D = (8\pi l_B c_0)^{-1/2}.$$

Only a few analytic solutions for this equation are known. In many works, it is linearized by expanding $\sinh\Phi$ and truncating at first order, yielding the linearized PB equation, also known as Debye–Hückel equation:

$$\Delta\phi = \kappa^2\phi$$

For a half space $x > 0$ bounded by a wall of constant potential ϕ_0 at $x = 0$, this equation is easily solved:

$$\phi = \phi_0 \exp\left(-x/l_\mathrm{D}\right).$$

This characteristic decay of the electrostatic potential, and correspondingly the density of the counterions, is the most characteristic feature of the PB equation. A good approximation of the Debye length in a univalent aqueous solution with a concentration c can be obtained from:

$$l_\mathrm{D} = \frac{10\,\mathrm{nm}}{\sqrt{c\,\mathrm{in\,mmol/l}}},$$

thus 10 nm at 1 mM, 1 nm at 100 mM and 0.3 nm at 1 M. At a distance of the Debye length from a charged surface, the electric field is reduced to a factor $1/e$, and on length scales larger than several Debye lengths, the electrostatic force between charges is negligible.

The same can be expected for the interaction of the DNA molecule with its image charge: We expect the effective charge entering equation 22.4 to be reduced by a factor of $\exp\left(-r/l_\mathrm{D}\right)$, which is 0.45 for 10 mM salt and a pore of radius 2.5 nm. This, however, is still not sufficient to explain the magnitude of the barrier, which we would expect to be $\sim 200 k_\mathrm{B}T$.

The fact that the barrier is much lower can be explained with the following consideration: The image charge forces between DNA and counterions lead to an enhanced attraction of DNA and counterions. This effect leads to better neutralization of the interior of the pore cylinder, than without dielectric contrast. We performed simulations with different pore lengths between 4 nm and 20 nm at 10 mM salt and measured the degree to which the DNA charge in the center of a pore was neutralized. This degree was defined as the total ion charge in a thin slab at the pore center divided by the DNA charge in the same slab. A neutralization degree of 1 thus means that each DNA charge is exactly compensated for by small ions.

The results are depicted in Fig. 22.3a. The dielectric contrast enhances the tendency that the interior of the pore is electrostatically neutral at much lower pore lengths than in the situation without dielectric contrast. In both cases, however, full neutralization is reached in the limit of an infinitely long pore. This is due to the fact that the self-energy of an infinitely long charged rod diverges

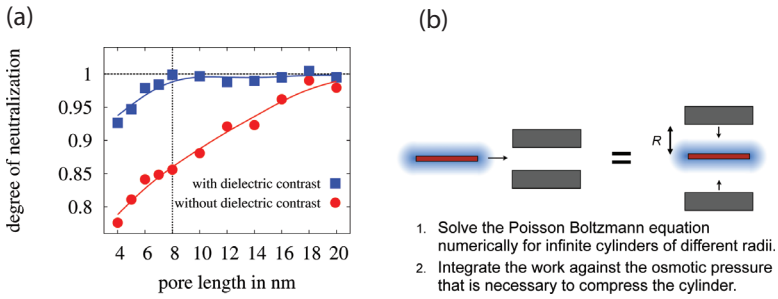

Figure 22.3 (a) The degree of neutralization as a function of the pore length. The vertical dotted line corresponds to the length for which free energy barriers are reported. (b) Sketch depicting the idea of the PB model applied to calculate free energy barriers.

and so must be compensated by counterions. In the limit of zero salt reservoir concentration as treated in [Manning (1969)], this divergence leads to the following: Even when decreasing the ion reservoir concentration to zero, a finite number of ions stays next to the charged cylinder, a fact that is known as Manning condensation.[a]

The effect of charge neutralization allows us to make the following consideration: If the interior of the pore is fully neutralized, no image charges are to be taken into account. Then, the effect of the pore confinement is nothing but compressing the counterion cloud into a radius r. This can be modeled with the PB equation:

We assume DNA to be a cylinder of radius 1 nm and one elementary charge per 0.167 nm and the pore to be a cylinder of radius R without surface charges. The boundary conditions thus are the following:

$$\left.\frac{\partial \Phi}{\partial r}\right|_{r=1\,\mathrm{nm}} = 4\pi l_{\mathrm{B}} \sigma_{\mathrm{DNA}}, \tag{22.5}$$

$$\left.\frac{\partial \Phi}{\partial r}\right|_{r=R} = 0, \tag{22.6}$$

where $\sigma_{\mathrm{DNA}} = 0.94e/\mathrm{nm}^2$. The second boundary condition corresponds to the requirement of charge neutrality of the system.

[a]Surprisingly in many cases, Manning condensation is wrongly attributed to be the reason for the "wrong" prefactor of the stall force in electrophoresis experiments (see Section 22.3). This underlines how common this misconception is.

The work to change the volume of the pore is determined by the osmotic pressure on the cylinder (see the sketch in Fig. 22.3b). In the PB approximation, this is just the ideal gas pressure of the ions at the boundary of the cell. We, however, do not want to compress the whole ion cloud but allow particle and volume exchange with the reservoir. Under these conditions, the excess osmotic pressure, thus the osmotic pressure minus the osmotic pressure in the reservoir, has to be taken. It reads as:

$$p^{\mathrm{e}}(R) = k_{\mathrm{B}}T\left(c_{+} + c_{-} - 2c_{0}\right)\Big|_{r=R} \tag{22.7}$$

$$= 2k_{\mathrm{B}}T\,c_{0}\left(\cosh\Phi(R) - 1\right). \tag{22.8}$$

This allows to calculate the work needed to shrink the pore to the desired size: it is the integral of $\mathrm{p}\,\mathrm{d}V$ taken from an infinitely large cylinder to a finite cylinder of radius R. In our case, we obtain the work per unit length as the integral:

$$\mathcal{W}/l = \int_{\infty}^{R} p^{\mathrm{e}}\left(R'\right) 2\pi R'\mathrm{d}R'.$$

We determine this work from a numerical solution of the PB equation with a simple finite difference scheme implemented in the programming language PYTHON using the NUMPY numeric library.

In Fig. 22.4, we report the results obtained with the PB model in comparison to the results of the coarse-grained MD model including dielectric contrast. We report the free energy barrier as a function of the pore radius for different salt concentration. The PB barriers are scaled to an effective DNA length of 7 nm (due to end effects of the pore). The agreement is surprisingly good: The deviations are within a few $k_{\mathrm{B}}T$. This indicates that the general physical effects are captured correctly by the PB model. Although our considerations make it plausible that the PB model is appropriate, it remains surprising even to the authors that the complex effect of dielectric boundary forces can be boiled down to a model that does not contain dielectrics at all. It however encourages us that other simple models in physics chosen with care and good physical intuition sometimes can explain more than expected at first sight.

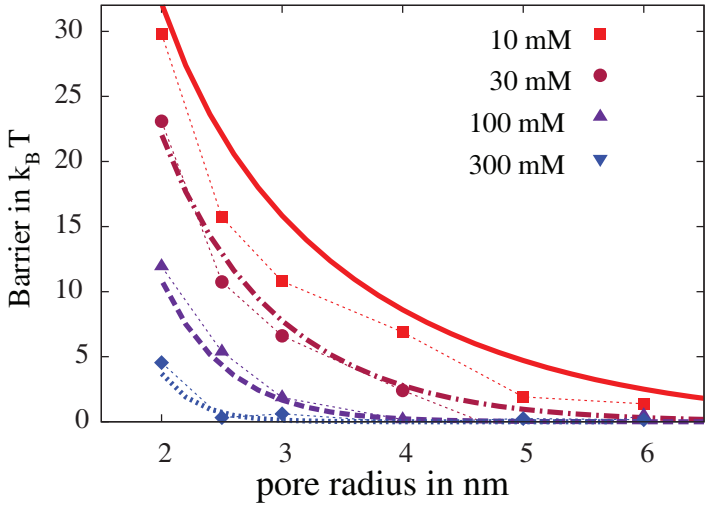

Figure 22.4 The free energy barrier calculated from MD simulations (symbols connected with thin lines) and PB model (thick lines).

22.5 Acknowledgments

The simulations were performed with the software package ESPResSo[Limbach *et al.* (2006)], published under the GNU Public License and free to use. The ICC* alogorithm requires to use ESPResSo in the release of version 3.1 (bugfixed in 3.1.1), which is described in [Arnold *et al.* (2012)]. We acknowledge financial support by the German Science Foundation (DFG) through the Collaborative Research Center 716 within project C5. The authors thank O. Hickey for critically reading the manuscript and M. Süzen and M. Sega for contributions in earlier phases of the project.

References

Arnold, A., Lenz, O., Kesselheim, S., Weeber, R., Fahrenberger, F., Roehm, D., Košovan, P. and Holm, C. (2012). Espresso 3.1—molecular dynamics software for coarse-grained models, in *Meshfree Methods for Partial Differential Equations VI*, no. 69, in Lecture Notes in Computational Science and Engineering (Springer).

Bell, N. A. W., Engst, C. R., Ablay, M., Divitini, G., Ducati, C., Liedl, T. and Keyser, U. F. (2012). DNA origami nanopores, *Nano Lett.* **12**, 1, pp. 512–517, doi:10.1021/nl204098n, http://pubs.acs.org/doi/abs/10.1021/nl204098n.

Branton, D., Kasianowicz, J. J., Brandin, E. and Deamer, D. W. (1996). Characterization of individual polynucleotide molecules using a membrane channel, *Proc. Natl. Acad. Sci. USA* **93**, pp. 13770–13773.

Chuang, J., Kantor, Y. and Kardar, M. (2001). Anomalous dynamics of translocation, *Phys. Rev. E* **65**, p. 011802.

Coulter, Wallace H. 1953. Means for counting particles suspended in a fluid. U.S. Patent 2,656,508, filed August 27, 1949, and issued October 20, 1953.

de Haan, H. and Slater, G. (2012). Memory effects during the unbiased translocation of a polymer through a nanopore, *The Journal of Chemical Physics* **136**, p. 154903.

Dekker, C. (2007). Solid-state nanopores, *Nature Nanotech* **2**, pp. 209–215.

Deserno, M. and Holm, C. (1998). How to mesh up Ewald sums. II. An accurate error estimate for the particle-particle-particle-mesh algorithm, *J. Chem. Phys.* **109**, p. 7694.

Doi, M. and Edwards, S. F. (1986). *The theory of polymer dynamics* (Oxford Science Publications).

Eisenstein, M. (2012). Oxford nanopore announcement sets sequencing sector abuzz, *Nature biotechnol.* **30**, 4, pp. 295–296.

Fischbein, M. and Drndic, M. (2008). Electron beam nanosculpting of suspended graphene sheets, *Appl. Phys. Lett.* **93**, 11, pp. 113107–113107.

Gauthier, M. and Slater, G. (2009). Nondriven polymer translocation through a nanopore: Computational evidence that the escape and relaxation processes are coupled, *Phys. Rev. E* **79**, 2, p. 21802.

Grass, K. and Holm, C. (2009). Polyelectrolytes in electric fields: Measuring the dynamical effective charge and effective friction, *Soft Matter* **5**, pp. 2079–2092, doi:10.1039/b822276b, http://arxiv.org/abs/0812.2557.

Grosberg, A. Y. and Khokhlov, A. R. (1994). *Statistical Physics of Macromolecules* (AIP Press).

Grosberg, A. Y. and Rabin, Y. (2010). DNA capture into a nanopore: Interplay of diffusion and electrohydrodynamics, *J. Chem. Phys* **133**, p. 165102.

Hall, J. (1975). Access resistance of a small circular pore. *The Journal of general physiology* **66**, 4, pp. 531–532.

He, Y., Tsutsui, M., Fan, C., Taniguchi, M. and Kawai, T. (2011). Gate manipulation of DNA capture into nanopores, *ACS nano* **5**, 10, pp. 8391–8397.

Henrickson, S. E., Misakian, M., Robertson, B. and Kasianowicz, J. J. (2000). Driven DNA transport into an asymmetric nanometer-scale pore, *Phys. Rev. Lett.* **85**, 14, p. 3057.

Hille, B. (1968). Pharmacological modifications of the sodium channels of frog nerve, *The Journal of general physiology* **51**, 2, pp. 199–219.

Hille, B. (1970). Ionic channels in nerve membranes, *Prog. Biophys. Mol. Bio.* **21**, pp. 1–32.

Hockney, R. W. and Eastwood, J. W. (1988). *Computer Simulation Using Particles* (IOP, London).

Howorka, S. and Siwy, Z. (2009). Nanopore analytics: Sensing of single molecules, *Chemical Society Reviews* **38**, 8, pp. 2360–2384.

Ivanov, A., Instuli, E., McGilvery, C., Baldwin, G., McComb, D., Albrecht, T. and Edel, J. (2011). DNA tunneling detector embedded in a nanopore, *Nano letters* **11**, 1, p. 279.

Jackson, J. D. (1999). *Classical Electrodynamics* (Wiley, New York, 3rd edition).

Kam, Z., Borochov, N. and Eisenberg, H. (2004). Dependence of laser light scattering of DNA on NaCl concentration, *Biopolymers* **20**, 12, pp. 2671–2690.

Kesselheim, S., Sega, M. and Holm, C. (2011). Applying ICC* to DNA translocation. Effect of dielectric boundaries, *Computer Physics Communications* **182**, 1, pp. 33–35, doi:10.1016/j.cpc.2010.08.014.

Kesselheim, S., Sega, M. and Holm, C. (2012). Effects of dielectric mismatch and chain flexibility on the translocation barriers of charged macromolecules through solid state nanopores, *Soft Matter* **8**, 36, pp. 9480–9486.

Keyser, U., van der Does, J., Dekker, C. and Dekker, N. (2006). Optical tweezers for force measurements on DNA in nanopores, *Rev. Sci. Instrum.* **77**, p. 105105.

Li, J., Stein, D., McMullan, C., Branton, D., Aziz, M. J. and Golovchenko, J. (2001). Ion-beam sculpting at nanometre length scales, *Nature* **412**, 6843, pp. 166–169.

Limbach, H. J., Arnold, A., Mann, B. A. and Holm, C. (2006). ESPResSo – an extensible simulation package for research on soft matter systems, *Comp. Phys. Comm.* **174**, 9, pp. 704–727.

Long, D., Viovy, J. L. and Ajdari, A. (1996). Simultaneous action of electric fields and nonelectric forces on a polyelectrolyte: Motion and deformation, *Phys. Rev. Lett.* **76**, 20, pp. 3858–3861.

Luan, B. and Aksimentiev, A. (2010). Electric and electrophoretic inversion of the DNA charge in multivalent electrolytes, *Soft Matter* **6**, 2, pp. 243–246.

Manning, G. (1969). Limiting laws and counterion condensation in polyelectrolyte solutions I. colligative properties, *J. Chem. Phys.* **51**, pp. 924–933.

Meller, A., Nivon, L., Brandin, E., Golovchenko, J. and Branton, D. (2000). Rapid nanopore discrimination between single polynucleotide molecules, *PNAS USA* **97**, pp. 1079–1084.

Moreira, A. G. and Netz, R. R. (2000). Strong-coupling theory for counter-ion distributions, *Europhysics Letters* **52**, 6, pp. 705–711, http://stacks.iop.org/0295-5075/52/705.

Muthukumar, M. (1999). Polymer translocation through a hole, *J. Chem. Phys.* **111**, 22, p. 10371.

Muthukumar, M. (2009). *Polymer Translocation* (Taylor and Francis), ISBN 9781420075168, http://books.google.de/books?id=PcuT-ibRtRIC.

Nkodo, A. E., Garnier, J. M., Tinland, B., Ren, H., Desruisseaux, C., McCormick, L. C., Drouin, G. and Slater, G. W. (2001). Diffusion coefficient of DNA molecules during free solution electrophoresis. *Electrophoresis* **22**, 12, pp. 2424–2432.

O'Brien, R. W. and White, L. R. (1978). Electrophoretic mobility of a spherical colloidal particle, *J. Chem. Soc. Faraday Trans.* **74**, 2, p. 1607.

Parsegian, A. (1969). Energy of an ion crossing a low dielectric membrane: Solutions to four relevant electrostatic problems, *Nature* **221**, p. 844.

Rothemund, P. (2006). Folding DNA to create nanoscale shapes and patterns, *Nature* **440**, 7082, pp. 297–302.

Rowghanian, P. and Grosberg, A. (2011). Force-driven polymer translocation through a nanopore: An old problem revisited, *The Journal of Physical Chemistry B* **115**, 48, pp. 14127–14135.

Rubinstein, M. and Colby, R. H. (2003). *Polymer Physics* (Oxford University Press, Oxford, UK).

Sakaue, T. (2010). Sucking genes into pores: Insight into driven translocation, *Phys. Rev. E* **81**, p. 041808, doi:10.1103/PhysRevE.81.041808, http://link.aps.org/doi/10.1103/PhysRevE.81.041808.

Shendruk, T. N., Hickey, O. A., Slater, G. W. and Harden, J. L. (2012). Electrophoresis: When hydrodynamics matter, *Curr. Opin. Colloid Interface Sc.* **17**, 2, pp. 74–82, doi:10.1016/j.cocis.2011.08.002.

Storm, A., Chen, J., Ling, X., Zandbergen, H. and Dekker, C. (2003). Fabrication of solid-state nanopores with single-nanometre precision, *Nature materials* **2**, 8, pp. 537–540.

Suezen, M. (2009). *Induced Charge Computation*, Ph.D. thesis, J.W. Goethe University of Frankfurt am Main.

Sung, W. and Park, P. J. (1996). Polymer translocation through a pore in a membrane, *Phys. Rev. Lett.* **77**, 4, p. 783.

Thacker, V. V., Hernandez-Ainsa, S. M., Gornall, J., Steinbock, L. J. and Keyser, U. F. (2012). Combining fluorescence imaging and ionic current detection in nanocapillaries, in *Nanopores for Bioanalytical Applications: Proceedings of the International Conference* (The Royal Society of Chemistry), ISBN 978-1-84973-416-5, pp. 43–45, doi:10.1039/9781849735278-00043, http://dx.doi.org/10.1039/9781849735278-00043.

Tsutsui, M., Taniguchi, M., Yokota, K. and Kawai, T. (2010). Identifying single nucleotides by tunnelling current, *Nat. Nanotechnol.* **5**, 4, pp. 286–290.

Tyagi, C., Süzen, M., Sega, M., Barbosa, M., Kantorovich, S. and Holm, C. (2010). An iterative, fast, linear-scaling method for computing induced charges on arbitrary dielectric boundaries, *J. Chem. Phys.* **132**, p. 154112 doi:10.1063/1.3376011.

Venkatesan, B. and Bashir, R. (2011). Nanopore sensors for nucleic acid analysis, *Nat. Nanotechnol.* **6**, 10, pp. 615–624.

Wanunu, M., Morrison, W., Rabin, Y., Grosberg, A. and Meller, A. (2009). Electrostatic focusing of unlabelled DNA into nanoscale pores using a salt gradient, *Nat. Nanotechnol.* **5**, 2, pp. 160–165.

Zhang, J. and Shklovskii, B. (2007). Effective charge and free energy of DNA inside an ion channel, *Phys. Rev. E* **75**, 2, p. 21906.

Chapter 23

Mean-Field Electrostatics of Stiff Rod-Like Ions

Sylvio May[a] and Klemen Bohinc[b]
[a] *Department of Physics, North Dakota State University, Fargo, ND 58108-6050, USA*
[b] *Faculty of Health Sciences, University of Ljubljana, SI-1000 Ljubljana, Slovenia*
klemen.bohinc@zf.uni-lj.si

23.1 Introduction

Electrostatic interactions between macroions in aqueous solution are omnipresent and therefore of fundamental interest for soft matter, colloid science, and biomolecular systems [10]. Macroions can appear in a multitude of forms such as surfactant micelles, polyelectrolytes (including DNA), gels, block copolymers, nanoparticles, extended solid surfaces (mica, clay, glass), lipid membranes, and proteins. Their charged moieties can be fixed or mobile, polarizable, or regulated through a dissociation process. What makes the interaction between macroions interesting from a basic physical point of view is the presence of small *mobile* ions in the aqueous solution. These ions often dissociate and become mobile because the high dielectric constant of water, $\epsilon_W \approx 80$, greatly reduces cation–anion attraction, thus favoring the entropic gain that comes

Electrostatics of Soft and Disordered Matter
Edited by David Dean, Jure Dobnikar, Ali Naji, and Rudolf Podgornik

ISBN 978-981-4411-85-1 (Hardcover), 978-981-4411-86-8 (eBook)
www.panstanford.com

with the dissociation process. The relation between electrostatic and thermal energy is often expressed in terms of the Bjerrum length $l_B = e^2/(4\pi\epsilon_0\epsilon_W k_B T)$, at which two monovalent ions have an interaction energy of $k_B T$. Here, k_B is Boltzmann's constant, T is the absolute temperature, ϵ_0 is the permittivity in vacuum, and e is the elementary charge.

The fundamental equation of electrostatics is Poisson's equation, $\epsilon_W\epsilon_0\triangle\Phi = -\rho$, a differential equation ($\triangle$ is the Laplacian) for the electrostatic potential Φ at given volume charge density ρ and uniform dielectric constant ϵ_W in the aqueous phase. Textbook problems typically fix ρ and ask the student reader to find the corresponding potential Φ. Mobile ions, however, will migrate toward regions of favorable potential. That is, the volume charge density ρ adjusts according to the potential Φ. More specifically, if the aqueous solution contains, say, a symmetric z:z salt solution (i.e., z-valent cations and anions with local concentrations n_+ and n_-, respectively), then $\rho = ez(n_+ - n_-)$ where both $n_+ = n_+(\Phi)$ and $n_+ = n_+(\Phi)$ depend on the electrostatic potential Φ.

Fortunately, finding the relation $\rho = \rho(\Phi)$ becomes a straightforward task in one particular situation, namely when the mobile ions are point-like and when correlations between ions are ignored. These two assumptions give rise to the classical Poisson–Boltzmann (PB) model, according to which the local ion concentrations follow the Boltzmann distributions $n_\pm = n_0 e^{\mp ze\Phi/k_B T}$. Here, the reference concentration n_0 equals the bulk concentration of cations and anions if a salt reservoir is present (otherwise n_0 follows from the condition of overall electroneutrality). Combination of the Poisson equation with the Boltzmann distributions yield the classical PB equation for a symmetric electrolyte

$$\triangle(z\Psi) = 8\pi l_B z^2 n_0 \sinh(z\Psi), \tag{23.1}$$

here conveniently expressed in terms of the dimensionless potential $\Psi = e\Phi/k_B T$.

For not too highly charged macroions and mobile ions that are monovalent, the classical PB model often makes qualitatively (sometimes even quantitatively) correct predictions, for example, concerning ion concentrations, predicting adsorption energies of macroions on surfaces [1], or capturing the effect of counterion

condensation [9]. For divalent or higher valent mobile ions, the classical PB model typically fails, even qualitatively. Among the most compelling examples is the condensation of double-stranded DNA in presence of trivalent cobalt hexamine [$Co(NH_3)_6^{3+}$] [2], resulting in compact toroidal aggregates in which DNA takes up a volume fraction of about 72% [12]. The mechanism how cobalt hexamine mediates attraction between like-charged DNA strands is related to the presence of ion–ion correlations. That is, DNA phosphate groups and cobalt hexamine counterions become engaged in the formation of an ordered structure of interlocked alternating charges—known as Wigner lattice—that mediate a short-range attractive force [22, 23]. The formation of a Wigner lattice is not possible in the framework of the classical PB model. This is because ion–ion correlations are generally ignored in mean-field models. Indeed, it has been shown rigorously [18] that the classical PB model always predicts a repulsive force between like-charged surfaces.

There is a second type of mobile ions that is well known to induce DNA condensation: short polyamines [7, 25], among them the trivalent spermidine and four-valent spermine, which are illustrated in Fig. 23.1. These polyamines are examples of rod-like ions wherein the individual positive charges that are attached to the mobile ions are spatially well separated from each other. We note that the separations between the individual charges are, in general, not small compared with the typical electrostatic screening length

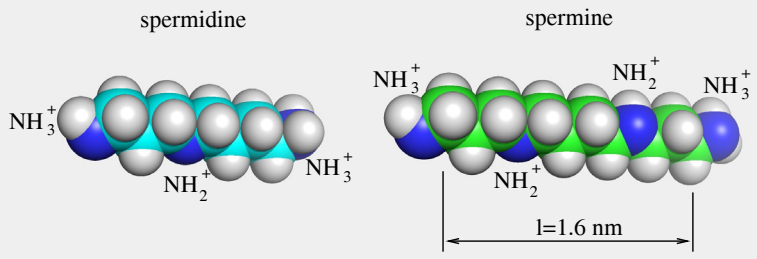

Figure 23.1 *Left*: spermidine, $[H_2N(CH_2)_3NH(CH_2)_4NH_2]^{3+}$. *Right*: spermine, $[H_2N(CH_2)_3NH(CH_2)_4NH(CH_2)_3NH_2]^{4+}$. Note that the spatial extension l of these polyamines is comparable to the electrostatic screening length, $l_D \approx 1$ nm, at physiological conditions. Molecular images were generated using PyMol.

(1 nm at physiological conditions). This has important consequences with regard to modeling this type of mobile ion: rather than being approximated as point-like ions of valence z, they should be described as z individual elementary charges that are attached uniformly to a rod of length l.

In this contribution, we discuss how to modify the PB approach so as to account for rod-like mobile ions. To this end, an appropriate free energy is introduced whose minimization yields a modified PB equation. We provide a brief account of the predictions that the modified PB approach makes. This includes, in particular, the *bridging* mechanism, which can explain the existence of a finite equilibrium distance between like-charged macroions. Here, the two ends of the rod-like ion form a bridge between the two macroions; see the illustration in the middle diagram of Fig. 23.2 below. The bridging mechanism has indeed been invoked to explain the condensation of DNA by spermine and spermidine [21]. Bridging also appears in the context of polyelectrolytes, which are able to mediate attractive interactions between like-charged surfaces [11].

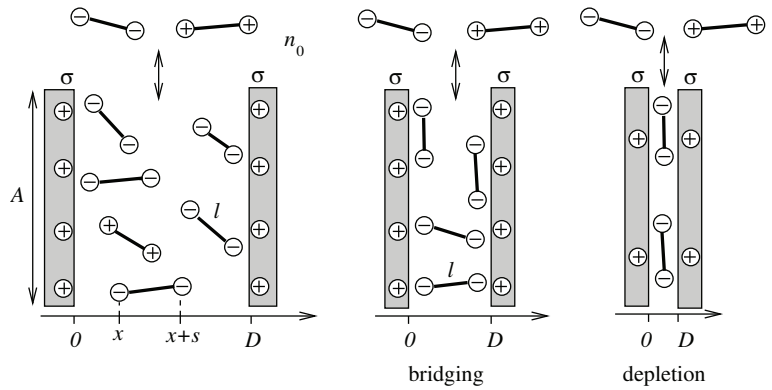

Figure 23.2 Schematic illustration of two like-charged planar surfaces (each of area A) embedded in an aqueous solution of mobile, rod-like, divalent cations and anions. The distance between the surfaces is D, their surface charge density is denoted by σ, and the length of each rod-like ion is l. Left, middle, and right diagrams correspond to $D \gg l$, $D \approx l$, and $D \ll l$, respectively. The latter two illustrate the bridging mechanism and the depletion interaction.

As modifications of the PB approach [5, 6] (and beyond [19, 20]) for polyelectrolytes already exist, we focus entirely on stiff rod-like ions.

23.2 PB Model for Stiff Rod-Like Ions

As indicated above, rod-like mobile ions are able to mediate attraction between like-charged macroions. Classical PB theory is not able to predict this kind of interaction, because it applies to point-charges and neglects correlations between charges. The question arises if one can modify the PB model so as to account for rod-like ions. This is the subject of the present contribution. We accurately account for the rod-like structure of each ion while continuing to neglect correlations between different rod-like ions. Differently expressed, we neglect *interionic* correlations but do account for *intraionic* correlations. If the individual monovalent charges of each rod-like ion are sufficiently separated (as compared with the electrostatic screening length of the system), this approach is expected to work as well as the PB model for monovalent point-like ions.

The following part focuses on a symmetric electrolyte of divalent ions, where the two elementary charges of each divalent ion are separated by a fixed distance l. There is no particular significance to having both cations and anions being rod-like other than the simplicity of this symmetric situation (the asymmetric case with only rod-like counterions was first analyzed by Carnie and McLaughlin [8]). We denote the concentration of rod-like cations and anions in the bulk of the electrolyte by n_0 (both must be the same to ensure electroneutrality). Embedded in the electrolyte are two planar and parallel, like-charged macroion surfaces of area A and with surface charge density $\sigma > 0$ each; see the illustration in Fig. 23.2 The surfaces are oriented normal to the x-axis of a Cartesian coordinate system and located at positions $x = 0$ and $x = D$. Note that all system properties depend only on the x-coordinate, thus being invariant with respect to the y- and z-directions.

Rod-like ions are able to change both their location and orientation. We can conveniently quantify both degrees of freedom by introducing an ionic distribution function $n_+(x, s)$ for the cationic

rod-like ions (and similarly $n_-(x, s)$ for the anionic rod-like ions). Here, x and $x + s$ denote the positions of the two charges of a given rod-like ion along the x-axis; see the left diagram of Fig. 23.2. Hence, s is the projected length of the rod-like ion along the x-axis. Orientational averaging over any given physical quantity $g(s)$ can then be expressed as $\langle g(s)\rangle = 1/(2l) \int_{-l}^{l} ds\, g(s)$. From $n_+(x, s)$, we obtain the local concentration of the divalent rod-like cations by $n_+(x) = \langle n_+(x, s)\rangle$ and the corresponding orientational probability distribution by $n_+(x, s)/n_+(x)$. Analogous relations apply to the divalent rod-like anions.

The key toward incorporating rod-like ions into the PB formalism is to express the electrostatic free energy F in terms of the ionic distribution functions $n_+(x, s)$ and $n_-(x, s)$. Recognizing that the free energy $F = U_{\rm el} - TS$ consists of the energy stored in the electrostatic field ($U_{\rm el}$) and the entropic (i.e., translational and orientational) contribution of the mobile ions ($-TS$), we arrive at the mean-field expression

$$\frac{F}{Ak_{\rm B}T} = \int_{-\infty}^{\infty} dx \left\{ \frac{\Psi'(x)^2}{8\pi l_{\rm B}} + \sum_{i=\{+,-\}} \left\langle n_i(x, s) \left(\ln \frac{n_i(x, s)}{n_0} - 1 + U(x, s) \right) \right\rangle + 2n_0 \right\}, \tag{23.2}$$

where a prime denotes a derivative with respect to the argument (i.e., $\Psi'(x) = d\Psi/dx$). The second term contains an additional external potential $U(x, s)$ that we can chose so as to prevent the rod-like ions from penetrating into one of the two planar surfaces. We point out that the dimensionless potential $\Psi(x) = e\Phi/k_{\rm B}T$ is related to the ionic distribution functions $n_+(x, s)$ and $n_-(x, s)$ through Poisson's equation

$$\Psi''(x) = -4\pi l_{\rm B} \sum_{i=\{+,-\}} i \langle n_i(x, s) + n_i(x - s, s)\rangle. \tag{23.3}$$

Hence, the only unconstrained quantities in the free energy F are the ionic distribution functions $n_+(x, s)$ and $n_-(x, s)$. We can find these through functional minimization of $F[n_+(x, s), n_-(x, s)]$ subject to Poisson's equation, yielding the Boltzmann distributions $n_\pm(x, s) = n_0 e^{\mp[\Psi(x)+\Psi(x+s)]-U(x,s)}$. Inserting these back into Poisson's equation

23.3 results in the PB equation for a symmetric electrolyte of divalent rod-like ions

$$2\Psi''(x) = 4 \times 8\pi l_B n_0 \left\langle e^{-U(x,s)} \sinh[\Psi(x) + \Psi(x+s)] \right\rangle \quad (23.4)$$
$$= \frac{4 \times 8\pi l_B n_0}{2l} \int_{-min(l,x)}^{min(l,D-x)} ds \sinh[\Psi(x) + \Psi(x+s)],$$

where the second equality follows from choosing the external potential $U(x, s)$ so as to prevent ions from moving beyond the two rigid surfaces (i.e., all rod-like ions are strictly confined to the region $0 < x < D$).

Equation 23.4 constitutes a nonlocal integro-differential equation that must be solved subject to the two boundary conditions $\Psi'(0) = -4\pi l_B \sigma/e$ and $\Psi'(D) = 4\pi l_B \sigma/e$. The two boundary conditions reflect the presence of the fixed charges on the two planar surfaces. Once known, the solution $\Psi(x)$ allows us to compute the ionic distribution functions $n_\pm(x, s)$ and thus the free energy in Eq. 23.2.

23.3 Predictions of the PB Model

In the following, we discuss predictions of the PB model for stiff rod-like ions as specified by Eqs. 23.2–23.4. Note first that in the limit $l \to 0$, we recover the classical PB equation for a symmetric 2:2 electrolyte, that is, Eq. 23.1 for $z = 2$. On the contrary, if all rod-like ions are cut in half (thus leaving two monovalent point-like mobile ions instead of one single divalent rod-like ion), then we obtain Eq. 23.1 for $z = 1$ and $n_0 \to 2n_0$. Both cases predict strictly repulsive interactions between the two like-charged surfaces.

Any nonvanishing rod length l entails a *depletion-induced* attraction between the two surfaces; see the illustration in the right diagram of Fig. 23.2. For example, upon (hypothetically) switching off all charges in the system (i.e., the charges on the surfaces and on all rod-like ions), the free energy in Eq. 23.2 becomes $F = F_{\text{depl}}$ with $F_{\text{depl}}/(Aln_0k_BT) = -(D/l)^2 + 2D/l$ for $D \le l$ and $F_{\text{depl}}/(Aln_0k_BT) = D/l$ for $D > l$. Here, the minimum of the free energy is located at $D = 0$; see curve g in Fig. 23.3 below. That is,

all rods become expelled from the space between the two surfaces to avoid loss in orientational entropy, leading to close contact of the two surfaces.

For weakly charged surfaces, the dimensionless potential becomes small. In this limit (i.e., $\Psi(x) \ll 1$), we can linearize the PB equation, thus replacing $\sinh[\Psi(x) + \Psi(x+s)]$ in Eq. 23.4 by $\Psi(x) + \Psi(x+s)$. As in classical PB theory, we refer to this regime as the Debye–Hückel limit. The free energy then separates into an electrostatic and a depletion-attraction contribution, $F = F_{\rm elec} + F_{\rm depl}$, where $F_{\rm elec} = Ak_{\rm B}T\,\Psi(0)\sigma/e$ can be computed directly from the surface potential $\Psi(0)$ and where $F_{\rm depl}$ is given above. In the Debye–Hückel limit, the electrostatic contribution is small and will thus only slightly shift the depletion minimum; see the illustration in the right diagram of Fig. 23.2. The question is what role

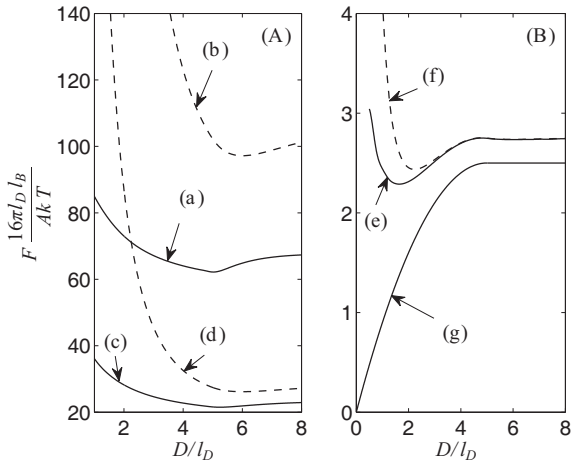

Figure 23.3 Scaled free energy $16\pi l_{\rm B} l_{\rm D} F/(Ak_{\rm B}T)$ as a function of the dimensionless distance $D/l_{\rm D}$ between the two like-charged surfaces. In both diagrams *A* and *B*, the solid curves are derived using the nonlinear theory (see Eqs. 23.2–23.4), whereas the dashed curves are based on the linearized Debye–Hückel limit. The surface charge densities correspond to $\sigma = 2 \times e/(2\pi l_{\rm B} l_{\rm D})$ (curves *a, b*), $\sigma = 1 \times e/(2\pi l_{\rm B} l_{\rm D})$ (curves *c, d*), $\sigma = 0.1 \times e/(2\pi l_{\rm B} l_{\rm D})$ (curves *e, f*), and, $p = 0$ (curve *g*). In the latter case, no electrostatic interactions are present, leaving only the bare depletion interaction. All curves correspond to a rod length $l = 5\,l_{\rm D}$. Figure is adapted from May *et al.* [16].

the electrostatic contribution F_{elec} plays for more highly charged surfaces, when electrostatic energies compete with or become larger than the depletion energies. In Fig. 23.3, we show the scaled free energy as a function of the surface separation D, calculated within both the linear (dashed lines) and nonlinear (solid lines) PB model for several different surface charge densities. Here, it is convenient to measure length in units of the electrostatic screening length l_{D} (defined through $1/l_{\text{D}}^2 = 4 \times 8\pi l_{\text{B}} n_0$) and surface charge density in units of $e/(2\pi l_{\text{B}} l_{\text{D}})$. All curves in Fig. 23.3 correspond to a rod length $l = 5\, l_{\text{D}}$ that is much longer than the electrostatic screening length l_{D}.

Indeed, for small σ, we observe an attractive interaction due to the steric depletion of the rod-like ions, leading to an equilibrium separation $D = D^{\text{eq}}$ with $D^{\text{eq}} \ll l$ (see curves *e, f, g* in Fig. 23.3). However, for larger σ, we consistently observe an optimal separation $D^{\text{eq}} \approx l$, which cannot be caused by the depletion interaction. The optimal separation $D^{\text{eq}} \approx l$ is predicted within both the linear and nonlinear PB approaches (with vastly different interaction energies though). A similar calculation for a small rod length, say $l = 0.5\, l_{\text{D}}$, would reveal the complete absence of a minimum other than the depletion-induced one. That is, for large σ, the surfaces would always repel each other as in the classical PB model. We conclude from Fig. 23.3 that for sufficiently large rod-lengths and surface charge densities, an equilibrium separation $D^{\text{eq}} \approx l$ between the two like-charged surfaces emerges.

An analysis based on the PB model according to Eqs. 23.2–23.4 has been carried out recently [16]. In the following, we summarize some results:

(1) The minimum $D^{\text{eq}} \approx l$ is caused by electrostatic interactions. This can be deduced within the Debye–Hückel limit directly from the electrostatic contribution F_{elec} to the total free energy. It is also indicated by the electrostatic potential $\Psi(x)$, which starts to oscillate above a certain critical rod length l^{crit}. The oscillations imply overcharging, which is a typical signature for the presence of attractive interactions [15, 17].
(2) The critical length l^{crit} above which attractive interactions between like-charged surfaces emerge can be estimated from a

series expansion of the linearized PB equation in terms of the scaled rod length l/l_D. Far away from the surfaces ($l < x < D - l$), we find up to fourth order

$$\frac{l^4}{240}\Psi''''(x) + \left[\frac{l^2}{12} - l_D^2\right]\Psi''(x) + \Psi(x) = 0. \qquad (23.5)$$

Solutions for $\Psi(x)$ can produce oscillating potentials. One can show [4] that within this fourth-order model a minimum in the electrostatic contribution to free energy F_{elec} can only be adopted for $l > l_{crit}$ with $l_{crit} = 2.170 l_D$. Carrying out the series expansion in Eq. 23.5 to higher orders shows that the critical length actually is $l_{crit} = 2.069 l_D$.

(3) Analysis of the orientational probability distribution $n_+(x, s)/n_+(x)$ indicates two preferential orientations of the rod-like ions when $D = D^{eq} \approx l$. One is parallel to the surfaces and the other is perpendicular; see the illustration in the middle diagram of Fig. 23.2. The latter, which is absent for isolated surfaces, embodies the bridging mechanism as origin for the existence of the equilibrium separation $D = D^{eq} \approx l$. Long, uniformly charged rods prefer to orient parallel to the surfaces [14].

We point out that the incorporation of rod-like ions into the PB formalism, which we have discussed here only for a symmetric electrolyte of divalent rod-like ions, has recently been generalized to mixtures of rod-like ions with arbitrary length and line charge distributions [4]. In addition, electrolytes composed of rod-like ions were also investigated using field theory [3] and computer simulations [14, 24].

23.4 Conclusion

The spatial extension of the charge distribution within multivalent mobile ions impacts electrolyte properties and affects the interactions between macroions [13]. This is, perhaps most dramatically, the case for rod-like ions, which even on the mean-field level give rise to attractive interactions between like-charged surfaces via a bridging mechanism. On the basis of a simple model system, we have discussed how to account for rod-like ions within the PB

formalism. Here, charge–charge correlations within the rod-like ions are accounted for accurately, whereas charge–charge correlations between different rod-like ions are neglected.

References

1. Ben-Tal, N., Honig, B., Miller, C. and McLaughlin, S. (1997). Electrostatic binding of proteins to membranes. Theoretical predictions and experimantal results with charybdotoxin and phospholipid vesicles, *Biophys. J.* **73**, pp. 1717–1727.
2. Bloomfield, V. A. (1997). DNA condensation by multivalent cations, *Biopolymers* **44**, pp. 269–282.
3. Bohinc, K., Grime, J. M. A. and Lue, L. (2012). The interactions between charged colloids with rod-like counterions, *Soft Matter* **8**, 20, pp. 5679–5686.
4. Bohinc, K., Rescic, J., Maset, S. and May, S. (2011). Debye–Hückel theory for mixtures of rigid rodlike ions and salt, *J. Chem. Phys.* **134**, 7.
5. Borukhov, I., Andelman, D. and Orland, H. (1995). Polyelectrolyte solutions between charged surfaces, *Europhysics Lett.* **32**, 6, pp. 499–504.
6. Borukhov, I., Andelman, D. and Orland, H. (1998). Scaling laws of polyelectrolyte adsorption, *Macromolecules* **31**, pp. 1665–1671.
7. Butler, J. C., Angelini, T., Tang, J. X. and Wong, G. C. L. (2003). Ion multivalence and like-charge polyelectrolyte attraction, *Phys. Rev. Lett.* **91**, 2, p. 028301.
8. Carnie, S. and McLaughlin, S. (1983). Large divalent-cations and electrostatic potentials adjacent to membranes—a theoretical calculation, *Biophys. J.* **44**, pp. 325–332.
9. Deserno, M., Holm, C. and May, S. (2000). Fraction of condensed counterions around a charged rod: Comparison of Poisson-Boltzmann theory and computer simulations, *Macromolecules* **33**, pp. 199–205.
10. Evans, D. F. and Wennerström, H. (1994). *The Colloidal Domain: Where Physics, Chemistry, Biology and Technology Meet* (Wiley-VCH, New York).
11. Huang, H. H. and Ruckenstein, E. (2004). The bridging force between two plates by polyelectrolyte chains, *Adv. Colloid Interface Sci.* **112**, 1–3, pp. 37–47.
12. Hud, N. V. and Vilfan, I. D. (2005). Toroidal DNA condensates: Unraveling the fine structure and the role of nucleation in determining size, *Annu. Rev. Biophys. Biomole. Struct.* **34**, pp. 295–318.

13. Kanduc, M., Naji, A., Jho, Y. S., Pincus, P. A. and Podgornik, R. (2009). The role of multipoles in counterion-mediated interactions between charged surfaces: strong and weak coupling, *J. Phys. Cond. Matter* **21**, 42, p. 424103.
14. Kim, Y. W., Yi, J. and Pincus, P. A. (2008). Attractions between like-charged surfaces with dumbbell-shaped counterions, *Phys. Rev. Lett.* **101**, 20, p. 208305.
15. Levin, Y. (2002). Electrostatic correlations: From plasma to biology, *Reports on Progress in Physics* **65**, 11, pp. 1577–1632.
16. May, S., Iglic, A., Rescic, J., Maset, S. and Bohinc, K. (2008). Bridging like-charged macroions through long divalent rodlike ions, *J. Phys. Chem. B* **112**, 6, pp. 1685–1692.
17. Messina, R., Gonzalez-Tovar, E., Lozada-Cassou, M. and Holm, C. (2002). Overcharging: The crucial role of excluded volume, *Europhysics Lett.* **60**, 3, pp. 383–389.
18. Neu, J. C. (1999). Wall-mediated forces between like-charged bodies in an electrolyte, *Phys. Rev. Lett.* **82**, pp. 1072–1074.
19. Podgornik, R. (2004). Polyelectrolyte-mediated bridging interactions, *J. Polymer Science Part B-polymer Phys.* **42**, 19, pp. 3539–3556.
20. Podgornik, R. and Licer, M. (2006). Polyelectrolyte bridging interactions between charged macromolecules, *Curr. Opin. Colloid Interface Sci.* **11**, 5, pp. 273–279.
21. Raspaud, E., de la Cruz, M. O., Sikorav, J. L. and Livolant, F. (1998). Precipitation of DNA by polyamines: A polyelectrolyte behavior, *Biophys. J.* **74**, 1, pp. 381–393.
22. Rouzina, I. and Bloomfield, V. A. (1996). Macroion attraction due to electrostatic correlation between screening counterions i. mobile surface-adsorbed ions and diffuse ion cloud, *J. Phys. Chem.* **100**, pp. 9977–9989.
23. Shklovskii, B. I. (1999). Wigner crystal model of counterion induced bundle formation of rodlike polyelectrolytes, *Phys. Rev. Lett.* **82**, 16, pp. 3268–3271.
24. Turesson, M., Forsman, J. and Akesson, T. (2006). Surface forces mediated by charged polymers: Effects of intrinsic chain stiffness, *Langmuir* **22**, 13, pp. 5734–5741.
25. Vijayanathan, V., Thomas, T., Shirahata, A. and Thomas, T. J. (2001). DNA condensation by polyamines: A laser light scattering study of structural effects, *Biochemistry* **40**, 45, pp. 13644–13651.

Chapter 24

Physics of Counterion-Mediated Attractions Between Double-Stranded DNAs

Fabien Paillusson
Department of Chemistry, Lensfield road, CB2 1EW, Cambridge, UK
fp286@cam.ac.uk

24.1 Introduction

Attraction between two indentical objects uniformly charged in solution seems intuitively surprising on one hand because we know that such objects do repel in vacuum and on another hand because this simple mental picture is still preserved within the Poisson–Boltzmann (PB) theory [40, 43, 47]. We recall that the PB theory is a mean field approximation [39] of a primitive model of electrolytes [16] in which ions are point-like and solvent is simply a uniform medium of dielectric constant ε. Attraction mechanisms mediated by counterions require therefore to modify at least one of the aforementioned assumptions. We will see that one can find attraction by (a) finding a situation in which two nonuniformly like charged objects can attract each other even in vacuum, (b) adopting

Electrostatics of Soft and Disordered Matter
Edited by David Dean, Jure Dobnikar, Ali Naji, and Rudolf Podgornik

ISBN 978-981-4411-85-1 (Hardcover), 978-981-4411-86-8 (eBook)
www.panstanford.com

another theoretical approximation for the same model of electrolyte, and (c) changing the model for the ions.

Before going onward, we introduce the characteristic length scales arising when studying counterions of valency q subject to thermal fluctuations of magnitude $k_B T$ next to a uniformly charged macroion with charge density σ in a solvent of permitivity ε. We note $q^2 l_B \equiv q^2 e^2/4\pi\varepsilon k_B T$ the Bjerrum length below which electrostatic repulsion dominates the thermal motion of counterions and $\mu_G \equiv (2\pi l_B q\sigma)^{-1}$ the Gouy–Chapman length that estimates the extent of the condensation layer on a plate owing to thermal fluctuations. Finally, we note $a_\perp$ as the typical lateral distance between two neighboring counterions on a plate such that $\pi a_\perp^2 \sigma = q$.

24.2 Planar Kornyshev–Leikin Theory

One possible way to get like charge attraction out of the PB theory is to find an electrostatic configuration that leads to attraction in vacuum. This is in fact possible as soon as the macroions are not uniformly charged but instead display, say, an assembly of quasi-dipoles. This is the idea behind the so-called Kornyshev–Leikin (KL) theory [9, 26, 28, 29] that was originally done considering a realistic model of the charge pattern on DNA. In what follows, we shall present a simplified version of it with a planar geometry to focus on the physics rather than the equations.

24.2.1 *One Plate in a Salt Solution*

We consider a plate at $z = 0$ whose surface charge distribution is composed of very thin stripes extending in the x direction of negative line charge density $-|\lambda_0|$. The distribution is periodic in the y direction such that there is a spacing H between two stripes. Let us put this object in an electrolyte solution with an inverse Debye length $\kappa = \sqrt{\sum_i 4\pi q_i^2 l_B n_i}$. If, moreover, the solution contains plate counterions with a high valency, then it is assumed that most of those will adsorb on the plate so as to neutralize its charge. In this section, we will consider that the adsorbed counterions mostly form positive stripes parallel to the original negative ones and each one of

them lies exactly in at equal distance from two neighboring negative stripes. Their line charge density is defined as $\theta|\lambda_0|$ with $0 < \theta < 1$. In the end, the fixed charge density on such a "dressed" plate can read $\rho_{\mathrm{L}}(y, z) = \delta(z)(\sigma_{\mathrm{d}}(y) + \sigma_{\mathrm{m}}(y))$ with:

$$\sigma_{\mathrm{d}}(y) \equiv |\lambda_0| \sum_{i\in\mathbb{Z}} (\delta(y - iH - H/2) - \delta(y - iH)) \quad (24.1)$$

$$\sigma_{\mathrm{m}}(y) \equiv |\lambda_0| \sum_{i\in\mathbb{Z}} (\theta - 1)\delta(y - iH - H/2) \quad (24.2)$$

where we simply used the identity $\theta = \theta + 1 - 1$ to subdivide the surface charge density into a purely dipolar contribution (alternating stripes of exactly opposite sign) and a contribution arising only from stripes of the same sign. Both $\sigma_{\mathrm{d}}(y)$ and $\sigma_{\mathrm{m}}(y)$ are even and periodic functions of period H and it is convenient to express them in term of their Fourier series components $\sigma_{\mathrm{d}}^{\mathrm{k}}$ and $\sigma_{\mathrm{m}}^{\mathrm{k}}$.[a] The $k = 0$ harmonic mode is nothing but the average surface charge density that is trivially $\sigma_{\mathrm{d}}^{0} = 0$ for $\sigma_{\mathrm{d}}(y)$ and $\sigma_{\mathrm{m}}^{0} = (\theta - 1)|\lambda_0|/H$ for $\sigma_{\mathrm{m}}(y)$. For the rest of the components, it easily found that $\sigma_{\mathrm{d}}^{\mathrm{k}} = 2|\lambda_0|[(-1)^{\mathrm{k}} - 1]/H$ and $\sigma_{\mathrm{m}}^{\mathrm{k}} = 2|\lambda_0|(\theta - 1)(-1)^{\mathrm{k}}/H$. Within a KL-like theory, we next consider that the mean electrostatic field φ satisfies the linearized PB equation [28, 29]. Expressing it directly in terms of its Fourier components φ_{k}, we get the following set of equations:

$$\frac{d^2\varphi_{\mathrm{k}}(z)}{dz^2} - \kappa_{\mathrm{k}}^2\varphi_{\mathrm{k}}(z) = -\frac{1}{\varepsilon}\delta(z)(\sigma_{\mathrm{d}}^{\mathrm{k}} + \sigma_{\mathrm{m}}^{\mathrm{k}}) \quad (24.3)$$

where $k \geq 0$. We notice from Eq. (24.3) that, the higher k, the higher the effective inverse screening length $\kappa_{\mathrm{k}} = \sqrt{\kappa^2 + k^2 4\pi^2/H^2}$. As we are interested in the far field generated by the plate, we will focus on the first two modes $k = 0$ and $k = 1$. The electrostatic potential then

[a] Any even and periodic function $f(y)$ of period H can be written as:

$$f(y) = f_0 + \sum_{i=1}^{\infty} f_k \cos\left(k\frac{2\pi y}{H}\right)$$

with

$$f_0 \equiv \lim_{h\to 0} \frac{1}{H} \int_{-H/2+h}^{H/2+h} dy\, f(y); \quad f_k \equiv \lim_{h\to 0} \frac{2}{H} \int_{-H/2+h}^{H/2+h} dy\, f(y) \cos\left(k\frac{2\pi y}{H}\right)$$

where the use of h prevents problems when integrating over Dirac combs of period H.

reads far from the plate:

$$\phi(y, z) \sim \frac{|\lambda_0|(\theta-1)}{2H\varepsilon} e^{-\kappa z} - \frac{|\lambda_0|(\theta+1)}{H\varepsilon} e^{-\kappa_1 z} \cos(\frac{2\pi}{H} y) \quad (24.4)$$

24.2.2 *Interaction Between Two Plates*

We now look at the interaction of the plate described in the previous section with a similar plate but shifted in the y direction by an amount $\delta y \leq H/2$ and at a distance $z = L$ from the former plate. Its fixed charge density reads then $\rho_{\mathrm{R}}(y, z) = \rho_{\mathrm{L}}(y - \delta y, z - L)$. We also assume that the plates are far enough to neglect the entropic contribution from the ions to the interaction energy. In this case, only the electrostatic contribution coming from the far field in Eq. (24.4) matters. The corresponding energy per unit area reads then:[d]

$$\mathcal{U}_{\mathrm{el}}(L) \approx \frac{\lambda_0^2}{2\varepsilon H^2} \left[(\theta-1)^2 e^{-\kappa L} + 2(\theta+1)^2 \cos\left(\frac{2\pi\delta y}{H}\right) e^{-\kappa_1 L} \right] \quad (24.5)$$

From Eq. (24.5), we see that as soon as the shift $\delta y > H/4$, the second term in the r.h.s. becomes attractive. This attractive interaction is maximum if the shift δy between the charged patterns on the plates equates exactly half the period H. As a matter of fact, in that case, each stripe on a plate would be facing an almost opposite stripe on the other plate, thus leading to an attraction. Overall, a net attraction is all the more likely if θ is close to unity, as the magnitude of the repulsion in Eq. (24.5) is proportional to the square of $(\theta - 1)$.

24.3 Strong Coupling Regime

The electrostatic coupling in a charged system with counterions can be described by a unique parameter $\Xi \equiv 2\pi q^3 l_{\mathrm{B}}^2 \sigma$ so that the limit of vanishing Ξ for an exact field theoretical description of the system gives the PB theory [39]. The SC regime can then be expressed as the opposite limit when Ξ goes to infinity. The following two subsections

[d] We define it as being:

$$\mathcal{U}_{\mathrm{el}} \approx \lim_{h\to 0} \frac{1}{H} \int_{-H/2+h}^{H/2+h} dy\, \phi(y, L)(\sigma_{\mathrm{d}}(y - \delta y) + \sigma_{\mathrm{m}}(y - \delta y))$$

summarize two different approaches of this SC regime, the virial strong coupling (VSC) approach and the Wigner strong coupling (WSC) approach.

24.3.1 *Virial Strong Coupling*

When Ξ tends to infinity, the counterions condense onto the macroions they neutralize [31, 32, 35, 46, 51]. At finite values of Ξ, few counterions are desorbed from the surfaces and the electrolyte is effectively decomposed into a condensed liquid phase on the macroions and a bulk vapor. The bigger Ξ, the smaller the vapor density and hence its fugacity λ. At equilibrium, the vapor fugacity has to equate that of the liquid so that the counterion fugacity tends to zero as Ξ tends to infinity. R. Netz suggested accordingly a Mayer expansion based [17] $1/\Xi$ expansion of the dimensionless one-particle density $\tilde{\rho}_1$ (in units of μ_{G}^{-3}) and the free energy βF of this system [38]. This theory has been discussed at length in the past [22, 34–37], although its capacity at capturing what is happening in the system has been questioned recently [19, 48]. For these reasons, we will simply present its single-particle picture predictions below:

$$\beta F(N) = \beta W_0 - N \ln \int d^3\tilde{r}\, e^{-\phi(\mathbf{r})} + \mathcal{O}(\Xi^{-1}) \tag{24.6}$$

$$\tilde{\rho}_1(\mathbf{r}) = \frac{C}{\Xi} e^{-\phi(\mathbf{r})} + \mathcal{O}(\Xi^{-2}) \tag{24.7}$$

where βW_0 is the energy of the system in absence of counterion, $\tilde{\mathbf{r}} \equiv \mathbf{r}/\mu_{\mathrm{G}}$ is a dimensionless position vector, and ϕ is the external potential (in units of $k_{\mathrm{B}}T$) owing to the macroions. The constant C in Eq. (24.7) can be found by requiring the integral of $q\rho_1$ to be equal to the total charge carried by the macroions.

24.3.2 *Wigner Strong Coupling*

The WSC approach starts from the fact that we know what is the exact ground state of a system of charges next to a plate (a Wigner crystal with a triangular lattice), and therefore, we can expand thermodynamic quantities around this ground state [19, 30–32, 41, 46, 48–50, 52]. If we focus on the one-particle density $\tilde{\rho}_1$, it is in fact exactly related to the fugacity λ and the excess chemical potential

$\mu_{\rm ex}$ via the relation [17]:

$$\tilde{\rho}_1(\tilde{\mathbf{r}}) = \lambda e^{-\phi(\tilde{\mathbf{r}})-\beta\mu_{\rm ex}(\tilde{\mathbf{r}})} \tag{24.8}$$

where ϕ is still the external potential in absence of any counterion. Contrary to the VSC approach that expands $\mu_{\rm ex}$ in powers of the fugacity λ (Mayer expansion), the aim here is to evaluate an exact expression valid for high values of Ξ in the planar geometry: the many-body problem is hence intrinsically accounted for in the WSC approach. One way to do it is to start from Widom's particle insertion method to compute the excess chemical potential [2, 12, 58]:

$$e^{-\beta\mu_{\rm ex}(\tilde{\mathbf{r}})} = \langle e^{-\beta\Delta U}\rangle_{N-1} \tag{24.9}$$

where ΔU is the variation of the whole interparticle energy when adding an Nth test particle at position $\tilde{\mathbf{r}}$ and $\langle . \rangle_{N-1}$ stands for a canonical average over all possible configurations of the $N-1$ other counterions.

24.3.2.1 Case of one plate

At high values of Ξ, the variation ΔU corresponds to a small perturbation of the interaction within a Wigner crystal formed by N counterions by moving the Nth one away at a distance $\tilde{z}$ from the plate. According to [19, 48], it reads within a harmonic approximation in the z direction:

$$\beta\Delta U = -\frac{\alpha}{\sqrt{\Xi}}\sum_{i=1}^{N-1}\frac{(\tilde{z}-\tilde{z}_i)^2}{(|\mathbf{R}-\mathbf{R}_i|/a)^3} + \mathcal{O}(\Xi^{-1}) \tag{24.10}$$

where $\alpha = 3^{3/4}/(16\pi^{3/2})$, $\mathbf{R}_i$ represents the position of the lattice site i and a is the lattice spacing. Note that the value of $|\tilde{z}-\tilde{z}_i|$ is totally unrelated to that of $|\mathbf{R}-\mathbf{R}_i|$, and therefore, the canonical average reads:[e]

$$\langle e^{-\beta\Delta U}\rangle_{N-1} = 1 + \frac{\alpha S}{\sqrt{\Xi}}\int_0^\infty d\tilde{z}'\, e^{-\tilde{z}'}(\tilde{z}-\tilde{z}')^2 + \mathcal{O}(\Xi^{-1}) \tag{24.11}$$

[e] We use the fact that first:

$$\langle e^{-\beta\Delta U}\rangle_{N-1} = \langle 1 - \beta\Delta U + \mathcal{O}(\Xi^{-1})\rangle_{N-1}$$

and second:

$$\left\langle \sum_{i=1}^{N-1}\frac{(\tilde{z}-\tilde{z}_i)^2}{(|\mathbf{R}-\mathbf{R}_i|/a)^3}\right\rangle_{N-1} = \sum_{i=1}^{N-1}\frac{\langle(\tilde{z}-\tilde{z}_i)^2\rangle_{N-1}}{(|\mathbf{R}-\mathbf{R}_i|/a)^3} = S\int_0^\infty d\tilde{z}'\, e^{-\tilde{z}'}(\tilde{z}-\tilde{z}')^2 + \mathcal{O}(\Xi^{-1/2})$$

This means that the average $\langle(\tilde{z}-\tilde{z}_i)^2\rangle_{N-1}$ is dominated by the cost it takes to take the ith ion away from the plate. Other contributions to the average are of order $\Xi^{-1/2}$.

where $S = \sum_i 1/(|\mathbf{R} - \mathbf{R}_i|/a)^3 \approx 11.034$. Evaluating the integral in (24.11) and plugging it back into Eq. (24.8) we get:

$$\tilde{\rho}_1(\tilde{z}) = \frac{e^{-\tilde{z}}}{2\pi\,\Xi}\left[1 + \frac{3^{3/4}S}{(4\pi)^{3/2}\sqrt{\Xi}}\left(\frac{\tilde{z}^2}{2} - \tilde{z}\right) + \mathcal{O}(\Xi^{-1})\right] \qquad (24.12)$$

where the prefactor solves the electroneutrality condition $\int dzq\rho_1 = 2|\sigma|$. In eq. (24.12), we see that corrections to the single-particle picture are of order $\Xi^{-1/2}$—instead of the order Ξ^{-1} prescribed in the VSC theory—and agree very well with existing simulation data [19, 48]. This discrepancy weakens reliability of VSC approach beyond the single particle for planar geometries and makes its applicability uncertain for other geometries.

24.3.3 *Case of Like-Charged Plates*

The expansion for the density can be carried out in a similar way as for one plate explained above. It is not as easy as for one plate because the ground state itself depends on the distance L between the plates [49], and therefore, we will not treat it fully in those lines. Three distance regimes can however be discriminated in a WSC approach and we shall see how they phenomenologically differ.

24.3.3.1 Short distances

At short distances, that is, when $L \ll a_\perp$, the single-particle picture can apply (i.e., ΔU in Eq. (24.9) is neglected at the single particle level) and yields an unbinding mechanism wherein the counterions detach from the plates[f] [34, 50]. The particle density $\rho_1(z)$ is uniform and satisfies $\rho_1(z) = Ce^{-\phi(z)}$, where $\phi(z) = cte$ for two equally charged plates and where C is a constant, too. Unsuring the electroneutrality condition (**??**), the density within the slab reads $\rho_1(z) = 2|\sigma|/qL$. Now, it is convenient to use the contact theorem that relates exactly the pressure βP to the particle density at contact

[f]The typical lateral distance $a_\perp$ used here is a bit tricky, as it depends on the distance between the plates [49]. Let us say here that for small enough distances L, $a_\perp$ is defined as $2\pi a_\perp^2|\sigma| = q$, whereas for infinite distances, we have $\pi a_\perp^2|\sigma| = q$.

$\rho_1(0)$ [18, 57]:

$$\beta P = \rho_1(0) - 2\pi l_B \sigma^2 = \frac{2|\sigma|}{qL} - 2\pi l_B \sigma^2 \qquad (24.13)$$

This expression can lead to attraction if $\tilde{L} = L/\mu_G > 2$.

24.3.3.2 Intermediate distances

This distance regime corresponds to separations L such that $a_\perp < L < q^2 l_B$. The unbinding mechanism responsible for a strong attractive pressure for short distances is not effective anymore and counterions start separating into two strongly correlated layers as L increases [49]. The density at the plate increases accordingly toward the zero pressure value $2\pi l_B \sigma^2$. At large enough distance, $\rho_1(0) \sim 2\pi l_B \sigma^2 - f(L)$ where $f(L)$ is a small correction for large L. It can be shown that in the limit of infinite Ξ, $f(L) \sim e^{-G_0 L}$ where the characteristic length G_0^{-1} depends on the Wigner crystal structure on the plates at large L [49]. This gives rise to an exponentially decaying attraction [31, 32, 49, 51] similar in spirit to the one found in the planar KL theory described above.

24.3.3.3 Large distances

If $L \gg q^2 l_B$, then counterions on a plate do not create anymore a proper correlation hole on the other plate and the condensed ionic layers are no longer strongly correlated with each other. Although the contact theorem (24.13) is valid for any L, it does not provide a simple understanding of the large distance physics. A simple way to understand it is to note that the two plates are so far away from each other that they are almost isolated and can be seen as dressed plates displaying a low charge density.[g] The counterion density far away from them is then described by a PB regime [8, 11, 41]. At that point, the condensed counterion layers become an intrinsic property of these dressed plates akin to surface plasmons on facing metallic plates. Still, they remain correlated through charge fluctuations and

[g]Roughly speacking, the effective charge density σ_{eff} scales as $\sim e^{-\sqrt{\Xi}}$ and goes rapidly to zero as the coupling parameter goes to infinity [11, 41].

yield a universal attraction at finite temperature [1, 7, 30, 32]:

$$\beta P_{\text{att}} = -\frac{\zeta(3)}{8\pi L^3} \tag{24.14}$$

where $\zeta(x)$ is the Riemann zeta function and $\zeta(3) \approx 1.2021$. For Eq. (24.14) to give a net attractive pressure, it has to be compared with the PB repulsion owing to the counterion-dressed plates.[h]

24.4 Dumbbell-Like Counterions

24.4.1 *The Model*

Among counterions of valency $n > 1$, some are molecules made of n repetitions of a single charged unit (principally monovalent) [4–6, 23, 24, 33]. For the sake of illustration, we will focus on divalent positive conterions that neutralize two like-charged plates in absence of salt. The simplest description for a divalent counterion would be two monovalent point-like ions of the same sign forming a dumbbell of length l.

Let us denote $p(\mathbf{r}, \hat{\mathbf{u}})$ the joint probability density to find a reference charge belonging to a dumbbell at $\mathbf{r}$ and having the dumbbell direction vector arising from it in direction $\hat{\mathbf{u}}$. The probability to find a dumbbell through its reference charge at position $\mathbf{r}$ reads:

$$p(\mathbf{r}) \equiv \int d\Omega \; p(\mathbf{r}, \hat{\mathbf{u}}) \tag{24.15}$$

where $d\Omega$ is the solid angle measure.

24.4.2 *Mean Field Theory*

24.4.2.1 A modified PB equation

Within a mean field theory, the joint probability density $p(\mathbf{r}, \hat{\mathbf{u}})$ for one dumbbell depends on the mean external electrostatic potential

[h] The physics becomes very similar to the DLVO theory [56] wherein ionic contributions are accounted for by the PB theory and separated from the medium-related van der Waals interactions.

φ generated by both its coions and the plates [5, 24, 33]:

$$p(\mathbf{r}, \hat{\mathbf{u}}) \propto e^{-\beta e\varphi(z)} e^{-\beta e\varphi(z+l\cos(\theta))} H(z + l\cos\theta) H(L - (z + l\cos\theta)) \tag{24.16}$$

where $\cos\theta$ is the projection of $\hat{\mathbf{u}}$ on the z-axis and $H(x)$ is the Heaviside step function that is zero if x is negative and one otherwise. The Heaviside functions in Eq. (24.16) prevent possible overlaps between the dumbbell and the plates. The volume density of dumbbells $n(z)$ is proportional to the probability (24.15) and the corresponding charge density is $2en(z)$ simply because there are two charges per dumbbell. Finally, for the definition of φ to be consistent, it has to satisfy the Poisson equation (in I.S. units), which yields the modified PB equation for dumbbells counterions in a slit geometry:

$$\frac{d^2\varphi}{dz^2} = -2en(z)/\varepsilon = -\frac{eC}{\varepsilon l} \int_{-l_{\min}(z)}^{l_{\max}(z)} ds\, e^{-\beta e\varphi(z)} e^{-\beta e\varphi(z+s)} \tag{24.17}$$

together with the boundary conditions:

$$\left.\frac{d\varphi}{dz}\right|_{z=0} = \frac{e|\sigma|}{\varepsilon}; \qquad \left.\frac{d\varphi}{dz}\right|_{z=L} = -\frac{e|\sigma|}{\varepsilon} \tag{24.18}$$

that ensure the global electroneutrality of the system. In Eq. (24.17), the change of variable $s = l\cos\theta$ has been made, the Heaviside measure appearing in Eq. (24.16) is unity in the interval $[l_{\min}(z), l_{\max}(z)]$, and C is a constant of arbitrary value.[i]

24.4.2.2 Plate–plate interaction

As before, we make use of the contact theorem that reads as follows for dumbbells [24, 33]:

$$\beta P = 2n(0) - 2\pi l_B \sigma^2 \tag{24.19}$$

The factor two in the osmotic part of Eq. (24.19) appears because there are two ends per dumbbell interacting with the plate at $z = 0$. The solution to Eqs. (24.17) and (24.18) is an inhomogeneous

[i] To be physically consistent, the r.h.s. of Eq. (24.17) has to be invariant under the (gauge) transformation $\varphi \to \varphi + g$ where g is a constant. This is only possible if, under this transformation, the constant C undergoes a change $C \to Ce^{2g}$. Choosing a specific value for C is thus equivalent to fixing the gauge g and any value can then be taken for it [53].

potential $\varphi(z)$ that increases rapidly from a low value at the plate to its highest value at the mid-plane [33]. Two distance regimes can then be discriminated [24]. The first regime is when the mid-interplate distance $L/2$ is larger than the size l of the dumbbells. In this case, the rapid decrease of the potential φ makes adsorbed counterions on a plate be oriented mostly parralel to it, as it is very favorable energetically. Second, when $L/2$ is smaller than l, then adsorbed dumbbells on a plate can also lie perpendicularly to it by reaching a not so unfavorable potential close to the other plate [33]. The increase of such bridging configurations when $L > l$ implies that, on average, there will be less point charges trapped directly at the wall, hence yielding a decrease in $n(0)$.[j] This drop can be sufficient enough for the electrostatic attraction to overcome the osmotic pressure and then generate an attraction. Now, if $L \leq l$, there is no lack of point charges at the plates and the interaction is repulsive again [24, 33]. This allows then to bound the equilibrium distance owing to a PB bridging mechanism $l < L_{\text{eq}} < 2l$.

24.4.3 *SC Regime for Dumbbells*

If the coupling parameter Ξ is big enough, then an SC description can be done on dumbbell counterions neutralizing two plates [4, 24]. In particular, if $l < a_\perp$, then a single particle picture can be used. In this case, the dumbbell density reads:

$$n(z) = \frac{\Omega(z)}{4\pi} K e^{-\tilde{L}} \tag{24.20}$$

where $\Omega(z)$ is the accessible solid angle for the dumbbell at location z, $\tilde{L} = L2\pi l_{\text{B}}|\sigma|q$ (with $q = 2$) is the constant external potential felt by the dumbbell, and K is a normalization constant. The constant K is chosen to satisfy electroneutrality and reads $K = |\sigma|e^{\tilde{L}}/(L - l/2)$

[j] If bridging configurations do exist then the dumbbell density will display four picks—one at each plate and two others at a distance l from the plates—instead of simply two at the plates. Let $n_>(0)$ be the density at a plate when $L > 2l$. The total number of dumbbells N_{d} is mostly dominated by the two picks at the plates and scales roughly as $N_{\text{d}} \sim 2n_>(0)$. Now, let $n_<(0)$ be the dumbbell density at a plate when $L < 2l$. It can be divided into parallel $n_p(0)$ and bridging $n_{\text{b}}(0)$ densities. In particular, $n_{\text{b}}(0) = n_{\text{b}}(l)$ by definition of a bridge. The integral of the dumbbell density is now dominated by the four picks enumerated above and the total number of particles scales as $N_{\text{d}} \sim 2n_<(0) + 2n_{\text{b}}(0)$. It then turns out that as long as $n_{\text{b}}(0)$ is nonzero and $L > l$, $n_<(0) < n_>(0)$.

when $l < L$.[k] We can then apply the contact theorem (24.19), which yields:

$$\beta P = \frac{|\sigma|}{(L-l/2)} - 2\pi l_B \sigma^2 \tag{24.21}$$

Hence, a stable bridging equilibrium arises at $\tilde{L}_{eq} = l + 2$. Likewise, when $l > L$, the accessible solid angle is $\Omega(z) = 2\pi L/l$ for any z [24] and the electroneutrality condition yields $n(z) = |\sigma|/L$. Inserting back this expression into the contact theorem (24.19), we get a stable equilibrium $\tilde{L}_{eq} = 4$ that is independent of the dumbbell size. Note also that it is twice the equilibrium length that would be obtained for point-like divalent ions in the SC regime from Eq. (24.13). This is because the attraction here is due to electrostatic correlations (and not a bridging mechanism) that are weaker with a divalent dumbbell than with a concentrated charge.

24.4.4 *Validity Domain and the Point-like Limit*

If l is small enough, we should recover the physics of point-like divalent ions. This happens when the dumbbell orientation is unaffected by the electrostatic potential gradient, that is, when $l \ll \mu_G < L$ [24, 33]. In this case, $n(z)$ becomes $n(z) = \rho_1(z)\Omega(z)/4\pi$ where $\rho_1(z)$ is the point-like divalent counterion density and $\Omega(z)$ is the accessible solid angle for the dumbbell. In particular, however small the dumbbell is, at $z = 0$, only half of the total solid angle is accessible to the dumbbell, and this allows us to recover the contact theorem for point-like ions (24.13) from the contact theorem for dumbbells Eq. (24.19).

24.5 DNA-DNA Attraction

It is now well established that molecular (e.g., polyamines) and atomic (e.g., Cr^{+3}) cations can lead to the formation of hexagonal arrays of double-stranded DNA (dsDNA) provided their valency is

[k] If $L > l$, the factor $\Omega(z)/4\pi$ is $1/2 + z/(2l)$ if $0 < z < l$, $1/2 + L/2 - z/(2l)$ if $L - l < z < L$ and unity otherwise. Its integrated value over the whole slab is thus simply $L - l/2$.

higher than $+2$ even though some divalent ions (e.g., Mn^{+2} and Cd^{+2}) are able to condense dsDNA [3, 26, 54]. Such arrays have been experimentally studied recently [10, 55] and both attractive and repulsive contributions to the interaction appear to be exponentially decaying. A long-ranged attraction as seen in Eq. (24.14) may still exist, but it does not seem to drive the array stability.

Todd et al. [55] also found the attractive decay length λ_{att} to be almost independent of the counterion type ($\lambda_{\text{att}} \sim 5$ Å) and to be roughly twice the repulsive characteristic length λ_{rep}. It seems unlikely for a bridging mechanism to be compatible with these observations, as its physics depends very much on the length of the molecular cations (see section 24.4.). Moreover, the corresponding equilibrium distance L_{eq} should be about the size l of the chains and thus should be increasingly big as the valency of the cations increases. This is in contradiction with what is observed in experiments [10, 55] in which the DNA–DNA equilibrium distance decreases while increasing the counterion valency. The KL theory and the WSC approach, however, are both compatible with an exponentially decaying attraction. Even though the WSC has yet to be fully treated for a realistic dsDNA, it is likely for the length G_0^{-1} (see section 24.3) to roughly equal dsDNA's mean helical pitch $H \approx 3.4\,\text{nm}$ [51]. This would then lead to an attractive decay length $\lambda_{\text{att}} \approx H/2\pi \approx 5.4$ Å (that is not so far from λ_{att}) as prescribed in the original KL theory [28, 29]. In addition, the ratio between DNA and water electrostatic permitivities being about $1/80$, it generates an exponentially decaying repulsion—owing to image charges of the dressed dsDNAs within each facing dsDNA [20]—with the same decay length as for the attraction but for a distance that is twice that of the spacing between the dsDNAs [10, 27]. In the end, it is equivalent to a repulsion whose decay length is exactly half that of the attraction decay length as measured in studies [55] and [10].

The KL theory seems in very good agreement with experiments [10, 25, 26, 55], although some of the assumptions it is based on are arguable[13–15]. An SC analysis seems potentially compatible and could provide some rational basis to the effective parameters of the KL theory [10, 21, 25, 26, 44].

Finally, the above discussion on dsDNA condensation only accounts for the improvements of the PB theory mentioned in the introduction. An obvious refinement that has not been treated in these lines is a better model for water. Such a thing goes way beyond the scope of this chapter. It is however worth mentioning that a phenomenological account of the way polyvalent counterions could affect the structure of water on dsDNA can give rise to an attraction [42, 45] whose quantitative features agree well with the work of [10, 55].

References

1. Attard, P., Kjellander, R., Mitchell, D. and Jönson, B. (1988). Electrostatic fluctuation interactions between neutral surfaces with adsorbed, mobile ions or dipoles, *J. Chem. Phys.* **89**, p. 1664.
2. Binder, K. (1997). Applications of monte carlo methods to statistical physics, *Rep. Prog. Phys.* **60**, p. 487.
3. Bloomfield, V. (1996). Dna condensation, *Curr. Opin. Struct. Biol.* **6**, pp. 334–341.
4. Bohinc, K., Grime, J. and Lue, L. (2012). The interactions between charged colloids with rod-like counterions, *Soft Matter* **8**, p. 5679.
5. Bohinc, K., Iglič, A. and May, S. (2004). Interaction between macroions mediated by divalent rod-like ions, *Europhys. Lett.* **68**, p. 494.
6. Bohinc, K., Reščič, J., Maset, S., and May, S. (2011). Debye-hückel theory for mixtures of rigid rodlike ions and salt, *J. Chem. Phys.* **134**, p. 074111.
7. Buenzli, P. and Martin, P. (2005). The casimir force at high temperature, *Europhys. Lett.* **72**, pp. 42–48.
8. Burak, Y., Andelman, D. and Orland, H. (2004). Test-charge theory for the electric double layer, *Phys. Rev. E* **70**, p. 016102.
9. Cortini, R., Kornyshev, A., Lee, D. and Leikin, S. (2011). Electrostatic braiding and homologous pairing of dna double helices, *Biophys. J.* **101**, pp. 875–884.
10. DeRouchey, J., V.A., P. and Rau, D. (2010). Cation charge dependence of the forces driving dna assembly, *Biophys. J.* **99**, pp. 2608–2615.
11. dos Santos, A., Diehl, A. and Levin, Y. (2009). Electrostatic correlations in colloidal suspensions: Density profiles and effective charges beyond the poisson-boltzmann theory, *J. Chem. Phys.* **130**, p. 124110.

12. Frenkel, D. and B., S. (2002). *Understanding molecular simulation (second edition)* (Academic Press).
13. Granot, J., Feignon, J. and Kearns, D. (1982). Interactions of dna with divalent metal ions. i. ^{31}p-nmr studies, *Biopolymers* **21**, p. 181.
14. Granot, J. and Kearns, D. (1982). Interactions of dna with divalent metal ions. ii. proton relaxation enhancement studies, *Biopolymers* **21**, p. 203.
15. Granot, J. and Kearns, D. (1982). Interactions of dna with divalent metal ions. iii. extent of metal binding: experiment and theory, *Biopolymers* **21**, p. 219.
16. Hansen, J.-P. and Löwen, H. (2000). *Annu. Rev. Phys. Chem.* **51**, p. 209.
17. Hansen, J.-P. and McDonald, I. (2006). *Theory of simple liquids (third edition)* (Academic Press).
18. Henderson, D. and Blum, L. (1978). *J. Chem. Phys.* **69**, p. 5441.
19. Šamaj, L. and Trizac, E. (2011). Counterions at highly charged interfaces: From one plate to like-charge attraction, *Phys. Rev. Lett.* **106**, 7, p. 078301.
20. Jackson, J. (1998). *Classical electrodynamics (third edition)* (Wiley).
21. Kanduc, M., Dobnikar, J. and Podgornik, R. (2009). Counterion-mediated electrostatic interactions between helical molecules, *Soft Matter* **5**, pp. 868–877.
22. Kanduč, M., Trulsson, M., Naji, A., Burak, Y., Forsman, J. and Podgornik, R. (2008). Weak- and strong-coupling electrostatic interactions between asymmetrically charged planar surfaces, *Phys. Rev. E* **78**, 6, p. 061105.
23. Kanduč, M., Naji, A., Jho, Y., Pincus, P. and Podgornik, R. (2009). Role of multipoles in counterion-mediated interactions between charged surfaces: Strong and weak coupling, *J.Phys.: Cond. Matt.* **21**, p. 424103.
24. Kim, Y., Yi, J. and Pincus, P. (2008). Attractions between like-charged surfaces with dumbbell-shaped counterions, *Phys. Rev. Lett.* **101**, p. 208305.
25. Kornyshev, A., Lee, D., Leikin, S., A., W. and Zimmermann, S. B. (2005). Direct observation of azimuthal correlations between dna in hydrated aggregates, *Phys. Rev. Lett.* **95**, p. 148102.
26. Kornyshev, A., Lee, D. J., Leikin, S. and Wynveen, A. (2007). Structure and interactions of biological helices, *Rev. Mod. Phys.* **79**, p. 943.
27. Kornyshev, A. and Leikin, S. (1997). Theory of interaction between helical molecules, *J. Chem. Phys.* **107**, pp. 3656–3674.
28. Kornyshev, A. and Leikin, S. (1999). Electrostatic zipper motif for dna aggregation, *Phys. Rev. Lett.* **82**, pp. 4138–4141.

29. Kornyshev, A. and Leikin, S. (2001). Sequence recognition in the pairing of dna duplexes, *Phys. Rev. Lett.* **86**, p. 3666.
30. Lau, A.-C., Levine, D. and Pincus, P. (2000). Novel electrostatic attraction from plasmon fluctuations, *Phys. Rev. Lett.* **84**, p. 4116.
31. Lau, A.-C., Pincus, P. and Levine, H., D. Fertig (2001). Electrostatic attraction of coupled wigner crystals: finite temperature effects, *Phys. Rev. E* **63**, p. 051604.
32. Lau, A. W.-C. (2000). *Fluctuation and Correlation effects in Electrostatics of Highly-Charged Surfaces (PhD thesis)*.
33. Maset, S., Reščič, J., May, S., Pavlič, J. and Bohinc, K. (2009). Attraction between like-charged surfaces induced by orientational ordering of divalent rigid rod-like counterions: theory and simulations, *J. Phys. A: Math. Theor.* **42**, p. 105401.
34. Moreira, A. and Netz, R. (2001). Field-theoretic approaches to classical charged systems, in *Electrostatic Effects in Soft Matter and Biophysics (C. Holm, P. Kékicheff and R Podgornik, Eds; NATO Science Series)* (Kluwer Academic Publishers), pp. 367–408.
35. Moreira, A. and Netz, R. (2002). Simulations of counterions at charged plates, *Eur. Phys. J. E* **8**, p. 33.
36. Naji, A., Arnold, A., Holm, C. and Netz, R. (2004). Attraction and unbinding of like-charged rods, *Europhys. Lett.* **67**, p. 130.
37. Naji, A. and Netz, R. (2004). Attraction of like-charged macroions in the strong-coupling limit, *Eur. Phys. J. E* **13**, p. 43.
38. Netz, R. (2001). Electrostatistics of counter-ions at and between planar charged walls: From poisson-boltzmann to the strong-coupling theory, *Eur. Phys. J. E* **5**, p. 557.
39. Netz, R. and Orland, H. (2000). Beyond poisson-boltzmann: Fluctuations and correlations, *Eur. Phys. J. E* **1**, pp. 203–214.
40. Neu, J. (1999). Wall-mediated forces between like-charged bodies in an electrolyte, *Phys. Rev. Lett.* **82**, p. 1072.
41. Paillusson, F. and Trizac, E. (2011). Interaction regimes for oppositely charged plates with multivalent counterions, *Phys. Rev. E* **82**, p. 052501.
42. Parsegian, V., Rand, R. and Rau, D. (1985). Hydration forces: What next? *Chem. Scr.* **25**, pp. 28–31.
43. Parsegian, V. A. and Gingell, D. (1972). On the electrostatic interaction across a salt solution between two bodies bearing unequal charges, *Biophys. J.* **12**, pp. 1192–1204.
44. Qiu, X., Parsegian, V. and Rau, D. (2010). Divalent counterion-induced condensation of triple-strand dna, *PNAS* **107**, pp. 21482–21486.

45. Rau, D. and Parsegian, V. (1992). Direct measurement of the intermolecular forces between counterion-condensed dna double helices: evidence for long range attractive hydration forces, *Biophys. J.* **61**, pp. 246–259.
46. Rouzina, I. and Bloomfield, V. (1996). Macroion attraction due to electrostatic correlation between screening counterions. 1. mobile surface-adsorbed ions and diffuse ion cloud, *J. Phys. Chem.* **100**, p. 9977.
47. Sader, J. and Chan, D. (1999). Long range electrostatic attractions between identically charged particles in confined geometries: an unresolved problem, *J. Coll. Int. Sci.* **213**, pp. 268–269.
48. Samaj, L. and Trizac, E. (2011). Wigner-crystal formulation of strong-coupling theory for counterions near planar charged interfaces, *Phys. Rev. E* **84**, p. 041401.
49. Samaj, L. and Trizac, E. (2012). Critical phenomena and phase sequence in classical bilayer wigner crystal at zero temperature, *Phys. Rev. B* **85**, p. 205131.
50. Samaj, L. and Trizac, E. (2012). Strong-coupling theory for a polarizable planar colloid, *Beit. Plasmaphys.-Cont.* **52**, p. 53.
51. Shklovskii, B. (1999). Wigner crystal model of counterion induced bundle formation of rodlike polyelectrolytes, *Phys. Rev. Lett.* **82**, p. 3268.
52. Shklovskii, B. I. (1999). Screening of a macroion by multivalent ions: Correlation-induced inversion of charge, *Phys. Rev. E* **60**, 5, pp. 5802–5811.
53. Tamashiro, M. and Schiessel, H. (2003). Where the linearized poisson-boltzmann cell model fails: The planar case as a prototype study, *Phys. Rev. E* **68**, p. 066106.
54. Teif, V. and Bohinc, K. (2011). Condensed dna: Condensing the concepts, *Prog. Biophys. Mol. Biol.* **105**, p. 208.
55. Todd, B., Parsegian, V., Shirahata, A., Thomas, T. and Rau, D. (2008). Attractive forces between cation condensed dna double helices, *Biophys. J.* **94**, p. 4775.
56. Vervey, J. and Overbeek, J. T. G. (1948). *Theory of the Stability of Lyophobic colloïds* (Elsevier: Amsterdam).
57. Wennerström, H., Jönsson, B. and Linse, P. (1982). The cell model for polyelectrolyte systems. exact statistical mechanical relations, monte carlo simulations, and the poisson-boltzmann approximation, *J. Chem. Phys.* **76**, pp. 4665–4670.
58. Widom, B. (1963). Some topics in the theory of fluids, *J. Chem. Phys.* **39**, p. 2802.

Part V

DISORDER EFFECTS IN COULOMB INTERACTIONS

Chapter 25

Coulomb Interactions between Disordered Charge Distributions

David S. Dean,[a] Ali Naji,[b] Ronald R. Horgan,[c] Jalal Sarabadani,[d] and Rudolf Podgornik[e]

[a] *Université de Bordeaux and CNRS, Laboratoire Ondes et Matière d'Aquitaine (LOMA), UMR 5798, F-33400 Talence, France*
[b] *School of Physics, Institute for Research in Fundamental Sciences (IPM), Tehran 19395-5531, Iran*
[c] *DAMTP CMS, Cambridge CB3 0WA, UK*
[d] *Department of Physics, Institute for Advanced Studies in Basic Sciences (IASBS), Zanjan 45137-66731, Iran, and Department of Physics, University of Isfahan, Isfahan 81746, Iran*
[e] *Department of Theoretical Physics, J. Stefan Institute, SI-1000 Ljubljana, Slovenia*
david.dean@u-bordeaux1.fr

25.1 Introduction

In most studies of electrostatic interactions between charged bodies, a number of simplifying assumptions are made. Beyond the purely geometric simplifications, the charge distribution is often taken to be uniform. This assumption is clearly always an idealization, as charge distributions in many systems will be inherently complex and/or disordered [1, 3, 5, 7, 21]. Examples of charge disorder are common in colloidal and soft matter systems [9, 12, 13], specific

Electrostatics of Soft and Disordered Matter
Edited by David Dean, Jure Dobnikar, Ali Naji, and Rudolf Podgornik

ISBN 978-981-4411-85-1 (Hardcover), 978-981-4411-86-8 (eBook)
www.panstanford.com

examples include surfactant-coated surfaces [10, 16] and random polyelectrolytes and polyampholytes [2]. Metallic and dielectric surfaces with local dielectric constant variation can also exhibit charge disorder, as local variations of the crystallographic axes of an exposed surface lead to a random surface potential, *the patch effect* [3, 5, 7, 20, 21]. Finally, the chemical preparation of samples is never perfect and charged impurities abound. The presence of charge disorder, even if the system is overall net neutral, can be shown to have strong effects on the interactions between bodies. Notably, charge disorder can lead to interactions that can mask the Casimir effect and may play an important role in the Casimir effect experiments, possibly making their interpretation rather delicate [3, 5, 7].

The disorder we will consider in this chapter is defined as *quenched*, as it is fixed once and for good in the preparation of the system, see Fig. 25.1, this is the case for charged impurities that are frozen in the boundaries of the materials and cannot move or react to electric fields acting upon them. It is for this reason that quenched disorder is sometimes referred to as *frozen*. In small systems, in which the objects are not held fixed and can move and/or rotate with respect to one another, the system will tend to lower its electrostatic energy by aligning and positioning its components appropriately. This effect is believed to be crucial for

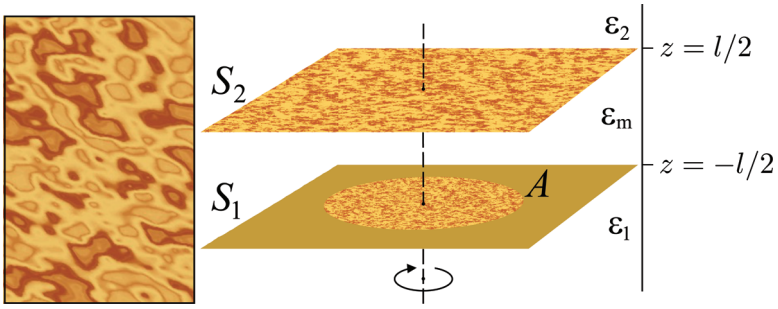

Figure 25.1 (Left) A schematic quenched surface charge distribution. (Right) Two parallel dielectric slabs S_1 and S_2, which are semi-infinite in the z directions and infinite in the $\mathbf{r} = (x, y)$ plane are placed at a separation distance l. The disorder charge is taken to be distributed over the whole surface in slab S_2 but is restricted to the finite region $\mathbf{r} \in A$ in slab S_1.

the so-called *lock and key mechanism*, which plays a fundamental role in the biological recognition mechanisms [8, 15]. In a typical Casimir force experiment in which one has a two-plate or a sphere-plate configuration, the surfaces in question are held fixed (not free to rotate or laterally to displace with respect to each other) and the two quenched charge distributions will be *completely uncorrelated*. If the sphere in a sphere-plate geometry is held close to one part of a large plate, the charge disorder will lead to *random* normal and lateral *forces* on the sphere, as well as *random torques*. If we carry out the same experiment between two different apposed parts of the sphere and the same surface, the fact that the sphere will feel a different charge distribution will lead to different normal and lateral forces and torques, in much the same way as if we had replaced the sphere and plates by new ones produced by the same productions process, i.e., giving the same statistical disorder. Carrying out a sequence of such experiments will lead to an ensemble of measured forces, which can then be averaged to obtain the average force. In most cases, we will see that the average normal force is non-zero. However, if the charge disorder in the plate is invariant under translation in space, that is to say it looks statistically the same everywhere across the plate, the average translational forces and torques will be zero. However, for the translational forces and torques, there will be a non-zero variance and they will fluctuate. The amplitude of these *sample-to-sample* fluctuations will give us additional information about the nature of the charge disorder and may be useful in unraveling the various components of the force measured in typical Casimir or other force detection setups [3, 5, 7].

25.2 Normal Electrostatic Forces Between Charge-Disordered Slabs

Consider a system of two parallel semi-infinite dielectrics S_1 and S_2, with local dielectric constants $\varepsilon(\mathbf{x})$. We take $\varepsilon(\mathbf{x}) = \varepsilon_1$ in S_1, $\varepsilon(\mathbf{x}) = \varepsilon_2$ in S_2 and $\varepsilon(\mathbf{x}) = \varepsilon_m$ in the intervening medium. We denote by l the separation between the two plates and by $\rho(\mathbf{x})$ the quenched charge distribution for a given configuration of the dielectric bodies.

The electrostatic energy is given by

$$E(l) = \frac{1}{2}\iint d\mathbf{y}d\mathbf{x}\,\rho(\mathbf{x})G(\mathbf{x},\mathbf{y};l)\rho(\mathbf{y}) \tag{25.1}$$

where $G(\mathbf{x},\mathbf{y};l)$ is the Green's function obeying

$$\varepsilon_0\nabla\cdot[\varepsilon(\mathbf{x})\nabla G(\mathbf{x},\mathbf{y};l)] = -\delta(\mathbf{x}-\mathbf{y}), \tag{25.2}$$

where ε_0 is the permittivity of vacuum. The Green's function depends explicitly on l, as the overall spatial dielectric function depends on l. The average electrostatic energy of this configuration is thus given by

$$\langle E(l)\rangle = \frac{1}{2}\int d\mathbf{x}d\mathbf{y}G(\mathbf{x},\mathbf{y};l)\langle\rho(\mathbf{x})\rho(\mathbf{y})\rangle, \tag{25.3}$$

where $\langle\cdots\rangle$ indicates the *disorder average* over the random charge distributions. The total charge distribution is given by $\rho(\mathbf{x}) = \rho_1(\mathbf{x}) + \rho_2(\mathbf{x})$, where $\rho_1(\mathbf{x})$ and $\rho_2(\mathbf{x})$ are the charge distributions in S_1 and S_2. In some cases, notably for the estimation of lateral forces and torques, it is useful to assign one of the bodies, say S_1, to have a charge distribution, which is restricted to a subregion of S_1, which we will denote by A, see Fig. 366.1.

Consider the case where the charge distributions on different bodies are uncorrelated and where the average charge on each body is zero, i.e. $\langle\rho_1(\mathbf{x})\rangle = \langle\rho_2(\mathbf{x}')\rangle = 0$ and $\langle\rho_1(\mathbf{x})\rho_2(\mathbf{x}')\rangle = 0$ for all $\mathbf{x}\in S_1$ and $\mathbf{x}'\in S_2$. Then

$$\langle E(l)\rangle = \frac{1}{2}\int d\mathbf{x}d\mathbf{y}G(\mathbf{x},\mathbf{y};l)[\langle\rho_1(\mathbf{x})\rho_1(\mathbf{y})\rangle + \langle\rho_2(\mathbf{x})\rho_2(\mathbf{y})\rangle]. \tag{25.4}$$

We note that the average interaction has just two self-interaction terms, as there is no interaction on average between charges on different slabs, i.e., the interaction energy between a charge in S_1 with a randomly chosen charge in S_2 is on average zero, as the charge in S_2 has an equal probability to have either the same sign or the opposite one to that in S_1. A nonzero interaction energy is only possible between a charge in a slab and its image charge in the opposing slab, the sign of this image charge depending on the charge in question and the dielectric constants of the system.

We notice that there is an interaction between S_1 and S_2, even if there is no charge in one of the slabs, stemming from a non-zero average interaction energy of a randomly charged slab (e.g., S_1) with

the induced image charges in the charge-free slab (e.g., S_2). The origin of a net interaction between overall neutral surfaces is thus easy to understand, but still rather subtle and surprising.

We now consider a simple model of the charge disorder, which can originate in either the surface charge or bulk charge. On the surface S_1, the surface charge distribution is

$$\rho_{1s}(\mathbf{x}) = \sum_{i=1}^{N_{1s}} q_i \delta(\mathbf{r} - \mathbf{r}_i)\delta\left(z + \frac{l}{2}\right), \tag{25.5}$$

where $\mathbf{r}$ is two dimensional in plane coordinate. If the area of the slab S_1 covered with charge disorder is A and the charges have the values $q_i = \pm q_{1s}$ with equal probability and $N_{1s} = n_{1s}A$ where n_{1s} is the surface concentration of charges, we easily find that $\langle \rho_s(\mathbf{r})\rangle = 0$ and

$$\langle \rho_{1s}(\mathbf{x})\rho_{1s}(\mathbf{x}')\rangle = g_{1s}\delta\left(z + \frac{l}{2}\right)\delta\left(z' + \frac{l}{2}\right)\delta(\mathbf{r} - \mathbf{r}'), \tag{25.6}$$

where $g_{1s} = n_{1s}q_{1s}^2$. Typical values of q_{1s} are given by the electron charge e and the bulk impurity charge densities are between 10^{10} and 10^{15} e/cm^3 [6, 17]. Using the size of a molecular layer, we can thus estimate the typical surface charge density of the surface, generated by cutting the bulk. Experimentally, the heterogeneous structure of the charge disorder on dielectric surfaces can be measured using Kelvin force microscopy [1].

Away from the surface, we assume that bulk charge distribution has the form

$$\rho_{1b}(\mathbf{x}) = \sum_{i=1}^{N_{1b}} q_i \delta(\mathbf{x} - \mathbf{x}_i), \tag{25.7}$$

where the charges q_i take the value $\pm q_{1b}$ with equal probability and have concentration n_{1b}. The bulk correlation function is then

$$\langle \rho_{1b}(\mathbf{x})\rho_{1b}(\mathbf{x}')\rangle = g_{1b}\delta(z - z')\delta(\mathbf{r} - \mathbf{r}'), \tag{25.8}$$

where $g_{1b} = n_{1b}q_{1b}^2$. The disorder assumed here has a short-range correlation, an assumption easily modified to more general forms [11, 18, 19]. To give explicit formulas, we will continue with short-range correlation functions and assume that the (infinite) surface areas $S_2 = S_1 = S$ (by taking A to infinity in the case of slab S_1) are

completely covered by charge disorder. From Eq. (366.4), we find that

$$\langle E(l)\rangle = \frac{S}{2}\left[g_{1s}G\left(\mathbf{0}, -\frac{l}{2}, -\frac{l}{2}; l\right) + g_{2s}G\left(\mathbf{0}, \frac{l}{2}, \frac{l}{2}; l\right)\right] + \frac{S}{2}\int_{-\infty}^{-l/2} dz\, g_{1b}G(\mathbf{0}, z, z; l) + \frac{S}{2}\int_{l/2}^{\infty} dz\, g_{2b}G(\mathbf{0}, z, z; l) \quad (25.9)$$

The Fourier transform in the in-plane coordinates is

$$\tilde{G}(\mathbf{k}, z, z'; l) = \int d\mathbf{r}\, G(\mathbf{r}, z, z'; l)\exp(-i\mathbf{k}\cdot\mathbf{r}) \quad (25.10)$$

and we can use equation (366.2) to show that

$$\varepsilon_0 \frac{d}{dz}\varepsilon(z)\frac{d}{dz}\tilde{G}(\mathbf{k}, z, z'; l) - \varepsilon_0\varepsilon(z)k^2\tilde{G}(\mathbf{k}, z, z'; l) = -\delta(z-z') \quad (25.11)$$

where $k = |\mathbf{k}|$. The above equation may be solved and we find that, for instance, when $z \leq -l/2$ we have

$$\tilde{G}(\mathbf{k}, z, z; l) = \frac{1}{2\varepsilon_1\varepsilon_0 k}\left(1 + \frac{[\Delta_1\exp(kl) - \Delta_2\exp(-kl)]\exp(2kz)}{1 - \Delta_1\Delta_2\exp(-2kl)}\right), \quad (25.12)$$

where Δ_a (for $a = 1$ or 2) is the *dielectric jump parameter*

$$\Delta_a = \frac{\varepsilon_a - \varepsilon_m}{\varepsilon_a + \varepsilon_m}. \quad (25.13)$$

With this result, we can evaluate the terms appearing in equation (366.4) using the inverse two-dimensional Fourier transform

$$G(\mathbf{0}, z, z; l) = \frac{1}{(2\pi)^2}\int d\mathbf{k}\, \tilde{G}(\mathbf{k}, z, z; l). \quad (25.14)$$

For short-range disorder, all the integrals can be evaluated analytically. It turns out that some integrals diverge due to self-energies that are independent of the separation of the plates and therefore do not contribute to the force. The total average force can be decomposed into the contribution coming from each of the charge distributions in the system. For instance, the average normal force $\langle f_{s1}^{(n)}\rangle$ due to the random surface charge on slab 1 is given by,

$$\frac{\langle f_{s1}^{(n)}\rangle}{S} = \frac{g_{1s}(1-\Delta_1^2)}{16\pi\,\Delta_1\varepsilon_1\varepsilon_0 l^2}\ln(1-\Delta_1\Delta_2) \quad (25.15)$$

and the contribution of the force from the surface charge on slab 2 is obtained by switching the index 1 for 2 and vice a versa in Eq. (366.15).

We first note that the interaction is an unscreened $1/l^2$ power law. Furthermore, we see that the sign of the interaction is rather nontrivial and depends on the signs of the dielectric jump parameters Δ_a [4, 11, 19]. We can make the following observations for, e.g., the force due to the slab 1, $f_{s1}^{(n)}$: (i) for $\Delta_1 > 0$ and $\Delta_2 > 0$, we find that $\langle f_{s1}^{(n)} \rangle < 0$ (attraction), (ii) for $\Delta_1 > 0$ and $\Delta_2 < 0$, $\langle f_{s1}^{(n)} \rangle > 0$ (repulsion) (iii) for $\Delta_1 < 0$ and $\Delta_2 > 0$, $\langle f_{s1}^{(n)} \rangle < 0$ (attraction) and (iv) for $\Delta_1 < 0$ and $\Delta_2 < 0$, $\langle f_{s1}^{(n)} \rangle > 0$ (repulsion). So, we see that the surface charge on slab 1 feels an attractive force toward slab 2 if $\Delta_2 > 0$, i.e., if the material composing slab 2 is more polarizable than the intervening medium. In the case of $\Delta_2 > 0$ but $\Delta_1 < 0$, the force due to the charge on slab 1 is attractive, but that due to the charge on slab 2 is repulsive! It is interesting to note that the sign of the thermal van der Waals interaction between two dielectric slabs depends only on the product $\Delta_1\Delta_2$ as we shall see below.

The normal force due to the bulk charge disorder in slab 1 can be shown [11] to be given by

$$\frac{\langle f_{b1}^{(n)} \rangle}{S} = -\frac{g_{1b}\Delta_2(1-\Delta_1^2)}{16\pi\varepsilon_1\varepsilon_0 l}\frac{1}{1-\Delta_1\Delta_2}. \tag{25.16}$$

The result for the force due to the charge distribution in the slab S_2 is obtained on switching indices. The sign of the force depends purely on that of Δ_2 (Δ_1) and behaves in the same way as the surface charge. However, we see that the force generated by bulk charge disorder is longer ranged than that due to the surface charges, decaying as $1/l$. In the above computation, it is important to bear in mind that slabs will have a finite thickness—changing the interslab separation should not introduce/remove quenched charge from the system, which will give an effective bulk term in the energy. A way of avoiding this, without complicating the dielectric problem, is to assume that the quenched charge disorder has a support that is in the interval $[-(L+l)/2, -l/2]$, in slab 1 for instance, while keeping L fixed upon changing l.

The components of the force due to both bulk and surface charge disorder in the same slab have the same sign; this means that the electrostatic component of the normal force is monotonic, having the same sign for all values of l. If one takes into account thermal

Casimir forces that are also monotonically attractive or repulsive, it is possible to find systems in which the overall force becomes zero, corresponding to a stable or unstable equilibrium [18, 19]. The normal thermal Casimir or the zero Matsubara frequency van der Waals (vdW) force interaction behaves as

$$\frac{f^{(n)}_{\mathrm{vdW}}}{S} = -\frac{k_B T\ \mathrm{Li}_3(\Delta_1\Delta_2)}{8\pi l^3}, \tag{25.17}$$

where $\mathrm{Li}_3(z)$ is the trilogarithm function. If the prefactor is chosen to be negative (by taking $\Delta_1\Delta_2 < 0$), the repulsive vdW interaction can stabilize the interaction, preventing collapse at short distances. It is theoretically possible to have an attractive charge disorder interaction, behaving as $1/l$ or $1/l^2$ at large separations, meaning that the overall interaction potential will possess a stable minimum [18, 19].

The above results can be easily generalized to the case wherein the charge disorder possesses a finite correlation length in the plane of the slabs [11, 19]. However, the case of a non-zero correlation normal to the slabs, in the z direction, is more difficult to deal with.

Finally, we should note that the physical usefulness of an average value depends on the scale of fluctuations of the force with respect to the average force. For simplicity, we will consider the variance of the normal force with just surface charge disorder. After a rather long computation for surface charge disorder with zero-correlation length, we find the variance of the *total* interaction force induced by surface charge disorder to be given by [4]

$$\langle \left(f^{(n)}_s\right)^2\rangle_c = \frac{S}{4\pi\varepsilon_0^2\varepsilon_m^2 l^2}\left(g^2_{1s}D_{11} + g^2_{2s}D_{22} + 2g_{1s}g_{2s}D_{21}\right) \tag{25.18}$$

where

$$D_{ij}\Delta_i\Delta_j = \frac{\varepsilon_m^4}{3(\varepsilon_m+\varepsilon_i)^2(\varepsilon_m+\varepsilon_j)^2}\left[\frac{2\Delta_1\Delta_2}{(1-\Delta_1\Delta_2)^2} + \alpha_{ij}\ln(1-\Delta_1\Delta_2)\right] \tag{25.19}$$

where we have defined $\alpha_{ij} = (1+\delta_{ij})(-1)^{i+j}$ for $i,\ j = 1, 2$ (note that no summation over the indices $i,\ j$ is assumed in Eq. (366.19)). The normal force fluctuations due to surface charge disorder then scale as

$$\delta f^{(n)}_s \sim \frac{\sqrt{S}}{l}. \tag{25.20}$$

The ratio of the force fluctuations to the average force $R = \delta f_s^{(n)}/\langle f_s^{(n)}\rangle$ thus scales as $R \sim l/\sqrt{S}$ and becomes smaller as the surface area is increased (as expected from self-averaging in the thermodynamic limit); however, they increase as the interslab separation l is increased. In most Casimir-type experimental setups, the linear dimensions of the interacting objects are typically much greater than their separation, keeping the force fluctuations small [5].

25.3 Lateral Electrostatic Forces Between Charge-Disordered Slabs

Suppose now that the region containing the charge disorder in the dielectric slab 1 is laterally smaller than the slab 2 whilst remaining large of area A, see Fig. 366.1. We furthermore assume that charge disorder is distributed only on the bounding surfaces of the two slabs. If we displace slab 1 laterally by a vector $\mathbf{a}$ within the plane of the slabs, this will induced a change in the charge distribution $\delta\rho(\mathbf{x})$ and give a change in energy

$$\delta E = \int d\mathbf{x}\, d\mathbf{y}\, \delta\rho(\mathbf{x}) G(\mathbf{x}, \mathbf{y}; l)\rho(\mathbf{y}). \tag{25.21}$$

Note that in this set up, we assume that there is no change in the dielectric function and so the only displaced charges are the quenched ones in slab 1. If we move slab 1 by an infinitesimal amount $\mathbf{a}$, it is clear that the only non-zero contribution to $\delta\rho$ is $\delta\rho_1$. The charge density associated with the slab 1 is again assumed to consist of point charges q_i at the points $\mathbf{x}_i = (\mathbf{r}_i, z_i)$ within the slab 1 (or on its surface in the case or surface charges). If the change in the system is to displace slab 1 by an infinitesimal vector $\mathbf{a}$, the new charge distribution associated with slab 1 corresponds to all the charges at $\mathbf{x}_i$ being displaced to $(\mathbf{r}_i + \mathbf{a}, z_i)$ when the whole body is displaced by $\mathbf{a}$. This then gives

$$\delta\rho(\mathbf{x}) = -\mathbf{a} \cdot \nabla_{\mathbf{r}} \rho_1(\mathbf{x}). \tag{25.22}$$

The change in energy on displacing body i through $\mathbf{a}$ is given only by the interaction of the charges and image charges in slab 1 with those

in 2, and therefore defines a lateral electrostatic force **f** that allows us to write the average of this interaction energy as

$$\langle \delta E(\mathbf{a}) \rangle = -\langle \mathbf{f}^{(l)} \cdot \mathbf{a} \rangle = -\mathbf{a} \cdot \int d\mathbf{x}\, d\mathbf{y}\, \langle \nabla \rho_1(\mathbf{x}) G(\mathbf{x}, \mathbf{y}; l) \rho_2(\mathbf{y}) \rangle, \tag{25.23}$$

The average lateral force is thus *zero*, as we assume that charge distributions on different bodies are uncorrelated.

Nevertheless, the variance of the lateral force will be non-zero and can be computed using the two-point correlation function of the charge disorder. For brevity, we state only results for surface charge disorder with spatially uncorrelated charge disorder [4]. We find that the lateral force components in the in-plane directions $i, j = 1, 2$ have the correlation function

$$\langle f_i^{(l)} f_j^{(l)} \rangle = -\frac{A \delta_{ij} g_{1s} g_{2s} \varepsilon_m^2}{4\pi \varepsilon_0^2 l^2 (\varepsilon_m + \varepsilon_1)^2 (\varepsilon_m + \varepsilon_2)^2 \Delta_1 \Delta_2} \ln(1 - \Delta_1 \Delta_2), \tag{25.24}$$

showing that the typical lateral force fluctuations scale as [4]

$$\delta f^{(l)} \sim \frac{\sqrt{A}}{l}, \tag{25.25}$$

the same scaling as for the fluctuations of the normal force. We note that in order for the variance to be non-zero, we do not require any dielectric discontinuities and find that for $\varepsilon_1 = \varepsilon_2 = \varepsilon_m$

$$\langle f_i^{(l)} f_j^{(l)} \rangle = \frac{A \delta_{ij} g_{1s} g_{2s}}{64\pi \varepsilon_0^2 \varepsilon_m^2 l^2}. \tag{25.26}$$

25.4 Electrostatic Torques Between Charge Disordered Slabs

On rotating the slab 1 by an angle θ around its symmetry axis [14], that is to say in the direction perpendicular to the normal between the bounding surfaces of the two dielectric media, we find (assuming that charge disorder is distributed only on the bounding surfaces) that the new charge distribution of slab 1 is given by

$$\rho_1'(\mathbf{x}) = \sum_{n \in S_1} q_n \delta(\mathbf{r} - \hat{R}_\theta\, \mathbf{r}_n) \delta(z - z_n), \tag{25.27}$$

where $\hat{R}_\theta$ is the two-dimensional rotation matrix. For an infinitesimal rotation angle $\delta\theta$, one has $\hat{R}_{\delta\theta} = 1 - \iota(\delta\theta)\,\hat{\sigma}_2$, where $\hat{\sigma}_2 = \begin{pmatrix} 0 & -\iota \\ \iota & 0 \end{pmatrix}$ is the Pauli matrix. The only non-zero contribution to $\delta\rho$ in this case (assuming the summation over the in-plane Cartesian components $i,\ j = 1, 2$) is then

$$\delta\rho(\mathbf{x}) = \iota(\delta\theta)\,(\hat{\sigma}_2)_{ij} r_j \frac{\partial}{\partial r_i}\rho_1(\mathbf{x}). \tag{25.28}$$

so that the change of the interaction energy, Eq. (366.21), on rotating the surface S_1, is due to the interaction of charges and image charges in S_1 with those in S_2. We may thus write

$$\delta E = \iota(\delta\theta)\,(\hat{\sigma}_2)_{ij} \int d\mathbf{r}' d\mathbf{r}\, dz\, dz' \left[r'_j \frac{\partial}{\partial r'_i}\rho_1(\mathbf{r}', z') \right] \times G(\mathbf{r} - \mathbf{r}', z, z'; l)\rho_2(\mathbf{r}, z), \tag{25.29}$$

where $\mathbf{r}'$ and $\mathbf{r}$ are again the two-dimensional coordinates in the planes of S_1 and S_2, respectively, and z' and z' are the coordinates normal to the planes. We again assume that the charge disorder is restricted to a subregion of area A of S_1, see Fig. 366.1. In an experimental set up, it would be more likely that S_1 is finite and the charge distribution is over all S_1; however, in the approach followed here, we avoid dielectric edge effects and the Green's functions involved then retain their planar symmetry.

Integration over the coordinate $\mathbf{r}'$ is over the finite area A, while that over $\mathbf{r}$ is unrestricted. The torque τ acting on the surface S_1 is then given by $\delta E = -\,(\delta\theta)\,\tau$. As the charge distribution on the surfaces S_1 and S_2 are uncorrelated, we find that $\langle \delta E \rangle = -(\delta\theta)\langle\tau\rangle = 0$. Thus, the mean torque is zero.

From here, one can derive [14] an intuitively clear physical relation between the lateral force fluctuations and the torque fluctuations of the form

$$\langle \tau^2 \rangle = \frac{1}{A} \langle f_i^{(l)} f_j^{(l)} \rangle I_{ij}, \tag{25.30}$$

where the moment of inertia tensor is defined as

$$I_{ij} = \int_A d\mathbf{r}\,(\delta_{ij} r^2 - r_i r_j).$$

The torque fluctuations are thus connected with the lateral force fluctuations through a geometric factor encoded by moment of

inertia tensor of the region A; thus, the torque fluctuations are not the same for a square and a disc of the same surface area. This result is completely general and valid for the assumed plane-parallel arrangement of the two disorder-carrying dielectric surfaces.

As the lateral force fluctuations have the scaling $\sqrt{A}/l$, (366.25), we find that

$$\langle f_i^{(l)} f_j^{(l)} \rangle \sim \frac{A}{l^2}. \tag{25.31}$$

It then follows that typical torque fluctuations scale as

$$\delta\tau \sim \frac{A}{l}, \tag{25.32}$$

being *extensive* in terms of the area A. This is as one might expect because torque is determined by the geometry of the area A even in the limit of large area (which is not the case for the random lateral force derived above). The geometry-dependence of the torque fluctuations and the scaling with area A are obtained simply from the moment of inertia tensor.

Again, we note that in order for the torque variance to be non-zero, we do not require any dielectric discontinuities and find that for $\varepsilon_1 = \varepsilon_2 = \varepsilon_m$, the torque fluctuations are given by

$$\langle \tau^2 \rangle = \frac{g_{1s} g_{2s} A^2}{128\pi^2 \varepsilon_0^2 \varepsilon_m^2 l^2}. \tag{25.33}$$

25.5 Conclusions

Charge disorder has important repercussions for electrostatic interactions between net-neutral dielectric slabs bearing random charges on their bounding surfaces and/or in the bulk. Quenched disorder leads to an additive contribution to the net (normal) interaction force that scales as $1/l$ (or $1/l^2$) for bulk (or surface) charge disorder, it may be attractive or repulsive, and depends on the dielectric contrast of the materials.

Because of the nature of electrostatic interactions between disordered media, there is a sample-to-sample variance in the lateral as well as normal forces and it can be substantial. In the ideal limit wherein the probe area is very large, the average force is much

larger than its fluctuations. However, in some experimental setups, the probe size may be quite small and the sample-to-sample force fluctuations could become important. In addition, force fluctuations become important at large separations where the normal force is weak. In the case of lateral force variance, as the average is zero, fluctuations are the only thing observable. Fluctuations in the normal and lateral directions are always comparable; for the special case of a uniform dielectric constant, the variance of the force fluctuations in the normal direction is exactly twice the magnitude of the one in the lateral direction [4].

The disorder-induced torque fluctuations scale differently with the surface area of the interfaces bearing charge disorder, with the typical torque fluctuation being *extensive* in the surface area A. This opens up a feasible way to measure charge disorder induced interactions between randomly charged media, in a way that is independent of normal force measurements and with a higher signal-to-noise ratio than lateral force measurements.

References

1. Baytekin, H. T., Patashinski, A. Z., Branicki, M., Baytekin, B., Soh, S. and Grzybowski, B. A. (2011). *Science* **333**, p. 308.
2. Borukhov, I., Andelman, D. and Orland, H. (1998). *Eur. Phys. J. B* **5**, p. 869.
3. de Man, S., Heeck, K. and Iannuzzi, D. (2009). *Phys. Rev. A* **79**, p. 024102.
4. Dean, D., Naji, A. and Podgornik, R. (2011). *Phys. Rev. E* **83**, p. 011102.
5. Decca, R., Fischbach, E., Klimchitskaya, G. L., Krause, D. E., López, D., Mohideen, U. and Mostepanenko, V. M. (2009). *Phys. Rev. A* **79**, p. 026101.
6. Kao, K. C. (2004). *Dielectric Phenomena in Solids* (Elsevier Academic Press, San Diego,).
7. Kim, W. J., Sushkov, A. O., Dalvit, D. A. R. and Lamoreaux, S. K. (2009). *Phys. Rev. Lett.* **103**, p. 060401.
8. Lukatsky, D. and Shakhnovich, E. (2008). *Phys. Rev E* **77**, p. 020901(R).
9. Mamasakhlisov, Y., Naji, A. and Podgornik, R. (2008). *J. Stat. Phys.* **133**, p. 659.
10. Meyer, E., Rosenberg, K. and Israelachvili, J. (2006). *Proc. Natl. Acad. Sci. USA* **103**, p. 15739.

11. Naji, A., Dean, D., Sarabadani, J., Horgan, R. and Podgornik, R. (2010). *Phys. Rev. Lett.* **104**, p. 060601.
12. Naji, A. and Podgornik, R. (2005). *Phys. Rev. E* **72**, p. 041402.
13. Podgornik, R. and Naji, A. (2006). *Europhys. Lett.* **74**, p. 712.
14. Naji, A., Sarabadani, J., Dean, D. and Podgornik, R. (2012). *Eur. Phys. J E* **35**, p. 24.
15. Panyukov, S. and Rabin, Y. (1997). *Phys. Rev E* **56**, p. 7055.
16. Perkin, S., Kampf, N. and Klein, J. (2006). *Phys. Rev. Lett.* **96**, p. 038301.
17. Pitaevskii, L. P. (2008). *Phys. Rev. Lett.* **101**, p. 163202.
18. Rezvani, V., Sarabadani, J., Naji, A. and Podgornik, R. (2012). *J. Chem. Phys.* **137**, p. 114704.
19. Sarabadani, J., Naji, A., Dean, D., Horgan, R. and Podgornik, R. (2010). *J. Chem. Phys.* **133**, p. 174702.
20. Speake, C. and Trenkel, C. (2003). *Phys. Rev. Lett.* **90**, p. 160403.
21. Zagonel, L., Barrett, N., Renault, O., Bailly, A., Baurer, M., Hoffmann, M., Shih, S. and Cockayne, D. (2008). *Surf. Interface Anal.* **40**, p. 1709.

Chapter 26

Short-Range Disorder and Electrostatic Interactions in Macromolecules

Y. Sh. Mamasakhlisov,[a] A. V. Badasyan,[b,c] and V. F. Morozov[a]

[a] *Yerevan State University, Str. A. Manoogian 1, 0025 Yerevan, Armenia*
[b] *Jozef Stefan Institute, Jamova 39, SI-1000 Ljubljana, Slovenia*
[c] *Materials Research Laboratory, University of Nova Gorica, Vipavska 13, SI-5000 Nova Gorica, Slovenia, EU*
y.mamasakhlisov@ysu.am

26.1 Introduction

The structure and properties of macromolecules are governed by interactions over different length scales including van der Waals and electrostatic, hydrogen bond forming, etc. In the present study, we will focus mainly on the biological polymers, which are heteropolymers composed of monomers of different types. At the same time, biological macromolecules are polyelectrolytes, that is, contain ionizable groups [Forster and Schmidt (1995)] able to disassociate in water, leaving charges on polymer chains and releasing counter ions in solution.

Polyelectrolytes are ubiquitous in nature and exhibit rich phase behavior. Some of them (e.g., proteins) are polyampholites and bear

Electrostatics of Soft and Disordered Matter
Edited by David Dean, Jure Dobnikar, Ali Naji, and Rudolf Podgornik

ISBN 978-981-4411-85-1 (Hardcover), 978-981-4411-86-8 (eBook)
www.panstanford.com

both cationic and anionic repeat groups. The others (e.g., nucleic acids) are polyanions, carrying negative charges on the nucleotides.

Polyelectrolytes have been extensively investigated both theoretically [Dobrynin and Rubinstein (2005); Khokhlov (1980); Muthukumar (1987); Borue and Erukhimovich (1988); Marko and Rabin (1991,1992); Muthukumar (2002); Holm *et al.* (2004); Podgornik (1989, 1990); Moreira and Netz (2002); Lukatsky and Safran (2002); Naji and Podgornik (2005); Podgornik and Naji (2006); Fleck and Netz (2005, 2007); Fleck, Netz, and von Grünberg (2002); Andelman (1995)] and experimentally [Nishida, Kaji, and Kanaya (2001); Eisenberg *et al.* (1995,1996,1998); Jenekhe and Chen (1998)]. The great progress was made in understanding their characteristics in solutions at different concentrations ranging from dilute to dense.

The phase behavior of polyelectrolytes substantially depends on the fact, whether the heterogeneity is coupled with the short or long-ranged interactions. For instance, a collapse transition for a neutral chain of a polyampholyte (heteropolymer with long-range interactions) in $d = 3$ has been reported in presence of salt [Victor and Imbert (1993); Kantor and Kardar (1994); Grassberger and Hegger (1995)]. However, a modulated or frozen phase for polyampholytes has not been observed, even at very low temperatures. This is different from the well-known phase behavior of heteropolymers with short-range interactions [Sfatos and Shakhnovich (1997); Pande *et al.* (1996)] where freezing transition is known to happen at temperatures low enough. The effect of long-range interactions (polyampholytes without salt) has been addressed in [Higgs and Joanny (1991); Gutin and Shakhnovich (1994); Dobrynin and Rubinstein (1995); Pande *et al.* (1996)]. Phase behavior of such a model system is distinguished depending on ensemble of averaging. If the neutrality constraint holds separately for each of the chains, the low-temperature phase is collapsed. The transition is similar to an ordinary Θ transition with effective excluded volume. At the same time, in the ensemble of globally neutral random chains, wherein each chain carries a typical charge $Q\pm \sim \sqrt{N}$, the presence of excess charge Q may lead to a swelling of the chains.

Systems containing biological polyelectrolytes are often governed by both long-range (electrostatic) and short-range interactions. In particular, when considering the problems of RNA folding, self-assembly of viruses, etc. [Mamasakhlisov *et al.* (2007); Siber and Podgornik (2008)] nonspecific electrostatic repulsion between chain segments of single-stranded RNA (ssRNA) competes with the sequence-specific Watson–Crick base pair formation. Such aninterplay needs to be properly accounted for, and in this chapter, we present an example of such consideration.

26.2 Polyelectrolytes with Short-Range Disorder

We consider a generic flexible polyelectrolyte composed of equally charged monomers with disorder conditioned by the short-range features only (e.g., ssRNA). Similar systems have been studied recently. Thus, the effect of ionic strength on the tertiary folding of ssRNA has been addressed, for example, in [Mamasakhlisov *et al.* (2007)]. Interactions between chain monomers were supposed to be saturated to mimic the formation of Watson–Crick base pairs. The melting temperature dependence on the ionic strength has been obtained in a qualitative agreement with experiment [Shiman and Draper (2000)]. The freezing transition exists at the temperature lower than the melting temperature. Thus, the experimentally observed stability difference between the secondary and tertiary structures could be assigned to the additional entropy loss at the freezing transition, but not to the different energies of the secondary and tertiary interactions. The salt effect on the secondary structure formation in ssRNA has been considered in Einert and Netz (2011). In Einert and Netz (2011), the theory has been developed that accounts for sequence effects, the entropic contributions associated with loop formation, and salt effects. Salt effects are modeled on the Debye–Huckel level that includes counterion condensation [Andelman (1995)]. For the P5ab RNA hairpin, the global phase diagram has been derived and a good agreement with the experiment has been obtained.

We are interested in the statistical mechanics of a three-dimensional polymer chain with randomly quenched interactions.

pe charge per monomer is assumed, where e is the electron charge and $0 < p < 1$. The position of a monomer is considered in a continuous way as $\mathbf{r}(\tau)$, where $\tau \in [0,\ N]$ and N is the dimensionless length of the chain. The random sequence of the chain assumes that the type of the τ-th monomer is described by the variable ξ_τ. $\{\xi\}$s are considered to be independent random variables drawn with the same probability law. Thus, the overall probability distribution of the sequence $\{\xi\}$ is

$$\mathcal{P}\{\xi\} = \prod_\tau p(\xi_\tau), \tag{26.1}$$

where the sequence disorder is supposed to be Gaussian

$$p(\xi_\tau) = \frac{\exp(-\frac{\xi_\tau^2}{2\xi^2})}{\sqrt{2\pi\xi^2}} \tag{26.2}$$

The Hamiltonian of the system in this case reads

$$\beta\mathcal{H} = \frac{3}{2\ell^2}\int_0^N d\tau\,(\partial_\tau \mathbf{r}(\tau))^2 + \frac{\beta}{2}\int_0^N d\tau \int_0^N d\tau' v_{\tau\tau'}(\mathbf{r}(\tau) - \mathbf{r}(\tau')) + \beta V\{\mathbf{r}\}, \tag{26.3}$$

where ℓ is the length of the Kuhn segment, $V_{\text{el}}\{\mathbf{r}\}$ describes the interaction between polyelectrolyte, counterions, viral capsid, etc., and

$$v_{\tau\tau'}(\mathbf{x}) = v_0\xi_\tau\xi_{\tau'}\delta(\mathbf{x}), \tag{26.4}$$

with the positive interaction constant $v_0 > 0$. Thus, the different monomers will attract, but the similar ones will repel.

The partition function of the polyelectrolyte for every fixed sequence $\{\xi\}$ writes

$$Z\{\xi\} = \int \mathcal{D}\mathbf{r} e^{-\beta\mathcal{H}}. \tag{26.5}$$

In the limit of $N \to \infty$, the free energy of a disordered system obeys the principle of self-averaging [Binder and Young (1986)]:

$$\mathcal{F} = -k_B T \langle \ln Z\{\xi\}\rangle_{\mathcal{P}}, \tag{26.6}$$

where $\langle \ldots \rangle_{\mathcal{P}}$ means averaging with the distribution function (26.1). Self-averaging physically means that the distribution of the free energy has a very narrow peak in the vicinity of the point of maximum, corresponding to the mean value of free energy (26.6).

26.3 Free Energy Calculation. Replica trick

The quenched free energy (26.6) can be estimated using the replica trick [Binder and Young (1986)]

$$-\beta\mathcal{F} = \lim_{n\to 0}\frac{\langle Z\{\xi\}^n\rangle_{\mathcal{P}} - 1}{n}, \tag{26.7}$$

where $\beta = (k_{\mathrm{B}}T)^{-1}$. Now we need to calculate the n-replica partition function as

$$\langle Z\{\xi\}^n\rangle_{\mathcal{P}} = \int \mathcal{D}\mathbf{r} e^{-\frac{3}{2\ell^2}\sum_{a=1}^{n}\int_0^N d\tau(\partial_\tau \mathbf{r}^a(\tau))^2 - \beta\sum_{a=1}^{n} V_{\mathrm{el}}\{\mathbf{r}^a\}} \times \int \mathcal{D}\xi\mathcal{P}\{\xi\} e^{-\frac{\beta v_0}{2}\int_0^N d\tau\int_0^N d\tau'\xi_\tau\xi_{\tau'}\sum_{a=1}^{n}\delta(\mathbf{r}^a(\tau)-\mathbf{r}^a(\tau'))}. \tag{26.8}$$

The average over the distribution function (26.1) in the equation (26.8) is transformed as

$$\int \mathcal{D}\xi\mathcal{P}\{\xi\} e^{-\frac{\beta v_0}{2}\int_0^N d\tau\int_0^N d\tau'\xi_\tau\xi_{\tau'}\sum_{a=1}^{n}\delta(\mathbf{r}^a(\tau)-\mathbf{r}^a(\tau'))} = \int \mathcal{D}\xi e^{-\frac{1}{2\xi^2}\int_0^N d\tau\xi_\tau^2} e^{-\frac{\beta v_0}{2}\int d^3\mathbf{x}\sum_{a=1}^{n} m_{\mathrm{a}}(\mathbf{x})^2}, \tag{26.9}$$

where the field $m_{\mathrm{a}}(\mathbf{x}) = \int_0^N d\tau\xi_\tau\delta(\mathbf{x}-\mathbf{r}^a(\tau))$ is introduced. The r.h.s. of the equation (26.9) is linearized using the Hubbard–Stratonovich transformation as

$$e^{-\frac{\beta v_0}{2}\int d^3\mathbf{x}\sum_{\mathrm{a}=1}^{n} m_{\mathrm{a}}(\mathbf{x})^2} = e^{-\frac{nV}{2}\ln(2\pi\beta v_0)} \int \mathcal{D}\Psi e^{-\frac{1}{2\beta v_0}\sum_{\mathrm{a}}\int d^3\mathbf{x}\Psi_{\mathrm{a}}(\mathbf{x})^2 + \imath\sum_{\mathrm{a}}\int d^3\mathbf{x}\Psi_{\mathrm{a}}(\mathbf{x})m_{\mathrm{a}}(\mathbf{x})}. \tag{26.10}$$

Insertion of Eqs. (26.9 and 26.10) into the Eq. (26.8) upon averaging over the $\{\xi\}$ variables yields the n-replica partition function as

$$\langle Z\{\xi\}^n\rangle_{\mathcal{P}} \propto e^{-\frac{nV}{2}\ln(2\pi\beta v_0)} \int \mathcal{D}\Psi e^{-\frac{1}{2\beta v_0}\sum_{\mathrm{a}}\int d^3\mathbf{x}\Psi_{\mathrm{a}}(\mathbf{x})^2} \times \int \mathcal{D}\mathbf{r} e^{-\frac{3}{2\ell^2}\sum_{a=1}^{n}\int_0^N d\tau(\partial_\tau \mathbf{r}^a(\tau))^2 - \beta\sum_{a=1}^{n} V_{\mathrm{el}}\{\mathbf{r}^a\}} \times e^{-\frac{\xi^2}{2}\sum_{a,b}\int_0^N d\tau\Psi_{\mathrm{a}}(\mathbf{r}^a(\tau))\Psi_{\mathrm{b}}(\mathbf{r}^b(\tau))}. \tag{26.11}$$

For further consideration, it is useful to introduce two order parameters, namely the inter-replica overlap $q_{ab}(\mathbf{x}, \mathbf{x}')$, with $a < b$, and the density of a-th replica monomers $\rho_{\mathrm{a}}(\mathbf{x})$ as

$$q_{ab}(\mathbf{x}, \mathbf{x}') = \int_0^N d\tau\delta(\mathbf{x} - \mathbf{r}^a(\tau))\delta(\mathbf{x}' - \mathbf{r}^b(\tau))$$
$$\rho_{\mathrm{a}}(\mathbf{x}) = \int_0^N d\tau\delta(\mathbf{x} - \mathbf{r}^a(\tau)). \tag{26.12}$$

Using these order parameters (26.12), the n-replica partition function (26.11) is transformed as

$$\begin{aligned}\langle Z\{\xi\}^n\rangle_{\mathcal{P}} \propto & \int \mathcal{D}\varphi \int \mathcal{D}c^{\pm} \int \mathcal{D}\Psi e^{-\frac{1}{2\beta v_0}\sum_{\mathrm{a}}\int d^3\mathbf{x}\Psi_{\mathrm{a}}(\mathbf{x})^2} \\ & \times \int \mathcal{D}\mathbf{r} e^{-\frac{3}{2\ell^2}\sum_{a=1}^{n}\int_0^N d\tau(\partial_\tau \mathbf{r}^a(\tau))^2} \\ & \times e^{-\beta\sum_{a=1}^{n} W_{el}(\rho_{\mathrm{a}},\varphi_{\mathrm{a}},c_a^{\pm})-\frac{\xi^2}{2}\sum_{\mathrm{a}}\int d^3\mathbf{x}\Psi_{\mathrm{a}}(\mathbf{x})^2\rho_{\mathrm{a}}(\mathbf{x})} \\ & \times e^{-\xi^2\sum_{a<b}\int d^3\mathbf{x}\int d^3\mathbf{x}'\Psi_{\mathrm{a}}(\mathbf{x})\Psi_{\mathrm{b}}(\mathbf{x}')q_{ab}(\mathbf{x},\mathbf{x}')}, \end{aligned} \tag{26.13}$$

where the electrostatic part of the free energy is written as a sum of electrostatic energies of polyelectrolyte segments, fixed charges residing on the capsid and charges of salt ions, as well as the entropies of the salt ions. As it was suggested in [Borukhov, Andelman, and Orland (1999); Shafir, Andelman, and Netz (2003); Siber and Podgornik (2008)],

$$\begin{aligned} W_{\mathrm{el}}(\rho_{\mathrm{a}},\varphi_{\mathrm{a}},c_a^{\pm}) = \int d^3\mathbf{x}\Big\{ & -\frac{\epsilon\epsilon_0}{2}(\nabla\varphi_{\mathrm{a}}(\mathbf{x}))^2 \\ & +\varphi_{\mathrm{a}}(\mathbf{x})\Big[ec_a^{+}(\mathbf{x})-ec_a^{-}(\mathbf{x})-pe\rho_{\mathrm{a}}(\mathbf{x})+\rho_{\mathrm{surf}}(\mathbf{x})\Big] \\ & +\sum_{i=\pm}\Big[k_{\mathrm{B}}T(c_a^i(\mathbf{x})\ln c_a^i(\mathbf{x})-c_a^i(\mathbf{x}) \\ & -(c_0^i\ln c_0^i-c_0^i))-\mu^i(c_a^i(\mathbf{x})-c_0^i)\Big]\Big\}. \end{aligned} \tag{26.14}$$

Here, $c^{\pm}$ are the concentrations of $\pm$ monovalent salt ions, with $c_0^{\pm}$ being their bulk concentrations, and $\mu^{\pm}$ their chemical potentials, $\epsilon\epsilon_0$ is the permittivity of water, and ρ_{surf} is the surface charge distribution over the capsid.

Introducing the Lagrange multipliers $\hat{q}_{ab}(\mathbf{x},\mathbf{x}')$ and the $\hat{\rho}_a(\mathbf{x})$ conjugated with the order parameters (26.12), the n-replica partition function reads [Garel, Orland, and Pitard (1997)]

$$\langle Z\{\xi\}^n\rangle_{\mathcal{P}} \propto e^{-\frac{nV}{2}\ln(2\pi\beta v_0)}\int \mathcal{D}\Psi\,\mathcal{D}\rho\,\mathcal{D}\hat{\rho}\,\mathcal{D}q\,\mathcal{D}\hat{q}e^{G(\Psi,\rho,\hat{\rho},q,\hat{q})+\ln\zeta(\hat{\rho},\hat{q})}, \tag{26.15}$$

where

$$G(\Psi, \rho, \hat{\rho}, q, \hat{q}, \varphi, c^{\pm}) = -\frac{1}{2\beta v_0}\sum_{\mathrm{a}}\int d^3\mathbf{x}\Psi_{\mathrm{a}}(\mathbf{x})^2$$
$$-\beta\sum_{a=1}^{n} W_{\mathrm{el}}(\rho_{\mathrm{a}}, \varphi_{\mathrm{a}}, c_a^{\pm}) - \frac{\xi^2}{2}\sum_{\mathrm{a}}\int d^3\mathbf{x}\Psi_{\mathrm{a}}(\mathbf{x})^2\rho_{\mathrm{a}}(\mathbf{x})$$
$$-\xi^2\sum_{a<b}\int d^3\mathbf{x}\int d^3\mathbf{x}'\Psi_{\mathrm{a}}(\mathbf{x})\Psi_{\mathrm{b}}(\mathbf{x}')q_{ab}(\mathbf{x}, \mathbf{x}')$$
$$+\imath\sum_{\mathrm{a}}\int d^3\mathbf{x}\rho_{\mathrm{a}}(\mathbf{x})\hat{\rho}_a(\mathbf{x})$$
$$\imath\sum_{a<b}\int d^3\mathbf{x}\int d^3\mathbf{x}' q_{ab}(\mathbf{x}, \mathbf{x}')\hat{q}_{ab}(\mathbf{x}, \mathbf{x}') \qquad (26.16)$$

and

$$\ln\zeta(\hat{\rho}, \hat{q}) = -N\min_{\psi}\Bigg\{\int d^{3n}\mathbf{x}\psi(\mathbf{x}_1, \ldots, \mathbf{x}_n)$$
$$\times\Bigg(-\frac{\ell^2}{6}\sum_{\mathrm{a}}\nabla_a^2 + \imath\sum_{\mathrm{a}}\hat{\rho}_a(\mathbf{x}_a) + \imath\sum_{a<b}\hat{q}_{ab}(\mathbf{x}_a, \mathbf{x}_b)\Bigg)$$
$$\times\psi(\mathbf{x}_1, \ldots, \mathbf{x}_n) - \epsilon_0\Bigg(\int d^{3n}\mathbf{x}\psi(\mathbf{x}_1, \ldots, \mathbf{x}_n)^2 - 1\Bigg)\Bigg\}. \qquad (26.17)$$

Here, ϵ_0 is the ground state energy and $\psi(\mathbf{x}_1, \ldots, \mathbf{x}_n)$ is the corresponding eigenfunction of the "quantum-like" Hamiltonian $\hat{\mathcal{H}}_n = -\frac{\ell^2}{6}\sum_{\mathrm{a}}\nabla_a^2 + \imath\sum_{\mathrm{a}}\hat{\rho}_a(\mathbf{x}_a) + \imath\sum_{a<b}\hat{q}_{ab}(\mathbf{x}_a, \mathbf{x}_b)$. As $v_0 > 0$, we have no trend of segregation between different kinds of monomers and we expect the high enough fluctuations of the fields $\{\Psi\}$. Thus, we need to take saddle-point in the equation (26.15) over the fields $\{\rho, \hat{\rho}, q, \hat{q}\}$ only and to integrate over the fields $\{\Psi\}$. Let us introduce $g(\rho, \hat{\rho}, q, \hat{q}, \varphi, c^{\pm}) = \ln\int\mathcal{D}\Psi e^{G(\Psi, \rho, \hat{\rho}, q, \hat{q})}$, where

$$\int\mathcal{D}\Psi e^{G(\Psi, \rho, \hat{\rho}, q, \hat{q})} = e^{-\beta\sum_{a=1}^{n} W_{\mathrm{el}}(\rho_{\mathrm{a}}, \varphi_{\mathrm{a}}, c_a^{\pm})}$$
$$\times e^{\imath\sum_{\mathrm{a}}\int d^3\mathbf{x}\rho_{\mathrm{a}}(\mathbf{x})\hat{\rho}_a(\mathbf{x}) + \imath\sum_{a<b}\int d^3\mathbf{x}\int d^3\mathbf{x}' q_{ab}(\mathbf{x}, \mathbf{x}')\hat{q}_{ab}(\mathbf{x}, \mathbf{x}')}$$
$$\times\int\mathcal{D}\Psi e^{-\frac{1}{2}\sum_{a,b}\int d^3\mathbf{x}\int d^3\mathbf{x}' P_{ab}(\mathbf{x}, \mathbf{x}')\Psi_{\mathrm{a}}(\mathbf{x})\Psi_{\mathrm{b}}(\mathbf{x}')}, \qquad (26.18)$$

and $P_{ab}(\mathbf{x}, \mathbf{x}') = \delta_{ab}\delta(\mathbf{x}-\mathbf{x}')[\frac{1}{\beta v_0} + \xi^2\rho_{\rm a}(\mathbf{x})] + \xi^2(1-\delta_{ab})q_{ab}(\mathbf{x}, \mathbf{x}')$. Thus, $g(\rho, \hat{\rho}, q, \hat{q})$ read

$$\begin{aligned} g(\rho, \hat{\rho}, q, \hat{q}, \varphi, c^{\pm}) &= -\frac{1}{2}\ln\det\frac{\hat{P}}{2\pi} \\ &-\beta\sum_{a=1}^{n} W_{\rm el}(\rho_{\rm a}, \varphi_{\rm a}, c_a^{\pm}) + \imath\sum_{\rm a}\int d^3\mathbf{x}\rho_{\rm a}(\mathbf{x})\hat{\rho}_a(\mathbf{x}) \\ &+\imath\sum_{a<b}\int d^3\mathbf{x}\int d^3\mathbf{x}' q_{ab}(\mathbf{x}, \mathbf{x}')\hat{q}_{ab}(\mathbf{x}, \mathbf{x}'). \end{aligned} \tag{26.19}$$

Let us consider the term $Tr\ln$ in the equation (26.19). These calculations may be carried out by employing properties of block-matrices and the operator algebra defined over the Hilbert space $\{|\mathbf{x}\rangle\}$. We shall use the compact notation by defining the operators $\langle\mathbf{x}|\hat{A}_{ab}|\mathbf{x}'\rangle = \delta_{ab}\delta(\mathbf{x}-\mathbf{x}')[\frac{1}{\beta v_0} + \xi^2\rho_{\rm a}(\mathbf{x})]$ as the $n\times n$ operator matrix and $\langle\mathbf{x}|\hat{P}_{ab}|\mathbf{x}'\rangle = P_{ab}(\mathbf{x}, \mathbf{x}')$ as an element of the $n\times n$ operator matrix

$$\hat{P} = \hat{A} + \xi^2\hat{B}, \tag{26.20}$$

where $\langle\mathbf{x}|\hat{B}_{ab}|\mathbf{x}'\rangle = (1-\delta_{ab})q_{ab}(\mathbf{x}, \mathbf{x}')$ is the $n\times n$ operator matrix. Therefore,

$$\begin{aligned} \ln\det\hat{P} = Tr\ln\hat{P} &= Tr\ln\left\{\hat{A} + \xi^2\hat{B}\right\} \\ &= Tr\ln\hat{A} + Tr\ln\left\{\hat{1}_n\otimes\hat{1} + \xi^2\hat{A}^{-1}\hat{B}\right\}, \end{aligned} \tag{26.21}$$

where $(\hat{1}_n)_{ab} = \delta_{ab}$ and $\langle\mathbf{x}|\hat{1}|\mathbf{x}'\rangle = \delta(\mathbf{x}-\mathbf{x}')$. Calculation of the first term on the r.h.s. of the equation (26.21) is straightforward

$$Tr\ln\hat{A} = \sum_{\rm a}\int d^3\mathbf{x}\ln\left(\frac{1}{\beta v_0} + \xi^2\rho_a(\mathbf{x})\right). \tag{26.22}$$

The second term can be expanded as

$$Tr\ln\left\{\hat{1}_n\otimes\hat{1} + \xi^2\hat{A}^{-1}\hat{B}\right\} = \sum_{k=1}^{\infty}(-1)^{k+1}\frac{\xi^{2k}}{k}Tr(\hat{A}^{-1}\hat{B})^k \tag{26.23}$$

26.4 Weak Disorder Expansion

In the case of weak disorder ($\xi \ll 1$), we may restrict ourselves by a few terms of the expansion up to the $\sim \mathcal{O}(\xi^4)$ order:

$$g(\rho, \hat{\rho}, q, \hat{q}, \varphi, c^{\pm}) = \frac{\xi^4(\beta v_0)^2}{2}\left\{\frac{1}{2}\sum_{\mathrm{a}}\int d^3\mathbf{x}\rho_{\mathrm{a}}(\mathbf{x})^2 + \sum_{a<b}\int d^3\mathbf{x}\int d^3\mathbf{x}' q_{ab}(\mathbf{x},\mathbf{x}')^2\right\} - \beta\sum_{a=1}^{n} W_{\mathrm{el}}(\rho_{\mathrm{a}}, \varphi_{\mathrm{a}}, c_a^{\pm}) + \imath\sum_{\mathrm{a}}\int d^3\mathbf{x}\rho_{\mathrm{a}}(\mathbf{x})\hat{\rho}_a(\mathbf{x}) + \imath\sum_{a<b}\int d^3\mathbf{x}\int d^3\mathbf{x}' q_{ab}(\mathbf{x},\mathbf{x}')\hat{q}_{ab}(\mathbf{x},\mathbf{x}'). \quad (26.24)$$

Thus, the functional of the reduced free energy reads

$$-\beta\mathcal{F}(\rho, \hat{\rho}, q, \hat{q}, \varphi, c^{\pm}) = g(\rho, \hat{\rho}, q, \hat{q}, \varphi, c^{\pm}) + \ln\zeta(\hat{\rho}, \hat{q}). \quad (26.25)$$

In the $\sim \mathcal{O}(\xi^4)$ approximation, saddle-point is satisfied by equations

$$0 = -\frac{\delta(\beta\mathcal{F})}{\delta\rho_{\mathrm{a}}(\mathbf{r})} = \frac{\xi^4(\beta v_0)^2}{2}\rho_{\mathrm{a}}(\mathbf{r}) + \beta pe\varphi_{\mathrm{a}}(\mathbf{r}) + \imath\hat{\rho}_a(\mathbf{r}) \quad (26.26)$$

$$0 = -\frac{\delta(\beta\mathcal{F})}{\delta\hat{\rho}_a(\mathbf{r})} = \imath\rho_{\mathrm{a}}(\mathbf{r}) - \imath N\int d^{3n}\mathbf{x}\psi(\mathbf{x}_1, \ldots, \mathbf{x}_n)^2\delta(\mathbf{x}_a - \mathbf{r}) \quad (26.27)$$

$$0 = -\frac{\delta(\beta\mathcal{F})}{\delta q_{ab}(\mathbf{r},\mathbf{r}')} = \xi^4(\beta v_0)^2 q_{ab}(\mathbf{r},\mathbf{r}') + \imath\hat{q}_{ab}(\mathbf{r},\mathbf{r}') \quad (26.28)$$

$$0 = -\frac{\delta(\beta\mathcal{F})}{\delta\hat{q}_{ab}(\mathbf{r},\mathbf{r}')} = \imath q_{ab}(\mathbf{r},\mathbf{r}') - \imath N\int d^{3n}\mathbf{x}\psi(\mathbf{x}_1, \ldots, \mathbf{x}_n)^2\delta(\mathbf{x}_a - \mathbf{r})\delta(\mathbf{x}_b - \mathbf{r}') \quad (26.29)$$

$$0 = -\frac{\delta(\beta\mathcal{F})}{\delta\varphi_a(\mathbf{r})} = -\beta\left[ec_a^+ - ec_a^- - pe\rho_a(\mathbf{r}) + \rho_{\mathrm{surf}}(\mathbf{r})\right] - \epsilon\epsilon_0\nabla^2\varphi_a(\mathbf{r}) \quad (26.30)$$

$$0 = -\frac{\delta(\beta\mathcal{F})}{\delta c_a^{\pm}(\mathbf{r})} = \pm\beta e\varphi_a(\mathbf{r}) + \ln c_a^{\pm}(\mathbf{r}) - \beta\mu^{\pm} \tag{26.31}$$

Equations (26.27, 26.29) give the standard relations between the eigenfunction $\psi(\mathbf{x}_1, \ldots, \mathbf{x}_n)$, the monomers' density, and the inter-replica overlapping, correspondingly [Garel, Orland, and Pitard (1997)]

$$\rho_{\mathrm{a}}(\mathbf{r}) = N \int d^{3n}\mathbf{x}\psi(\mathbf{x}_1, \ldots, \mathbf{x}_n)^2\delta(\mathbf{x}_a - \mathbf{r}), \tag{26.32}$$

$$q_{ab}(\mathbf{r}, \mathbf{r}') = N \int d^{3n}\mathbf{x}\psi(\mathbf{x}_1, \ldots, \mathbf{x}_n)^2\delta(\mathbf{x}_a - \mathbf{r})\delta(\mathbf{x}_b - \mathbf{r}'). \tag{26.33}$$

Equations (26.30, 26.31) give the generalized polyelectrolyte Poisson–Boltzmann equation

$$\epsilon\epsilon_0\nabla_r^2\varphi(\mathbf{r}) = 2ec_0\sinh(\beta e\varphi(\mathbf{r})) - \rho_{\mathrm{surf}}(\mathbf{r}) + pe\rho(\mathbf{r}). \tag{26.34}$$

Minimization of the free energy (26.25) over the "wave function" $\psi(\mathbf{x}_1, \ldots, \mathbf{x}_n)$ yields the generalized Edwards equation [Edwards (1965)] for any integer n

$$\frac{\ell^2}{6}\nabla^2\psi(\mathbf{x}_1, \ldots, \mathbf{x}_n) = \Bigg[- \beta pe\sum_{\mathrm{a}}\varphi(\mathbf{x}_a) - \epsilon_0$$
$$-\xi^4(\beta v_0)^2\Bigg(\sum_{\mathrm{a}}\rho(\mathbf{x}_a) + \sum_{a<b}q_{ab}(\mathbf{x}_a, \mathbf{x}_b)\Bigg)\Bigg]\psi(\mathbf{x}_1, \ldots, \mathbf{x}_n) \tag{26.35}$$

We need to solve the system of Eqs. (26.34, 26.35) and to take the limit of $n \to 0$ for the number of replicas. Solution is strictly dependent on the boundary conditions and charge distribution $\rho_{\mathrm{surf}}(\mathbf{r})$. The proposed approach permits to consider the effect of the short-range disorder on the polyelectrolyte chain behavior in different geometries.

Next step requires the introduction of assumptions about the particular form of charge distribution $\rho_{\mathrm{surf}}(\mathbf{r})$ to solve the system of Eqs. 26.34 and 26.35, followed by taking the limit of $n \to 0$ for the number of replicas. Solution is also strictly dependent on the boundary conditions. The proposed approach permits to consider the effect of the short-range disorder on the polyelectrolyte chain behavior in different geometries.

References

D. Andelman, in *Handbook of Biological Physics: Structure and Dynamics of Membranes*, R. Lipowsky, E. Sackmann (eds.), Vol. 1B. Elsevier, Amsterdam (1995), Chap. 12.

K. Binder and A. P. Young, *Rev. Mod. Phys.* **58**, 801 (1986).

V. Yu. Borue and I. Ya. Erukhimovich, *Macromolecules* **21**, 3240 (1988).

I. Borukhov, D. Andelman, and H. Orland, *J. Phys. Chem. B* **103**, 5042 (1999).

A. V. Dobrynin and M. Rubinstein, *J. Phys. (France) II* **5**, 677 (1995).

A. V. Dobrynin and M. Rubinstein, *Prog. Polym. Sci.* **30** 1049 (2005).

S. F. Edwards, *Proc. Phys. Soc. London* **85**, 613 (1965).

T. R. Einert and R. R. Netz, *Biophys. J.* **100**, 2475 (2011).

C. Fleck, R. R. Netz, and H. H. von Grünberg, *Biophys. J.* **82**, 76 (2002).

C. Fleck and R. R. Netz, *Europhys. Lett.* **70**, 341 (2005).

S. Forster and M. Schmidt, *Adv. Polym. Sci.* **120** 51 (1995).

C. Fleck and R. R. Netz, *Eur. J. Phys.* E **22**, 261 (2007).

T. Garel, H. Orland, and E. Pitard in *Spin glasses and random fields*, A.P. Young (ed.), World Scientific (1997).

P. Grassberger and R. Hegger, *Europhys. Lett.* **31**, 351 (1995).

A. M. Gutin and E. I. Shakhnovich, *Phys. Rev. E* **50**, R3322 (1994).

P. G. Higgs and J. F. Joanny, *J. Chem. Phys.* **94**, 1543 (1991).

C. Holm, J. F. Joanny, K. Kremer, R. R. Netz, P. Reineker, C. Seidel, et al. *Adv. Polym. Sci.* **166**, 67 (2004).

S. A. Jenekhe and X. L. Chen, *Science* **279**, 1903 (1998).

Y. Kantor and M. Kardar, *Europhys. Lett.* **28**, 169 (1994).

A.R. Khokhlov, *J.Phys.A: Math. Gen.* **13**, 979 (1980).

D. B. Lukatsky and S. A. Safran, *Europhys. Lett.* **60**, 629 (2002).

J. F. Marko and Y. Rabin, *Macromolecules* **24**, 2134 (1991); *ibid.* **25**, 1503 (1992).

M. Mezard and G. Parisi, *J. Phys. I* **1**, 809 (1991).

Y. Sh. Mamasakhlisov, Sh. Hayryan, V. F. Morozov, and C.-K. Hu, *Phys. Rev. E* 75, 061907 (2007).

A. G. Moreira and R. R. Netz, *Europhys. Lett.* **57**, 911 (2002).

M. Muthukumar, *J. Chem. Phys.* **86**, 7230 (1987).

M. Muthukumar, *Macromolecules* **35**, 9142 (2002).

A. Naji and R. Podgornik, *Phys. Rev. E* **72**, 041402 (2005).

K. Nishida, K. Kaji, and T. Kanaya, *J. Chem. Phys.* **114**, 8671 (2001); *ibid.* **115**, 8217 (2001).

V. S. Pande, A. Y. Grosberg, C. Joerg, M. Kardar, and T. Tanaka, *Phys. Rev. Lett.*, 76, 3565 (1996).

R. Podgornik, *J. Chem. Phys.* **91**, 5840 (1989).

R. Podgornik, *J. Phys. A: Math. Gen.* **23**, 275 (1990).

R. Podgornik and A. Naji, *Europhys. Lett.* **74**, 712 (2006).

C. D. Sfatos and E. I. Shakhnovich, *Physics Reports* **288**, 77 (1997).

A. Shafir, D. Andelman, and R. R. Netz, *J. Chem. Phys.* **119**, 2355 (2003).

E. I. Shakhnovich and A. M. Gutin, *J. Phys. A* **22**, 1647 (1989).

R. Shiman and D. E. Draper, *J. Mol. Biol.* **302**, 79 (2000).

A. Siber and R. Podgornik, *Phys. Rev. E* 78, 051915 (2008).

J. M. Victor and J. B. Imbert, *Europhys. Lett.* **24**, 189 (1993).

L. Zhang and A. Eisenberg, *Science* **268**, 1728 (1995); L. Zhang and A. Eisenberg, Macromolecules **29**, 8805 (1996); K. Yu and A. Eisenberg, *Macromolecules* **31**, 3509 (1998).

Chapter 27

Interaction between Disordered Heterogeneous Charged Surfaces

Gilad Silbert and Jacob Klein
Department of Materials and Interfaces, Weizmann Institute of Science, Rehovot 76100, Israel
Jacob.klein@weizmann.ac.il

Long-ranged attractions across water between two surfaces that are randomly covered with positive and negative charge domains have been attributed to induced correlation of the charges (positive lining up with negative) as the surfaces approach. Here we show, by directly measuring normal forces under a rapid shear field, that these attractions are not in fact due to such correlations. It is rather the inherent interaction-asymmetry between equally and between oppositely charged domains that results in the long-ranged attraction between two such surfaces. This happens even in the complete absence of any charge correlation between the disordered domains on the opposing, overall-neutral surfaces. Our results may also account for the long-ranged attraction frequently observed between surfaces hydrophobized by surfactant layers, which were previously attributed to "hydrophobic interactions."

This chapter is based on a work published in [1] and was presented at the CECAM meeting on "New challenges in electrostatics of soft and disordered matter" in Toulouse, May 2012.

Electrostatics of Soft and Disordered Matter
Edited by David Dean, Jure Dobnikar, Ali Naji, and Rudolf Podgornik

ISBN 978-981-4411-85-1 (Hardcover), 978-981-4411-86-8 (eBook)
www.panstanford.com

27.1 Introduction

The stability of colloidal dispersions, as recognized since the work of Faraday and Graham some 150 years ago, hinges largely on the balance between attractive and repulsive surface forces [2]. In aqueous media, the electrostatic double-layer repulsion between like-charged surfaces plays the dominant role in the stabilization, keeping particles from aggregating under van der Waals attraction [2–4]. Such forces have been studied for decades [2–7], but although nearly all understanding of the interactions relate to uniformly charged surfaces, most real surfaces are in fact heterogeneous and disordered.

Theoretical models of interactions between heterogeneously charged surfaces in aqueous media have mainly treated the effect of charge correlations, rather than that of fully disordered heterogeneity. Theoretical studies of surfaces bearing patterned charge domains predicted a long-range attraction as a result of net correlations—more opposite charges facing each other than equal charges facing each other—between the domains [8–12]. Miklavic *et al.* [10] computed the interaction opposing periodic charge patterns, which were correlated, anti-correlated, or the charge domains were free to migrate in order to minimize the free energy of the interaction. Podgornik and co-workers have studied extensively interactions between disordered charged surfaces. Naji and Podgornik [11] calculated effective electrostatic interactions between charged surfaces with charge-domain disorder, defined via a mean surface charge density with a Gaussian-distributed quenched surface charge. They considered correlation between the charge fluctuations on both surfaces, and in particular showed that fully quenched—that is, fully disordered and uncorrelated—small charge patches on the opposing surfaces resulted in little interaction at the mean-field level. More recently, Mamasakhlisov *et al*. [13] computed the inter-surface forces for two planar surfaces of equal mean surface charge, which are partially annealed, enabling correlation between surface charges as surfaces approach: it was shown that such partial annealing of the quenched disorder can lead to a reduction of the inter-plate repulsion at the mean-field level. It is fair to say that all mean-field theoretical models to date show that

long-ranged attractions between heterogeneously charged surfaces across water arise essentially through net correlations of opposing charges, whether through patterning, charge fluctuations, or charge migration.

In contrast to these theoretical models, experimentally one frequently encounters random (fully disordered), heterogeneously distributed charge domains. A particular example arises from the adsorption of amphiphilic surfactants with positively charged headgroups onto negatively charged surfaces, which is widely used in surface modification. Such surfactant layers initially expose their alkyl tails to form a hydrophobic monolayer, but under a thermodynamic driving force may reorganize in water to form mosaic-like structures consisting of positively charged bilayer domains on a negatively charged substrate [14–19]. Several independent studies revealed that such surfaces experience an attraction at separations up to many tens of nanometers [14–18], that at their onset are orders of magnitude stronger than those due to van der Waals attraction. These strong, long-ranged attractive forces were attributed to the correlation of charge domains (positive facing negative) evolving on approach of the surfaces as a result of the domain mobility [14–18, 20, 21]. As such, charge domains form through reorganization of hydrophobic surfactant layers, understanding that these forces may shed light on the puzzling long-range attractions attributed to "hydrophobic" interactions between such layers [15, 21, 22]. Indeed, it was explicitly suggested earlier [14–18] that the origin of the long-ranged "hydrophobic" attraction between surfactant-coated surfaces is due to positive vs. negative correlations forming, through lateral charge migration, when opposing surfaces with charge domains (that form through the surfactant reorganization) approach each other.

Here, we demonstrate that two surfaces covered with disordered charge patches experience a long-ranged attraction across water that is orders of magnitude stronger than van der Waals forces, and which persists, remarkably, even in the complete absence of any correlations between opposing positive and negative domains (so-called "quenched disorder"). The origin of this attraction is, as we show, the counterintuitive observation that two oppositely charged surfaces attract each other across water (or other ion-containing

liquids) much more strongly than equally charged surfaces repel, for identical surface separations and charge densities. This striking asymmetry may result in strong, long-ranged attraction between randomly charged surfaces even when they are overall neutral. It sheds new light on interactions of hydrocolloids and in biological systems, in which such surfaces are ubiquitous. It may also account for the long-ranged attraction frequently observed between surfaces coated with surfactants (and with other species), which was long attributed to a hydrophobic surface interaction.

27.2 Results and Discussion

Heterogeneous surfaces with random positive and negative charge domains were created via an initially uniform, self-assembled surfactant layer that re-arranged with time under water (Methods). Figure 27.1 shows typical AFM micrographs of the monolayers, as

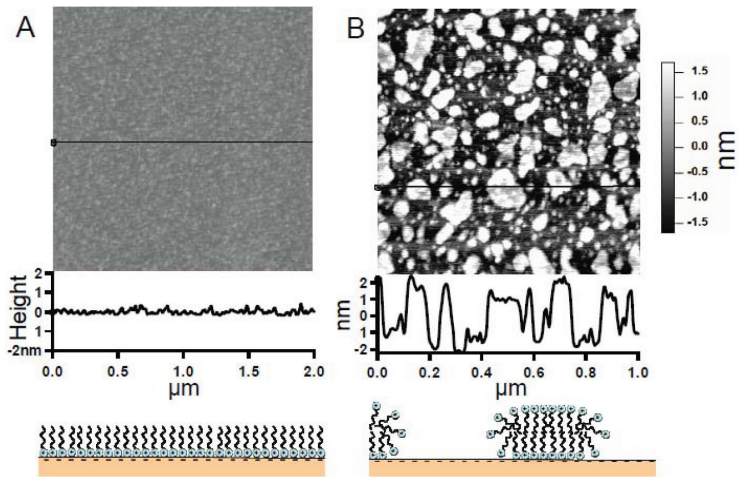

Figure 27.1 Surfaces with random charge domains. AFM tapping-mode images of the model surfactant (octadecyltrimethylammonium bromide) on mica: (A) in air, (B) after 22 h immersion time in pure water. The cartoons illustrate the break-up of the initially uniform monolayer into positively charged bilayer domains on a negatively charged substrate. For the micrograph shown, the bilayer domains (white, positively charged) cover some 45% of the total area in B, while those over lateral dimensions > 150 nm cover 7% of the total area.

freshly deposited and following immersion in water. As observed previously with many other surfactants [14–18], the initially smooth monolayer breaks up with immersion time in water into a random mosaic of positively charged bilayers (mean thickness 3.2 ± 0.4 nm) on a background of negatively charged bare mica. Earlier studies revealed that such surfaces—bearing positively and negatively charged domains of random size and distribution—experience an attraction at separations of several tens of nanometers [14–18], which is orders of magnitude stronger than can be due to van der Waals forces. This strong, long-ranged attraction was attributed to the correlation of charge domains (positive facing negative) developing on approach of the surfaces [14–18, 20, 21]. Here, we carried out experiments to examine directly the crucial point whether such charge correlations were occurring: Normal forces $F_{\mathrm{n}}(\mathrm{D})$ between the two surfaces at closest distance D apart were determined using a surface force balance (SFB, Methods) in two different modes, illustrated in the insets A and B to Fig. 27.2. The first, inset A, termed the straight-approach mode, is the one used in all earlier studies of surface forces: The surface separation D has progressively decreased by moving them normally with respect to each other, to construct the force vs. separation profile $F_{\mathrm{n}}(\mathrm{D})$. In the second mode, termed the shear-approach mode, the surfaces are again made to approach, but now the sectored piezoelectric tube on which the upper surface is mounted is used, during this normal approach, to apply a rapid lateral (shear) motion parallel to the lower surface (inset B to Fig. 27.2), over a range of frequencies ν and amplitudes A. The amplitude, A, of this lateral motion (120–600 nm) is much larger than the characteristic size of the charge domains (from ca. 10 to 200 nm, Fig. 27.1). The lateral velocity $v_{\mathrm{s}} = 2\ \nu A$ ranges to values (5.1 μm/s) that are up to three orders of magnitude larger than the estimated value of v_{domain}, the velocity of the charge domains during their assumed motion to correlation, at the onset of attraction [15, 23]. Such applied lateral motion $v_{\mathrm{s}} \gg v_{\mathrm{domain}}$ must thus frustrate any directed translation of the charge domains on either surface to a correlated configuration with the opposing charge regions. If indeed therefore it was the charge correlations postulated earlier that were leading to the long-ranged attraction in the straight-approach mode, then the attractive normal interactions measured using the shear-approach mode should be much weaker,

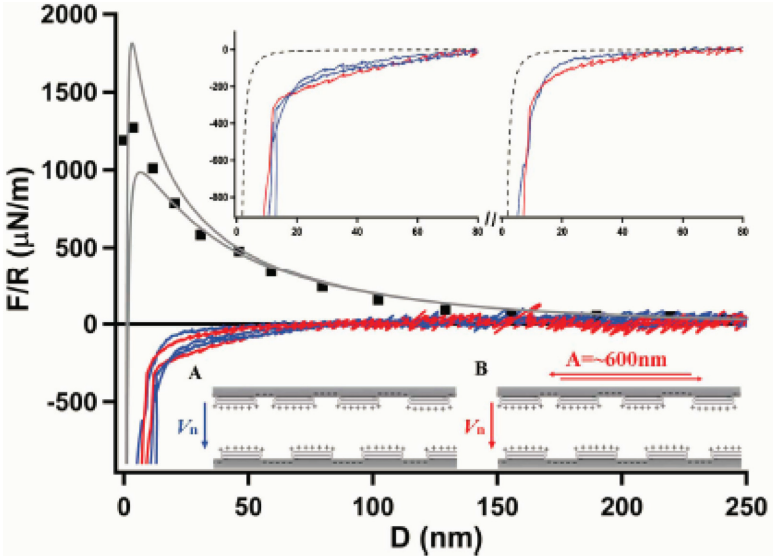

Figure 27.2 Surface energy of the random charge domain-coated surfaces (as seen in Fig. 27.1). Surface energies are shown as a function of time in water and of multiple approaches at given contact point, for several different contact points and two independent experiments, calculated via the force to separate the two adhered surfaces using the Johnson—Kendal–Roberts model [41]. Consecutive approaches at a given contact point are alternately in the straight- and in the shear-approach modes. (●) First approach at a contact point. (■) Second entry at a contact point. (▲) Third entry at a contact point. (▼) Fourth entry at a contact point.

and, in particular, they would onset at a much shorter range. Likewise, as the surfaces come into adhesive contact, correlation between opposing charges—as on the straight approach—would lead to larger adhesion energies than with the shear-approach in which such correlation is absent. Several typical surface interaction profiles using these two modes are shown in Fig. 27.2, for surfactant-coated surfaces that had been immersed in water for extended periods. As clearly seen (and suggested also by earlier preliminary measurements [19]), there is no systematic difference within the experimental scatter at a given contact point between force profiles measured in the straight approach mode (as used in all earlier studies), and those measured in the shear-approach mode

designed to frustrate any formation of a correlated (positive-faces-negative) charge distribution: Both show the characteristic long-ranged attraction reported earlier [14–18]. Likewise, as shown in Fig. 27.3, there is no systematic difference in the measured adhesion energy—as determined from the pull-off force—between the two modes of approach. We conclude, unambiguously, that the suppression of correlations does not result in the disappearance of the long-ranged attraction between the surfaces bearing randomly distributed charge domains. If, therefore, correlation is not the reason, what then is the origin of this attraction, which at its onset is a 100-fold larger than can be accounted for by dispersion forces alone?

We attribute the attraction to the asymmetry in the forces between equally and between oppositely charged surfaces across water (or other ion-containing liquids, see Methods). This is a counter-intuitive observation that has not earlier been remarked on. The interaction between two uniformly charged surfaces is well described by the Poisson–Boltzmann (PB) equation, which for a 1:1 electrolyte (in the effectively one-dimensional configuration of our experiment) is given by [2–4]:

$$\frac{d^2\psi(x)}{dx^2} = \frac{2c_0 e}{\varepsilon\varepsilon_0} \cdot \sinh\left[\frac{e\psi(x)}{kT}\right] \tag{27.1}$$

where $\psi(x)$ is the potential at distance x from the surface, c_0 is the concentration of ions in the bulk solution, ε_0 is the permittivity of free space, ε is the dielectric constant, k_B the Boltzmann constant, T the absolute temperature, and e the electronic charge. This mean-field model, originally developed for the symmetric case of surfaces with a uniform, equal surface charge density, has been extensively validated experimentally and has been extended in several directions [24–29]. The pressure between two approaching surfaces can be calculated by integration of the PB equation [30], yielding the net pressure Π after the subtraction of the bulk osmotic pressure:

$$\Pi = c_0 kT\left(e^{\frac{-e\psi}{kT}} + e^{\frac{e\psi}{kT}} - 2\right) - \frac{\varepsilon\varepsilon_0}{2} \cdot \left(\frac{d\psi}{dx}\right)^2 \tag{27.2}$$

The first term corresponds to the net osmotic pressure in the gap (repulsive except when the potential vanishes) while the second

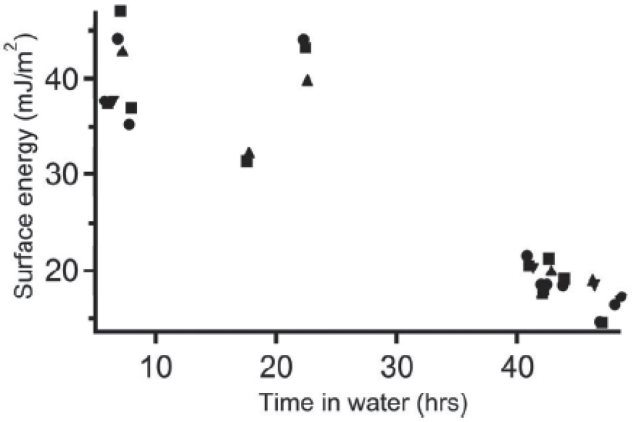

Figure 27.3 Surfaces with random charge domains. Normalized force vs. distance profiles [$F_n(D)/R$ between surfaces with random charge domains, in the Derjaguin approximation, where R is the surface radius of curvature] between random charge domain-coated surfaces (arising as in Fig. 27.1B) on mica, carried out both in the straight-approach mode (blue profiles) and in the shear-approach mode (red profiles). Surfaces were immersed for 40 h and 43 h in water, and force profiles from two independent contact points are shown (typical of many others); the upper insets show the profiles on a magnified scale, wherein the broken curves are the van der Waals interaction alone (Hamaker constant as below). Consecutive force profiles alternating between shear-approach (red) and straight-approach (blue) were carried out at each of the contact points. Amplitudes of shearing during "shear approach" were ca. 600 nm or more with frequencies up to 4 Hz resulting in shear velocities of 3.8–5.1 m/s. First approach in both contact points was carried out using "straight approach" (inset A), followed by a "shear approach" (inset B). A control profile between two bare mica surfaces (prior to coating with C_{18}TAB) across water is shown (■) and fitted to the solution of Eq. 27.2 together with the vdW interaction (with Hamaker constant $A = 2 \times 10^{-20}$ J) under limits of constant potential and constant charge boundary conditions (lower and upper grey curves, respectively). The corresponding parameters are surface potential $\psi_0 = -117$ mV, Debye length $\lambda_D = 75$ nm, surface charge density $\sigma = e/70$ nm^2. The data points, intermediate between the two curves, suggest boundary conditions somewhere between these limits.

term corresponds to the Maxwell stress, which is always attractive. The equilibrium pressure between two similarly charged surfaces can be obtained by considering Eq. (27.2) at the midplane of the inter-surface gap wherein the gradient of potential is equal to zero; thus, the only contribution to the pressure is the osmotic term. However, for two oppositely charged surfaces, the Maxwell stress never vanishes at finite separations. This result implies that two oppositely charged surfaces across water may attract more than two similarly charged ones will repel, for the same interacting areas, absolute surface charge densities and separations. Physically, this arises because of the qualitatively different mechanisms of repulsion and attraction across water between equally charged and oppositely charged surfaces, respectively. The former may be viewed as due to the osmotic pressure of trapped counterions at the midplane, whereas the latter may be seen as arising from the entropy gain upon release of counterion pairs from within the gap between the approaching surfaces [31].

To demonstrate that substantial long-ranged attraction between heterogeneous surfaces may be expected on the basis of PB even without any correlation of opposing charges, we use a simple heuristic model, illustrated in the inset to Fig. 27.4, based on the following assumptions: randomly distributed charged domains on each surface; equal magnitude of charge density $|\sigma|$ on oppositely charged domains; a similar total area of the negatively and positively charged domains, for overall neutrality of each surface (a reasonable assumption for our system, see Fig. 27.1); and, in particular, domains that are substantially larger than the surface separation, enabling the neglect of domain edge effects and allowing us to treat the interactions as between flat uniform charge domains for which the PB equation applies. Under these assumptions, the average interactions per unit area become simply 25% (+ vs. +, like/like, repulsive), 25% (– vs. –, like/like, repulsive), and 50% (– vs. +, like/unlike, attractive), as indicated schematically in the cartoon inset Fig 27.4. The dominant electrostatic interactions are then symmetric repulsive (+ vs. + and – vs. – with resulting pressures $\Pi_{+/+}$), or antisymmetric attractive (+ vs. –; $\Pi_{+/-}$): It may readily be shown analytically (Methods) that, in the conditions of

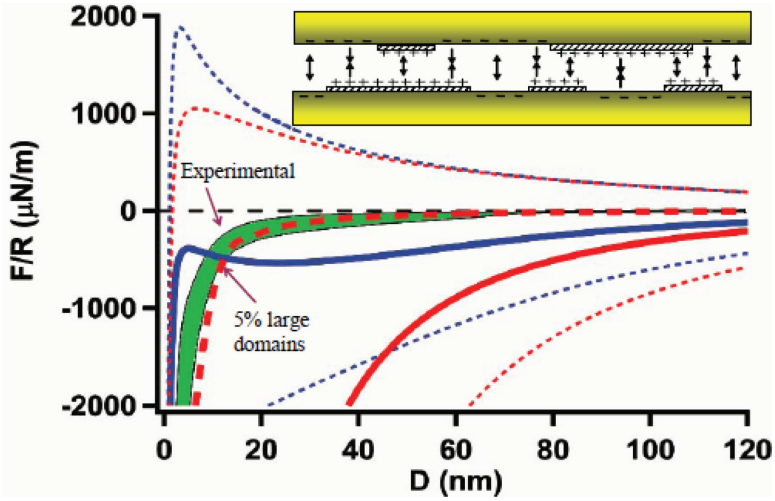

Figure 27.4 Numerical solutions for the interaction between two surfaces with uniform and with random charge domains. Results are based on the PB equation (27.1) combined with *vdW* attraction, under constant charge (blue curves) and under constant potential (red curves) boundary conditions. The upper (repulsive) broken curves show the interaction between two equally charged surfaces (symmetric interaction). The lower (attractive) broken curves show the interaction between two oppositely charged surfaces (antisymmetric interaction). The thicker smooth curves represent half the sum of both interactions (i.e., symmetric interaction/2 + antisymmetric interaction/2), which corresponds to that expected from our model of random charge domains described in the text. The green shaded region corresponds to the range of experimental attractions in Fig. 27.2. The inset cartoon illustrates the model, wherein outward pointing arrows indicate like–like repulsion, and inward pointing ones are like–unlike attraction. The calculations were carried out for surface charge density of $|\sigma_+| = |\sigma_-| = 1/70$ nm^2 (constant charge) or for $\psi_0 = -117$ mV (constant potential), with Debye length $\lambda_D = 75$ nm and Hamaker constant $A = 2 \times 10^{-20}$ J for the van der Waals attraction. The thick broken red curve corresponds to the net interaction, where only 5% of the domains contribute to the interaction, as suggested from the relative areas of the large domains in Fig. 27.1 (calculated with constant potential BC).

our experiments, $\Pi_{+/-} > \Pi_{+/+}$; the detailed behavior requires numerical solution of the PB model.

This is shown in Fig. 27.4, where the force vs. distance profile in our model (inset) is plotted from numerical solutions of the PB equation, under either constant charge or constant potential boundary conditions (BCs), incorporating also *vdW* attraction, using parameters typical for mica in water with no added salt, as for our experiments (Fig. 27.2). Also plotted (green band) is the spread of experimental profiles from Fig. 27.2. We see clearly that our model—in which there is no charge correlation and repulsive and attractive interactions cover equal areas—does indeed predict a net long-ranged attraction in the absence of any charge correlation (red and blue solid curves), though its range and magnitude are larger than our measured attractions (see below). We note that at small separations, it is constant potential rather than constant charge BCs that apply (Methods), implying a monotonic attraction (red curve)—as observed experimentally—rather than the nonmonotonic interaction (blue curve).

Our PB-based treatment, although transparent and qualitatively demonstrating the long-ranged attraction, contains a number of assumptions: We ignore the effect of domain edges (which assumes that all domains are much larger than the surface separation); and we assume that $\sigma_+ = |\sigma|$, and that the overall area of negative and positive charge patches is the same (Fig. 27.1 indicates this is a reasonable assumption), so that each surface is overall neutral. However, the most significant factor responsible for the weaker measured attraction (green band in Fig. 27.4) relative to the prediction of our model (thick solid red curve in Fig. 27.4) is the fact that, as clearly seen in Fig. 27.1, many of the charge patches are quite small, indeed smaller than the surface separation over much of the range D less than 50 nm. Such patches, equivalent to quenched disorder of small charge domains, have—as noted in the Introduction—been shown to result in little interaction at the PB level [11]. Thus, the effective area of the charge domains contributing to the attraction (those larger than ca. 150 nm say) is much smaller than the full coverage assumed in Fig. 27.4 (solid red and blue curves), which explains qualitatively the much smaller measured attraction than the calculated one. When this is taken into

account from the relative area of large domains, Fig. 27.1, we find a far closer fit to the data (thick broken red curve in Fig. 27.4). The essential point evident from Fig. 27.4, however, is that there is no need for correlation of opposing charges to explain the strong attraction between randomly charged surfaces that we (and many others [14–18] earlier) have observed: it can be readily accounted for using the well-tested PB model.

It is instructive to calculate the behavior predicted by our model also under conditions of different salt concentrations c_0 (corresponding to different Debye screening lengths λ_D) and different surface charge densities. The resulting profiles are shown in Fig. 27.5, for BCs) both of constant charge and of constant surface potential ψ_0. The most notable feature is that the range of the net attraction is closely comparable to the Debye screening lengths, that is, at higher salt concentration, the attractions are weaker and shorter ranged. The nonmonotonic form of the interaction for constant charge BC arises from the fact that repulsion due to counterion trapping between like-charged surfaces rises sharply at small separations D, whereas the attraction due to counterion release between oppositely charged surfaces saturates at small D.

Our findings may also account for the long-ranged attractions observed in very many studies between surfaces hydrophobised by physically attached surfactant layers, which were previously attributed to "hydrophobic interactions" (these experiments are reviewed in ref. [22]). It has long been pointed out [32] that such long-ranged attractions are strongly correlated with high mobility of the surfactant molecules: this in turn implies that the corresponding surfactant layers are able to rearrange in a facile manner. This correlation of long-ranged attraction with ease of surfactant-layer rearrangement makes it very conceivable that, under water, such layers undergo a thermodynamically driven rearrangement to form random positive and negative charge patches similar to those observed in our study (Fig. 27.1), and in earlier work. Taken together with our present findings that such random charge domains lead to long-ranged attraction even in the absence of any charge correlation (in contrast to earlier suggestions [10, 14–18], which all involved correlations), such a break-up would readily account for these long-ranged attractions earlier attributed to "hydrophobic effects." This

is further supported by the observation—as seen in Fig. 27.4—that a rather small coverage of the surface by larger charge domains may be sufficient to result in the observed attractions. Moreover, the puzzling long-range attractions earlier observed between surfaces bearing nucleic acid residues [33, 34], attached to a physisorbed surfactant coating the substrate, may also be accounted for by a small extent of charge domain formation arising from the rearrangement of the underlying surfactant layer. In other words, our results suggest that it is not the "hydrophobic effect" that is responsible for the long-ranged [ca. 20 nm − O(100 nm)] attraction noted between surfactant-coated surfaces, but, rather, a random, uncorrelated charge-patch formation arising from thermodynamically driven surfactant rearrangements as discussed above. Moreover, the earlier suggestions [35–37] that such "hydrophobic" interactions have an electrostatic origin, due to their dependence on salt concentration, are indeed borne out—see Fig. 27.5—and may now be understood in terms of the explicit mechanism that we described, which arises from the symmetry breaking between like–like and like–unlike charge domain interactions across water.

In summary, we have found that long-ranged attractions between surfaces bearing random charge domains across water persist unchanged under conditions designed to frustrate correlated motion of charges as the surfaces approach. This shows directly that these attractions are not the result of correlations between oppositely charged domains, that is, positive facing negative, developing on approach, as first proposed many years ago [10, 14–18]. It is shown rather that such attractions may arise as the consequence of classically understood electrostatic double-layer interactions (via the PB equation) between large, random, uncorrelated charge domains on the opposing surfaces, once the counterintuitive like–like vs. like–unlike interaction asymmetry is recognized. Our results immediately explain the recently observed, long-ranged attractions between surfaces made hydrophobic by surfactant monolayers that subsequently rearrange into positive and negative charged domains [14–18, 20, 21], with no need to invoke charge correlations. We believe that they may account also for the many earlier long-ranged interactions measured between surfactant-coated surfaces and attributed to the "hydrophobic interaction" [22]. More generally,

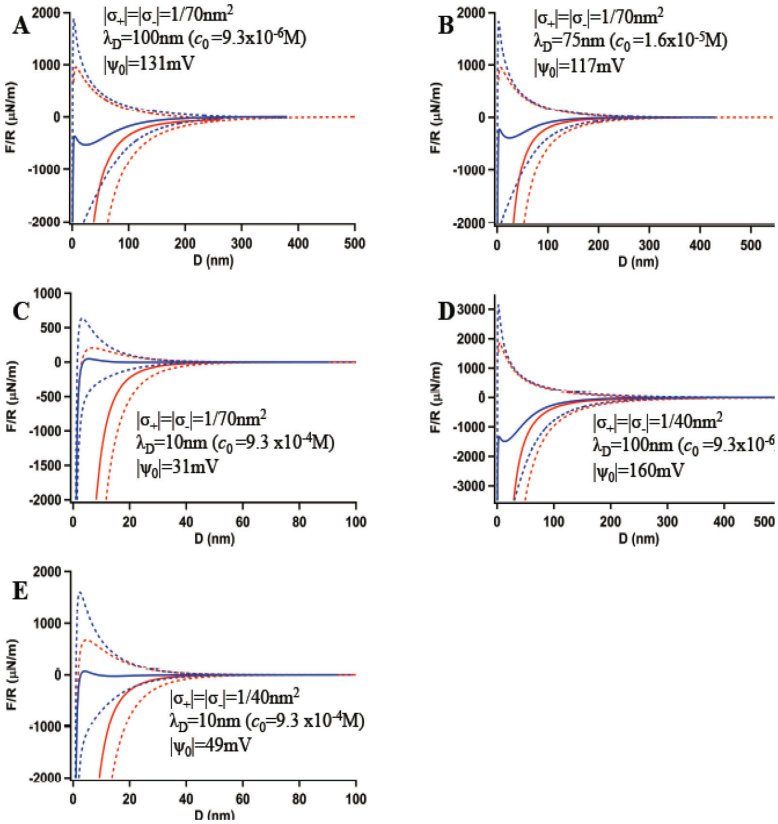

Figure 27.5 Numeric solutions for the interaction between two charged surfaces (Eq. 27.2) based on the PB equation, combined with *vdW* attraction (with Hammaker constant $A = 2 \times 10^{-20}$ J), under constant charge (blue) and constant potential (red) boundary condition at different salt concentrations c_0 (and corresponding Debye lengths λ_D) and surface potentials $|\psi_0|$. In each panel, the upper broken lines are the repulsions between two equally charged surfaces (symmetric interaction). The lower broken lines are the attraction between two oppositely charged surfaces (antisymmetric interaction). The smooth lines represent half the sum of both interactions (i.e., symmetric interaction/2 + antisymmetric interaction/2), corresponding to our model of random charge domains.

our findings shed new light on the stability of hydrocolloids and on interactions between heterogeneously charged surfaces, which are ubiquitous in biological systems.

27.3 Materials and Methods

27.3.1 *Surfactant Coating*

Monolayers of the polar surfactant octadecyltrimethylammonium bromide ($CH_3(CH_2)_{17}N^+(CH_3)_3Br^-$, Sigma–Aldrich purity 98%+, used as received) were deposited on mica surfaces by self-assembly from aqueous solution at concentration 6–8 fold higher than the critical micelle concentration, at 70 $\pm$ 5°C, well above the Krafft temperature for this system. The freshly cleaved molecularly smooth mica sheets were dipped for 30 s in the solution and then rinsed in heated pure water. All water was purifed (Barnsted NanoPure, resistivity 18.2 MMΩ/cm, nominal total organic content $<$1 ppb). Layers were characterized by atomic force microscopy (AFM, Asylum MFP 3-D), contact angle goniometry (FTA200 goniometer), and SFB measurements as described below. Following break-up of the monolayer on immersion in water, the overall area of the bilayers and their stability with time suggests little loss of the surfactant to solution.

27.3.2 *Surface Force Balance Measurements*

The SFB enables the measurement of forces between two molecularly smooth mica surfaces (coated if appropriate, as in the present study) to be measured directly with angstrom-level resolution in the surface separation, and has been described in detail previously [38]. In particular, it enables both normal motion between the surfaces and controlled lateral motion between them, as the upper surface is moved parallel to the lower one via a sectored piezocrystal, as for the shear-approach mode described above. Force [$F(D)$] versus surface-separation (D) profiles were generated both manually, via a step-wise approach, and dynamically, where surfaces are made to approach at velocity v_n. The variation with time t of surface

separation $D(t)$ is determined via fast video recording, frame grabbing, and analysis of the optical interference fringes of equal chromatic order. The corresponding force $F(D)$ is then evaluated using the instantaneous balance of forces through the Newtonian relation [39]:

$$F(D) = m\ddot{D} - K_{\mathrm{n}}\delta D(t) + \frac{6\pi\eta R^2\dot{D}}{D(t)} \tag{27.3}$$

where m is the total mass of the lower surfaces attached to the spring, K_{n} is the spring constant: 200N/m , η is the dynamic viscosity of water, and R is the mean radius of curvature of the surfaces. The time derivative of the data, $\dot{D}$, at large separation is constant and equal to the approach velocity, v_{n}, of the surface due to the applied approach motion (ranging from 4 nm/s to 20 nm/s in different runs). Any deviation from this slope is due to the deflection $\delta D(t)$of the spring connected to the lower lens, $\delta D(t) = D_{t=0} - D(t) + v_{\mathrm{n}}t$. The last term in the equation for $F(D)$ is the hydrodynamic force given by the Taylor equation under the assumption of no slip BC.

27.3.3 *Electrostatic Double-Layer Interactions*

Analytical solutions of Eq. (27.2) for equally and for oppositely charged surfaces may be obtained for certain regimes determined by the relation between the length scales in the PB model [30, 40], the so-called Gouy–Chapman length b and the Debye screening length λ_{D}. These are given by $b = \frac{1}{2\pi l_{\mathrm{B}}\sigma}$ and $\lambda_{\mathrm{D}} = \sqrt{\frac{\varepsilon\varepsilon_0 k_{\mathrm{B}}T}{2c_0e^2}}$, where l_{b} is the Bjerrum length, defined as the separation between elementary charges at which the electrostatic interaction equal to the thermal energy: $l_{\mathrm{b}} = \frac{e^2}{4\pi\varepsilon\varepsilon_0 kT}$[= 7 Å for water at 300 K), which yields $b =$ 160Å (evaluated at $\sigma = (e/70\ \mathrm{nm}^2)$, a typical value for mica]. λ_{D} in purified water with no added salt can range from about 50 nm up to about 1 μm (depending on the amount of dissolved carbon dioxide and ions leaching from the glassware in the water). The Gouy–Chapman regime [30, 40], which is when $\lambda_{\mathrm{D}} \gg D$ and $b \ll D$, is most relevant for our experiments in water with no added salt in which the long-ranged attractions are observed experimentally. The expressions for the pressure between the surfaces in this regime are [30] $\Pi_{+/+} \cong \frac{\pi}{2l_{\mathrm{B}}D^2}$ and [40] $\Pi_{+/-} \cong -\frac{2}{\pi l_{\mathrm{B}}D^2}\ln^2(\frac{D}{8\lambda_{\mathrm{D}}})$, giving the ratio

Ra between the repulsive and attractive interactions in this regime as $\left|\frac{\Pi_{+/-}}{\Pi_{+/+}}\right| = Ra \cong \frac{4}{\pi^2}\ln^2\left(\frac{D}{8\lambda_D}\right)$.

Ra > 1 throughout the Gouy–Chapman range, increasing significantly for $D < \lambda_D/2$. This implies that in this regime—corresponding to our experiments in no added salt water—the attraction will dominate the repulsion (the terms defining Ra were derived under constant charge BCs), but as seen in the numerical simulations, the ratio of attractive to repulsive pressure is even higher when constant potential BC are used.

Acknowledgments

We thank Dan Ben-Yaakov, Yael Dror, Susan Perkin and NirKampf, our co-authors on Ref [1], for their help. We thank Sam Safranand Rudolf Podgornick for useful discussions. Support from the Israel Science Foundation, from the European Research Council and from the Minerva Foundation is acknowledged with thanks.

References

1. Silbert, G., *et al*., Long-ranged attraction between heterogeneous surfaces, *Physical Review Letters*, 2012, **109**(16), p. 168305.
2. Lyklema, J., *Fundamentals of Interface and Colloid Science*, 1991, Amsterdam: Elsevier.
3. Derjaguin, B. V., N. V. Churaev, and V. M. Muller, *Surface Forces*, 1987, New York: Plenum Publishing Corporation.
4. Israelachvili, J. N., *Intermolecular and surface forces*, 2nd ed, 1992, London: Academic Press Limited.
5. Parsegian, V. A. and D. Gingell, Electrostatic interaction across a salt solution between 2 bodies bearing unequal charges, *Biophysical Journal*, 1972, **12**(9), p. 1192.
6. Pashley, R. M., DLVO and hydration forces between mica surfaces in Li+, Na+, K+, and Cs+ electrolyte solutions: A correlation of double-layer and hydration forces with surface cation exchange properties, *Journal of Colloid and Interface Science*, 1981, **83**(2), pp. 531–546.

7. Raviv, U., P. Laurat, and J. Klein, Time dependence of forces between mica surfaces in water and its relation to the release of surface ions, *Journal of Chemical Physics*, 2002, **116**(12), pp. 5167–5172.
8. Brewster, R., P. A. Pincus, and S. A. Safran, Self assembly modulated by interactions of two heterogeneously charged surfaces. *Physical Review Letters*, 2008, **101**(12), p. 128101.
9. Evans, D. F. and H. Wennerström, *The colloidal domain*, 2nd ed., 1999, New York: Wiley.
10. Miklavic, S. J., *et al.*, Double-layer forces between heterogeneous charged surfaces, *Journal of Physical Chemistry*, 1994, **98**(36), pp. 9022–9032.
11. Naji, A. and R. Podgornik, Quenched charge disorder and Coulomb interactions, *Physical Review E*, 2005. **72**(4), p. 041402.
12. Tsao, Y. H., D. F. Evans, and H. Wennerstrom, Long-range attractive force between hydrophobic surfaces observed by atomic force microscopy. *Science*, 1993, **262**(5133), pp. 547–550.
13. Mamasakhlisov, Y. S., A. Naji, and R. Podgornik, Partially annealed disorder and collapse of like-charged macroions. *Journal of Statistical Physics*, 2008, **133**(4), pp. 659–681.
14. Meyer, E. E., *et al.*, Origin of the long-range attraction between surfactant-coated surfaces. Proceedings of the National Academy of Sciences of the United States of America, 2005, **102**(19), pp. 6839–6842.
15. Meyer, E. E., K. J. Rosenberg, and J. Israelachvili, Recent progress in understanding hydrophobic interactions. Proceedings of the National Academy of Sciences of the United States of America, 2006, **103**(43), pp. 15739–15746.
16. Perkin, S., N. Kampf, and J. Klein, Stability of self-assembled hydrophobic surfactant layers in water. *Journal of Physical Chemistry B*, 2005, **109**(9), pp. 3832–3837.
17. Perkin, S., N. Kampf, and J. Klein, Long-range attraction between charge-mosaic surfaces across water. *Physical Review Letters*, 2006, **96**(3), p. 038301.
18. Zhang, J., *et al.*, Effects of degassing and ionic strength on AFM force measurements in octadecyltrimethylammonium chloride solutions, *Langmuir*, 2005, **21**(13), pp. 5831–5841.
19. Silbert, G., J. Klein, and S. Perkin, The effect of counterions on surfactant-hydrophobized surfaces. *Faraday Discussions*, 2010, **146**, pp. 309–324.
20. Ball, P., Water as an active constituent in cell biology, *Chemical Reviews*, 2008, **108**(1), pp. 74–108.

21. Hammer, M. U., *et al.*, The search for the hydrophobic force law. *Faraday Discussions*, 2010, **146**, pp. 299–308.
22. Christenson, H. K. and P. M. Claesson, Direct measurements of the force between hydrophobic surfaces in water, *Advances in Colloid and Interface Science*, 2001, **91**(3), pp. 391–436.
23. Perkin, S., *et al.*, Forces between mica surfaces, prepared in different ways, across aqueous and nonaqueous liquids confined to molecularly thin films, *Langmuir*, 2006, **22**(14), pp. 6142–6152.
24. Ben-Yaakov, D., *et al.*, Beyond standard Poisson-Boltzmann theory: ion-specific interactions in aqueous solutions. *Journal of Physics: Condensed Matter*, 2009, **21**(42), p. 424106.
25. Gregory, J., Interaction of unequal double layers at constant charge. *Journal of Colloid and Interface Science*, 1975, **51**(1), pp. 44–51.
26. Ninham, B. W. and V. Yaminsky, Ion binding and ion specificity: the Hofmeister effect and Onsager and Lifshitz theories, *Langmuir*, 1997, **13**(7), pp. 2097–2108.
27. Onsager, L. and N. T. N. Samaras, The surface tension of Debye-Hückel electrolytes. *J. Chem. Phys.*, 1934, **2**(8), pp. 528–536.
28. Kjellander, R. and S. Marcelja, Inhomogeneous Coulomb fluids with image interactions between planar surfaces. I. *J. Chem. Phys.*, 1985, **82**(4), pp. 2122–2135.
29. Ruckenstein, E. and D. Schiby, Effect of the excluded volume of the hydrated ions on double-layer forces, *Langmuir*, 1985, **1**(5), pp. 612–615.
30. Andelman, D., Introduction to electrostatics in soft and biological matter, in *Handbook of Physics of Biological Systems*, R. S. E. Lipowsky, Editor, 1995, Amsterdam: Elsevier Science.
31. Safran, S. A., Scaling relations for counterion release and attraction of oppositely charged surfaces, *Europhysics Letters*, 2005, **69**(5), pp. 826–831.
32. Christenson, H. K. and V. V. Yaminsky, Is the long-range hydrophobic attraction related to the mobility of hydrophobic surface groups? *Colloids and Surfaces a-Physicochemical and Engineering Aspects*, 1997, **130**, pp. 67–74.
33. Berndt, P., K. Kurihara, and T. Kunitake, Measurement of forces between surfaces composed of two-dimensionally organized, complementary and noncomplementary nucleobases, *Langmuir*, 1995, **11**(8), pp. 3083–3091.

34. Pincet, F., *et al.*, Long-range attraction between nucleosides with short-range specificity: Direct measurements, *Physical Review Letters*, 1994, **73**(20), pp. 2780–2783.
35. Christenson, H. K., *et al.*, *Forces between fluorocarbon surfactant monolayers: salt effects on the hydrophobic interaction.* The Journal of Physical Chemistry, 1989, **93**(4), pp. 1472–1478.
36. Christenson, H. K., P. M. Claesson, and J. L. Parker, Hydrophobic attraction: A reexamination of electrolyte effects. *The Journal of Physical Chemistry*, 1992, **96**(16), pp. 6725–6728.
37. Kekicheff, P. and O. Spalla, Long-range electrostatic attraction between similar, charge-neutral walls. *Physical Review Letters*, 1995, **75**(9), pp. 1851–1854.
38. Klein, J. and E. Kumacheva, Simple liquids confined to molecularly thin layers. I. Confinement-induced liquid-to-solid phase transitions. *Journal of Chemical Physics*, 1998, **108**(16), pp. 6996–7009.
39. Kampf, N., *et al.*, Direct measurement of sub-Debye-length attraction between oppositely charged surfaces, *Physical Review Letters*, 2009, **103**(11), p. 118304.
40. Ben-Yaakov, D., *et al.*, Electrostatic interactions of asymmetrically charged membranes. *Europhysics Letters*, 2007, **79**(4), p. 48002.